

Dissertation zur Erlangung des Doktorgrades
der Fakultät für Chemie und Pharmazie
der Ludwig-Maximilians-Universität München

Photoswitchable lipids:

targeting the membrane with photopharmacology

James Allen Frank

aus

Edmonton, Kanada

2017

Erklärung

Diese Dissertation wurde im Sinne von § 7 der Promotionsordnung vom 28. November 2011 von Herrn Prof. Dr. Dirk Trauner betreut.

Eidesstattliche Versicherung

Diese Dissertation wurde eigenständig und ohne unerlaubte Hilfe erarbeitet.

München, den 01. März 2017.

James A. Frank

Dissertation eingereicht am:	15.12.2016
1. Gutachter:	Prof. Dr. Dirk Trauner
2. Gutachter:	Prof. Dr. Thomas Carell
Mündliche Prüfung am:	26.1.2017

This work is dedicated to my friend Camille Gregory B.Sc. (1989-2012). Her love for chemistry and adventure has driven me to explore science in Europe, and her strength and optimism through difficult times has kept me going through many of the rough days. SatNam.

Acknowledgements

“Society does not consist of individuals but expresses the sum of interrelations, the relations within which these individuals stand.” – Karl Marx

I am mostly grateful to my parents, Jill and Martin Frank, and my brother Sean Frank for continuous support throughout my degree and beyond. Without this pillar to stand on, none of this work would have been possible. I acknowledge my supervisor and mentor Prof. Dr. Dirk Trauner for providing an incredible working environment where anything seemed possible. Not only did he provide unmatched financial, inspirational and intellectual support, he was instrumental in providing the connections which we needed to push the work and my career to the next level.

I gratefully acknowledge the contributions and support of my collaborators, both in the Trauner lab (Dr. Martin Sumser, Dr. Johannes Broichhagen, David Konrad, Benjamin Williams, Dr. Matthias Scönberger, Philipp Leippe, Dr. Arunas Damijonaitis, Dr. Henry Toombs-Ruane, Johannes Morstein and Nina Vrieling) and elsewhere (Prof. Dr. Gary Lewin, Dr. Mirko Moroni, Dr. Rabih Moshourab, Prof. Dr. Carsten Schultz, Dr. Dmytro Yuschenko, Dr. David Hodson, Prof. Dr. Petra Schwille, Dr. Henri Franquelim). I am grateful to the students who worked with me and contributed to the work described in this dissertation (Simone Wouters, Felix Metzner, Margherita Duca, Nadja Klipfel, and Sarah Schiffers), whose drive and attentiveness permitted the rapid progression of our work. Finally, I must acknowledge the so-far-not-mentioned colleagues from Clown College (AK Trauner) who made my stay in Germany a pleasant one (Daniel Terwilliger, Klaus Speck, Dr. Cedric Hugelshofer, Katharina Hüll, Antonio Rizzo, Giulio Volpin and Bichu Cheng). I would also like to thank Johannes Morstein and Philipp Leippe for proof-reading this dissertation. Finally, I am very grateful to the technical staff of AK Trauner (Heike Traub, Aleksandra Grilc, Luis de la Osa de la Rosa, and Mariia Palchyk). Due to the contributions of all the above-mentioned individuals, this work was made possible. Thank you!

“How long will this last, this delicious feeling of being alive, of having penetrated the veil which hides beauty and the wonders of celestial vistas? It doesn't matter, as there can be nothing but gratitude for even a glimpse of what exists for those who can become open to it.”

- **Alexander T. Shulgin**

Sections of this work has been published in peer-reviewed journals:

1. Photoswitchable fatty acids enable optical control of TRPV1, **Frank, J.A.**; Moroni, M.; Moshourab, R.; Sumser M.; Lewin, G.R.; Trauner, D.* *Nature Commun.* **2015**, *6*, 7118.
2. Synthesis of redshifted azobenzene photoswitches by late-stage functionalization, Konrad, D.B.; **Frank, J.A.**; Trauner, D.* *Chem. Eur. J.* **2016**, *22*, 4364.
3. Photoswitchable diacylglycerols enable optical control of protein kinase C, **Frank, J.A.**; Yushchenko, D.A.; Hodson, D.J.; Lipstein, N.; Nagpal, J.; Rutter, G.A.; Rhee, J.S.; Gottschalk, A.; Brose, N.; Schultz, C.*; Trauner, D.* *Nature Chem. Biol.* **2016**, *12*, 755.
4. Optical control of lipid rafts with photoswitchable ceramides, **Frank, J.A.**; Franquelim, H.G.; Schwille, P.*; Trauner, D.* *J. Am. Chem. Soc.* **2016**, *138*, 12981.

Further publications in peer-reviewed journals include:

1. Optical control of insulin release using a photoswitchable sulfonylurea, Broichhagen, J.; Schönberger, M.; Cork, S.; **Frank, J.A.**; Marchetti, P.; Bugliani, M.; Shapiro, A.M.J.; Trapp, S.; Rutter, G.A.; Hodson, D.J.; Trauner, D.* *Nature Commun.* **2014**, *5*, 5116.
2. A red-shifted photochromic sulfonylurea for the remote control of pancreatic beta cell function, Broichhagen, J.; **Frank, J.A.**; Johnston, N. R.; Mitchell, K.; Smid, K.; Marchetti, P.; Bugliani, M.; Rutter, G. A.; Trauner. D.*; Hodson, D.* *Chem. Commun.* **2015**, *51*, 6018.
3. A roadmap to success in photopharmacology, Broichhagen, J.; **Frank, J.A.**; Trauner, D.* *Acc. Chem. Res.* **2015**, *48*, 1947.

Table of contents

1 – Abstract	1
2 – Introduction to photolipids	2
3 – Project affiliation disclosure	9
4 – Photoswitchable fatty acids enable optical control of TRPV1	12
4.1 – Introduction	12
4.2 – Results.....	13
4.2.1 – Photolipid synthesis.....	13
4.2.2 – Optical control over TRPV1 in HEK293T cells	17
4.2.3 – Capsazepine antagonizes AzCA-4 activity	21
4.2.4 – AzCA-4 enables precision control of TRPV1 at varied stimulation wavelengths.....	22
4.2.5 – AzCA-4 permits optical control over cultured DRG neurons.....	24
4.2.6 – AzCA-4 is selective for TRPV1 sensitive neurons in the DRG	27
4.2.7 – Optical control of C-fiber nociceptors.....	28
4.2.8 – Serotonin and bradykinin sensitize DRG neurons to AzCA-4.....	30
4.2.9 – AzCA-4 is compatible with genetic tools	32
4.2.10 – QX-314 can be selectively transported into DRG neurons	32
4.2.11 – Synthesis and characterization of a red-shifted AzCA derivative	34
4.2.12 – Red-shifted optical control of TRPV1 with tetra- <i>ortho</i> chlorinated azobenzenes	35
4.3 – Discussion	37
4.4 – Supporting information.....	40
4.4.1 – Whole-cell electrophysiology in HEK293T cells	40
4.4.2 – Determination of AzCA photoswitching properties	41
4.4.3 – Dorsal root ganglion neuronal culture	41
4.4.4 – Whole-cell electrophysiology in cultured DRG neurons	42
4.4.5 – Intracellular Ca ²⁺ imaging.....	42
4.4.6 – Ex vivo skin nerve preparation.....	43
4.4.7 – Compound switching	44
4.4.8 – Compound synthesis and characterization	45
4.4.8.1 – 4-((4-Heptylphenyl)diazenyl)benzoic acid (FAAzo-1)	49
4.4.8.2 – <i>N</i> -(4-Hydroxy-3-methoxybenzyl)-4-((4-heptylphenyl)diazenyl)benzamide (AzCA-1).....	52

4.4.8.3 – 2-(4-((4-Hexylphenyl)diazenyl)phenyl)acetic acid (FAAzo-2)	54
4.4.8.4 – <i>N</i> -(4-Hydroxy-3-methoxybenzyl)-2-(4-((4-hexylphenyl)diazenyl)phenyl).....	56
acetamide (AzCA-2)	56
4.4.8.5 – 3-(4-((4-Pentylphenyl)diazenyl)phenyl)propanoic acid (FAAzo-3)	58
4.4.8.6 – <i>N</i> -(4-Hydroxy-3-methoxybenzyl)-3-(4-((4-pentylphenyl)diazenyl)phenyl) ...	60
propanamide (AzCA-3)	60
4.4.8.7 – 4-(4-((4-Butylphenyl)diazenyl)phenyl)butanoic acid (FAAzo-4)	62
4.4.8.8 – <i>N</i> -(4-Hydroxy-3-methoxybenzyl)-4-(4-((4-butylphenyl)diazenyl)phenyl)	64
butanamide (AzCA-4)	64
4.4.8.9 – Methyl pent-4-ynoate (1a)	66
4.4.8.10 – Methyl 5-(4-nitrophenyl)pent-4-ynoate (2a)	68
4.4.8.11 – Methyl 5-(4-aminophenyl)pentanoate (3a)	70
4.4.8.12 – Methyl 5-(4-((4-propylphenyl)diazenyl)phenyl)pentanoate (4a)	72
4.4.8.13 – 5-(4-((4-Propylphenyl)diazenyl)phenyl)pentanoic acid (FAAzo-5)	74
4.4.8.14 – <i>N</i> -(4-Hydroxy-3-methoxybenzyl)-5-(4-((4-propylphenyl)diazenyl)phenyl) .	76
pentanamide (AzCA-5)	76
4.4.8.15 – Methyl hex-5-ynoate (1b)	78
4.4.8.16 – Methyl 6-(4-nitrophenyl)hex-5-ynoate (2b)	80
4.4.8.17 – Methyl 6-(4-aminophenyl)hexanoate (3b).....	82
4.4.8.18 – Methyl 6-(4-((4-ethylphenyl)diazenyl)phenyl)hexanoate (4b).....	84
4.4.8.19 – 6-(4-((4-Ethylphenyl)diazenyl)phenyl)hexanoic acid (FAAzo-6).....	86
4.4.8.20 – <i>N</i> -(4-Hydroxy-3-methoxybenzyl)-6-(4-((4-ethylphenyl)diazenyl)phenyl) ...	88
hexanamide (AzCA-6)	88
4.4.8.21 – Methyl hept-6-ynoate (1c)	90
4.4.8.22 – Methyl 7-(4-nitrophenyl)hept-6-ynoate (2c)	91
4.4.8.23 – Methyl 7-(4-aminophenyl)heptanoate (3c).....	93
4.4.8.24 – Methyl 7-(4-(<i>p</i> -tolylidiazanyl)phenyl)heptanoate (4c)	95
4.4.8.25 – 7-(4-(<i>p</i> -Tolylidiazanyl)phenyl)heptanoic acid (FAAzo-7).....	97
4.4.8.26 – <i>N</i> -(4-Hydroxy-3-methoxybenzyl)-7-(4-(<i>p</i> -tolylidiazanyl)phenyl)	99
heptanamide (AzCA-7)	99
4.4.8.27 – Oct-7-ynoic acid (1d)	101
4.4.8.28 – Methyl oct-7-ynoate (2d).....	103
4.4.8.29 – Methyl 8-(4-nitrophenyl)oct-7-ynoate (3d)	105
4.4.8.30 – Methyl 8-(4-aminophenyl)octanoate (4d)	107
4.4.8.31 – Methyl 8-(4-(phenyldiazanyl)phenyl)octanoate (5d)	109

4.4.8.32 – 8-(4-(Phenyldiazenyl)phenyl)octanoic acid (FAAzo-8).....	111
4.4.8.33 – <i>N</i> -(4-Hydroxy-3-methoxybenzyl)-8-(4-(phenyldiazenyl)phenyl).....	113
octanamide (AzCA-8)	113
5 – Photoswitchable diacylglycerols enable optical control of protein kinase C	115
5.1 – Introduction	115
5.2 – Results.....	116
5.2.1 – Design and synthesis of photoswitchable DAGs.....	116
5.2.2 – Optical control of C1 domain translocation	119
5.2.3 – PhoDAGs modulate intracellular Ca ²⁺ levels in HeLa cells	126
5.2.4 – Optical control of protein kinase C	127
5.2.5 – Optical control of [Ca ²⁺] _i oscillations in β-cells.....	130
5.2.6 – Optical control of insulin secretion in pancreatic islets	134
5.2.7 – Optical control of synaptic transmission.....	137
5.2.8 – Control of <i>Caenorhabditis elegans</i> synaptic transmission.....	142
5.3 – Discussion	143
5.4 – Supporting information.....	145
5.4.1 – List of utilized cDNA constructs	145
5.4.2 – Cell culture	146
5.4.3 – Culture of primary mouse pancreatic islets	147
5.4.4 – Laser scanning confocal microscopy	148
5.4.5 – Quantification of insulin secretion	148
5.4.6 – Whole-cell electrophysiology in MIN6 and dissociated β-cells	149
5.4.7 – Electrophysiology in mouse hippocampal neurons	150
5.4.8 – Aldicarb assay	151
5.4.9 – Compound synthesis and characterization	152
5.4.9.1 – <i>S</i> -2,3- <i>O</i> -Isopropylidene-1- <i>O</i> -stearoyl- <i>sn</i> -glycerol (6).....	152
5.4.9.2 – 1- <i>O</i> -Stearoyl-3- <i>O</i> -triethylsilyl- <i>sn</i> -glycerol (7)	155
5.4.9.3 – 2- <i>O</i> -(4-(4-((4-butylphenyl)diazenyl)phenyl)butanoyl)-1- <i>O</i> -stearoyl-3- <i>O</i> - triethylsilyl- <i>sn</i> -glycerol (8)	158
5.4.9.4 – 2- <i>O</i> -(4-(4-((4-Butylphenyl)diazenyl)phenyl)butanoyl)-1- <i>O</i> -stearoyl- <i>sn</i> - glycerol (PhoDAG-1, 1).....	161
5.4.9.5 – <i>S</i> -2,3- <i>O</i> -Isopropylidene-1- <i>O</i> -octanoyl- <i>sn</i> -glycerol (9)	164
5.4.9.6 – 1- <i>O</i> -Octanoyl-3- <i>O</i> -triethylsilyl- <i>sn</i> -glycerol (10)	166
5.4.9.7 – 2- <i>O</i> -(4-(4-((4-Butylphenyl)diazenyl)phenyl)butanoyl)-1- <i>O</i> -octanoyl-3- <i>O</i> - triethylsilyl- <i>sn</i> -glycerol (11)	168

5.4.9.8 – 2-O-(4-(4-((4-Butylphenyl)diazenyl)phenyl)butanoyl)-1-O-octanoyl- <i>sn</i> -glycerol (PhoDAG-2, 2)	171
5.4.9.9 – 4-(Phenyldiazenyl)phenyl butanoic acid (FAAzo-9, 4).....	173
5.4.9.10 – 2-O-(4-(4-(Phenyldiazenyl)phenyl)butanoyl)-1-O-octanoyl-3-O-triethylsilyl- <i>sn</i> -glycerol (12).....	175
5.4.9.11 – 2-O-(4-(4-(Phenyldiazenyl)phenyl)butanoyl)-1-O-octanoyl- <i>sn</i> -glycerol (PhoDAG-3, 3).....	178
6 – Synthesis of photoswitchable glycerophospholipids	180
6.1 – Introduction.....	180
6.2 – Results	181
6.2.1 – Synthesis and characterization of a photoswitchable phosphatidylcholine.....	181
6.2.2 – Design and synthesis of cell-permeable, photoswitchable PI(4,5)P ₂	183
6.3 – Discussion	185
6.4 – Supporting information.....	186
6.4.1 – Compound synthesis and characterization	186
6.4.1.1 – 2-O-(4-(4-((4-Butylphenyl)diazenyl)phenyl)butanoyl)-3-bis-(9 <i>H</i> -fluoren-9-ylmethyl)- <i>N,N</i> -diisopropylamidophosphite)-1-O-stearoyl- <i>sn</i> -glycerol (13) - (<i>P</i> -diastereomeric mixture)	186
6.4.1.2 – 2-O-(4-(4-((4-Butylphenyl)diazenyl)phenyl)butanoyl)-3-1-O-stearoyl- <i>sn</i> -glycero-3-phosphocholine (<i>azo</i> -PC)	190
6.4.1.3 – 2,3,6- <i>O,O,O</i> -Tris(butyryl)-4,5- <i>O,O</i> -bis(9 <i>H</i> -fluoren-9-ylmethyl)diphosphoryl-1- <i>O</i> -(9 <i>H</i> -fluoren-9-ylmethyl)-(2'- <i>O</i> -(4'-(4'-((4'-butylphenyl)diazenyl)phenyl)butanoyl)-1'- <i>O</i> -stearoyl- <i>sn</i> -glycero)phosphoryl- <i>myo</i> -inositol (14)	195
6.4.1.4 – 2,3,6- <i>O,O,O</i> -Tris-(butyryl)-4,5- <i>O,O</i> -bis(phosphoryl)-1- <i>O</i> -(2'- <i>O</i> -(4'-(4'-((4'-butylphenyl)diazenyl)phenyl)butanoyl)-1'- <i>O</i> -stearoyl- <i>sn</i> -glycero)phosphoryl- <i>myo</i> -inositol pentakis(acetoxymethyl) ester (<i>apo-azo</i> -PIP ₂) - (<i>P</i> -diastereomeric mixture).....	199
7 – Optical control of arachidonate signalling in pancreatic β-cells	204
7.1 – Introduction.....	204
7.2 – Results	206
7.2.1 – Design and synthesis of photoswitchable arachidonate mimics.....	206
7.2.2 – Photolipids enable optical control of GRP40 in HeLa cells	208
7.2.3 – Optical control of K ⁺ channel activity in β-cells.....	211
7.2.4 – Optical control of [Ca ²⁺] _i oscillations in pancreatic islets.....	215
7.3 – Discussion	217
7.4 – Supporting information.....	218
7.4.1 – Cell culture	218
7.4.2 – Culture of primary mouse pancreatic islets.....	218

7.4.3 – List of utilized cDNA constructs	219
7.4.4 – Laser scanning confocal microscopy	219
7.4.5 – Whole-cell electrophysiology in dissociated mouse β -cells	220
7.4.6 – Compound synthesis and characterization	221
7.4.6.1 – 3-(4-((3-Phenoxyphenyl)diazenyl)phenyl)propanoic acid (FAAzo-10).....	221
7.4.7 – Crystallographic data.....	224
7.4.7.1 – 4-(((4-Butylphenyl)diazenyl)phenyl)butanoic acid (FAAzo-4).....	224
8 – Optical control of lipid rafts with photoswitchable ceramides.....	225
8.1 – Introduction.....	225
8.2 – Results.....	227
8.2.1 – Synthesis of photoswitchable ceramides	227
8.2.2 – Confocal fluorescence microscopy of supported lipid bilayers	230
8.2.3 – Isomerization to <i>cis</i> -ACe-1 triggers a fluidification of ordered domains	232
8.2.4 – Dynamic control of raft fluidification and rigidification.....	236
8.2.5 – ACe-2 and ACe-3 affect domain structure on isomerization.....	240
8.3 – Discussion	243
8.4 – Supporting information.....	244
8.4.1 – Supported lipid bilayer formation	244
8.4.2 – Combined atomic force and confocal microscopy.....	244
8.4.3 – Compound switching on supported lipid bilayers	245
8.4.4 – Compound synthesis and characterization	246
8.4.4.1 – <i>N</i> -(4-(((4-Butylphenyl)diazenyl)phenyl)butanamide)-(2 <i>S</i> ,3 <i>R</i>)-2-aminooctadec-4-ene-1,3-diol (ACe-1).....	246
8.4.4.2 – <i>N</i> -(4-((4-Heptylphenyl)diazenyl)benzamide)-(2 <i>S</i> ,3 <i>R</i>)-2-aminooctadec-4-ene-1,3-diol (ACe-2)	249
8.4.4.3 – <i>N</i> -(7-(4-(<i>p</i> -Tolyldiazenyl)phenyl)heptanamide)-(2 <i>S</i> ,3 <i>R</i>)-2-aminooctadec-4-ene-1,3-diol (ACe-3)	251
9 – Appendix.....	253
9.1 – Abbreviations	253
9.2 – General synthetic methods and spectroscopic characterization	255
9.3 – Data reporting and error analysis	256
9.4 – References	257

1 – Abstract

Lipids are amphiphilic molecules which function not only as sources of energy and structural components of cells, but are involved in signal transduction. Fatty acids (FAs) are the simplest lipid building block, and contain an unbranched carbon chain that can be decorated with *cis* double bonds. They serve as modular components of more complex lipids through further functionalization of the polar headgroup, affording an expansive collection of molecules whose structures are as diverse as their functions. Although lipids are vital to most, if not all, cellular processes, few tools exist which allow researchers to perturb lipid-dependent processes with a high degree of spatiotemporal precision. To achieve greater control over the function of small molecules, our lab designs photoswitchable ligands that interact with their target under the control of light, a field we call *photopharmacology*. This technique has enabled optical control of a variety of transmembrane and intracellular proteins, but has been mostly focused on soluble small-molecule ligands that interact directly with their target.

Here, we aim to place lipid signaling under photopharmacological control using photoswitchable lipids, or *photolipids*. We prepared a series of photoswitchable FAs, the FAAzos, which contain an azobenzene photoswitch replacing the double bonds in the FA aliphatic chain. This allows the researcher to fine-tune the pharmacological and biophysical properties of each molecule in a reversible manner on illumination. Given the ubiquity of protein-lipid interactions in cell physiology, the photolipids are broadly applicable tools for controlling signal transduction. The FAAzos themselves can be used to control FA-signaling through interactions with voltage-activated K⁺ channels and G protein-coupled receptors (GPCRs) such as GPR40. They can also be further derivatized to create more sophisticated photolipids; including vanilloids, glycerolipids, phosphoinositides, and sphingolipids. These photolipids enable optical control of ion channels such as TRPV1 or enzymes like protein kinase C (PKC), providing researchers with tools to manipulate nociception, synaptic transmission, and excretion. In contrast to optogenetic approaches, these tools do not require genetic encoding. As such, they are applicable to a variety of different cell types, and can even be used *in vivo*. The photolipids can also be incorporated into synthetic membranes, where they affect membrane properties such as permeability, fluidity, and curvature. Taken together, we demonstrate how discrete alterations in lipid properties are crucial towards their effects within the cell. More generally, this work directs photopharmacology towards the plasma membrane, and provides researchers with tools to manipulate lipid signaling with the high spatiotemporal precision of light.

2 – Introduction to photolipids

Lipids are fundamental to compartmentalized organic life, as they define the permeability barriers between cells and organelles¹⁻³. They serve as stores of energy, and are also essential signaling molecules which act as first and second-messengers, ligands or allosteric modulators in most, if not all, signaling events⁴. Lipids can be generically defined as hydrophobic or amphiphilic molecules that are soluble in nonpolar organic solvents, however their chemical structures are as diverse as their functions⁵. The characterization of a cellular lipid content, alongside the individual functions of each molecule, has been coined lipidomics⁶. In contrast to genomics, which developed rapidly alongside technology enabling the efficient analysis and manipulation of genetic information and proteins⁴, lipidomics was late to gain momentum as technology for precise and quantitative lipid detection was limited. However, recent advances in mass spectrometry and computational methods for storing and processing data have triggered an explosion in lipidomics⁷. We now know that the lipidome of an average cell contains over 1000 unique molecules^{8,9}, and a significant portion of the proteome is dedicated to controlling the amount and location of specific lipids¹⁰. Lipids are the solvent in which transmembrane proteins function, and the clustering of lipids into distinct microdomains is thought to organize signaling events within the plane of the membrane^{11,12}. As our ability to observe and manipulate lipids grows, we are only now beginning to grasp the complex roles of lipids in cell physiology.

FAs are aliphatic carboxylic acids that represent the simplest lipid unit. They most often contain a unbranched chain of 4 to 28 carbon atoms, and can possess one or more degrees of unsaturation in the form of *cis* double bonds¹³ (**Fig. 2.1a**). The chain length and degree of unsaturation determines the biophysical and pharmacological properties of each FA, and this has a significant effect on the fluidity and curvature of the membrane in which they are embedded. As a particularly noteworthy example, arachidonic acid (AA) possesses a linear 20 carbon chain with four skipped *cis* double bonds that are vital for its effects in the cell (**Fig. 2.1b**). AA acts as a second messenger, and is a ligand for several ion channels and GPCRs^{14,15}. It also and serves as a precursor to highly potent signaling hormones such as leukotrienes and eicosanoids¹⁶. More generally, FAs serve as the hydrophobic components of more elaborate lipids through conjugation to polar headgroups of varying complexity. These range from simple net-neutral units such as phosphocholine, to the chiral charged headgroups of phosphoinositides or glycolipids (**Fig. 2.1c**). The different headgroups and acyl chains are mixed in near-endless combinations to afford thousands of different lipid species, each with a

distinct role within the membrane. As our understanding of these molecules becomes more sophisticated, novel chemical and genetic tools must be developed to manipulate individual lipid species with greater precision. These tools may be useful for understanding lipid function, both in normal cell physiology and disease states.

To enable greater control over signal transduction, researchers often endow proteins or small molecules with light sensitivity¹⁷. Light can be applied with an unmatched degree of spatial and temporal precision, and a light-responsive effector can translate the applied stimulus towards a target protein, initiating a cellular response. Optogenetics, for example, utilizes light-responsive proteins with naturally occurring chromophores¹⁸ to enable optical control of specific cells or signaling pathways^{19–21}. This approach allows researchers to control complex tissues and organisms with light using relatively well-established genetic methods²². Alternatively, synthetic small molecules can be rendered light-responsive and used to target proteins that are not normally associated with a natural chromophore. Caged ligands²³, including caged lipids²⁴, have already been developed and used extensively in a variety of applications^{25–31}. In this case, the active pharmacophore is masked with a light-labile protecting group³², allowing the free ligand to be released almost instantaneously upon a flash of light. This approach dramatically increases the precision at which a ligand can be applied, however uncaging is an irreversible process, and once switched ON the activity relies on metabolism or active transport to be turned OFF.

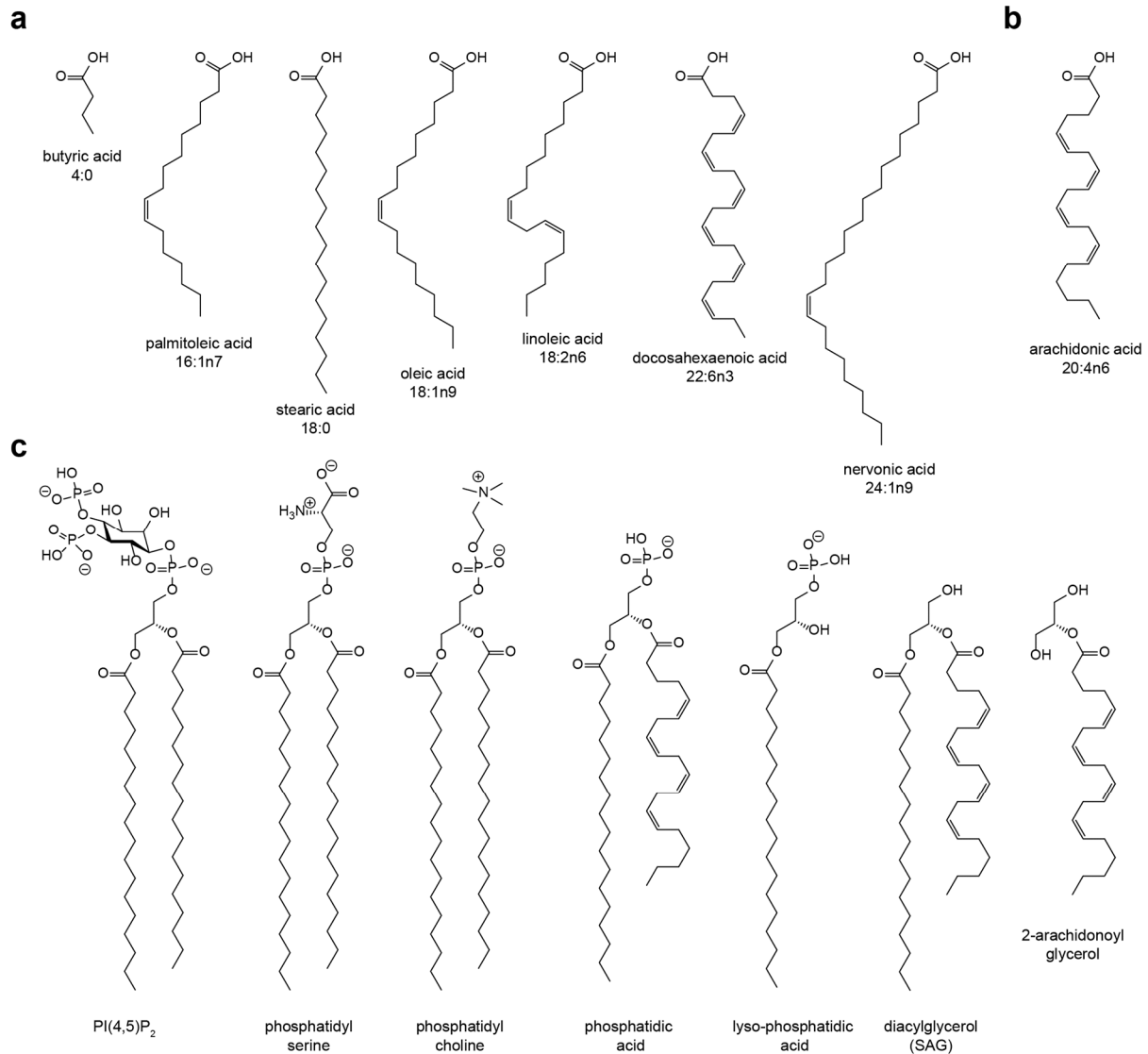


Figure 2.1 | Fatty acids are modular components of more complex lipids. (a) Chemical structures of various FAs of different lengths and degrees of unsaturation. (b) The chemical structure of AA, a second messenger lipid with unique biophysical properties. (c) The chemical structures of various glycerolipids with polar headgroups of increasing complexity.

Complementary to this technique, *photoswitchable* small molecules can be used to enable reversible optical control of cellular function³³. This approach has been coined *photopharmacology*³⁴. A synthetic photoswitch can be incorporated into the target molecule, and permits cycling between distinct conformations with light in a reversible manner. Research in our lab has focused primarily on the azobenzene photoswitch, which can be rapidly isomerized from the thermally more stable *trans*-configuration to the higher-energy *cis*-form with UV-A light (**Fig. 2.2a**). This process can be reversed by irradiation with blue light, and photoswitching can be performed over hundreds of cycles without photobleaching or the generation of harmful singlet oxygen species³⁵ (**Fig. 2.2b**). The azobenzene is a relatively small photoswitch (about 9 Å long in the *trans*-form) and exhibits a large conformational change (about 3 Å shortening between the *para*-positions) alongside a significant increase in polarity on isomerization to *cis*. Azobenzenes can be readily synthesized using a variety of methods, and can be spectrally tuned to respond to longer irradiation wavelengths^{36,37} (**Fig. 2.2c,d**). This lower energy and deeper-penetrating light facilitates application to more complex tissues^{38,39}. Photopharmacology was first successfully applied to ion channels⁴⁰, where a photoswitchable pharmacophore was covalently tethered to an engineered cysteine on the protein of interest via maleimide chemistry⁴¹ (**Fig. 2.3a**). More recently, this approach has been extended to utilize new bioconjugation techniques such as self-labeling protein tags⁴², and enables optical control of a target protein with a high degree of specificity driven by the protein-ligand conjugation. Alternatively, freely diffusible photoswitchable small molecules, the so-called photochromic ligands (PCLs), can place endogenous protein function under optical control without the need for genetic manipulation (**Fig. 2.3b**)⁴³. In both cases, the ligand has been rendered photoswitchable through synthetic modifications, and exhibits a change in efficacy towards its target on isomerization between the two distinct conformational states (**Fig. 2.3c**). Photopharmacology has now been expanded to GPCRs, enzymes, and transcription factors, enabling reversible control of a number of proteins with the spatiotemporal precision of light^{35,44}.

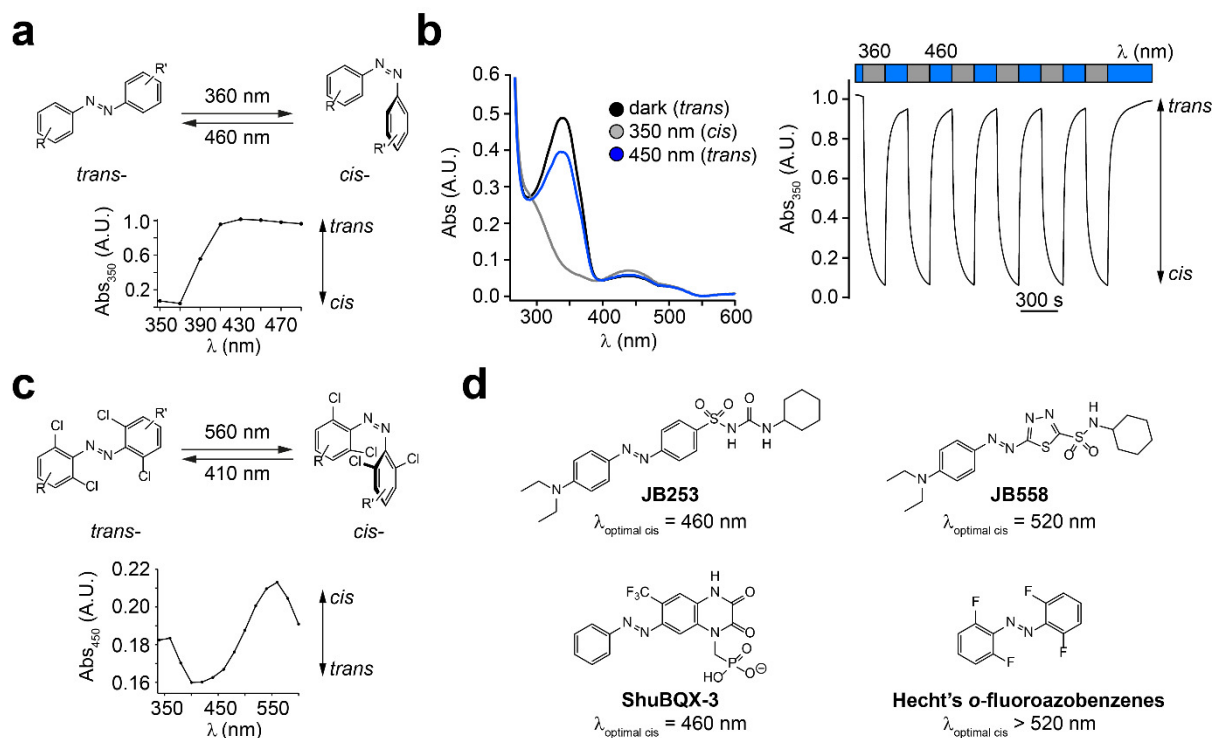


Figure 2.2 | The azobenzene as a photoswitch. (a) Chemical structure of the azobenzene in its *trans* and *cis* states. (b) UV-Vis spectra demonstrate that a standard azobenzene can be isomerized between its *cis* and *trans* states over many cycles with UV-A and blue light, respectively. (c) Chemical structure of the tetra-*ortho*-chloro azobenzene in its *trans* and *cis* states. The *cis*-form can be generated by green ($\lambda = 560$ nm) irradiation. (d) The chemical structures of various functionalized azobenzene derivatives, which can be isomerized to the *cis*-form with different irradiation wavelengths.

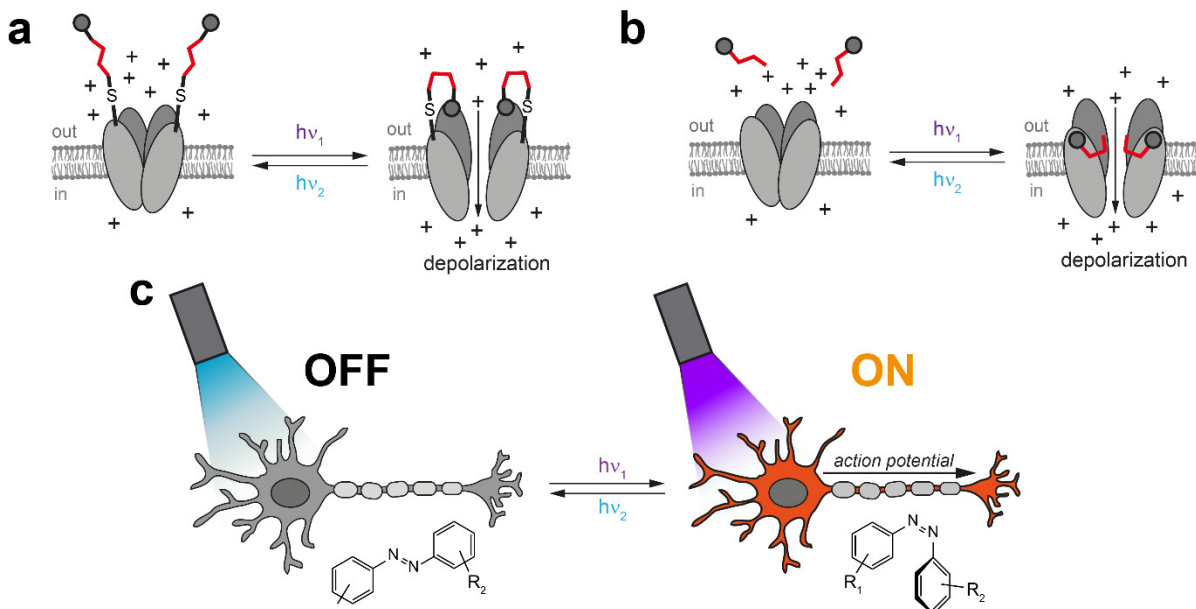


Figure 2.3 | Photopharmacology enables optical control of cell signaling. (a) Photoswitched tethered ligands (PTLs) can be tethered to an engineered cysteine on a target protein, enabling optical control with high specificity. (b) Photochromic ligands (PCLs) are freely diffusing photoswitchable ligands which change in efficacy on isomerization between two distinct states. (c) PCLs or PTLs can enable optical control of cellular signaling. For example, action potential (AP) firing in neurons can be triggered by a flash of light.

In this thesis, I describe our efforts in extending the reach of photopharmacology to control lipid signaling. Although photoswitchable lipids, also called *photolipids*, have been investigated before, this work was limited and mostly restricted to biophysical studies in artificial membranes^{45–48}. In some cases, the photoswitch was incorporated into the polar headgroup of the molecule, which often defines the identity and function of a given lipid for its effector proteins^{49,50}. Given the modularity of FAs across almost all lipid classes, we recognized that incorporating a photoswitch into the fatty acyl chain would allow us to construct a wide range of photolipids from only a few synthetic building blocks. This approach would also retain the identity of the headgroup, preserving the lipids identity and native activity within the cell. Photoisomerization within the acyl chain(s) would allow us to fine-tune the molecule's efficacy towards its target effectors, either through direct interaction with the target protein, or with the surrounding membranes. To this end, we designed and synthesized a set of photoswitchable FAs, the FAAzos, which consist of an aliphatic carboxylic acid and an azobenzene photoswitch to mimic the double bonds. We discovered that the azobenzene can

be easily incorporated into the fatty acyl chain without disrupting the compounds biological activities. In some cases, the FAAZos behave as an AA that can be turned ON and OFF with light. By attaching the FAAZos to different polar headgroups, we created a library of photolipids which enable optical control of lipid-mediated signaling events^{37,51,52}, and can also be applied to model membrane systems⁵³. By harnessing the spatiotemporal precision of light, the photolipids are broadly applicable tools to study the roles of lipids in cell signaling and membrane structure.

3 – Project affiliation disclosure

In this statement, I proclaim that the findings in the following dissertation are the result of a team-driven effort involving many individuals. I will discuss the findings of our group and our collaborators, compiling the work of many into a description of our findings. Alongside the supervision of Prof. Dr. Dirk Trauner, the following individuals added significantly to this work through conceptual and/or experimental contributions:

Chapter 4 – Photoswitchable fatty acids enable optical control of TRPV1

Dr. Mirko Moroni¹ (electrophysiology), Dr. Med. Rabih Moshourab^{1,2} (C-fiber experiments), David Konrad³ (synthesis of *red-AzCA-4*), Dr. Martin Sumser³ (supervision and electrophysiology), Prof. Dr. Gary R. Lewin¹ (supervision).

¹Molecular Physiology of Somatic Sensation, Max Delbrück Center for Molecular Medicine, 13125 Berlin, Germany. ²Department of Anesthesiology, Campus Charité Mitte und Virchow-Klinikum, Charité – Universitätsmedizin Berlin, Augustburgerplatz 1, 13353 Berlin, Germany. ³Department of Chemistry and Center for Integrated Protein Science, Ludwig Maximilians University Munich, Butenandtstraße 5–13, 81377 Munich, Germany.

Chapter 5 – Photoswitchable diacylglycerols enable optical control of protein

kinase C

Prof. Dr. Carsten Schultz¹ (supervision), Dr. Dmytro A. Yushchenko^{1,2} (imaging), Dr. David J. Hodson^{3,4,5} (imaging and secretion experiments), Dr. Noa Lipstein⁶ (electrophysiology), Dr. Jatin Nagpal^{7,8} (*C. elegans* experiments), Prof. Dr. Guy A. Rutter³ (supervision), Dr. Jeong-Seop Rhee⁶ (supervision), Prof. Dr. Alexander Gottschalk^{7,8} (supervision), Prof. Dr. Nils Brose⁶ (supervision).

¹European Molecular Biology Laboratory (EMBL), Cell Biology & Biophysics Unit, Meyerhofstraße 1, 69117 Heidelberg, Germany. ²Institute of Organic Chemistry and Biochemistry, Academy of Sciences of the Czech Republic, Flemingovo namesti 2, 16610 Prague 6, Czech Republic. ³Section of Cell Biology and Functional Genomics, Department of Medicine, Imperial College London, ICTEM, Hammersmith Hospital, Du Cane Road, London W12 0NN, UK. ⁴Institute of Metabolism and Systems Research (IMSR), University of Birmingham, Birmingham B15 2TT, UK. ⁵Centre for Endocrinology, Diabetes and Metabolism, Birmingham Health Partners, Birmingham,

B15 2TH, UK. ⁶Department of Molecular Neurobiology, Max Planck Institute of Experimental Medicine, Hermann-Rein Straße 3, 37075 Göttingen, Germany. ⁷Buchmann Institute for Molecular Life Sciences, Goethe University, Max von Laue Strasse 15, D-60438 Frankfurt, Germany. ⁸Institute of Biochemistry, Department for Biochemistry, Chemistry and Pharmacy, Goethe University, Max von Laue Strasse 9, D-60438 Frankfurt, Germany.

Chapter 6 – Synthesis of photoswitchable glycerophospholipids

Prof. Dr. Carsten Schultz¹ (supervision), Dr. Rainer Müller¹ (synthesis).

¹European Molecular Biology Laboratory (EMBL), Cell Biology & Biophysics Unit, Meyerhofstraße 1, 69117 Heidelberg, Germany.

Chapter 7 – Optical control of arachidonate signalling in pancreatic β -cells

Prof. Dr. Carsten Schultz¹ (supervision), Dr. Dmytro A. Yushchenko^{1,2} (imaging), Dr. David J. Hodson^{3,4,5} (β -cell imaging and secretion experiments), Nick Fine^{3,4,5} (β -cell imaging and secretion experiments), Margherita Duca⁶ (synthesis).

¹European Molecular Biology Laboratory (EMBL), Cell Biology & Biophysics Unit, Meyerhofstraße 1, 69117 Heidelberg, Germany. ²Institute of Organic Chemistry and Biochemistry, Academy of Sciences of the Czech Republic, Flemingovo namesti 2, 16610 Prague 6, Czech Republic. ³Section of Cell Biology and Functional Genomics, Department of Medicine, Imperial College London, ICTEM, Hammersmith Hospital, Du Cane Road, London W12 0NN, UK. ⁴Institute of Metabolism and Systems Research (IMSR), University of Birmingham, Birmingham B15 2TT, UK. ⁵Centre for Endocrinology, Diabetes and Metabolism, Birmingham Health Partners, Birmingham, B15 2TH, UK. ⁶Department of Chemistry and Center for Integrated Protein Science, Ludwig Maximilians University Munich, Butenandtstraße 5-13, 81377 Munich, Germany.

Chapter 8 – Optical control of lipid rafts with photoswitchable ceramides

Dr. Henri G. Franquelim¹ (atomic force microscopy), Prof. Dr. Petra Schwille¹ (supervision), Margherita Duca² (synthesis).

¹Department of Cellular and Molecular Biophysics, Max Planck Institute of Biochemistry, Am Klopferspitz 18, 82152 Martinsried, Germany. ²Department of Chemistry and Center for Integrated Protein Science, Ludwig Maximilians University Munich, Butenandtstraße 5-13, 81377 Munich, Germany.

The minds and wills of many individuals have come together and our combined efforts have enabled me to write this dissertation. However, this thesis has been compiled under my own initiative, and I am solely responsible for any errors contained within the following text.

4 – Photoswitchable fatty acids enable optical control of TRPV1

This work has been published in *Nature Communications* (2015)⁵¹ and *Chemistry - a European Journal* (2016)³⁷.

4.1 – Introduction

Lipids serve not only as sources of energy and integral components of membranes, but are also involved in cellular communication through participation in a variety of signaling cascades and the modulation of transmembrane proteins⁵⁴. Over the past several decades, interest in lipid chemistry has been overshadowed by advancements in proteomic and genomic technologies. However, recent developments in lipid research, including analysis of the lipidome⁴, have shed new light on the roles of these molecules at all levels of biology. Many lipids are comprised of FAs. These ancient molecular building blocks typically feature a long linear carbon chain (up to 28 carbons)¹³ that often contains one or several *cis*- double bonds.

The Vanilloid Receptor 1 (TRPV1), is the most studied of the transient receptor potential (TRP) ion channels^{55,56}. This family of non-selective cation channels is renowned for its ability to respond to a wide variety of chemical and physical inputs^{57,58}. TRPV1 is involved in the regulation of body temperature⁵⁹ and the transduction of painful stimuli from the periphery towards the central nervous system⁶⁰. It is expressed in sub-populations of sensory nerve fibers within the dorsal root and trigeminal ganglia⁶¹ where it responds to temperatures greater than 43 °C⁶², protons⁶³, as well as environmental toxins and poisons^{64,65}. Importantly, TRPV1 is modulated by a plethora of FA amides, including the endogenous AA derivatives anandamide⁶⁶ and *N*-arachidonoyl dopamine⁶⁷. Its most famous exogenous agonist is the vanilloid capsaicin (CAP), the pungent component of chili peppers⁶². Synthetic TRPV1 agonists include olvanil⁶⁸ and arvanil⁶⁹, which are FA-derived vanilloids developed as non-pungent CAP analogs.

TRPV1 is not only involved in responses to noxious stimuli, but is also believed to initiate the neurogenic inflammatory response⁷⁰ which has made it an attractive target for novel analgesics⁶². However, these attempts have proven more challenging than anticipated as TRPV1 is involved in a variety of other biological pathways that can lead to unwanted side effects. An agonist or antagonist that could be applied globally but activated only locally could offer a solution to this problem. In addition to this, such a tool would be highly valuable for

untangling the complex interactions that TRPV1 has with other proteins, such as the serotonin (5-HT), bradykinin (BK), and recently GABA_{B1} receptors^{56,71,72}.

Precision control can be achieved through photoswitchable small molecules that act as transducers between a light stimulus and protein function^{33,34,73}. In 2013, our group was the first to place TRPV1 under reversible optical control when we developed a series of photoswitchable *antagonists* which could optically control TRPV1 in the presence of CAP to activate the channel⁷⁴. Based on the structure of CAP and other TRPV1 agonists, we saw the opportunity to develop a photoswitchable TRPV1 *agonist*, which would permit optical control over the ion channel without the use of a second factor.

In this study, we present a toolkit of photolipids that allow us to place lipid-modulated biological targets, such as TRPV1, under the precise spatial and temporal control of light. We show that **AzCA-4** permits optical control over TRPV1 in complex neural systems with a higher degree of spatiotemporal precision than what is currently possible via other methods. More generally, this work represents the first example of the fusion of photopharmacology with lipid signaling, and consequently sets the groundwork for future research in this field.

4.2 – Results

4.2.1 – Photolipid synthesis

In an effort to mimic FAs with a chain length of 18 carbons, we prepared a series of eight photoswitchable FA-derivatives, **FAAzo-1-8**. Each of these compounds contained an azobenzene photoswitch which allowed for controllable *cis/trans*-isomerization along the length of the chain (**Fig. 4.1a**). **FAAzo-1-8** were prepared in between 2 and 6 steps in moderate yield (**Fig. 4.2**)⁷⁵. In their dark-adapted state, the FAAzos existed predominantly in the *trans*-configuration. UV-Vis spectroscopy showed that isomerization from *trans*- to *cis*- could be achieved by irradiation at $\lambda = 365$ nm, and this process could be reversed by $\lambda = 460$ nm light.

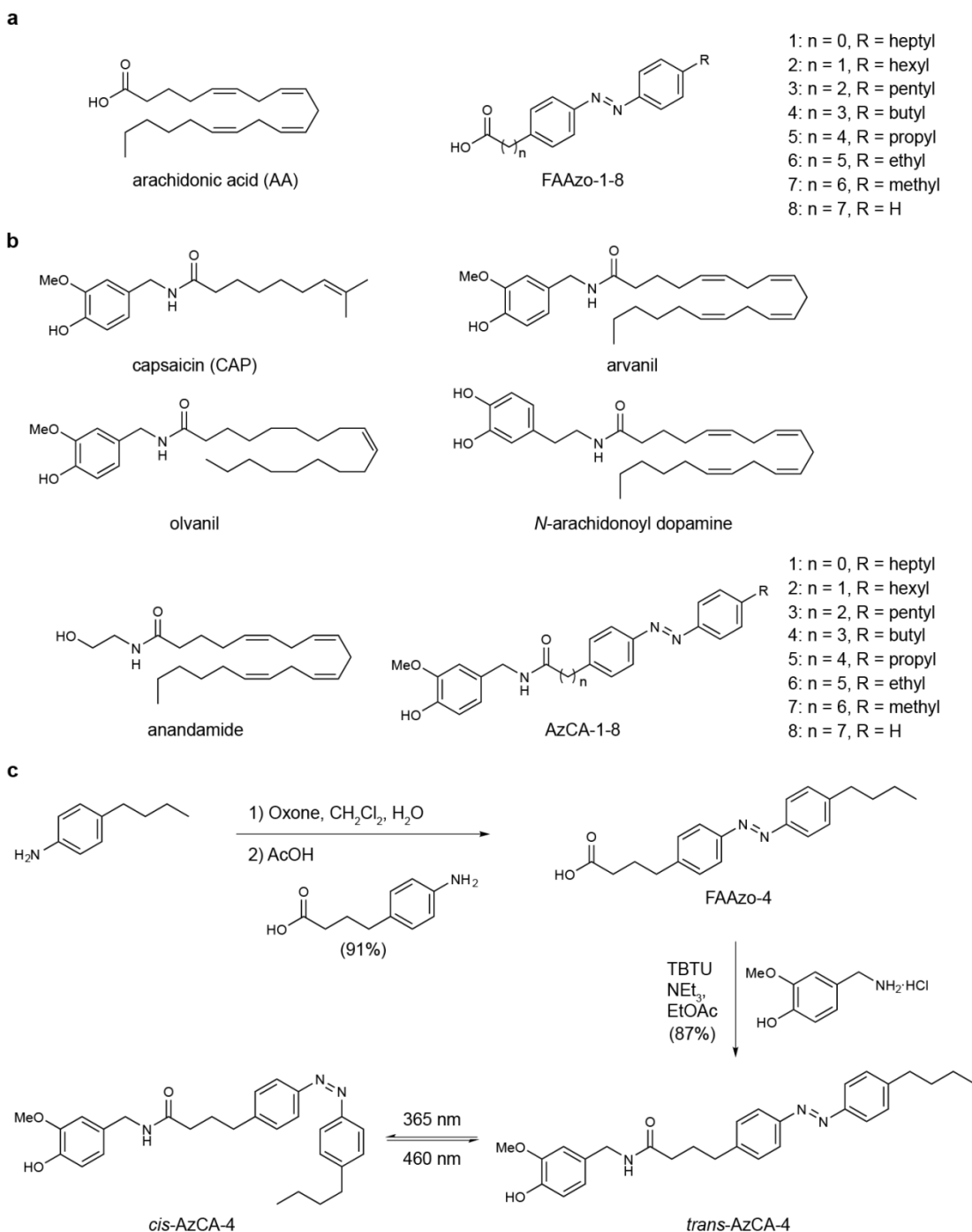


Figure 4.1 | Photolipids for the optical control of TRPV1. (a) Chemical structures of AA and **FAAzo-1-8**. (b) Chemical structures of TRPV1 agonists capsaicin (CAP), arvanil, olvanil, *N*-arachidonoyl dopamine and anandamide alongside photoswitchable vanilloids, **AzCA-1-8**. (c) Chemical synthesis of **AzCA-4**. Isomerization between *cis*- and *trans*-**AzCA-4** could be induced by irradiation with $\lambda = 365$ nm (*trans* to *cis*) and $\lambda = 460$ nm (*cis* to *trans*), respectively.

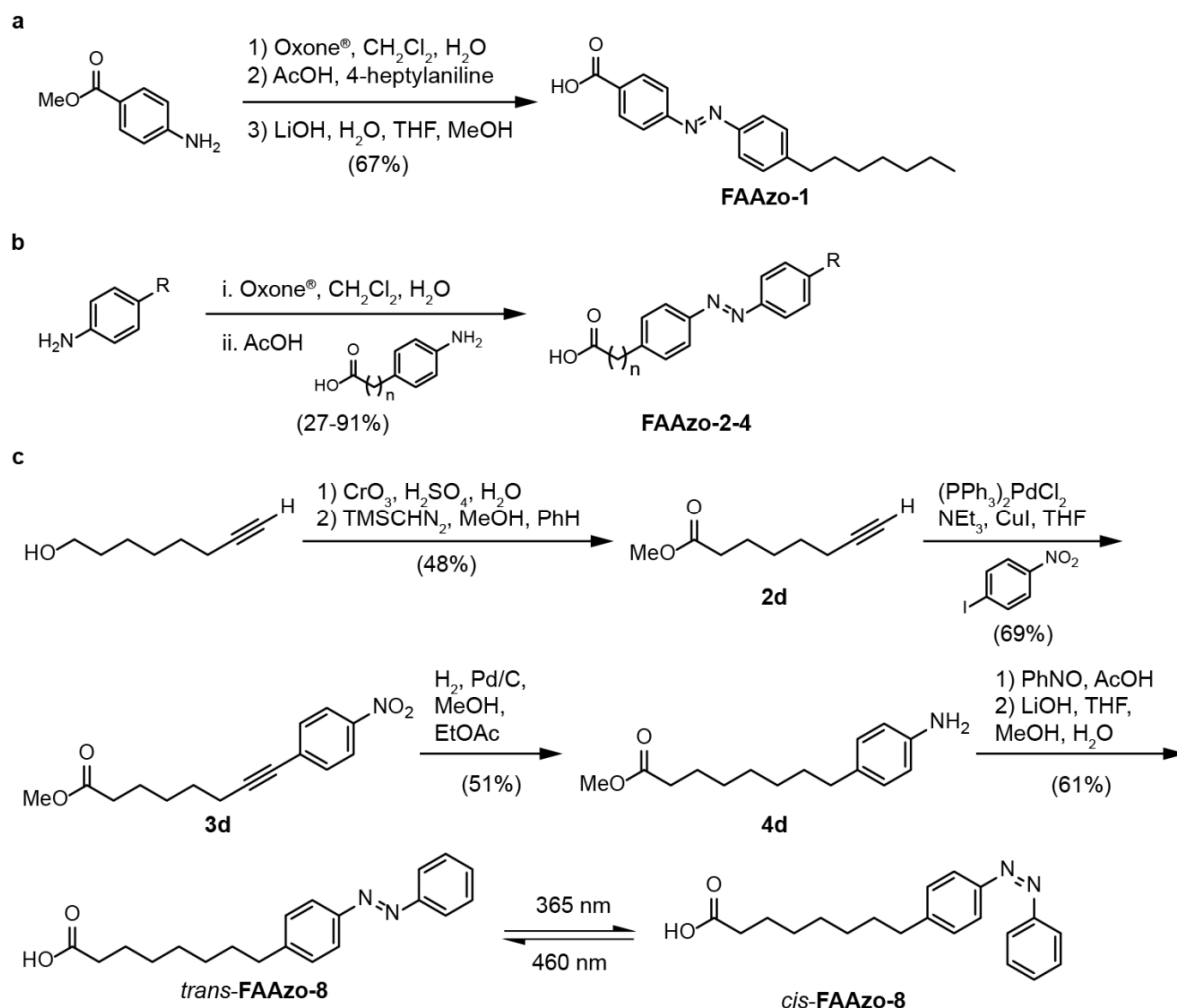


Figure 4.2 | The syntheses of photoswitchable fatty acids, FAAzo-1-8. (a) The synthesis of **FAAzo-1**. (b) **FAAzo-2-4** were synthesized via the Mills reaction. **FAAzo-2**: $n = 1$, R = hexyl (27%). **FAAzo-3**: $n = 2$, R = pentyl (27%). **FAAzo-4**: $n = 3$, R = butyl (91%). (c) **FAAzo-8** was synthesized in 6 steps from 7-octyn-1-ol in 10% overall yield. **FAAzo-5-7** were synthesized in an analogous fashion.

Supported by structure activity relationships (SAR) and recent structural data⁷⁶, we envisioned a unique opportunity to create a series of photoswitchable vanilloids for the optical control of TRPV1. Our approach combined the vanilloid head group of CAP with the FAAzos which would act as a photoswitchable tail mimicking that of *N*-arachidonoyl dopamine, anandamide, olvanil or arvanil (**Fig. 4.1b**). The preparation of these compounds (**Fig. 4.1c**, **Fig. 4.3**) required only a peptide coupling between vanillylamine and the appropriate FAAzo to afford 8 photoswitchable vanilloids, **AzCA-1-8**, in good yields (**Fig. 4.1b**). Photoswitching of **AzCA-1-8** was also achieved using $\lambda = 365/460$ nm, and they showed similar photoswitching properties when compared to the FAAzos (**Fig. 4.4**). As such, both FAAzos and AzCAs could be classified as “regular” azobenzenes that require UV-A light for isomerization to their thermally unstable *cis*-form.

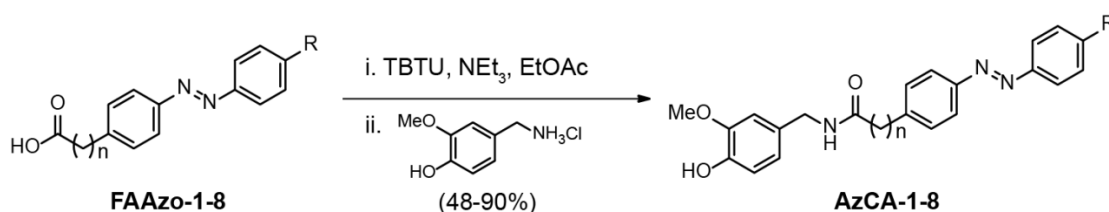


Figure 4.3 | The syntheses of photoswitchable vanilloids, AzCA-1-8. Photoswitchable vanilloids, **AzCA-1-8**, were prepared from the corresponding FAAzo via peptide coupling with vanillylamine. **AzCA-1**: $n = 0$, R = heptyl (89%). **AzCA-2**: $n = 1$, R = hexyl (48%). **AzCA-3**: $n = 2$, R = pentyl (89%). **AzCA-4**: $n = 3$, R = butyl (87%). **AzCA-5**: $n = 4$, R = propyl (90%). **AzCA-6**: $n = 5$, R = ethyl (86%). **AzCA-7**: $n = 6$, R = methyl (81%). **AzCA-8**: $n = 7$, R = H (88%).

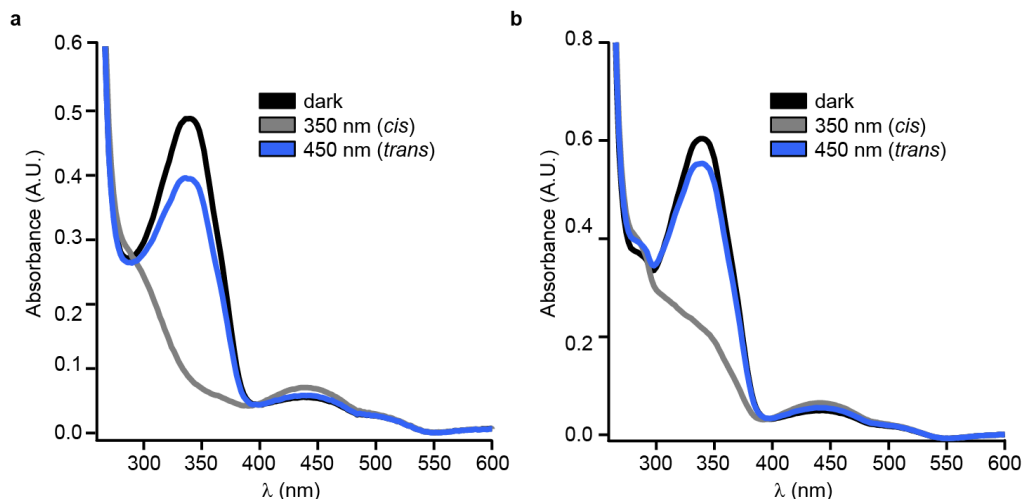


Figure 4.4 | UV-Vis spectra of FAAzo- and AzCA-derivatives. Photoswitching of (a) FAAzo-4 and (b) AzCA-4 could be visualized with UV-Vis spectroscopy. The spectra for all FAAzo- and AzCA-derivatives showed nearly identical profiles among the group. An initial spectrum was recorded (*dark* adapted state, black) and then again following illumination at the λ_{max} for the π - π^* transition ($\lambda = 350$ nm) for 3 min (*cis*-adapted state, grey). A third spectrum was recorded after irradiation at the λ_{max} for the n - π^* transition ($\lambda = 450$ nm) for 3 min (*trans*-adapted state, blue).

4.2.2 – Optical control over TRPV1 in HEK293T cells

We evaluated the photopharmacology of **AzCA-1-8** using whole-cell electrophysiology in human embryonic kidney (HEK) 293T cells transiently expressing the YFP-tagged ion channel (TRPV1-YFP)⁷⁷. Each compound (1 μM) was continuously applied while alternating between irradiation at $\lambda = 350$ nm and $\lambda = 450$ nm until a steady state of activity/desensitization was achieved upon photoswitching. Their relative light-dependent activities were then assessed by performing voltage ramps (-100 to $+100$ mV over 5 s) under irradiation at both wavelengths (**Fig. 4.5a**, **Fig. 4.6a**). Among the 8 derivatives tested, three compounds: **AzCA-2**, **AzCA-3**, and **AzCA-4** (at 1 μM), showed the most profound TRPV1 photoswitching effect (**Fig. 4.5b**, **Fig. 4.6b**). For all 3 derivatives, larger currents were observed under irradiation at $\lambda = 350$ nm, indicating that these compounds had higher efficacies towards TRPV1 in their *cis*-configuration. At higher concentrations (>300 nM, bath application), smaller cellular currents were observed upon application of the AzCAs in their dark-adapted states. This showed that in both configurations, the AzCAs were TRPV1 agonists, however in all cases a larger current was observed under $\lambda = 350$ nm irradiation. Working at an optimized concentration (1 μM by

puff pipette), the AzCAs could be applied to cells in the dark without any observable effect, and allowed immediate TRPV1 activation upon irradiation with UV-A light (**Fig. 4.7**). Photoswitching could be repeated over multiple cycles and only minor channel desensitization was observed (**Fig. 4.5c**).

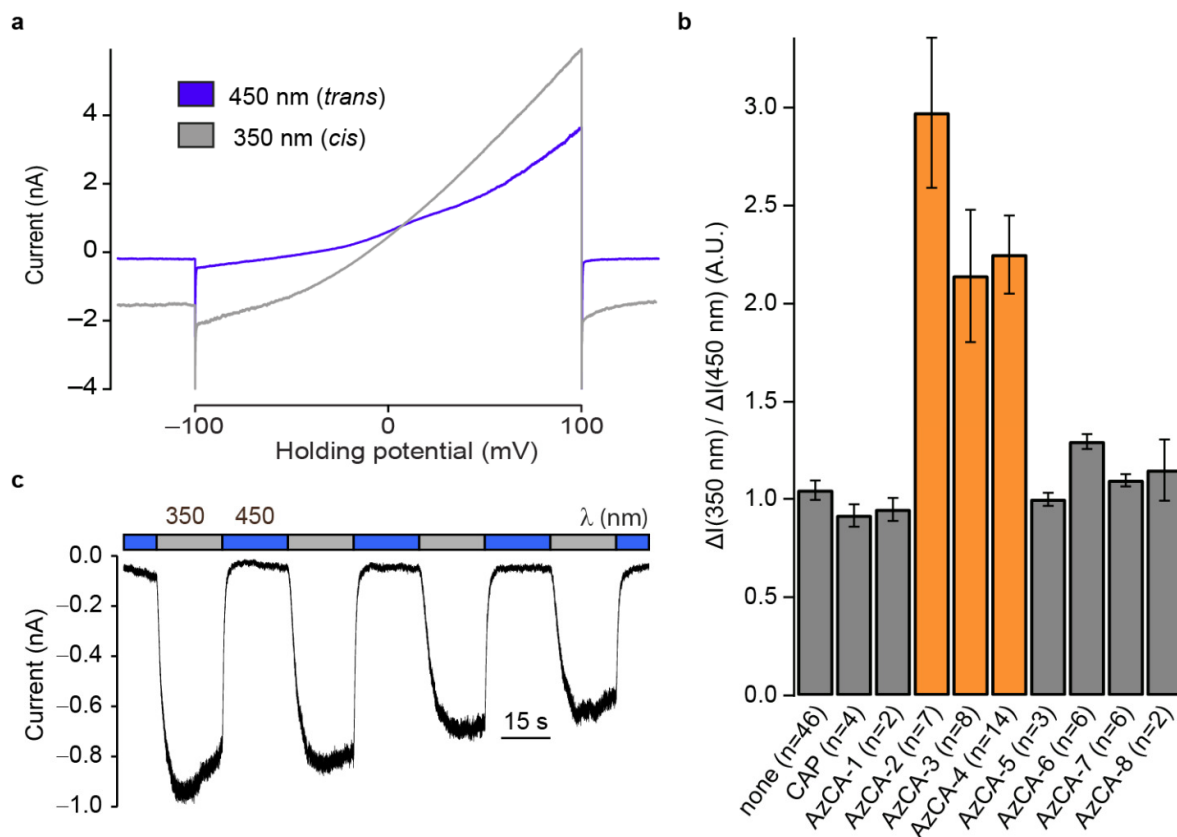


Figure 4.5 | AzCAs permit optical control of TRPV1 in HEK293T cells. HEK293T cells expressing TRPV1-YFP were observed using whole-cell patch-clamp electrophysiology after the application of an AzCA-derivative (1 μ M). **(a)** Voltage ramps were applied under both $\lambda = 350 \text{ nm}$ and $\lambda = 450 \text{ nm}$ irradiation. Larger currents were observed under $\lambda = 350 \text{ nm}$ irradiation (**AzCA-4**). **(b)** **AzCA-2**, **AzCA-3** and **AzCA-4** emerged as photoswitchable TRPV1 agonists. **(c)** When voltage clamped, photoswitching could be repeated over many cycles (**AzCA-3**). Error bars were calculated as \pm s.e.m.

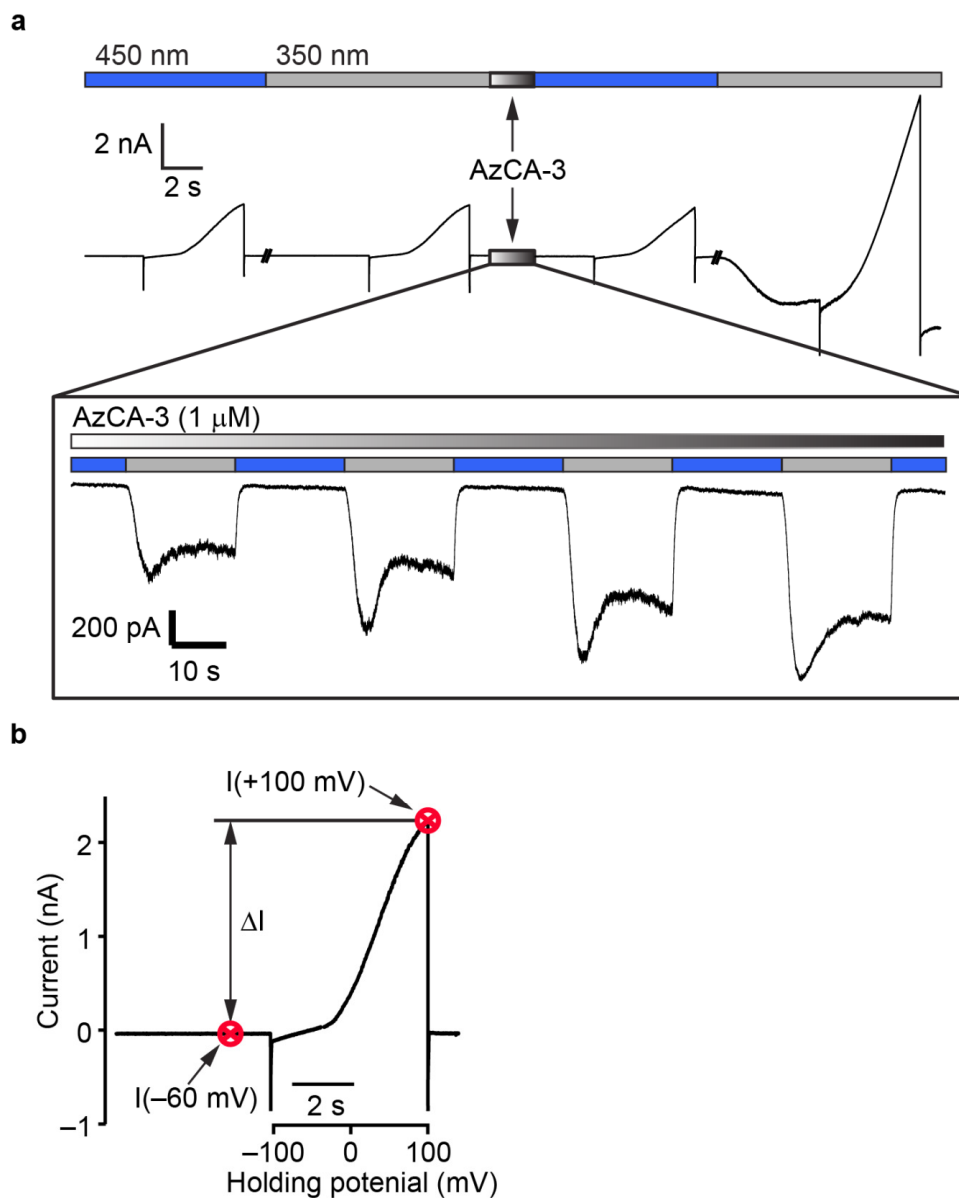


Figure 4.6 | AzCA photoswitching characterization. A representative electrophysiological recording for **AzCA-3** (1 μ M) is displayed here. **(a)** The typical procedure which was used to apply and assess each AzCA-derivative. **(b)** ΔI determination by voltage ramp analysis.

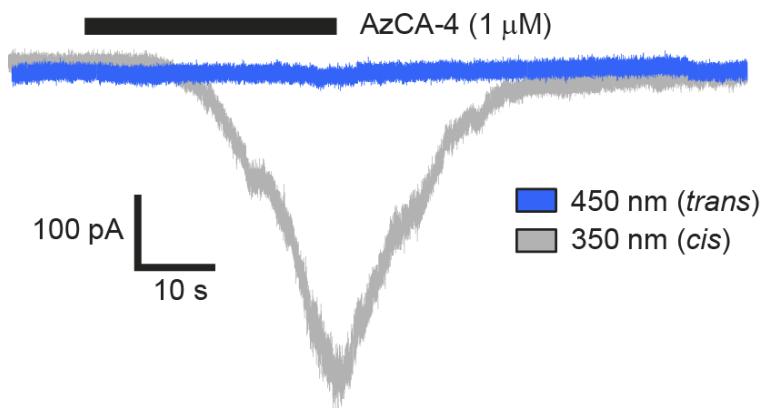


Figure 4.7 | AzCA-4 possesses a higher efficacy towards TRPV1 in its *cis*-configuration. **AzCA-4** was applied (1 μM) to HEK293T cells transiently expressing TRPV1-YFP under both $\lambda = 350$ nm (grey) and $\lambda = 450$ nm (blue) irradiation. When the membrane potential was clamped at -60 mV, an inward current was only observed upon irradiation with $\lambda = 350$ nm (*cis*), but not under $\lambda = 450$ nm (*trans*) upon application of **AzCA-4**. This showed that **AzCA-4** was a more potent TRPV1 agonist in its *cis*-configuration. Both traces are sequential recordings from the same cell, and the first **AzCA-4** application was under $\lambda = 350$ nm irradiation.

4.2.3 – Capsazepine antagonizes AzCA-4 activity

The washout of **AzCA-4** with buffer was very slow and photoswitching currents persisted for minutes under constant perfusion. However, application of capsazepine (CPZ, 5 μ M), a TRPV1 antagonist known to bind competitively against CAP, was capable of displacing **AzCA-4** and rapidly abolished inward currents upon UV-stimulation (**Fig. 4.8**)^{78,79}. In control experiments, no light-induced activity was observed in cells lacking TRPV1, before the application of an AzCA-derivative (**Fig. 4.9a**) or after the application of CAP (1 μ M) (**Fig. 4.9b**). The application of **FAAzo-2**, **FAAzo-3** and **FAAzo-4** caused no effect (5 μ M, $n \geq 3$ for each) in TRPV1-responding cells.

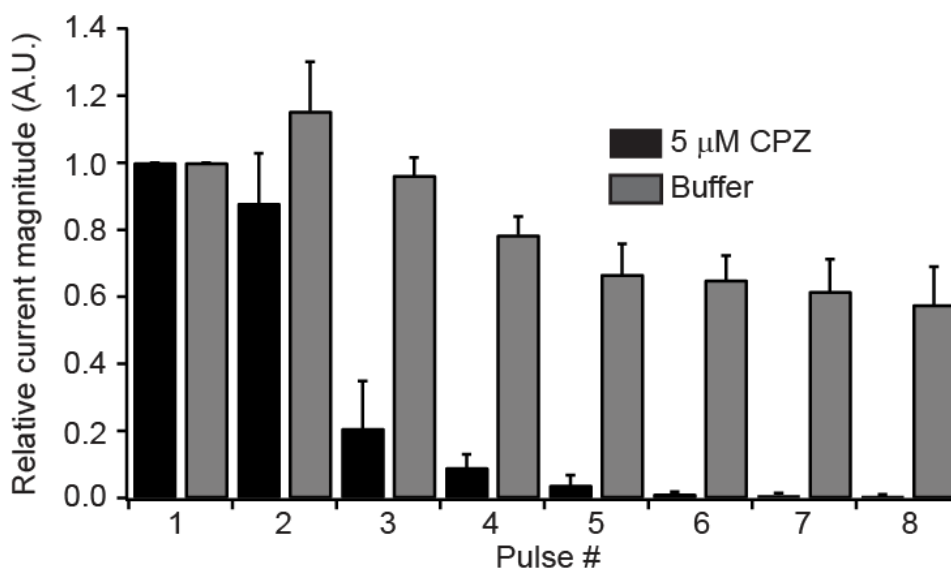


Figure 4.8 | Capsazepine blocked AzCA-4 photoswitching activity. **AzCA-4** (1 μ M, puff application) was continuously applied upon photoswitching between $\lambda = 350$ nm and $\lambda = 450$ nm (10 s alternating pulses). After a steady state of activity/desensitization had been reached, the cells were washed with either capsazepine (CPZ, 5 μ M in extracellular buffer, $n = 4$, black) or extracellular buffer (control, $n = 4$, grey). The maximum current amplitude for each UV pulse was calculated relative to the steady-state inward current and plotted as a function of pulse number after the washing was started. With buffer only, **AzCA-4** washout was slow and photoswitching persisted for >8 pulses. Addition of CPZ rapidly blocked TRPV1 currents upon photoswitching. Error bars were calculated as \pm s.e.m.

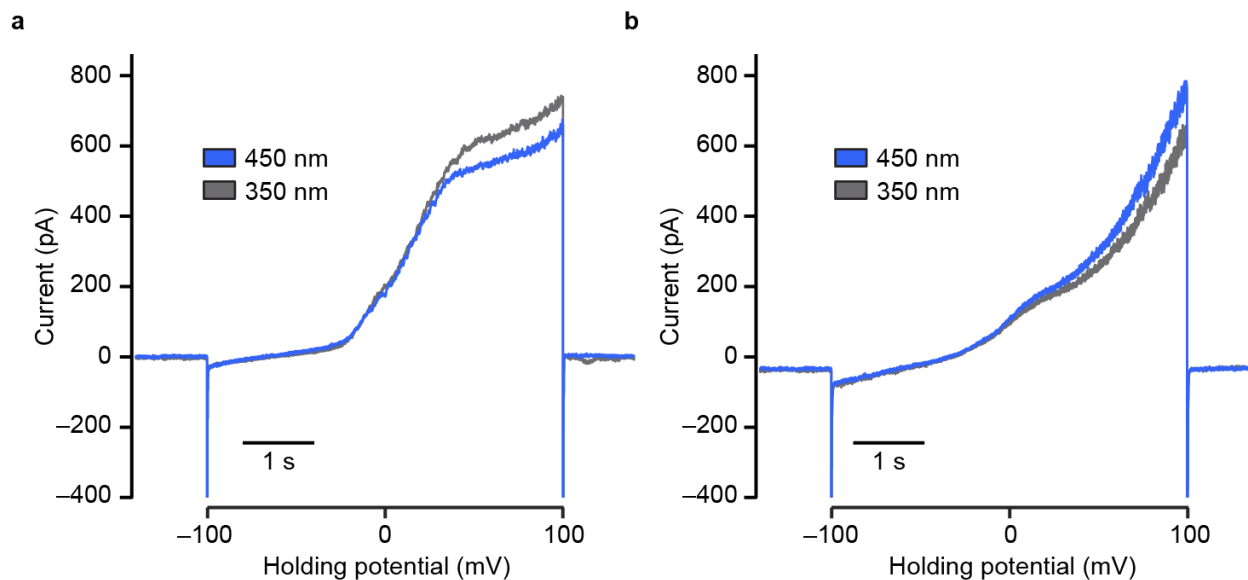


Figure 4.9 | Capsaicin did not permit the optical control of TRPV1. Control experiments using whole-cell voltage clamp electrophysiology showed that capsaicin (CAP) did not endow optical control over TRPV1-YFP in HEK293T cells. Voltage ramps (from -100 mV to $+100$ mV over 5 s) were applied (a) before and (b) after the application of CAP ($1 \mu\text{M}$). The ramp profile changed between the two measurements due to residual TRPV1 activation, but no significant light-dependent currents were observed.

4.2.4 – AzCA-4 enables precision control of TRPV1 at varied stimulation wavelengths

In voltage clamp experiments, the magnitude of the cellular currents could be controlled by adjusting the ON wavelength between $\lambda = 350$ - 390 nm. As shown by an action spectrum, the largest currents were observed under $\lambda = 350$ nm and they became smaller towards $\lambda = 390$ nm (Fig. 4.10a, Fig. 4.11). Current clamp experiments revealed that the cellular membrane potential could be controlled in a similar fashion, with $\lambda = 360$ nm yielding the largest depolarization (Fig. 4.10b). Through exponential curve fitting, we evaluated the effects of irradiation on the TRPV1 activation kinetics. The fastest ON response was observed at $\lambda = 360$ nm and all other τ_{on} values were normalized to this τ -value for comparison (Fig. 4.10c). At longer wavelengths, a slower response was observed. Taken together, these results indicate that the AzCAs permit precise, optical control over the activity of TRPV1 that cannot be achieved with other lipophilic agonists, such as CAP, alone. Because **AzCA-4** could be prepared in high yield at low cost, we decided to focus our future investigations on this compound.

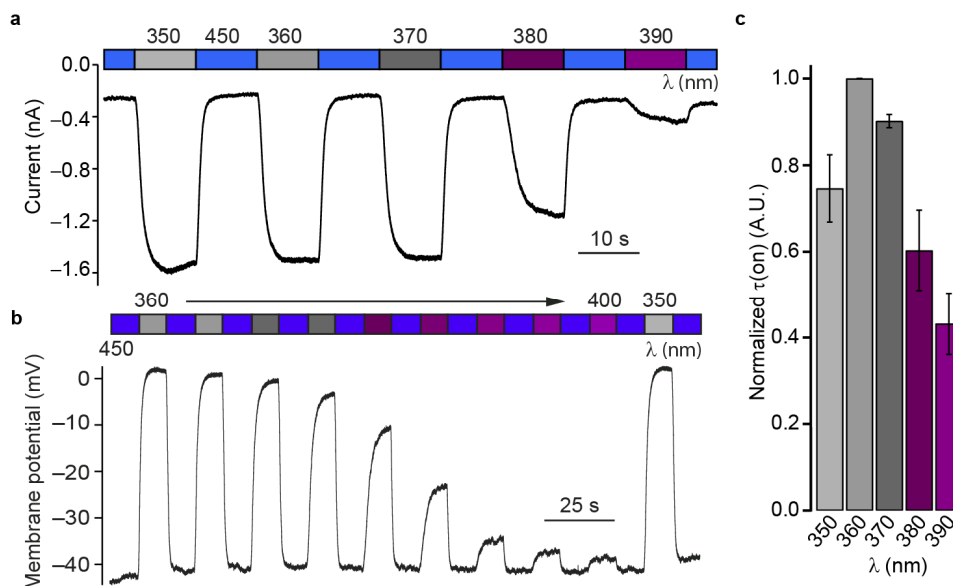


Figure 4.10 | TRPV1 activation can be precisely controlled with light. Cellular currents were observed using whole-cell patch-clamp electrophysiology in HEK293T cells expressing TRPV1-YFP after the application of an AzCA-derivative (1 μ M). (a) The current magnitude could be controlled by adjusting the ON wavelength between $\lambda = 350$ -390 nm (**AzCA-3**). (b) When current clamped, the membrane potential could be controlled by adjusting the ON wavelength between $\lambda = 350$ -400 nm (**AzCA-4**). (c) The activation rate could be controlled by adjusting the ON wavelength between $\lambda = 350$ -390 nm (**AzCA-3**, $n = 3$). Error bars were calculated as \pm s.e.m.

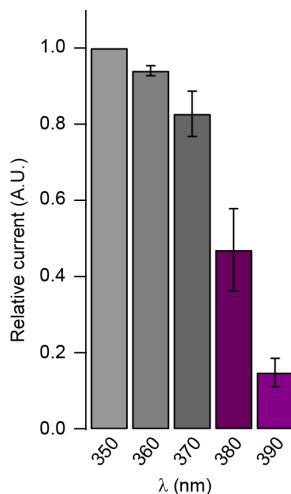


Figure 4.11 | The magnitude of cellular currents was a function of the ON wavelength. When voltage clamped at -60 mV, the magnitude of the cellular current could be precisely controlled by adjusting the ON wavelength in HEK293T cells expressing TRPV1-YFP after the application of **AzCA-3** (1 μ M). The values were calculated as the current change from the baseline while irradiating with $\lambda = 450$ nm, and the maximum inward current observed upon irradiation at the ON wavelength ($\lambda = 350$ -390 nm) for 5 s. The resulting currents were normalized to the largest current value (with $\lambda = 350$ nm) and averaged over multiple cells ($n = 3$) to yield a relative current. Error bars were calculated as \pm s.e.m.

4.2.5 – AzCA-4 permits optical control over cultured DRG neurons

Having demonstrated that **AzCA-4** acts as a photoswitchable TRPV1 agonist that is relatively inactive in the dark, we next evaluated its activity in isolated wild type (wt) mouse DRG neurons using both electrophysiology and intracellular Ca^{2+} imaging. Whole-cell patch-clamp electrophysiology showed that **AzCA-4** (200 nM) enabled reversible optical control over DRG neuronal activity. Switching between $\lambda = 365$ nm and $\lambda = 460$ nm in the voltage-clamp configuration at a holding potential of -60 mV resulted in reversible control over the transmembrane currents (**Fig. 4.12a**). Accordingly, the membrane potential and excitability of DRG neurons could be optically controlled as well. Action potential (AP) firing was reversibly switched ON and OFF by irradiation with $\lambda = 365$ nm and $\lambda = 460$ nm, respectively (**Fig. 4.12b**).

Bath application of **AzCA-4** (100 nM) and irradiation at $\lambda = 365$ nm (5 s), caused an increase in intracellular Ca^{2+} concentration ($[\text{Ca}^{2+}]_i$) in about 30% of DRG neurons cultured from 2-3 week old mice (**Fig. 4.12c**, **Fig. 4.13**). The remaining 70% of the DRG neurons did not respond to **AzCA-4** but still responded to a high potassium (Hi- K^+) solution (100 mM) (**Fig. 4.12d**). The percentage of **AzCA-4** responding neurons was consistent with the percentage of TRPV1 containing DRG neurons at this stage of mouse development ($33.6 \pm 1.3\%$ at P15, $30.5 \pm 3\%$ at P22)⁸⁰.

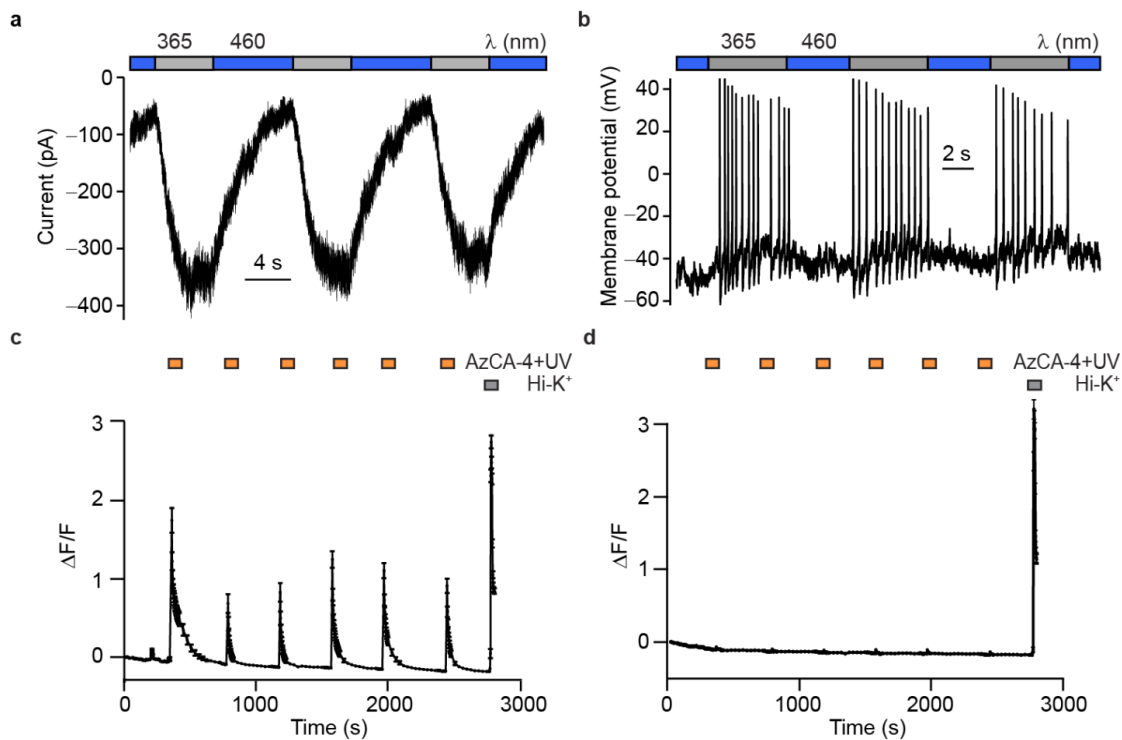


Figure 4.12 | AzCA-4 enabled optical control over cultured wt DRG neurons. (a) After the bath application of **AzCA-4** (200 nM), neuronal currents could be modulated by monochromatic irradiation. When clamped at a holding potential of -60 mV, an inward current was observed upon irradiation with $\lambda = 365$ nm and this effect could be reversed with irradiation at $\lambda = 460$ nm. (b) When clamped at a current of 0 pA and after the application of **AzCA-4** (200 nM), the neuronal membrane potential could be controlled. AP firing could be induced by irradiation at $\lambda = 365$ nm, and halted with $\lambda = 460$ nm. This process could be repeated over many cycles. (c) Intracellular Ca^{2+} imaging showed that **AzCA-4** (100 nM) significantly increased the $[\text{Ca}^{2+}]_i$ in TRPV1-positive neurons only after irradiation at $\lambda = 365$ nm (5 s). (d) Cells which did not respond to **AzCA-4** showed no increase in $[\text{Ca}^{2+}]_i$ after the bath application of **AzCA-4** and a UV pulse (6 pulses, 100 nM, 5 s at $\lambda = 365$ nm). These cells still responded to a Hi-K⁺ solution (100 mM), suggesting that they did not possess TRPV1. Error bars were calculated as \pm s.e.m.

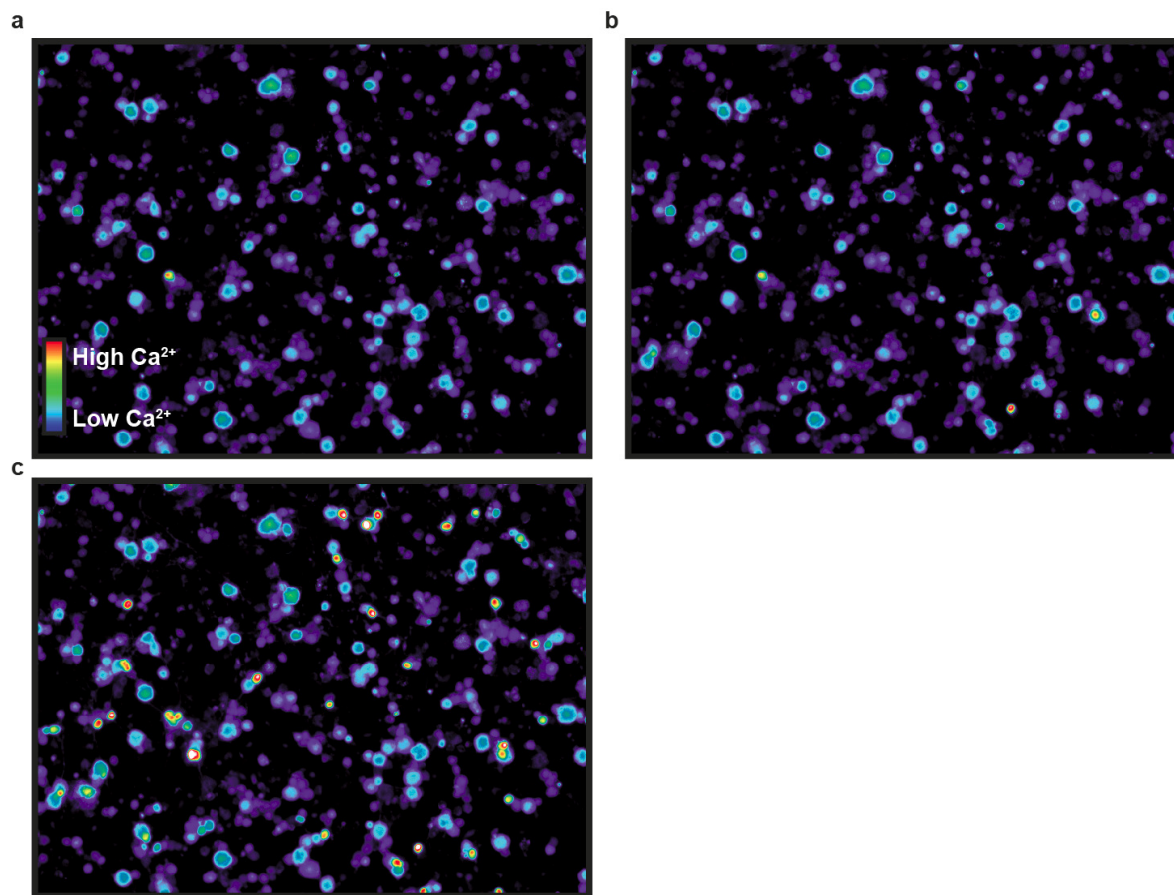


Figure 4.13 | AzCA-4 caused a significant increase in $[Ca^{2+}]_i$ after a UV pulse in DRG neurons. (a) A baseline fluorescence image was recorded before the application of any compound. (b) A fluorescence image was then recorded 45 s after the application of **AzCA-4** (100 nM, bath application) and directly before UV irradiation. (c) A fluorescence image was then recorded immediately after a 5 s flash of $\lambda = 365$ nm irradiation. A marked increase in fluorescence was observed after UV irradiation in about 30% of the cultured neurons.

4.2.6 – AzCA-4 is selective for TRPV1 sensitive neurons in the DRG

TRPV1 knockout mutant mice (*Trpv1*^{-/-}) have proven to be an excellent negative control to study the functional aspects of TRPV1 and the role of CAP-sensitive afferent neurons in the mammalian nervous system⁸¹. We utilized this mouse line to assay the selectivity of **AzCA-4** in DRG neurons. As expected, Ca²⁺ imaging in *Trpv1*^{-/-} mouse DRG neurons showed no neural activity in response to **AzCA-4** (300 nM) or CAP (300 nM). Control experiments showed that these neurons still responded to menthol (100 μM, data not shown), adenosine 5'-triphosphate (ATP, 20 μM) and Hi-K⁺ (100 mM) solutions (**Fig. 4.14**). Combined, these results indicate that **AzCA-4** acted solely on TRPV1-positive neurons in the DRG.

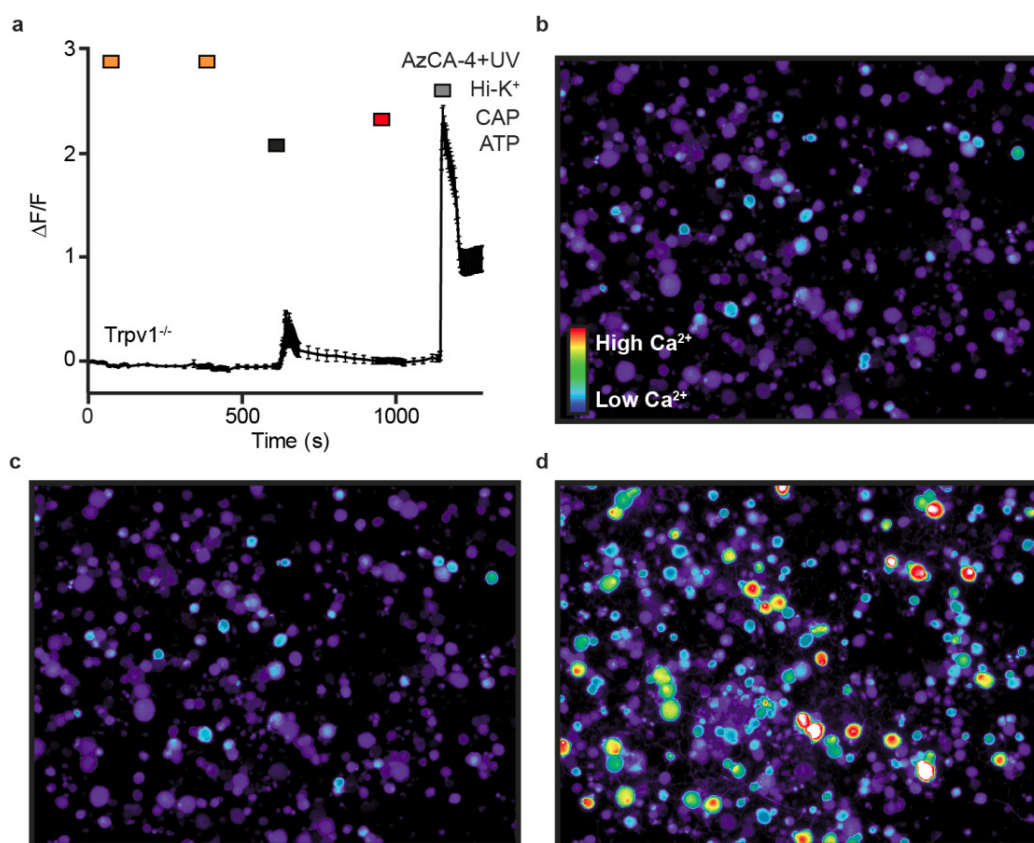


Figure 4.14 | AzCA-4 was selective for TRPV1-positive DRG neurons. Intracellular Ca²⁺ imaging revealed that **AzCA-4** had no action in cultured mouse *Trpv1* knockout mutant (*Trpv1*^{-/-}) DRG neurons. (a) No fluorescence increase was observed upon application of **AzCA-4** (300 nM) and a UV pulse ($\lambda = 365$ nm, 5 s) or CAP (300 nM). The neurons were still responsive to ATP (20 μM) and a Hi-K⁺ (100 mM) solution (n = 11). (b) A baseline fluorescence image was recorded before the application of any compound. (c) Another image was then recorded after the application of **AzCA-4** (300 nM, bath application) and a UV pulse ($\lambda = 365$ nm, 5 s). No response was observed in any of the DRG neurons. (d) After application of a Hi-K⁺ solution (100 mM), a large increase in [Ca²⁺]_i was observed.

4.2.7 – Optical control of C-fiber nociceptors

We next evaluated the effects of **AzCA-4** on heat sensitive C-fiber nociceptors (C-MH) in the *ex vivo* skin nerve preparation of the saphenous nerve. In wt mice, 19 out of 35 C-MH responded to **AzCA-4** photoswitching compared to none of the 11 C-MH examined in *Trpv1*^{-/-} mice ($P < 0.001$, χ^2 test; **Fig. 4.15a**). We compared the activation of **AzCA-4** to that of CAP on C-MH in terms of the latency time to the first AP spike, as well as the AP discharge rates. Peak discharge rates during photostimulation with $\lambda = 365$ nm surged rapidly to 9.6 spikes/s and lasted on average 11.0 ± 6.9 s (**Fig. 4.15b**). The average peak discharge rates of C-MH due to **AzCA-4** photoswitching were not significantly different from CAP stimulation (**Fig. 4.15c**). However, the mean latency time to the first AP spike upon irradiation with $\lambda = 365$ nm in the presence of **AzCA-4** was significantly shorter (1.9 ± 0.5 s; mean \pm SEM) when compared to the latencies to the first spike after CAP application (9.5 ± 3.5 s) (**Fig. 4.15d**, Mann-Whitney Test, $P < 0.05$). The discharges of C-MH in response to **AzCA-4** were usually transient and adapted during the 20 s photostimulation period. These responses were completely reproducible after a 5 min recovery interval, during which **AzCA-4** was kept on the receptive field with no signs of desensitization (**Fig. 4.15e**). Therefore, the photoswitching of **AzCA-4** could selectively activate TRPV1 receptors on the peripheral terminals of cutaneous C-MH to a similar magnitude as CAP. Advantageously, **AzCA-4** had the ability to trigger a more rapid neuronal response, and did not require washout of the drug.

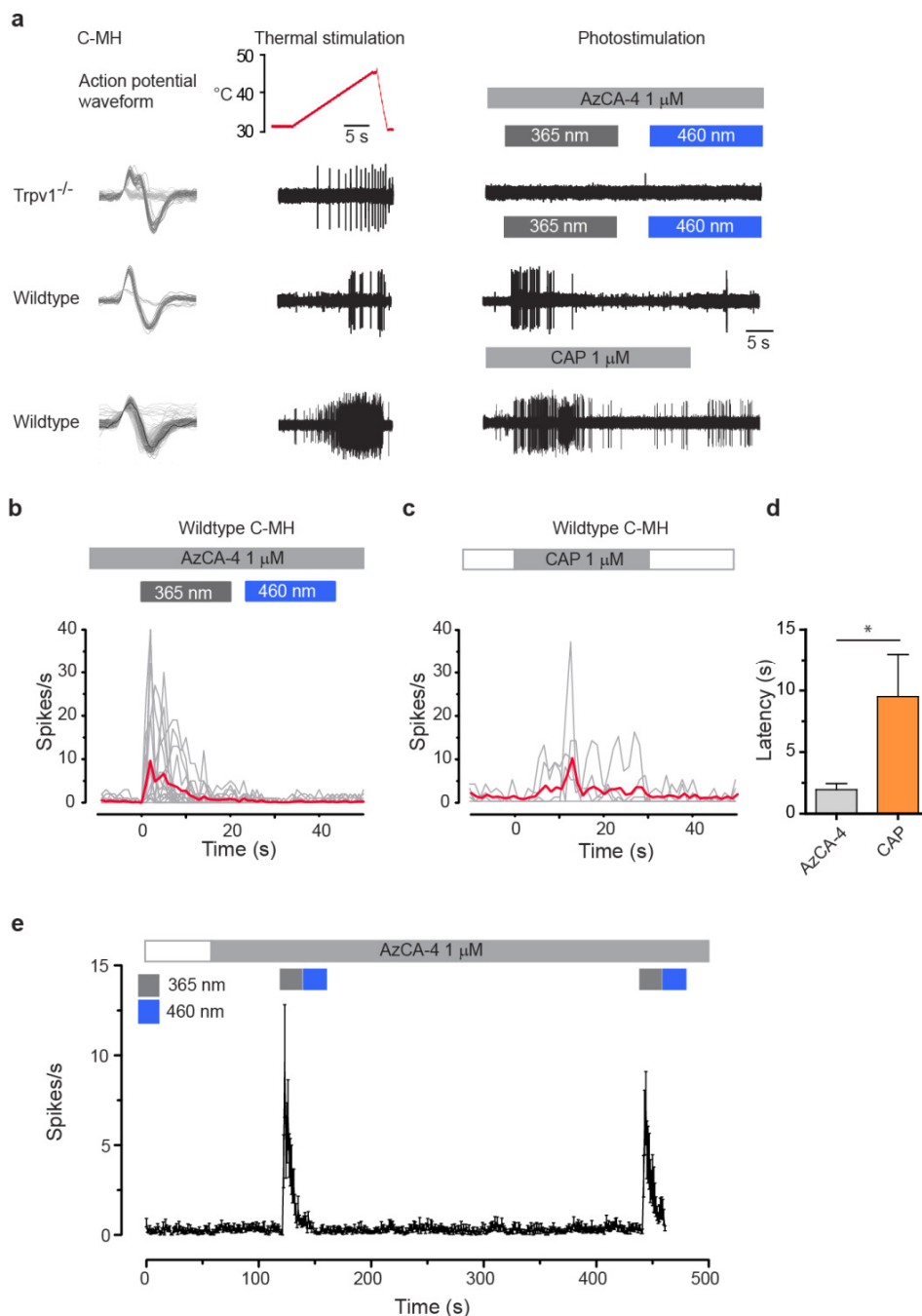


Figure 4.15 | Optical activation of TRPV1 in C-fiber nociceptors. (a) A typical sample trace showing the activation of a heat sensitive C-fiber nociceptor (C-MH) by optical switching of **AzCA-4** (1 μ M) with $\lambda = 365$ nm light, and CAP (1 μ M) application in wt mice. No photostimulation occurred in *Trpv1*^{-/-} mice. (b,c) The average AP spiking rate (red) and the spiking rate for individual C-MHs (grey) in response to photostimulation in the presence of **AzCA-4** (1 μ M, n = 19), and activation by CAP (1 μ M, n = 6). (d) The latencies to the occurrence of the first AP spikes after photostimulation and after the application of CAP (*P < 0.05, Mann-Whitney Test). (e) A second photostimulation in the presence of **AzCA-4** by $\lambda = 460$ nm light can be triggered 5 min after the first photostimulation; the data is represented as the mean and SD of the number of spikes per 1 s bins of all activated C-MH.

4.2.8 – Serotonin and bradykinin sensitize DRG neurons to AzCA-4

TRPV1 mediated hyperalgesia is a complex process which underlies inflammatory pain^{70,82}. At sites of tissue injury, a number of chemical agents are released which cause an inflammatory response resulting in an increased thermal pain sensation in response to normally non-painful stimuli. Several GPCRs mediate TRPV1 sensitization^{82,83}. Bradykinin (BK)- and serotonin (5-HT)-triggered GPCR cascades are able to decrease the threshold for TRPV1 activation and increase the number of receptors at the cell surface^{56,82,84,85}.

We utilized intracellular Ca^{2+} imaging in cultured wt mouse DRG neurons to determine whether these endogenous inflammatory agents still sensitized TRPV1 towards **AzCA-4**. Our experiments showed that TRPV1 became sensitized to **AzCA-4** (200 nM) after the application of both BK (200 nM) and 5-HT (100 μM) (**Fig. 4.16a,b**). After 5 pulses of **AzCA-4** and UV irradiation, a steady-state of TRPV1 desensitization was reached and the cells were washed with the sensitizing agent for 5 min (**Fig. 4.16a**). In both cases, a final pulse of **AzCA-4** and UV irradiation resulted in increased $[\text{Ca}^{2+}]_i$ when compared to the previous pulse. Experiments with both inflammatory agents produced similar results to those achieved when using CAP as the channel agonist (**Fig. 4.16b, Fig. 4.17**). These results suggest that **AzCA-4** could be used as a tool to study the involvement of TRPV1 in inflammatory pain.

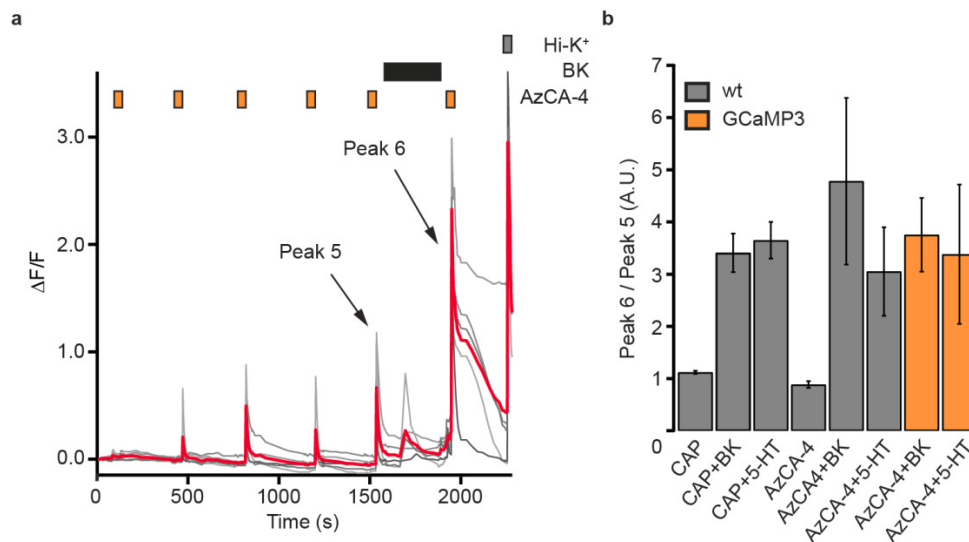


Figure 4.16 | Serotonin and bradykinin sensitized TRPV1 to AzCA-4. Intracellular Ca^{2+} imaging showed that both BK and 5-HT sensitized TRPV1 to CAP (100 nM), and **AzCA-4** (200 nM) with UV irradiation ($\lambda = 365$ nm, 5 s) in cultured wt DRG neurons. **(a)** After the application of BK (200 nM), an increased intensity and duration of Ca^{2+} influx was observed upon application of **AzCA-4** with UV irradiation when compared to the previous pulse. The neurons responded to a Hi- K^+ solution (100 mM). Shown here are 5 representative traces (grey) and average $\Delta\text{F}/\text{F}$ value (red). **(b)** TRPV1 sensitization experiments in wt mouse DRG neurons (grey) and the *Trpv1*^{Cre/GCaMP3} mouse line (orange). The results were plotted as the ratio of peak heights for Peak 6/Peak 5 for the wt mouse as: CAP with no sensitization agent (n = 520), CAP with BK (n = 210), CAP with 5-HT (n = 175), **AzCA-4** with no sensitizing agent (n = 36), **AzCA-4** with BK (n = 15), and **AzCA-4** with 5-HT (n = 12). For the *Trpv1*^{Cre/GCaMP3} mouse line the results are plotted for: **AzCA-4** with BK (n = 28) and **AzCA-4** with 5-HT (n = 10). Error bars were calculated as \pm s.e.m.

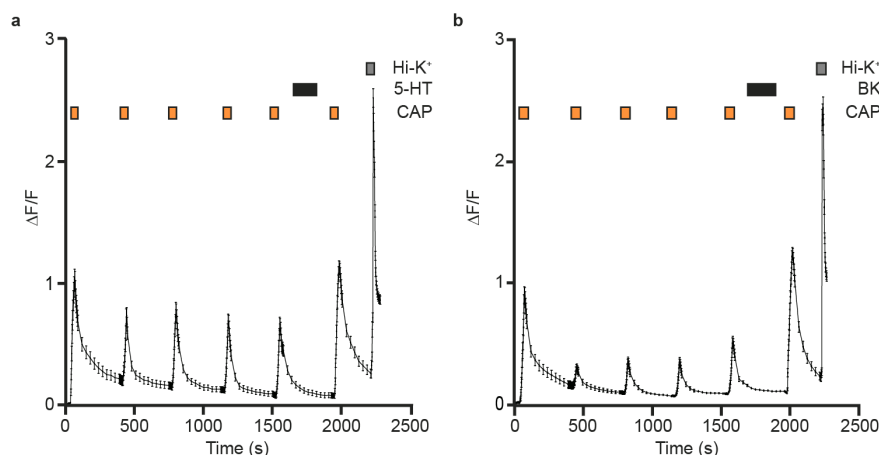


Figure 4.17 | Bradykinin and serotonin sensitized TRPV1 to capsaicin. Intracellular Ca^{2+} imaging showed that cultured wild type mouse DRG neurons were sensitized towards CAP (100 nM) by both **(a)** serotonin (5-HT, 100 μM , n = 175) and **(b)** bradykinin (BK, 200 nM, n = 210). The cells were pulsed 5 times with CAP, followed by a 5 min wash with the sensitizing agent. A final CAP pulse showed a marked increase in both intensity and duration of the fluorescence increase in CAP-responding DRG neurons when compared with the previous pulse. The neurons still responded to a Hi- K^+ solution (100 mM).

4.2.9 – AzCA-4 is compatible with genetic tools

Genetically encoded $[Ca^{2+}]_i$ indicators, such as GCaMP3⁸⁶, have proven very useful for the study of neuronal activity *in vitro* and *in vivo*. We therefore tested the ability of **AzCA-4** to work in combination with this genetic tool. We crossed a mouse line that expresses the Cre-recombinase under the promoter of TRPV1⁸⁷, with a reporter mouse line that expresses GCaMP3 in a Cre-dependent manner (*Trpv1^{Cre/GCaMP3}*). Since the majority of DRG neurons express TRPV1 at embryonic stage E14.5⁸⁰, we observed that 90% of the DRG neurons in culture showed a faint basal fluorescence, confirming that recombination had occurred in most neurons at an earlier developmental stage.

However, upon application of CAP or **AzCA-4** alongside UV irradiation, only 30% of the neurons showed a Ca^{2+} dependent increase in fluorescence. This confirmed not only the correct function and localization of GCaMP3 in TRPV1-positive DRG neurons, but also that this small molecular photoswitch, **AzCA-4**, can be used in combination with a genetic tool.

To further confirm the applicability of **AzCA-4** and the use of genetically encoded $[Ca^{2+}]_i$ indicators to address physiologically relevant issues, we repeated the sensitization experiments on the *Trpv1^{Cre/GCaMP3}* mouse line (**Fig. 4.16b**, orange). These results again confirmed that TRPV1 could be sensitized to **AzCA-4** by BK or 5-HT, even in the *Trpv1^{Cre/GCaMP3}* mouse line.

4.2.10 – QX-314 can be selectively transported into DRG neurons

QX-314 is a permanently charged lidocaine derivative that blocks sodium channels from the intracellular side but is unable to penetrate the plasma membrane due to its charged nature⁸⁸. It has been shown that QX-314, and its photoswitchable derivative QAQ⁴³, could be shuttled into cells via TRPV1 when co-applied with CAP to open the channel⁸⁹. We hypothesized that $[Ca^{2+}]_i$ build-up is not only caused by Ca^{2+} -influx through TRPV1, but is a consequence of AP firing leading to Ca^{2+} release from intracellular stores. We showed **AzCA-4** (200 nM) in combination with $\lambda = 365$ nm irradiation, opened TRPV1 and allowed QX-314 to enter TRPV1-positive neurons in the DRG. The cells were first washed with a Hi-K⁺ solution (40 mM) causing massive electrical activity. After the cells recovered, 4 pulses of **AzCA-4** (200 nM, 5 s at $\lambda = 365$ nm) reached a steady state of TRPV1 desensitization. Next, **AzCA-4** was co-applied with QX-314 (5 mM), followed by another pulse of **AzCA-4** and a final pulse of the

Hi-K⁺ solution. By comparing the peak heights of the first and final Hi-K⁺ pulses (HK₁ and HK₂, respectively), we observed that the cells which were responsive to **AzCA-4** showed a lower HK₂/HK₁ ratio when compared to cells which did not respond to **AzCA-4** (Fig. 4.18). These results indicate that in combination with **AzCA-4**, TRPV1 could be used as an import channel to localize a charged anesthetic in TRPV1-positive cells, only.

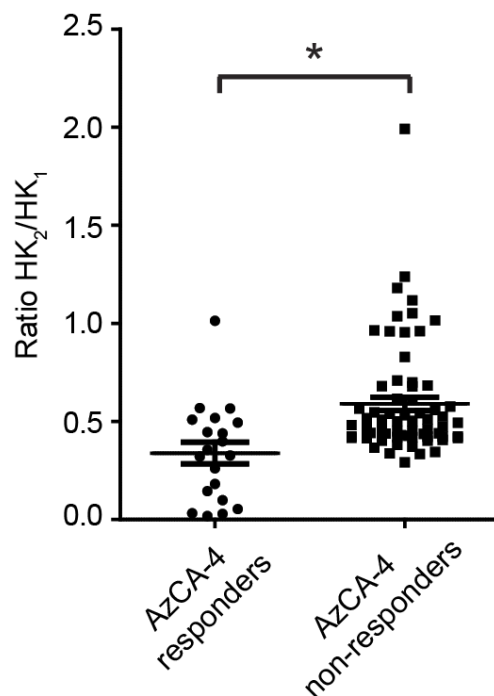


Figure 4.18 | QX-314 could be shuttled into TRPV1-positive DRG neurons using AzCA-4. After the co-application of **AzCA-4** (200 nM) and QX-314 (5 mM), the peak heights of the Ca²⁺ signals of the Hi-K⁺ (40 mM) pulses before (HK₁), and after (HK₂) drug application were compared. The results were plotted as the peak-height ratio of two pulses, HK₂/HK₁, calculated for both **AzCA-4** responding, and **AzCA-4** non-responding neurons. Error bars were calculated as \pm s.e.m.

4.2.11 – Synthesis and characterization of a red-shifted AzCA derivative

Azobenzenes can be synthetically modified to allow isomerization between the *trans*- and *cis*-states with longer-wavelength irradiation⁹⁰. This lower-energy light is less damaging to cells and allows deeper penetration into tissue. Tetra-*ortho*-chlorination of the azobenzene core enables photoswitching between the *trans*- and *cis*-states with violet/blue and green light, respectively⁹¹. This bioisosteric modification eliminates the need for UV light during photostimulation, and causes a relatively minimal change to the azobenzene structure. Recently, our lab developed a method to synthesize tetra-*ortho*-chloro azobenzenes via late-stage functionalization of an already existing azobenzene core³⁷. This method utilizes a Pd-catalyzed C-H activation in AcOH, with *N*-chlorosuccinimide as a chlorine source. We applied this method to synthesize the first red-shifted fatty acid, *red*-FAAzo-4 (Fig. 4.19a). Sequential attachment of the vanilloid headgroup afforded *red*-AzCA-4 in high yield. The activation wavelength of *red*-AzCA-4 was significantly shifted by 200 nm towards the visible range, as it could be isomerized to its active *cis*-form with green light. The maximum *cis*-content was achieved on irradiation at $\lambda = 560$ nm green light, and maximum *trans*-content under $\lambda = 400$ nm violet light (Fig 4.19b).

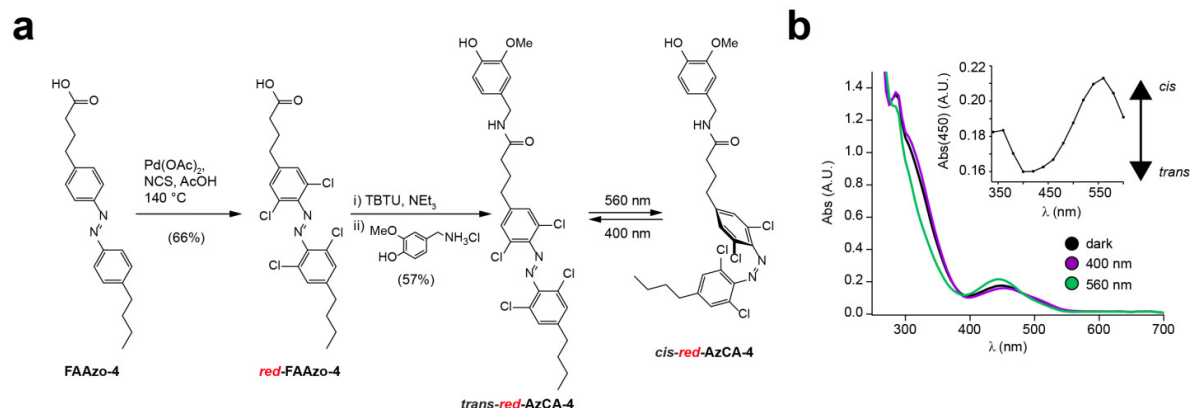


Figure 4.19 | Synthesis and characterization of a red-shifted AzCA. (a) The tetra-*ortho* chlorinated photoswitch *red*-AzCA-4 was synthesized from the red-shifted FA, *red*-FAAzo-4. (b) The UV-Vis absorption spectra of *red*-AzCA-4 in its dark-adapted, violet-adapted ($\lambda = 400$ nm) and green-adapted ($\lambda = 560$ nm) states. The greatest *trans*-content was achieved under $\lambda = 400$ nm irradiation, while the greatest *cis*-content was achieved with $\lambda = 560$ nm light.

4.2.12 – Red-shifted optical control of TRPV1 with tetra-*ortho* chlorinated azobenzenes

We then tested the utility of *red-AzCA-4* as a photoswitchable vanilloid in HEK293T cells expressing TRPV1-YFP. Like its parent compound, *red-AzCA-4* displayed an increased efficacy towards the ion channel when isomerized to its *cis*-configuration on irradiation with green light. Whole-cell voltage clamp experiments revealed an increased current in the presence of *cis-red-AzCA-4* when compared to *trans-red-AzCA-4* (**Fig. 4.20a**). The application of *red-AzCA-4* (500 nM) under $\lambda = 400$ nm irradiation caused only a small inward current when the cell was held at -60 mV, which could be greatly potentiated by green light (**Fig. 4.20b**). As previously described for other tetra-*ortho-chloro* substituted azobenzene derivatives⁹¹, *red-AzCA-4* could be photoactivated with UV-A light as well (**Fig. 4.20c,d**). These results demonstrate that the tetra-*ortho*-chlorination of **AzCA-4** did not hinder its utility as a photoswitchable TRPV1-agonist, and will facilitate the compounds use in more complex tissues by eliminating the need for high-energy UV-A light for photoactivation.

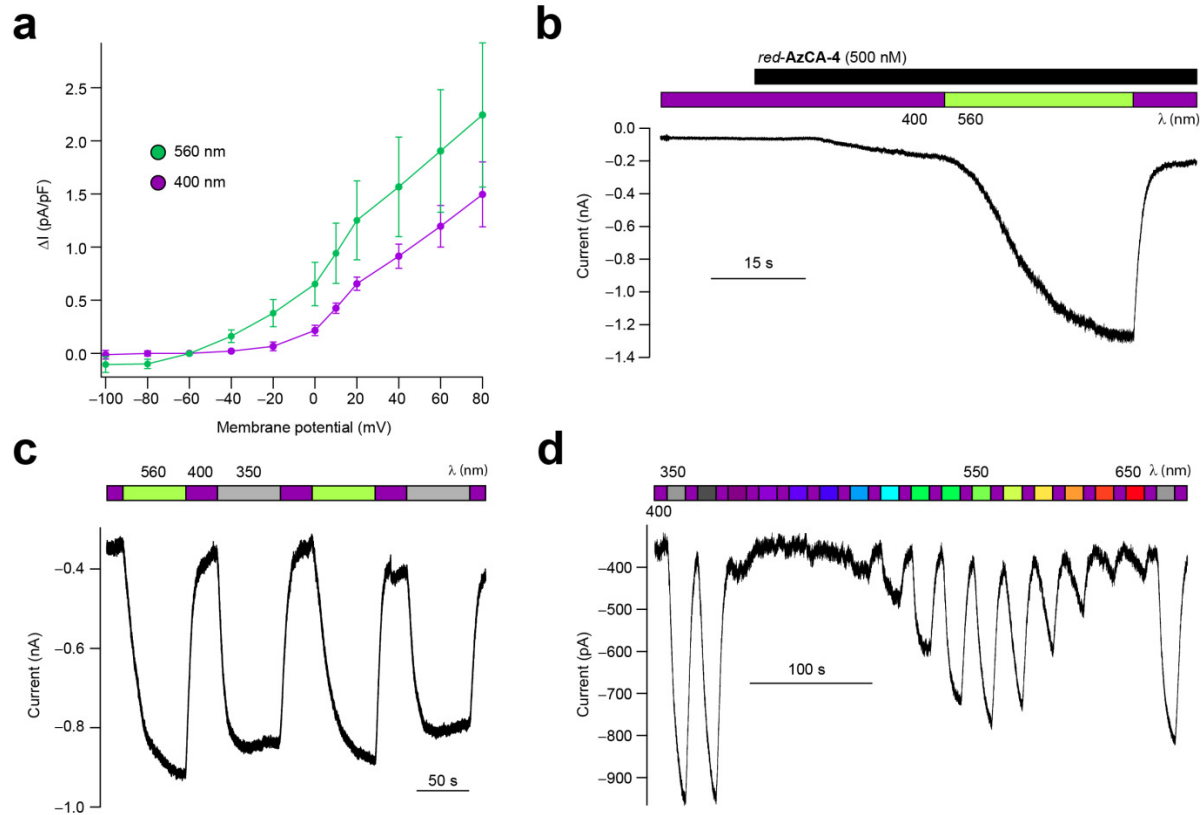


Figure 4.20 | *red-AzCA-4* enables control of TRPV1 with green light. In HEK293T cells transiently expressing TRPV1-YFP: (a) the current-voltage plot showed that *red-AzCA-4* (500 nM) was a more potent TRPV1-agonist in its *cis*-configuration ($n = 3$), displayed as the change in current from the baseline holding potential (-60 mV, pA/pF) as a function of the IV holding potential (mV). (b) Application of *red-AzCA-4* (500 nM) under violet light produced only a small inward current, which was reversibly potentiated with green light. (c) TRPV1 could be repeatedly cycled ON and OFF with UV-A ($\lambda = 350$ nm)/green ($\lambda = 560$ nm) and violet light ($\lambda = 400$ nm), respectively, as was also shown by (d) an action spectrum. Holding potential -60 mV. Error bars were calculated as \pm s.e.m.

4.3 – Discussion

In this study, we present eight photoswitchable FAs, the FAAzos. We expect that these lipophilic modules will allow us to place a variety of lipid-modulated biological targets under photopharmacological control. The FAAzos are FAs mimetics, resembling in particular highly unsaturated FAs like AA. These compounds could be used as molecular building blocks for the construction of more complicated photolipids which could facilitate the optical control of a wide range of ion channels, GPCRs, and enzymes associated with FA signaling.

We hypothesized that an azobenzene photoswitch would be best suited towards integration into the FA backbone, as its hydrophobic nature may cause only a minimal disruption to the properties of a natural aliphatic chain. The FAAzos allow the position of the switch to be fine-tuned in order to complement SARs between the ligand and its target. As a first installment illustrating this concept, we showed that the FAAzos could be incorporated into other photolipids through a simple amide coupling reaction. In HEK293T cells, three AzCAs stood out as the most promising candidates to enable the optical control of TRPV1 and showed significant, light-dependent efficacy at concentrations as low as 100 nM. All three compounds were more potent in their *cis*-configuration. Due to the structural similarities between the AzCAs and other vanilloid TRPV1 agonists, we presume that the AzCAs act on the same vanilloid binding site as CAP, olvanil and arvanil. This is further supported by the requirement of the vanilloid headgroup, as was shown by the inactivity of **FAAzo-2-4**. Channel activation by **AzCA-4** can also be completely blocked by the application of CPZ, a known competitive antagonist for CAP, suggesting a common binding site and mode of activation.

We then demonstrated that **AzCA-4** was a powerful modulator of DRG neurons in wt mice and the *Trpv1^{Cre/GCaMP3}* mouse line. Control experiments in untransfected HEK293T cells and *Trpv1^{-/-}* mice showed no response to **AzCA-4**, even upon light stimulation. These results rule out the possibility of action through off-target mechanisms. This characteristic is essential for the study of signal transduction in the nociceptive neurons involved in inflammatory pain. To this end, we envision that **AzCA-4** could be used to study TRPV1-mediated hyperalgesia and the physiological processes involved with the inflammatory state that occurs at sites of tissue injury. We showed that application of components of the so-called “inflammatory soup”, such as BK or 5-HT, could sensitize TRPV1 to **AzCA-4** in DRG neurons. Furthermore, we proved that **AzCA-4** could be used in conjunction with genetic tools such as the GCaMP3 $[Ca^{2+}]_i$ indicator selectively expressed in TRPV1-positive mouse neurons.

Importantly, **AzCA-4** allowed for greater temporal control over TRPV1 than that which can be achieved by other small molecule agonists such as CAP, olvanil and arvanil. By working at an optimized concentration, **AzCA-4** showed no activity towards TRPV1 in its *trans*-configuration, but rapid TRPV1 activation was observed when it was isomerized to its *cis*-configuration. This ON and OFF effect became even more pronounced in neuronal systems when the non-linear, “all or nothing,” nature of the AP took effect. Previous studies have suggested that the rate of TRPV1 activation determines the balance between agonist potency and pungency⁴²⁻⁴⁵. Molecular weight and lipophilicity normally define the pharmacodynamics of TRPV1 agonists^{92,93}. In the case of AzCAs, light provides another level of control. We showed that the magnitude and rate of cellular activation could be precisely tuned by adjusting the ON wavelength between $\lambda = 350-390$ nm. Therefore, AzCAs could provide a platform for the further understanding of hyperalgesia and could lead to the development of new anesthetics.

When using CAP to stimulate C-fibers in the saphenous nerve, a relatively slow increase in AP firing was observed. This effect was likely caused by the time required for CAP to diffuse through the skin and plasma membrane to reach the vanilloid binding site⁹⁶⁻⁹⁸. We showed that **AzCA-4** could be applied to neurons its dark-adapted, relatively inactive configuration. Upon isomerization, TRPV1 was activated and AP firing was immediately observed. It is this characteristic which makes **AzCA-4** a useful tool for the study of nociception, a process that relies on the rapid transmission of noxious stimuli from the periphery towards the coordinating centers of the central nervous system. **AzCA-4** also possesses significant advantages when compared to other small molecules that have been used to place TRPV1 under the control of light. Caged CAP is a useful tool that has increased the level of control with which we are able to activate TRPV1⁹⁹. However, compound uncaging and TRPV1 activation is a non-reversible, one-shot process. Repeated activation by uncaging relies on fast acting transporters or deactivating enzymes to clear the synapse of the free ligand²⁴. The fact that CAP and its analogs exhibit long-lasting effects suggests that they do not undergo transporter-mediated reuptake or significant enzymatic hydrolysis. These aspects are circumvented by the use of **AzCA-4**, which allows for successive rounds of activation/inactivation without the requirement for washout of the drug. Previously, we showed that photoswitchable TRPV1 *antagonists* can optically control the activity of a constitutively active agonist upon photoswitching⁷⁴. In comparison, **AzCA-4** greatly simplifies this system and is capable of activating TRPV1 directly. This permits the optical control of neuronal excitability without the use of a second factor. Advantageously, **AzCA-4** is relatively inactive

in the dark, therefore a more rapid and reproducible initiation of activity can be achieved after it has distributed itself uniformly within more complex tissues.

We also demonstrated that the tetra-*ortho*-chlorination of the FAAzos is a useful method to red-shift their activation wavelength. In this case, the *ortho*-hydrogen atoms on the azobenzene are substituted with chlorine atoms, enabling isomerization to the *cis*-state with longer-wavelength irradiation. In this case, this bioisosteric modification did not affect the activity of the pharmacophore. *red-AzCA-4* possessed similar potency to the parent compound **AzCA-4**. This suggests that TRPV1 efficacy is generally quite tolerant of modifications in the hydrophobic portion of the molecule. We envision that this new red-shifted tool will enable the optical control of TRPV1 in more complex tissues, and facilitate *in vivo* applications.

In conclusion, this study provides the first application of photopharmacology to lipid signaling. Given the ubiquitous distribution of FA derivatives at all levels of nature, we envision that the FAAzos and their conjugates will emerge as broadly applicable tools for the optical control of biological functions which rely on protein-lipid interactions.

4.4 – Supporting information

4.4.1 – Whole-cell electrophysiology in HEK293T cells

HEK293T cells (obtained from the Leibniz-Institute DSMZ: #305) were incubated at 37 °C (10% CO₂) in Dulbecco's Modified Eagle Medium (DMEM) + 10% fetal bovine serum (FBS) and were split at 80-90% confluency. For cell detachment, the medium was removed and the cells were washed with Ca²⁺-free PBS buffer and treated with trypsin for 2 min at 37 °C. The detached cells were diluted in growth medium and plated on acid-etched coverslips coated with poly-L-lysine in a 24-well plate. 50,000 cells were added to each well in 500 μL standard growth medium along with the DNA (per coverslip: 500 ng TRPV1-YFP⁷⁷) and JetPRIME[®] transfection reagents according to the manufacturer's instructions (per coverslip: 50 μL JetPRIME[®] buffer, 0.5 μL JetPRIME[®] transfection reagent). The transfection medium was exchanged for normal growth media 4 h after transfection and electrophysiological experiments were carried out 20-40 h later. Whole cell patch clamp experiments were performed using a standard electrophysiology setup equipped with a HEKA Patch Clamp EPC10 USB amplifier and PatchMaster software (HEKA Elektronik). Micropipettes were generated from "Science Products GB200-F-8P with filament" pipettes using a Narishige PC-10 vertical puller. The patch pipette resistance varied between 5-9 MΩ. The bath solution contained: Solution A (in mM): 150 NaCl, 6.0 CsCl, 1.0 MgCl₂, 1.5 CaCl₂, 10 HEPES, 10 D-glucose (adjusted to pH 7.4 with 3 M NaOH)¹⁰⁰ or Solution B (in mM): 140 NaCl, 5 KCl, 5 HEPES, 1 MgCl, 5 D-glucose (adjusted to pH 7.4 with 3 M NaOH). The pipette solution contained: Solution A' (in mM): 150 NaCl, 3 MgCl₂, 10 HEPES, 5 EGTA (adjusted to pH 7.2 with 3M NaOH) or solution B' (in mM): 100 K-gluconate, 40 KCl, 5 HEPES, 5 MgATP, 1 MgCl₂ (adjusted to pH 7.2 with 1M KOH). The cells were first visualized to contain TRPV1-YFP by irradiation at λ = 480 nm using a Polychrome V (Till Photonics) monochromator. All cells had a leak current between -15 to -300 pA upon break-in at -60 mV. All voltage clamp measurements were carried out at a holding potential of -60 mV. The cells were held at 0 pA for current clamp measurements. The compounds were applied by puff pipette using a "Toohey Spritzer pressure system IIe" at 25 psi. The puff pipette resistance varied between 3-5 MΩ. All experiments were performed at room temperature.

4.4.2 – Determination of AzCA photoswitching properties

The photoswitching properties of the prepared compounds were assessed using whole-cell voltage clamp electrophysiology in HEK293T cells transiently expressing TRPV1-YFP⁷⁷. The compounds were dissolved as stock solutions in DMSO (2-6 mM) and then diluted into warmed extracellular solution at a concentration of 1 μ M. The cell was held at -60 mV and voltage ramps (-100 to $+100$ mV over 5 s) were applied under both $\lambda = 450$ nm and $\lambda = 350$ nm irradiation. The AzCA-derivative (1 μ M) was then constantly applied (puff pipette application) while switching between the two wavelengths until a steady state of activity/desensitization was observed upon photoswitching (**Fig. 4.6a**). The voltage ramps were applied again under each wavelength and the current change (ΔI) between the baseline (-60 mV) and the ramp maximum ($+100$ mV) was recorded (**Fig. 4.6b**). $\Delta I(350$ nm) was normalized to $\Delta I(450$ nm) and this potentiation factor was averaged over multiple cells and plotted in **Fig. 4.5b**. TRPV1 activation and inactivation kinetics were determined by exponential curve fitting in Igor Pro.

4.4.3 – Dorsal root ganglion neuronal culture

Dorsal root ganglia (DRG) were quickly dissected, collected in ice-cold DRG medium and digested in 1 mg/mL Collagenase IV (Gibco) at 37 °C for 50 min to dissociate the tissue followed by incubation in 0.05% trypsin (Gibco) in phosphate-buffered saline (PBS) at 37 °C for 15 min. The trypsin was removed and cells were re-suspended in 1 mL of DRG medium. After gentle trituration, the DRGs were loaded onto a 2 mL BSA pillow and centrifuged at 250 g for 10 min to separate the myelin and debris. The resulting cell pellet was suspended in 50 μ L fresh DRG medium and plated onto poly-D-lysine (100 μ g/mL) and laminin (10 μ g/mL) coated coverslips. The cells were flooded with medium 30 min after plating.

4.4.4 – Whole-cell electrophysiology in cultured DRG neurons

Electrophysiological recordings of DRG neurons from 14-21 days old mice were performed using a HEKA 10 amplifier (HEKA instrument) and an ITC Analog Digital Converter (HEKA) in whole-cell voltage clamp or current clamp configuration. The currents were filtered with a built-in 5 kHz 8-pole Bessel filter and digitized at 50 kHz. The currents were analyzed using Clampfit 10.3 (Molecular Devices) and graphs were plotted in Prism 5 (Graphpad). Experiments were performed 1-3 days after plating. The *Trpv1^{Cre}* and the *GCaMP3* reporter mice were acquired from Jackson laboratory. DRG neurons were prepared for imaging from 25 wk old *Trpv1^{Cre/GCaMP3}* mice. The extracellular solution contained in mM: 150 NaCl, 5 KCl, 10 HEPES, 10 D-glucose, 2 CaCl₂, 1 MgCl₂. The intracellular solution contained (values in mM): 130 KCl, 10 HEPES, 10 EGTA, 1 CaCl₂, 1 MgCl₂, 2 MgATP, 1 NaGTP, 4 NaCl, 4 PhosphoCreatine.

Thick walled electrodes (Harvard apparatus, 1.17x0.87 mm, external and internal diameter respectively) were pulled with a Sutter P-197 puller to a final resistance of 3-5 MΩ. After the break-through, the intracellular solution was dialyzed with the intracellular medium for at least 1 min prior to the beginning of the recordings. Series resistance compensation reached values between 70-90%. Neurons were selected to have a leak current less than -100 pA upon break-in at -60 mV. All experimental procedures were carried out in accordance with the State of Berlin Animal Welfare requirements and were approved by this authority.

4.4.5 – Intracellular Ca²⁺ imaging

DRG neurons plated on a 5 mm glass coverslip were placed in a recording chamber of 300 μL volume (Harvard Apparatus) and were continuously perfused with extracellular solution at a rate of 2 mL/min. Wild type (wt) neurons cells were loaded with Cal-520 (5 μM, AAT-Bioquest) Ca²⁺ dye for 1 h at 37 °C in the presence of pluronic acid 0.02% dissolved in Ringer solution (values in mM): 140 NaCl, 5 KCl, 2 CaCl₂, 2 MgCl₂, 10 HEPES and 10 D-glucose, adjusted to pH 7.4. CAP (100 nM, Tocris) was dissolved in extracellular solution from a stock concentration of 10 mM in ethanol. Fluorescent images were acquired with Metafluor Software (Molecular Devices) and analyzed in Clampfit. All experiments were performed at room temperature. The dye excitation was performed at $\lambda = 480$ nm. The results were plotted as the change in fluorescence over baseline fluorescence ($\Delta F/F$) as a function of time (s).

4.4.6 – Ex vivo skin nerve preparation

**Note: ex vivo skin nerve experiments were performed by Dr. Med. Rabih Moshourab (MDC Berlin) and are included here for clarity.*

The skin-nerve preparation was used as previously described to record from single primary afferents¹⁰¹. Mice were sacrificed with CO₂ inhalation for 2-4 min followed by cervical dislocation. The saphenous nerve and the shaved skin of the hind limb were dissected free and placed in an organ bath at 32 °C. The chamber was perfused with a synthetic interstitial fluid (SIF buffer) the composed of (in mM): 123 NaCl; 3.5 KCl; 0.7 MgSO₄; 1.7 NaH₂PO₄; 2.0 CaCl₂; 9.5 Na-gluconate; 5.5 D-glucose; 7.5 sucrose; and 10 HEPES, at a pH of 7.4. The skin was placed with the corium side up in the organ bath for pharmacological application to the receptive fields of single sensory units. The saphenous nerve was placed in an adjacent chamber on a mirror and under microscopy, fine filaments were teased from the nerve and placed on the recording electrode. Electrical isolation was achieved with mineral oil. Signals from the filaments were amplified (Neurolog System, Digitimer Ltd) and sampled using a data acquisition system (PowerLab 4.0, ADInstruments). The receptive fields of individual mechanically sensitive C-fiber units were identified by manually probing the skin with the blunted tip of a glass probe. Their conduction velocities (calculated by dividing conduction distance over electrical latency for the first spike) were determined using an electrical stimulator (1 MΩ). All C-fibers studied were identified by mechanical probing and were heat sensitive (C-MH). The conduction velocities were in the C-fiber range (< 1 m/s). The thermal sensitivity of identified C-fibers was tested with a computer controlled peltier device (3x5 mm, Yale University medical school, Medical Instruments, New Haven, USA). A heat ramp was delivered from 32 to 48 °C at a rate of 1 °C/s to the mechanically localized receptive fields of single C-fibers. The receptive fields of heat sensitive C-fibers were isolated with a metal cylinder ring (5 mm inner diameter, 10 mm in height, and 1.44 g weight) for the administration of the drugs (**AzCA-4** or CAP). The metal ring was tested for leakage before drug application. A stock solution of **AzCA-4** was prepared in dimethyl sulfoxide and diluted in SIF buffer. 100 µL of a 1 µM **AzCA-4** solution dissolved in SIF buffer was applied into the ring. The pharmacological testing protocol with **AzCA-4** had 4 distinct successive phases: 1) 60 s recording time prior to the application of **AzCA-4**; 2) 60 s recording after application of **AzCA-4**; 3) 20 s of recording during photostimulation of **AzCA-4** with LED light, $\lambda = 365$ nm (Mic-LED-365, Prizmatix); 4) 20 s of recording during photoinhibition of **AzCA-4** with LED light,

$\lambda = 460$ nm (UHP-LED-460, Prizmatix). **AzCA-4** was kept in the ring for 300 s and a second photostimulation with LED light $\lambda = 360$ nm for 20 s was applied to test the reproducibility of the initial responses. 100 μ L of CAP (1 μ M, Sigma) were administered onto the receptive field of another set of heat sensitive C-fibers for 20 s before wash out. Recordings were obtained for 1 min prior-to, and 2 min after CAP administration. Spikes were discriminated off-line with the spike histogram extension of the software. Data was obtained from 6 skin-nerve preparations (2 *Trpv1*^{-/-} and 4 wt C57Bl/6N mice). All experimental procedures were carried out in accordance with the State of Berlin Animal Welfare requirements and were approved by this authority.

4.4.7 – Compound switching

Compound switching for electrophysiology in HEK293T cells was achieved using a Polychrome V (Till Photonics) monochromator and the light beam was guided via a fiber-optic cable through the microscope objective and operated by the amplifier and PatchMaster software (HEKA Elektronik).

Compound switching for electrophysiology in DRG neurons was achieved using a Prizmatix Mic-LED-365 high power UV LED light source for illumination at $\lambda = 365$ nm, and the Prizmatix UHP-Mic-LED-460 ultra-high power LED light source for illumination at $\lambda = 460$ nm. The light beam was guided by a fiber-optic cable and pointed directly towards the cells from above at an angle of about 45 ° from the side. The distance between the end of the cable and the cells was no greater than 2 cm. UV illumination during intracellular Ca²⁺ imaging was also performed using this light source.

4.4.8 – Compound synthesis and characterization

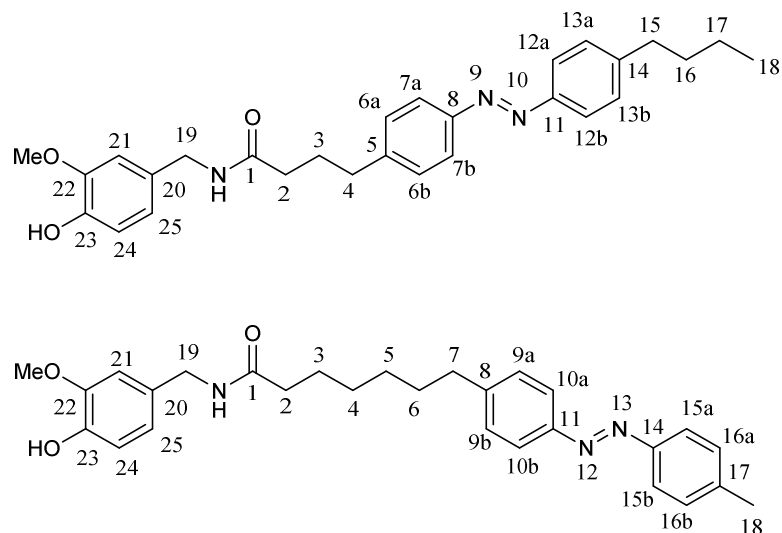


Figure 4.21 | Photolipid numbering system. Numbering of the atoms in the lipid chains was set in relation to the carboxylic acid, which was labelled atom #1, and then increasing towards the distal end of the carbon chain.

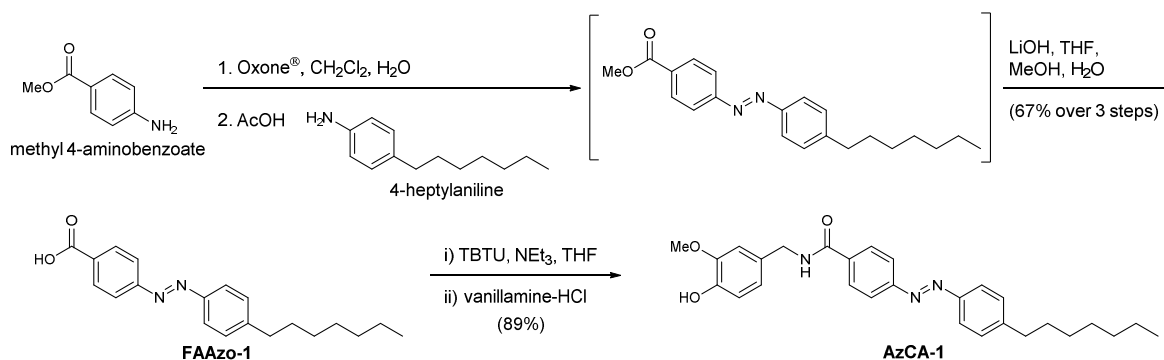


Figure 4.22 | Chemical synthesis of AzCA-1.

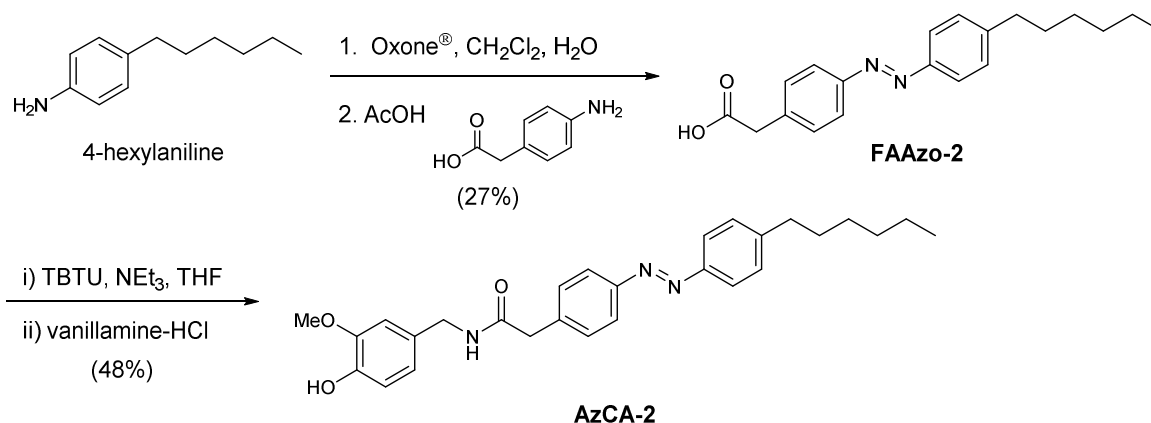


Figure 4.23 | Chemical synthesis of AzCA-2.

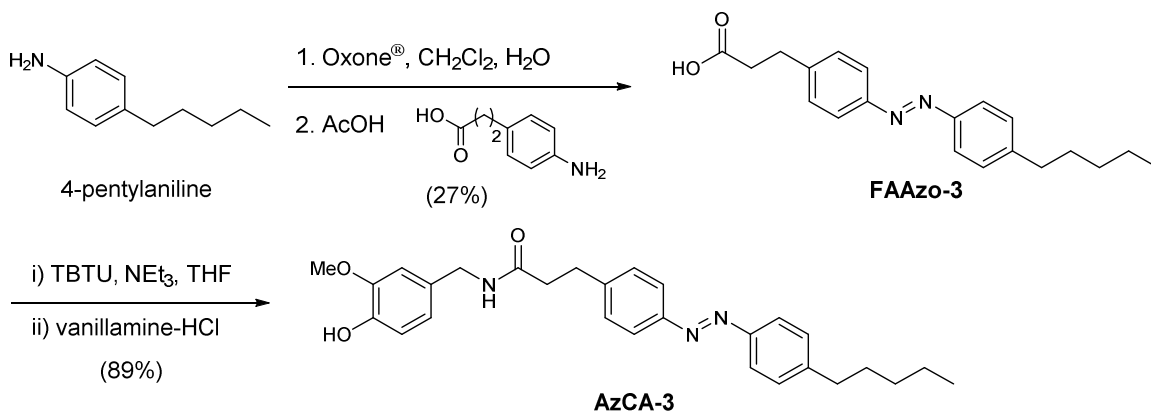


Figure 4.24 | Chemical synthesis of AzCA-3.

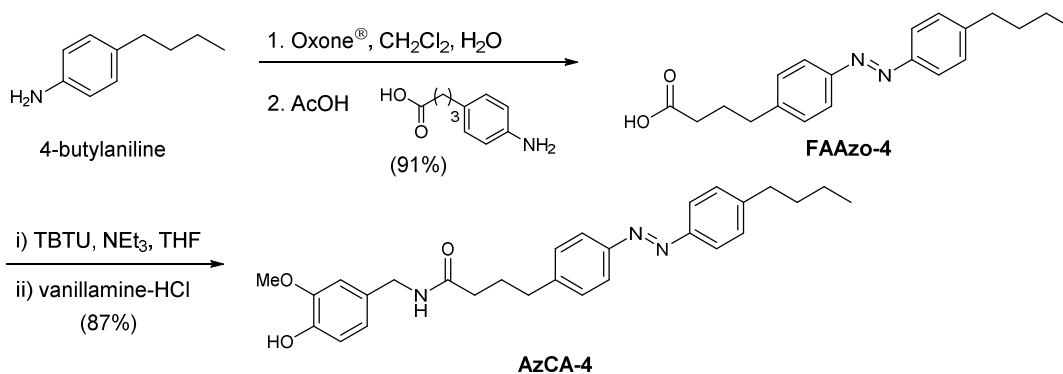


Figure 4.25 | Chemical synthesis of AzCA-4.

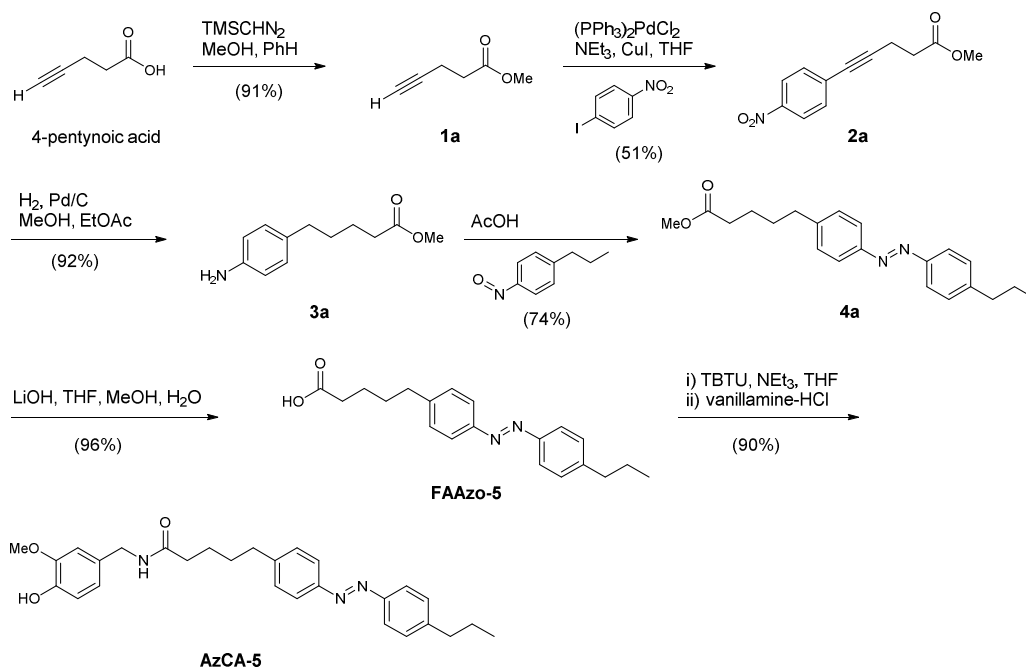


Figure 4.26 | Chemical synthesis of AzCA-5.

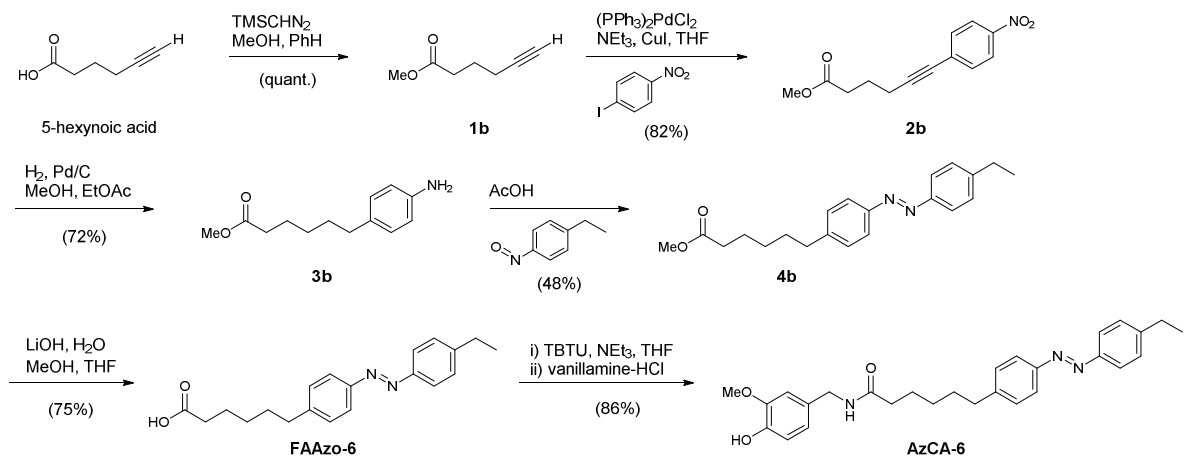


Figure 4.27 | Chemical synthesis of AzCA-6.

4 – Photoswitchable fatty acids enable optical control of TRPV1

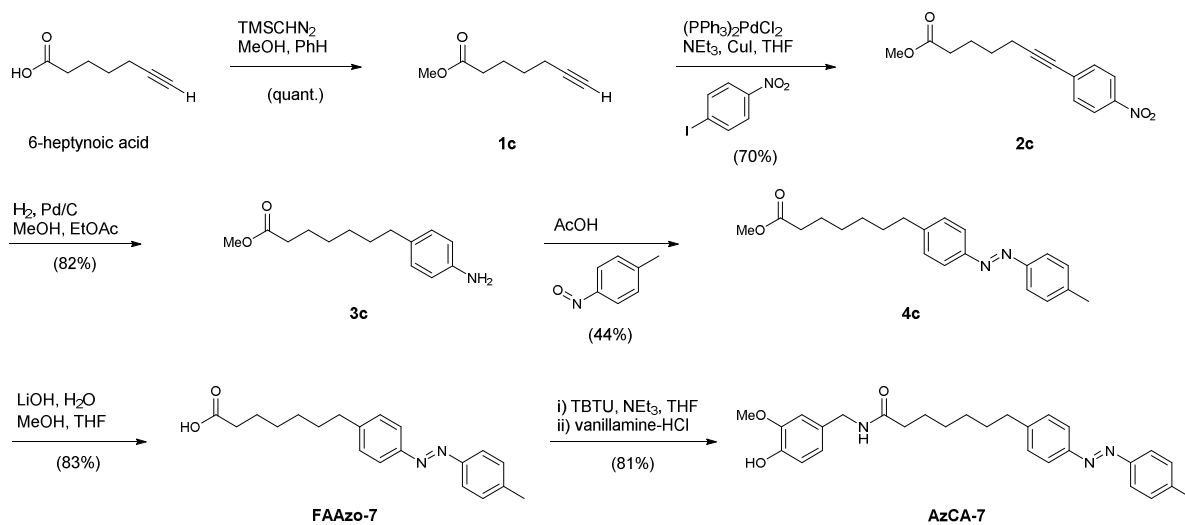


Figure 4.28 | Chemical synthesis of AzCA-7.

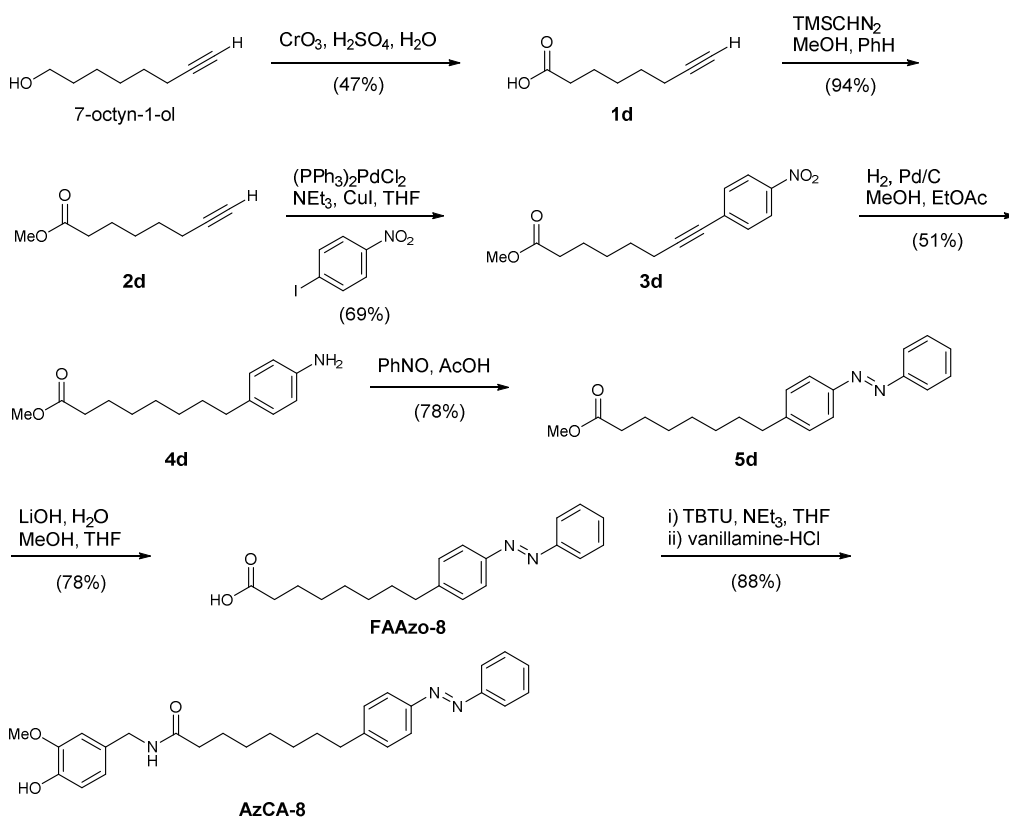
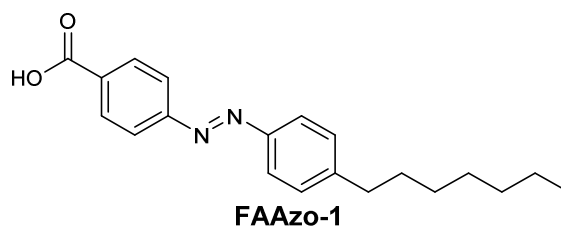


Figure 4.29 | Chemical synthesis of AzCA-8.

4.4.8.1 – 4-((4-Heptylphenyl)diazenyl)benzoic acid (FAAzo-1)

A solution of methyl 4-aminobenzoate (0.30 g, 2.0 mmol, 1.0 equiv.) in CH_2Cl_2 (20 mL) was treated with a solution of Oxone[®] (1.52 g, 5 mmol, 2.5 equiv.) in H_2O (20 mL) at 23 °C. The resulting biphasic reaction mixture was stirred vigorously at room temperature overnight or until all the aniline was consumed, as observed by TLC analysis. Subsequently, the phases were separated and the aqueous phase was extracted with CH_2Cl_2 (2x20 mL). The combined organic extracts were washed with H_2O (2x30 mL) and to the washed organic solution was then added 4-heptylaniline (0.38 g, 2.0 mmol, 1.0 equiv.) followed by AcOH (20 mL). The CH_2Cl_2 was removed under reduced pressure and the solution was left to stir overnight. The reaction mixture was then concentrated under reduced pressure and the residue was dissolved in CH_2Cl_2 (200 mL). The organic phase was washed with a saturated aqueous NaHCO_3 solution (2x50 mL), followed by H_2O (3x75 mL). The washed organic phase was dried over anhydrous Na_2SO_4 and then filtered. The filtrate was then concentrated under reduced pressure. The residue was dissolved in THF (18 mL) and MeOH (18 mL). This solution was treated with a 1 M aqueous lithium hydroxide solution (9 mL), and this solution was stirred for 2 h. The organic solvent was then removed under reduced pressure. The mixture was then acidified with a 2 M aqueous hydrochloric acid solution, and extracted with EtOAc (2x30 mL). The combined organic phases were washed with H_2O (2x40 mL), the washed solution was dried over anhydrous Na_2SO_4 and the dried solution was filtered. The filtrate was then concentrated under reduced pressure, and after being pre-absorbed onto SiO_2 (5 g, loaded from THF), the residue was purified by flash silica gel chromatography (50 g SiO_2 , 99:1 CH_2Cl_2 : H_2O) to yield **4-((4-heptylphenyl)diazenyl)benzoic acid (FAAzo-1)**, 450 mg, 67%) as a red solid.

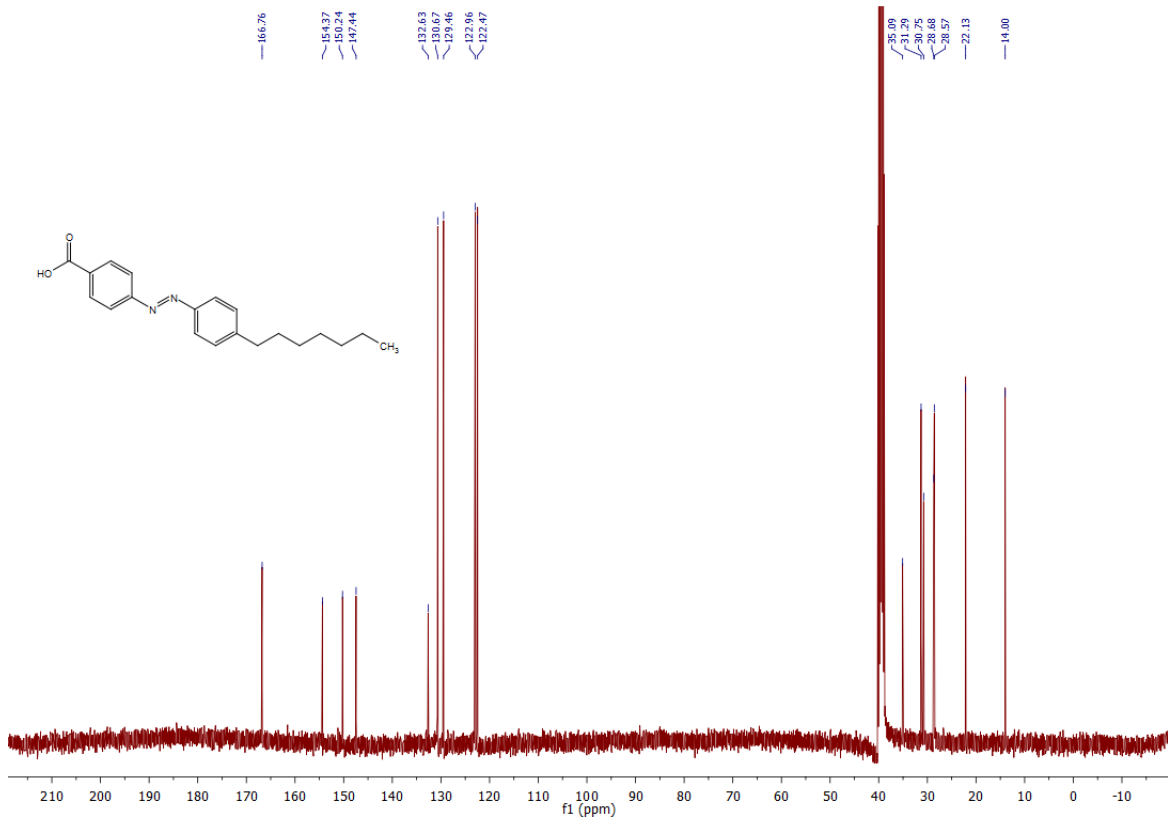
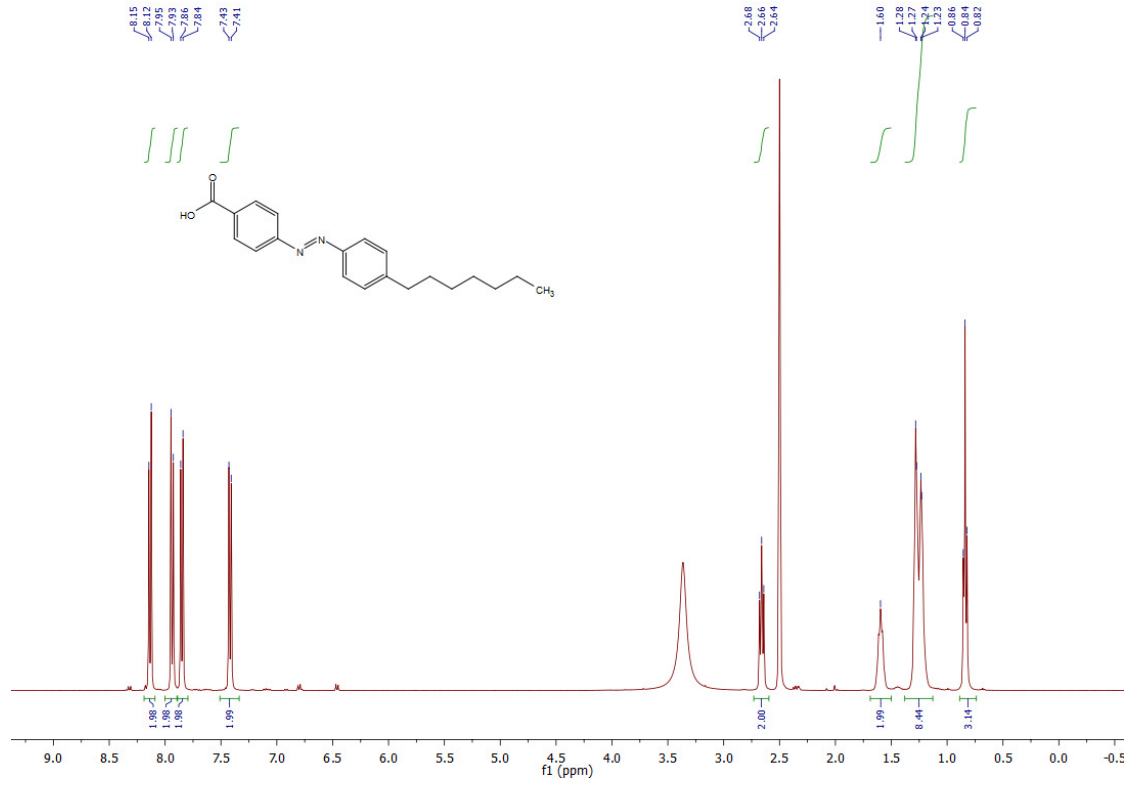
TLC (CH₂Cl₂): R_f = 0.35 (*cis*), 0.52 (*trans*).

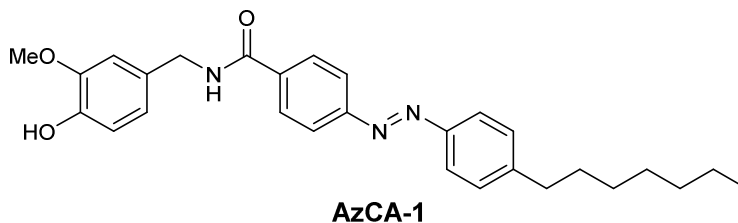
¹H NMR (D₆-DMSO, 400 MHz, 25 °C): δ 8.13 (d, 2H, H_{3_{a,b}}, J_{3,4} = 8.6 Hz), 7.94 (d, 2H, H_{4_{a,b}}, J_{4,3} = 8.6 Hz), 7.86 (d, 2H, H_{9_{a,b}}, J_{9,10} = 8.4 Hz), 7.43 (d, 2H, H_{10_{a,b}}, J_{10,9} = 8.4 Hz), 2.66 (m, 2H, H_{12_{a,b}}), 1.64-1.54 (m, 2H, H_{13_{a,b}}), 1.31-1.19 (m, 8H, H_{14_{a,b}}, H_{15_{a,b}}, H_{16_{a,b}}, H_{17_{a,b}}), 0.84 (t, 3H, H_{18_{a,b,c}}, J_{18,17} = 6.9 Hz).

¹³C NMR (D₆-DMSO, 101 MHz, 25 °C): δ 166.8 (C1), 154.4 (C5), 150.2 (C8), 147.4 (C11), 132.6 (C2), 130.6 (C_{3_{a,b}}), 129.5 (C_{10_{a,b}}), 123.0 (C_{9_{a,b}}), 122.5 (C_{4_{a,b}}), 35.1 (C12), 31.3 (C_{alk}), 30.8 (C13), 28.7 (C_{alk}), 28.6 (C_{alk}), 22.1 (C_{alk}), 14.0 (C18).

IR (neat, ATR): $\tilde{\nu}$ = 2952, 2920, 2850, 2662, 2543, 1678, 1601, 1582, 1501, 1424, 1289, 1221, 1143, 1125, 1111, 1098, 1011, 944, 868, 840, 805, 755, 722, 690, 672.

HRMS (EI⁺): *m/z* calcd. for [C₂₀H₂₄N₂O₂]⁺: 324.1838, found: 324.1834 ([M-e]⁺).



4.4.8.2 – *N*-(4-Hydroxy-3-methoxybenzyl)-4-((4-heptylphenyl)diazenyl)benzamide (AzCA-1)

A solution of **4-((4-heptylphenyl)diazenyl)benzoic acid (FAAzo-1, 25 mg, 77 μ mol, 1.0 equiv.)** and TBTU (25 mg, 77 μ mol, 1.0 equiv.) in EtOAc (3.0 mL) was treated with NEt_3 (24 mg, 3.0 equiv.) under an argon atmosphere at room temperature. After 1 h, vanillylamine hydrochloride (29 mg, 0.15 mmol, 2.0 equiv.) was added and stirring was continued at room temperature for 2 h. The solution was then diluted with EtOAc (15 mL) and washed with H_2O (2x20 mL). The phases were separated and the organic layer was dried over anhydrous Na_2SO_4 . The solvent was removed under reduced pressure and the residue was purified by flash silica gel chromatography (9.0 g SiO_2 , 40:1 CH_2Cl_2 :MeOH) to yield ***N*-(4-hydroxy-3-methoxybenzyl)-4-((4-heptylphenyl)diazenyl)benzamide (AzCA-1, 31 mg, 89%)** as a red solid.

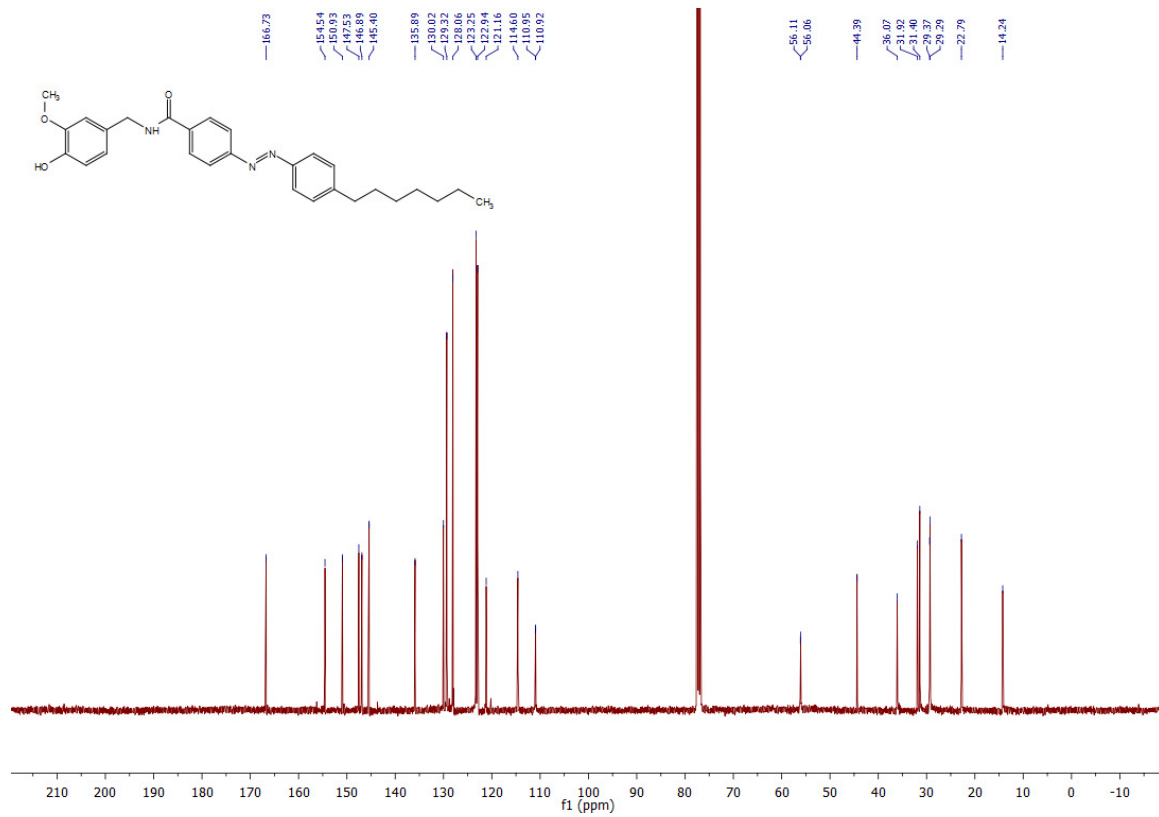
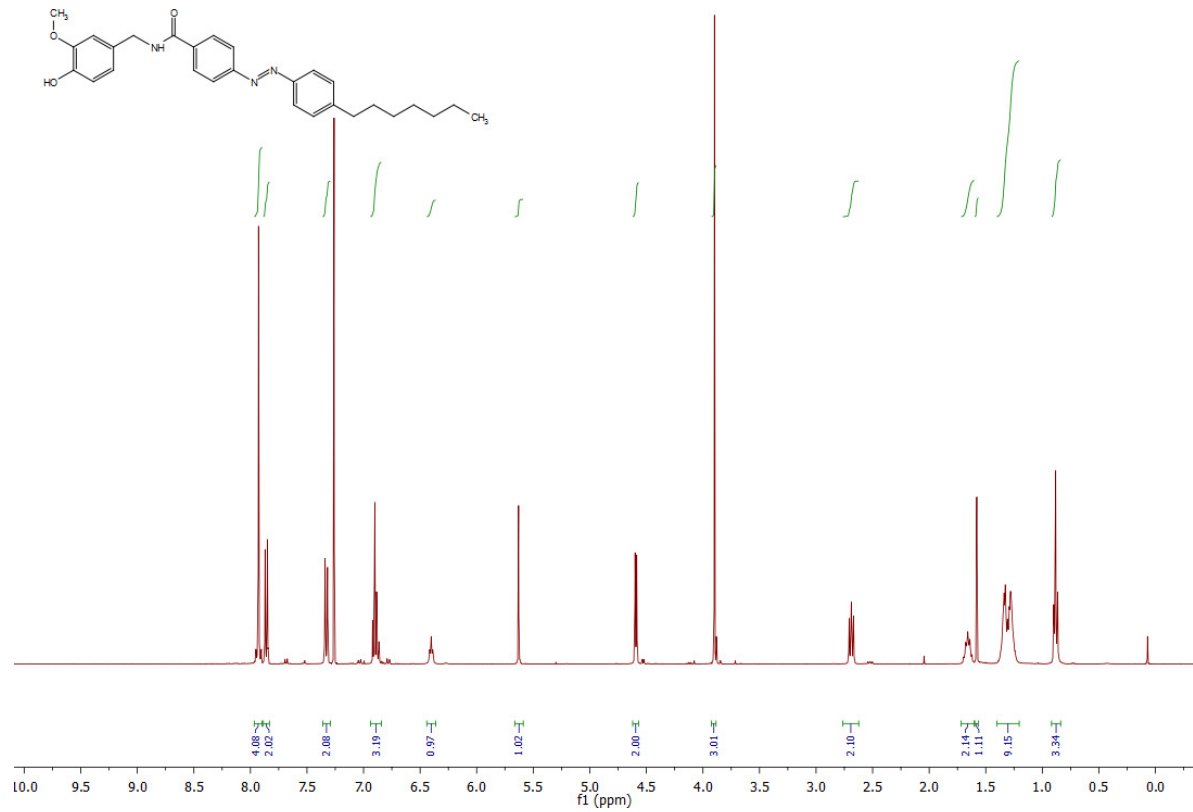
TLC (hexane/EtOAc, 1:1): $R_f = 0.48$.

$^1\text{H NMR}$ (CDCl_3 , 400 MHz, 25 $^\circ\text{C}$): δ 7.95-7.90 (m, 4H, H_{3a,b}, H_{4a,b}), 7.88-7.84 (m, 2H, H_{9a,b}, J_{9,10} = 8.4 Hz), 7.35-7.31 (m, 2H, H_{10a,b}, J_{10,9} = 8.4 Hz), 6.92-6.86 (m, 3H, H₂₁, H₂₄, H₂₅), 6.40 (t, 1H, NH, J_{NH,19} = 6.5 Hz), 5.63 (s, 1H, OH), 4.59 (d, 2H, H_{19a,b}, J_{19,NH} = 6.5 Hz), 3.90 (s, 3H, H_{26a,b,c}), 2.69 (t, 2H, H_{12a,b}, J_{12,13} = 7.6 Hz), 1.70-1.61 (m, 2H, H_{13a,b}), 1.37-1.23 (m, 8H, H_{14a,b}, H_{15a,b}, H_{16a,b}, H_{17a,b}), 0.88 (t, 3H, H_{18a,b,c}, J_{18,17} = 6.5 Hz).

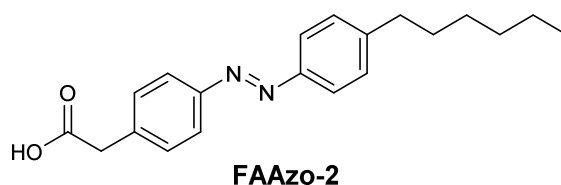
$^{13}\text{C NMR}$ (CDCl_3 , 101 MHz, 25 $^\circ\text{C}$): δ 166.7 (C1), 154.5 (C_{azo}), 150.9 (C_{azo}), 147.5 (C2), 146.9 (C22), 145.4 (C23), 135.9 (C11), 130.0 (C20), 129.3 (2C, C_{azo}), 128.1 (2C, C_{azo}), 123.3 (2C, C_{azo}), 122.9 (2C, C_{azo}), 121.2 (C21), 114.6 (C24), 111.0 (C25), 56.1 (C26), 44.4 (C19), 36.1 (C12), 31.9 (C_{alk}), 31.4 (C13), 29.4 (C_{alk}), 29.3 (C_{alk}), 22.8 (C17), 14.2 (C18).

IR (neat, ATR): $\tilde{\nu}$ = 3350, 3199, 2922, 2851, 1627, 1605, 1572, 1547, 1523, 1491, 1452, 1360, 1287, 1214, 1159, 1127, 1040, 868, 809, 773.

HRMS (ESI⁺): m/z calcd. for $[\text{C}_{28}\text{H}_{34}\text{N}_3\text{O}_3]^+$: 460.2600, found: 460.2592 ($[\text{M}+\text{H}]^+$).



4.4.8.3 – 2-(4-((4-Hexylphenyl)diazenyl)phenyl)acetic acid (FAAzo-2)



A solution of 4-hexylaniline (3.0 g, 17 mmol, 1.5 equiv.) in CH₂Cl₂ (200 mL), was treated with a solution of Oxone[®] (30.4 g, 99 mmol, 9.0 equiv.) in H₂O (200 mL) at 23 °C. The resulting biphasic reaction mixture was stirred vigorously at room temperature overnight or until all the aniline was consumed, as observed by TLC analysis. Subsequently, the phases were separated and the aqueous phase was extracted with CH₂Cl₂ (2x140 mL). The combined organic extracts were washed sequentially with a 1 M aqueous hydrochloric acid solution (240 mL), saturated aqueous NaHCO₃ (240 mL), and H₂O (3x240 mL). The washed organic layer was treated with 4-aminophenylacetic acid (1.7 g, 11 mmol, 1.0 equiv.) and AcOH (150 mL). The CH₂Cl₂ was then removed under reduced pressure at 35 °C and the solution was stirred overnight. The AcOH was then removed under reduced pressure and the red oil was azeotroped from toluene (PhMe, 100 mL). The residue was then purified by flash silica gel chromatography (0.30 kg SiO₂, 99:1 CH₂Cl₂:AcOH) to yield **2-(4-((4-hexylphenyl)diazenyl)phenyl)acetic acid (FAAzo-2)**, 1.00 g, 27%) as a red solid.

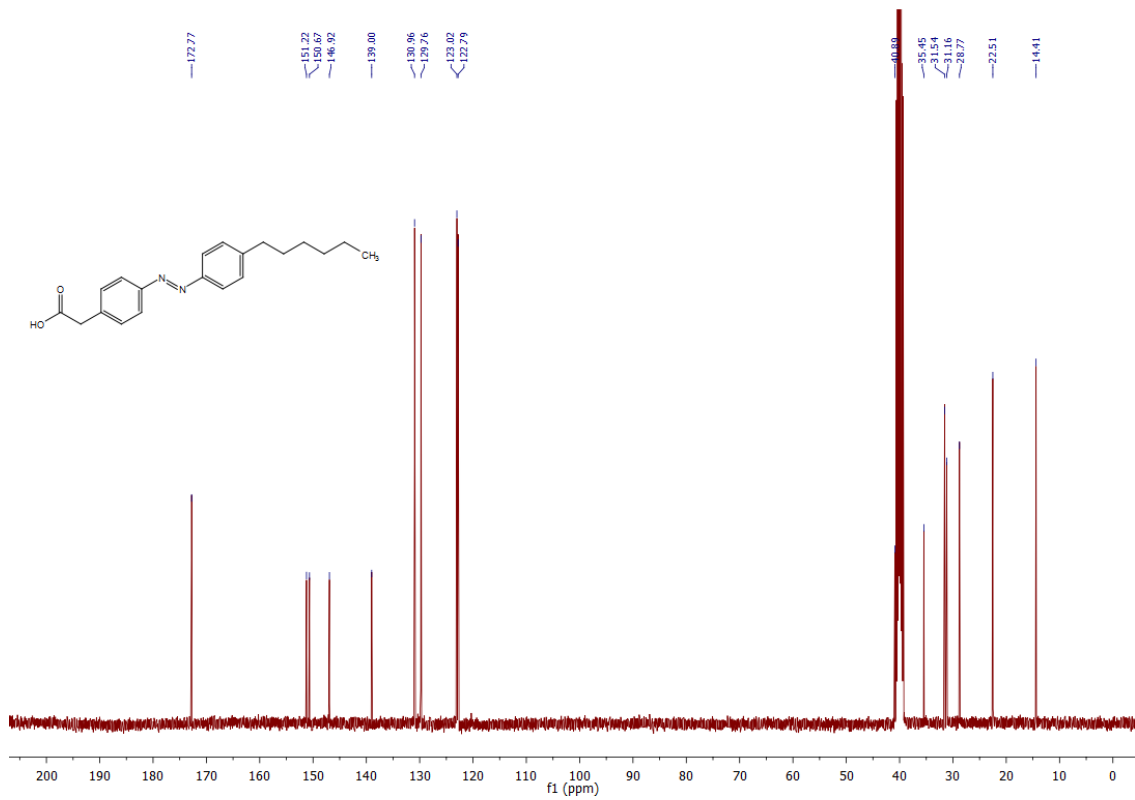
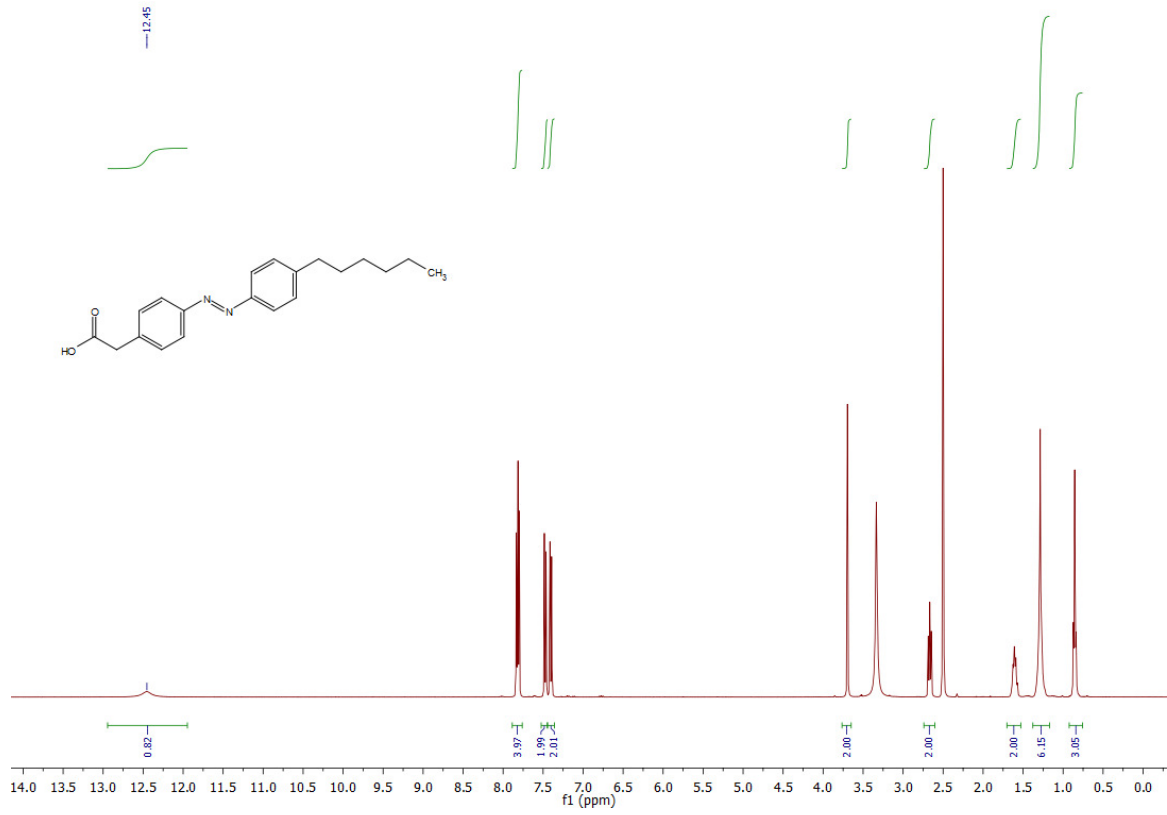
TLC (hexane/EtOAc, 1:1): R_f = 0.79.

¹H NMR (D₆-DMSO, 400 MHz, 25 °C): δ 12.45 (s, 1H, H_{COOH}), 7.84-7.79 (m, 4H, H_{5a,b}, H_{10a,b}, J_{5,4} ≈ J_{10,11} ≈ 8.3 Hz), 7.49-7.46 (m, 2H, H_{11a,b}, J_{11,10} ≈ 8.4 Hz), 7.42-7.38 (m, 2H, H_{4a,b}, J_{4,5} ≈ 8.4 Hz), 3.69 (s, 2H, H_{2a,b}), 2.66 (t, 2H, H_{13a,b}, J_{13,14} = 7.4 Hz), 1.65-1.56 (m, 2H, H_{14a,b}), 1.35-1.22 (m, 6H, H_{15a,b}, H_{16a,b}, H_{17a,b}), 0.85 (t, 3H, H_{18a,b,c}, J_{18,17} = 7.0 Hz).

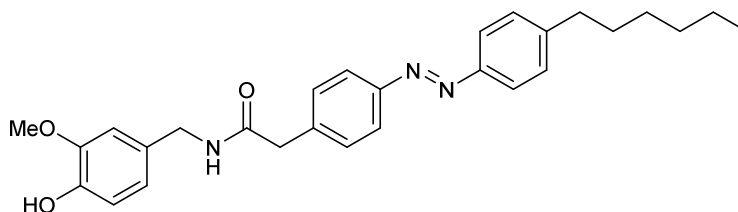
¹³C NMR (D₆-DMSO, 101 MHz, 25 °C): δ 172.8 (C1), 151.1 (C6), 150.7 (C9), 146.9 (C12), 139.0 (C3), 131.0 (C_{4a,b}), 129.8 (C_{11a,b}), 123.0 (C_{10a,b}), 122.8 (C_{5a,b}), 40.9 (C2), 35.5 (C13), 31.5 (C_{alk}), 31.2 (C4), 28.8 (C_{alk}), 22.5 (C_{alk}), 14.4 (C18).

IR (neat, ATR): $\tilde{\nu}$ = 3022, 2952, 2926, 2850, 2728, 2636, 1691, 1601, 1497, 1465, 1413, 1377, 1301, 1249, 1197, 1171, 1153, 1114, 1010, 904, 866, 844, 825, 783, 726, 677.

HRMS (EI⁺): *m/z* calcd. for [C₂₀H₂₄N₂O₂]: 324.1838, found: 324.1832 ([M-e]⁺).



4.4.8.4 – *N*-(4-Hydroxy-3-methoxybenzyl)-2-(4-((4-hexylphenyl)diazenyl)phenyl)acetamide (AzCA-2)



AzCA-2

***N*-(4-((4-Hexylphenyl)diazenyl)phenyl)acetic acid (FAAzo-2, 25 mg, 77 μ mol, 1.0 equiv.)** was converted to red solid ***N*-(4-hydroxy-3-methoxybenzyl)-2-(4-((4-hexylphenyl)diazenyl)phenyl)acetamide (AzCA-2, 17 mg, 48%)** in an analogous manner as described above for the preparation of ***N*-(4-hydroxy-3-methoxybenzyl)-4-((4-heptylphenyl)diazenyl)benzamide (AzCA-1)**. *Note: all reagents and solvents were scaled according to molarity.*

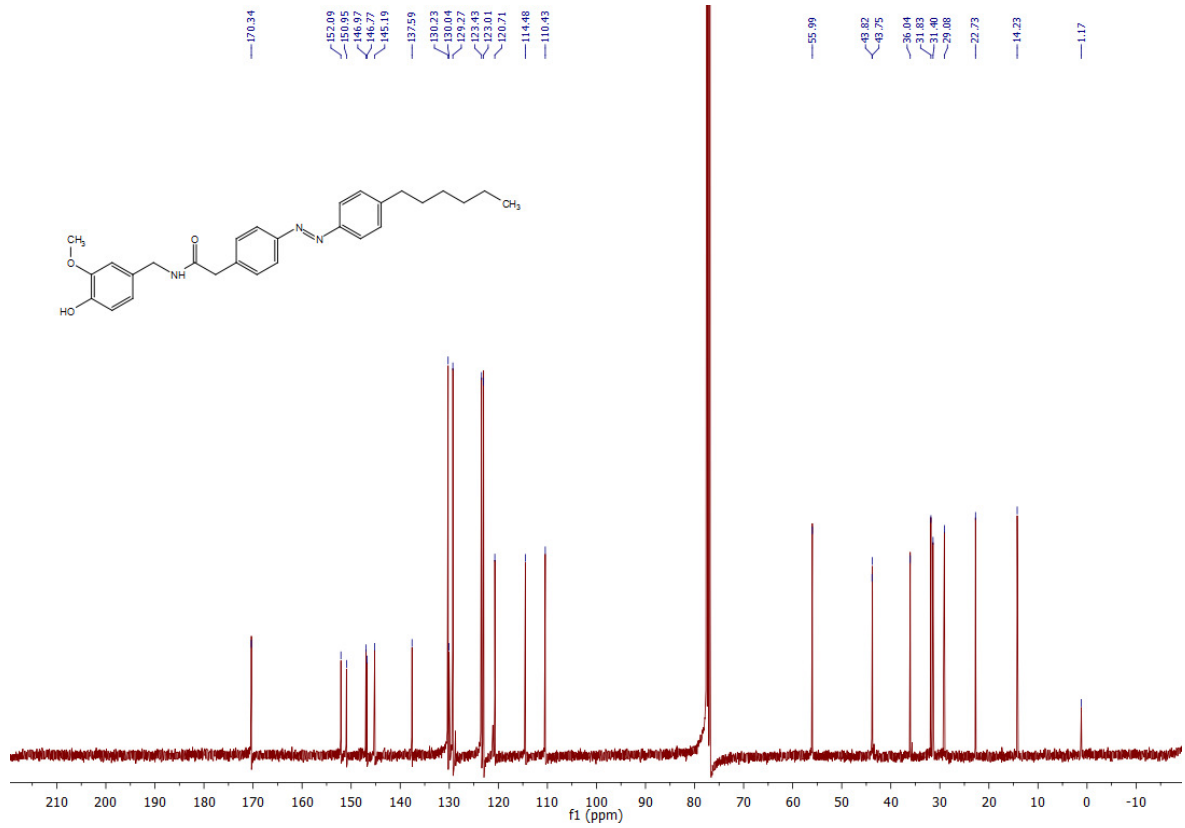
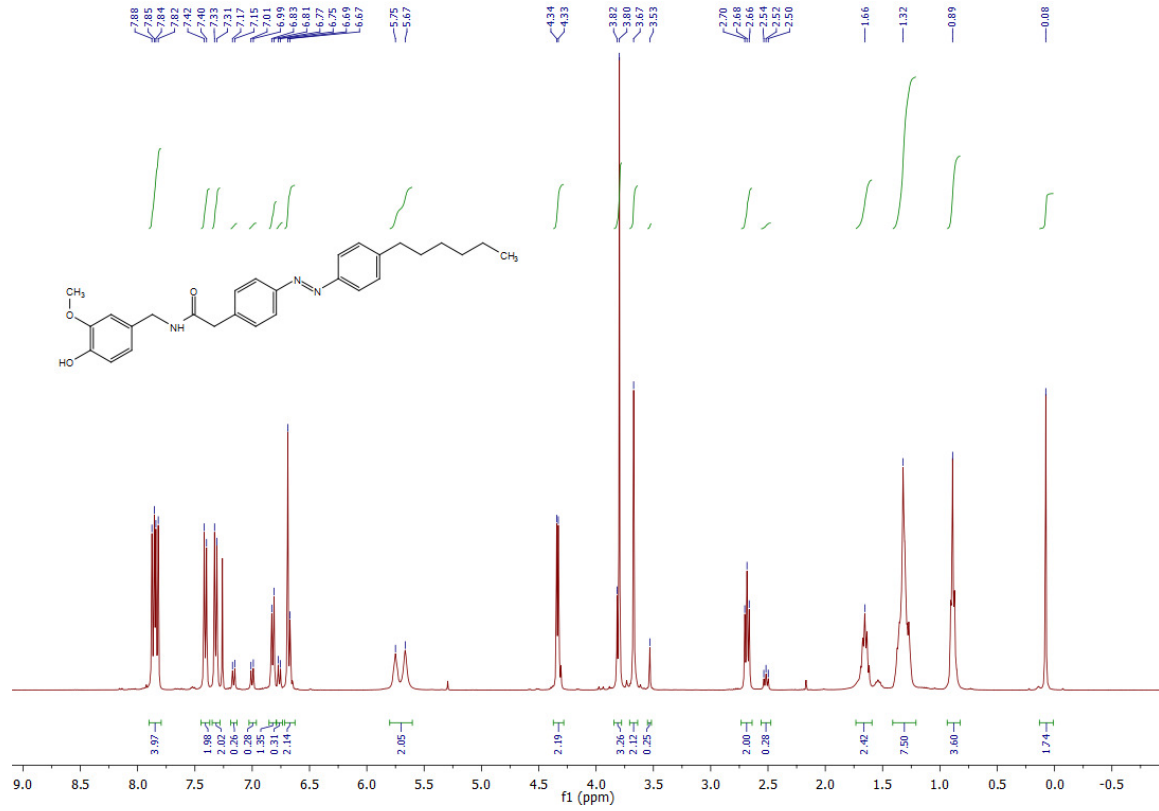
TLC (hexane/EtOAc, 1:2): $R_f = 0.40$.

$^1\text{H NMR}$ (CDCl_3 , 400 MHz, 25 $^\circ\text{C}$): δ 7.88-7.81 (m, 2H, H_{5a,b}, H_{10a,b}, $J_{5,4} \approx J_{10,11} \approx 8.3$ Hz), 7.41 (d, 2H, H_{4a,b}, $J_{4,5} = 8.3$ Hz), 7.32 (d, 2H, H_{11a,b}, $J_{11,10} = 8.3$ Hz), 6.84-6.80 (m, 1H, H₂₄), 6.71-6.64 (m, 2H, H₂₅, H₂₁), 5.75 (t, 1H, NH), 5.66 (s, 1H, OH), 4.34 (d, 2H, H_{19a,b}, $J_{19,\text{NH}} = 5.7$ Hz), 3.80 (s, 3H, H_{OMe}), 3.67 (s, 2H, H_{2a,b}), 2.68 (t, 2H, H_{13a,b}, $J_{13,14} = 7.7$ Hz), 1.72-1.61 (m, 2H, H_{14a,b}), 1.40-1.23 (m, 6H, H_{15a,b}, H_{16a,b}, H_{17a,b}), 0.89 (t, 3H, H_{18a,b,c}, $J_{18,17} = 6.7$ Hz).

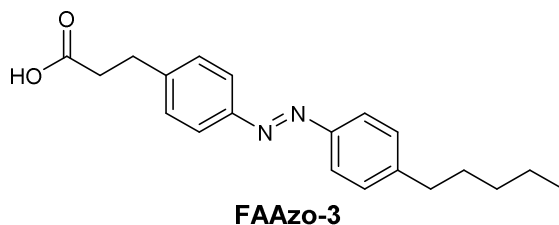
$^{13}\text{C NMR}$ (CDCl_3 , 101 MHz, 25 $^\circ\text{C}$): δ 170.3 (C₁), 152.1 (C_{azo}), 151.0 (C_{azo}), 147.0 (C₃), 146.8 (C₂₂), 145.2 (C₂₃), 137.6 (C₁₂), 130.2 (2C, C_{azo}), 130.0 (C₂₀), 129.3 (2C, C_{azo}), 123.4 (2C, C_{azo}), 123.0 (2C, C_{azo}), 120.7 (2C, C_{azo}), 114.5 (C₂₄), 110.4 (C₂₅), 56.0 (C₂₆), 43.8 (C₂), 43.8 (C₁₉), 36.0 (C₁₃), 31.8 (C₁₅), 31.4 (C₁₄), 29.1 (C₁₆), 22.7 (C₁₇), 14.2 (C₁₈).

IR (neat, ATR): $\tilde{\nu} = 3457, 3285, 2953, 2922, 2852, 1648, 1635, 1601, 1518, 1462, 1434, 1428, 1339, 1276, 1248, 1234, 1194, 1152, 1120, 1039, 1019, 1011, 838, 797, 716, 677$.

HRMS (ESI⁺): m/z calcd. for [C₂₈H₃₄N₃O₃]⁺: 460.2600, found: 460.2592 ([M+H]⁺).



4.4.8.5 – 3-(4-((4-pentylphenyl)diazenyl)phenyl)propanoic acid (FAAzo-3)



4-Pentylaniline (1.5 g, 9.2 mmol, 1.5 equiv.) and 4-aminophenylpropionic acid (1.0 g, 6.1 mmol, 1.0 equiv.) were converted to red solid **3-(4-((4-pentylphenyl)diazenyl)phenyl)propanoic acid (FAAzo-3)**, 1.0 g, 27%) in an analogous manner as described above for the preparation of **2-(4-((4-hexylphenyl)diazenyl)phenyl)acetic acid (FAAzo-2)**. *Note: all reagents and solvents were scaled according to molarity.*

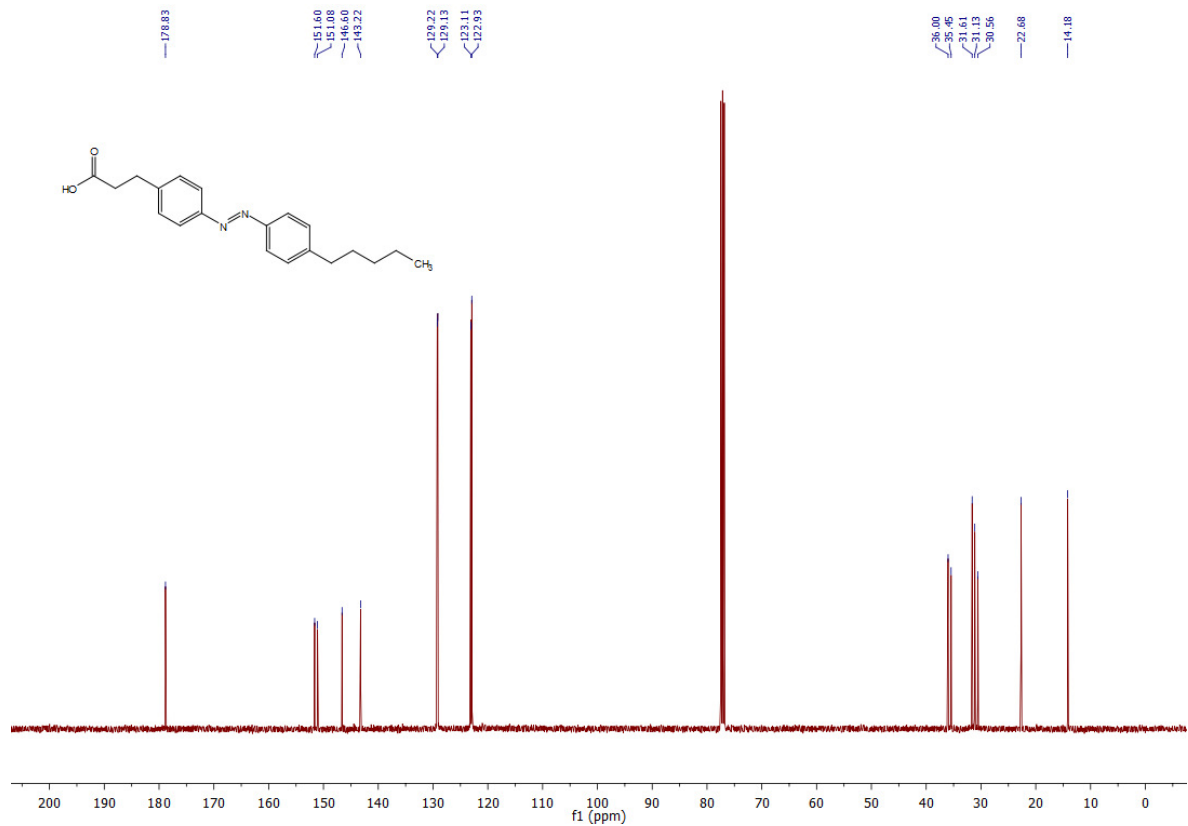
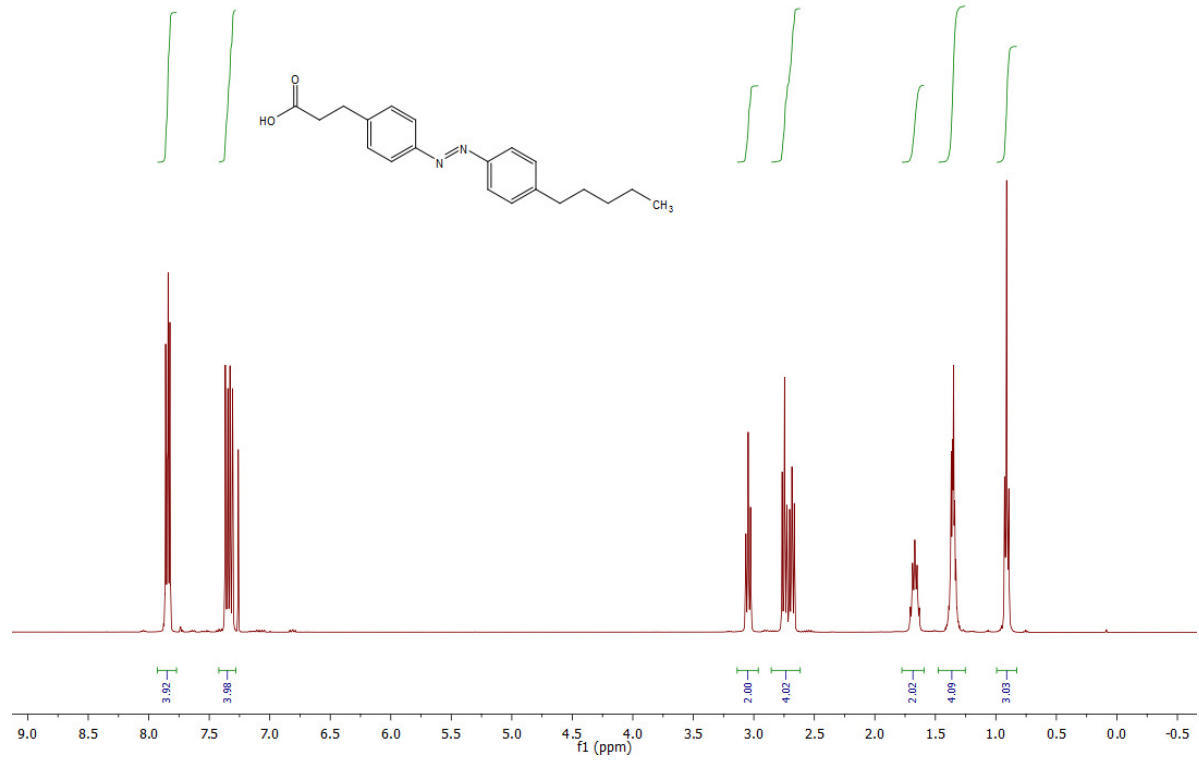
TLC (hexane/EtOAc, 10:1): $R_f = 0.74$.

$^1\text{H NMR}$ (CDCl_3 , 400 MHz, 25 °C): δ 7.87-7.81 (m, 4H, H_{6a,b}, H_{11a,b}), 7.37-7.30 (m, 4H, H_{5a,b}, H_{12a,b}, $J_{12,11} \approx J_{5,6} \approx 8.4$ Hz), 3.05 (t, 2H, H_{2a,b}, $J_{2,3} = 7.6$ Hz), 2.75 (t, 2H, H_{3a,b}, $J_{3,2} = 7.7$ Hz), 2.68 (t, 2H, H_{14a,b}), 1.71-1.62 (m, 2H, H_{15a,b}), 1.40-1.32 (m, 4H, H_{16a,b}, H_{17a,b}), 0.91 (t, 3H, H_{18a,b,c}, $J_{18,17} = 6.9$ Hz).

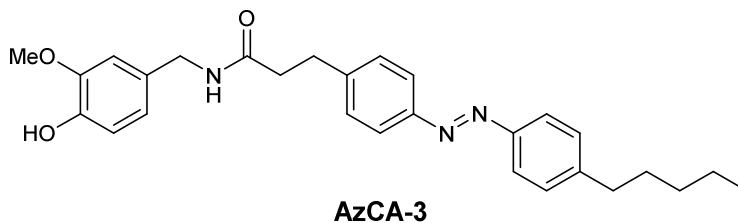
$^{13}\text{C NMR}$ (CDCl_3 , 101 MHz, 25 °C): δ 178.8 (C₁), 151.6 (C_{azo}), 151.1 (C_{azo}), 146.6 (C_{azo}), 143.2 (C_{azo}), 129.2 (2C, C_{azo}), 129.1 (2C, C_{azo}), 123.1 (2C, C_{azo}), 122.9 (2C, C_{azo}), 36.0 (C₁₄), 35.5 (C₂), 31.6 (C₃), 31.1 (C₁₆), 30.6 (C₁₅), 22.7 (C₁₇), 14.2 (C₁₈).

IR (neat, ATR): $\tilde{\nu} = 3026, 2950, 2924, 2853, 2616, 1691, 1599, 1579, 1494, 1431, 1417, 1358, 1315, 1286, 1217, 1186, 1153, 1105, 1011, 932, 837, 806, 725, 678$.

HRMS (EI⁺): m/z calcd. for [C₂₀H₂₄N₂O₂]: 324.1838, found: 324.1831 ([M-e]⁺).



4.4.8.6 – N-(4-Hydroxy-3-methoxybenzyl)-3-(4-((4-pentylphenyl)diazenyl)phenyl)propanamide (AzCA-3)



3-(4-((4-Pentylphenyl)diazenyl)phenyl)propanoic acid (FAAzo-3, 25 mg, 77 μ mol, 1.0 equiv.) was converted to red solid **N-(4-hydroxy-3-methoxybenzyl)-3-(4-((4-pentylphenyl)diazenyl)phenyl)propanamide (AzCA-3, 17 mg, 89%)** in an analogous manner as described above for the preparation of **N-(4-hydroxy-3-methoxybenzyl)-4-((4-heptylphenyl)diazenyl)benzamide (AzCA-1)**. *Note: all reagents and solvents were scaled according to molarity.*

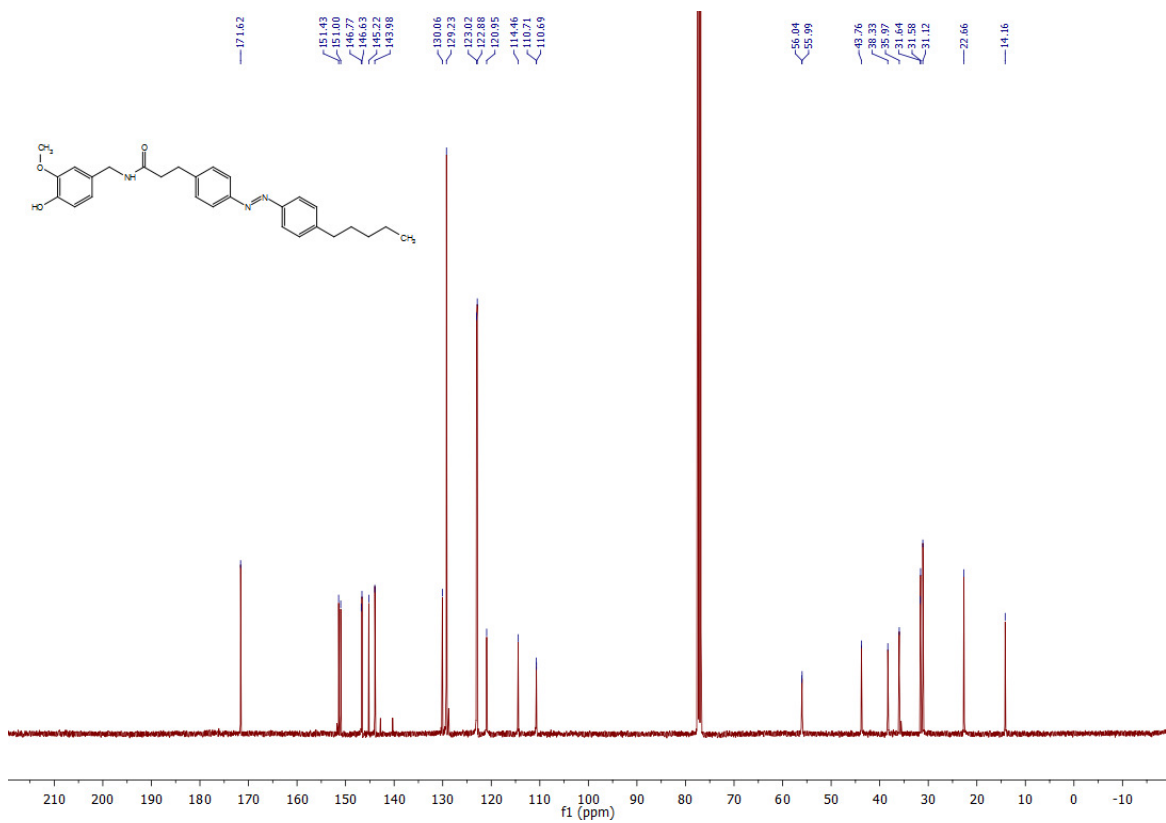
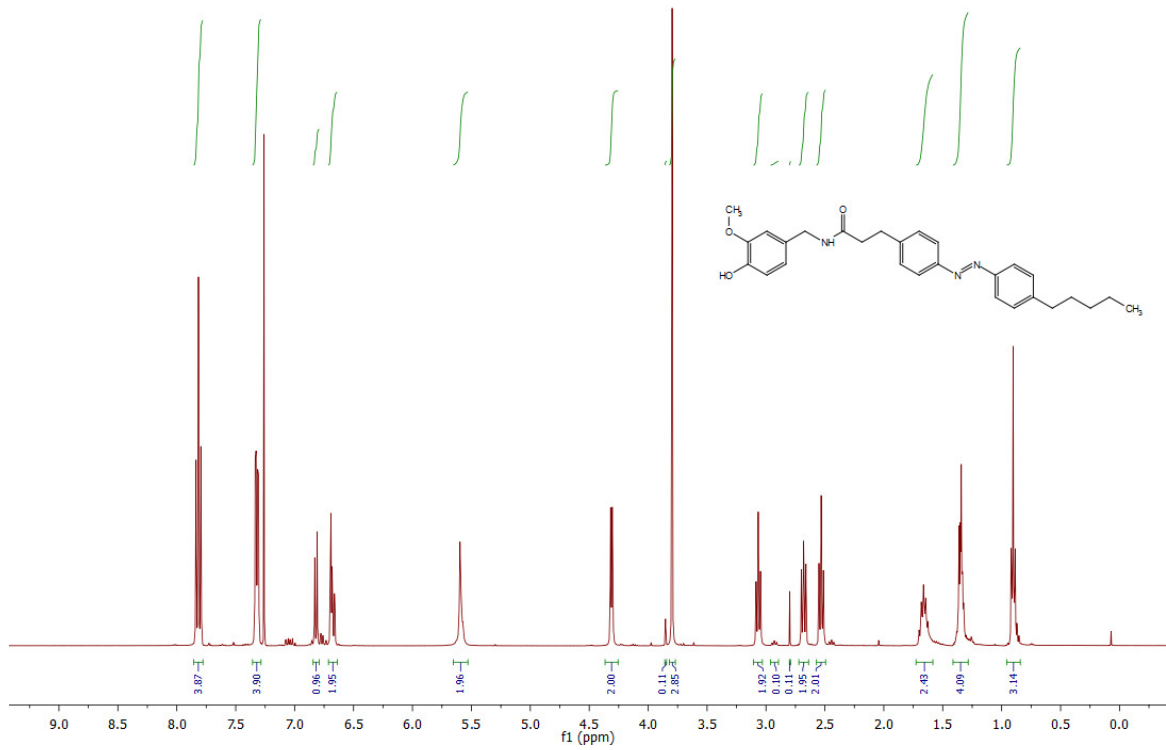
TLC (CH₂Cl₂:MeOH:AcOH, 95:5:1): R_f = 0.47.

¹H NMR (CDCl₃, 400 MHz, 25 °C): δ 7.85-7.78 (m, 4H, H_{6a,b}, H_{11a,b}, J_{6,5} \approx J_{11,12} \approx 8.3 Hz), 7.35-7.30 (m, 4H, H_{5a,b}, H_{12a,b}, J_{5,6} \approx J_{12,11} \approx 8.4 Hz), 6.82 (d, 1H, H₂₂, J_{22,21} = 7.8 Hz), 6.71-6.65 (m, 2H, H₂₁, H₂₅), 5.62-5.56 (m, 2H, NH, OH), 4.31 (d, 2H, H_{19a,b}, J_{19,NH} = 5.8 Hz), 3.80 (s, 3H, H_{26a,b,c}), 3.07 (t, 2H, H_{3a,b}, J_{3,2} = 7.5 Hz), 2.68 (t, 2H, H_{14a,b}, J_{14,15} = 8.0 Hz), 2.53 (t, 2H, H_{2a,b}, J_{2,3} = 7.4 Hz), 1.70-1.60 (m, 2H, H_{15a,b}), 1.39-1.31 (m, 4H, H_{16a,b}, H_{17a,b}), 0.90 (t, 3H, H_{18a,b,c}, J_{18,17} = 6.8 Hz).

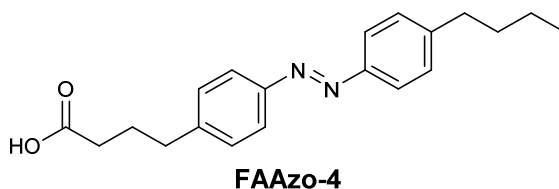
¹³C NMR (CDCl₃, 101 MHz, 25 °C): δ 171.6 (C₁), 151.4 (C_{azo}), 151.0 (C_{azo}), 146.8 (C₂₂), 146.6 (C_{azo}), 145.2 (C₂₃), 144.0 (C_{azo}), 130.1 (C₂₀), 129.2 (4C, C_{azo}), 123.0 (2C, C_{azo}), 122.9 (2C, C_{azo}), 121.0 (C₂₁), 114.5 (C₂₄), 110.7 (C₂₅), 56.0 (C₂₆), 43.8 (C₁₉), 38.3 (C₂), 36.0 (C₁₄), 31.6 (C₃), 31.6 (C₁₆), 31.1 (C₁₅), 22.7 (C₁₇), 14.2 (C₁₈).

IR (neat, ATR): $\tilde{\nu}$ = 3285, 3052, 2953, 2927, 2855, 1642, 1600, 1513, 1462, 1451, 1429, 1375, 1272, 1235, 1155, 1123, 1034, 1012, 848, 735, 731.

HRMS (ESI⁺): *m/z* calcd. for [C₂₈H₃₄N₃O₃]⁺: 460.2600, found: 460.2591 ([M+H⁺]⁺).



4.4.8.7 – 4-(4-((4-Butylphenyl)diazenyl)phenyl)butanoic acid (FAAzo-4)



4-Butylaniline (2.27 g, 15 mmol, 3.0 equiv.) and 4-(4-aminophenyl)butyric acid (0.90 g, 5.1 mmol, 1.0 equiv.) were converted to red solid **4-(4-((4-butylphenyl)diazenyl)phenyl)-butanoic acid (FAAzo-4)**, 1.49 g, 91%) in an analogous manner as described above for the preparation of **2-(4-((4-hexylphenyl)diazenyl)phenyl)acetic acid (FAAzo-2)**. *Note: all reagents and solvents were scaled according to molarity.*

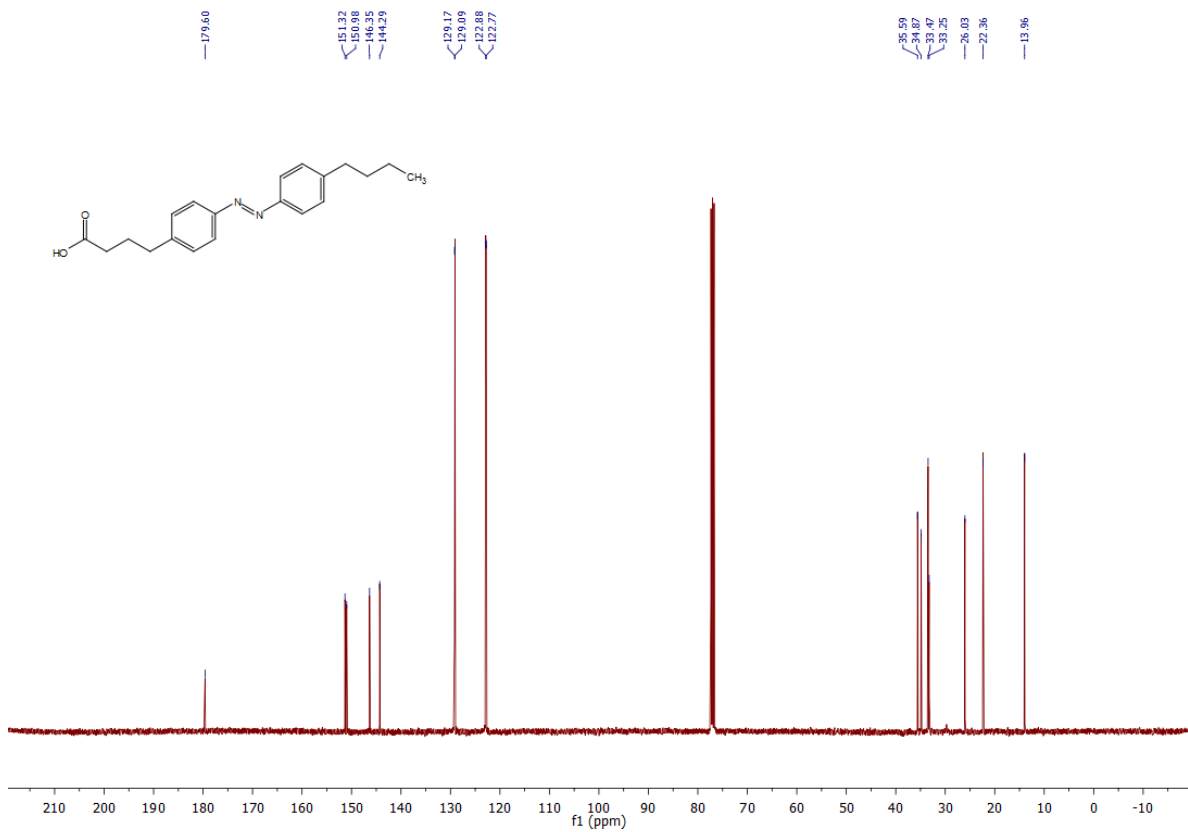
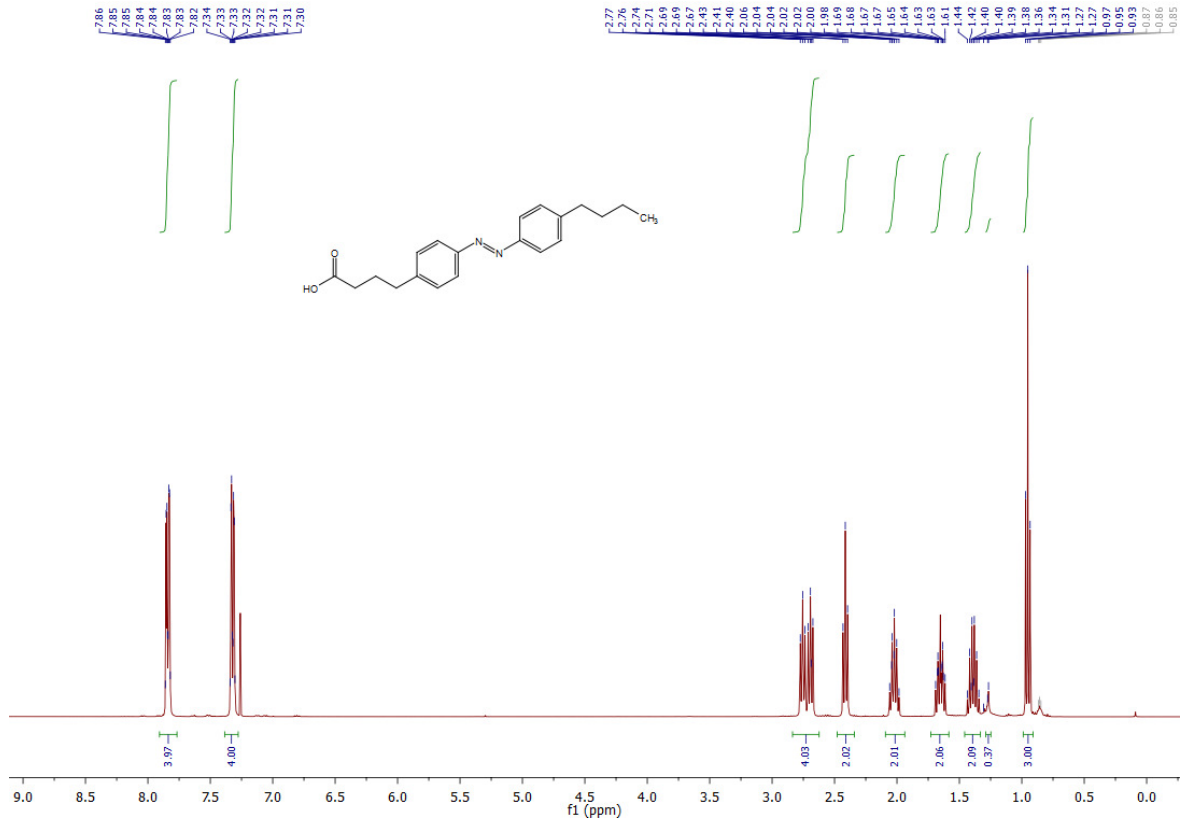
TLC (CH₂Cl₂/AcOH, 99:1): R_f = 0.15.

¹H NMR (CDCl₃, 400 MHz, 25 °C): δ 7.86-7.81 (m, 4H, H7_{a,b}, H12_{a,b}, J_{7,6} ≈ J_{12,13} ≈ 8.4 Hz), 7.35-7.29 (m, 4H, H6_{a,b}, H13_{a,b}, J_{6,7} ≈ J_{13,12} ≈ 8.4 Hz), 2.76 (t, 2H, H4_{a,b}, J_{4,3} = 7.8 Hz), 2.71 (t, 2H, H15_{a,b}, J_{15,16} = 7.8 Hz), 2.43 (t, 2H, H2_{a,b}, J_{2,3} = 7.3 Hz), 2.08-1.98 (m, 2H, H3_{a,b}), 1.70-1.61 (m, 2H, H16_{a,b}), 1.44-1.34 (m, 2H, H17_{a,b}), 0.95 (t, 3H, H18_{a,b,c}, J_{18,17} = 7.3 Hz).

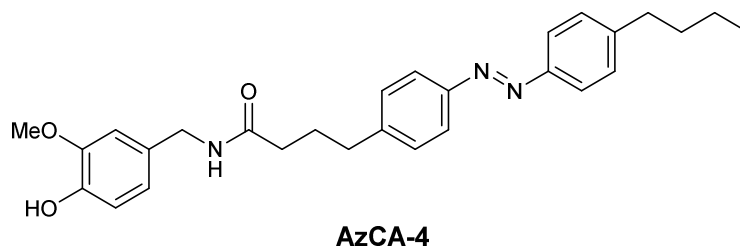
¹³C NMR (CDCl₃, 101 MHz, 25 °C): δ 179.6 (C1), 151.3 (C8), 151.0 (C11), 146.4 (C14), 144.3 (C5), 129.2 (2C, C_{azo}), 129.1 (2C, C_{azo}), 122.9 (2C, C_{azo}), 122.8 (2C, C_{azo}), 35.6 (C15), 34.9 (C4), 33.5 (C16), 33.3 (C2), 26.0 (C3), 22.4 (C17), 14.0 (C18).

IR (neat, ATR): $\tilde{\nu}$ = 3021, 2950, 2927, 2869, 2853, 2685, 2599, 1689, 1600, 1580, 1497, 1461, 1434, 1409, 1337, 1279, 1212, 1152, 1113, 1102, 1060, 1024, 1010, 901, 842, 824, 772, 730, 671.

HRMS (EI⁺): *m/z* calcd. for [C₂₀H₂₄N₂O₂]: 324.1838, found: 324.1836 ([M-e]⁺).



4.4.8.8 – *N*-(4-Hydroxy-3-methoxybenzyl)-4-(4-((4-butylphenyl)diazenyl)phenyl)butanamide (AzCA-4)



4-(4-((4-Butylphenyl)diazenyl)phenyl)butanoic acid (FAAzo-4, 16 mg, 77 μ mol, 1.0 equiv.) was converted to red solid ***N*-(4-hydroxy-3-methoxybenzyl)-4-(4-((4-butylphenyl)diazenyl)phenyl)butanamide (AzCA-4, 20 mg, 87%)** in an analogous manner as described above for the preparation of ***N*-(4-hydroxy-3-methoxybenzyl)-4-((4-heptylphenyl)diazenyl)benzamide (AzCA-1)**. *Note: all reagents and solvents were scaled according to molarity.*

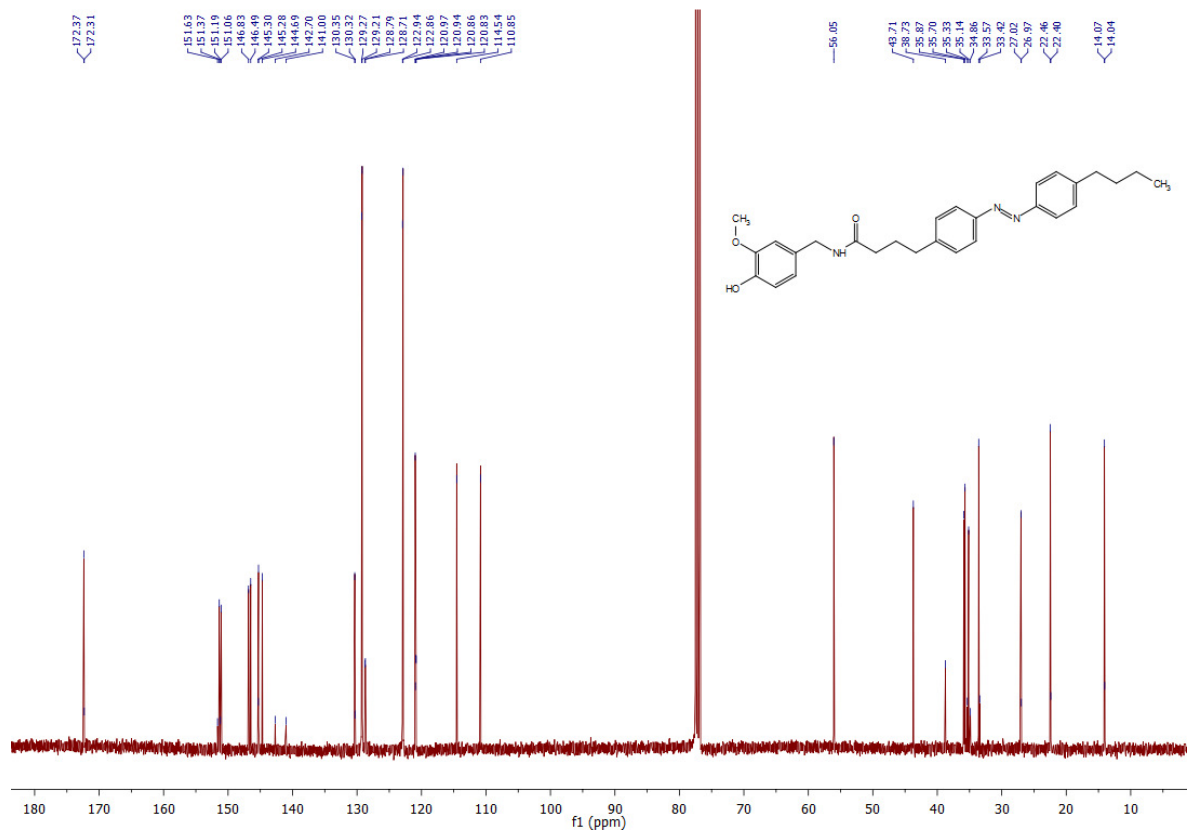
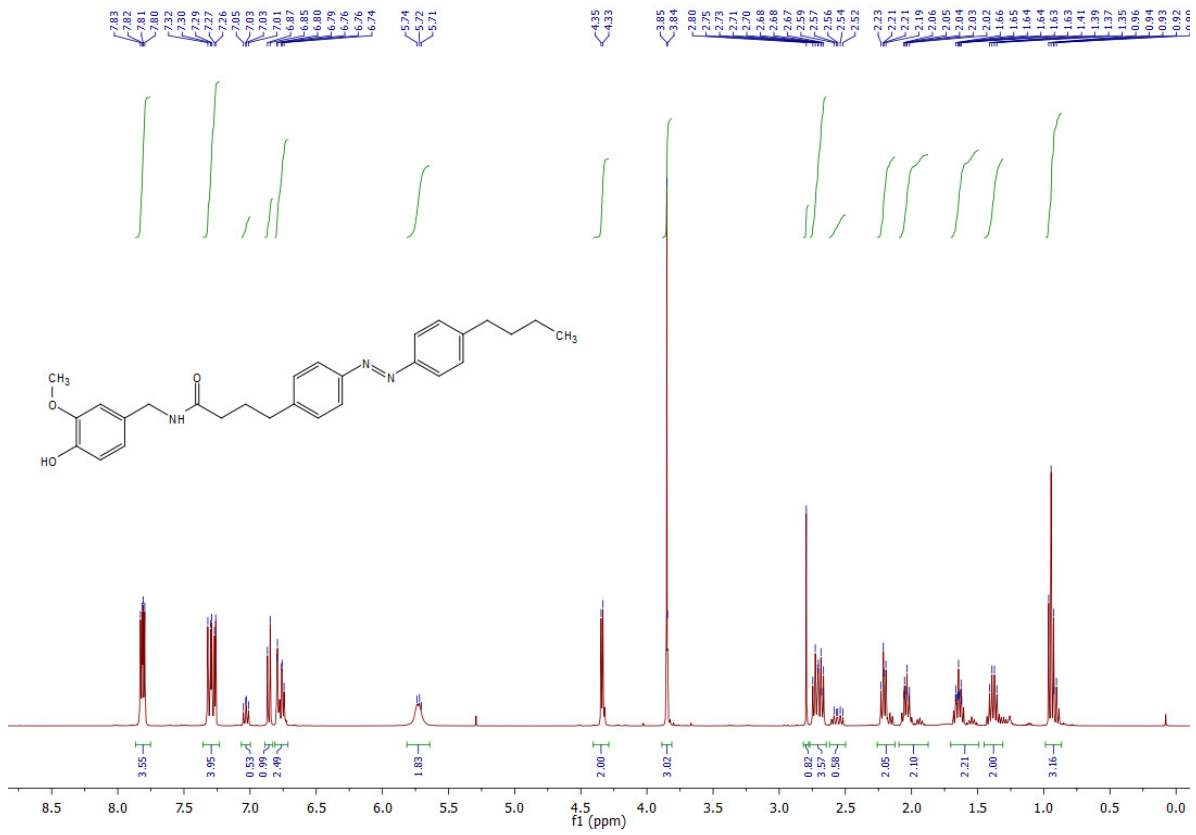
TLC (hexane/EtOAc, 1:1): R_f = 0.34.

$^1\text{H NMR}$ (CDCl_3 , 400 MHz, 25 $^\circ\text{C}$): δ 7.84-7.78 (m, 4H, H_{12a,b}, H_{7a,b}, $J_{12,13} \approx J_{7,6} \approx 8.4$ Hz), 7.33-7.25 (m, 4H, H_{6a,b}, H_{13a,b}, $J_{6,7} \approx J_{13,12} \approx 8.4$ Hz), 6.86 (d, 1H, H₂₄, $J_{24,25} = 8.0$ Hz), 6.80-6.73 (m, 2H, H₂₁, H₂₅), 5.77-5.68 (m, 2H, NH, OH), 4.34 (d, 2H, H_{19a,b}, $J_{19,\text{NH}} = 5.60$ Hz), 3.85 (s, 3H, H₂₆), 2.73 (t, 2H, H_{4a,b}, $J_{4,3} = 7.4$ Hz), 2.68 (t, 2H, H_{15a,b}, $J_{15,16} = 7.6$ Hz), 2.21 (t, 2H, H_{2a,b}, $J_{2,3} = 7.6$ Hz), 2.08-1.99 (m, 2H, H_{3a,b}), 1.68-1.59 (m, 2H, H_{16a,b}), 1.44-1.30 (m, 2H, H_{17a,b}), 0.94 (t, 3H, H_{18a,b,c}, $J_{18,17} = 7.4$ Hz).

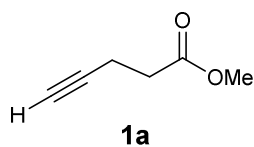
$^{13}\text{C NMR}$ (CDCl_3 , 101 MHz, 25 $^\circ\text{C}$): δ 172.4 (C1), 151.4 (C8), 151.1 (C11), 146.8 (C22), 146.5 (C14), 145.3 (C23), 144.7 (C5), 130.3 (C20), 129.3 (2C, C_{azo}), 129.2 (2C, C_{azo}), 122.9 (2C, C_{azo}), 122.9 (2C, C_{azo}), 121.0 (C21), 114.5 (C24), 110.9 (C25), 56.1 (C26), 43.7 (C19), 35.9 (C2), 35.7 (C15), 35.1 (C4), 33.6 (C16), 27.0 (C3), 22.5 (C17), 14.1 (C18).

IR (neat, ATR): $\tilde{\nu}$ = 3285, 3054, 2953, 2929, 2857, 1643, 1600, 1514, 1462, 1430, 1377, 1275, 1237, 1155, 1124, 1034, 1013, 845, 736, 677.

HRMS (EI⁺): m/z calcd. for [C₂₈H₃₃N₃O₃]: 459.2522, found: 459.2516 ([M-e]⁺).



4.4.8.9 – Methyl pent-4-ynoate (1a)

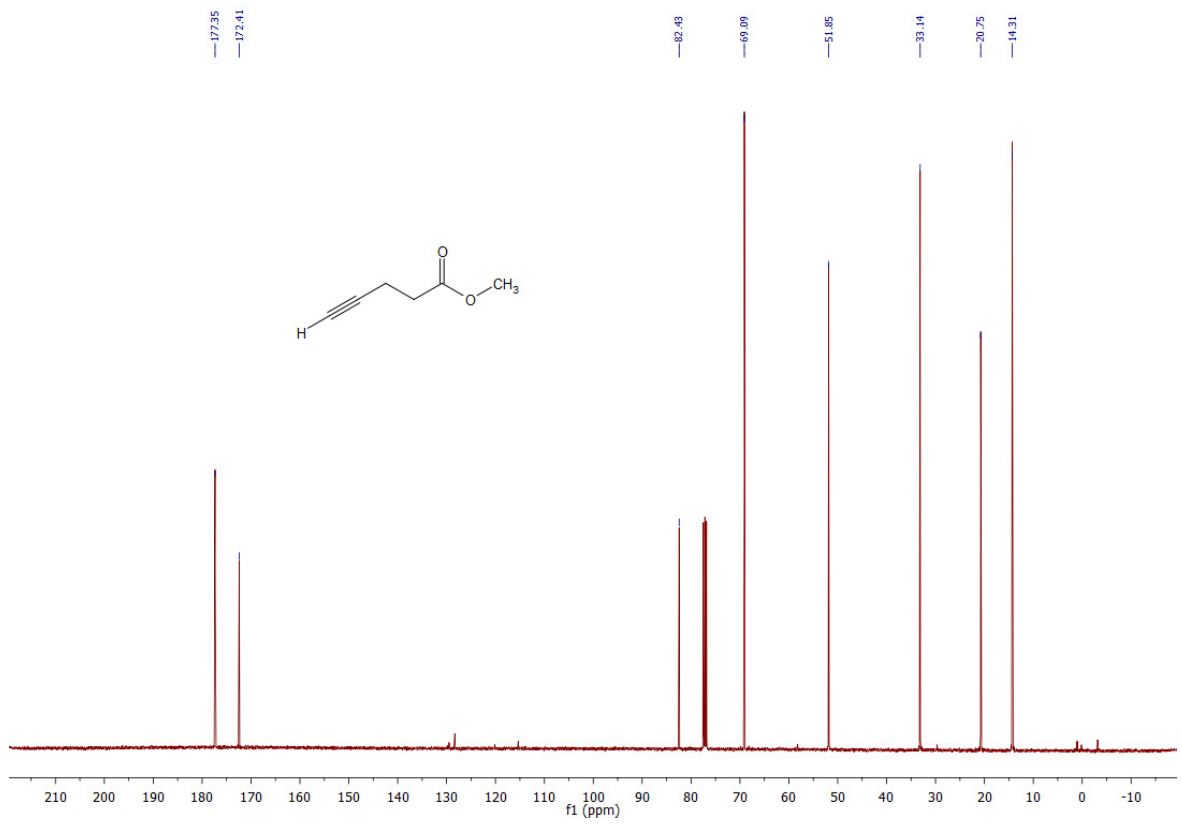
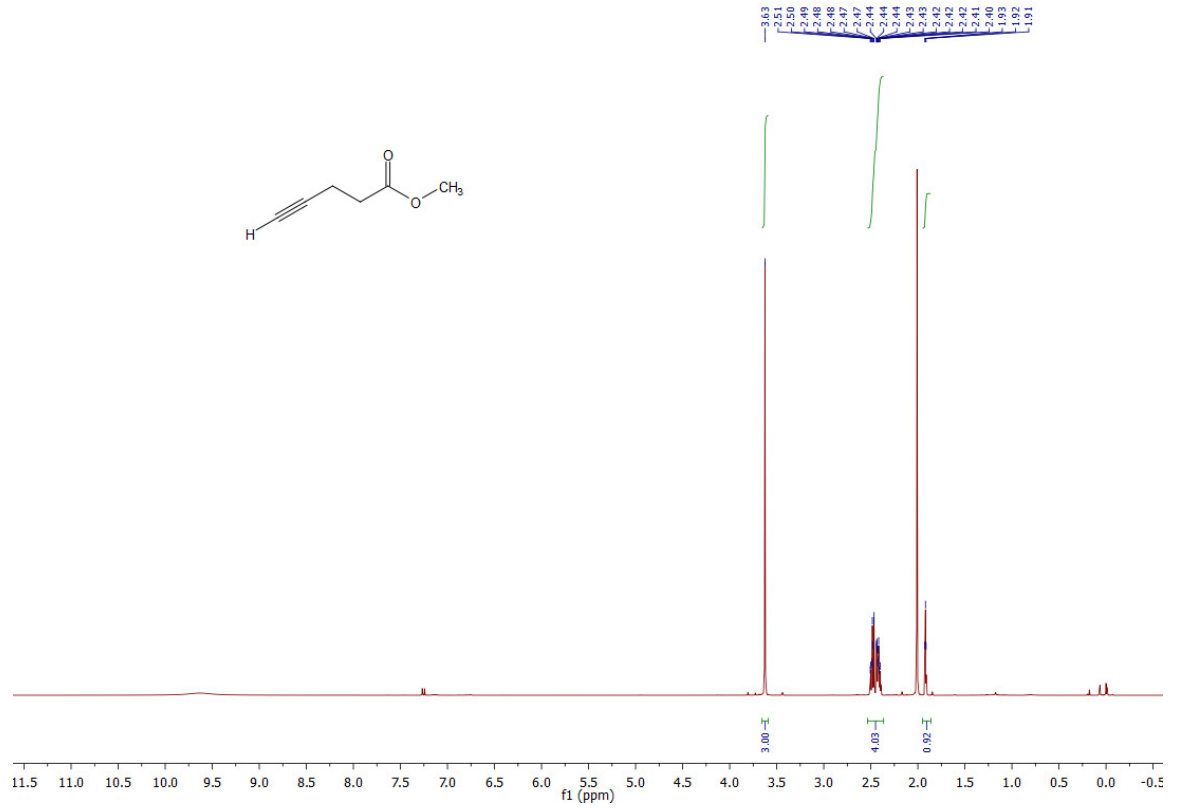


4-Pentynoic acid (0.36 g, 3.6 mmol, 1.0 equiv.) was dissolved in dry MeOH (7.0 mL) and benzene (25 mL) under an argon atmosphere. Trimethylsilyldiazomethane (2.4 mL, 0.20 M in diethyl ether, 4.7 mmol, 1.3 equiv.) was slowly added at room temperature until the solution retained a faint yellow color. The mixture was then titrated with AcOH until a colorless solution was obtained and the gas evolution had ceased. The reaction mixture was concentrated under reduced pressure (0.25 bar, 40 °C). The resulting oily residue was diluted with diethyl ether (50 mL) and the mixture was washed with H₂O (2x25 mL). The layers were separated and the organic layer was dried over anhydrous Na₂SO₄. The dried solution was filtered, and the filtrate was concentrated under reduced pressure (0.25 bar, 40 °C) to yield **methyl pent-4-ynoate (1a)**, 0.37 g, 91%) as a volatile colorless liquid.

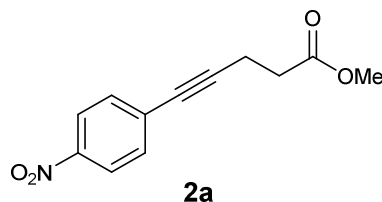
TLC (hexane/EtOAc, 4:1): R_f = 0.71.

¹H NMR (CDCl₃, 400 MHz, 25 °C): δ 3.64 (s, 3H, H_{OMe}), 2.51-2.38 (m, 4H, H_{2a,b}, H_{3a,b}), 1.94 (t, 1H, H₅, J_{5,3} = 2.5 Hz).

¹³C NMR (CDCl₃, 101 MHz, 25 °C): δ 172.4 (C1), 82.4 (C4), 69.1 (C5), 51.9 (C_{OMe}), 33.1 (C2), 14.3 (C3). Spectral characteristics matched those previously reported.¹⁰² *The product still contained AcOH but this did not affect the following reaction.*



4.4.8.10 – Methyl 5-(4-nitrophenyl)pent-4-ynoate (2a)



Methyl 5-(4-nitrophenyl)pent-4-ynoate (2a) was prepared utilizing a modified method described by Sugimoto et al.¹⁰³

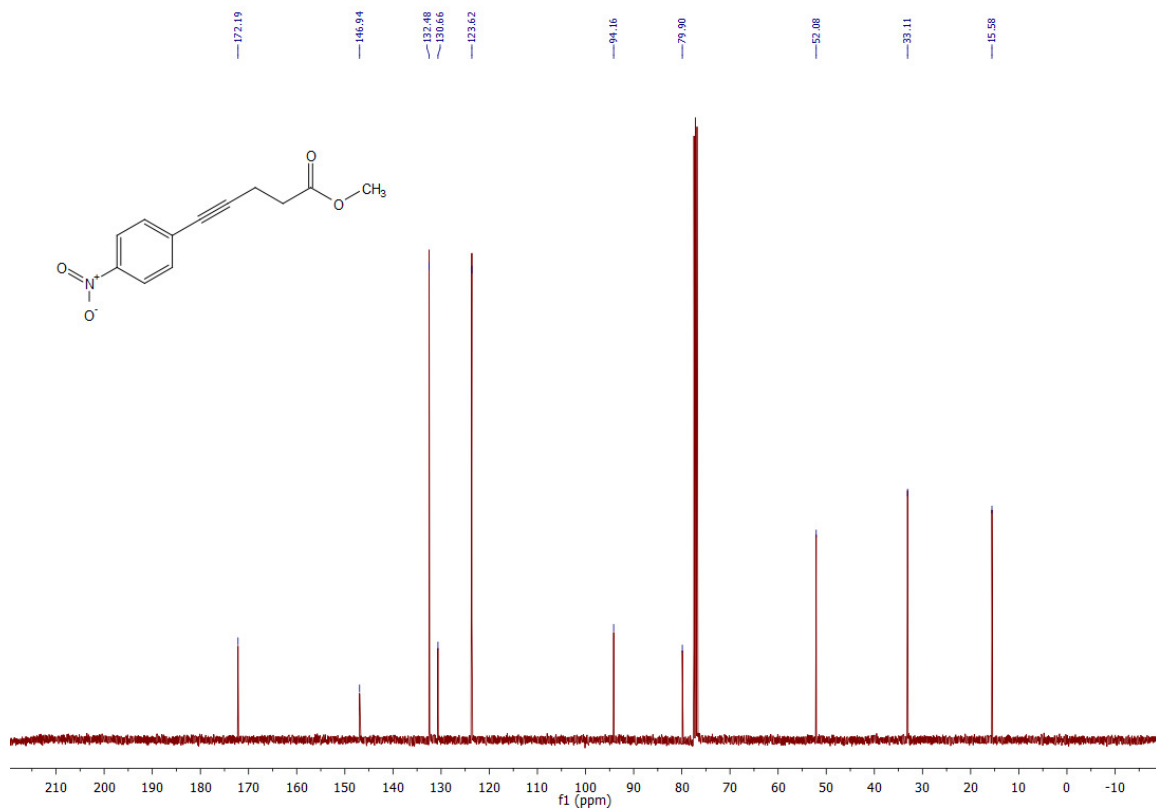
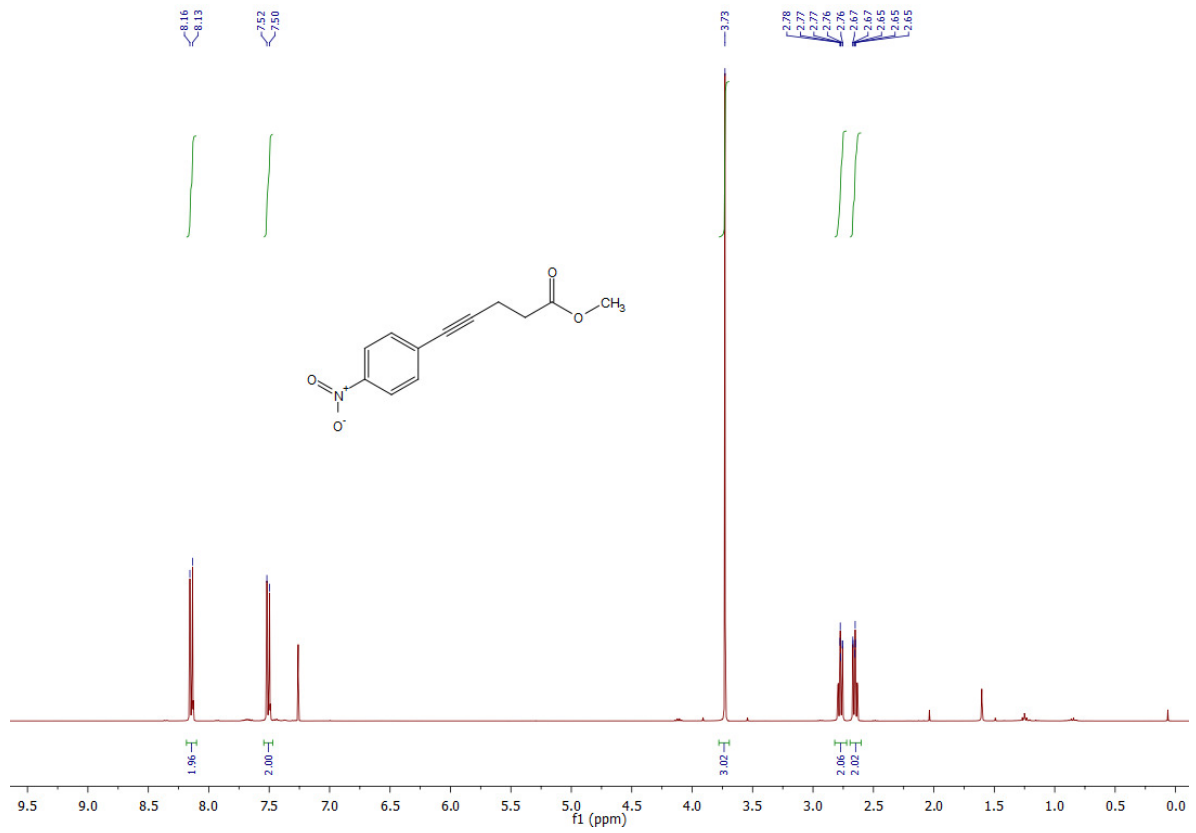
Methyl pent-4-ynoate (1a, 0.40 g, 3.6 mmol, 1.0 equiv.) and 4-iodonitrobenzene (1.1 g, 4.3 mmol, 1.2 equiv.) were combined in a round-bottomed flask under an argon atmosphere and were dissolved in degassed/dry THF (28 mL). NEt₃ (1.5 g, 14 mmol, 4.0 equiv.) was then added, followed by the addition of CuI (0.12 g, 0.64 mmol, 0.18 equiv.) and (PPh₃)₂PdCl₂ (0.12 g, 0.18 mmol, 0.050 equiv.) at room temperature. The resulting brown solution was heated to 50 °C. After 2 h, the dark red mixture was cooled to room temperature and was diluted with EtOAc (50 mL), and washed with saturated aqueous ammonium chloride solution (50 mL, then 25 mL), water (25 mL) and then half saturated aqueous NaCl solution (25 mL). The organic phase was dried over anhydrous Na₂SO₄ and the dried solution was filtered. The filtrate was concentrated under reduced pressure and after being preadsorbed onto silica gel (4.0 g SiO₂, loaded from THF), the residue was purified by flash silica gel chromatography (0.10 kg SiO₂, 10:1 hexane:EtOAc) to yield **methyl 5-(4-nitrophenyl)pent-4-ynoate (2a**, 0.42 g, 51%) as an orange solid.

TLC (hexane/EtOAc, 4:1): R_f = 0.56.

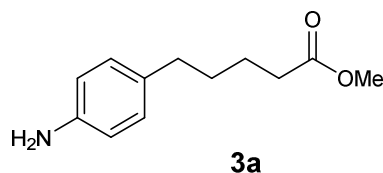
¹H NMR (CDCl₃, 400 MHz, 25 °C): δ 8.17-8.13 (m, 2H, H_{8,a,b}, J_{8,7} ≈ 9.0 Hz), 7.53-7.48 (m, 2H, H_{7,a,b}, J_{7,8} ≈ 9.0 Hz), 3.73 (s, 3H, H_{OMe}), 2.77 (t, 2H, H_{2,a,b}, J_{2,3} = 7.3 Hz), 2.65 (t, 2H, H_{3,a,b}, J_{3,2} = 7.3 Hz).

¹³C NMR (CDCl₃, 101 MHz, 25 °C): δ 172.2 (C1), 146.9 (C9), 132.5 (2C, C_{7,a,b}), 130.7 (C6), 123.6 (2C, C_{8,a,b}), 94.2 (C4), 79.9 (C5), 52.1 (C_{OMe}), 33.1 (C2), 15.6 (C3).

HRMS (EI⁺): *m/z* calcd. for [C₁₂H₁₁NO₄]: 233.0688, found: 233.0674 ([M-e]⁺).



4.4.8.11 – Methyl 5-(4-aminophenyl)pentanoate (3a)



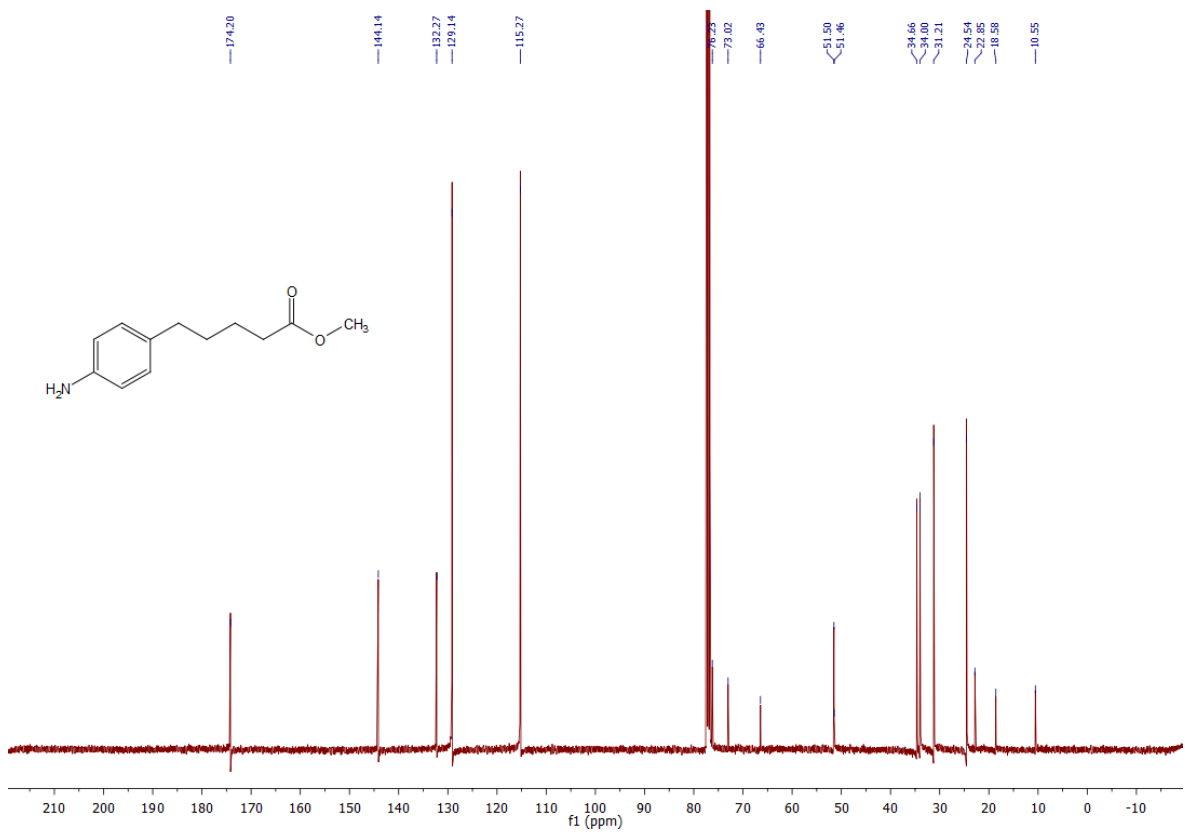
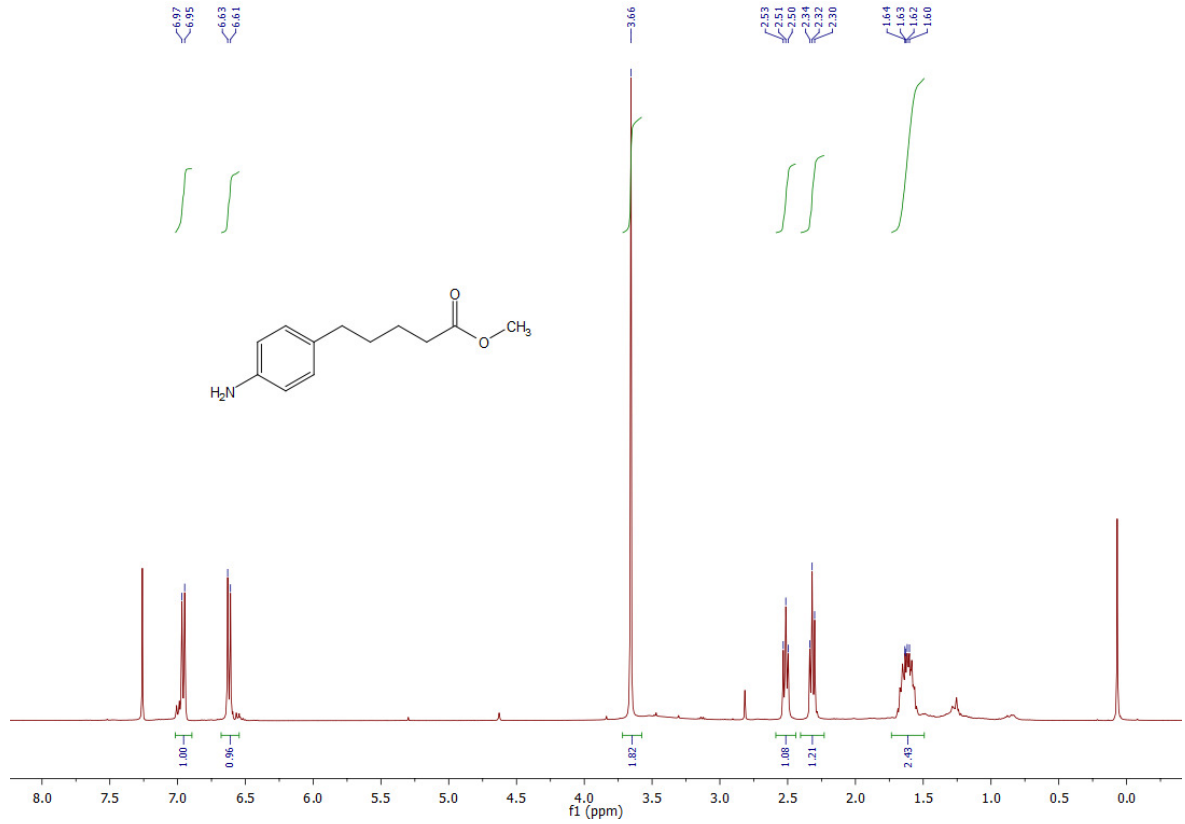
Methyl 5-(4-nitrophenyl)pent-4-ynoate (2a, 0.42 g, 1.8 mmol, 1.0 equiv.) was dissolved in 2:1 EtOAc:MeOH (v:v, 30 mL total) and this solution was degassed by sparging with argon gas. Pd/C (10 wt%, 0.13 g) was added and the suspension was again degassed and placed under a hydrogen atmosphere (H₂ pressure applied with a balloon). The mixture was stirred vigorously at room temperature overnight. Upon completion of the reaction as observed by TLC analysis, the mixture was filtered through a pad of celite and the filtrate was concentrated under reduced pressure. The residue was purified by flash silica gel chromatography (50 g SiO₂, 3:1 hexane:EtOAc) to yield **5-(4-aminophenyl)pentanoate (3a, 0.34 g, 1.6 mmol, 92%)** as an orange oil.

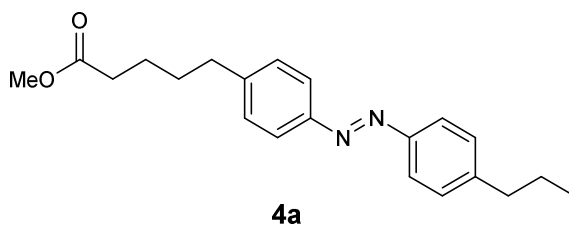
TLC (hexane/EtOAc, 4:1): R_f = 0.13.

¹H NMR (CDCl₃, 400 MHz, 25 °C): δ 6.98-6.93 (m, 2H, H7_{a,b}, J_{7,8} ≈ 8.3 Hz), 6.64-6.60 (m, 2H, H8_{a,b}, J_{8,7} ≈ 8.3 Hz), 3.66 (s, 3H, H_{OMe}), 3.56 (s_{br}, NH₂), 2.51 (t, 2H, H5_{a,b}, J_{5,4} = 7.2 Hz), 2.32 (t, 2H, H2_{a,b}), 1.69-1.54 (m, 4H, H3_{a,b}, H4_{a,b}).

¹³C NMR (CDCl₃, 101 MHz, 25 °C): δ 174.2 (C1), 144.1 (C9), 132.3 (C6), 129.1 (2C, C7_{a,b}), 115.3 (2C, C8_{a,b}), 51.5 (C_{OMe}), 34.7 (C5), 34.0 (C2), 31.2 (C4), 24.5 (C3).

HRMS (EI⁺): *m/z* calcd. for [C₁₂H₁₇NO₂]: 207.1259, found: 207.1238 ([M-e]⁺).



4.4.8.12 – Methyl 5-(4-((4-propylphenyl)diazenyl)phenyl)pentanoate (**4a**)

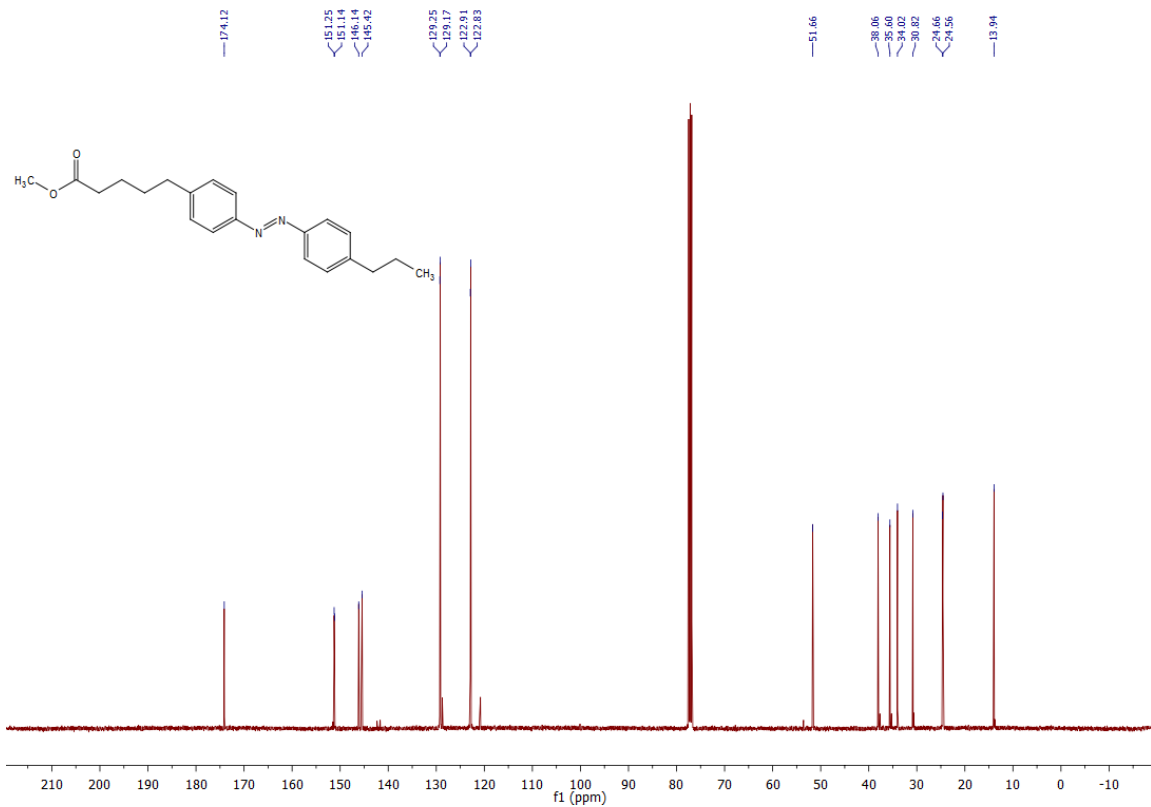
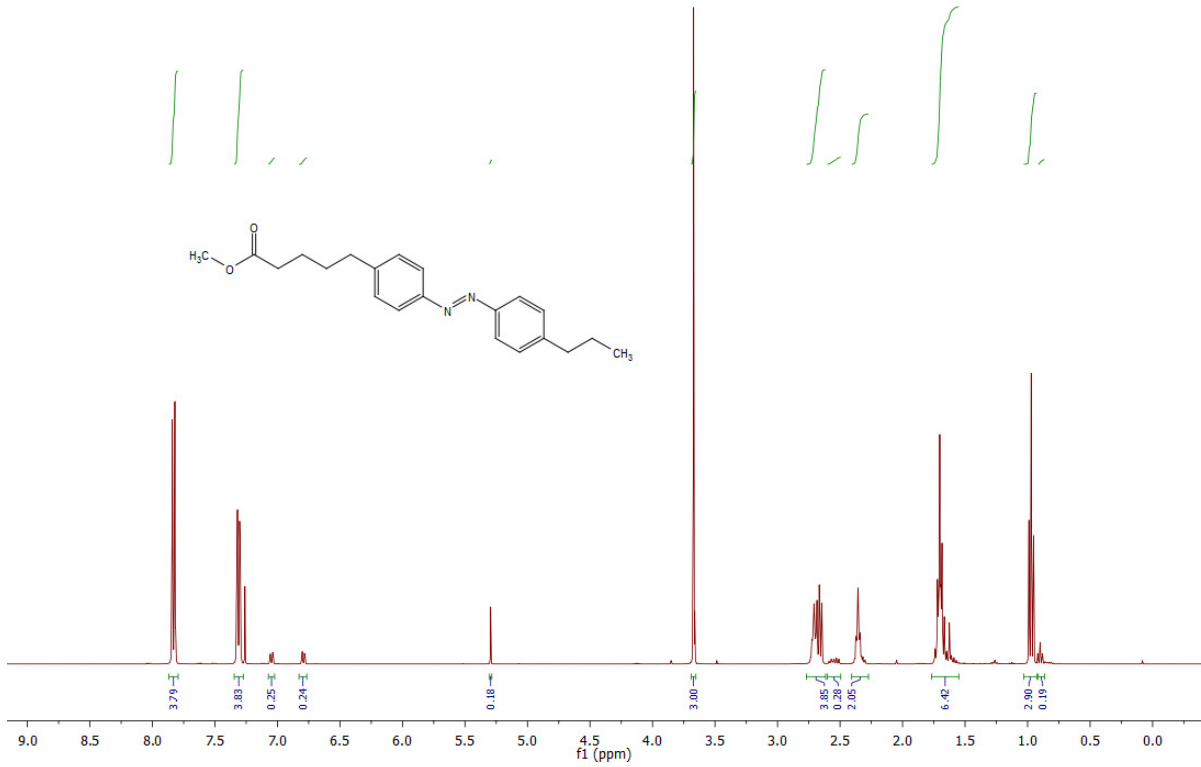
A solution of 4-propylaniline (0.64 g, 4.7 mmol, 3.0 equiv.) in CH₂Cl₂ (50 mL) was treated with Oxone[®] (3.0 g, 9.6 mmol, 6.0 equiv.) dissolved in H₂O (50 mL) and the resulting biphasic mixture was stirred rapidly at room temperature overnight. The two phases were then separated and the organic phase was washed with H₂O (60 mL). The washed organic phase was concentrated under reduced pressure to approximately 5 mL volume and this residue was then directly purified by flash silica gel chromatography (20 g SiO₂, CH₂Cl₂). The collected green fractions were combined and a solution of **5-(4-aminophenyl)pentanoate (3a)**, 0.33 g, 1.6 mmol, 1.0 equiv.) in CH₂Cl₂ (2.0 mL) was added followed by AcOH (25 mL). The CH₂Cl₂ was then removed under reduced pressure (0.50 bar, 40 °C) and the resulting solution was stirred at room temperature for 40 h. Upon complete consumption of **3a** as determined by TLC analysis, the AcOH was removed under reduced pressure and the residue was azeotroped from PhMe (40 mL). The resulting brown oil was purified by flash silica gel chromatography (0.12 kg SiO₂, gradient: 20:1 to 10:1 pentane:EtOAc) to yield **methyl 5-(4-((4-propylphenyl)diazenyl)phenyl)pentanoate (4a)**, 0.39 g, 74%) as a red oil.

TLC (hexane/EtOAc, 20:1): R_f = 0.73.

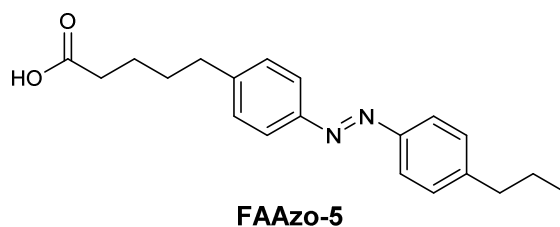
¹H NMR (CDCl₃, 400 MHz, 25 °C): δ 7.85-7.81 (m, 4H, H_{8a,b}, H_{13a,b}, J_{8,7} ≈ J_{13,14} ≈ 8.4 Hz), 7.33-7.29 (m, 4H, H_{7a,b}, H_{14a,b}, J_{7,8} ≈ J_{14,13} ≈ 8.4 Hz), 3.67 (s, 3H, H_{OMe}), 2.74-2.64 (m, 4H, H_{5a,b}, H_{16a,b}), 2.38-2.32 (m, 2H, H_{2a,b}), 1.75-1.64 (m, 6H, H_{3a,b}, H_{4a,b}, H_{17a,b}), 0.97 (t, 3H, H_{18a,b,c}, J_{18,17} = 7.4 Hz).

¹³C NMR (CDCl₃, 101 MHz, 25 °C): δ 174.1 (C₁), 151.3 (C_{Azo}), 151.1 (C_{Azo}), 146.1 (C_{Azo}), 145.4 (C_{Azo}), 129.3 (2C, C_{Azo}), 129.2 (2C, C_{Azo}), 122.9 (2C, C_{Azo}), 122.8 (2C, C_{Azo}), 51.7 (C_{OMe}), 38.1 (C₁₆), 35.6 (C₅), 34.0 (C₂), 30.8 (C_{alk}), 24.7 (C_{alk}), 24.6 (C_{alk}), 13.9 (C₁₈).

HRMS (EI⁺): *m/z* calcd. for [C₂₁H₂₆N₂O₂]: 338.1994, found: 338.1986 ([M-e]⁺).



4.4.8.13 – 5-(4-((4-Propylphenyl)diazenyl)phenyl)pentanoic acid (FAAzo-5)



Methyl 5-(4-((4-propylphenyl)diazenyl)phenyl)pentanoate (4a, 0.36 g, 1.1 mmol, 1.0 equiv.) was dissolved in 1:1 MeOH:THF (v:v, 42 mL total). To this solution was added aqueous 1 M lithium hydroxide solution (11 mL, 10 equiv.) and the mixture was stirred at room temperature for 2 h. Upon consumption of the starting material as observed by TLC analysis, the organic solvent was removed under reduced pressure. The resulting solution was acidified to pH = 1 with aqueous 2 M hydrochloric acid solution and the aqueous layer was extracted with EtOAc (2x30 mL). The combined organic phases were washed with H₂O (30 mL), and the washed solution was dried over anhydrous Na₂SO₄. The dried solution was filtered, and the filtrate was concentrated under reduced pressure. The residue was purified by flash silica gel chromatography (32 g SiO₂, 99:1 CH₂Cl₂:AcOH) to yield **5-(4-((4-propylphenyl)diazenyl)phenyl)pentanoic acid (FAAzo-5**, 0.33 g, 96%) as a red solid.

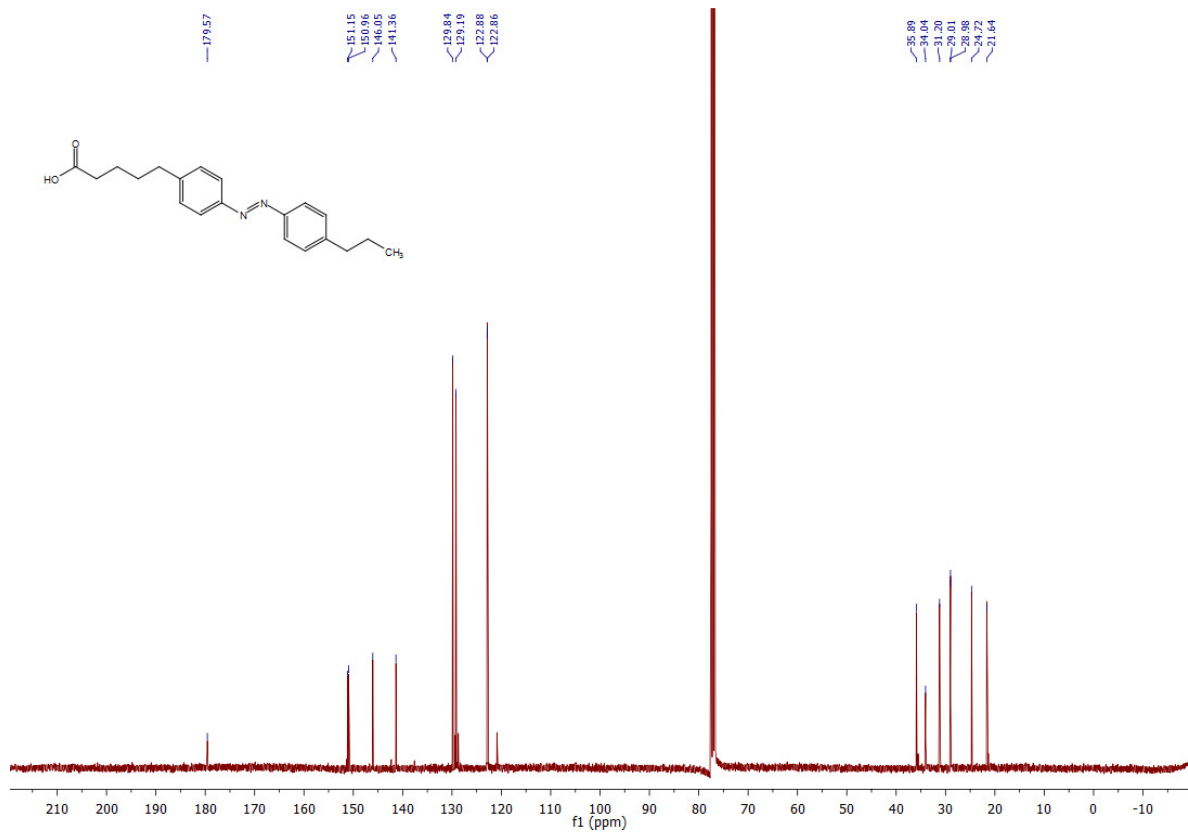
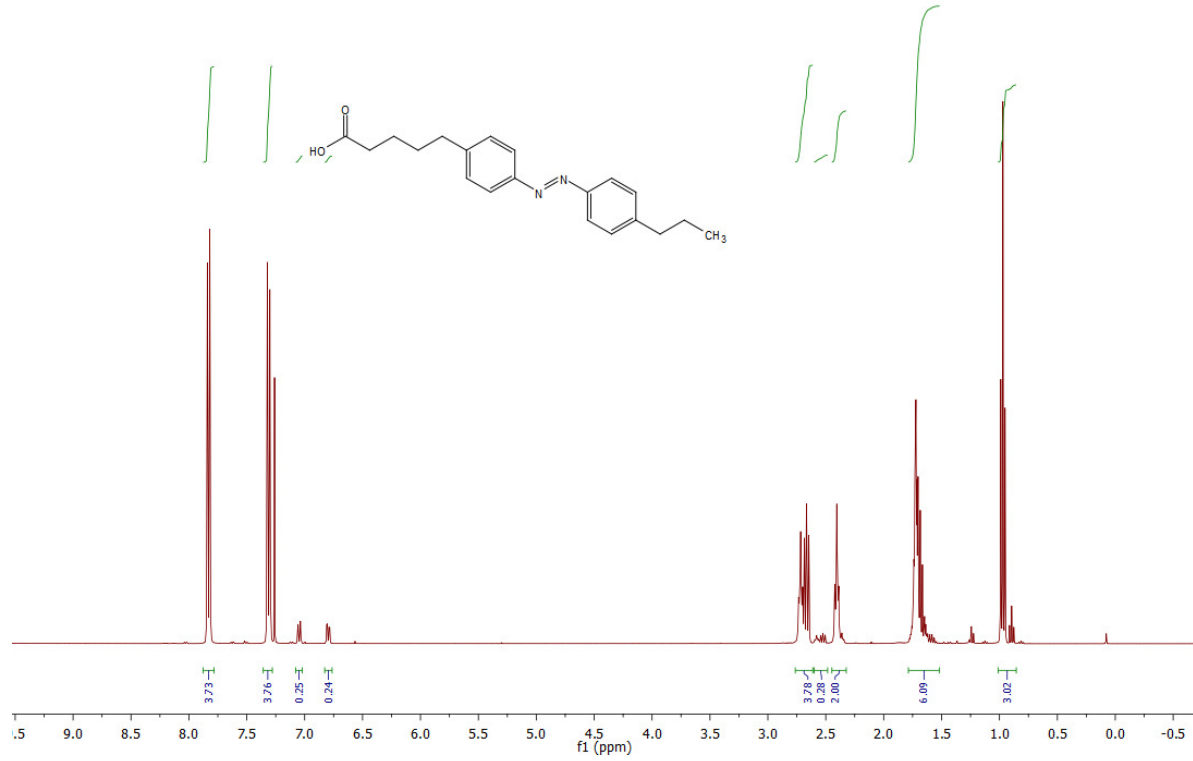
TLC (hexane/EtOAc, 4:1): R_f = 0.18.

¹H NMR (CDCl₃, 400 MHz, 25 °C): δ 7.85-7.81 (m, 4H, H_{8a,b}, H_{13a,b}, J_{8,7} ≈ J_{13,14} ≈ 8.3 Hz), 7.33-7.29 (m, 4H, H_{17a,b}, H_{14a,b}, J_{7,8} ≈ J_{14,13} ≈ 8.2 Hz), 2.75-2.63 (m, 4H, H_{5a,b}, H_{16a,b}), 2.40 (t, 2H, H_{2a,b}, J_{2,3} = 7.0 Hz), 1.76-1.67 (m, 6H, H_{3a,b}, H_{4a,b}, H_{17a,b}), 0.97 (t, 3H, H_{18a,b,c}).

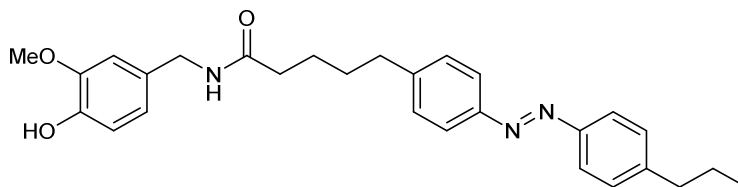
¹³C NMR (CDCl₃, 101 MHz, 25 °C): δ 179.6 (C1), 151.2 (C_{azo}), 151.0 (C_{azo}), 146.1 (C_{azo}), 141.4 (C_{azo}), 129.8 (2C, C_{azo}), 129.2 (2C, C_{azo}), 122.9 (2C, C_{azo}), 122.9 (2C, C_{azo}), 35.9 (C5), 34.0 (C2), 31.2 (C17), 29.0 (C3), 29.0 (C18), 24.7 (C4), 21.6 (C16).

IR (neat, ATR): $\tilde{\nu}$ = 2925, 2856, 1701, 1697, 1693, 1599, 1497, 1462, 1420, 1409, 1303, 1255, 1200, 1154, 1109, 1090, 1074, 1012, 932, 851, 834, 744, 731, 677.

HRMS (EI⁺): *m/z* calcd. for [C₂₀H₂₄N₂O₂]: 324.1838, found: 324.1831 ([M-e]⁺).



4.4.8.14 – N-(4-Hydroxy-3-methoxybenzyl)-5-(4-((4-propylphenyl)diazenyl)phenyl)pentanamide (AzCA-5)



AzCA-5

5-(4-((4-Propylphenyl)diazenyl)phenyl)pentanoic acid (FAAzo-5, 21 mg, 65 μ mol, 1 equiv.) was converted to red solid **N-(4-hydroxy-3-methoxybenzyl)-5-(4-((4-propylphenyl)diazenyl)phenyl)pentanamide (AzCA-5, 27 mg, 90%)** in an analogous manner as described above for the preparation of **N-(4-hydroxy-3-methoxybenzyl)-4-((4-heptylphenyl)diazenyl)benzamide (AzCA-1)**. *Note: all reagents and solvents were scaled according to molarity.*

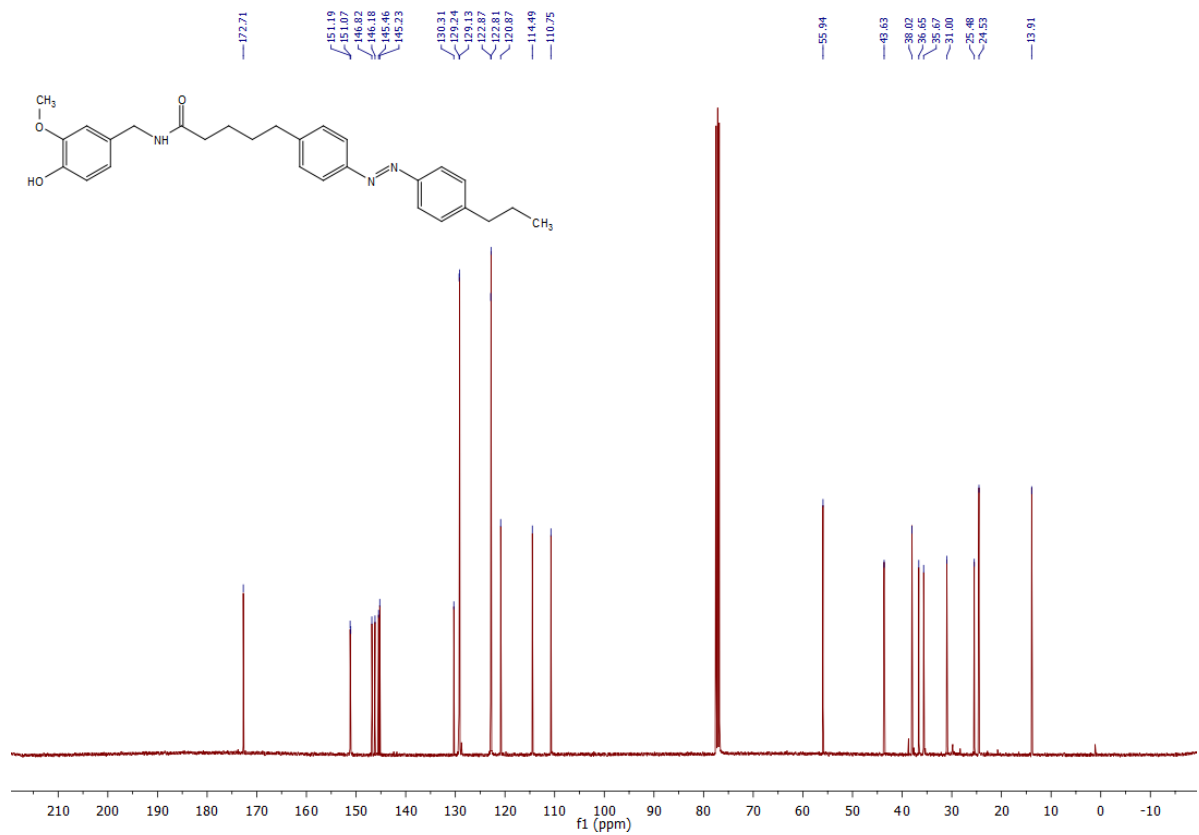
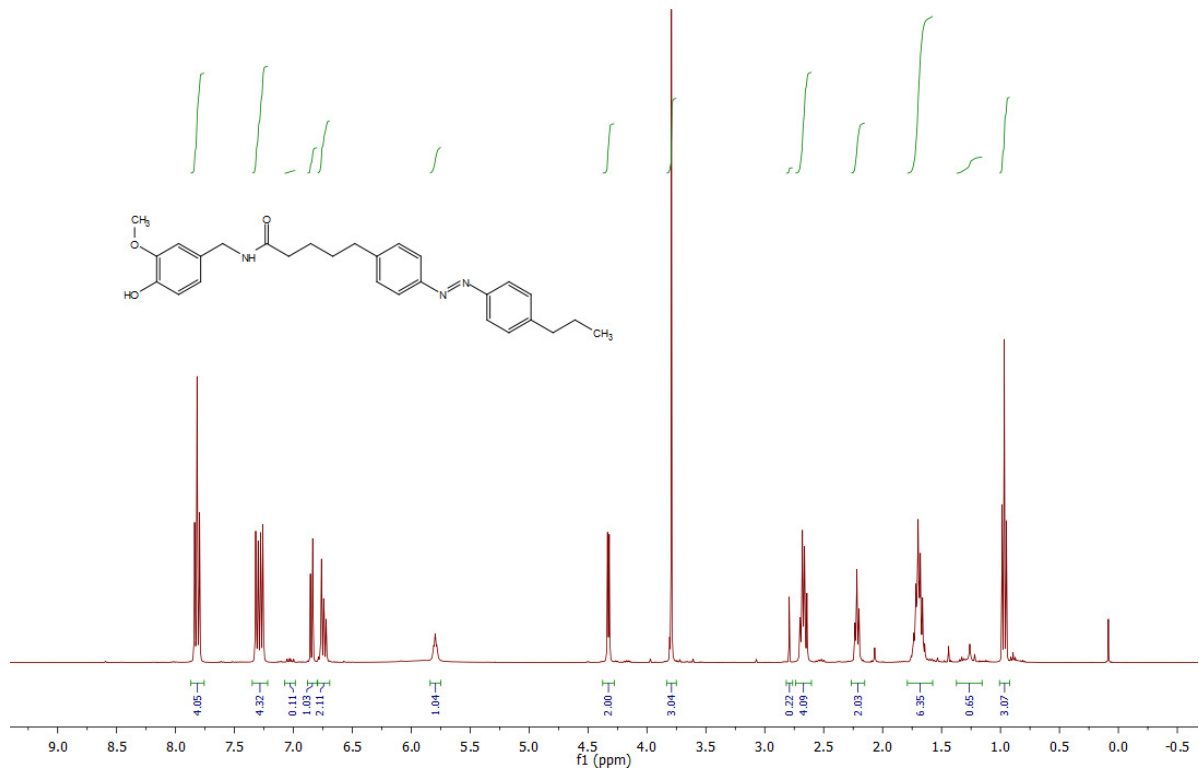
TLC (CH₂Cl₂/AcOH, 99:1): R_f = 0.43.

¹H NMR (CDCl₃, 400 MHz, 25 °C): δ 7.84-7.79 (m, 4H, H_{8a,b}, H_{13a,b}, J_{8,7} \approx J_{13,14} \approx 8.4 Hz), 7.33-7.24 (m, 4H, H_{7a,b}, H_{14a,b}, J_{7,8} \approx J_{14,13} \approx 8.4 Hz), 6.85 (d, 1H, H₂₄, J_{24,25} = 8.0 Hz), 6.77-6.71 (m, 2H, H₂₁, H₂₅), 5.80 (t, 1H, NH, J_{NH,19} = 5.8 Hz), 4.33 (d, 2H, H_{19a,b}, J_{19,NH} = 5.7 Hz), 3.79 (s, 3H, H_{26a,b,c}), 2.71-2.63 (m, 4H, H_{5a,b}, H_{16a,b}), 2.22 (t, 2H, H_{2a,b}, J_{2,3} = 7.0 Hz), 1.77-1.63 (m, 6H, H_{3a,b}, H_{4a,b}, H_{17a,b}), 0.97 (t, 3H, H_{18a,b,c}, J_{18,17} = 7.3 Hz).

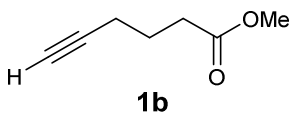
¹³C NMR (CDCl₃, 101 MHz, 25 °C): δ 172.7 (C₁), 151.2 (C_{azo}), 151.1 (C_{azo}), 146.8 (C₂₂), 146.2 (C_{azo}), 145.5 (C_{azo}), 145.2 (C₂₃), 130.3 (C₂₀), 129.2 (2C, C_{azo}), 129.1 (2C, C_{azo}), 122.9 (2C, C_{azo}), 122.8 (2C, C_{azo}), 120.9 (C₂₅), 114.5 (C₂₄), 110.8 (C₂₁), 55.9 (C₂₆), 43.6 (C₁₉), 38.0 (C₁₆), 36.7 (C₂), 35.7 (C₅), 31.0 (C_{alk}), 25.5 (C_{alk}), 24.5 (C₁₇), 13.9 (C₁₈).

IR (neat, ATR): $\tilde{\nu}$ = 3291, 3054, 2956, 2930, 2859, 1644, 1600, 1515, 1463, 1430, 1376, 1274, 1236, 1155, 1124, 1035, 1013, 849, 736.

HRMS (EI⁺): *m/z* calcd. for [C₂₈H₃₃N₃O₃]: 459.2522, found: 459.2507 ([M-e]⁺).



4.4.8.15 – Methyl hex-5-ynoate (**1b**)

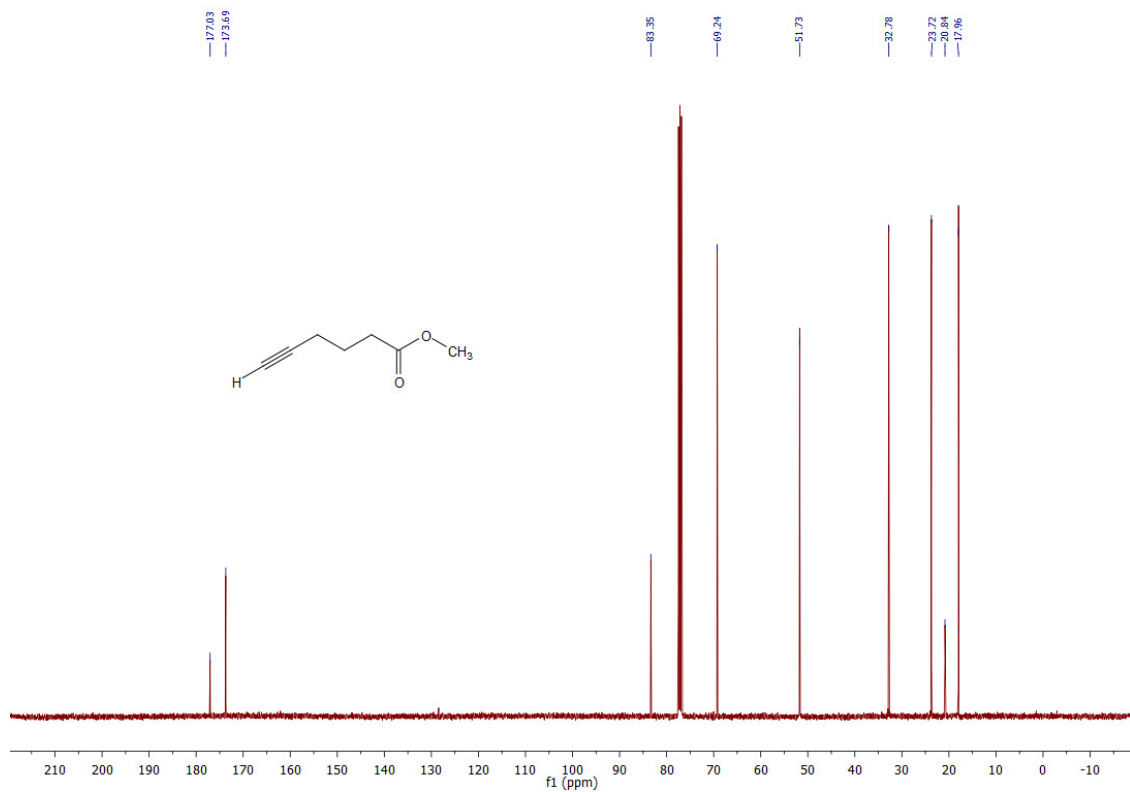
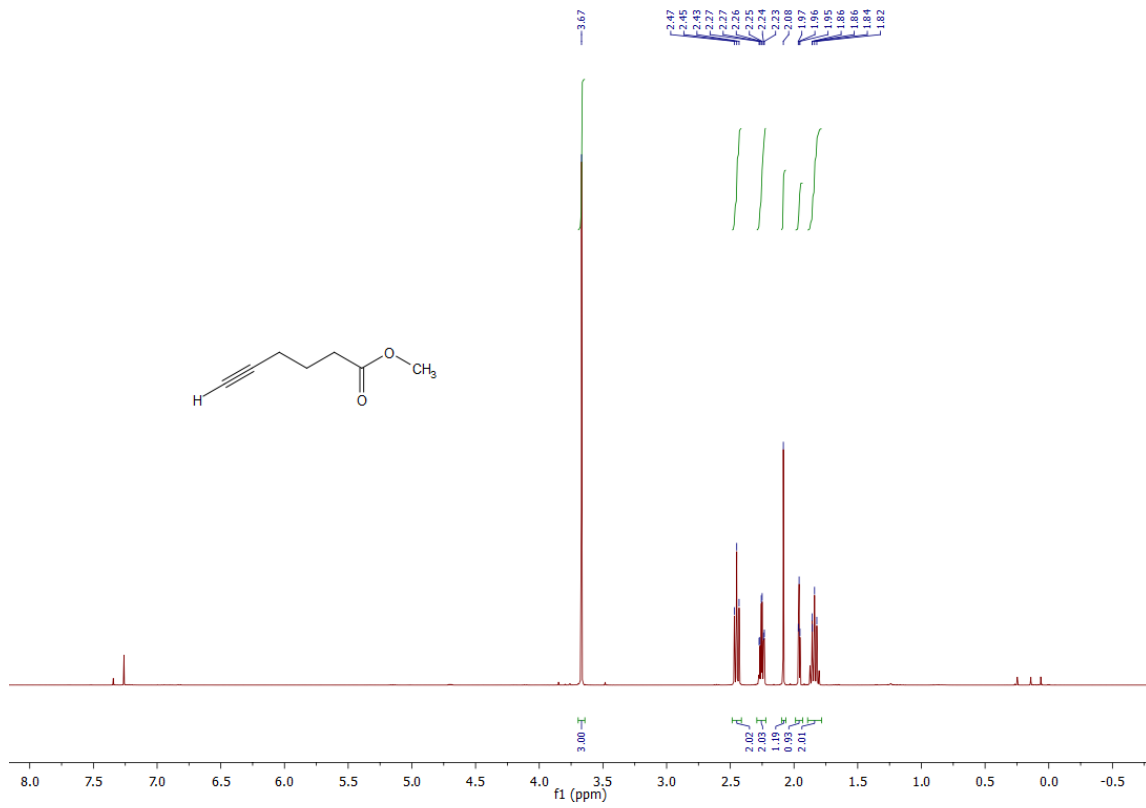


5-Hexynoic acid (0.10 g, 0.89 mmol, 1.0 equiv.) was converted to **methyl hex-5-ynoate (1b)**, 0.12 g, quant.) in an analogous manner as described above for the preparation of **methyl pent-4-ynoate (1a)**. *Note: all reagents and solvents were scaled according to molarity.*

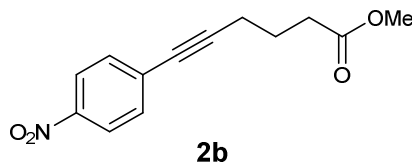
TLC (hexane/EtOAc, 4:1): $R_f = 0.73$.

$^1\text{H NMR}$ (CDCl_3 , 400 MHz, 25 °C): δ 3.67 (s, 3H, H_{OMe}), 2.45 (t, 2H, $\text{H}_{2\text{a,b}}$, $J_{2,3} = 7.4$ Hz), 2.25 (dt, 2H, $\text{H}_{4\text{a,b}}$, $J_{4,3} = 6.7$ Hz, $J_{4,6} = 2.7$ Hz), 1.96 (t, 1H, H_6 , $J_{6,4} = 2.7$ Hz), 1.84 (quint, 2H, $\text{H}_{3\text{a,b}}$, $J_{3,2} \approx J_{3,4} \approx 7.4$ Hz).

$^{13}\text{C NMR}$ (CDCl_3 , 101 MHz, 25 °C): δ 173.7 (C1), 83.4 (C5), 69.2 (C6), 51.7 (C_{OMe}), 32.8 (C2), 23.7 (C3), 18.0 (C4). Spectral characteristics matched those previously reported¹⁰⁴. *The product still contained AcOH but this did not affect the following reaction.*



4.4.8.16 – Methyl 6-(4-nitrophenyl)hex-5-ynoate (2b)

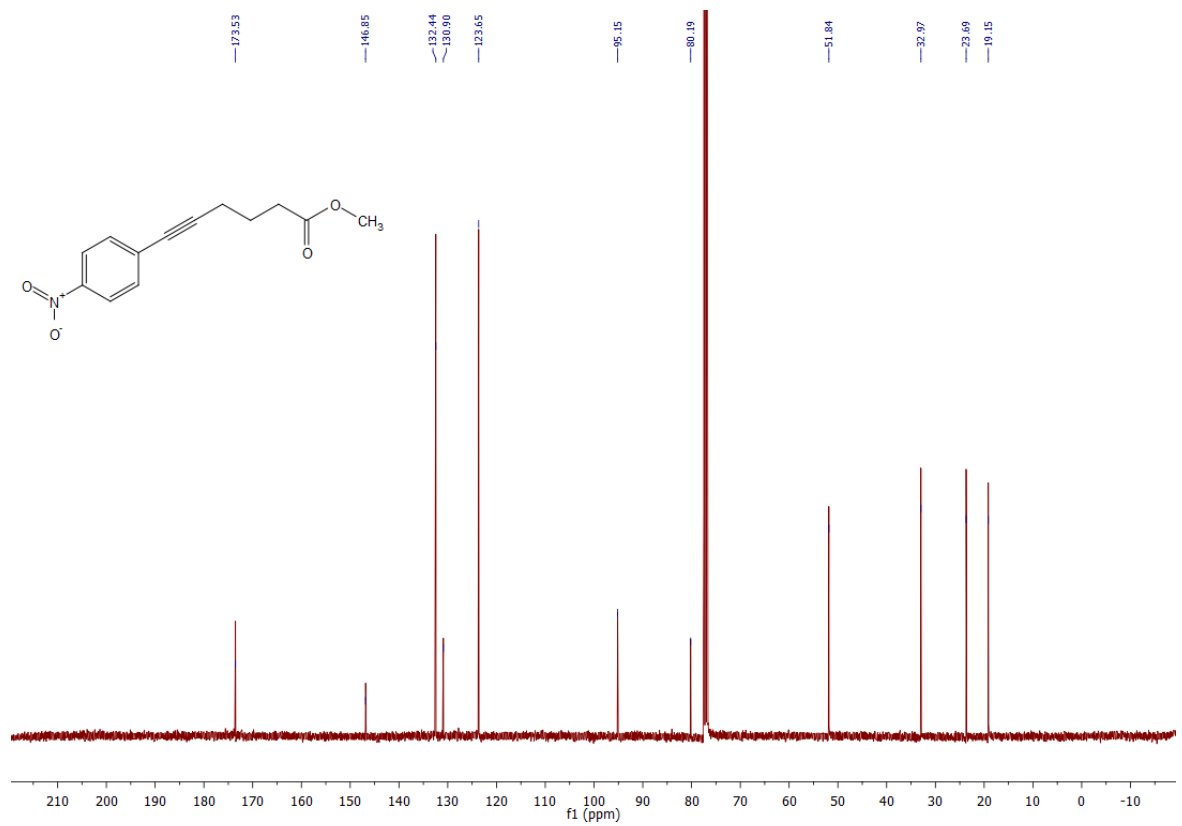
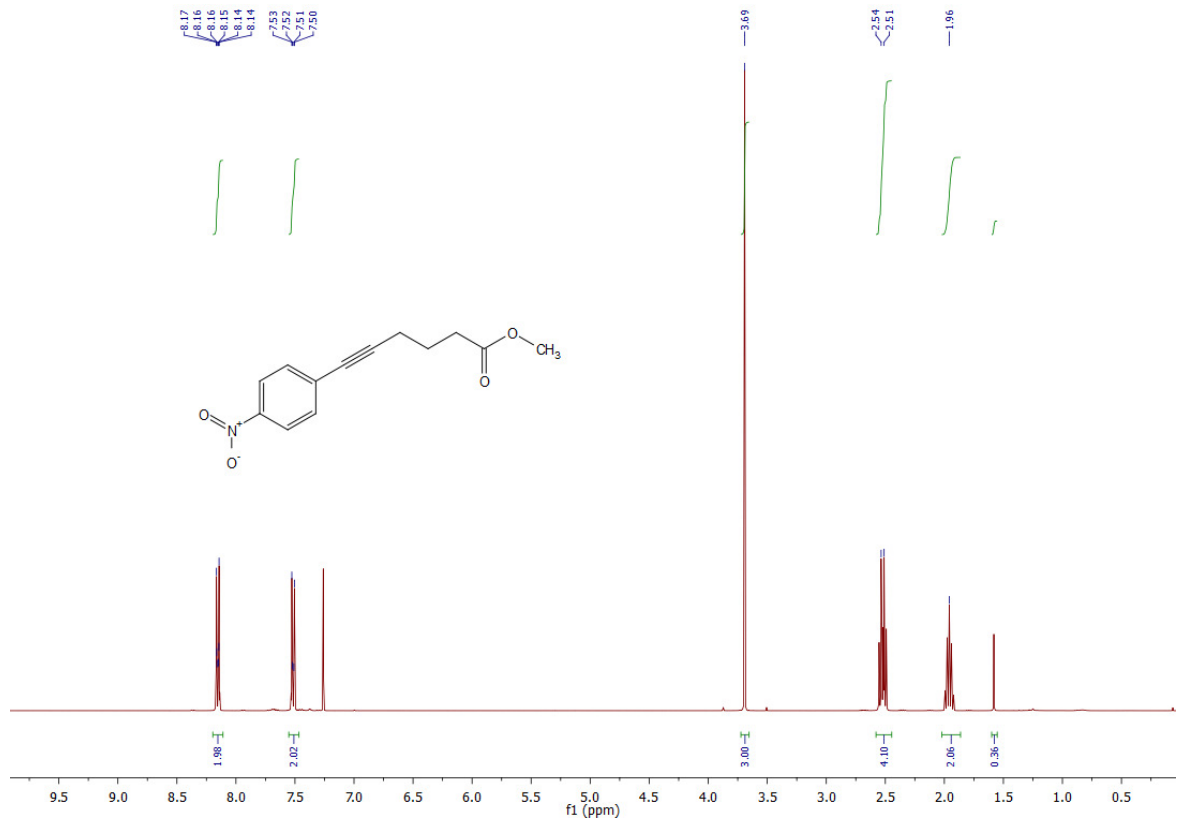


Methyl hex-5-ynoate (1b, 94 mg, 0.75 mmol, 1.0 equiv.) was converted to **methyl 6-(4-nitrophenyl)hex-5-ynoate (2b**, 0.15 g, 0.61 mmol, 82%) in an analogous manner as described above for the preparation of **methyl 5-(4-nitrophenyl)pent-4-ynoate (2a)**. *Note: all reagents and solvents were scaled according to molarity.*

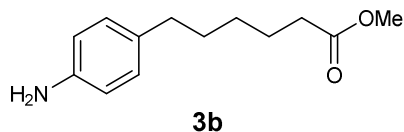
TLC (hexane/EtOAc, 4:1): $R_f = 0.46$.

$^1\text{H NMR}$ (CDCl_3 , 400 MHz, 25 °C): δ 8.18-8.14 (m, 2H, $\text{H}_{9\text{a,b}}$, $J_{9,8} \approx 9.0$ Hz), 7.53-7.49 (m, 2H, $\text{H}_{8\text{a,b}}$, $J_{8,9} \approx 9.0$ Hz), 3.69 (s, 3H, H_{OMe}), 2.56-2.49 (m, 4H, $\text{H}_{2\text{a,b}}$, $\text{H}_{4\text{a,b}}$), 1.96 (quint, 2H, $\text{H}_{3\text{a,b}}$, $J_{3,2} = J_{3,4} \approx 7.2$ Hz).

$^{13}\text{C NMR}$ (CDCl_3 , 101 MHz, 25 °C): δ 173.5 (C1), 146.9 (C10), 132.4 (2C, $\text{C}_{8\text{a,b}}$), 130.9 (C7), 123.7 (2C, $\text{C}_{9\text{a,b}}$), 95.2 (C5), 80.2 (C6), 51.8 (C_{OMe}), 33.0 (C2), 23.7 (C3), 19.2 (C4).



4.4.8.17 – Methyl 6-(4-aminophenyl)hexanoate (3b)



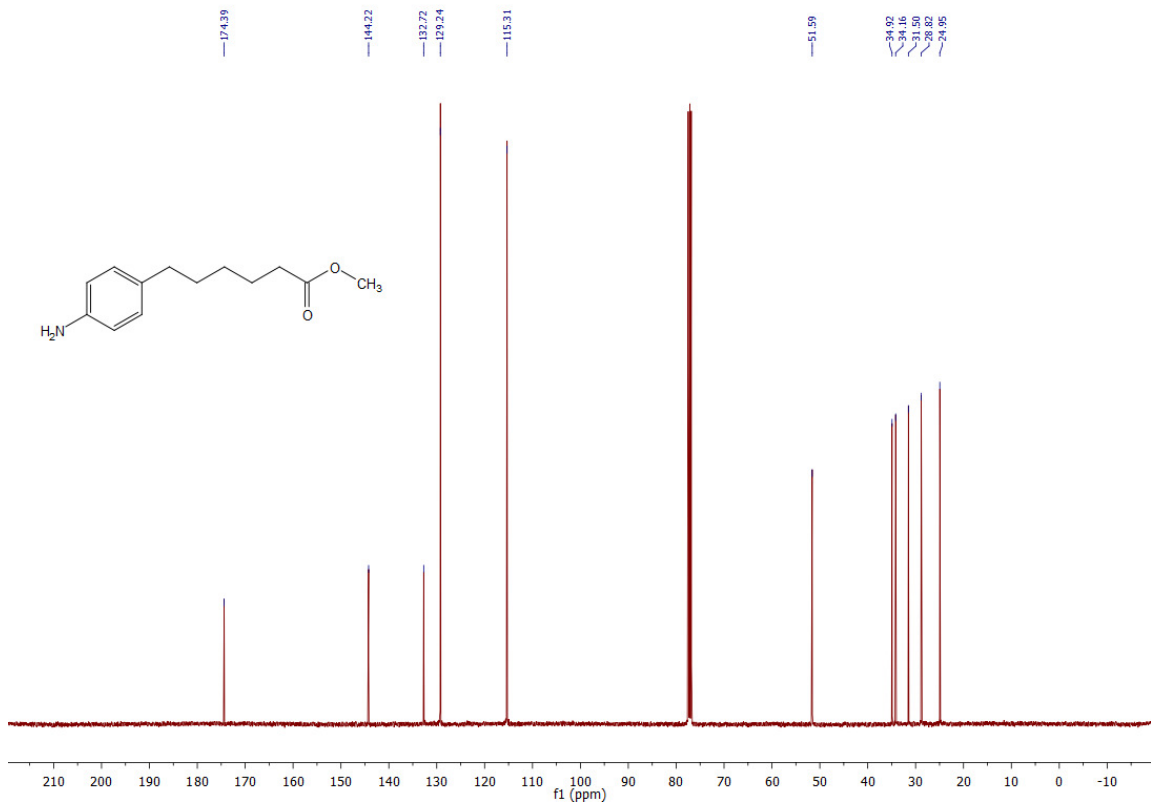
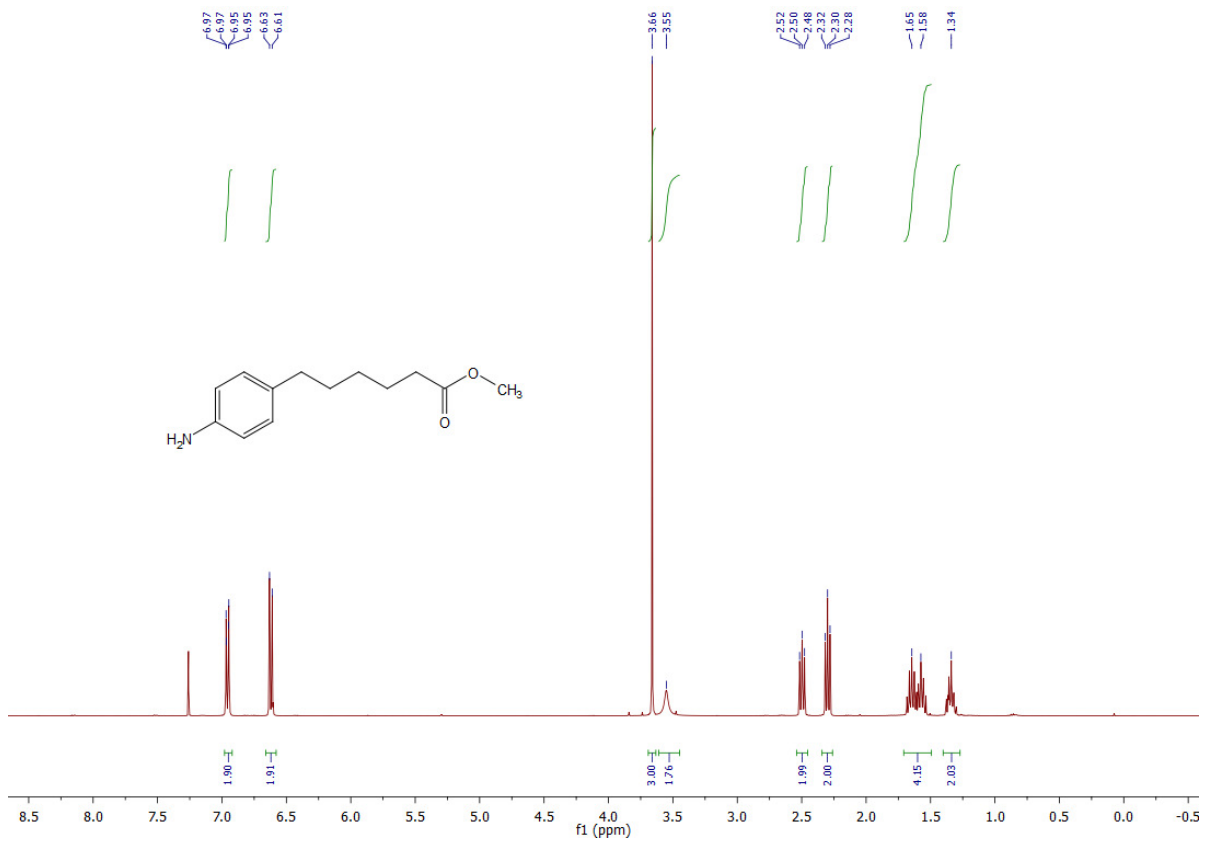
Methyl 6-(4-nitrophenyl)hex-5-ynoate (2b), 0.12 g, 0.5 mmol, 1 equiv.) was converted to **methyl 6-(4-aminophenyl)hexanoate (3b)**, 79 mg, 0.36 mmol, 72%) in an analogous manner as described above for the preparation of **methyl 5-(4-aminophenyl)pentanoate (3a)**. *Note: all reagents and solvents were scaled according to molarity.*

TLC (hexane/EtOAc, 4:1): $R_f = 0.13$.

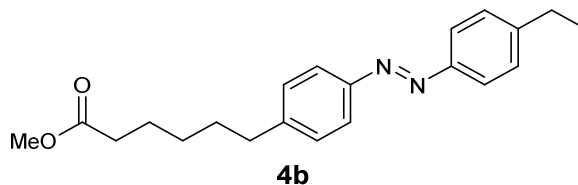
$^1\text{H NMR}$ (CDCl_3 , 400 MHz, 25 °C): δ 6.98-6.93 (m, 2H, $\text{H}_{8\text{a,b}}$, $J_{8,9} \approx 8.5$ Hz), 6.64-6.60 (dt, 2H, $\text{H}_{9\text{a,b}}$, $J_{9,8} \approx 8.4$ Hz), 3.66 (s, 3H, H_{OMe}), 3.55 (s_{br}, 2H, NH_2), 2.50 (t, 2H, $\text{H}_{6\text{a,b}}$, $J_{6,5} = 7.6$ Hz), 2.30 (t, 2H, $\text{H}_{2\text{a,b}}$, $J_{2,3} = 7.5$ Hz), 1.69-1.52 (m, 4H, $\text{H}_{3\text{a,b}}$, $\text{H}_{5\text{a,b}}$), 1.38-1.28 (m, 2H, $\text{H}_{4\text{a,b}}$).

$^{13}\text{C NMR}$ (CDCl_3 , 101 MHz, 25 °C): δ 174.4 (C1), 144.2 (C10), 132.7 (C7), 129.2 (2C, $\text{C}_{8\text{a,b}}$), 115.3 (2C, $\text{C}_{9\text{a,b}}$), 51.6 (C_{OMe}), 34.9 (C6), 34.2 (C2), 31.5 (C5), 28.8 (C3), 25.0 (C4).

HRMS (EI^+): m/z calcd. for $[\text{C}_{13}\text{H}_{19}\text{NO}_2]$: 221.1416, found: 221.1408 ($[\text{M}-\text{e}]^+$).



4.4.8.18 – Methyl 6-(4-((4-ethylphenyl)diazenyl)phenyl)hexanoate (4b)



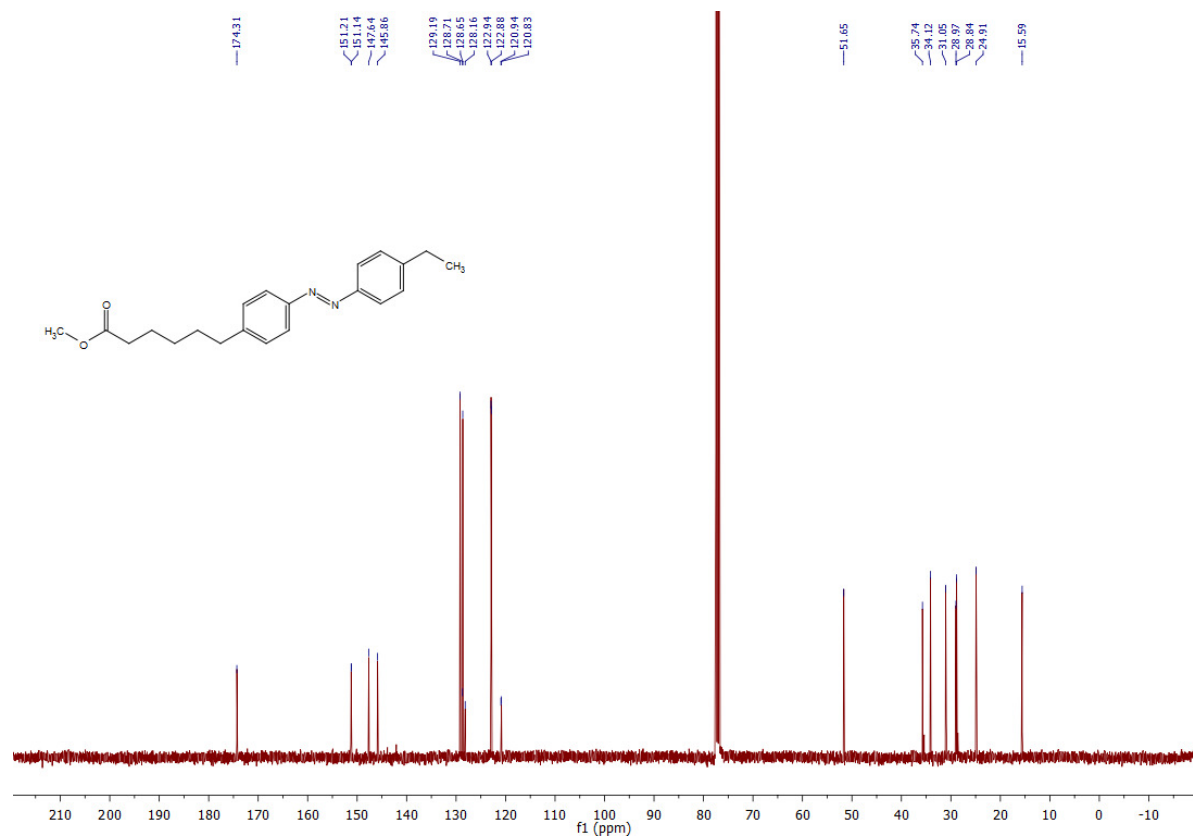
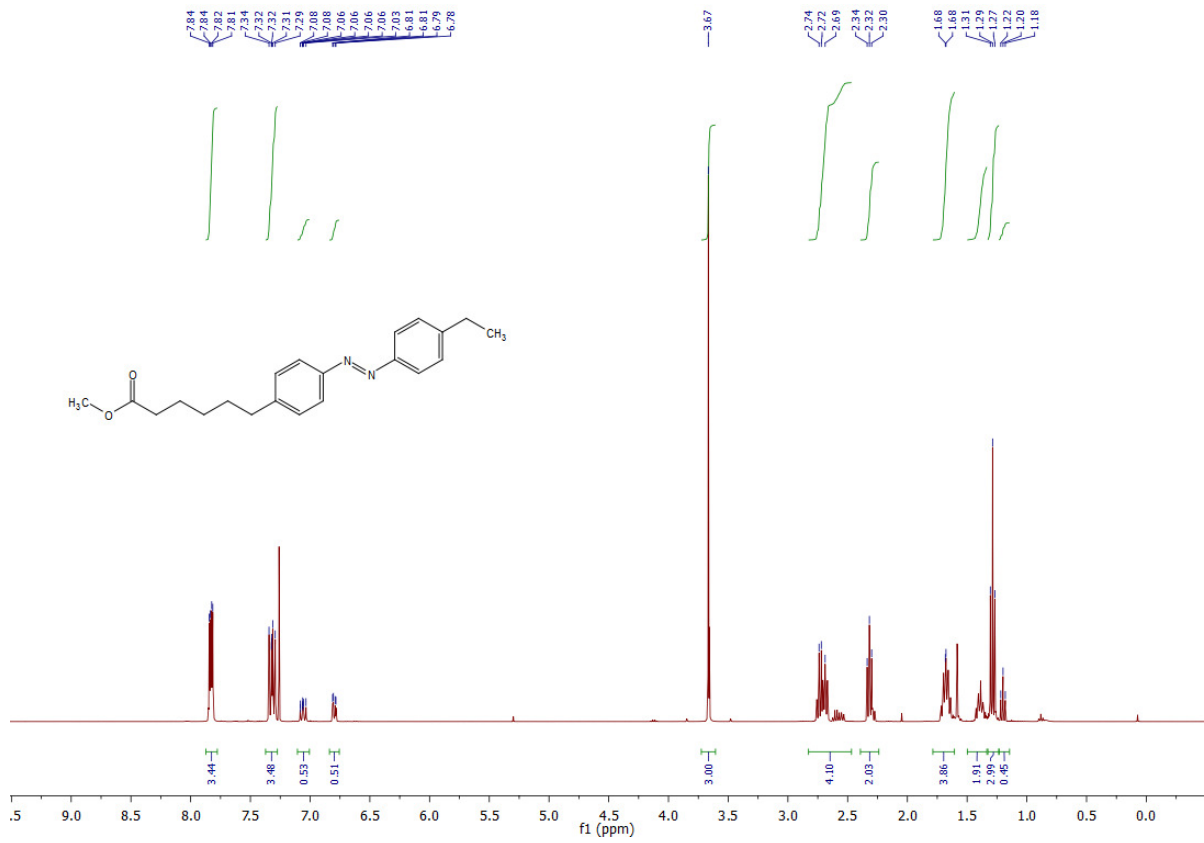
4-Ethylaniline (0.12 g, 0.95 mmol, 3.0 equiv.) and **methyl 6-(4-aminophenyl)hexanoate (3b)**, 70 mg, 0.32 mmol, 1.0 equiv.) were converted to orange oil **methyl 6-(4-((4-ethylphenyl)diazenyl)phenyl)hexanoate (4b)**, 52 mg, 48%) in an analogous manner as described above for the preparation of **methyl 5-(4-((4-propylphenyl)diazenyl)phenyl) pentanoate (4a)**.
Note: all reagents and solvents were scaled according to molarity.

TLC (pentane/EtOAc, 20:1): $R_f = 0.24$ (*trans*), 0.10 (*cis*).

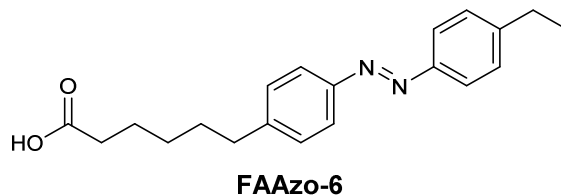
$^1\text{H NMR}$ (CDCl_3 , 400 MHz, 25 °C): δ 7.85-7.80 (m, 4H, H_{9a,b}, H_{14a,b}, $J_{9,8} \approx J_{14,15} \approx 8.4$ Hz), 7.35-7.28 (m, 4H, H_{8a,b}, H_{15a,b}, $J_{8,9} \approx J_{15,14} \approx 8.5$ Hz), 3.67 (s, 3H, H_{OMe}), 2.77-2.65 (m, 4H, H_{6a,b}, H_{17a,b}), 2.32 (t, 2H, H_{2a,b}), 1.73-1.62 (m, 4H, H_{3a,b}, H_{5a,b}), 1.43-1.34 (m, 2H, H_{4a,b}), 1.29 (t, 3H, H_{18a,b,c}, $J_{18,17} = 7.6$ Hz).

$^{13}\text{C NMR}$ (CDCl_3 , 101 MHz, 25 °C): δ 174.3 (C₁), 151.2 (C_{azo}), 151.1 (C_{azo}), 147.6 (C_{azo}), 145.9 (C_{azo}), 129.2 (2C, C_{azo}), 128.7 (2C, C_{azo}), 122.9 (2C, C_{azo}), 122.9 (2C, C_{azo}), 51.7 (C_{OMe}), 35.7 (C_{alk}), 34.1 (C₂), 31.1 (C_{alk}), 29.0 (C_{alk}), 28.9 (C_{alk}), 24.9 (C_{alk}), 15.6 (C₁₈).

HRMS (EI⁺): m/z calcd. for [C₂₁H₂₆N₂O₂]: 338.1994, found: 338.1983 ([M-e]⁺).



4.4.8.19 – 6-(4-((4-Ethylphenyl)diazenyl)phenyl)hexanoic acid (FAAzo-6)



Methyl 6-(4-((4-ethylphenyl)diazenyl)phenyl)hexanoate (4b, 45 mg, 0.13 mmol, 1.0 equiv.) was converted to red solid **6-(4-((4-ethylphenyl)diazenyl)phenyl)hexanoic acid (FAAzo-6, 32 mg, 75%)** in an analogous manner as described above for the preparation of **5-(4-((4-propylphenyl)diazenyl)phenyl)pentanoic acid (FAAzo-5)**. *Note: all reagents and solvents were scaled according to molarity.*

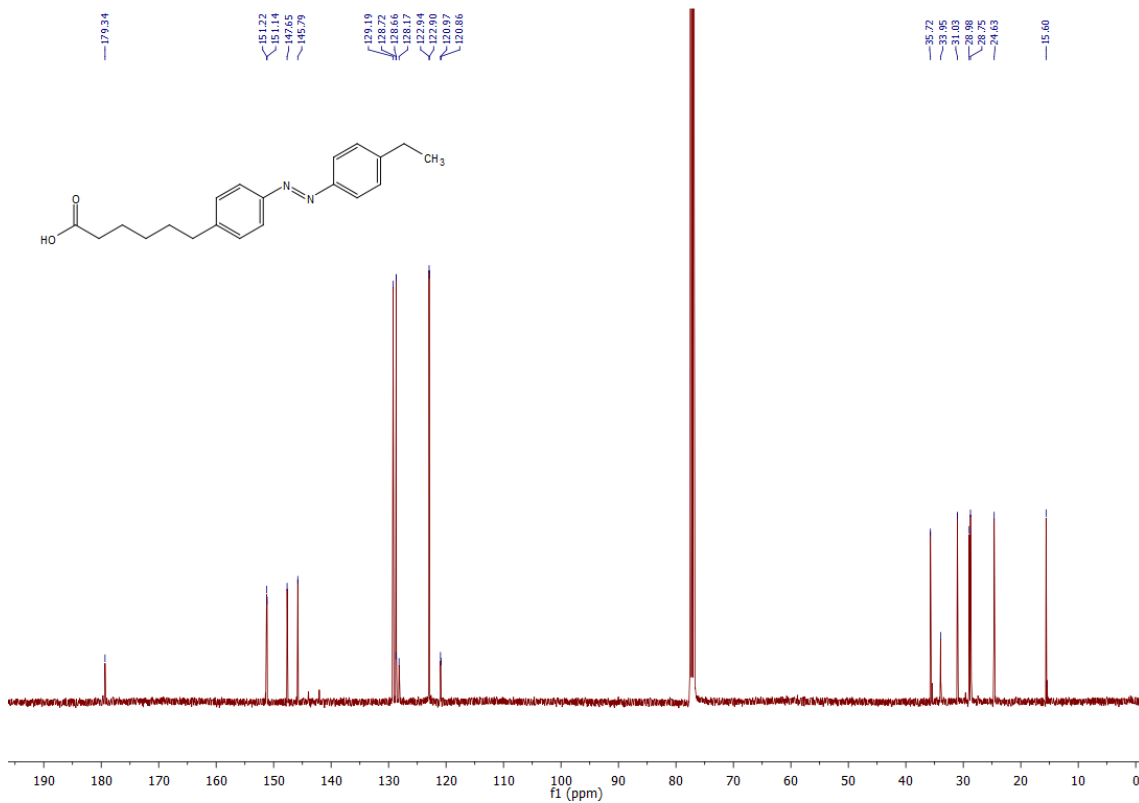
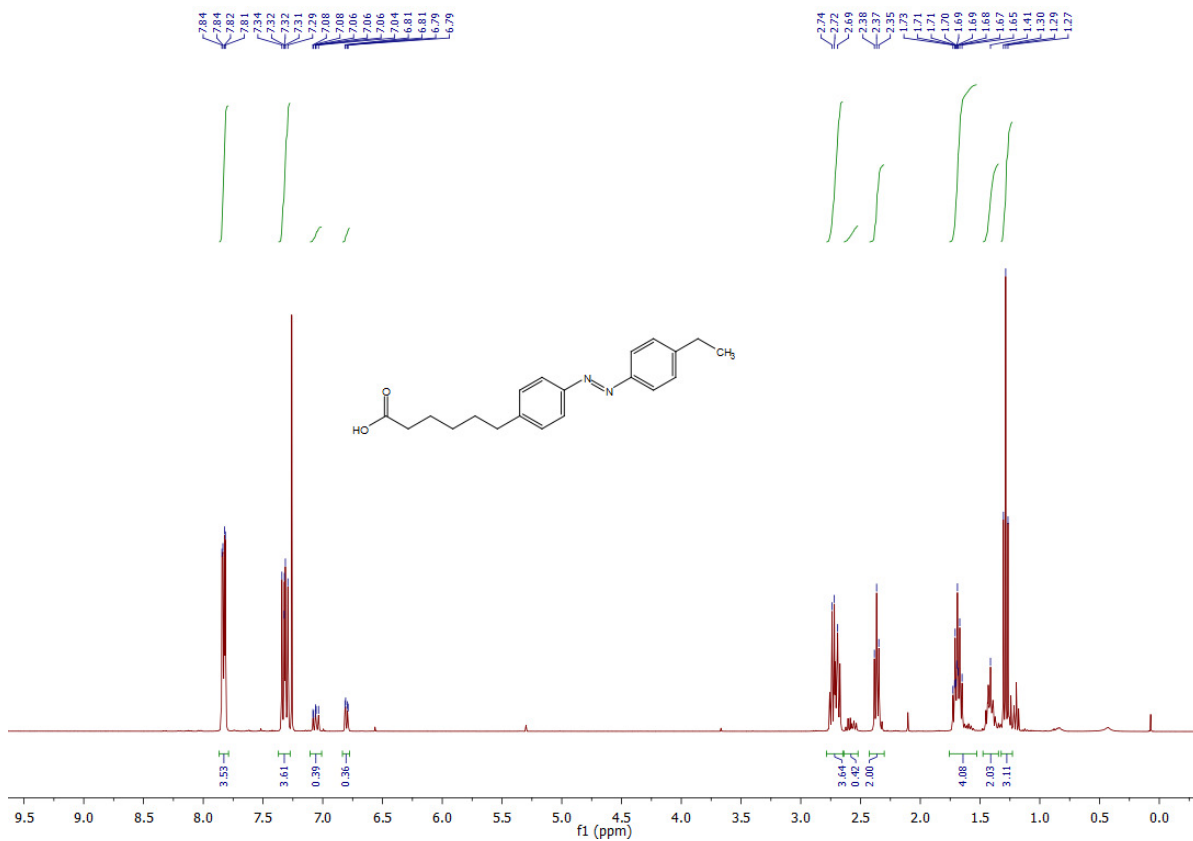
TLC (CH₂Cl₂:AcOH, 99:1): R_f = 0.22.

¹H NMR (CDCl₃, 400 MHz, 25 °C): δ 7.85-7.80 (m, 4H, H_{9,a,b}, H_{14,a,b}, J_{9,10} ≈ J_{14,15} ≈ 8.3 Hz), 7.35-7.28 (m, 4H, H_{8,a,b}, H_{15,a,b}, J_{8,9} ≈ J_{15,14} ≈ 8.4 Hz), 2.77-2.65 (m, 4H, H_{6,a,b}, H_{17,a,b}), 2.39-2.33 (t, 2H, H_{2,a,b}, J_{2,3} = 7.4 Hz), 1.73-1.64 (m, 4H, H_{3,a,b}, H_{5,a,b}), 1.46-1.37 (m, 2H, H_{4,a,b}), 1.29 (t, 3H, H_{18,a,b,c}, J_{18,17} = 7.5 Hz).

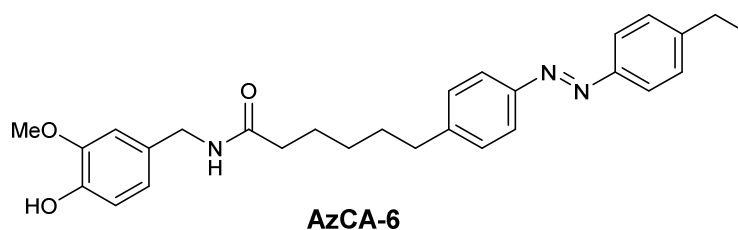
¹³C NMR (CDCl₃, 101 MHz, 25 °C): δ 179.4 (C₁), 151.2 (C_{azo}), 151.1 (C_{azo}), 147.7 (C_{azo}), 145.8 (C_{azo}), 129.2 (2C, C_{azo}), 128.7 (2C, C_{azo}), 122.9 (2C, C_{azo}), 122.9 (2C, C_{azo}), 35.7 (C_{alk}), 34.0 (C₂), 31.0 (C_{alk}), 29.0 (C_{alk}), 28.8 (C_{alk}), 24.6 (C_{alk}), 15.6 (C₁₈).

IR (neat, ATR): $\tilde{\nu}$ = 3022, 2956, 2927, 2851, 1692, 1600, 1497, 1466, 1438, 1410, 1355, 1293, 1249, 1200, 1152, 1056, 1010, 913, 848, 826, 729, 685.

HRMS (EI⁺): *m/z* calcd. for [C₂₀H₂₄N₂O₂]: 324.1838, found: 324.1838 ([M-e]⁺).



4.4.8.20 – N-(4-Hydroxy-3-methoxybenzyl)-6-(4-((4-ethylphenyl)diazenyl)phenyl)hexanamide (AzCA-6)



6-(4-((4-Ethylphenyl)diazenyl)phenyl)hexanoic acid (FAAzo-6, 16 mg, 49 μ mol, 1 equiv.) was converted to red solid **N-(4-hydroxy-3-methoxybenzyl)-6-(4-((4-ethylphenyl)diazenyl)phenyl)hexanamide (AzCA-6, 19 mg, 86%)** in an analogous manner as described above for the preparation of **N-(4-hydroxy-3-methoxybenzyl)-4-((4-heptylphenyl)diazenyl)benzamide (AzCA-1)**. *Note: all reagents and solvents were scaled according to molarity.*

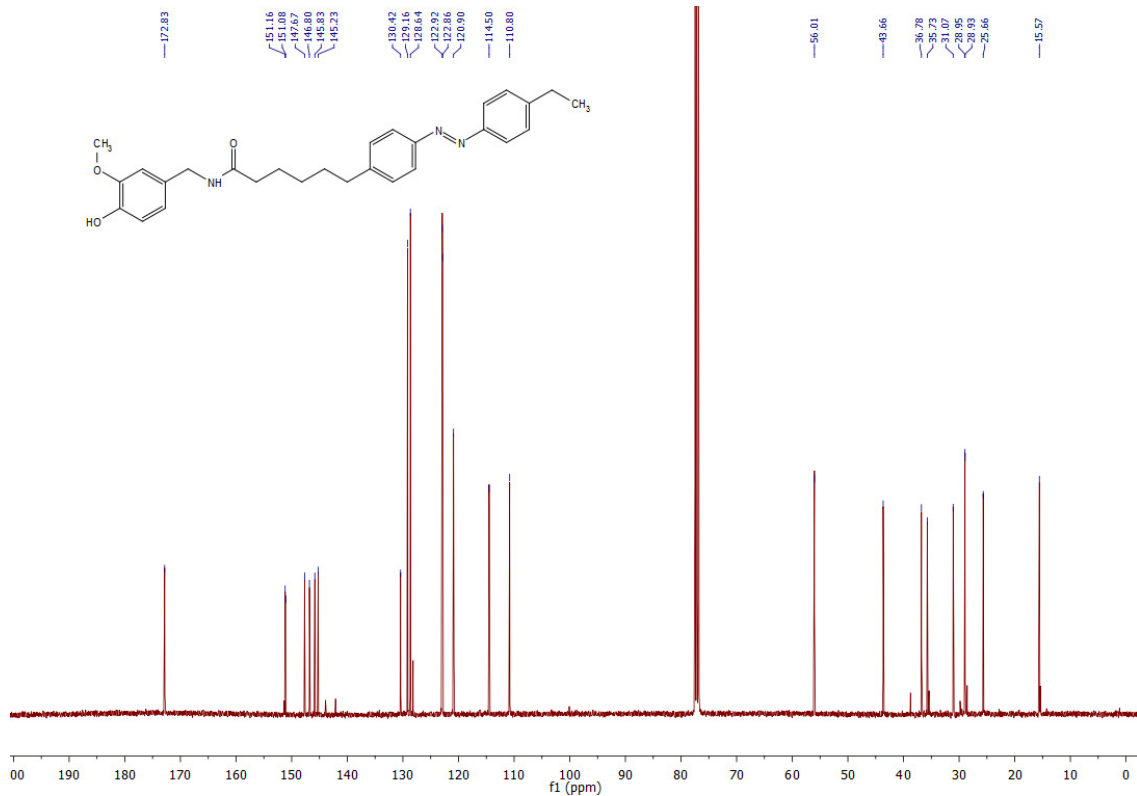
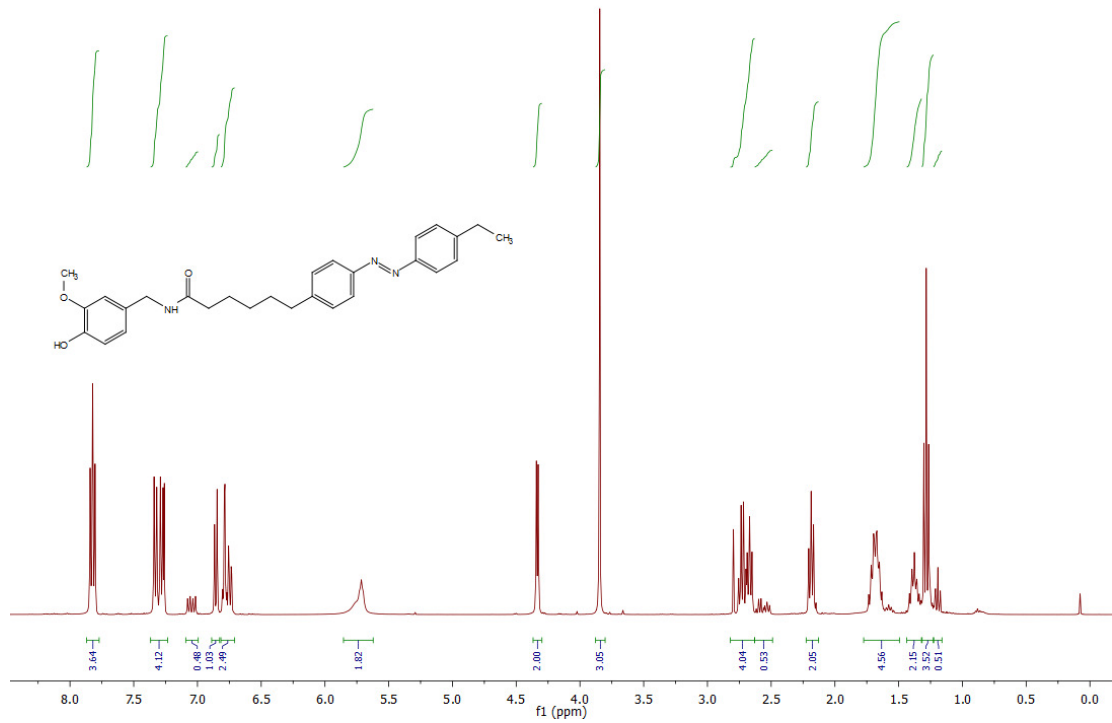
TLC (hexane/EtOAc, 1:2): $R_f = 0.31$.

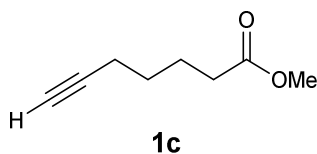
$^1\text{H NMR}$ (CDCl_3 , 400 MHz, 25 $^\circ\text{C}$): δ 7.85-7.79 (m, 4H, H_{9a,b}, H_{14a,b}, $J_{9,8} \approx J_{14,15} \approx 8.3$ Hz), 7.35-7.25 (m, 4H, H_{8a,b}, H_{15a,b}, $J_{8,9} \approx J_{15,14} \approx 8.3$ Hz), 6.86 (d, 1H, H₂₄, $J_{24,25} = 8.1$ Hz), 6.81-6.72 (m, 2H, H₂₁, H₂₅), 5.82-5.66 (m, 2H, NH, OH, $J_{\text{NH},19} = 5.3$ Hz), 4.33 (d, 2H, H_{19a,b}, $J_{19,\text{NH}} = 5.7$ Hz), 3.84 (s, 3H, H_{26a,b,c}), 2.77-2.63 (m, 4H, H_{6a,b}, H_{17a,b}), 2.19 (t, 2H, H_{2a,b}, $J_{2,3} = 7.5$ Hz), 1.74-1.62 (m, 4H, H_{5a,b}, H_{3a,b}), 1.42-1.32 (m, 2H, H_{4a,b}), 1.28 (t, 3H, H_{18a,b,c}, $J_{18,17} = 7.8$ Hz).

$^{13}\text{C NMR}$ (CDCl_3 , 101 MHz, 25 $^\circ\text{C}$): δ 172.8 (C₁), 151.2 (C_{azo}), 151.1 (C_{azo}), 147.7 (C_{azo}), 146.8 (C₂₂), 145.8 (C_{azo}), 145.2 (C₂₃), 130.4 (C₂₀), 129.2 (2C, C_{azo}), 128.6 (2C, C_{azo}), 122.9 (2C, C_{azo}), 122.9 (2C, C_{azo}), 120.9 (C₂₅), 114.5 (C₂₄), 110.8 (C₂₁), 56.0 (C₂₆), 43.7 (C₁₉), 36.8 (C₂), 35.7 (C_{alk}), 31.1 (C_{alk}), 29.0 (C_{alk}), 28.9 (C_{alk}), 25.7 (C_{alk}), 15.6 (C_{alk}).

IR (neat, ATR): $\tilde{\nu} = 3291, 3053, 2961, 2930, 2856, 1651, 1645, 1600, 1557, 1539, 1515, 1546, 1530, 1373, 1274, 1237, 1155, 1124, 1035, 1013, 845, 795, 736$.

HRMS (EI⁺): m/z calcd. for [C₂₈H₃₃N₃O₃]: 459.2522, found: 459.2520 ([M-e]⁺).

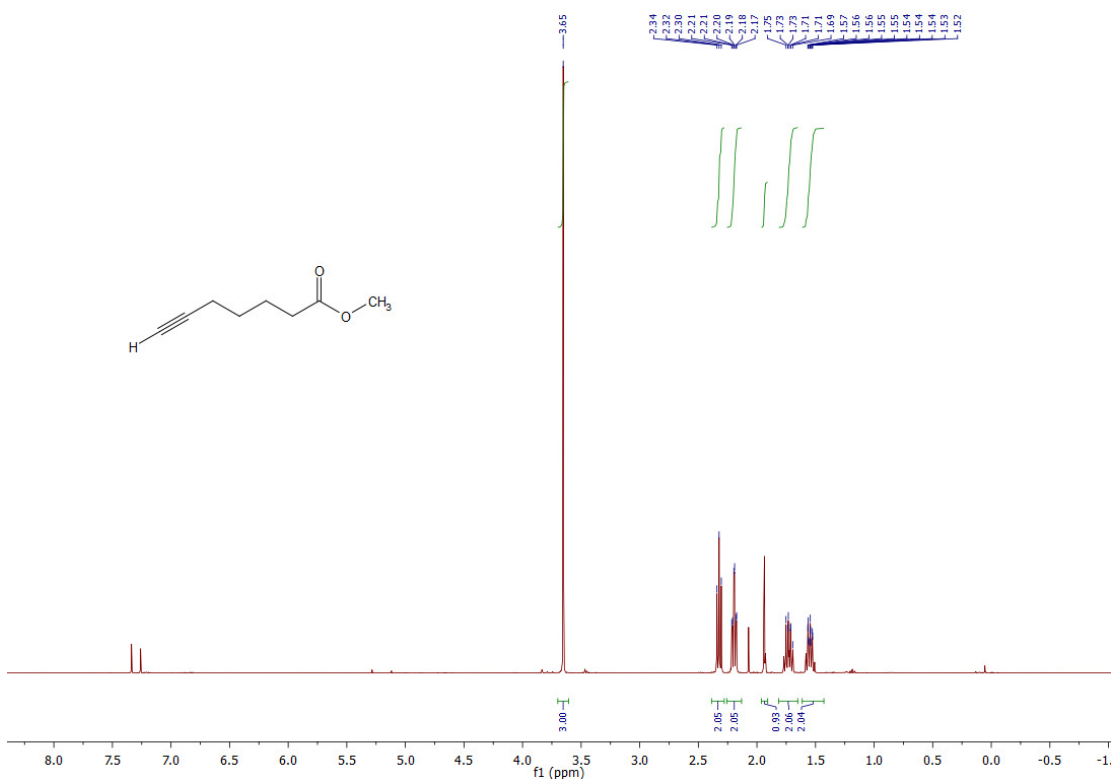


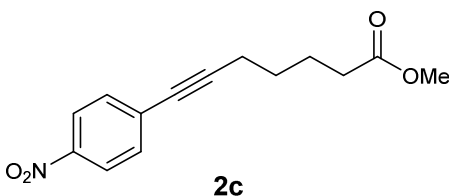
4.4.8.21 – Methyl hept-6-ynoate (**1c**)

6-Heptynoic acid (0.10 g, 0.79 mmol, 1.0 equiv.) was converted to **methyl hept-6-ynoate (1c)**, 0.11 g, quant.) in an analogous manner as described above for the preparation of **methyl pent-4-ynoate (1a)**. *Note: all reagents and solvents were scaled according to molarity.*

TLC (hexane/EtOAc, 4:1): $R_f = 0.71$.

$^1\text{H NMR}$ (CDCl_3 , 400 MHz, 25 °C): δ 3.65 (s, 3H, H_{OMe}), 2.32 (t, 2H, $\text{H}_{2,\text{a,b}}$, $J_{2,3} = 7.4$ Hz), 2.19 (dt, 2H, $\text{H}_{5,\text{a,b}}$, $J_{5,4} = 7.1$ Hz, $J_{5,7} = 2.6$ Hz), 1.94 (t, 1H, H_7 , $J_{7,5} = 2.5$ Hz), 1.78-1.69 (m, 2H, H_{alk}), 1.59-1.50 (m, 2H, H_{alk}). *The product still contained AcOH but this did not affect the next reaction.*



4.4.8.22 – Methyl 7-(4-nitrophenyl)hept-6-ynoate (2c)

Methyl hept-6-ynoate (1c, 96 mg, 0.69 mmol, 1.0 equiv.) was converted to **methyl 7-(4-nitrophenyl)hept-6-ynoate (2c, 0.12 g, 0.47 mmol, 70%)** in an analogous manner as described above for the preparation of **methyl 5-(4-nitrophenyl)pent-4-ynoate (2a)**. *Note: all reagents and solvents were scaled according to molarity.*

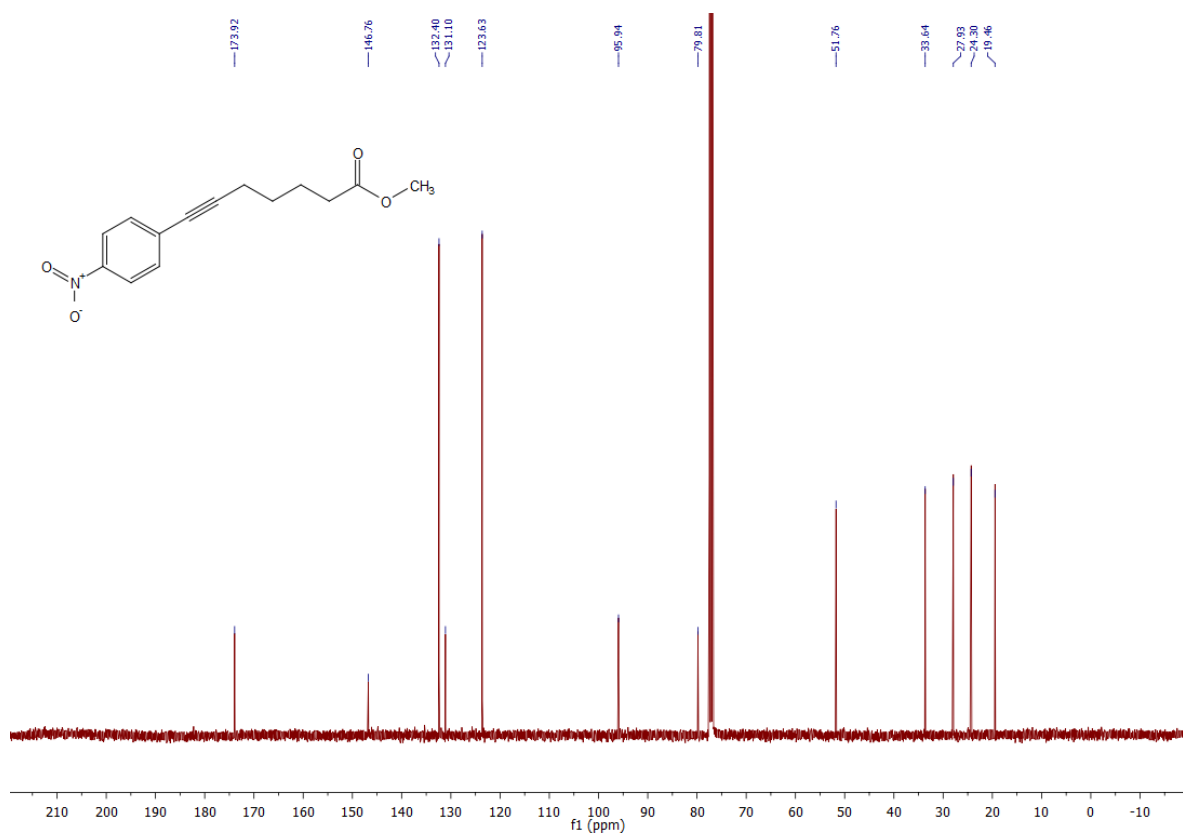
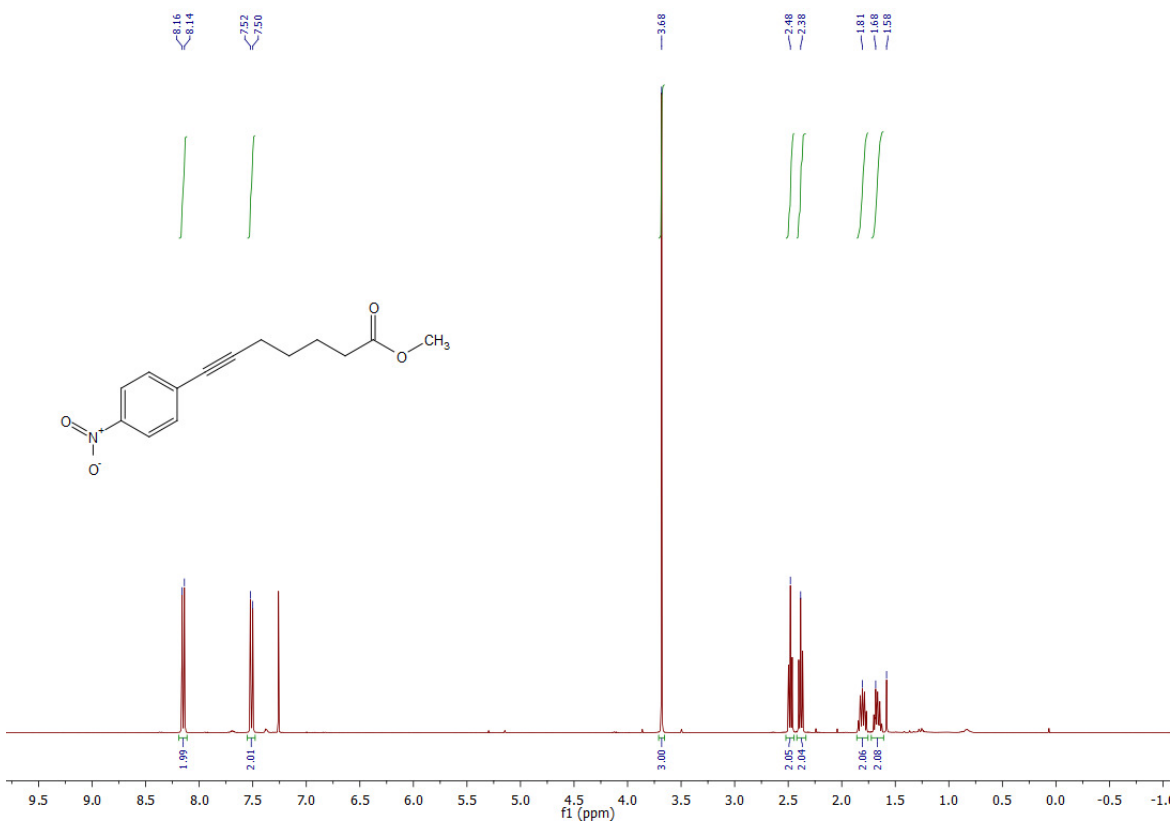
TLC (hexane/EtOAc, 4:1): $R_f = 0.53$.

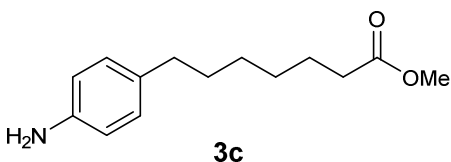
$^1\text{H NMR}$ (CDCl_3 , 400 MHz, 25 °C): δ 8.17-8.13 (m, 2H, H_{10a,b}, $J_{10,9} \approx 8.9$ Hz), 7.53-7.49 (m, 2H, H_{9a,b}, $J_{9,10} \approx 8.9$ Hz), 3.68 (s, 3H, H_{OMe}), 2.48 (t, 2H, H_{2a,b}, $J_{2,3} = 7.0$ Hz), 2.38 (t, 2H, H_{5a,b}, $J_{5,4} = 7.3$ Hz), 1.85-1.76 (m, 2H, H_{4a,b}), 1.70-1.62 (m, 2H, H_{3a,b}).

$^{13}\text{C NMR}$ (CDCl_3 , 101 MHz, 25 °C): δ 173.9 (C1), 146.8 (C11), 132.4 (2C, C_{9a,b}), 131.1 (C8), 123.6 (2C, C_{10a,b}), 95.9 (C6), 79.8 (C7), 51.8 (C_{OMe}), 33.6 (C2), 27.9 (C3), 24.3 (C4), 19.5 (C5).

HRMS (EI⁺): m/z calcd. for [C₁₅H₁₇N₁O₄]: 275.1158, found: 275.1134 ([M-e]⁺).

4 – Photoswitchable fatty acids enable optical control of TRPV1



4.4.8.23 – Methyl 7-(4-aminophenyl)heptanoate (3c)

Methyl 7-(4-nitrophenyl)hept-6-ynoate (2c), 0.12 g, 0.4 mmol, 1 equiv.) was converted to orange oil **methyl 7-(4-aminophenyl)heptanoate (3c)**, 85 mg, 0.36 mmol, 82%) in an analogous manner as described above for the preparation of **methyl 5-(4-aminophenyl)pentanoate (3a)**. *Note: all reagents and solvents were scaled according to molarity.*

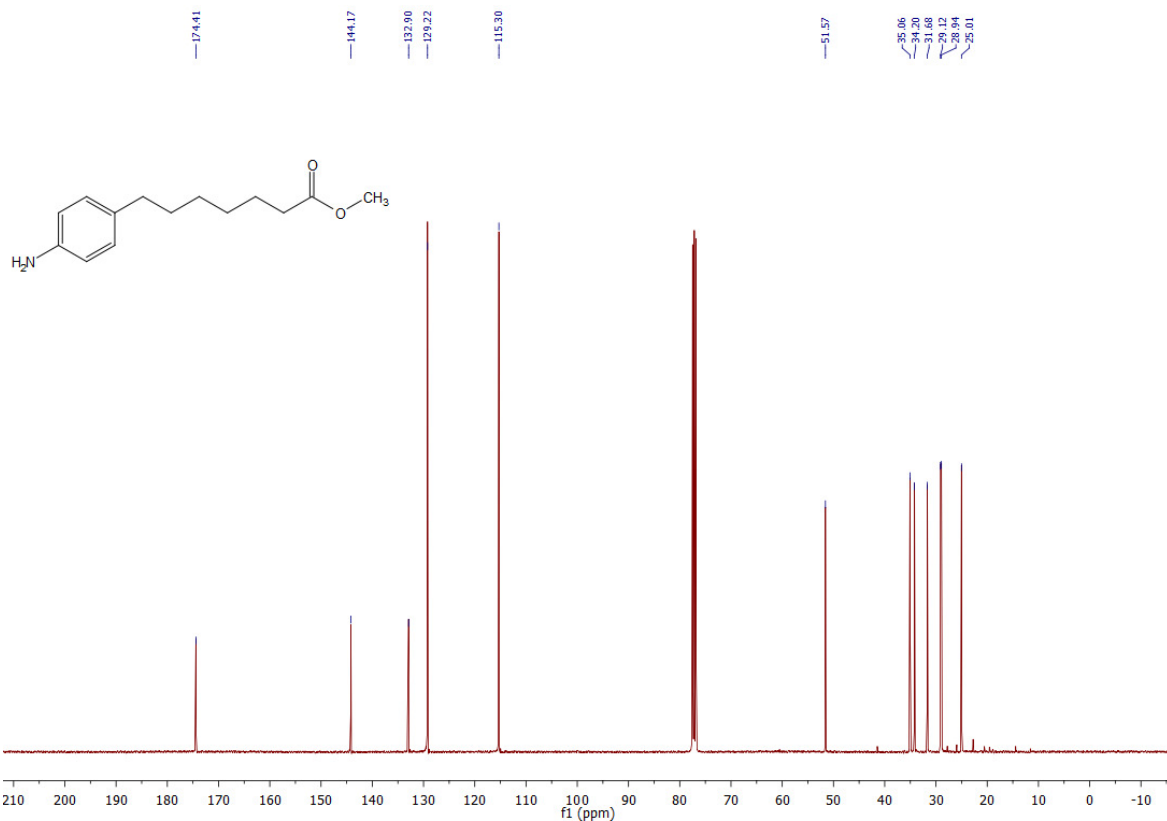
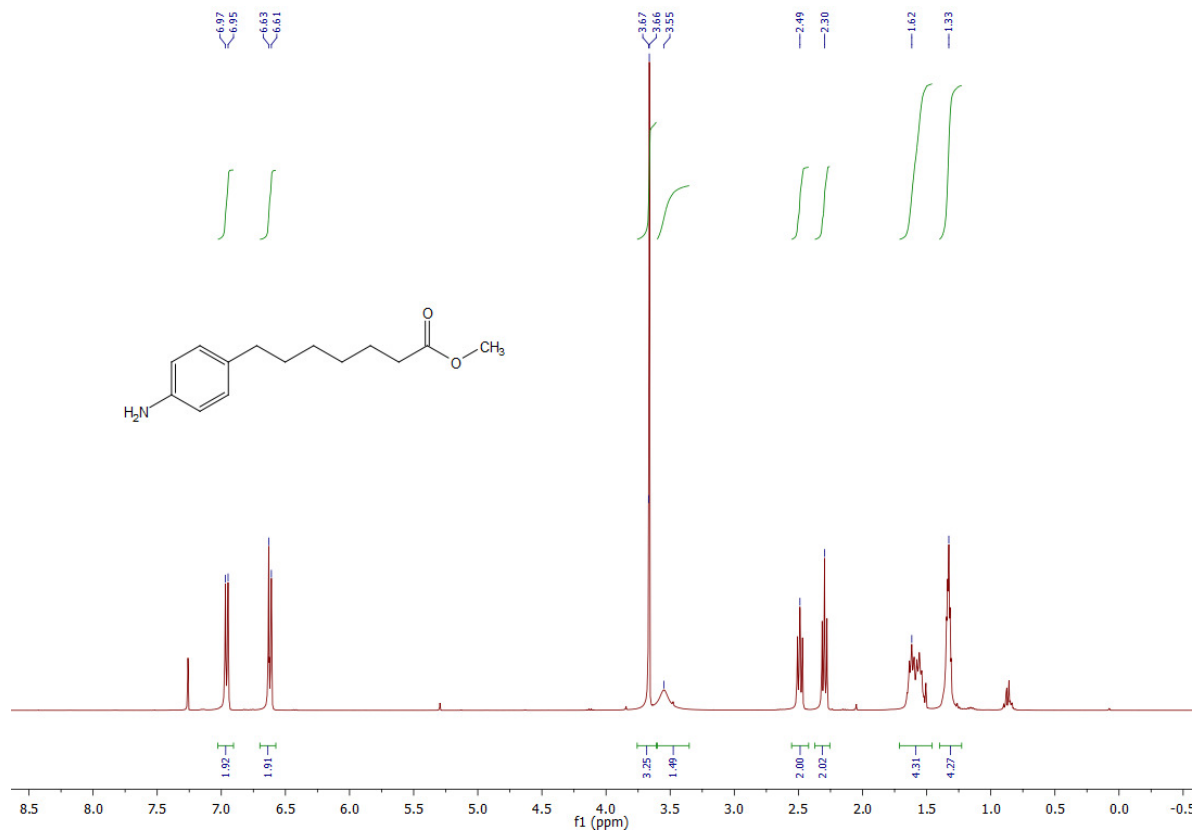
TLC (hexane/EtOAc, 4:1): $R_f = 0.12$.

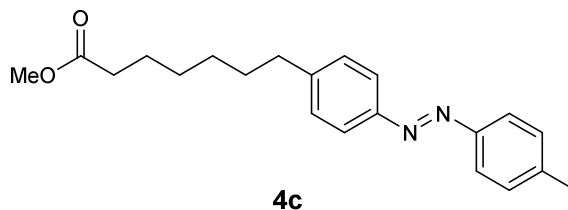
$^1\text{H NMR}$ (CDCl_3 , 400 MHz, 25 °C): δ 6.99-6.93 (m, 2H, $\text{H}_{9\text{a,b}}$, $\text{H}_{9,10} \approx 8.2$ Hz), 6.65-6.60 (m, 2H, $\text{H}_{10\text{a,b}}$, $J_{10,9} \approx 8.3$ Hz), 3.66 (s, 3H, H_{OMe}), 3.55 (s_{br}, NH_2), 2.49 (t, 2H, $\text{H}_{7\text{a,b}}$, $J_{7,6} = 8.1$ Hz), 2.30 (t, 2H, $\text{H}_{2\text{a,b}}$), 1.66-1.50 (m, 4H, $\text{H}_{3\text{a,b}}$, $\text{H}_{6\text{a,b}}$), 1.39-1.28 (m, 4H, $\text{H}_{4\text{a,b}}$, $\text{H}_{5\text{a,b}}$).

$^{13}\text{C NMR}$ (CDCl_3 , 101 MHz, 25 °C): δ 174.4 (C1), 144.2 (C11), 132.9 (C8), 129.2 (2C, $\text{C}_{9\text{a,b}}$), 115.3 (2C, $\text{C}_{10\text{a,b}}$), 51.6 (C_{OMe}), 35.1 (C7), 34.2 (C2), 31.7 (C_{alk}), 29.1 (C_{alk}), 28.9 (C_{alk}), 25.0 (C_{alk}).

HRMS (ESI⁺): m/z calcd. for $[\text{C}_{15}\text{H}_{24}\text{NO}_2]^+$: 250.1807, found: 250.1801 ($[\text{M}+\text{H}]^+$).

4 – Photoswitchable fatty acids enable optical control of TRPV1



4.4.8.24 – Methyl 7-(4-(*p*-tolylidiazenyl)phenyl)heptanoate (**4c**)

p-Toluidine (0.10 g, 0.96 mmol, 3.0 equiv.) and **methyl 7-(4-aminophenyl)heptanoate (3c)**, 70 mg, 0.32 mmol, 1.0 equiv.) were converted to orange oil **methyl 7-(4-(*p*-tolylidiazenyl)phenyl)heptanoate (4c)**, 48 mg, 44%) in an analogous manner as described above for the preparation of **methyl 5-(4-((4-propylphenyl)diazenyl)phenyl)pentanoate (4a)**. *Note: all reagents and solvents were scaled according to molarity.*

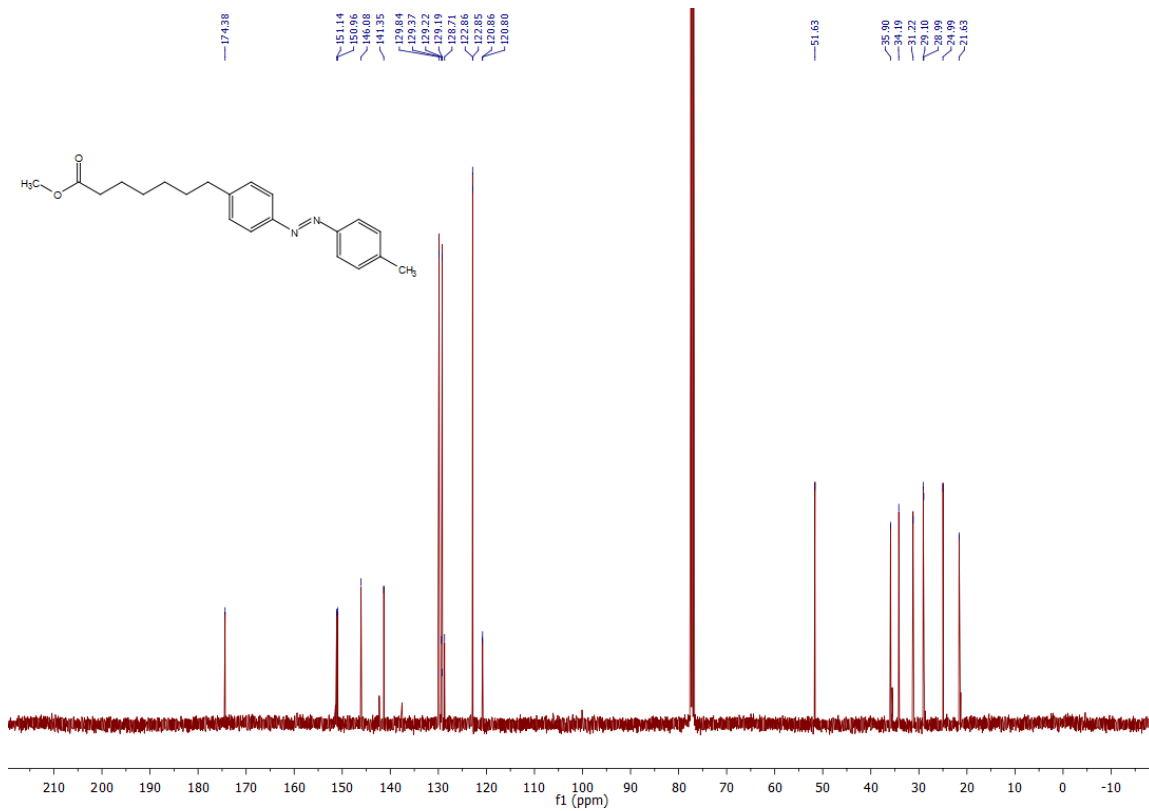
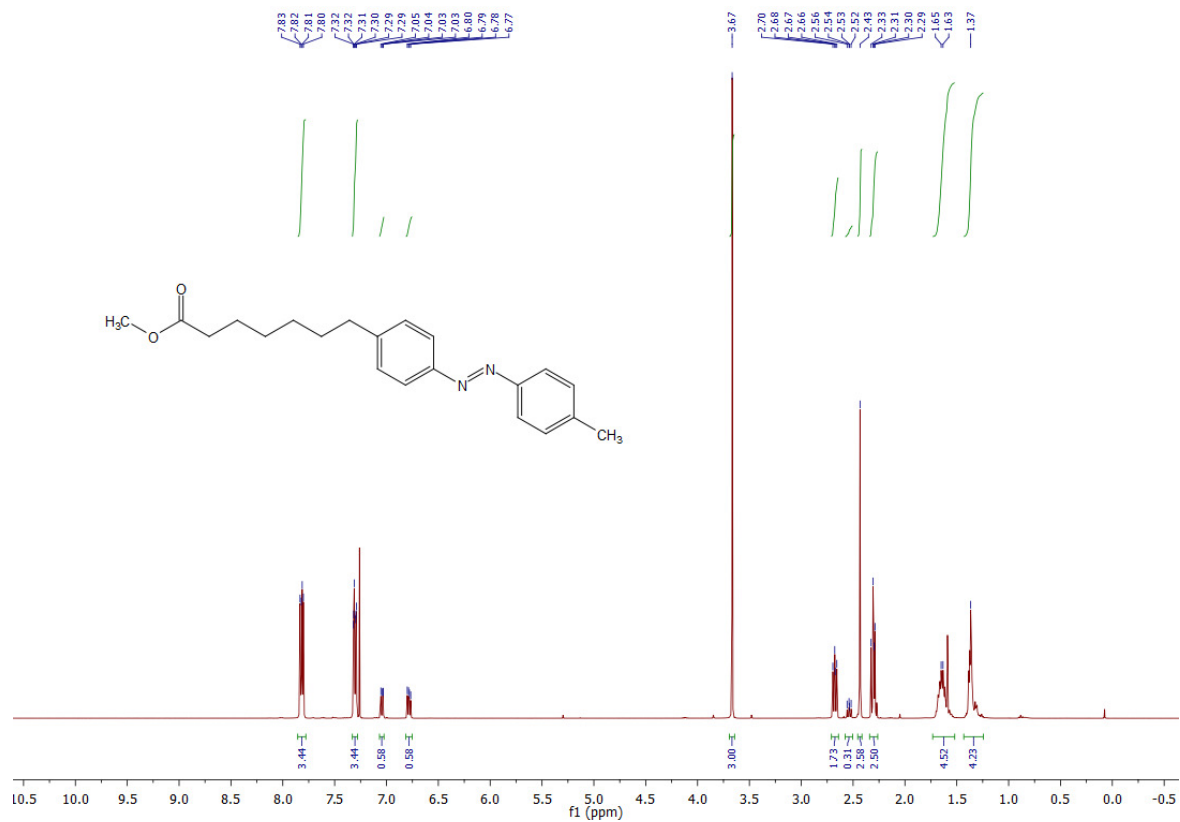
TLC (hexane/EtOAc, 4:1): $R_f = 0.74$ (*trans*), 0.55 (*cis*).

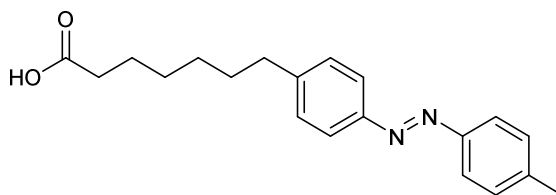
$^1\text{H NMR}$ (CDCl_3 , 400 MHz, 25 °C): δ 7.84-7.79 (m, 4H, H_{10a,b}, H_{15a,b}), 7.33-7.28 (m, 4H, H_{9a,b}, H_{16a,b}, $J_{9,10} \approx J_{16,15} \approx 8.5$ Hz), 3.67 (s, 3H, H_{OMe}), 2.68 (t, 2H, H_{7a,b}, $J_{7,6} = 7.5$ Hz), 2.43 (s, 3H, H_{18a,b}), 2.32-2.27 (m, 2H, H_{2a,b}), 1.71-1.54 (m, 4H, H_{3a,b}, H_{6a,b}), 1.41-1.28 (m, 4H, H_{4a,b}, H_{5a,b}).

$^{13}\text{C NMR}$ (CDCl_3 , 101 MHz, 25 °C): δ 174.4 (C₁), 151.1 (C_{azo}), 151.0 (C_{azo}), 146.1 (C_{azo}), 141.4 (C_{azo}), 129.8 (2C, C_{azo}), 129.2 (2C, C_{azo}), 122.9 (2C, C_{azo}), 122.9 (2C, C_{azo}), 51.6 (C_{OMe}), 35.9 (C₇), 34.2 (C₂), 31.2 (C_{alk}), 29.1 (C_{alk}), 29.0 (C_{alk}), 25.0 (C_{alk}), 21.6 (C₁₈).

HRMS (EI⁺): m/z calcd. for [C₂₁H₂₆N₂O₂]: 338.1994, found: 338.1991 ([M-e]⁺).

4 – Photoswitchable fatty acids enable optical control of TRPV1



4.4.8.25 – 7-(4-(*p*-Tolyldiazenyl)phenyl)heptanoic acid (FAAzo-7)

FAAzo-7

Methyl 7-(4-(*p*-tolyldiazenyl)phenyl)heptanoate (4c, 35 mg, 0.10 mmol, 1 equiv.) was converted to red solid **7-(4-(*p*-tolyldiazenyl)phenyl)heptanoic acid (FAAzo-7**, 28 mg, 83%) in an analogous manner as described above for the preparation of **5-(4-(4-propylphenyl)diazenyl)phenyl)pentanoic acid (FAAzo-5)**. *Note: all reagents and solvents were scaled according to molarity.*

TLC (hexane/EtOAc, 4:1): $R_f = 0.13$.

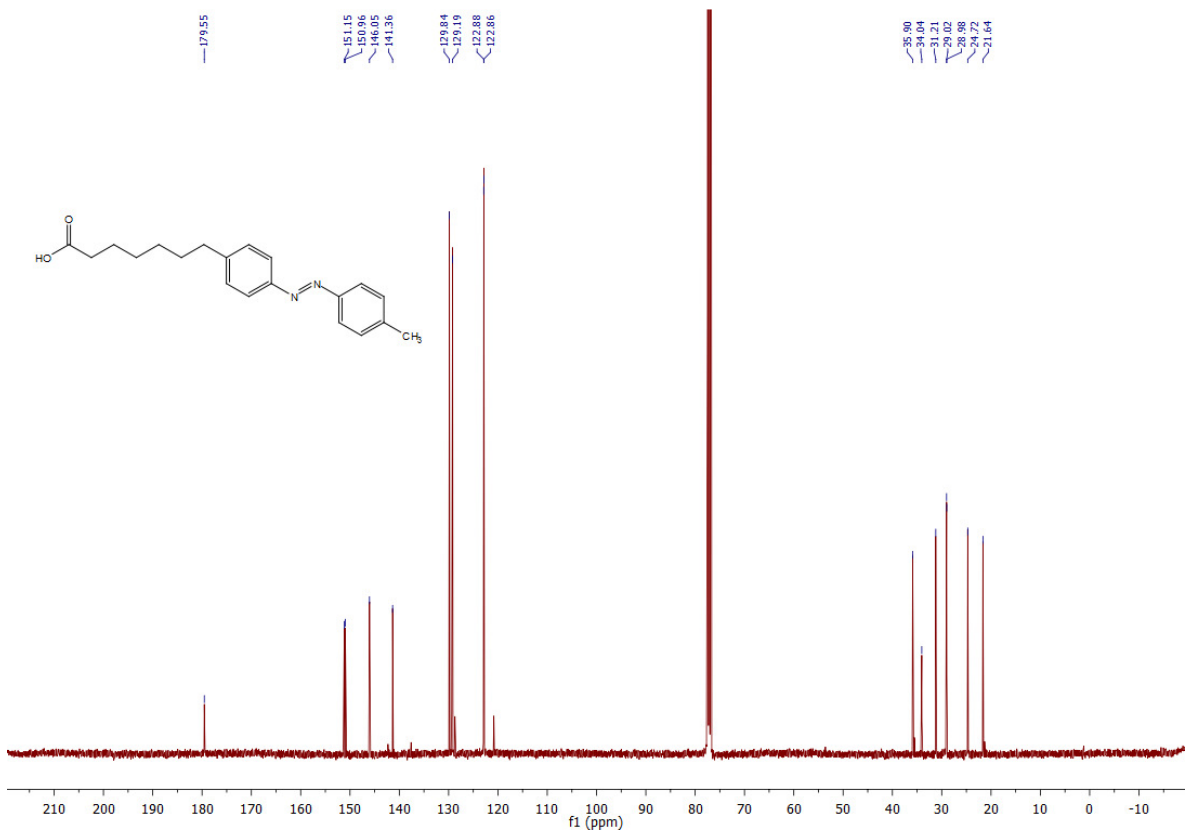
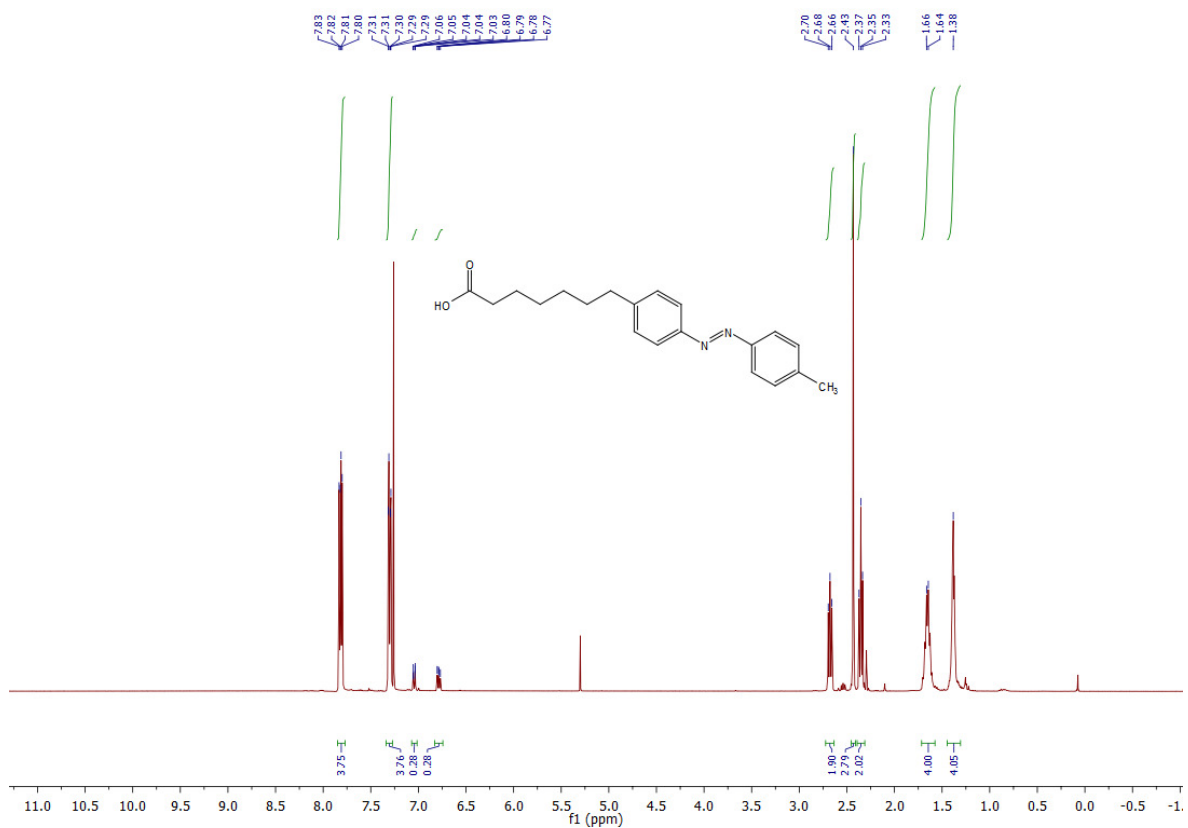
$^1\text{H NMR}$ (CDCl_3 , 400 MHz, 25 °C): δ 7.84-7.79 (m, 4H, H10_{a,b}, H15_{a,b}), 7.32-7.28 (m, 4H, H9_{a,b}, H16_{a,b}, $J_{9,10} \approx J_{16,15} \approx 8.3$ Hz), 2.68 (t, 2H, H7_{a,b}, $J_{7,6} = 7.6$ Hz), 2.43 (s, 3H, H18_{a,b}), 2.35 (t, 2H, H2_{a,b}, $J_{2,3} = 7.5$ Hz), 1.71-1.58 (m, 4H, H3_{a,b}, H6_{a,b}), 1.42-1.31 (m, 4H, H4_{a,b}, H5_{a,b}).

$^{13}\text{C NMR}$ (CDCl_3 , 101 MHz, 25 °C): δ 179.6 (C1), 151.2 (C_{azo}), 151.0 (C_{azo}), 146.1 (C_{azo}), 141.4 (C_{azo}), 129.8 (2C, C_{azo}), 129.2 (2C, C_{azo}), 122.9 (2C, C_{azo}), 122.9 (2C, C_{azo}), 35.9 (C7), 34.0 (C2), 31.2 (C_{alk}), 29.0 (C_{alk}), 29.0 (C_{alk}), 24.7 (C_{alk}), 21.6 (C18).

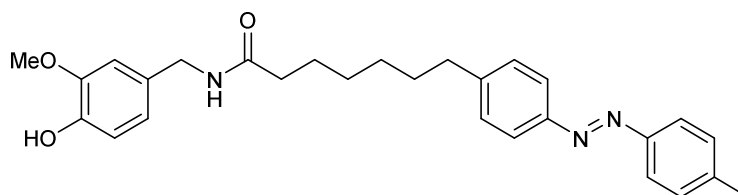
IR (neat, ATR): $\tilde{\nu} = 2927, 2851, 1720, 1702, 1697, 1693, 1600, 1497, 1465, 1438, 1413, 1314, 1295, 1280, 1241, 1208, 1152, 1109, 1010, 954, 850, 826, 727$.

HRMS (ESI): m/z calcd. for $[\text{C}_{20}\text{H}_{23}\text{N}_2\text{O}_2]^-$: 323.1765, found: 323.1762 ($[\text{M}-\text{H}^+]$).

4 – Photoswitchable fatty acids enable optical control of TRPV1



4.4.8.26 – N-(4-Hydroxy-3-methoxybenzyl)-7-(4-(p-tolyldiazenyl)phenyl) heptanamide (AzCA-7)



AzCA-7

7-(4-(p-Tolyldiazenyl)phenyl)heptanoic acid (FAAzo-7, 14 mg, 43 μ mol, 1.0 equiv.) was converted to red solid **N-(4-hydroxy-3-methoxybenzyl)-7-(4-(p-tolyldiazenyl)phenyl) heptanamide (AzCA-7, 16 mg, 81%)** in an analogous manner as described above for the preparation of **N-(4-hydroxy-3-methoxybenzyl)-4-((4-heptylphenyl)diazenyl)benzamide (AzCA-1)**. *Note: all reagents and solvents were scaled according to molarity.*

TLC (hexane/EtOAc, 2:1): $R_f = 0.31$.

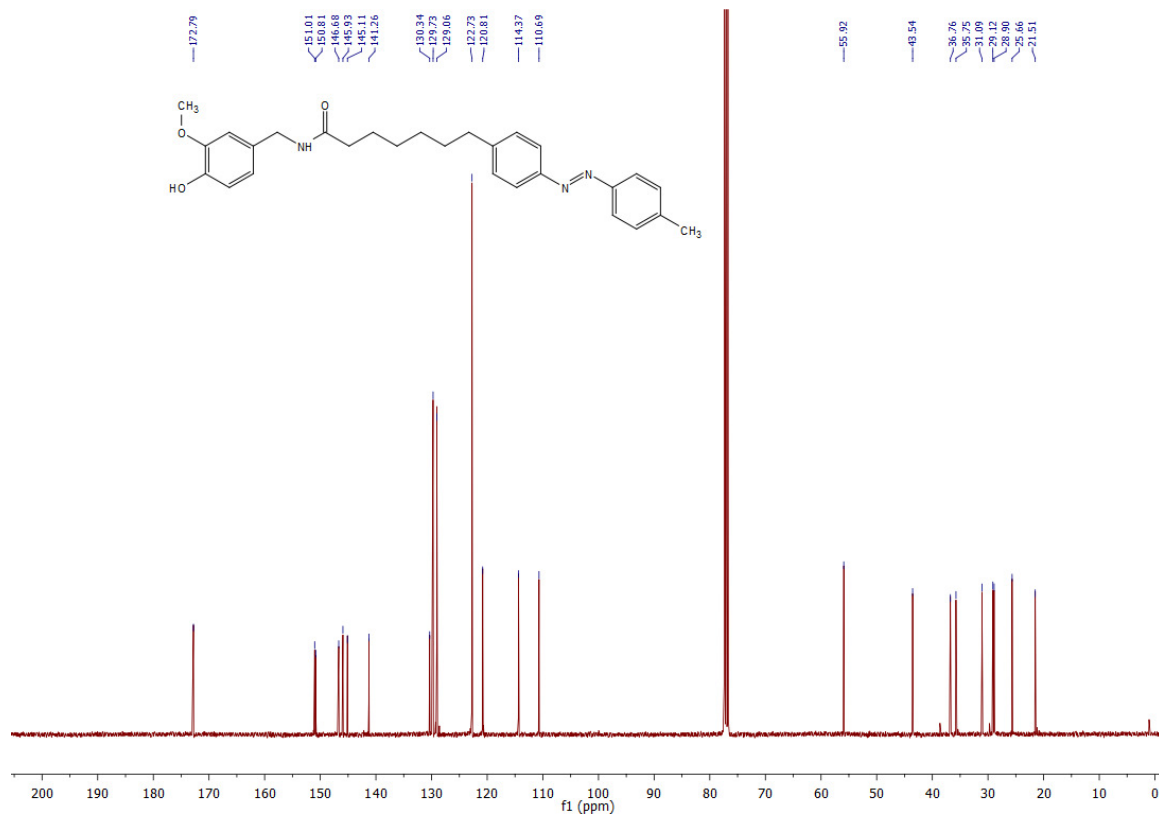
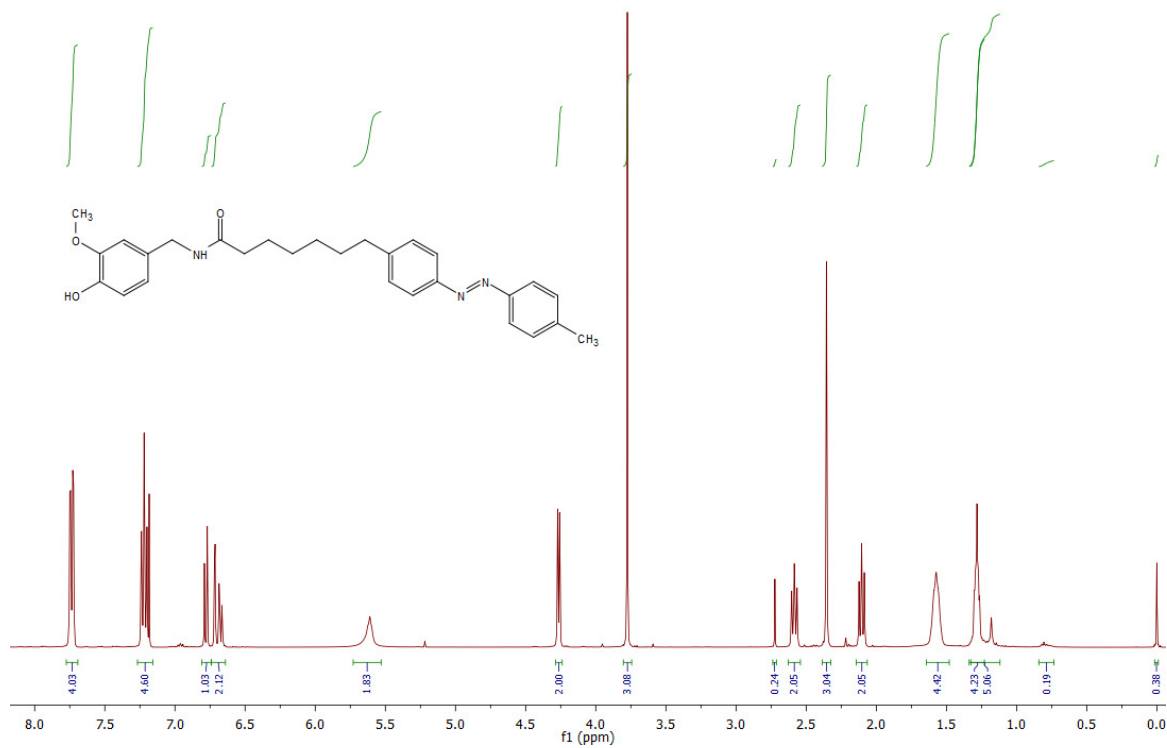
$^1\text{H NMR}$ (CDCl_3 , 400 MHz, 25 °C): δ 7.76-7.71 (m, 4H, H10_{a,b}, H15_{a,b}, $J_{10,9} \approx J_{15,16} \approx 8.4$ Hz), 7.25-7.19 (m, 4H, H9_{a,b}, H16_{a,b}, $J_{9,10} \approx J_{16,15} \approx 8.3$ Hz), 6.78 (d, 1H, H24, $J_{24,25} = 8.0$ Hz), 6.73-6.65 (m, 2H, H21, H25), 5.71-5.56 (m, 2H, NH, OH, $J_{\text{NH},19} = 5.3$ Hz), 4.26 (d, 2H, H19, $J_{19,\text{NH}} = 5.4$ Hz), 3.77 (s, 3H, H26_{a,b,c}), 2.58 (t, 2H, H7_{a,b}, $J_{7,6} = 7.5$ Hz), 2.36 (s, 3H, H18_{a,b,c}), 2.10 (t, 2H, H2_{a,b}, $J_{2,3} = 7.4$ Hz), 1.62-1.51 (m, 4H, H3_{a,b}, H6_{a,b}), 1.32-1.24 (m, 4H, H4_{a,b}, H5_{a,b}).

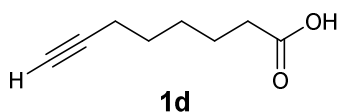
$^{13}\text{C NMR}$ (CDCl_3 , 101 MHz, 25 °C): δ 172.8 (C1), 151.0 (C_{azo}), 150.9 (C_{azo}), 146.8 (C22), 145.9 (C_{azo}), 145.1 (C23), 141.3 (C_{azo}), 130.3 (C20), 129.7 (2C, C_{azo}), 129.1 (2C, C_{Azo}), 122.7 (4C, C_{Azo}), 120.8 (C25), 114.4 (C24), 110.7 (C21), 55.9 (C26), 43.5 (C19), 36.8 (C2), 35.8 (C7), 31.1 (C_{alk}), 29.1 (C_{alk}), 28.9 (C_{alk}), 25.7 (C_{alk}), 21.5 (C18).

IR (neat, ATR): $\tilde{\nu} = 3292, 2927, 2854, 1652, 1645, 1600, 1558, 1539, 1515, 1464, 1456, 1429, 1373, 1275, 1237, 1155, 1124, 1035, 823, 727$.

HRMS (EI⁺): m/z calcd. for [C₂₈H₃₃N₃O₃]: 459.2522, found: 459.2524 ([M-e]⁺).

4 – Photoswitchable fatty acids enable optical control of TRPV1



4.4.8.27 – Oct-7-ynoic acid (1d)

Oct-7-ynoic acid (1d) was prepared from 7-octyn-1-ol according to a modified procedure reported by *Reyes et al*¹⁰⁵.

CrO₃ (0.78 g, 7.8 mmol, 1.5 equiv.) was dissolved in H₂O (10 mL) and cooled to 0 °C. H₂SO₄ (96%, 2.4 mL, 45 mmol, 8.7 equiv.) was slowly added and the mixture was allowed to warm to room temperature over 10 min. The solution was again cooled to 0 °C whereupon **7-octyn-1-ol** (0.65 g, 5.2 mmol, 1.0 equiv.) dissolved in acetone (3.3 mL) was added slowly. Upon complete addition of the alcohol, the reaction mixture was allowed to warm to room temperature and stirring was continued for 2 h. The reaction mixture was then diluted with EtOAc (40 mL) and the phases were separated. The aqueous phase was extracted with EtOAc (40 mL) and the combined organic phases were concentrated. The resulting oil was purified by flash column chromatography (65 g SiO₂, 4:1 hexane:EtOAc to 3:1 hexane:EtOAc) to yield **oct-7-ynoic acid (1d)**, 0.34 g, 47%) as a clear, volatile liquid. *This product still contained CH₂Cl₂ which was not further removed due to its volatile nature. This did not affect the following reaction.*

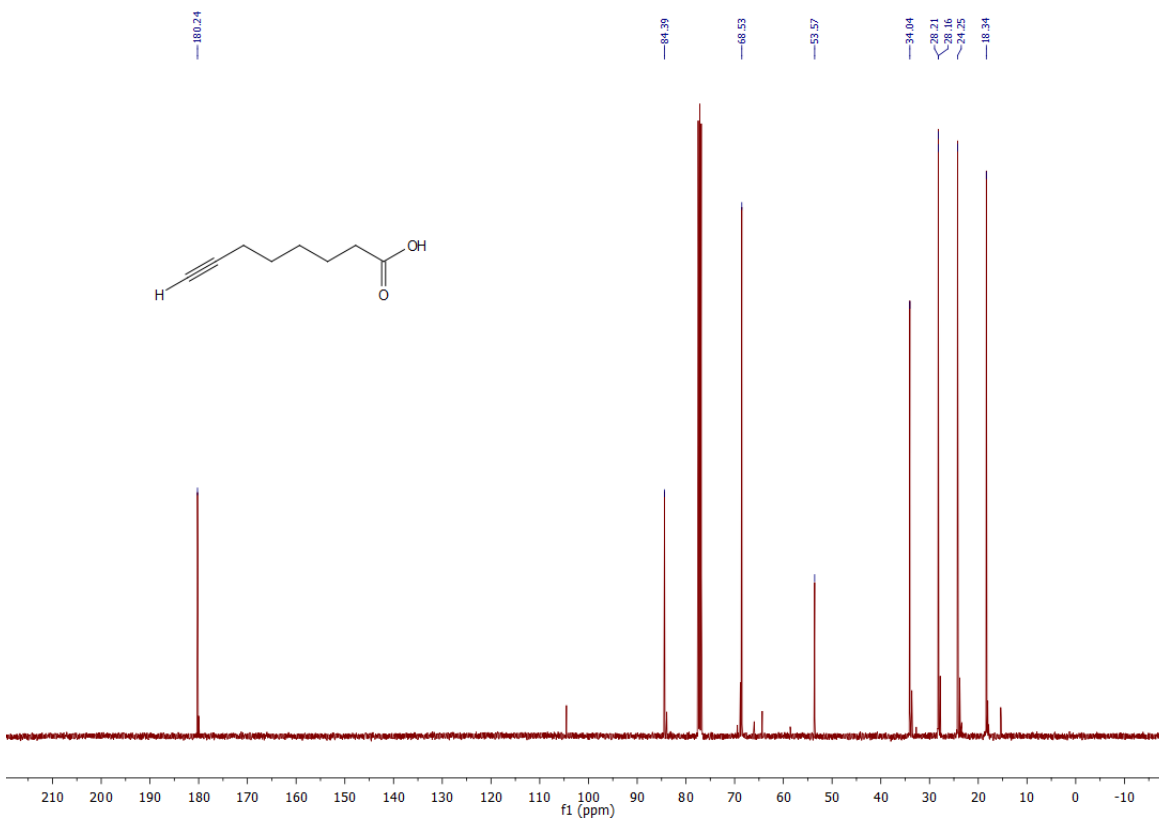
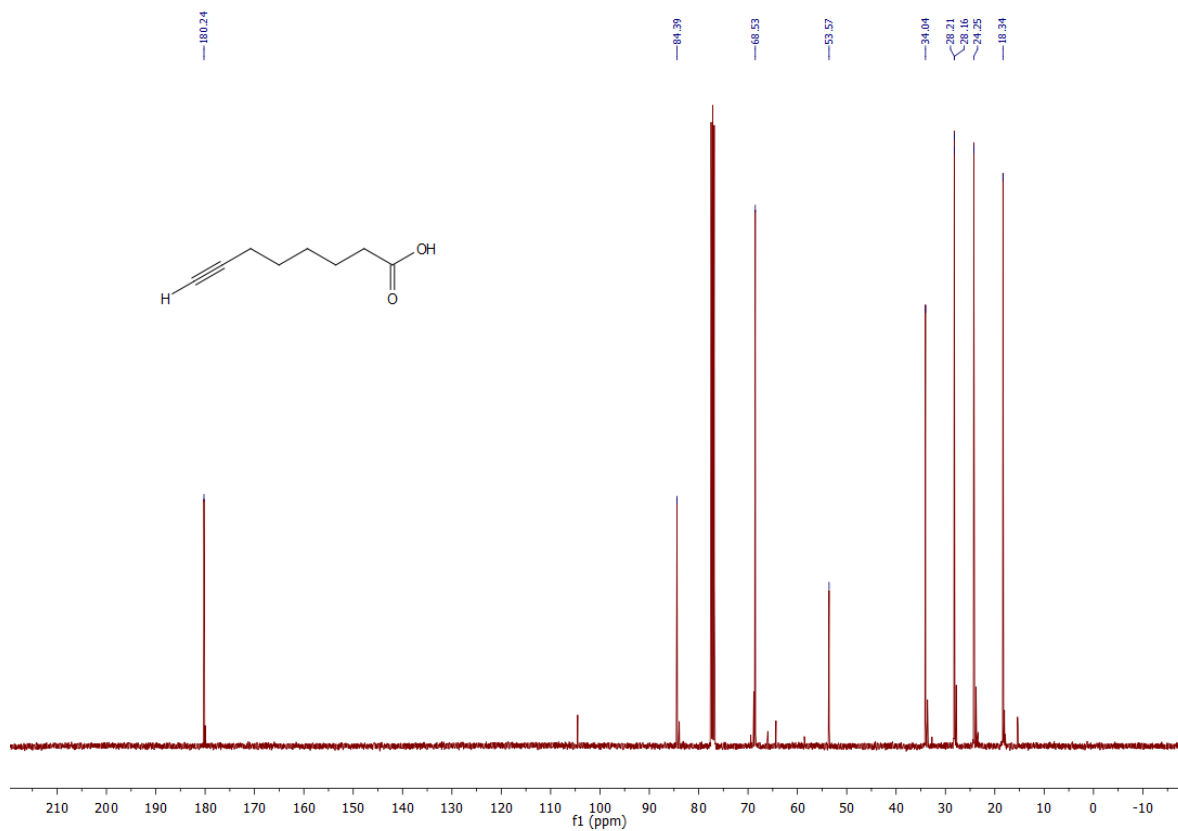
TLC (hexane/EtOAc, 4:1): R_f = 0.16.

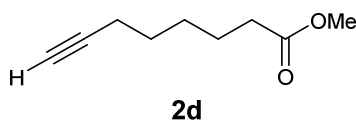
¹H NMR (CDCl₃, 400 MHz, 25 °C): δ 10.23 (s_{br}, 1H, H_{COOH}), 2.36 (t, 2H, H_{2,a,b}, J_{2,3} = 7.6 Hz), 2.19 (dt, 2H, H_{6,a,b}, J_{6,5} = 6.9 Hz, J_{6,8} = 2.8 Hz), 1.98 (t, 1H, H₈, J_{8,6} = 2.8 Hz), 1.69-1.59 (m, 2H, H_{alk}), 1.58-1.50 (m, 2H, H_{alk}), 1.50-1.40 (m, 2H, H_{4,a,b}).

¹³C NMR (CDCl₃, 101 MHz, 25 °C): δ 180.2 (C₁), 84.4 (C₅), 68.5 (C₆), 34.0 (C₂), 28.2 (C_{alk}), 28.2 (C_{alk}), 24.3 (C_{alk}), 18.3 (C_{alk}).

HRMS (EI⁺): *m/z* calcd. for [C₈H₁₂O₂]⁺: 140.0837, found: 140.0764 ([M-e]⁺).

4 – Photoswitchable fatty acids enable optical control of TRPV1



4.4.8.28 – Methyl oct-7-ynoate (2d)

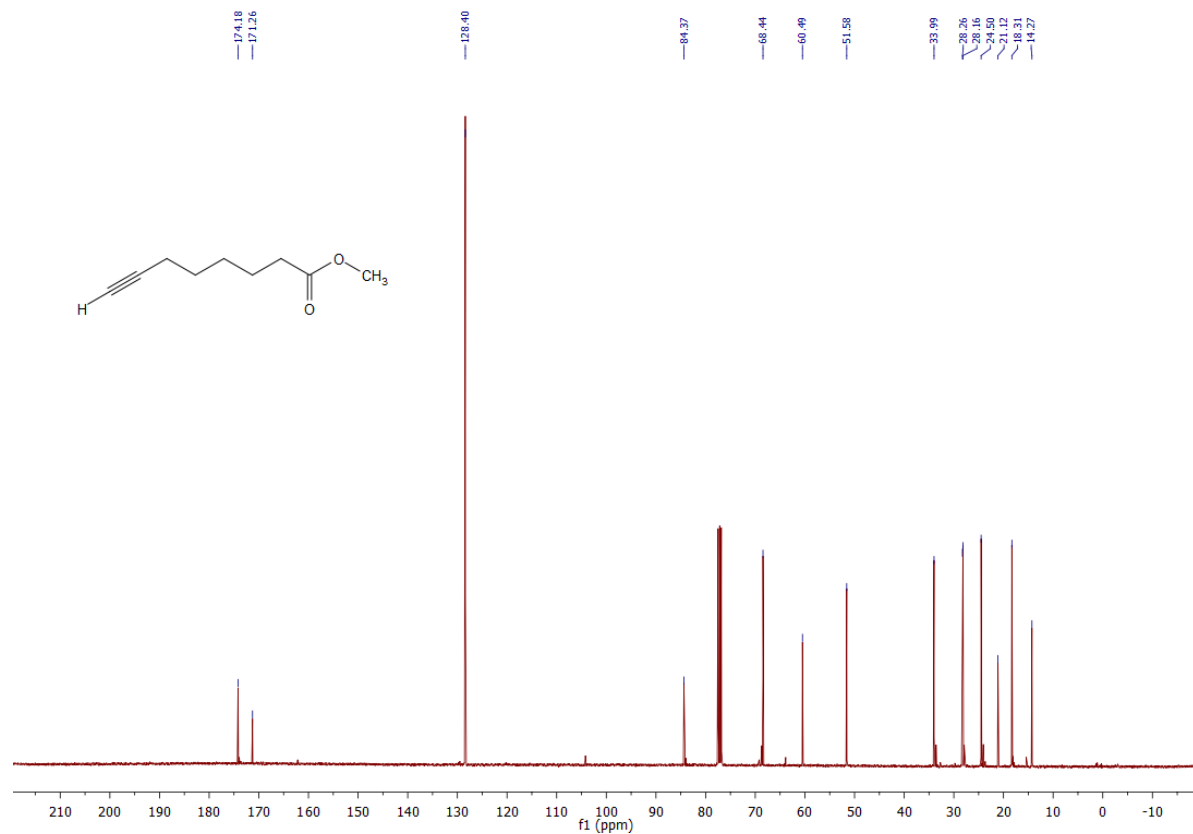
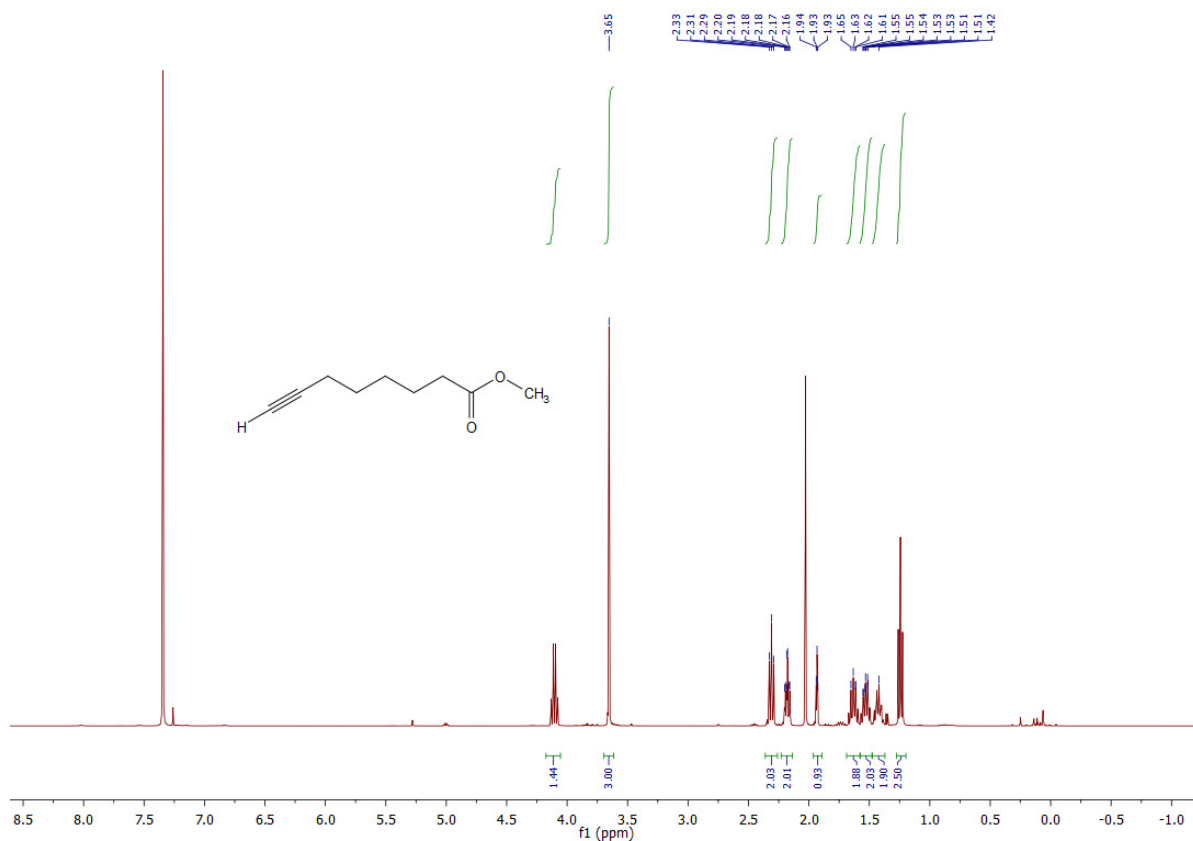
7-Octynoic acid (1d), 0.34 g, 2.4 mmol, 1.0 equiv.) was converted to **methyl oct-7-ynoate (2d)**, 0.35 g, 94% in an analogous manner as described above for the preparation of **methyl pent-4-ynoate (1a)**. *Note: all reagents and solvents were scaled according to molarity.*

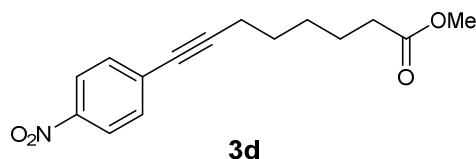
TLC (hexane/EtOAc, 4:1): $R_f = 0.50$.

$^1\text{H NMR}$ (CDCl_3 , 400 MHz, 27 °C): δ 3.65 (s, 3H, H_{OMe}), 2.31 (t, 2H, $\text{H}_{2\text{a,b}}$, $J_{2,3} = 7.5$ Hz), 2.18 (dt, 2H, $\text{H}_{6\text{a,b}}$, $J_{6,5} = 7.0$ Hz, $J_{6,8} = 2.7$ Hz), 1.93 (t, 1H, H_8 , $J_{8,6} = 2.7$ Hz), 1.67-1.58 (m, 2H, H_{alk}), 1.56-1.49 (m, 2H, H_{alk}), 1.47-1.39 (m, 2H, $\text{H}_{4\text{a,b}}$).

$^{13}\text{C NMR}$ (CDCl_3 , 101 MHz, 27 °C): δ 174.2 (C_1), 84.4 (C_5), 68.4 (C_6), 51.6 (C_{OMe}), 34.0 (C_2), 28.3 (C_{alk}), 28.2 (C_{alk}), 24.5 (C_{alk}), 18.3 (C_{alk}).

4 – Photoswitchable fatty acids enable optical control of TRPV1



4.4.8.29 – Methyl 8-(4-nitrophenyl)oct-7-ynoate (3d)

Methyl oct-7-ynoate (2d, 350 mg, 2.30 mmol, 1.0 equiv.) was converted to **methyl 8-(4-nitrophenyl)oct-7-ynoate (3d, 430 mg, 69%)** in an analogous manner as described above for the preparation of **methyl 5-(4-nitrophenyl)pent-4-ynoate (2a)**. *Note: all reagents and solvents were scaled according to molarity.*

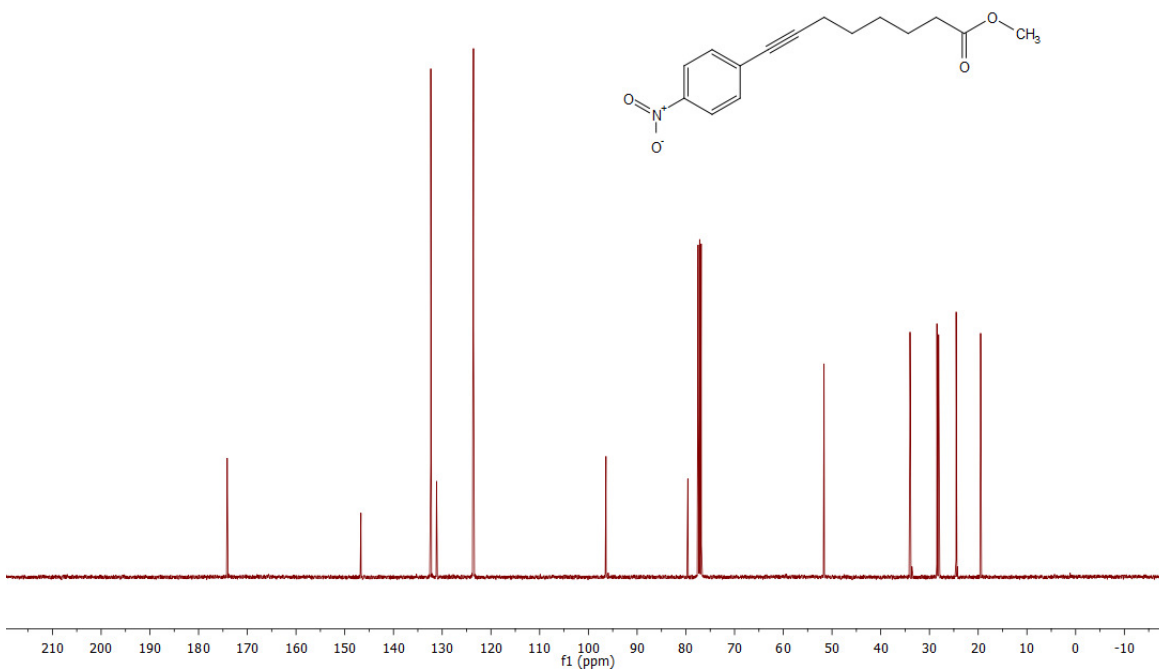
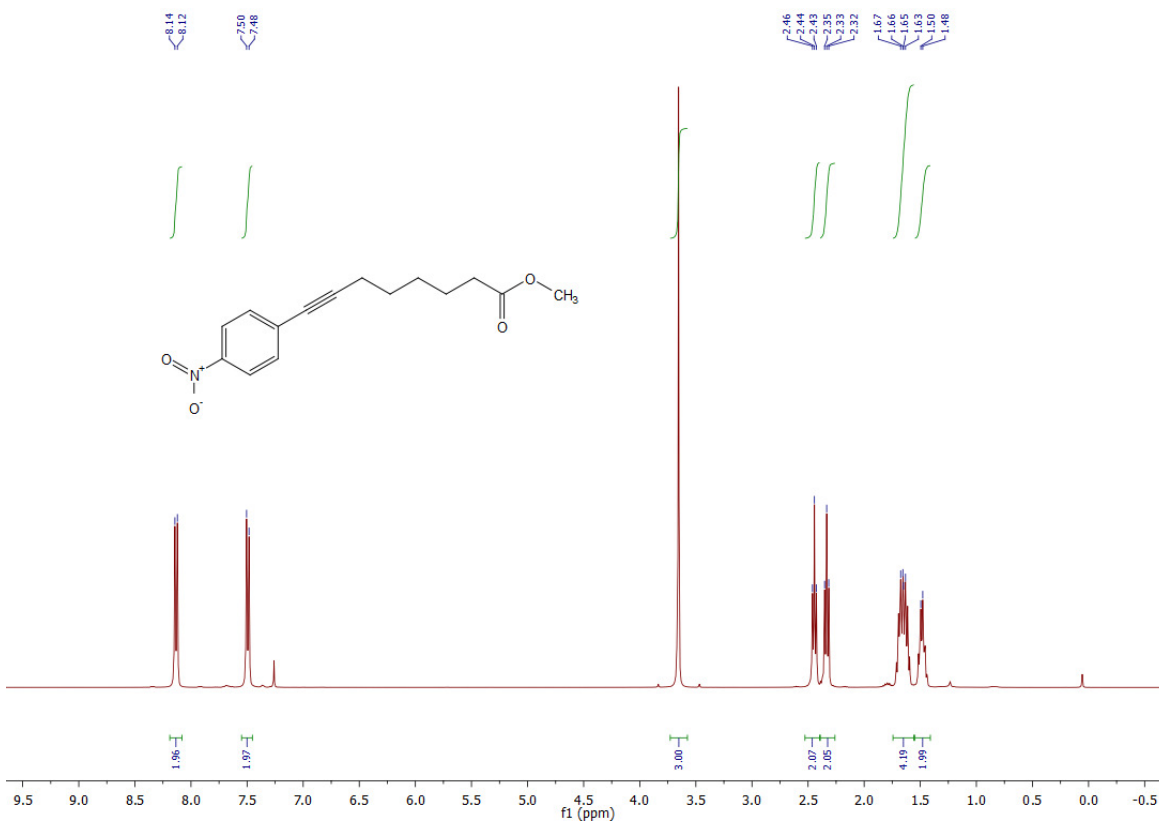
TLC (hexane/EtOAc, 4:1): $R_f = 0.59$.

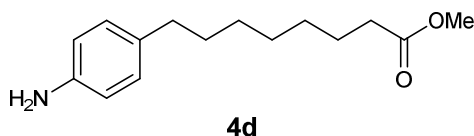
$^1\text{H NMR}$ (CDCl_3 , 400 MHz, 25 °C): δ 8.13 (d, 2H, $\text{H}_{11\text{a,b}}$, $J_{11,10} = 8.8$ Hz), 7.49 (d, 2H, $\text{H}_{10\text{a,b}}$, $J_{10,11} = 8.8$ Hz), 3.65 (s, 3H, H_{OMe}), 2.44 (t, 2H, $\text{H}_{2\text{a,b}}$, $J_{2,3} = 6.9$ Hz), 2.33 (t, 2H, $\text{H}_{6\text{a,b}}$, $J_{6,5} = 7.4$ Hz), 1.72-1.58 (m, 4H, $\text{H}_{3\text{a,b}}$, $\text{H}_{5\text{a,b}}$), 1.53-1.43 (m, 2H, $\text{H}_{4\text{a,b}}$).

$^{13}\text{C NMR}$ (CDCl_3 , 101 MHz, 25 °C): δ 174.1 (C1), 146.7 (C12), 132.3 (2C, $\text{C}_{10\text{a,b}}$), 131.2 (C9), 123.6 (2C, $\text{C}_{11\text{a,b}}$), 96.4 (C7), 79.6 (C8), 51.6 (C_{OMe}), 34.0 (C2), 28.5 (C_{alk}), 28.1 (C_{alk}), 24.5 (C_{alk}), 19.5 (C6).

HRMS (EI⁺): m/z calcd. for $[\text{C}_{15}\text{H}_{17}\text{NO}_4]^+$: 275.1158, found: 275.1134 ($[\text{M}-\text{e}]^+$).

4 – Photoswitchable fatty acids enable optical control of TRPV1



4.4.8.30 – Methyl 8-(4-aminophenyl)octanoate (4d)

Methyl 8-(4-nitrophenyl)oct-7-ynoate (3d), 43 mg, 0.16 mmol, 1.0 equiv.) was converted to orange oil **methyl 8-(4-aminophenyl)octanoate (4d)**, 20 mg, 51%) in an analogous manner as described above for the preparation of **methyl 5-(4-aminophenyl)pentanoate (3a)**. *Note: all reagents and solvents were scaled according to molarity.*

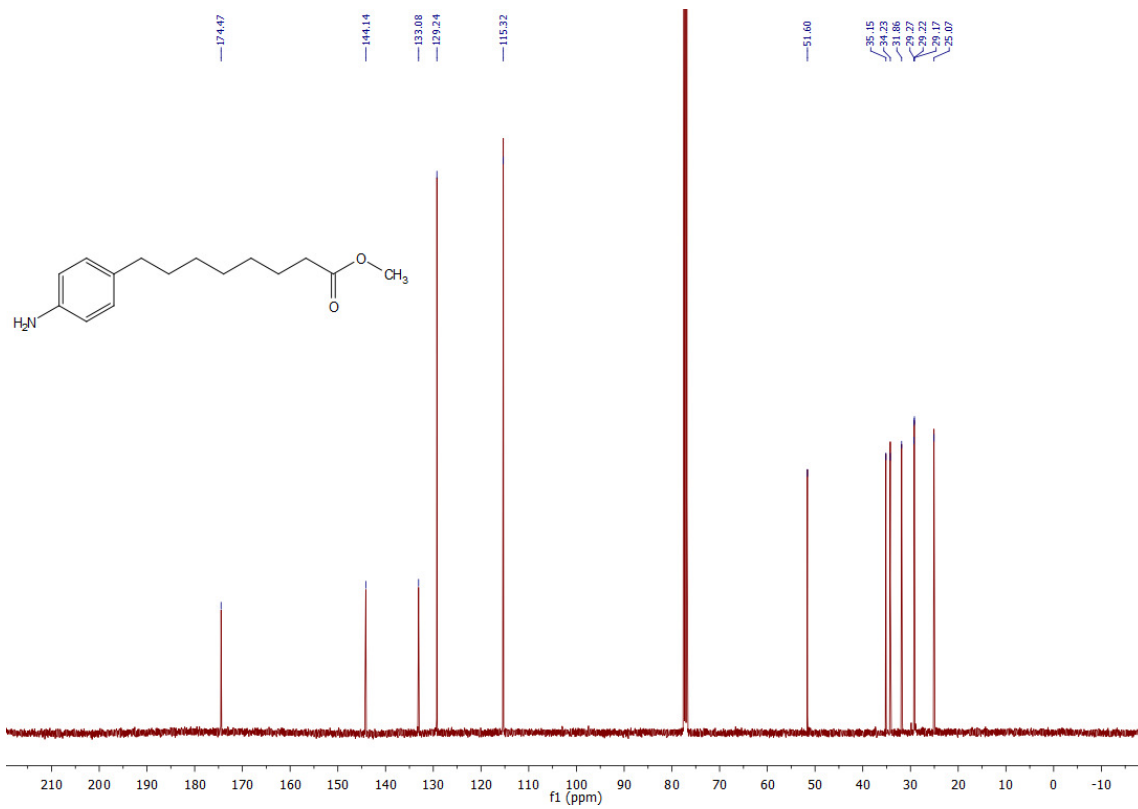
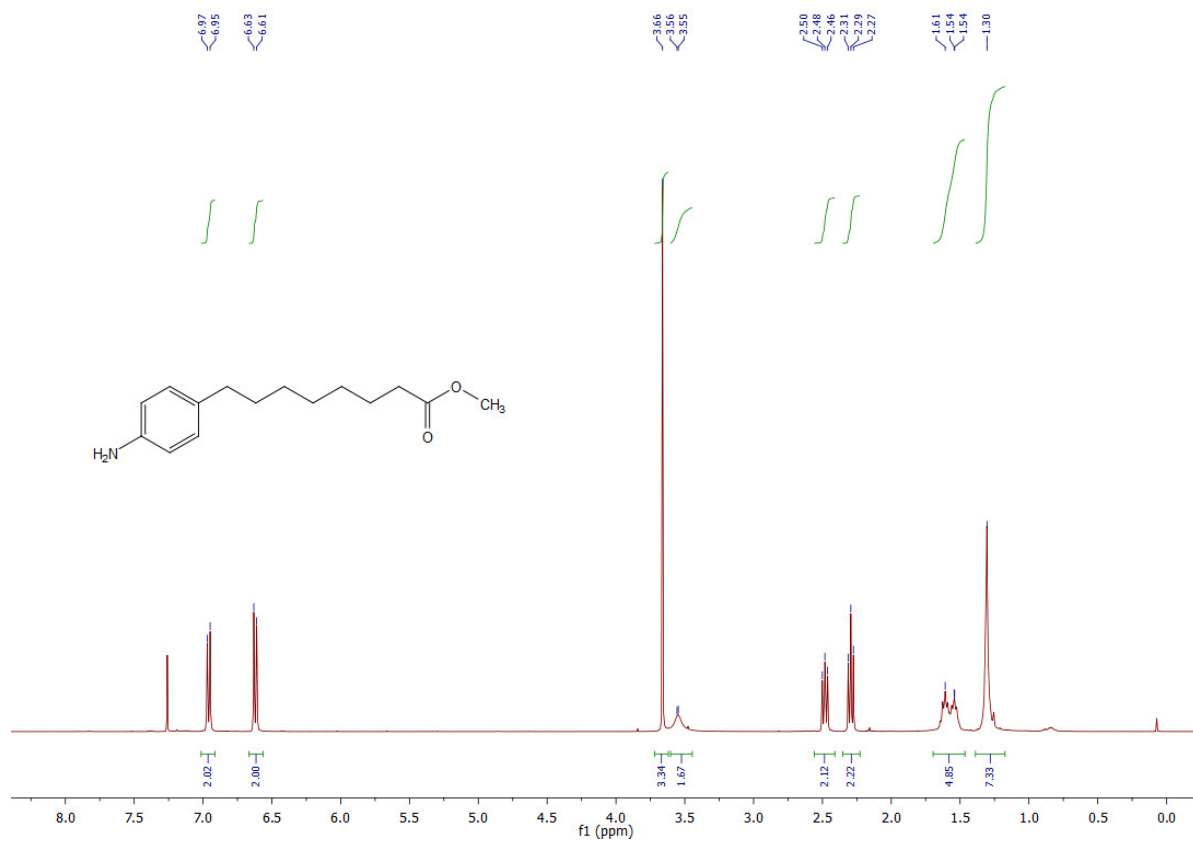
TLC (hexane/EtOAc, 4:1): $R_f = 0.19$.

$^1\text{H NMR}$ (CDCl_3 , 400 MHz, 25 °C): δ 6.97-6.95 (m, 2H, $\text{H}_{10\text{a,b}}$, $J_{10,11} \approx 8.5$ Hz), 6.64-6.60 (m, 2H, $\text{H}_{11\text{a,b}}$, $J_{11,10} \approx 8.5$ Hz), 3.66 (s, 3H, H_{OMe}), 3.55 (s_{br}, 2H, NH_2), 2.48 (t, 2H, $\text{H}_{8\text{a,b}}$, $J_{8,7} = 7.4$ Hz), 2.29 (t, 2H, $\text{H}_{2\text{a,b}}$, $J_{2,3} = 7.5$ Hz), 1.65-1.49 (m, 4H, $\text{H}_{3\text{a,b}}$, $\text{H}_{7\text{a,b}}$), 1.36-1.22 (m, 6H, $\text{H}_{4\text{a,b}}$, $\text{H}_{5\text{a,b}}$, $\text{H}_{6\text{a,b}}$).

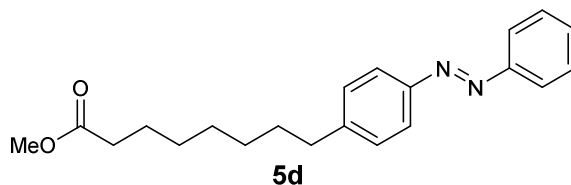
$^{13}\text{C NMR}$ (CDCl_3 , 101 MHz, 25 °C): δ 174.5 (C1), 144.1 (C12), 133.1 (C9), 129.2 (2C, $\text{C}_{10\text{a,b}}$), 115.3 (2C, $\text{C}_{11\text{a,b}}$), 51.6 (C_{OMe}), 35.2 (C8), 34.2 (C2), 31.9 (C_{alk}), 29.3 (C_{alk}), 29.2 (C_{alk}), 29.2 (C_{alk}), 25.1 (C_{alk}).

HRMS (ESI⁺): m/z calcd. for $[\text{C}_{14}\text{H}_{24}\text{NO}_2]^+$: 250.1807, found: 250.1801 ($[\text{M}+\text{H}^+]^+$).

4 – Photoswitchable fatty acids enable optical control of TRPV1



4.4.8.31 – Methyl 8-(4-(phenyldiazenyl)phenyl)octanoate (5d)



Methyl 8-(4-aminophenyl)octanoate (4d, 15 mg, 60 μmol , 1.0 equiv.) was dissolved in CH_2Cl_2 (1 mL). Nitrosobenzene (8 mg, 72 μmol , 1.2 equiv.) followed by AcOH (36 mg, 0.60 mmol, 10 equiv.) were added to this solution and the resulting mixture was stirred at room temperature for 7 h. Upon completion of the reaction, the mixture was diluted with EtOAc (5 mL), and the organic phase was washed with a saturated aqueous NaHCO_3 solution (10 mL) and water (2x10 mL). The layers were separated, and the organic phase was dried over anhydrous Na_2SO_4 . The dried solution was filtered and the filtrate was then concentrated under reduced pressure. The residue was purified by flash column chromatography (5 g SiO_2 , 20:1 pentane:EtOAc) to yield **methyl 8-(4-(phenyldiazenyl)phenyl)octanoate (5d**, 16 mg, 78%) as an orange oil.

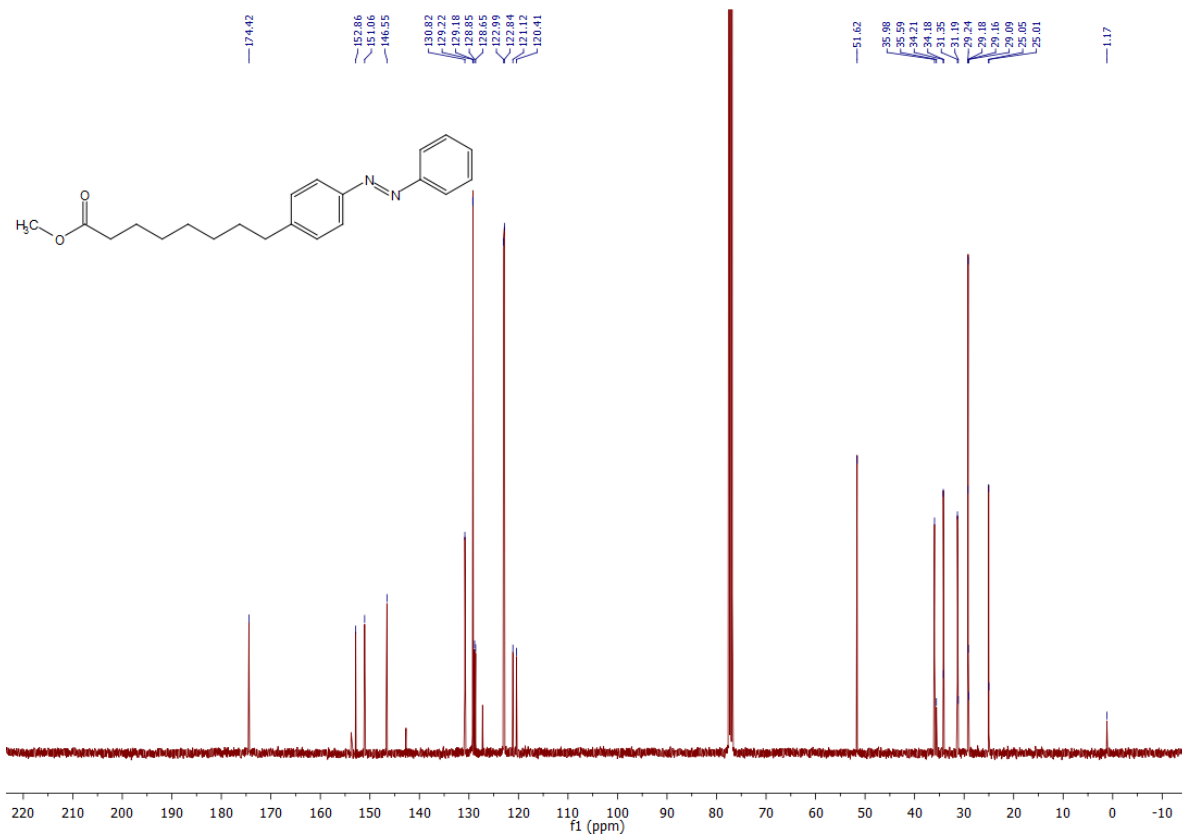
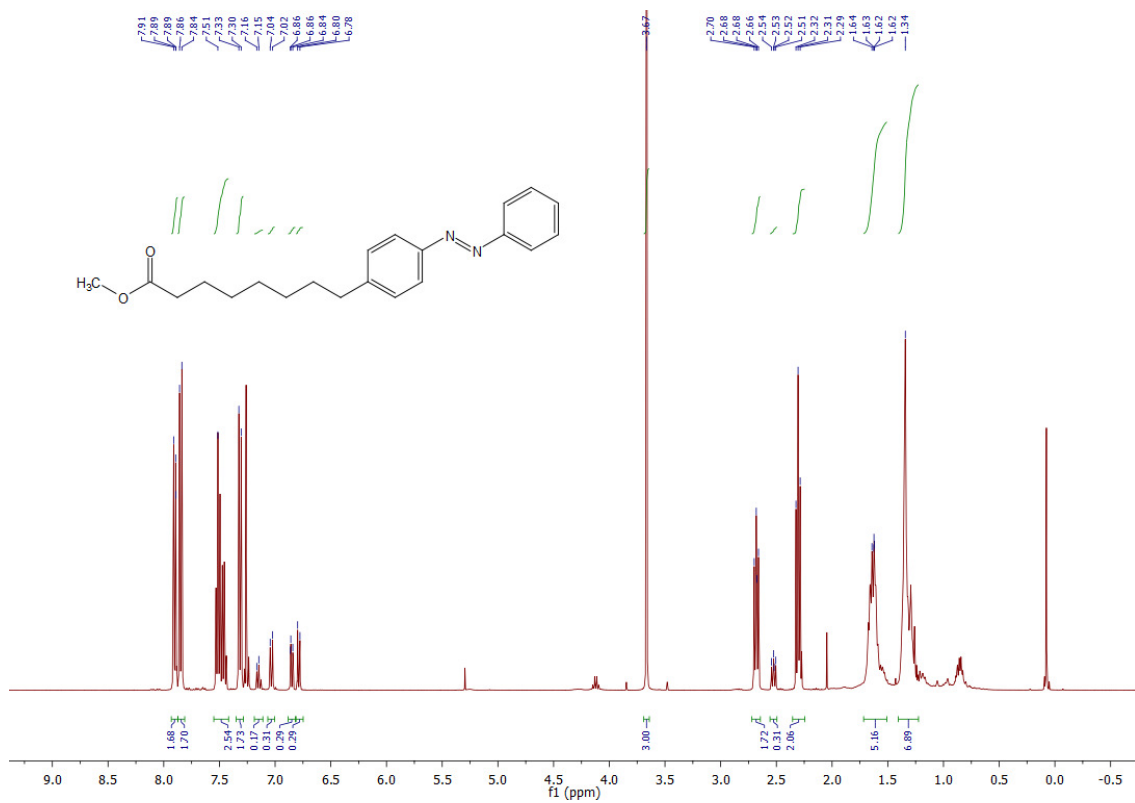
TLC (hexane/EtOAc, 20:1): R_f = 0.36 (*trans*), 0.10 (*cis*).

$^1\text{H NMR}$ (CDCl_3 , 400 MHz, 25 $^\circ\text{C}$): δ 7.92-7.88 (m, 2H, H11_{a,b}, $J_{11,10} \approx 8.4$ Hz), 7.87-7.82 (m, 2H, H16_{a,b}, $J_{16,17} \approx 8.4$ Hz), 7.54-7.43 (m, 3H, H17_{a,b}, H18), 7.32 (d, 2H, H10_{a,b}, $J_{10,11} = 8.4$ Hz), 3.67 (s, 3H, H_{OMe}), 2.68 (t, 2H, H8_{a,b}, $J_{8,7} = 7.4$ Hz), 2.30 (t, 2H, H2_{a,b}, $J_{2,3} = 7.5$ Hz), 1.70-1.50 (m, 4H, H3_{a,b}, H7_{a,b}), 1.41-1.25 (m, 6H, H4_{a,b}, H5_{a,b}, H6_{a,b}).

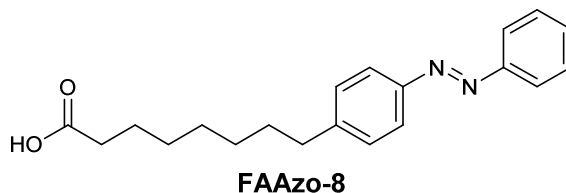
$^{13}\text{C NMR}$ (CDCl_3 , 101 MHz, 25 $^\circ\text{C}$): δ 174.4 (C1), 152.9 (C_{azo}), 151.1 (C_{azo}), 146.6 (C9), 130.8 (C18), 129.2 (2C, C_{azo}), 129.2 (2C, C_{azo}), 123.0 (2C, C_{azo}), 122.9 (2C, C_{azo}), 51.6 (C_{OMe}), 36.0 (C8), 34.2 (C2), 31.4 (C_{alk}), 29.2 (C_{alk}), 29.2 (C_{alk}), 29.2 (C_{alk}), 25.1 (C_{alk}).

HRMS (ESI⁺): m/z calcd. for $[\text{C}_{21}\text{H}_{27}\text{N}_2\text{O}_2]^+$: 339.2073, found: 339.2065 ($[\text{M}+\text{H}^+]^+$).

4 – Photoswitchable fatty acids enable optical control of TRPV1



4.4.8.32 – 8-(4-(Phenyldiazenyl)phenyl)octanoic acid (FAAzo-8)



Methyl 8-(4-(phenyldiazenyl)phenyl)octanoate (5d, 16 mg, 47 μ mol, 1 equiv.) was converted to red solid **8-(4-(phenyldiazenyl)phenyl)octanoic acid (FAAzo-8, 12 mg, 78%)** in an analogous manner as described above for the preparation of **5-(4-((4-propylphenyl)diazenyl)phenyl)pentanoic acid (FAAzo-5)**. *Note: all reagents and solvents were scaled according to molarity.*

TLC (hexane/EtOAc, 4:1): $R_f = 0.13$.

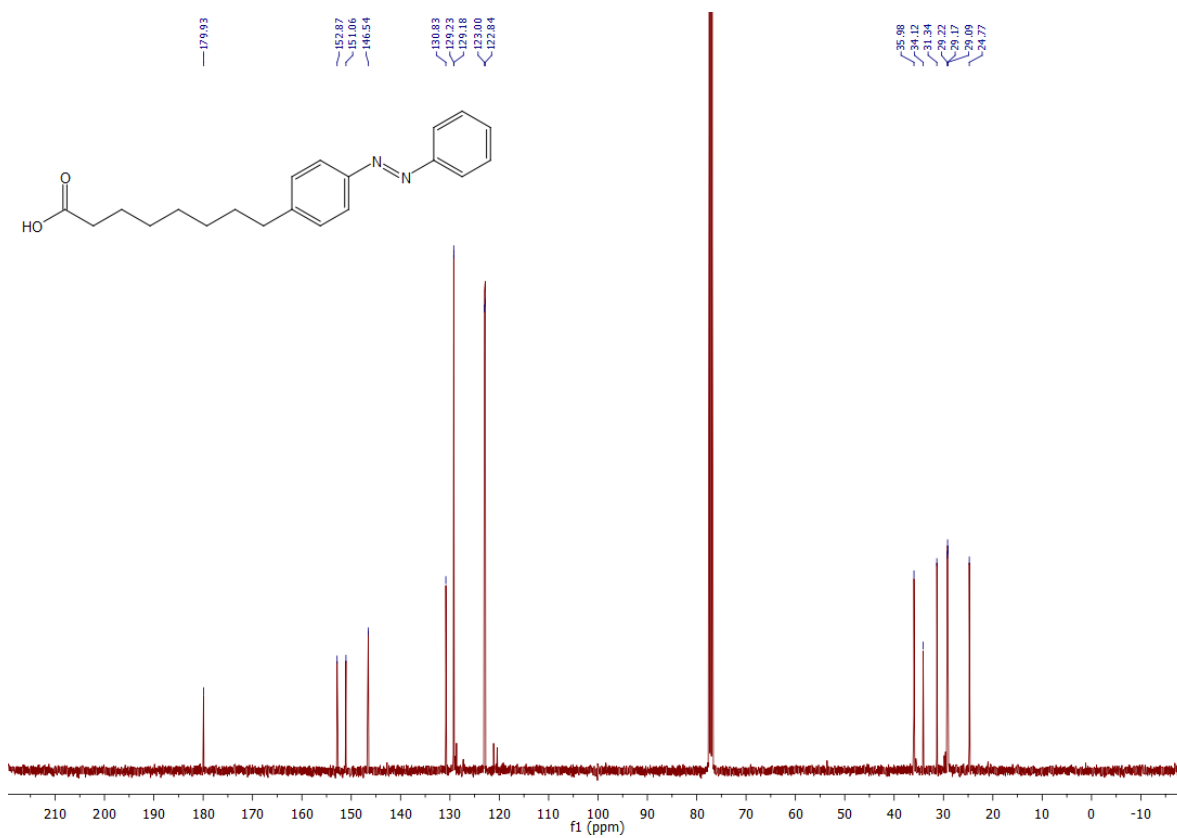
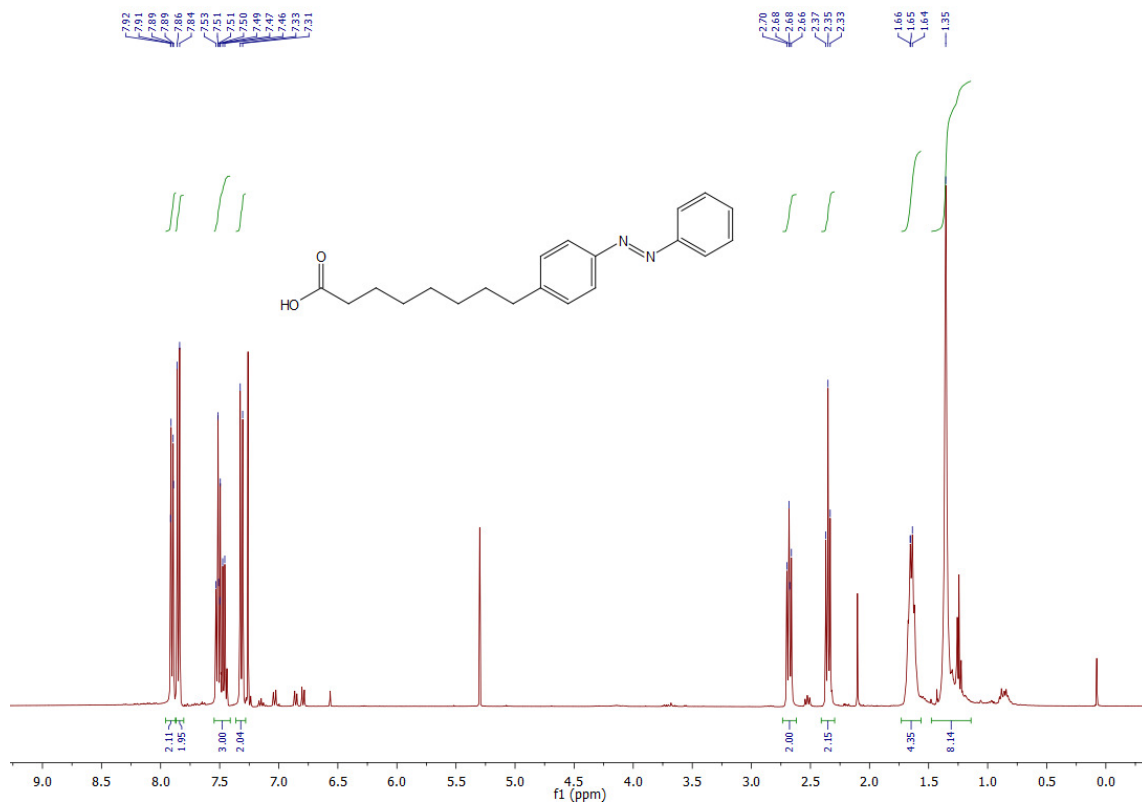
$^1\text{H NMR}$ (CDCl_3 , 400 MHz, 25 °C): δ 7.92-7.88 (m, 2H, H11_{a,b}, $J_{11,10} \approx 8.5$ Hz), 7.87-7.82 (m, 2H, H16_{a,b}, $J_{16,17} \approx 8.5$ Hz), 7.54-7.43 (m, 3H, H17_{a,b}, H18), 7.32 (d, 2H, H10_{a,b}, $J_{10,11} = 8.4$ Hz), 2.68 (t, 2H, H8_{a,b}, $J_{8,7} = 7.5$ Hz), 2.35 (t, 2H, H2_{a,b}, $J_{2,3} = 7.4$ Hz), 1.70-1.59 (m, 4H, H3_{a,b}, H7_{a,b}), 1.41-1.28 (m, 6H, H4_{a,b}, H5_{a,b}, H6_{a,b}).

$^{13}\text{C NMR}$ (CDCl_3 , 101 MHz, 25 °C): δ 179.9 (C1), 152.9 (C_{azo}), 151.1 (C_{azo}), 146.5 (C9), 130.8 (C18), 129.2 (2C, C_{azo}), 129.2 (2C, C_{azo}), 123.0 (2C, C_{azo}), 122.8 (2C, C_{azo}), 36.0 (C8), 34.1 (C2), 31.3 (C_{alk}), 29.2 (C_{alk}), 29.2 (C_{alk}), 29.1 (C_{alk}), 24.8 (C_{alk}).

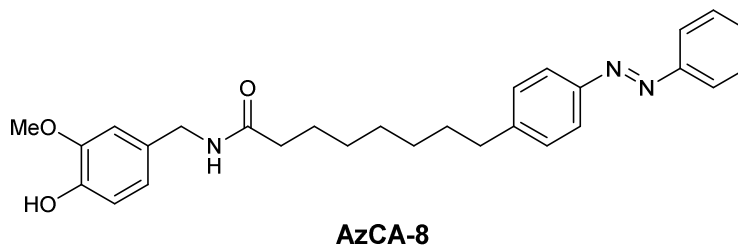
IR (neat, ATR): $\tilde{\nu} = 3180, 2921, 2848, 1701, 1602, 1486, 1464, 1428, 1409, 1343, 1303, 1289, 1264, 1226, 1198, 1154, 1088, 1012, 925, 840, 806, 767, 759, 725, 685$.

HRMS (ESI): m/z calcd. for $[\text{C}_{20}\text{H}_{23}\text{N}_2\text{O}_2]^-$: 323.1765, found: 323.1762 ($[\text{M}-\text{H}^+]$).

4 – Photoswitchable fatty acids enable optical control of TRPV1



4.4.8.33 – *N*-(4-Hydroxy-3-methoxybenzyl)-8-(4-(phenyldiazenyl)phenyl) octanamide (AzCA-8)



8-(4-(phenyldiazenyl)phenyl)octanoic acid (FAAzo-8, 12 mg, 37 μ mol, 1.0 equiv.) was converted to red oil ***N*-(4-hydroxy-3-methoxybenzyl)-8-(4-(phenyldiazenyl)phenyl) octanamide (AzCA-8, 15 mg, 88%)** in an analogous manner as described above for the preparation of ***N*-(4-hydroxy-3-methoxybenzyl)-4-((4-heptylphenyl)diazenyl)benzamide (AzCA-1)**. *Note: all reagents and solvents were scaled according to molarity.*

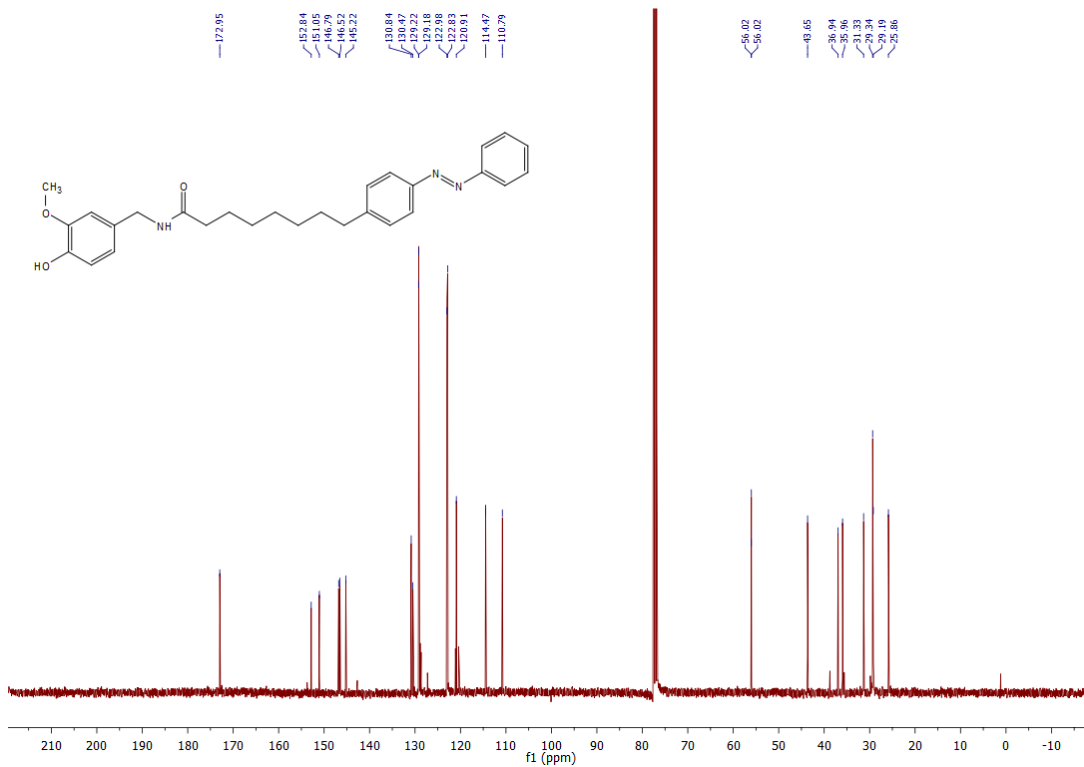
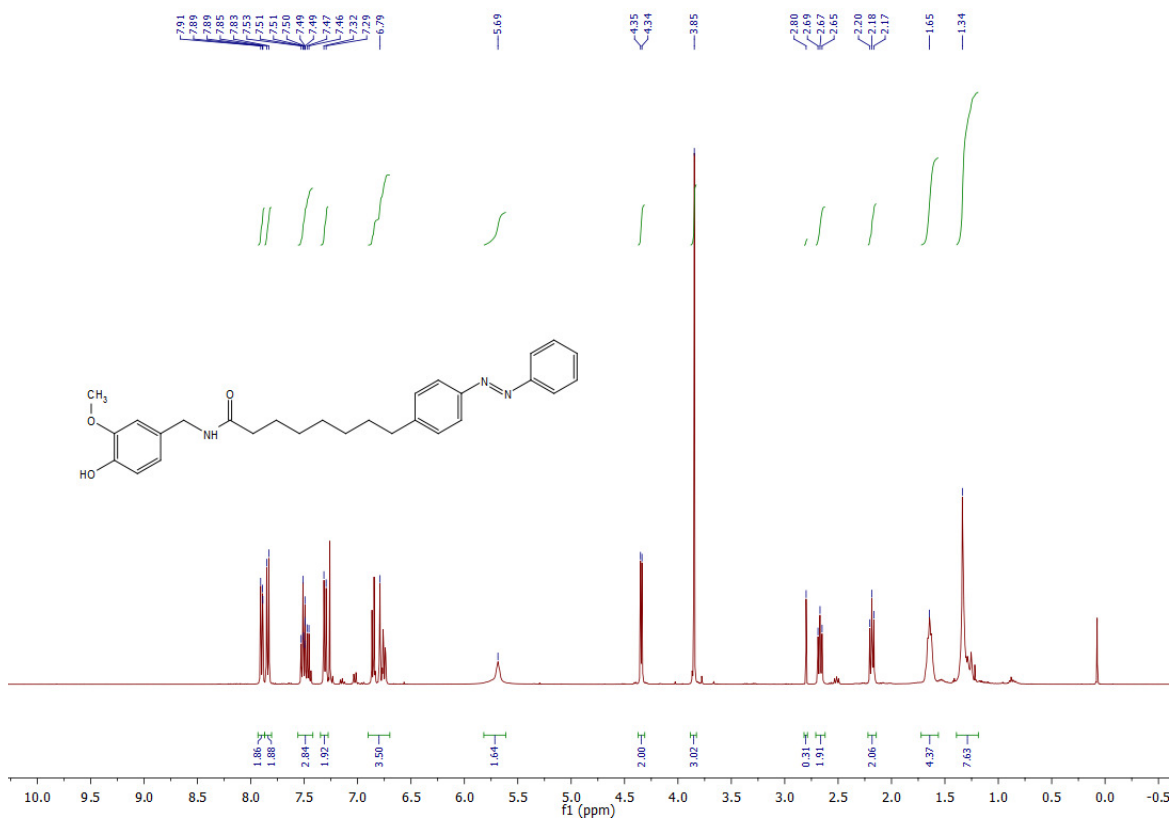
TLC (hexane/EtOAc, 1:2): $R_f = 0.26$.

$^1\text{H NMR}$ (CDCl_3 , 400 MHz, 25 $^\circ\text{C}$): δ 7.92-7.88 (m, 2H, H11_{a,b}), 7.86-7.82 (m, 2H, H16_{a,b}, $J_{16,17} \approx 8.4$ Hz), 7.54-7.43 (m, 3H, H17_{a,b}, H18), 7.31 (d, 2H, H10_{a,b}, $J_{10,11} = 8.4$ Hz), 6.88-6.72 (m, 3H, H21, H24, H25), 5.77-5.63 (m, 2H, NH, H_{OH}), 4.34 (d, 2H, H19_{a,b}, $J_{19,\text{NH}} = 5.6$ Hz), 3.85 (s, 3H, H_{OMe}), 2.67 (t, 2H, H8_{a,b}, $J_{8,7} = 7.6$ Hz), 2.18 (t, 2H, H2_{a,b}, $J_{2,3} = 7.5$ Hz), 1.70-1.58 (m, 4H, H3_{a,b}, H6_{a,b}), 1.38-1.22 (m, 6H, H4_{a,b}, H5_{a,b}, H6_{a,b}).

$^{13}\text{C NMR}$ (CDCl_3 , 101 MHz, 25 $^\circ\text{C}$): δ 173.0 (C1), 152.8 (C_{azo}), 151.1 (C_{azo}), 146.8 (C22), 146.5 (C9), 145.2 (C23), 130.8 (C18), 130.5 (C20), 129.2 (2C, C_{azo}), 129.2 (2C, C_{azo}), 123.0 (2C, C_{azo}), 122.8 (2C, C_{azo}), 120.9 (C25), 114.5 (C24), 110.8 (C20), 56.0 (C_{OMe}), 43.7 (C19), 36.9 (C2), 36.0 (C8), 31.3 (C_{alk}), 29.3 (C_{alk}), 29.2 (2C, C_{alk}), 25.9 (C_{alk}).

IR (neat, ATR): $\tilde{\nu} = 3286, 2928, 2853, 1733, 1717, 1699, 1683, 1674, 1652, 1645, 1634, 1616, 1600, 1557, 1538, 1516, 1464, 1456, 1436, 1418, 1373, 1274, 1153, 1124, 1035, 768, 688, 667$. **HRMS (EI⁺):** m/z calcd. for $[\text{C}_{28}\text{H}_{33}\text{N}_3\text{O}_3]^+$: 459.2522, found: 459.2506 ($[\text{M-e}]^+$).

4 – Photoswitchable fatty acids enable optical control of TRPV1



5 – Photoswitchable diacylglycerols enable optical control of protein kinase C

This work has been published in *Nature Chemical Biology* (2016)⁵².

5.1 – Introduction

Diacylglycerol (DAG) is not only an integral component of plasma membrane phospholipids, but is also known for its role as a second messenger¹⁰⁶. Cellular DAG concentrations are tightly regulated by enzymes including phospholipase C (PLC), as well as DAG lipases and kinases¹⁰⁷. The bulk of DAG originates from phosphatidylcholine, or the PLC-mediated hydrolysis of phosphoinositides. Rapid changes in DAG levels occur following the extracellular stimulation of receptors¹⁰⁸. Over 50 different DAGs have been identified in humans¹⁰⁹, and the length and degree of unsaturation of the lipid chains determines the biophysical and pharmacological properties of individual DAG species¹¹⁰.

DAGs interact with both transmembrane and soluble proteins, and are known to activate TRP cation channels, including TRPC3 and TRPC6¹¹¹. Importantly, DAG generation also triggers the translocation towards the plasma membrane of a number of proteins that contain C1 domains¹¹². These small, highly conserved, zinc-binding protein domains were originally characterized as the DAG-sensing regulatory elements of the protein kinase C (PKC) family¹¹³. C1-mediated translocation plays a key role in the activation of various other factors, including kinases and nucleotide exchange factors¹⁰⁷. DAGs were also reported to affect the protein machinery involved in synaptic transmission and exocytosis^{107,114}. Thus, a tool which enables reversible control of C1 domain translocation would be widely applicable towards the control of intra- and intercellular signaling.

Precision pharmacological manipulation of lipid signaling is often difficult due to the restricted localization and diffusion of these hydrophobic molecules. Experimentally, the activation of C1 domain-containing proteins is usually achieved by addition of bryostatins or phorbol-esters, which can be viewed as highly potent DAG mimics¹¹⁵. So far, the greatest control over DAG concentrations has been achieved with the photochemical uncaging of DAGs, such as caged 1,2-*O*-dioctanoyl-*sn*-glycerol (*cg*-1,2-DOG)¹¹⁶. However, once triggered, the activity cannot be switched OFF and the decay of the DAG signal depends on its metabolism or diffusion from the cell. Alternatively, chemical dimerizers^{117,118} or optogenetic techniques¹⁹ may be employed to modulate the levels of signaling lipids in cells on the addition of a small molecule or a flash of light, respectively. While these systems hold great promise

for rapid switching within signaling networks, they require recombinant expression of non-native proteins, and frequently depend on the presence of exogenous co-factors.

Previously, we prepared a series of photoswitchable FAs, termed FAAzos⁵¹, which can mimic highly unsaturated FAs such as AA. They are useful modular building blocks for synthetic incorporation into more elaborate photolipids. We now report the incorporation of the FAAzos into the DAG scaffold. The resulting photoswitchable DAGs, PhoDAGs, allow us to mimic the effects of natural DAGs in living cells with unprecedented kinetics and reversibility, especially in regards to pattern formation.

5.2 – Results

5.2.1 – Design and synthesis of photoswitchable DAGs

The design of the PhoDAGs was guided by our previous work which suggested that the azobenzene derivative **FAAzo-4** (**Fig. 1a**), in its *cis*-configuration, is able to mimic AA⁵¹. Therefore, we synthesized **PhoDAG-1** (**1**) as a photoswitchable analog of 2-*O*-arachidonyl-1-*O*-stearoyl-*sn*-glycerol (1,2-SAG) (**Fig. 5.1b**). **PhoDAG-1** was intended to be less active with the azobenzene in the *trans*-form, and become more active upon isomerization to the *cis*-form with UV-A light. The more hydrophilic DAG derivatives, **PhoDAG-2** (**2**) and **PhoDAG-3** (**3**), were designed as cell-permeable analogs mimicking 1,2-*O*-dioctanoyl-*sn*-glycerol (1,2-DOG)¹¹⁹, and contain shorter alkyl chains at the *sn*1 and *sn*2 positions, including the shorter chain azobenzene **FAAzo-9** (**4**) (**Fig. 5.2**).

PhoDAG-1 was synthesized in four steps in 57% overall yield (**Fig. 5.3a**). When handled under ambient lighting conditions, **PhoDAG-1** existed predominantly in its thermally stable *trans*-configuration and contained approximately 10% *cis*-isomer (**Fig. 5.3b**). On irradiation with UV-A light ($\lambda = 350\text{--}375$ nm), **PhoDAG-1** isomerized to its *cis*-configuration (**Fig. 5.1c**). Thermal back-relaxation of *cis*-**PhoDAG-1** occurred with a τ -value of about 60 h in DMSO and 22 h in water, while blue irradiation increased the rate of isomerization from *cis* to *trans*. As such, **PhoDAG-1** behaves as a regular azobenzene, and can be switched over many cycles without fatigue (**Fig. 5.1d**). The remaining PhoDAGs were prepared in an analogous fashion (**Fig. 5.3c**), and possessed comparable spectral characteristics to **PhoDAG-1**.

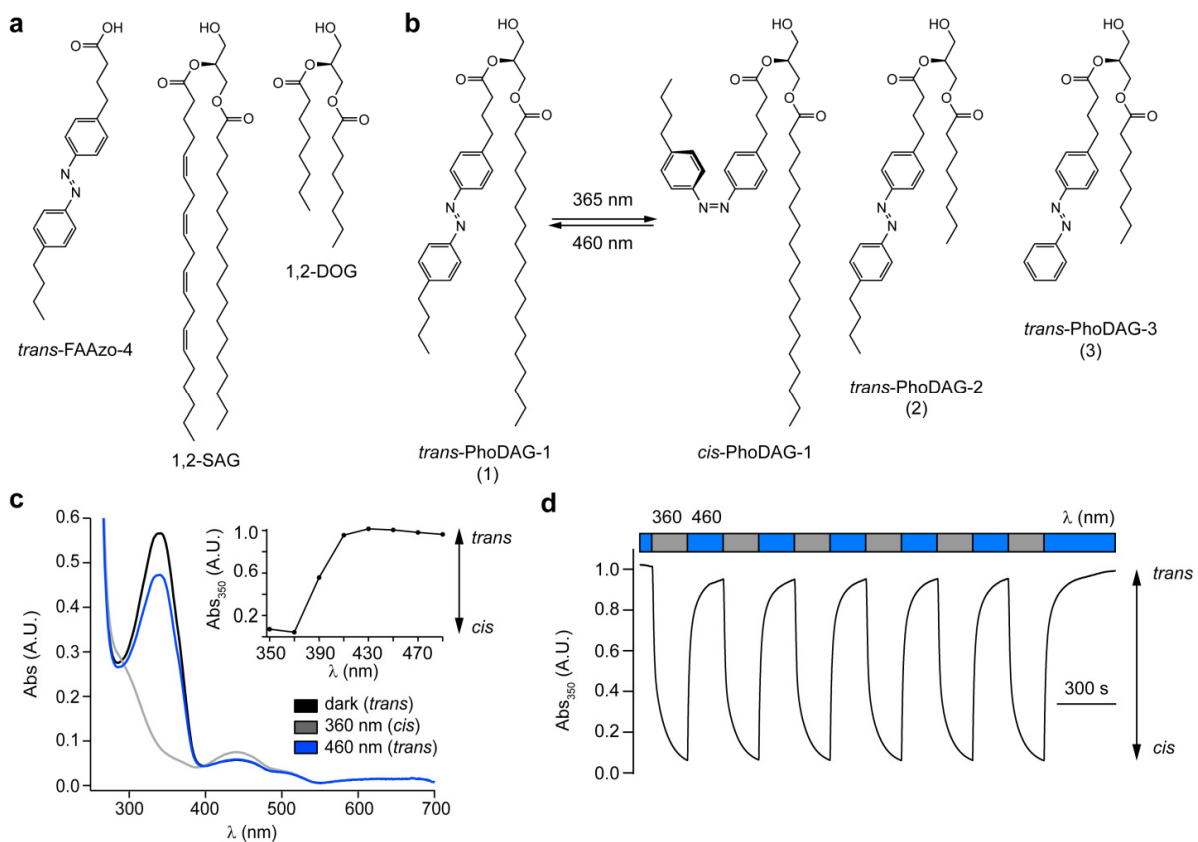


Figure 5.1 | Design and synthesis of photoswitchable DAGs. (a) The chemical structures of the photoswitchable fatty acid **FAAzo-4**, 2-*O*-arachidonyl-1-*O*-stearoyl-*sn*-glycerol (1,2-SAG) and 1,2-DOG. (b) The chemical structures of photoswitchable DAGs **PhoDAG-1 (1)**, **PhoDAG-2 (2)** and **PhoDAG-3 (3)**. (c) The UV-Vis spectra of **PhoDAG-1** (25 μ M in DMSO) in its *dark*-adapted (black), *UV*-adapted (gray) and *blue*-adapted (blue) photostationary states. The absorbance at $\lambda = 350$ nm was plotted as a function of the irradiation wavelength, demonstrating that **PhoDAG-1** existed primarily in its *trans*- and *cis*-configurations under blue and UV-A irradiation, respectively. (d) **PhoDAG-1** was cycled between the two states over many cycles without fatigue. The absorbance at $\lambda = 350$ nm was plotted over multiple cycles of alternating UV-A and blue irradiation.

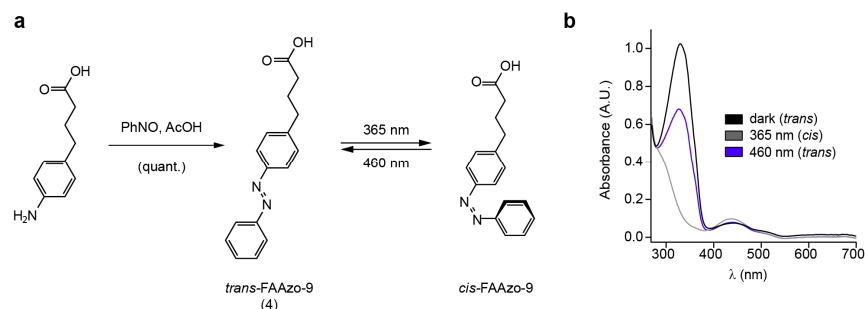


Figure 5.2 | Synthesis and characterization of a short-chain photoswitchable fatty acid. (a) The chemical synthesis of **FAAzo-9 (4)**. (b) UV-Vis spectroscopy showed that **FAAzo-9** (50 μ M in DMSO) could be isomerized between its *cis*- and *trans*-configurations with UV-A and blue light, respectively. Absorption spectra are shown for the *dark*-adapted (black), *UV*-adapted (grey) and *blue*-adapted (blue) photostationary states.

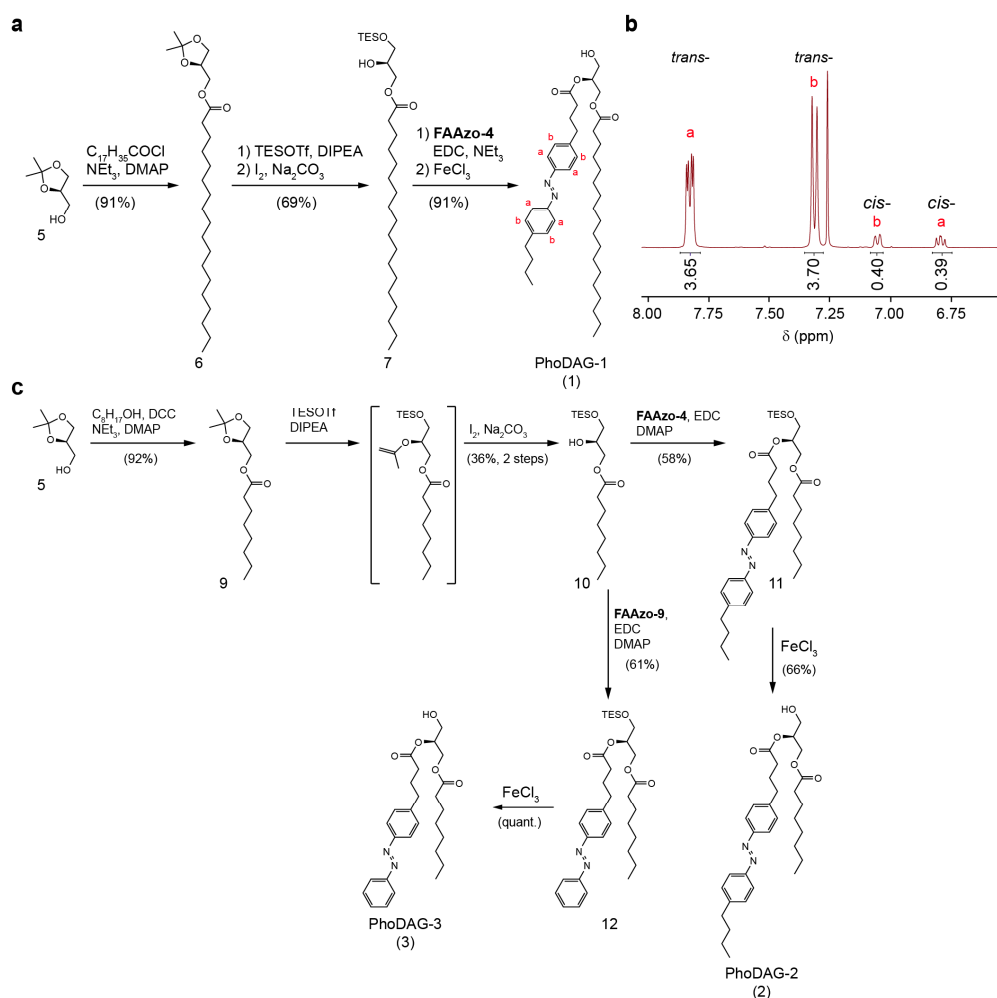


Figure 5.3 | Synthesis and characterization of the photoswitchable DAGs. (a) **PhoDAG-1** was synthesized in four steps and 57% overall yield. (b) A representative NMR spectrum of **PhoDAG-1** (in CDCl_3), displaying the aromatic region. Both the *trans*- and *cis*-azobenzene protons give signals under ambient lighting conditions, where **PhoDAG-1** exists as $\approx 10\%$ the *cis*-isomer. (c) The chemical syntheses of the short-chain photoswitchable DAGs, **PhoDAG-2** and **PhoDAG-3**.

5.2.2 – Optical control of C1 domain translocation

We evaluated the effects of the PhoDAGs in HeLa cells transiently expressing a fluorescent C1 domain translocation reporter (C1-GFP)^{120,121}. Before the addition of any compound, C1-GFP was evenly distributed within the cytoplasm, and the application of *trans*-PhoDAG-1 did not affect its localization (Fig. 5.4a). Illumination with UV-A light ($\lambda = 375$ nm) and isomerization to *cis*-PhoDAG-1 rapidly induced the translocation of C1-GFP towards the plasma membrane (Fig. 5.4b, Fig. 5.5, Fig. 5.6). After termination of the irradiation, C1-GFP diffused back into the cytoplasm, and translocation was again triggered on repeated stimulation (Fig. 5.4c). C1-GFP localization could be controlled with a high degree of spatial precision, as only cells that were directly irradiated were affected (Fig. 5.7). Shorter UV-A pulses triggered a small and transient translocation, while longer periods of irradiation caused a larger and more sustained response (Fig. 5.4d), permitting the generation of oscillation patterns. After incubation with PhoDAG-1 followed by washing and removal of extracellular compound, translocation of C1-GFP was still observed on photoactivation (Fig. 5.8a). The magnitude of the translocation induced by *cis*-PhoDAG-1 was comparable to that triggered by the uncaging of 1,2-DOG from its coumarin-caged form, *cg*-1,2-DOG (Fig. 5.8b-d).

Interestingly, PhoDAG-2 and PhoDAG-3 did not induce pronounced translocation of C1-GFP towards the plasma membrane. Instead, C1-GFP mostly accumulated on the inner membranes on PhoDAG application (Fig. 5.9a). We monitored the localization and uptake of the PhoDAGs by exploiting the quenching of coumarin fluorescence by the azobenzene. We loaded HeLa cells with coumarin-labelled AA (*cg*-AA) (Fig. 5.9b), which localizes predominantly at the inner cellular membranes¹²². Application of PhoDAG-1 caused a slow but small decrease in the observed coumarin fluorescence (<20% of total, $\tau = 295$ s) (Fig. 5.4e black, Fig. 5.9c). In comparison, PhoDAG-3 caused a more rapid and significant decrease in coumarin fluorescence (>70% in total, $\tau = 85$ s) (Fig. 5.4e gray, Fig. 5.9d). These results suggest that PhoDAG-1 internalizes more slowly and remains trapped on the plasma membrane, while PhoDAG-3 quickly diffuses and accumulates at inner membranes. UV-A irradiation alone did not trigger the translocation of C1-GFP to the plasma membrane (Fig. 5.10a).

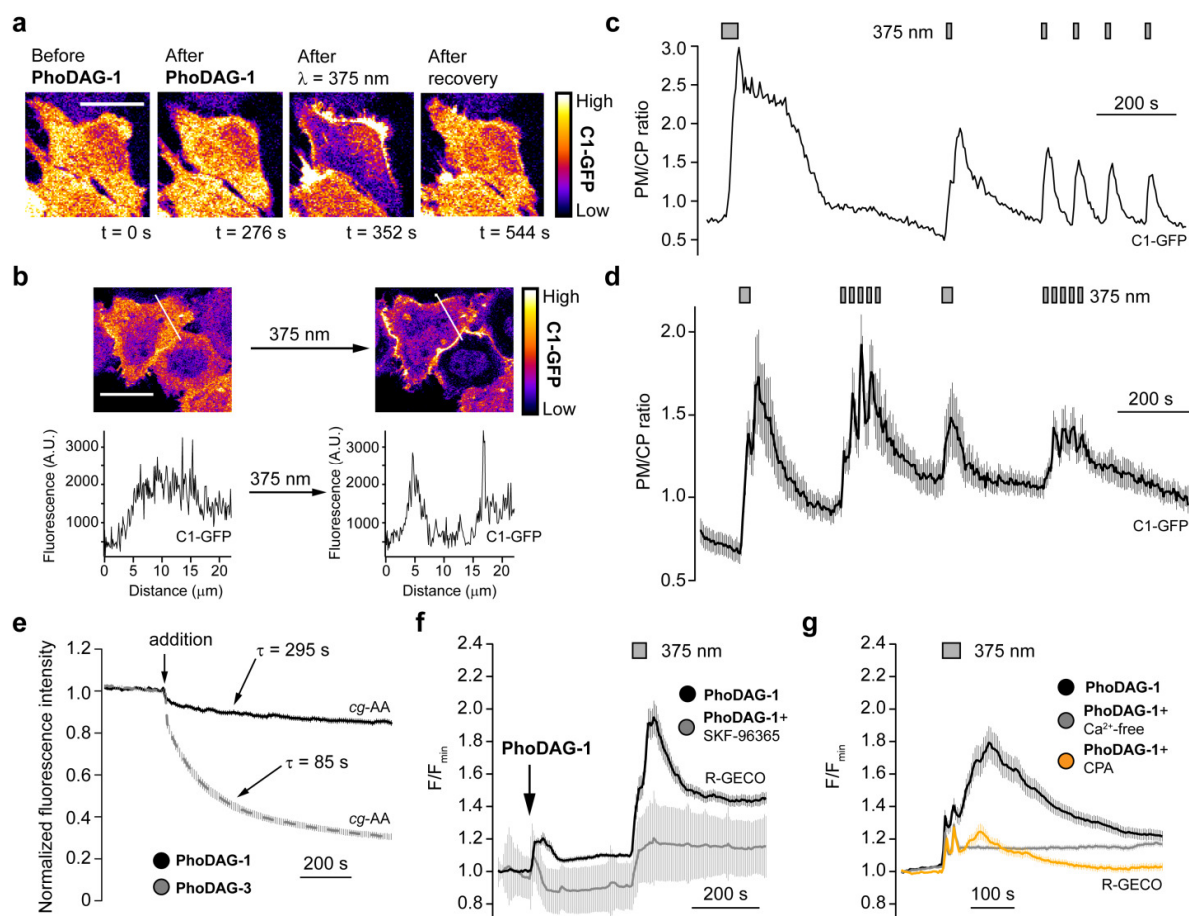


Figure 5.4 | PhoDAG-1 enables optical control of C1-GFP translocation and $[Ca^{2+}]_i$ in HeLa cells. (a) Fluorescence images showed that **PhoDAG-1** (150 μ M) promotes reversible translocation of C1-GFP in HeLa cells towards the plasma membrane only after irradiation with $\lambda = 375$ nm light. (b) C1-GFP fluorescence intensity was measured across a representative cell (white line) loaded with **PhoDAG-1** before (left image) and after (right image) illumination with $\lambda = 375$ nm light. (c) Translocation could be triggered over multiple cycles in the presence of **PhoDAG-1**, and was quantified by plotting the plasma membrane to cytoplasm (PM/CP) fluorescence intensity ratio of a representative cell. (d) Patterns of C1-GFP translocation were generated by irradiation at $\lambda = 375$ nm in the presence of **PhoDAG-1** ($n = 16$, 2 experiments). (e) Fluorescence quenching dynamics of coumarin-labelled AA (*cg*-AA, 100 μ M) localized at the internal cell membranes after application of **PhoDAG-1** (150 μ M, $n = 18$, 2 experiments, black) or **PhoDAG-3** (150 μ M, $n = 19$, 2 experiments, gray). (f) The TRPC channel blocker SKF-96365 (50 μ M) decreased the Ca^{2+} influx on application and photoactivation of **PhoDAG-1** ($n = 54$, 2 experiments, gray) when compared to **PhoDAG-1** alone ($n = 16$, 2 experiments, black). $[Ca^{2+}]_i$ levels were monitored with the R-GECO $[Ca^{2+}]_i$ sensor. (g) After incubation with **PhoDAG-1** followed by the removal of extracellular compound, both cyclopiazonic acid (CPA, 50 μ M, $n = 64$, 4 experiments, orange) and $NiCl_2$ (5 mM) combined with a Ca^{2+} -free extracellular buffer (0.1 mM EGTA, $n = 73$, 4 experiments, gray) reduced the Ca^{2+} response. Error bars were calculated as \pm s.e.m. All scale bars = 20 μ m.

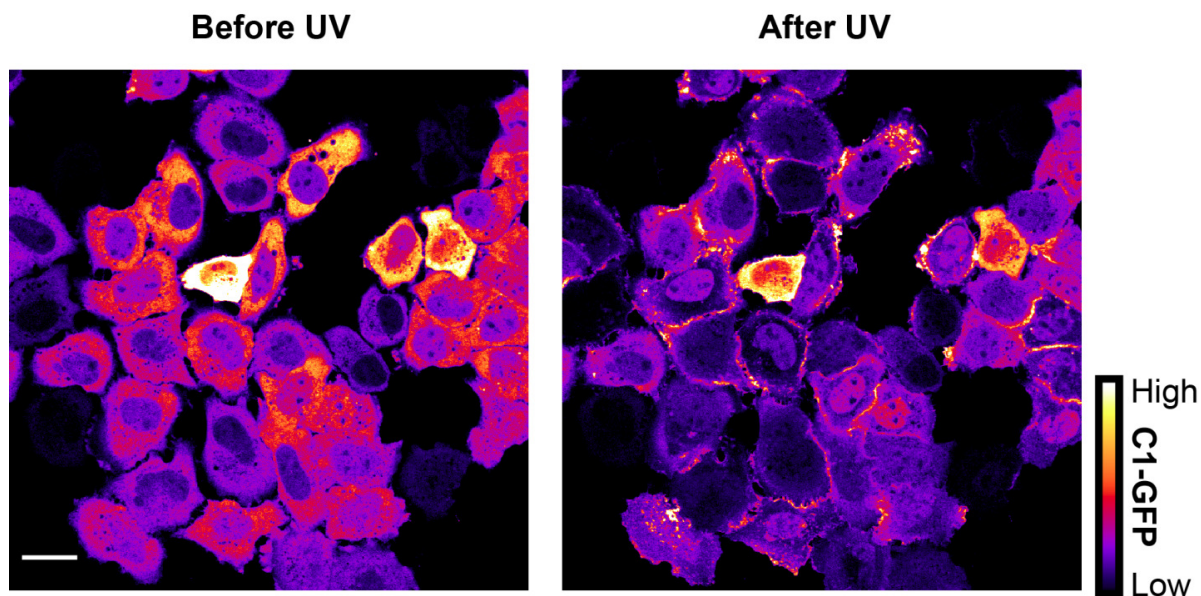


Figure 5.5 | Optical control of C1-GFP translocation. In HeLa cells, **PhoDAG-1** (150 μM) triggered the translocation of C1-GFP towards the plasma membrane on $\lambda = 375 \text{ nm}$ irradiation. Scale bar = 20 μM .

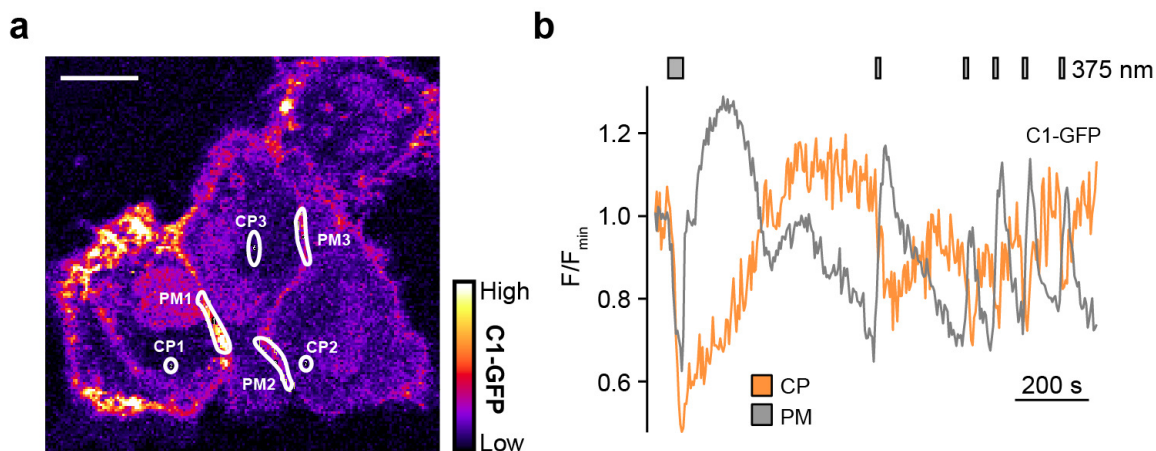


Figure 5.6 | Quantification of C1-GFP translocation. (a) A representative fluorescence image of HeLa cells expressing C1-GFP, detailing the cytoplasm (CP) and plasma membrane (PM) sample regions used for translocation quantification. Displayed here is C1-GFP fluorescence after the application of **PhoDAG-1** (400 μM) and $\lambda = 375 \text{ nm}$ irradiation. Scale bar = 20 μM . (b) The GFP fluorescence intensities at the plasma membrane and cytoplasm of a representative cell after the application of **PhoDAG-1** (200 μM). In the main text, C1 domain translocation is quantified by measuring the ratio of the GFP intensities in the PM and CP, and then plotted as the plasma membrane to cytoplasmic (PM/CP) fluorescence ratio.

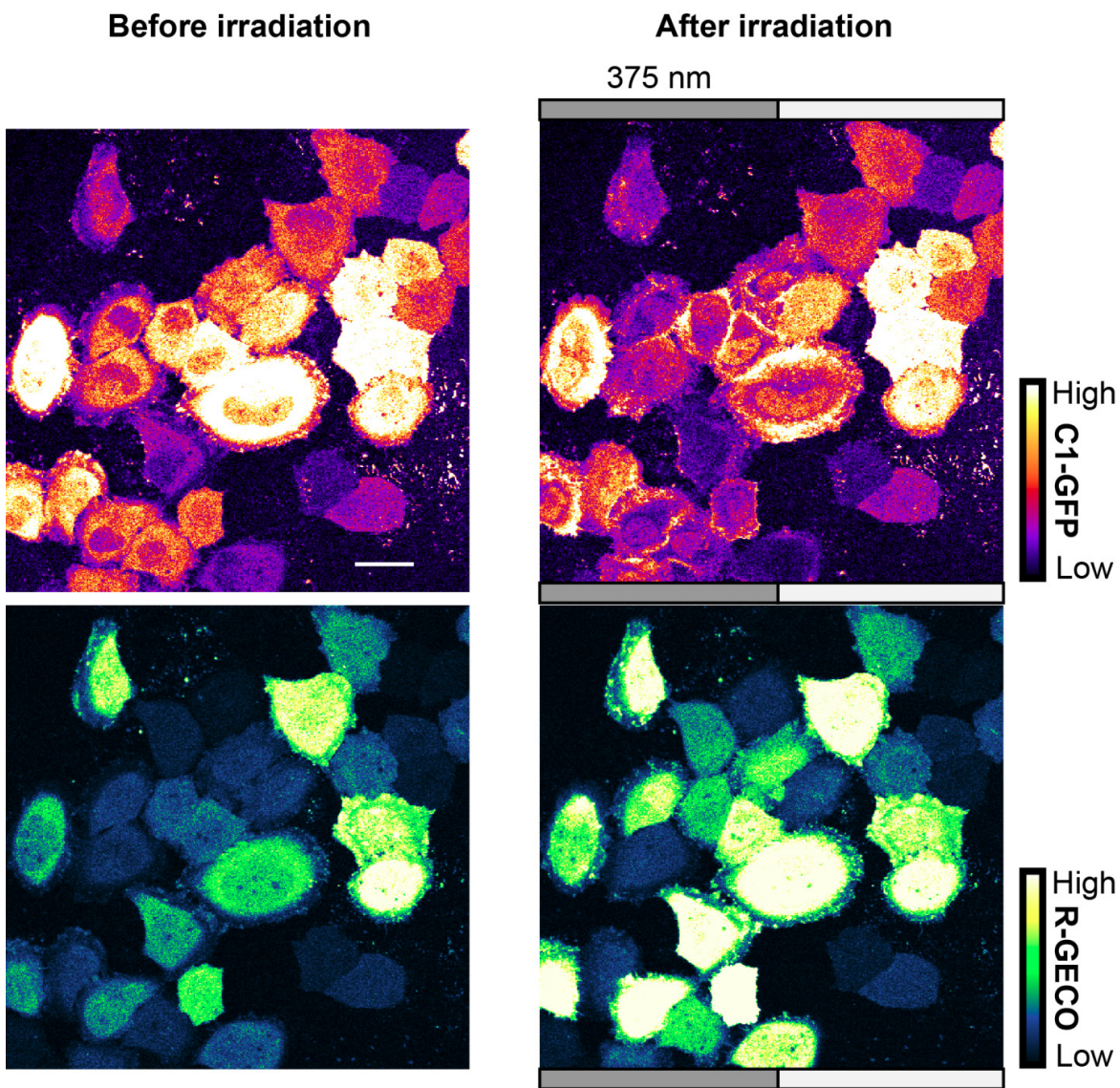


Figure 5.7 | PhoDAG-1 enables spatial control of DAG signaling. In HeLa cells expressing C1-GFP and R-GECO, PhoDAG-1 (150 μM) activation could be targeted to specific cells. In this case, only the left half of the frame (gray bar) was irradiated at $\lambda = 375 \text{ nm}$. In these cells, C1 GFP translocated towards the plasma membrane, alongside an increase in $[\text{Ca}^{2+}]_i$. The right half of the frame remained largely unaffected (white bar). Scale bar = 20 μM .

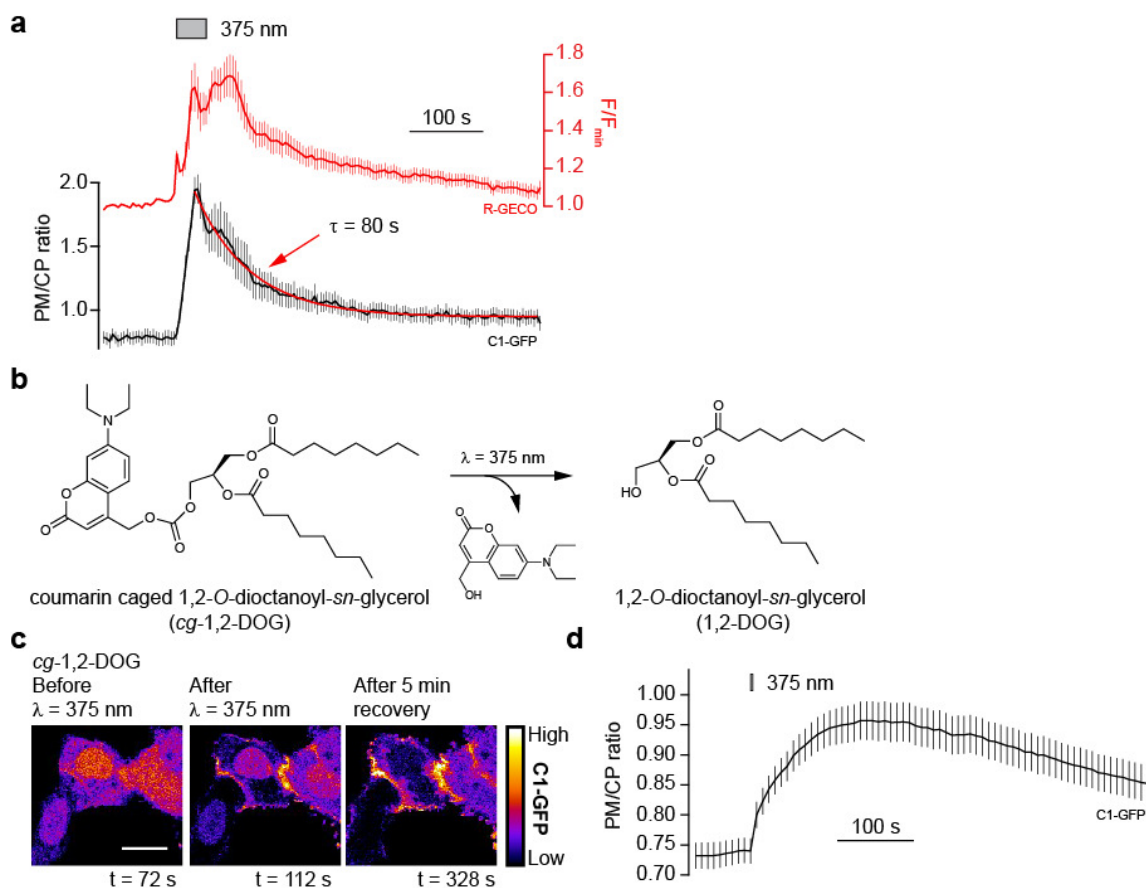


Figure 5.8 | Optical control of C1-GFP translocation. (a) HeLa cells expressing C1-GFP and R-GECO were incubated **PhoDAG-1** (150 μ M) followed by washing with buffer to remove extracellular compound. Translocation of C1-GFP towards the plasma membrane was observed on $\lambda = 375$ nm irradiation. An increase in $[Ca^{2+}]_i$ was also observed in the same cells ($n = 12$, 2 experiments). (b) The chemical structure of 1,2-DOG being liberated from caged 1,2-DOG (cg-1,2-DOG) on $\lambda = 375$ nm irradiation. (c,d) The uncaging of cg-1,2-DOG (100 μ M) triggered C1-GFP translocation towards the plasma membrane in HeLa cells. After uncaging, the recovery was relatively slow. Shown are (c) fluorescence images of two representative cells, and (d) data averaged from multiple cells ($n = 25$ cells, 1 experiment), displayed as the plasma membrane to cytoplasm (PM/CP) fluorescence ratio. Error bars were calculated as \pm s.e.m. Scale bar = 20 μ M.

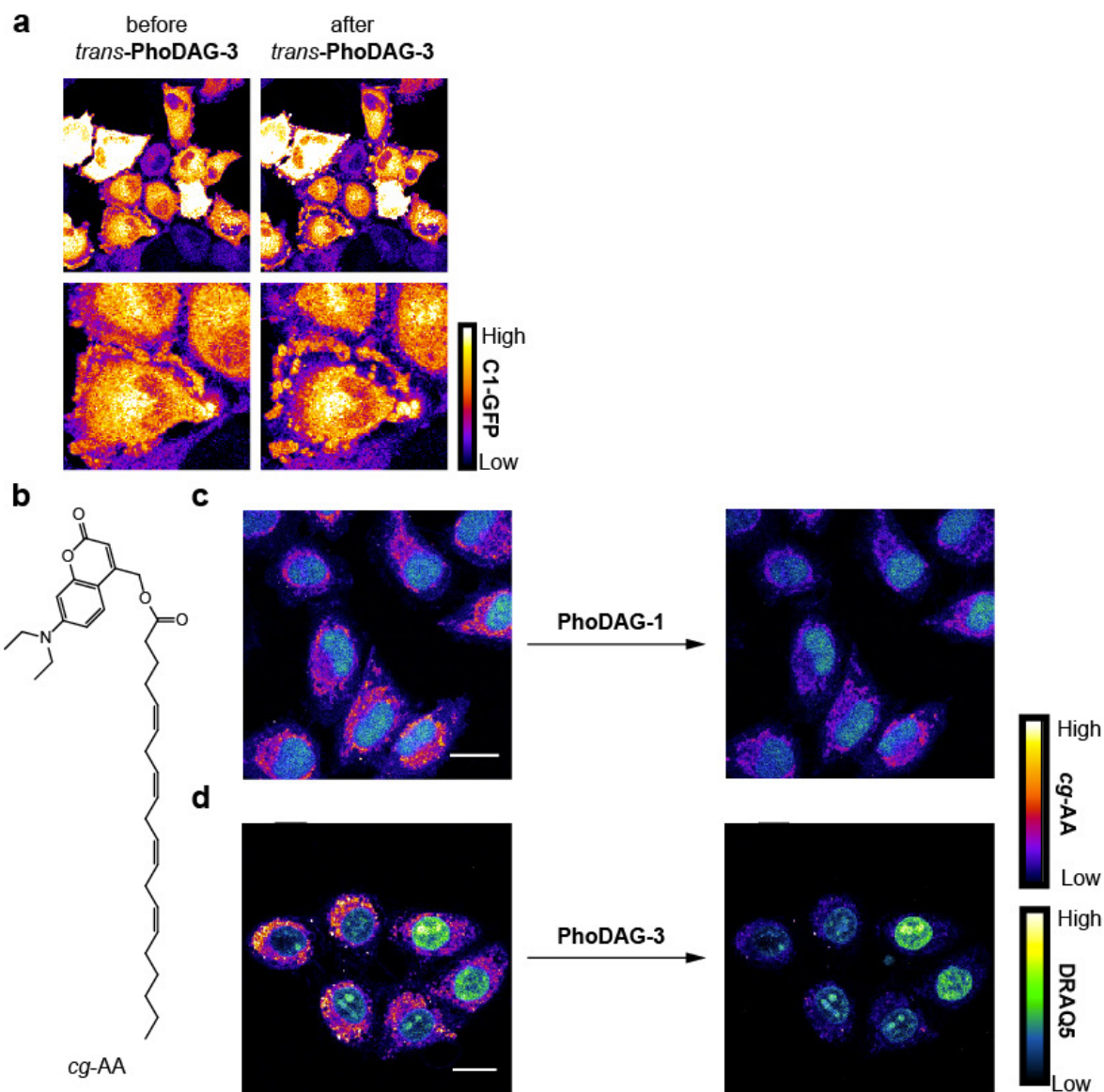


Figure 5.9 | Lipid chain length determines the localization and activity of the PhoDAGs. (a) In HeLa cells, *trans*-PhoDAG-3 (150 μ M) caused translocation of C1-GFP towards internal membranes on application. (b) The chemical structure of coumarin-labeled AA (*cg*-AA), which localizes in internal membranes. (c,d) Representative fluorescence images showing the localization of *cg*-AA (100 μ M, fire) before (left) and after (right) the addition of (c) **PhoDAG-1** (150 μ M) or (d) **PhoDAG-3** (150 μ M). **PhoDAG-3** quenched the coumarin fluorescence more quickly than **PhoDAG-1**. Cell nuclei were stained with DRAQ-5 (green) as a reference. Scale bar = 20 μ M.

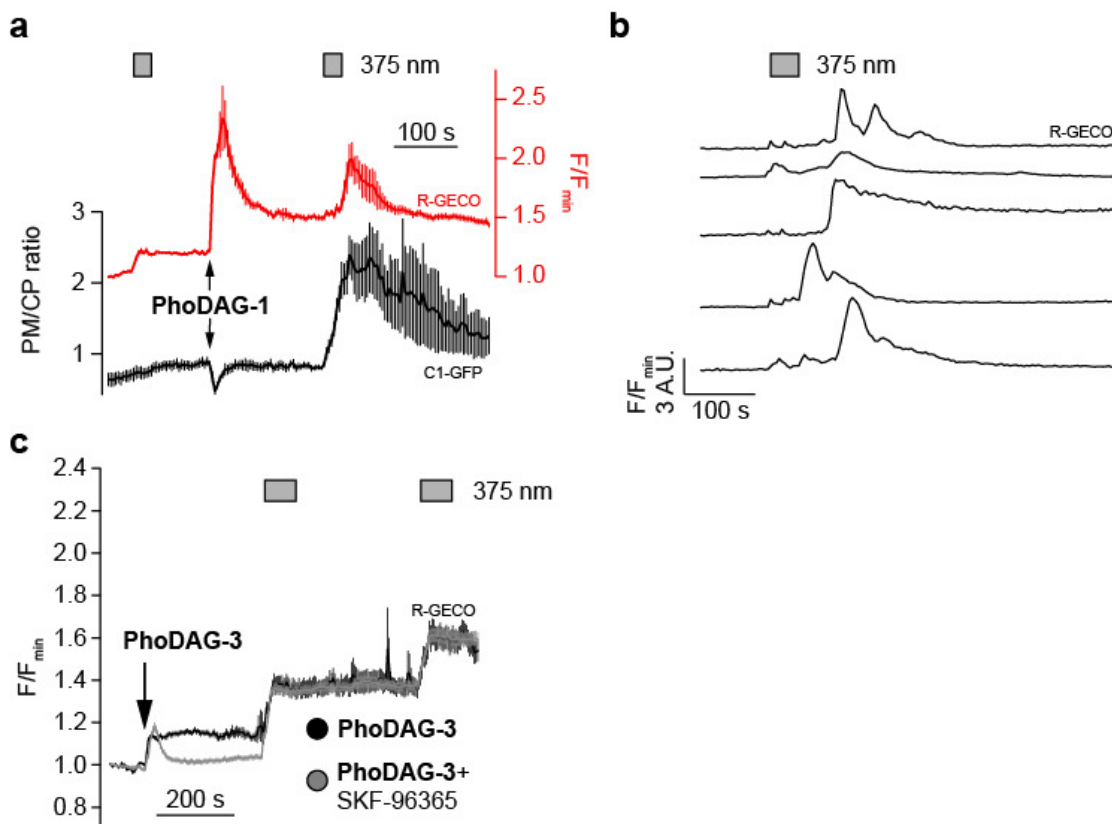


Figure 5.10 | PhoDAG-1 affects $[Ca^{2+}]_i$ levels in HeLa cells. HeLa cells were transfected with C1-GFP and R-GECO. (a) Before the application of **PhoDAG-1**, UV-A irradiation alone did not catalyze C1-GFP translocation. Application of *trans*-**PhoDAG-1** (300 μ M) caused an increase in $[Ca^{2+}]_i$ levels, however no translocation was observed until triggered by $\lambda = 375$ nm irradiation ($n = 6$, 1 experiment). Translocation is displayed as the PM/CP C1-GFP fluorescence ratio, while $[Ca^{2+}]_i$ levels were plotted as the R-GECO fluorescence intensity normalized to the baseline fluorescence (F/F_{min}). (b) In the presence of **PhoDAG-1**, a small increase in $[Ca^{2+}]_i$ was observed on photoactivation, followed by a delayed, larger increase. Shown are representative traces from individual cells. (c) The TRPC channel inhibitor SKF-96365 (50 μ M) slightly decreased the Ca^{2+} influx after application of **PhoDAG-3** (150 μ M), but not on photoactivation ($n = 54$, 2 experiments, gray), when compared to **PhoDAG-3** alone ($n = 16$, black). Error bars were calculated as \pm s.e.m.

5.2.3 – PhoDAGs modulate intracellular Ca^{2+} levels in HeLa cells

1,2-SAG was previously reported to increase $[\text{Ca}^{2+}]_i$ levels in HeLa cells via activation of TRPC channels¹¹⁶. Using the genetically encoded Ca^{2+} sensor, R-GECO¹²³, we observed that application of *trans*-**PhoDAG-1** stimulated a small rise in $[\text{Ca}^{2+}]_i$ (**Fig. 5.4f**). Upon isomerization to *cis*-**PhoDAG-1**, a much larger $[\text{Ca}^{2+}]_i$ increase was observed. The TRPC channel blocker SKF-96365 suppressed the rise in $[\text{Ca}^{2+}]_i$ (**Fig. 5.4f**). After incubation with **PhoDAG-1** followed by washing and removal of extracellular compound, an increase in $[\text{Ca}^{2+}]_i$ was still observed on photoactivation (**Fig. 5.4g**, **Fig. 5.8a**, **Fig. 5.10b**). Incubation with cyclopiazonic acid, which depletes endoplasmic reticulum (ER) Ca^{2+} stores¹²⁴, diminished the Ca^{2+} response (**Fig. 5.4g**, orange). NiCl_2 in combination with a Ca^{2+} -free extracellular buffer¹¹⁶ abolished the Ca^{2+} signal by preventing the entry of extracellular Ca^{2+} (**Fig. 5.4g**, gray). Together, these results suggest that *cis*-**PhoDAG-1** promotes Ca^{2+} influx by activation of TRPC3 and/or TRPC6 channels, which in turn triggers Ca^{2+} -induced Ca^{2+} release from intracellular stores. Interestingly, application and photoactivation of **PhoDAG-3** only caused a small increase in $[\text{Ca}^{2+}]_i$, which was not affected by SKF-96365 (**Fig. 5.10c**).

5.2.4 – Optical control of protein kinase C

PKCs are a group of serine/threonine kinases that are involved in cell cycle regulation, proliferation, apoptosis and migration¹⁰⁸. The PKC family is grouped into three different subtypes; conventional, novel and atypical, according to their cofactor requirements as determined by the regulatory elements linked to the kinase domain¹²⁵. These regulatory domains allow different PKC isoforms to decode different signals at the plasma membrane, such as the generation of DAG.

Novel PKCs, such as PKC δ , contain two C1 domains that orchestrate their activation alongside translocation toward the plasma membrane in a Ca²⁺-independent fashion¹²⁶. In HeLa cells, **PhoDAG-1** triggered translocation of fluorescently labeled PKC δ (PKC δ -RFP) towards the plasma membrane following a UV-A flash (**Fig. 5.11a**). After termination of the irradiation, PKC δ -RFP translocated back to the cytosol with a τ -value of ~ 102 s (**Fig. 5.11b**). Translocation could be repeated over several cycles, however the magnitude of translocation often diminished with repeated UV-A flashes of the same duration (**Fig. 5.12a**). To overcome this limitation, we developed a protocol that allowed us to perform many translocation cycles without a decrease in efficiency by increasing the irradiation time on each sequential photostimulation (**Fig. 5.11c**). Increasing the interval time between the UV-A pulses did not affect the translocation magnitude, suggesting that *trans*-**PhoDAG-1** metabolism was not a significant factor (**Fig. 5.12b**).

Conventional PKCs, such as PKC α , were also placed under optical control. **PhoDAG-1** triggered the translocation of PKC α -GFP¹²⁷ towards the plasma membrane on photoactivation (**Fig. 5.12c**). In contrast to C1-GFP and PKC δ -RFP, PKC α -GFP translocation efficiency decreased quickly alongside Ca²⁺-influx on sequential photostimulations, reflecting its known Ca²⁺-sensitivity¹²⁵.

Although PKC translocation to the plasma membrane is normally associated with its activation¹²⁸, translocation alone is not sufficient to conclude whether **PhoDAG-1** can trigger PKC phosphorylation. To this end, we utilized the C kinase activity reporter (CKAR)¹²⁹, which displays a decrease in FRET efficiency on phosphorylation (**Fig. 5.11d,e**). In line with previous reports¹²⁹, the addition of 1,2-DOG (**Fig. 5.12d**) to HeLa cells expressing CKAR caused a 5.5% increase in the CFP/YFP fluorescence ratio, while the application of phorbol 12-myristate 13-acetate (PMA) (**Fig. 5.12e**) caused a 4.8% increase. The application of *trans*-**PhoDAG-1** did not cause a significant CKAR FRET change. However, a 4.4% increase in the CFP/YFP fluorescence ratio was observed on isomerization to *cis*,

corresponding to 80% of the response evoked by 1,2-DOG (Fig. 5.11e). The application of *trans*-PhoDAG-3 also caused a small increase (2.2%) in the CFP/YFP ratio on application, and a further 2.0% increase was induced by photoactivation (Fig. 5.12f,g). The overall response after the application and photoactivation of PhoDAG-3 was similar to that which was evoked by PhoDAG-1 (95%) or 1,2-DOG (76%). Interestingly, this effect was observed even in the absence of a clear translocation to the outer plasma membrane, suggesting that PKC δ -RFP could be activated on internal membranes as well. In all cases, the effect was reversed by the application of the broad-spectrum PKC inhibitors Gö-6983 or chelerythrine chloride (C-CI) (Fig. 5.11d,e, Fig. 5.12d–h)^{130,131}.

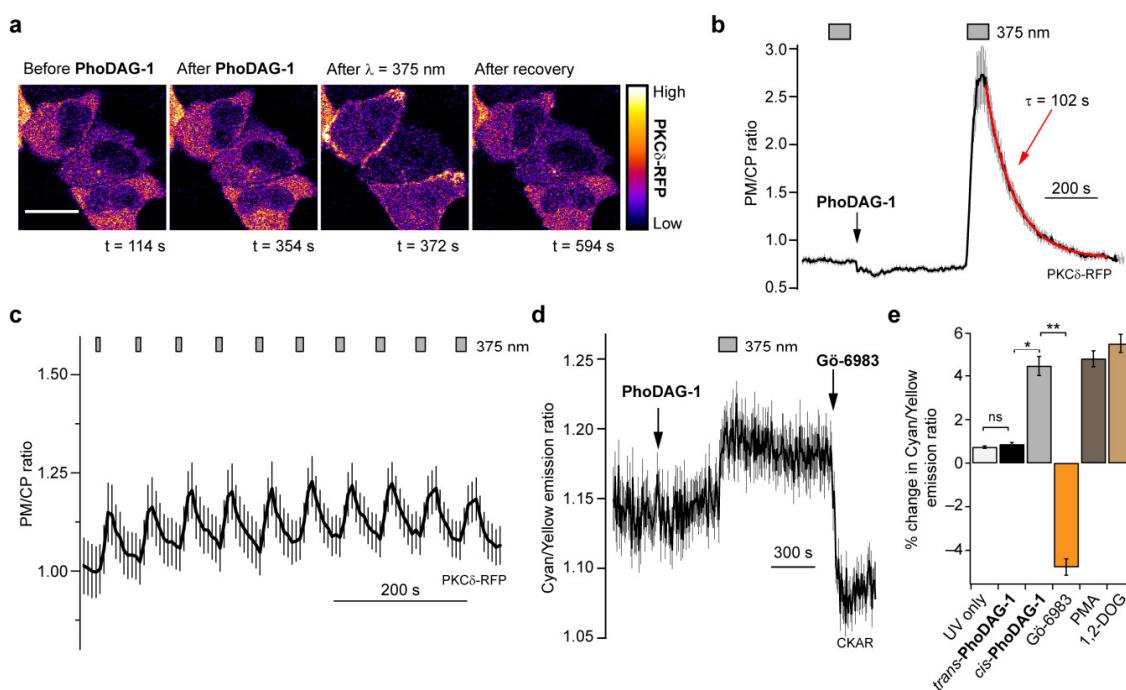


Figure 5.11 | PhoDAG-1 enables optical control of PKC. (a) Fluorescence images of HeLa cells expressing PKC δ -RFP showed that PhoDAG-1 (100 μ M) triggered reversible translocation of PKC δ -RFP towards the plasma membrane on $\lambda = 375$ nm irradiation. Scale bar = 20 μ m. (b) After photoactivation, PKC δ -RFP redistributed back to the cytoplasm ($n = 19$, 2 experiments). Translocation was quantified as the plasma membrane to cytoplasm (PM/CP) fluorescence intensity ratio. (c) Oscillations of PKC δ -RFP translocation were generated by sequential pulses of UV-A irradiation with increasing length ($n = 11$ cells, 1 representative experiment). (d,e) PKC activation was evaluated in HeLa cells expressing PKC δ -RFP and the cytosolic C kinase activation reporter, CKAR¹²⁹. (d) PhoDAG-1 (300 μ M) triggered an increase in the cyan/yellow fluorescence emission ratio on isomerization to *cis* ($n = 49$, 3 experiments). (e) Photoactivation of PhoDAG-1 ($n = 49$, 3 experiments) produced a similar FRET change when compared to 1,2-DOG (300 μ M, $n = 32$, 1 experiment) and PMA (5 μ M, $n = 31$, 2 experiments). Application of Gö-6983 (10 μ M, $n = 49$, 3 experiments) reversed this effect. The Mann-Whitney test was used to determine statistical significance. ns = not significant $P > 0.05$, * $P < 0.005$, ** $P < 0.001$. Error bars were calculated as \pm s.e.m.

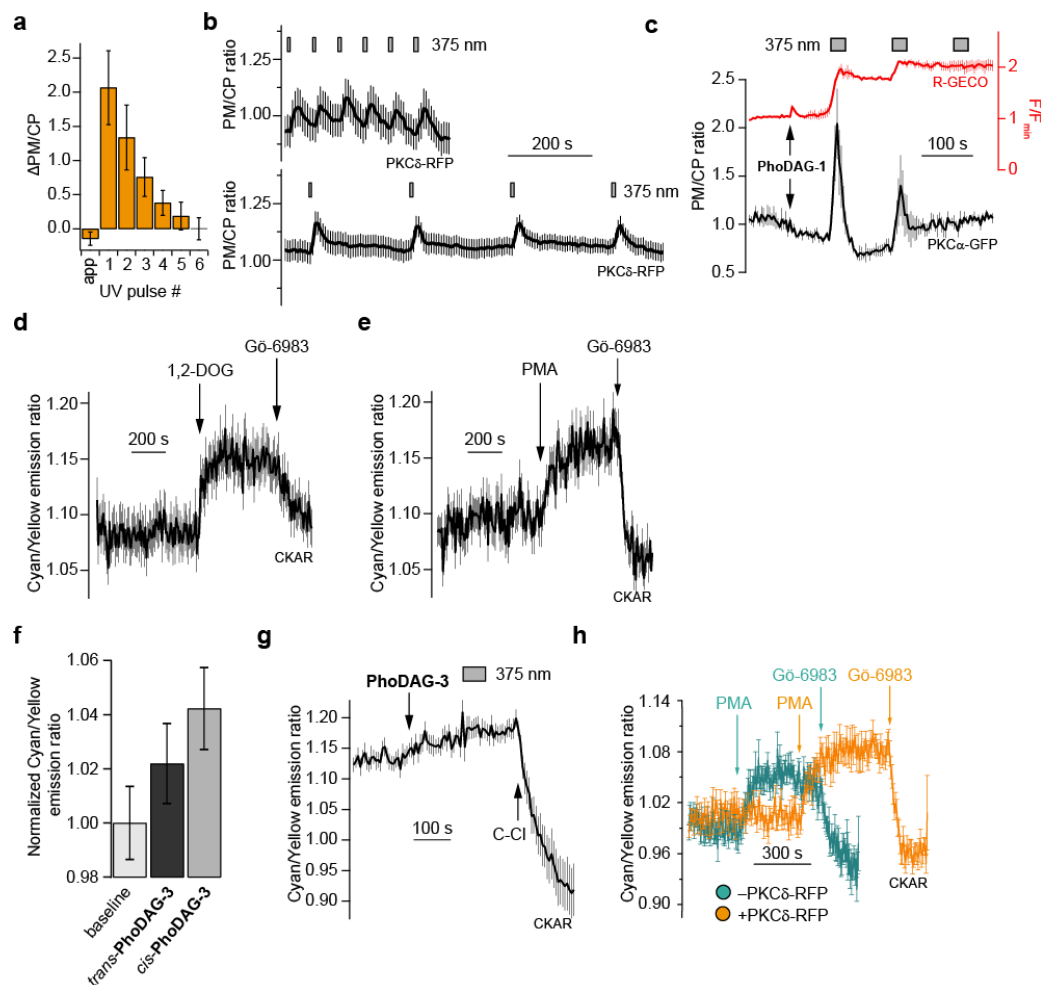


Figure 5.12 | Optical control of PKC. In HeLa cells: **(a)** PKC δ -RFP translocation efficiency induced by **PhoDAG-1** (100 μ M) decayed over multiple irradiation cycles of the same length (28 s pulses at $\lambda = 375$ nm, $n = 11$, 2 experiments). **(b)** Changing the time between UV-A pulses did not affect the magnitude of the translocation. Both the 60 s ($n = 13$, 1 experiment) and 240 s ($n = 15$, 1 experiment) intervals showed similar efficiencies. **(c)** PKC α -GFP translocated towards the plasma membrane on isomerization to *cis*-**PhoDAG-1** (150 μ M) ($n = 3$, 1 experiment). Sequential photostimulations led to diminished efficiency, corresponding to a reduced Ca^{2+}_i response. $[Ca^{2+}]_i$ levels (R-GECO) are displayed as the RFP fluorescence intensity and normalized to the baseline fluorescence (F/F_{min}). **(d,e)** As shown by the cytosolic C kinase activity reporter (CKAR), the application of **(d)** 1,2-DOG (300 μ M, $n = 32$, 1 experiment) and **(e)** PMA (5 μ M, $n = 31$, 2 experiments) triggered an increase in the CFP/YFP emission ratio, indicating kinase activation. In both cases, the FRET change was reversed on addition of the broadband PKC inhibitor Gō-6983 (10 μ M). **(f,g)** **PhoDAG-3** (15 μ M) caused an increase in the CFP/YFP emission ratio on application, and a further increase on photoactivation. This effect was reversed by the application of C-Cl (100 μ M) ($n = 14$, 1 experiment). **(h)** The CKAR response in HeLa cells was compared between cells with ($n = 37$, 1 experiment, orange) and without ($n = 20$, 1 experiment, teal) the expression of exogenous PKC δ -RFP. Overexpression of PKC δ -RFP increased the CKAR response by 1.2-fold when compared to endogenous PKC expression only. Error bars were calculated as \pm s.e.m.

5.2.5 – Optical control of $[Ca^{2+}]_i$ oscillations in β -cells

In pancreatic β -cells, glucose induces oscillations in $[Ca^{2+}]_i$ levels, the frequency of which strongly correlate with insulin secretion¹³². Similarly, DAG levels are known to oscillate in β -cells¹²¹, implicating a connection between glucose and lipid metabolism. The exact mechanism by which DAGs regulate insulin secretion remains elusive, however increased DAG levels were reported to terminate $[Ca^{2+}]_i$ oscillations in the mouse insulinoma-derived β -cell line, MIN6^{133,134}. The addition of *trans*-**PhoDAG-1** did not affect $[Ca^{2+}]_i$ oscillations in MIN6 cells stimulated by a high glucose concentration (20 mM). Photoactivation with $\lambda = 375$ nm for 3 min caused a rapid decline in both the intensity and frequency of the $[Ca^{2+}]_i$ oscillations (**Fig. 5.13a,b**), as well as the overall $[Ca^{2+}]_i$ level (**Fig. 5.14a**). In the majority of cells examined, this termination was transient and lasted on average 5 min. **PhoDAG-3** behaved in a similar manner, but was active at a much lower concentration (**Fig. 5.13c**).

$[Ca^{2+}]_i$ oscillations in β -cells are driven by a dynamic interplay between voltage-gated ion channels. DAGs modulate the conductance of L-type voltage-activated Ca^{2+} channels (Ca_v) in mouse β -cells, and 1,2-DOG is known to inhibit the whole-cell Ca_v current¹³⁵. Using whole-cell patch clamp electrophysiology in MIN6 cells, we evaluated the effects of PhoDAGs on Ca_v conductance. Photoactivation of **PhoDAG-3** with UV-A light triggered a decrease in the Ca_v current (**Fig. 5.13d, Fig. 5.14b**). This effect could be reversed by irradiation with blue light, and could be repeated over several cycles (**Fig. 5.13e**). Application of diltiazem, which blocks L-type Ca^{2+} channels, diminished the Ca_v current in a similar fashion (**Fig. 5.14c**). UV-A irradiation alone did not affect the oscillatory behavior (**Fig. 5.15**) or the Ca_v current (**Fig. 5.14c**).

To compare the responses observed in MIN6 to those of primary β -cells, we cultured β -cells from dissociated mouse pancreatic islets. As in MIN6 cells, **PhoDAG-3** triggered a light-dependent decrease in $[Ca^{2+}]_i$ oscillation frequency (**Fig. 5.13f**) and the whole-cell Ca_v conductance (**Fig. 5.13g**). Surprisingly, in these cells *cis*-**PhoDAG-1** caused an increase in the oscillation frequency and $[Ca^{2+}]_i$ level (**Fig. 5.13h**). Patch clamp experiments revealed that, whereas photoactivation of **PhoDAG-1** had little effect on Ca_v conductance (**Fig. 5.16a**), it caused a reduction in the conductance of delayed rectifier voltage-gated K^+ channels (K_v) (**Fig. 5.13i**). Ablation of K_v has been shown to increase Ca^{2+} fluxes in β -cells by extending the AP duration¹⁵. Similar effects can be also induced by AA, which is known to block $K_v2.1$ channels¹³⁶. In control experiments, the application of 1,2-DOG indeed decreased the

magnitude of β -cell Ca_v conductance (**Fig. 5.16b**), while the addition of AA reduced the K_v current (**Fig. 5.16c**). Neither UV-A nor blue-irradiation alone affected the Ca_v or K_v currents (**Fig. 5.16b,c**).

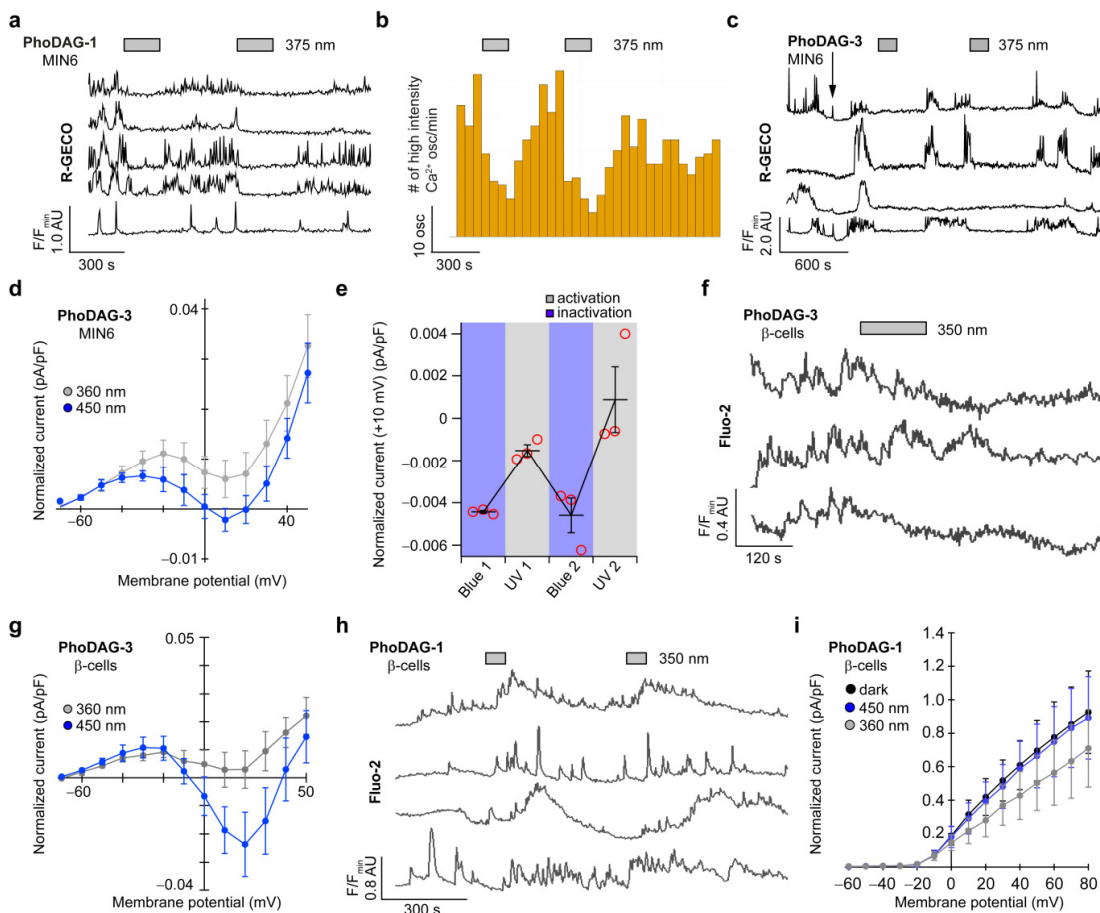


Figure 5.13 | Optical control of $[\text{Ca}^{2+}]_i$ oscillations in MIN6 and dissociated primary mouse β -cells. (a-c) $[\text{Ca}^{2+}]_i$ oscillations in glucose-stimulated (20 mM) MIN6 cells were monitored using R-GECO. **PhoDAG-1** (300 μM) decreased $[\text{Ca}^{2+}]_i$ levels on photoactivation with $\lambda = 375$ nm light, displayed as (a) individual $[\text{Ca}^{2+}]_i$ traces from four representative cells, and (b) a statistical analysis of the oscillation frequency ($n = 38$, 3 experiments). Bar graphs represent the number of high intensity $[\text{Ca}^{2+}]_i$ oscillations ($>50\%$ of highest transient in each trace) detected within every 60 s interval. (c) **PhoDAG-3** (35 μM) also triggered a decrease in glucose-stimulated (20 mM) $[\text{Ca}^{2+}]_i$ oscillations on photoactivation. (d) Isomerization to *cis*-**PhoDAG-3** (35 μM , $n = 6$) induced a decrease in whole-cell voltage-gated Ca^{2+} channel (Ca_v) current. (e) This effect was reversed by blue light and could be repeated over several cycles ($n = 3$). (f-i) In dissociated mouse β -cells: (f) *cis*-**PhoDAG-3** (10 μM) caused a decrease in glucose-stimulated (11 mM) $[\text{Ca}^{2+}]_i$ oscillations, corresponding to (g) a reduction in the Ca_v current (15 μM , $n = 3$). (h) In contrast, *cis*-**PhoDAG-1** (200 μM) led to an increase in the $[\text{Ca}^{2+}]_i$ oscillation frequency. (i) A reduction in the delayed rectifier voltage-activated K^+ channel (K_v) current was observed on isomerization to *cis*-**PhoDAG-1** ($n = 3$). Error bars were calculated as \pm s.e.m.

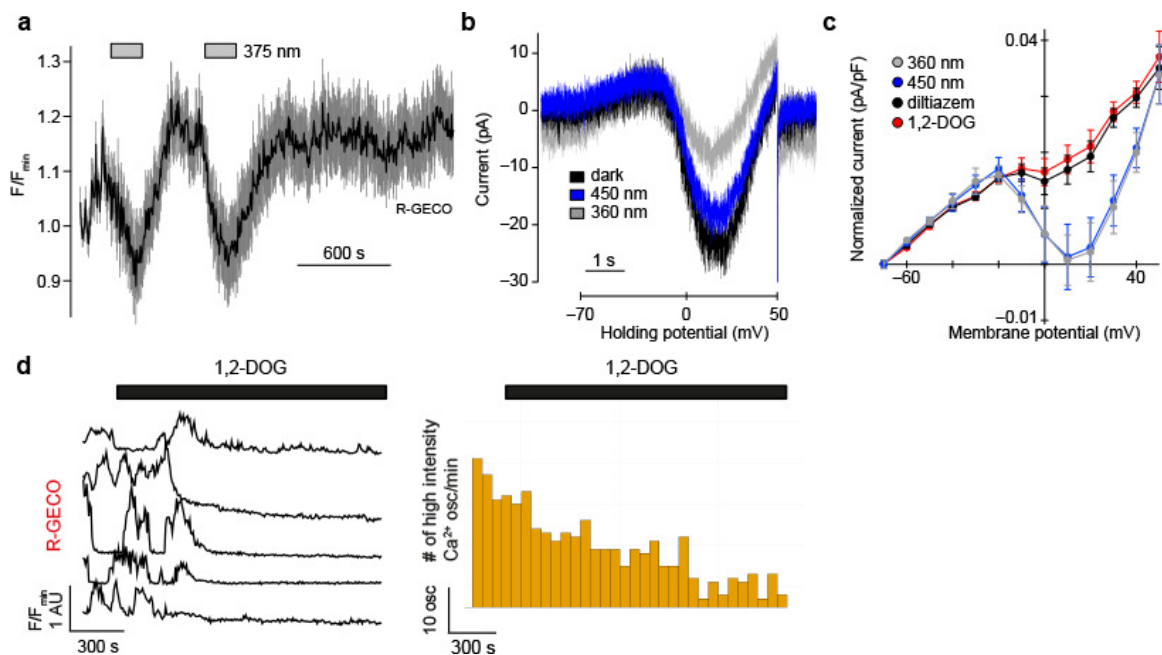


Figure 5.14 | Optical control of $[Ca^{2+}]_i$ oscillations in MIN6 cells. $[Ca^{2+}]_i$ oscillations in glucose stimulated (20 mM) MIN6 cells were monitored using R-GECO (a) **PhoDAG-1** (300 μ M) caused a decrease in the overall $[Ca^{2+}]_i$ level on photoactivation. Data was averaged over multiple cells ($n = 23$, 2 experiments). (b) **PhoDAG-3** (35 μ M) triggered a decrease in the whole-cell voltage activated L-type Ca^{2+} channel (Ca_v) current, as shown by voltage ramps (-70 to $+50$ mV over 5 s) from a representative cell. (c) UV-A or blue irradiation alone did not affect the Ca_v current ($n = 8$), while the application of 1,2-DOG (100 μ M, $n = 3$) and the L-type Ca^{2+} channel blocker diltiazem (500 μ M, $n = 3$) decreased the magnitude of the whole-cell Ca_v current. (d) The application of 1,2-DOG (100 μ M) led to a slow and permanent decrease in the frequency and intensity of $[Ca^{2+}]_i$ oscillations ($n = 25$, 1 experiment).

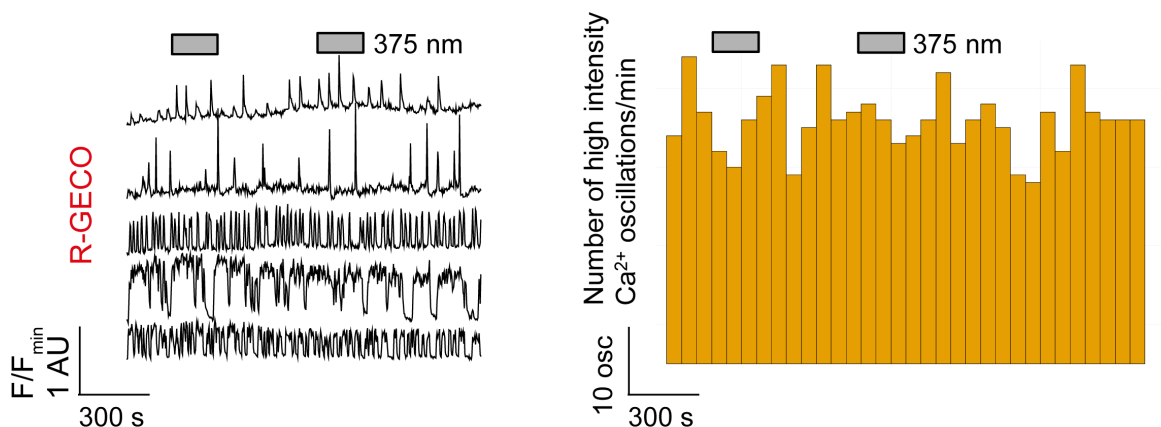


Figure 5.15 | UV-A illumination alone has no effect on MIN6 $[Ca^{2+}]_i$ oscillations. $[Ca^{2+}]_i$ oscillations in glucose-stimulated (20 mM) MIN6 cells were monitored using R-GECO. UV-A irradiation alone did not affect the oscillation frequency. Shown are individual $[Ca^{2+}]_i$ traces from representative cells (left), and a statistical analysis of the oscillation frequency averaged over multiple cells ($n = 30$, one experiment, right). Bar graphs represent the number of detected high intensity $[Ca^{2+}]_i$ oscillations (>50% of highest transient in each trace) within every 60 s interval.

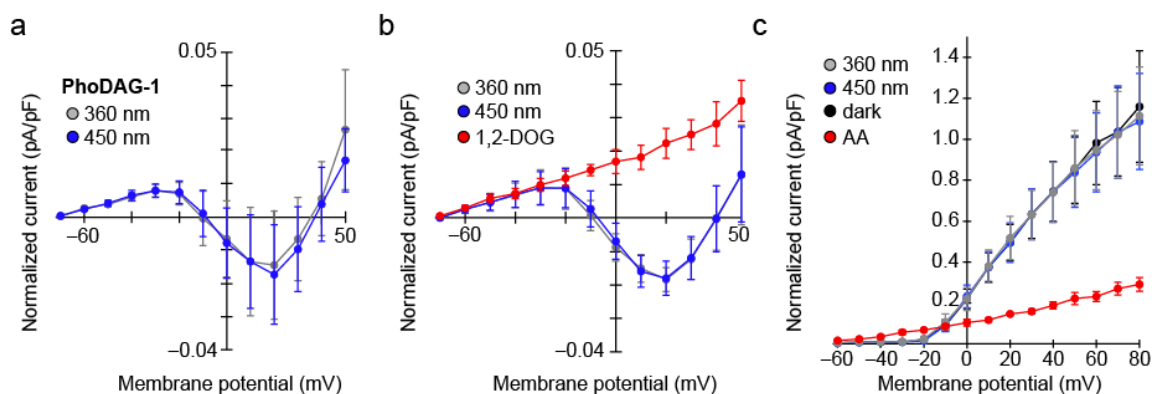


Figure 5.16 | Electrophysiological studies in dissociated mouse β -cells. In primary mouse β -cells: (a) PhoDAG-1 (200 μ M) had no effect on the Ca_v current ($n = 5$). (b) UV-A or blue-irradiation alone did not affect the Ca_v current ($n = 8$), while the application of 1,2-DOG (15 μ M) decreased the magnitude of the Ca_v current ($n = 3$). (c) UV-A or blue-irradiation alone did not affect the K_v current ($n = 4$). AA (10 μ M) decreased the magnitude of the K_v current ($n = 4$). Error bars were calculated as \pm s.e.m.

5.2.6 – Optical control of insulin secretion in pancreatic islets

Islets of Langerhans are endocrine micro-organs comprised of hundreds of β -cells together with α -, δ - and pancreatic polypeptide cells¹³⁷. We therefore examined whether responses in intact islets were similar to MIN6 and dissociated β -cells. In contrast to the effects observed in dissociated cells, intact mouse pancreatic islets pre-treated with either **PhoDAG-1** (**Fig. 5.17a,b**) or **PhoDAG-3** (**Fig. 5.18a,b**) responded to illumination with a marked and reproducible increase in the glucose-stimulated (11 mM) $[\text{Ca}^{2+}]_i$ oscillation frequency. These results could be mimicked by the application of 1,2-DOG (**Fig. 5.17c**). Strikingly, islets treated with **PhoDAG-1** were rendered light-responsive, displaying almost a 3-fold increase in insulin secretion (at 16.7 mM glucose) following photoactivation (**Fig. 5.17d**). UV-A irradiation alone did not significantly affect $[\text{Ca}^{2+}]_i$ oscillation frequency or the amount of insulin secreted (**Fig. 5.18c,d**). These results suggest that photoactivation of the PhoDAGs in intact pancreatic islets increases the $[\text{Ca}^{2+}]_i$ oscillation frequency, and consequently elevates insulin secretion.

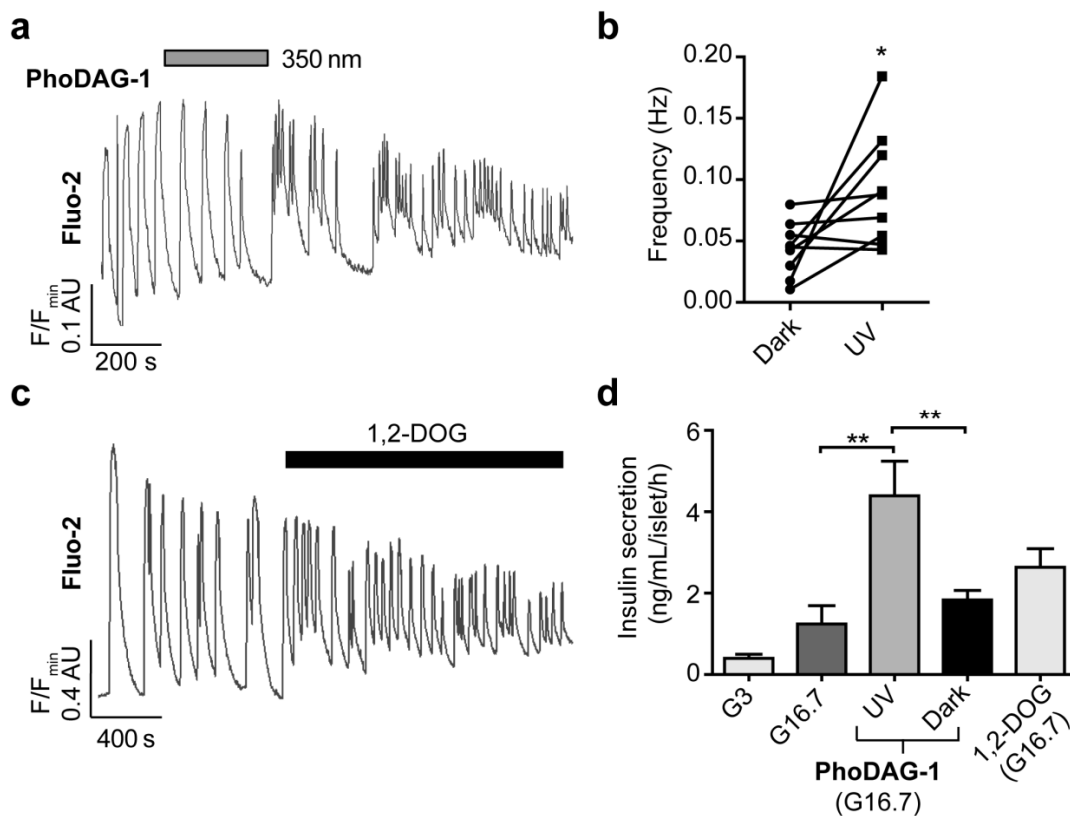


Figure 5.17 | Optical control of insulin secretion in intact mouse pancreatic islets. Glucose-stimulated (11 mM) $[Ca^{2+}]_i$ oscillations in whole mouse pancreatic islets were monitored using Fluo-2. **(a,b)** Photoactivation of **PhoDAG-1** (200 μ M) triggered an increase in the oscillation frequency, displayed as **(a)** a representative trace from a single islet and **(b)** the average oscillation frequencies for several islets before and after $\lambda = 350$ nm irradiation ($n = 9$ recordings from 4 animals). **(c)** The application of 1,2-DOG (100 μ M) led to an increase in the oscillation frequency ($n = 8$ recordings from 4 animals). **(d)** As determined by an HTRF assay, *cis*-**PhoDAG-1** (200 μ M) at 16.7 mM glucose led to a 3-fold increase in insulin secretion when compared to either *trans*-**PhoDAG-1** or glucose-stimulated conditions (16.7 mM) alone. Similar effects were observed with 1,2-DOG (100 μ M) ($n = 3$ assays from 6 animals). G3 = 3 mM glucose, G16.7 = 16.7 mM glucose. The Mann-Whitney test was used to determine statistical significance. ns = not significant, * $P < 0.05$, ** $P < 0.01$. Error bars were calculated as \pm s.e.m.

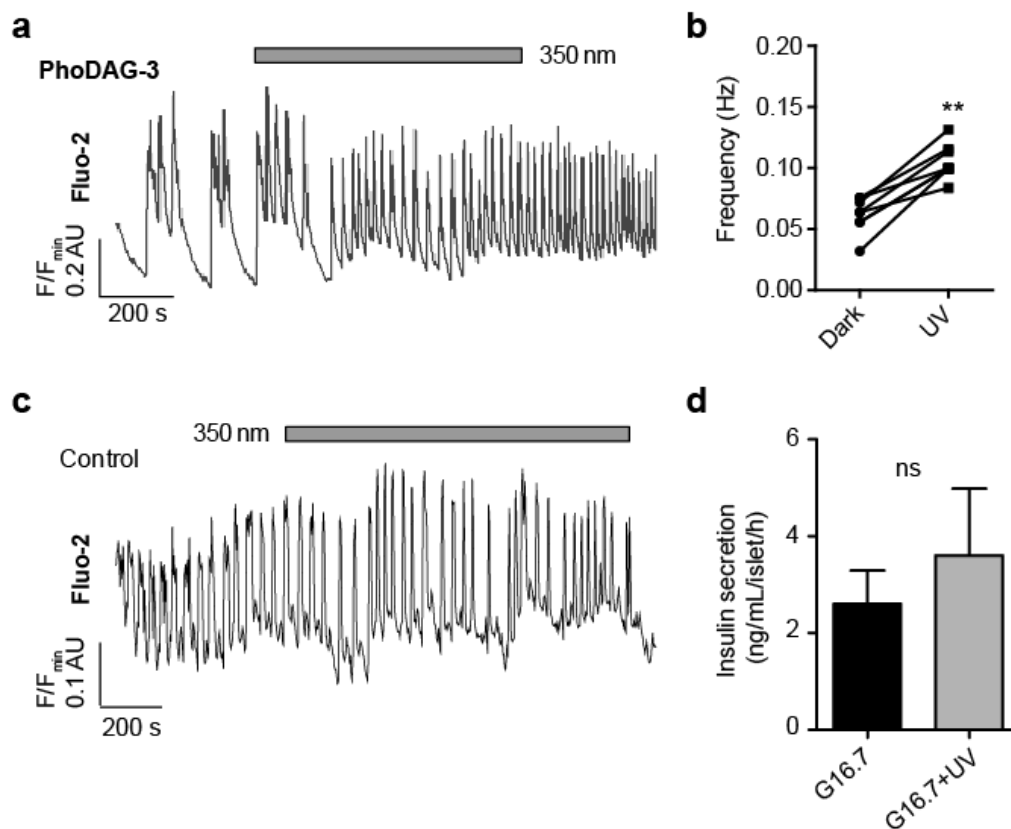


Figure 5.18 | Optical control of pancreatic islet activity. $[Ca^{2+}]_i$ oscillations in intact mouse pancreatic islets were monitored by Fluo-2. **(a,b)** Photoactivation of **PhoDAG-3** (100 μ M) triggered an increase in the oscillation frequency, displayed as **(a)** a representative trace from a single islet and **(b)** the average oscillation frequencies for several islets before and after $\lambda = 350$ nm irradiation ($n = 8$ recordings from 3 animals). **(c,d)** UV-A irradiation ($\lambda = 350$ nm) alone did not affect **(c)** the speed of the $[Ca^{2+}]_i$ oscillations in islets stimulated by 11 mM glucose or **(d)** the insulin secretion stimulated by 16.7 mM glucose (G16.7) ($n = 3$ experiments from 3 animals). The Mann-Whitney test was used to determine statistical significance. ns = not significant $P > 0.05$, $**P < 0.01$. Error bars were calculated as \pm s.e.m.

5.2.7 – Optical control of synaptic transmission

DAG is known as a regulator of neuronal activity^{114,138}. Multiple downstream effectors of DAG signaling have been described¹³⁹, including the PKC-dependent phosphorylation of Munc18 and the direct binding of DAG to Munc13 proteins, and have been linked to an increase in synaptic transmission^{140,141}. Munc13s function as essential priming factors for synaptic vesicles, preparing them for fusion with the plasma membrane at the active zone, thereby facilitating the release of neurotransmitters into the synaptic cleft^{142–144}. We found that **PhoDAG-1** could indeed trigger the translocation of the fluorescent translocation reporter Munc13-1-GFP towards the plasma membrane on photoactivation in HeLa cells over multiple cycles (**Fig. 5.19a**). The DAG-insensitive Munc13-1^{H567K}-GFP mutant reporter¹⁴² did not respond to **PhoDAG-1** (**Fig. 5.20**).

We then examined the effects of all three PhoDAGs in primary cultures of mouse autaptic hippocampal neurons. In this case, **PhoDAG-2** produced the most dramatic and reproducible effect on synaptic transmission. Synaptic transmission was measured by recording evoked excitatory postsynaptic currents (EPSCs) that were elicited by depolarization-induced APs. The initial EPSC amplitude was not affected by the presence of *trans*-**PhoDAG-2** when compared to control neurons (**Fig. 5.19b**). However, on activation with $\lambda = 365$ nm light (30 s), we observed a prominent increase in the EPSC amplitude (**Fig. 5.19c,d**). This activation was sustained until inactivation with $\lambda = 425$ nm light (20 s), which triggered a rapid and significant decrease of the EPSC amplitude. This effect was absent in control neurons and could be repeated over multiple cycles with little to no decay in efficacy. The first activation of **PhoDAG-2** led to a 1.19 ± 0.07 -fold increase of the EPSC amplitude, and was similar in the following two rounds of activation (1.19 ± 0.1 fold and 1.18 ± 0.07 fold) (**Fig. 5.19e**). Similarly, the first inactivation led to a 0.80 ± 0.03 fold decrease in the EPSC amplitude, and was similar in the two following cycles (0.77 ± 0.03 and 0.76 ± 0.03 fold, respectively). We did not observe any change in the series resistance of the patch pipette during activation or inactivation of **PhoDAG-2**, which could have generated artifacts mimicking changes in the EPSC size (**Fig. 5.21**). Similarly, **PhoDAG-2** affected the frequency of spontaneous miniature postsynaptic currents (sEPSCs), pointing to an acute effect on the presynaptic release machinery (**Fig. 5.19f**). An increase in the sEPSC frequency was observed during periods of activation, by 1.68 ± 0.3 , 1.55 ± 0.4 and 1.62 ± 0.2 fold over three rounds. Inactivation led to a decrease in the sEPSC frequency, by 0.65 ± 0.1 , 0.82 ± 0.14 , and 0.63 ± 0.06 fold over three inactivation cycles, respectively. **PhoDAG-3** produced similar

results (**Fig. 5.22**), however the variability of the response of the neurons to photoactivation was larger, and some neurons did not respond consistently during all rounds of activation/inactivation. **PhoDAG-1** did not yield a consistent effect on synaptic transmission, likely due to its limited solubility at these high concentrations during incubation.

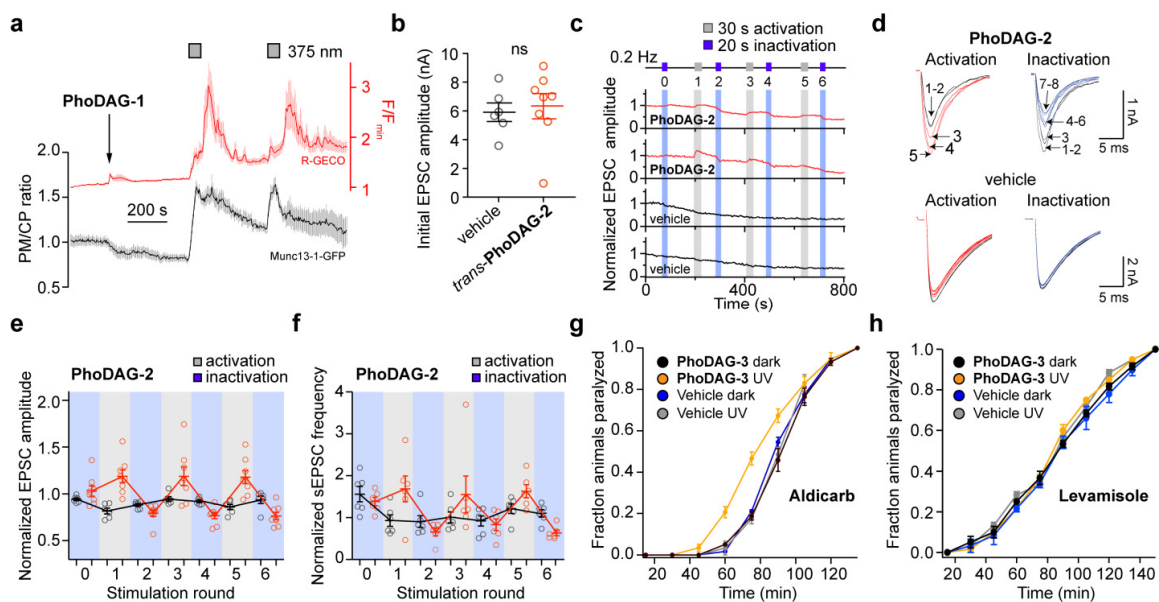


Figure 5.19 | PhoDAGs enable optical control of Munc13 and synaptic transmission. (a) In HeLa cells, **PhoDAG-1** (150 μ M) triggered reversible translocation of Munc13-1-GFP on photoactivation ($n = 14$, 3 experiments). (b-f) Mouse hippocampal neurons were pre-incubated with **PhoDAG-2** (500 μ M, 20–25 min, 37 $^{\circ}$ C) and excitatory post synaptic currents (EPSCs) were monitored by whole-cell voltage clamp electrophysiology. (b) *trans*-**PhoDAG-2** (red, $n = 8$) did not affect the EPSC amplitude when compared to control neurons (black, $n = 6$). (c) Photoactivation of **PhoDAG-2**-treated neurons with $\lambda = 365$ nm light caused an increase in the EPSC amplitude, while deactivation with $\lambda = 425$ nm light reversed the effect. Shown are two neurons pre-incubated with **PhoDAG-2** (red) and two control neurons (black). (d) Representative EPSC traces during activation and inactivation. Numbers indicate the EPSC number. Black traces are the EPSC before irradiation. (e,f) The normalized change in (e) the EPSC amplitude (red = **PhoDAG-2**, $n = 8$; black = vehicle, $n = 6$) and (f) sEPSC frequency (red = **PhoDAG-2**, $n = 6$; black = vehicle, $n = 6$) over six rounds of alternating activation and inactivation. Values for individual neurons are presented as open circles. (g) *cis*-**PhoDAG-3** (1 mM) increased the rate of aldicarb-induced (1 mM) paralysis in *Caenorhabditis elegans* ($n = 3$ experiments, 20 animals each) when compared to animals exposed to *trans*-**PhoDAG-3** (black). The paralysis rate was not affected by UV-A irradiation alone (blue, gray). (h) *cis*-**PhoDAG-3** (1 mM) did not affect the rate of levamisole-induced (0.1 mM) paralysis in *C. elegans* ($n = 3$ experiments, 20 animals each) when compared to animals exposed to *trans*-**PhoDAG-3** (black). The paralysis rate was not affected by UV-A irradiation alone (blue, gray). A Mann-Whitney test was used to determine statistical significance. Error bars were calculated as \pm s.e.m.

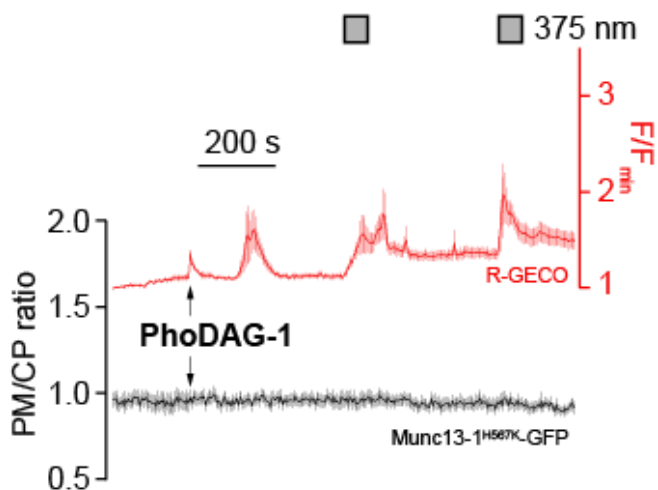


Figure 5.20 | A C1 domain point mutant abolishes the sensitivity of Munc13-1 to PhoDAG-1. In HeLa cells, the DAG-insensitive Munc13-1^{H567K}-GFP mutant translocation reporter did not translocate on the application of **PhoDAG-1** (150 μ M) or after photoactivation with $\lambda = 375$ nm light, even though an increase in $[Ca^{2+}]_i$ levels was observed using R-GECO (n = 13, 2 experiments). Error bars were calculated as \pm s.e.m.

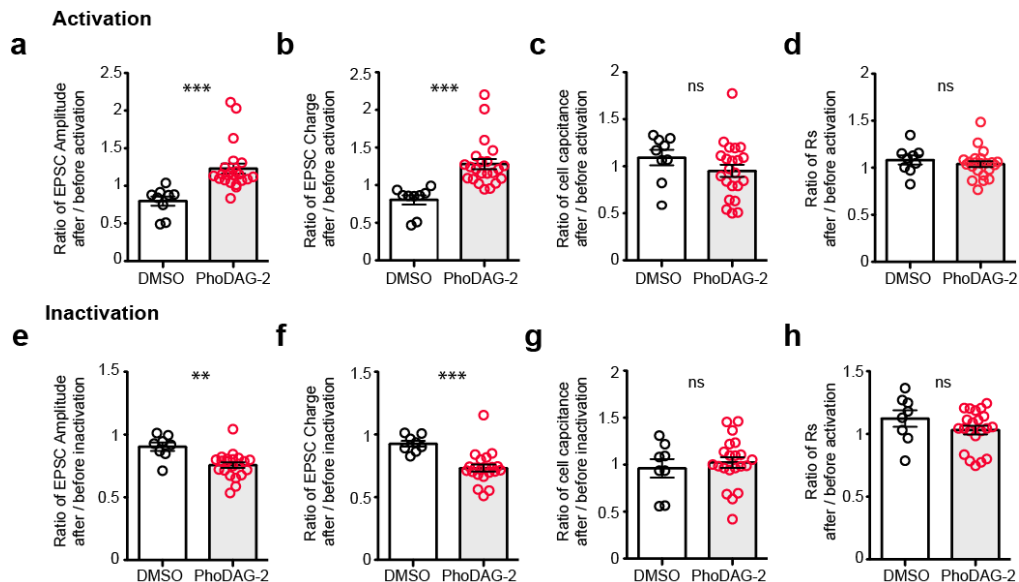


Figure 5.21 | PhoDAG-2 does not affect the pipette series resistance in patch-clamp experiments. The PhoDAGs are lipid compounds, and therefore might affect the series resistance (R_s) of the patch pipette, which could lead to artifacts in the EPSC amplitude. Moreover, the compound integrates in the cell membrane where it might lead to changes in the cell size or membrane conductance. To exclude these effects, we performed a control experiment with **PhoDAG-2** and monitored series resistance and membrane capacitance, before and after illumination (n represents the number of illumination cycles; DMSO, black, for activation $n = 9$, for inactivation $n = 8$; **PhoDAG-2**, red, for activation $n = 22$, for inactivation $n = 21$). (a) The ratio of the change in the EPSC amplitude was calculated by dividing the average amplitude after photoactivation, by that before photoactivation. (b) The ratio of the change in EPSC charge was calculated by dividing the average charge after activation by that before activation. (c) The ratio of the change in the cell capacitance, a measure of the cell body size and conductance, was calculated by dividing the average capacitance after activation by that before activation. (d) The ratio of the change in R_s was calculated by dividing the average capacitance after activation by that before activation. (e) The ratio of the change in EPSC amplitude after inactivation. (f) The ratio of the change in EPSC charge after inactivation (g) The ratio of the change in cell capacitance after inactivation. (h) The ratio of the change in R_s after inactivation. Error bars were calculated as \pm s.e.m. The Mann-Whitney test was used to determine statistical significance. ns = not significant $P > 0.05$, ** $P < 0.01$, *** $P < 0.001$.

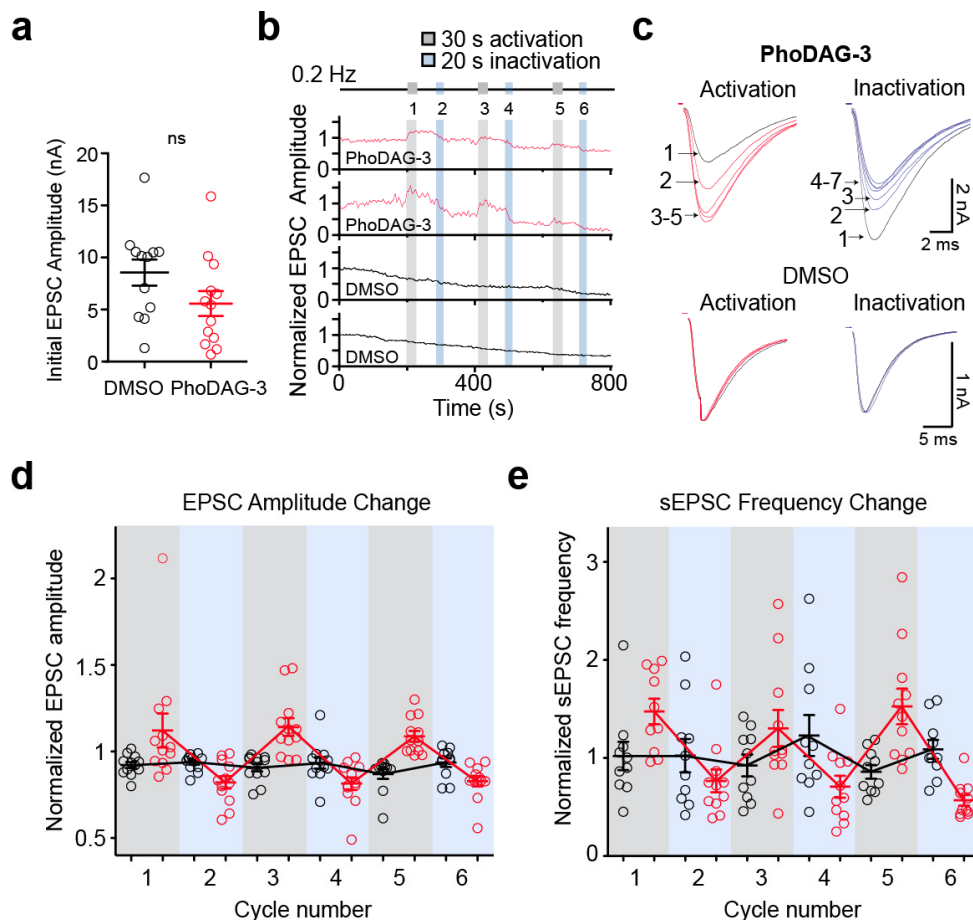


Figure 5.22 | PhoDAG-3 modulates synaptic transmission in hippocampal neurons. Wild type mouse hippocampal neurons were pre-incubated at 37 °C in the extracellular recording solution containing 500 μ M **PhoDAG-3** or DMSO (vehicle). The neurons were then whole-cell voltage clamped at room temperature and stimulated at 0.2 Hz, and the evoked EPSCs were monitored. **(a)** The initial EPSC amplitudes measured in control neurons (black, $n = 12$), or in neurons where *trans*-**PhoDAG-3** was applied (red, $n = 13$), were not significantly different. **(b)** The normalized EPSC amplitude is plotted for two neurons preincubated with **PhoDAG-3** (red) and for two control neurons (black) on photostimulation. **(c)** Example traces of EPSCs during activation and inactivation for **PhoDAG-3**. **(d)** Activation and inactivation by **PhoDAG-3** could be repeated over several cycles, corresponding to an increase and decrease in the EPSC amplitude, respectively (red = **PhoDAG-3**, $n = 13$; black = vehicle, $n = 12$). **(e)** The sEPSC frequency could also be increased by photoactivation with UV-A light, and decreased by inactivation with blue light (red = **PhoDAG-3**, $n = 11$; black = vehicle, $n = 10$). Data from individual neurons are presented by open circles, summaries are presented as mean \pm s.e.m. The Mann-Whitney test was used to determine statistical significance. ns = not significant $P > 0.05$.

5.2.8 – Control of *Caenorhabditis elegans* synaptic transmission

Caenorhabditis elegans has been used extensively to study synaptic transmission¹⁴⁵. At the neuromuscular junction, acetylcholine is released from cholinergic motor neurons and activates post-synaptic cholinergic receptors of the body-wall muscles, inducing muscle contraction¹⁴⁶. This process is terminated by the action of acetylcholinesterase. Sensitivity to aldicarb, an acetylcholinesterase inhibitor, is therefore commonly used to study synaptic transmission at the neuromuscular junction¹⁴⁷. *C. elegans* become hypersensitive to aldicarb under conditions of excess acetylcholine release and display a faster onset of paralysis on exposure to the drug. Animals cultivated in the presence of *cis*-**PhoDAG-3** (1 mM) showed a faster onset of paralysis induced by aldicarb (1 mM) as compared to animals cultivated only with ethanol (vehicle), with or without UV-A irradiation. Animals that were exposed to *trans*-**PhoDAG-3** showed no aldicarb hypersensitivity (**Fig. 5.19g**). To exclude post-synaptic effects (e.g. a possible **PhoDAG-3**-induced increase in the sensitivity of nicotinic acetylcholine receptors (nAChRs)), we used levamisole, which paralyzes animals due to hyperstimulation of muscle-specific nAChRs^{148,149}. Animals grown in the presence of *trans*- or *cis*-**PhoDAG-3** showed similar rates of levamisole-induced paralysis when compared to the vehicle controls (**Fig. 5.19h**). These results suggest that **PhoDAG-3** affects pre-synaptic transmission via modulating neurotransmitter release at the *C. elegans* neuromuscular junction.

5.3 – Discussion

Here, we have demonstrated that the three PhoDAGs are versatile tools for controlling DAG signaling in a variety of experimental settings, and can even be applied *in vivo*. In all cases, the PhoDAGs were more potent in their *cis*-configuration, which is characterized by an increased molecular dipole moment and a more bent orientation¹⁵⁰. We hypothesize that these changes mimic the transition from a less bent (ex. saturated) fatty acid, to a highly bent acyl chain like AA. Effectively, this action mimics an increase in DAG levels on the membrane, potentially by making the headgroup more accessible for C1 domain binding.

The length of each acyl chain is crucial, as hydrophobicity determines the localization and site of activity. We envision that **PhoDAG-1** could be used as a general tool, by virtue of C1-fusion, to translocate other effector proteins towards the plasma membrane in a reversible manner. This approach can be extended to other kinases, lipases, or glycosidases, and could be invaluable in understanding how plasma membrane localization affects these proteins. Although the shorter chain PhoDAGs triggered translocation towards intracellular membranes preferentially, we demonstrated that this does not limit their utility in other settings. As photochromic ligands, they are applied to cells extracellularly without the need for genetic manipulation. Although their activity cannot be genetically targeted to specific organelles, activation can still be induced with the spatial precision of light, enabling specific cells or organelles to be activated on command.

As with the metabolic generation of endogenous DAGs, the PhoDAGs stimulate a mosaic of effector proteins, similar to the downstream activation of the G_q-pathway. Although the small dynamic range of the CKAR sensor might limit our detection of PKC phosphorylation to quite low activation levels, our results in more complex systems suggest that the PhoDAGs indeed are capable of stimulating the cell in a physiologically relevant manner. In pancreatic β -cells, DAG signaling can be manipulated with a degree of precision and reproducibility currently unavailable to other chemical tools. These effects likely involve the activation of PKC alongside other partners including Munc13, affecting glucose-stimulated [Ca²⁺]_i oscillations via effects on K_v/Ca_v channels, intracellular Ca²⁺ stores, the SNARE apparatus, granule sensitivity and combinations thereof¹⁵¹. Similarly, our experiments in both hippocampal neurons and *C. elegans* suggest that the PhoDAGs increases neurotransmitter release by affecting the pre-synaptic release machinery. *cis*-PhoDAGs likely activate Munc13 or cause the phosphorylation of Munc18^{114,141}, promoting vesicle release. Combined, these results

demonstrate that the PhoDAGs are useful tools to study the effects of DAG on the exocytosis of both hormones and neurotransmitters.

Most notably, the PhoDAGs revealed the cell and tissue-context of DAG signaling in pancreatic β -cells. When PhoDAGs are activated on β -cell inner membranes, an overall decrease in the $[Ca^{2+}]_i$ oscillation frequency is observed. Conversely, DAG-activation on the outer plasma membrane preferentially leads to an increase in oscillation speed. Similar effects were also observed for the uncaging of AA on the inner vs outer membranes of MIN6 cells¹²², which is not surprising given the metabolic connection between these two lipids. The divergent effects observed between MIN6 and dissociated β -cells highlight the importance of the acyl chain length for DAG activity. This may stem from subtle differences in ion channel expression, membrane composition, and endogenous DAG levels between immortalized and primary cells. In the case of intact islets, a greater amount of extracellular matrix likely increases the surface availability of both long- and short-chain PhoDAGs, resulting in a reduced effect on the Ca_v channels. This work highlights the limitations of model cell lines, and may explain some of the contrasting reports in the literature on the effects of DAG in pancreatic β -cells.

The PhoDAGs permit control over C1-containing proteins with unmatched spatiotemporal precision. They possess the main advantage of caged DAGs, as they can be applied to cells in the inactive *trans*-configuration where they can be switched ON in seconds with a light stimulus. Importantly, these small molecule tools stand alone in their ability to switch OFF. This characteristic will enable researchers to mimic the natural oscillations observed in both DAG levels and PKC activation in a fully time-controlled fashion¹²⁹. As the PhoDAGs require high energy UV-A irradiation to become activated, their use could be partially restricted to primary research applications due to the cytotoxicity associated with high intensity UV-A light. Future studies will be directed towards preparing “red-shifted” PhoDAGs³⁷, or those which can be activated by two-photon irradiation. This will permit the use of longer wavelength, and lower energy irradiation for photoactivation. This deeper-penetrating light will increase the PhoDAGs applicability in more complex intact tissues, and as potential therapeutics.

As a lipid precursor, DAG is incorporated into a collection of more complicated glycerolipids that serve as structural components, protein anchors, and signaling molecules. We expect that novel photolipids built around the DAG scaffold will emerge as useful tools to control a variety of proteins, alongside the membranes with which they interact.

5.4 – Supporting information

5.4.1 – List of utilized cDNA constructs

Name	Characterization
R-GECO ¹²³	Red intensiometric [Ca ²⁺] _i sensor
C1-GFP ¹²⁰	Green DAG-sensing translocation probe
PKC δ -RFP*	Protein kinase C δ reporter
PKC α -GFP ¹²⁷	Protein kinase C α reporter
CKAR ¹²⁹	Cytosolic C kinase activity reporter
Munc13-1-GFP ¹⁴²	Munc13-1 translocation reporter
Munc13-1 ^{H567K} -GFP ¹⁴²	Munc13-1 ^{H567K} mutant translocation reporter

**The PKC δ -RFP construct was prepared by exchanging the eGFP from the original construct¹⁵² with mRFP via the EcoRI and EcoRV sites in the MCS of pcDNA3 backbone.*

5.4.2 – Cell culture

HeLa Kyoto cells were grown in 1.0 g/L D-glucose DMEM (GIBCO, cat # 31885-023) supplied with 10% FBS (GIBCO, cat # 10270-106) and 0.1 mg/mL antibiotic Primocin (Invitrogen, cat # ant-pm-1). HeLa cells were first seeded in an 8-well Lab-Tek™ chambered coverslip (ThermoScientific # 155411) 24-48 h before transfection at 37 °C and 5% CO₂. Transfection was carried out with FugeneHD (Promega, cat # E2311) in DMEM free of FBS and antibiotic according to the manufacturer's instructions. First, the media was aspirated and the wells were charged with DMEM (200 μL per well). A transfection solution containing DMEM (20 μL per well), cDNA (300 ng total DNA per well) and FugeneHD (1.5 μL per well) was then added to each well of the 8-well Lab-Tek™. Cells were incubated at 37 °C and 5% CO₂ for 20–24 h before the microscopy experiments were performed.

The mouse insulinoma derived cell line, MIN6, used in this study was initially developed and provided as a kind gift by Miyazaki *et al.*¹⁵³. The cells were grown at 37 °C and 5% CO₂ in high glucose DMEM (41965-039, Life Technologies) supplied with 15% FBS (10270098, Lifetechnologies), penicillin-streptomycin (Pen Strep, 100 U/mL, 15140122, Lifetechnologies) and β-mercaptoethanol (70 μM, P07-05100, PAN-Biotech) that was always added freshly to the cell culture flasks. Cells were seeded in 8-well Lab-Tek™ microscope dishes 48–64 h (to reach 50–80% confluence) prior to imaging. For [Ca²⁺]_i imaging, MIN6 cells were transfected with cDNA coding for the R-GECO¹²³ [Ca²⁺]_i reporter, and cDNA coding for the C1-GFP¹²⁰ DAG sensor (as a control) usually 24-48 h after seeding. A transfection cocktail of C1-GFP (200 ng per well) and R-GECO (200 ng per well) in Opti-MEM (20 μL per well, 31985-070, Life Technologies) and Lipofectamine2000® transfection reagent (1.5 μL per well, 11668030, Life Technologies) was added to each well of an 8-well Lab-Tek™ microscope dish loaded with 200 μL Opti-MEM (37 °C, immediately before the addition). After 24 h incubation at 37 °C and 8.5% CO₂, the media was exchanged to culture media, followed by incubation for another 24 h before the microscopy experiments were performed.

5.4.3 – Culture of primary mouse pancreatic islets

***Note: Culture of mouse pancreatic islets was performed by Dr. David Hodson (IMSR Birmingham), and the experimental details are included here for clarity.*

Islets were isolated from C57BL6 mice using collagenase digestion, as previously detailed¹⁵⁴. Briefly, following euthanasia by cervical dislocation, the bile duct was injected with a collagenase solution (1 mg/mL) before digestion at 37 °C for 10 min and separation of islets using a Histopaque gradient (1.083 and 1.077 g/mL). Islets were cultured for 24-72 h in Roswell Park Memorial Institute (RPMI) medium supplemented with 10% fetal calf serum (FCS), 100 U/mL penicillin and 100 µg/mL streptomycin. Islets were dissociated into single β -cells using trypsin digestion for 5 min at 37 °C and allowed to attach to poly-L-lysine-coated and acid-etched coverslips. All animal work was regulated by the Home Office according to the Animals Act 1986 (Scientific Procedures) of the United Kingdom (PPL 70/7349, Dr Isabelle Leclerc), as well as EU Directive 2010/63/EU.

5.4.4 – Laser scanning confocal microscopy

The cells were incubated in 250 μ L imaging buffer containing (in mM): 115 NaCl, 1.2 CaCl₂, 1.2 MgCl₂, 1.2 K₂HPO₄, 20 HEPES, D-glucose (20 for MIN6, 11 for islets and β -cells unless otherwise stated), adjusted to pH 7.4 with NaOH at 37 °C and 5% CO₂ for at least 10 min. Compounds were first solubilized in DMSO at a concentration of 10 mM. This stock (2-5 μ L) was then diluted into imaging buffer (50 μ L) and added directly to the well containing the cells in imaging buffer.

Imaging of HeLa, MIN6, or primary rodent pancreatic β -cells was performed cells was performed on one of two microscopes: 1) Olympus Fluoview 1200 with a 20x objective, or a 63x oil objective. GFP excitation was performed with λ = 488 nm laser at low laser power (<3%) and emission was collected at λ = 500-550 nm. CFP excitation was performed with a λ = 405 nm laser at low laser power and emission was collected at λ = 425-475 nm. For FRET experiments, YFP emission was collected at λ = 510-560 nm. RFP/R-GECO excitation was performed with a λ = 559 nm laser at low laser power (<3%) and emission was collected at λ = 570-670 nm. Compound irradiation at λ = 375 nm was triggered using the quench function in the Olympus software. Photoactivation was carried out with λ = 375 nm laser at 100% intensity. 2) Zeiss Axiovert M200 coupled to a Yokogawa CSU10 spinning disk head and 10x and 20x objectives. Fluo-2 excitation was performed using a solid-state λ = 491 nm laser, and emission was collected using a highly sensitive back-illuminated EM-CCD (Hamamatsu C9100-13) at λ = 500-550 nm. Photoactivation was carried out using an X-Cite 120 epifluorescence source and a λ = 350 \pm 20 nm band-pass filter. Images were processed with Fiji software (<http://fiji.sc/Fiji>) and the resulting data was analyzed in Microsoft Excel, MATLAB and R. The data were then plotted with Igor Pro, Origin and R.

5.4.5 – Quantification of insulin secretion

Insulin secretion was measured using static incubation of 6-8 islets for 30 min at 37 °C in Krebs-HEPES bicarbonate solution containing (in mM): 130 NaCl, 3.6 KCl, 1.5 CaCl₂, 0.5 MgSO₄, 0.5 NaH₂PO₄, 2 NaHCO₃, 10 HEPES and 0.1% (wt/vol) bovine serum albumin (BSA), pH 7.4¹⁵⁵. Treatments were applied as indicated, and photoswitching performed at λ = 340 \pm 10 nm using a BMG Fluostar Optima platereader. Insulin concentration secreted into the supernatant was determined using a homogeneous time-resolved fluorescence (HTRF) assay (Cisbio), according to the manufacturer's instructions and low-range protocol.

5.4.6 – Whole-cell electrophysiology in MIN6 and dissociated β -cells

MIN6 cells (passage 26-33) were cultured as described above at 37 °C and 5% CO₂. For cell detachment, the medium was removed and the cells were washed with Ca²⁺-free PBS buffer and treated with trypsin for 5 min at 37 °C. The detached cells were diluted in growth medium and plated on acid-etched coverslips in a 24-well plate. 50,000 cells were added to each well in 500 μ L growth medium. The growth medium was exchanged every 48 h, and electrophysiological experiments were carried out 2-7 days later.

Whole cell patch clamp experiments were performed using a standard electrophysiology setup equipped with a HEKA Patch Clamp EPC10 USB amplifier and PatchMaster software (HEKA Elektronik). Micropipettes were generated from “Science Products GB200-F-8P with filament” pipettes using a Narishige PC-10 vertical puller. The patch pipette resistance varied between 4-7 M Ω . For recording of the Ca²⁺-channel current¹⁵⁶, the bath solution contained (in mM): 82 NaCl, 20 tetraethylammonium chloride, 0.1 tolbutamide, 30 CaCl₂, 5 CsCl, 1 MgCl₂, 0.1 EGTA, 10 D-glucose, 5 HEPES (adjusted to pH 7.4 with NaOH). The intracellular solution contained (in mM): 102 CsCl, 10 tetraethylammonium chloride, 0.1 tolbutamide, 10 EGTA, 1 MgCl₂, 3 Na₂ATP, 5 HEPES (adjusted to pH 7.4 with CsOH). In voltage clamp mode, voltage steps were applied to the cells from the baseline at –70 mV to +50 mV in 10 mV intervals for 0.5 s. All cells had a leak current below 15 pA on break-in at –70 mV. For recording of the K_v current, the bath solution contained (in mM): 119 NaCl, 2 CaCl₂, 4.7 KCl, 10 HEPES, 1.2 MgSO₄, 1.2 KH₂PO₄, 14.4 D-glucose (adjusted to pH 7.3 with NaOH). The intracellular solution contained (in mM): 140 KCl, 1 MgCl₂, 10 EGTA, 10 HEPES, 5 MgATP (adjusted to pH 7.25 with KOH). The data was analyzed in Igor Pro using the Patcher’s Power Tools (MPI Göttingen) plugin. Current values were extrapolated and processed in Microsoft Excel, and the results were again plotted in Igor Pro.

5.4.7 – Electrophysiology in mouse hippocampal neurons

***Note: Patch-clamp experiments in mouse hippocampal neurons were performed by Dr. Noa Lipstein (MPI Göttingen), and the experimental details are included here for clarity.*

Microisland cultures of wild type mouse hippocampal neurons were prepared as described¹⁵⁷. For experiments, a 12-well plate was filled with 480 μL /well of extracellular recording solution contained (in mM): 140 NaCl, 2.4 KCl, 10 HEPES, 10 D-glucose, 4 CaCl₂, and 4 MgCl₂ (320 mOsmol/L), and 20 μL of a 12.5 M stock solution of **PhoDAG-2** or **PhoDAG-3** in DMSO was added. For controls, 20 μL of DMSO were added. The coverslips containing day *in vitro* 14–16 neurons were broken and a piece was moved into one well in the 12-well plate. The neurons were incubated at 37 °C, and 5% CO₂ for 10 min with **PhoDAG-3** and respective controls; or for 20–25 min for **PhoDAG-2** and respective controls. Neurons were incubated with PhoDAG, and were whole-cell voltage clamped directly post-incubation. EPSCs were elicited by depolarization-induced APs at a frequency of 0.2 Hz. For vehicle controls, neurons from the same culture were incubated in DMSO for the same time. Beyond these times, we did not find a correlation between the length of incubation and the presence of an effect or its strength. Longer incubation periods of >1 h resulted in astrocyte death. In the case of **PhoDAG-2** patching the incubated neurons was usually easier 1 h after the stock solution was diluted in the extracellular solution. 3–4 coverslips were subsequently incubated in one well where either **PhoDAG-2** or **PhoDAG-3** was diluted.

Whole-cell voltage clamp recordings were acquired using the Axon Multiclamp 700B amplifier, Digidata 1440A data acquisition system, and the pCLAMP 10 software (Molecular Devices). The standard internal solution contained (in mM): 136 KCl, 17.8 HEPES, 1 EGTA, 4.6 MgCl₂, 4 NaATP, 0.3 Na₂GTP, 15 creatine phosphate, and 5 U/mL phosphocreatine kinase (315–320 mOsmol/liter), pH 7.4. APs were stimulated at 0.2 Hz (by depolarizing the cell from –70 to 0 mV for 2 ms) to evoke excitatory post synaptic currents (EPSCs). The sEPSCs were derived from the traces where EPSCs were recorded (last 600 ms of a 1 s recording) and were recorded without tetrodotoxin (TTX). However, in the autapse-system, sEPSCs predominantly represent miniature EPSCs. Light illumination was performed by a CoolLED pE-2 lamp that was fixed to the setup. Photoactivation was performed at $\lambda = 365$ nm (80% strength) and inactivation at $\lambda = 425$ nm (40% strength). The normalized responses following illumination were calculated by dividing by the averaged response before illumination. All analyses were performed using Axograph 1.4.3.

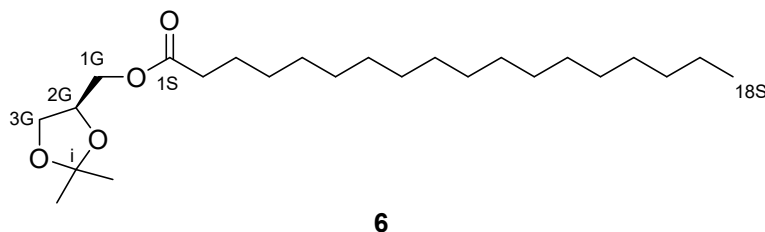
5.4.8 – Aldicarb assay

***Note: Experiments in *Caenorhabditis elegans* were performed by Dr. Jatin Nagpal (Frankfurt), and the experimental details are included here for clarity.*

Caenorhabditis elegans wild-type (N2) strain was cultivated at 20 °C on nematode growth medium (NGM) plates seeded with *E. coli* strain OP50-1¹⁵⁸. A 100 mM stock solution of **PhoDAG-3** was prepared in 100% EtOH. For application to *C.elegans*, the stock solution was diluted to the working concentration of 1 mM **PhoDAG-3** using OP50-1 and 200 µL of the resulting solution was applied to the NGM plate. For the vehicle control, an equivalent volume of 100% EtOH was used instead of the stock solution. L4 stage larvae were picked onto 1 mM **PhoDAG-3**/EtOH NGM plates and left overnight. The young adult hermaphrodites were used on the following day for the aldicarb and levamisole-sensitivity assays^{147,149}. The assay was performed in the dark, except for the picking and counting of animals which was performed under red light. To study aldicarb or levamisole sensitivity, 20 animals were transferred onto NGM plates containing 1 mM aldicarb (Sigma) or 0.1 mM tetramisole hydrochloride (Racemic form of levamisole, Sigma) and the fraction of animals paralysed was scored every 15 min by assessing movement following three gentle touches with a platinum wire. The animals were illuminated with UV-A light ($\lambda = 366 \text{ nm}$, $18 \text{ }\mu\text{W}/\text{mm}^2$) provided by a UV-A lamp (Benda, Wiesloch, Germany) for the first 5 min after being placed on the aldicarb/levamisole plates and then subsequently for the last 3 min of each 15 min time interval. The assays were performed blinded regarding the absence/presence of **PhoDAG-3**, and on the same day with the same batch of aldicarb or levamisole plates.

5.4.9 – Compound synthesis and characterization

5.4.9.1 – S-2,3-O-Isopropylidene-1-O-stearoyl-*sn*-glycerol (6)



S-2,3-O-Isopropylidene-1-O-stearoyl-*sn*-glycerol (6) was prepared using a modified procedure as previously described by Gaffney *et al.*¹⁵⁹ Spectral characteristics matched those previously reported¹⁶⁰.

R(-)-2,3-O-Isopropylidene-*sn*-glycerol (5), 2.85 g, 22.0 mmol, 1.0 equiv.) and 4-(dimethylamino)pyridine (DMAP, 268 mg, 2.20 mmol, 0.1 equiv.) were dissolved in dry CH₂Cl₂ (75 mL) under an argon atmosphere. To this solution was added dry NEt₃ (6.16 mL, 4.48 g, 44.0 mmol, 2.0 equiv.) and the reaction was cooled to 0 °C. Stearoyl chloride was dissolved in dry CH₂Cl₂ (25 mL) and slowly added to the previously prepared solution. The reaction was allowed to slowly warm to room temperature and stirred for 2 h. H₂O (28 mL) was slowly added and the biphasic solution was stirred rapidly for 10 min. The phases were then separated, and the organic phase was washed with aqueous HCl (2 M, 50 mL), followed by saturated aqueous NaHCO₃ (2x50 mL) and brine (2x50 mL) solutions. The organic phase was then dried over anhydrous Na₂SO₄ and filtered. The filtrate was then concentrated and purified by flash silica gel chromatography (150 g SiO₂, 20:1 hexane:EtOAc) to yield **S-2,3-O-isopropylidene-1-O-stearoyl-*sn*-glycerol (6)**, 6.99 g, 81%) as an off-white solid.

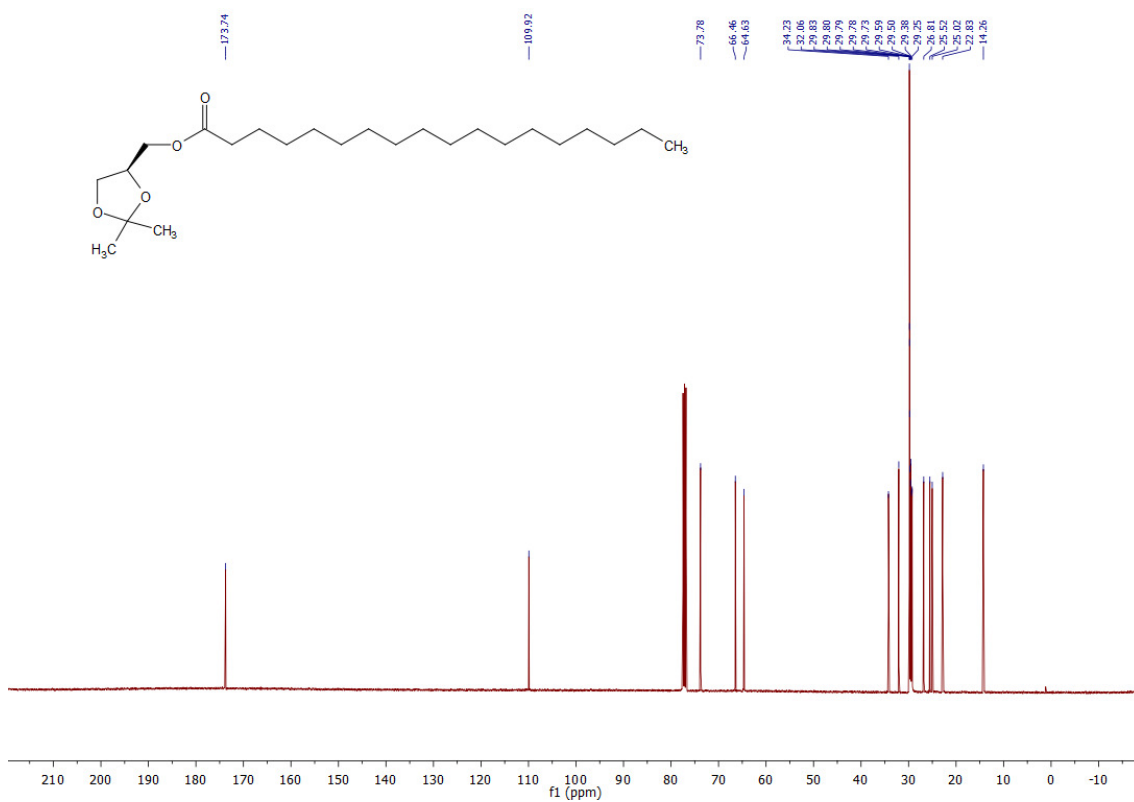
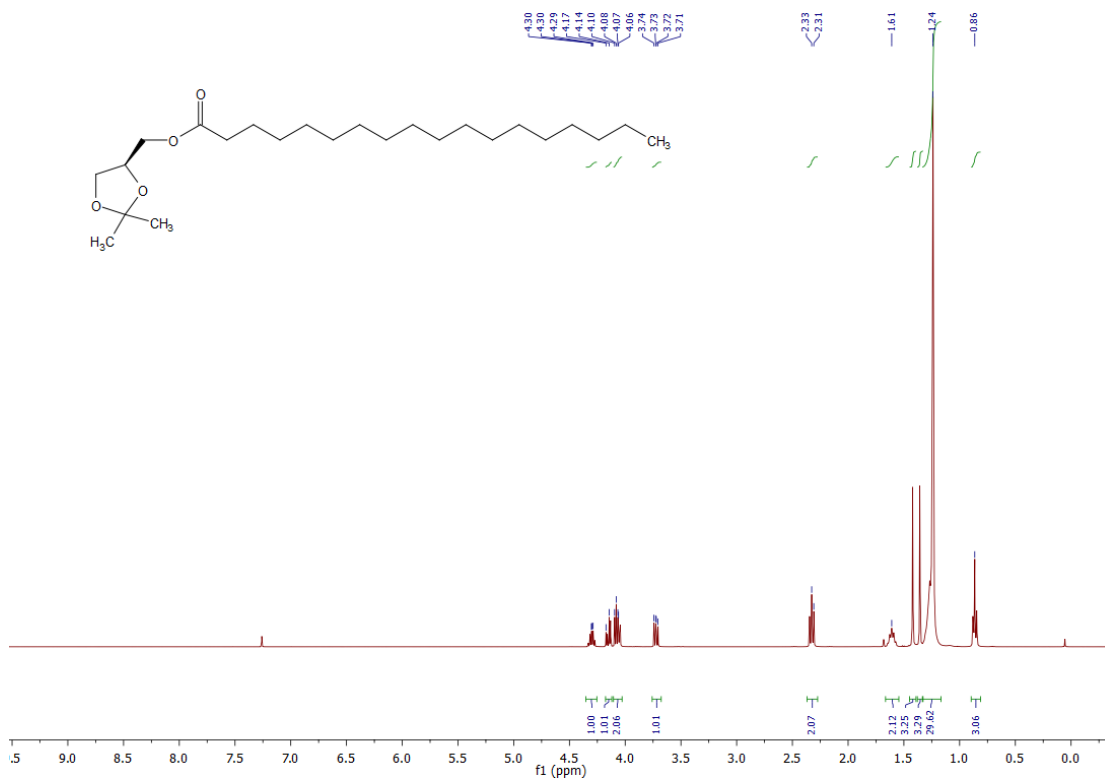
TLC (20:1 hexane:EtOAc): $R_f = 0.25$.

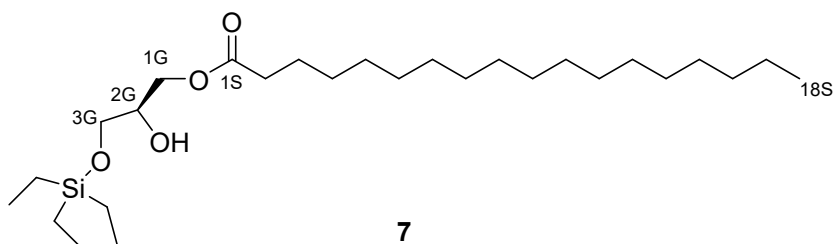
$^1\text{H NMR}$ (CDCl_3 , 400 MHz, 25 °C): δ 4.35-4.28 (m, 1 H, H_{2G}), 4.17 (dd, 1 H, HG_{1a}, $J = 11.7$, 4.7 Hz), 4.12-4.05 (m, 2 H, HG_{1b}, HG_{3a}), 3.75 (dd, 1H, H_{3b}, $J = 8.4$, 6.2 Hz) 2.34 (t, 2 H, H_{2L_{a,b}}, $J = 7.4$ Hz), 1.67-1.58 (m, 2 H, H_{3L_{a,b}}), 1.43 (s, 3 H, H_{CH₃}), 1.37 (s, 3 H, H_{CH₃}), 1.33-1.21 (m, 28 H, H_{alk}), 0.87 (t, 3 H, H_{8L_{a,b,c}}, $J = 6.5$ Hz).

$^{13}\text{C NMR}$ (CDCl_3 , 101 MHz, 25 °C): δ 173.1 (C_{1S}), 109.9 (C_i), 73.8 (C_{Glycerol}), 66.5 (C_{Glycerol}), 64.6 (C_{Glycerol}), 34.2 (C_{2S}), 32.1 (C_{3S}), 29.9-29.8 (m, C_{alk}, 2xCH₃), 29.7 (C_{alk}), 29.6 (C_{alk}), 29.5 (C_{alk}), 29.4 (C_{alk}), 29.3 (C_{alk}), 26.8 (C_{alk}), 25.5 (C_{alk}), 25.0 (C_{alk}), 22.8 (C_{alk}), 14.3 (C_{18S}).

HRMS (EI⁺): m/z calcd. for [C₂₃H₄₃O₄]⁺: 383.3156, found: 383.3172 ([M-CH₃]⁺).

5 – Photoswitchable diacylglycerols enable optical control of protein kinase C



5.4.9.2 – 1-O-Stearoyl-3-O-triethylsilyl-*sn*-glycerol (7)

1-O-Stearoyl-3-O-triethylsilyl-*sn*-glycerol (7) was prepared using a modified procedure as previously described by Nadler *et al.*¹¹⁶ Spectral characteristics matched those previously reported.

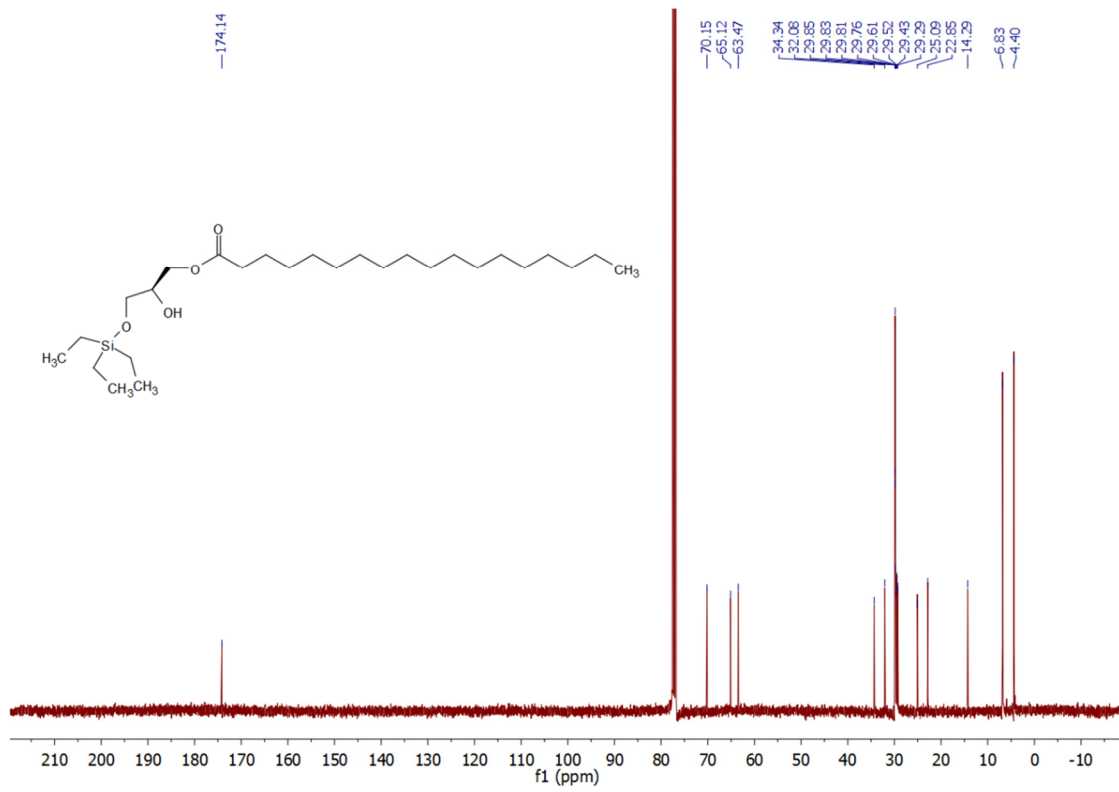
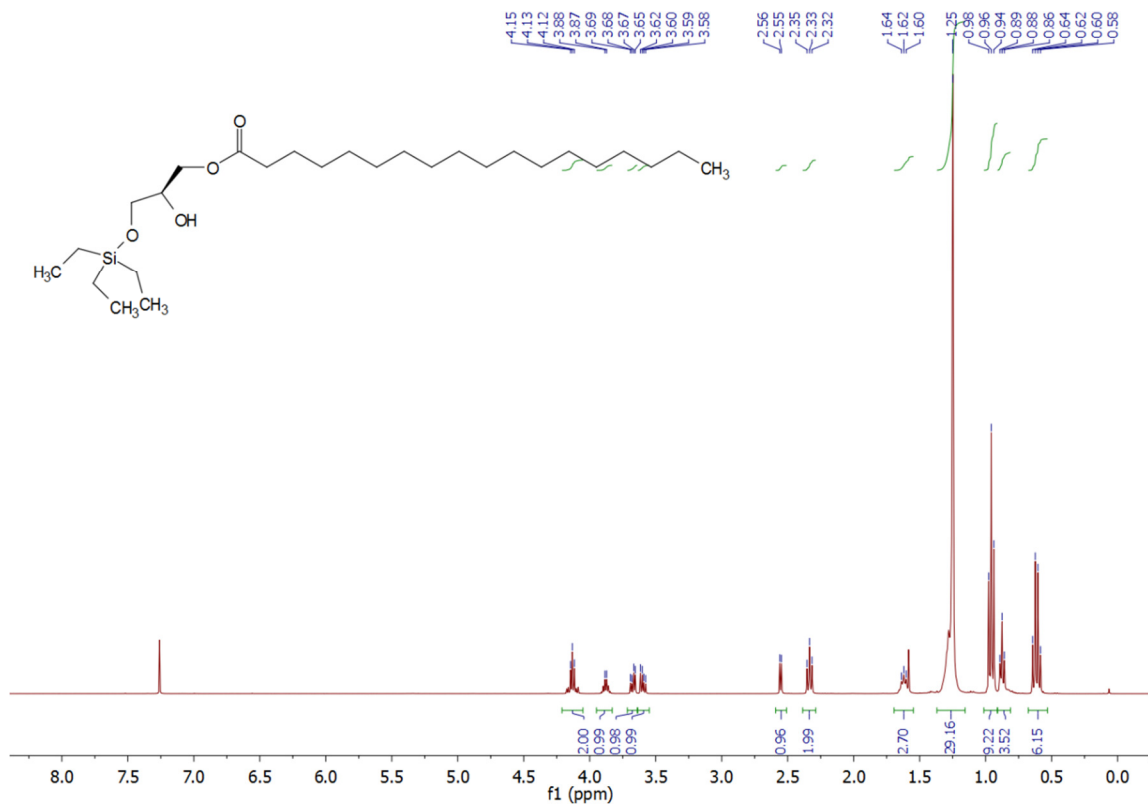
S-2,3-O-Isopropylidene-1-O-stearoyl-*sn*-glycerol (6, 500 mg, 1.25 mmol, 1.0 equiv.) was dissolved in dry 1,2-dichloroethane (DCE, 20 mL) under an argon atmosphere. *N,N*-Diisopropylethylamine (DIPEA, 1.20 mL, 6.88 mmol), followed by triethylsilyl trifluoromethanesulfonate (TESOTf, 496 mg, 0.425 mL, 1.88 mmol, 1.5 equiv.) were added at room temperature and the reaction was stirred at 90 °C. After 1 h, a second portion of TESOTf (169 mg, 0.145 mL, 0.5 equiv.) was added and the reaction was stirred at 90 °C for 2.5 h. Upon consumption of the starting material as determined by TLC, the solution was cooled to room temperature, diluted with EtOAc, and then washed with aqueous HCl (0.1 M, 50 mL) and brine (50% saturated, 2x50 mL). The organic phase was concentrated under reduced pressure and the resulting oil was dissolved in THF (20 mL). To this solution was added an aqueous Na₂CO₃ solution (10%, 10 mL) followed by I₂ (610 mg, 2.4 mmol, 1.95 equiv.). The solution was stirred rapidly for 2.5 h at room temperature. A further portion of I₂ was added (300 mg, 1.2 mmol, 1.0 equiv.) and the solution was stirred at room temperature for 1 h. The solution was diluted with EtOAc (50 mL) and washed with saturated aqueous Na₂S₂O₃ (50 mL), H₂O (2x50 mL) and brine (50 mL) solutions. The organic phase was then dried over anhydrous Na₂SO₄ and filtered. The filtrate was concentrated under reduced pressure and the resulting oil was purified by flash column chromatography (50 g SiO₂, 20:1 hexane:EtOAc) to yield **1-O-stearoyl-3-O-triethylsilyl-*sn*-glycerol (7, 412 mg, 69%)** as a colorless liquid.

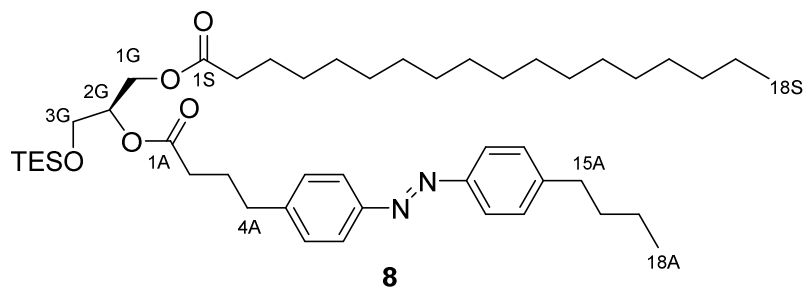
TLC (10:1 hexane:EtOAc): $R_f = 0.23$.

$^1\text{H NMR}$ (CDCl_3 , 400 MHz, 25 °C): δ 4.18 (m, 2 H, H1G_{a,b}), 3.92-3.82 (m, 1 H, H2G), 3.67 (dd, 1 H, H3G_a, $J = 10.3$ Hz, 4.5 Hz), 3.60 (dd, 1 H, H3G_b, $J = 10.0$ Hz, 5.7 Hz), 2.55 (d, 1 H, OH, $J = 5.3$ Hz), 2.33 (t, 2 H, H2S_{a,b}, $J = 7.6$ Hz), 1.66-1.58 (m, 2 H, H3S_{a,b}), 1.34-1.20 (m, 28 H, 14xCH₂(stearoyl)), 0.96 (t, 9 H, 3xCH₃(TES), $J = 7.8$ Hz), 0.88 (t, 3 H, H18S_{a,b,c}, $J = 6.9$ Hz), 0.61 (q, 6 H, 3xCH₂(TES), $J = 7.9$ Hz).

$^{13}\text{C NMR}$ (CDCl_3 , 101 MHz, 25 °C): δ 174.1 (C1S), 70.2 (C2G), 65.1 (C1G), 63.5 (C3G), 34.3 (C2S), 32.1 (C_{alk}), 29.9-29.7 (m, C_{alk}), 29.6 (C_{alk}), 29.5 (C_{alk}), 29.4 (C_{alk}), 29.3 (C_{alk}), 25.1 (C3S), 22.9 (C_{alk}), 14.3 (C18S), 6.8 (3C, 3xCH₃(TES)), 4.4 (3C, 3xCH₂(TES)).

HRMS (ESI⁺): m/z calcd. for [C₂₇H₅₆NaO₄Si]⁺: 495.3846, found: 495.3850 ([M+Na]⁺).



5.4.9.3 – 2-O-(4-(4-((4-butylphenyl)diazenyl)phenyl)butanoyl)-1-O-stearoyl-3-O-triethylsilyl-*sn*-glycerol (8)

FAAzo-4⁵¹ (1.08 g, 3.3 mmol, 2.0 equiv.), *N*-(3-dimethylaminopropyl)-*N'*-ethylcarbodiimide (EDC, 773 mg, 4.38 mmol, 3.0 equiv.) and DMAP (20.2 mg, 166 μ mol, 0.1 equiv.) were dissolved in dry CH_2Cl_2 (50 mL) under an argon atmosphere. This solution was stirred at room temperature for 15 min. After cooling to 0 $^\circ\text{C}$, a solution of **1-O-stearoyl-3-O-triethylsilyl-*sn*-glycerol (7)**, 787 mg, 1.66 mmol, 1.0 equiv.) in dry CH_2Cl_2 (30 mL) was slowly added. The solution was warmed to room temperature and stirred overnight under an argon atmosphere. The solution was then diluted with CH_2Cl_2 (200 mL) and washed with H_2O (2x100 mL) and brine (100 mL). The solution was then filtered and the filtrate was concentrated under reduced pressure. The resulting red oil was purified by flash silica gel chromatography (170 g SiO_2 , 30:1 hexane:EtOAc) to yield **2-O-(4-(4-((4-butylphenyl)diazenyl)phenyl)butanoyl)-1-O-stearoyl-3-O-triethylsilyl-*sn*-glycerol (8)**, 944 mg, 72%) as a red oil.

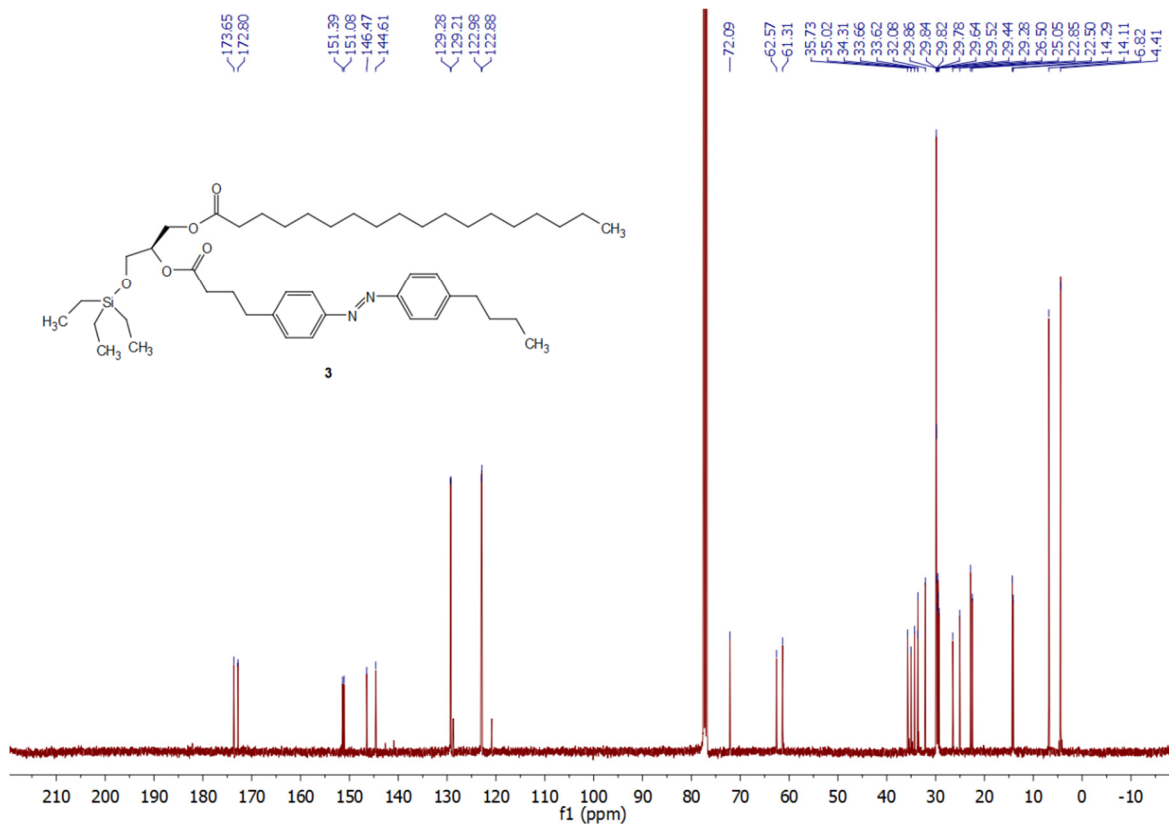
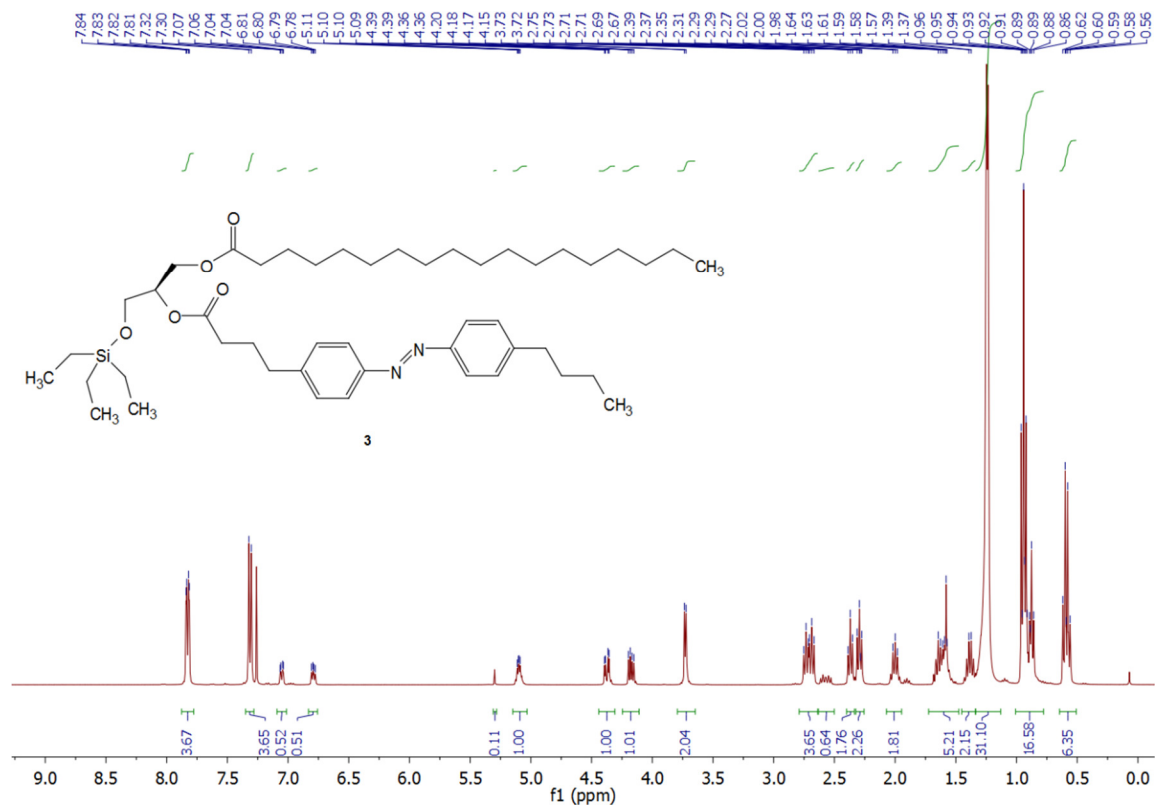
TLC (10:1 hexane:EtOAc): $R_f = 0.50$.

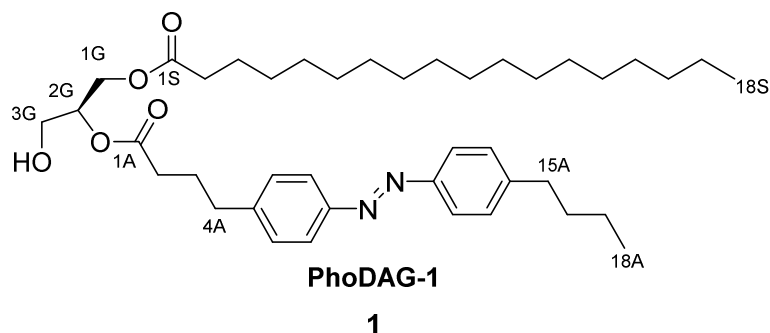
$^1\text{H NMR}$ (CDCl_3 , 400 MHz, 25 °C): δ 7.85-7.80 (m, 4 H, H7A_{a,b}, H12A_{a,b}), 7.31 (d, 4 H, H6A_{a,b}, H13A_{a,b}, $J = 8.2$ Hz), 5.13-5.05 (m, 1 H, H2G), 4.38 (dd, 1 H, H1G_a, $J = 12.1$ Hz, 3.6 Hz), 4.17 (dd, 1 H, H1G_b, $J = 12.1$ Hz, 6.1 Hz), 3.73 (d, 2 H, H3G_{a,b}, $J = 5.3$ Hz), 2.73 (t, 2 H, H4A_{a,b}, $J = 7.7$ Hz), 2.69 (t, 2 H, H15A_{a,b}, $J = 7.8$ Hz), 2.37 (t, 2 H, H2A_{a,b}, $J = 7.5$ Hz), 2.29 (t, 2 H, H2S_{a,b}, $J = 7.6$ Hz), 2.00 (quin, 2 H, H3A_{a,b}, $J = 7.4$ Hz), 1.69-1.53 (m, 4 H, H3S_{a,b}, H16A_{a,b}), 1.43-1.34 (m, 2 H, H17A_{a,b}), 1.33-1.21 (m, 28 H, H17S_{a,b}, 13xCH₂(alk)), 0.97-0.85 (m, 15 H, H18A_{a,b,c}, H17S_{a,b,c}, 3xCH₃(TES)), 0.59 (q, 6 H, 3xCH₂(TES), $J = 8.0$ Hz).

$^{13}\text{C NMR}$ (CDCl_3 , 101 MHz, 25 °C): δ 173.7 (C1S), 172.8 (C1A), 151.4 (C_{azo}), 151.1 (C_{azo}), 146.5 (C_{azo}), 144.6 (C_{azo}), 129.3 (2 C, C_{azo}), 129.2 (2 C, C_{azo}), 123.0 (2 C, C_{azo}), 122.9 (2 C, C_{azo}), 72.1 (C2G), 62.6 (C3G), 61.3 (C1G), 35.7 (C15A), 35.0 (C4A), 34.3 (C2S), 33.7 (C2A), 33.6 (C2S), 32.1 (C3S), 29.9-29.7 (m, C_{alk}), 29.6 (C_{alk}), 29.5 (C_{alk}), 29.4 (C_{alk}), 29.3 (C_{alk}), 26.5 (C3A), 25.1 (C16A), 22.9 (C17S), 22.5 (C17A), 14.3 (C18S), 14.1 (C18A), 6.8 (3 C, 3xCH₃(TES)), 4.4 (3 C, 3xCH₂(TES)).

HRMS (EI⁺): m/z calcd. for [C₂₀H₂₄N₂O₂]⁺: 778.5680, found: 778.5675 ([M-e⁻]⁺).

5 – Photoswitchable diacylglycerols enable optical control of protein kinase C



5.4.9.4 – 2-O-(4-(4-((4-Butylphenyl)diazenyl)phenyl)butanoyl)-1-O-stearoyl-*sn*-glycerol (PhoDAG-1, 1)

2-O-(4-(4-((4-Butylphenyl)diazenyl)phenyl)butanoyl)-1-O-stearoyl-3-O-triethylsilyl-*sn*-glycerol (8, 500 mg, 0.641 mmol, 1.0 equiv.) was first dissolved in CH₂Cl₂ (5 mL) and added to a solution of FeCl₂·6H₂O (5 mM in 25 mL 3:1 MeOH:CH₂Cl₂). This solution was stirred at room temperature for 30 min. The solution was then diluted with EtOAc (200 mL) and washed with H₂O (2x200 mL). The organic phase was then dried over Na₂SO₄. The mixture was filtered and the filtrate was concentrated under reduced pressure. The resulting oil was purified by flash silica gel chromatography (3:1 hexane:EtOAc) to yield **2-O-(4-(4-((4-butylphenyl)diazenyl)phenyl)butanoyl)-1-O-stearoyl-*sn*-glycerol (PhoDAG-1, 425 mg, quant.)** as an orange solid. *Note: Short reaction time and quick chromatography are essential to avoid acyl chain migration.*

TLC (3:1 hexane:EtOAc): $R_f = 0.45$ (*trans*), 0.35 (*cis*).

$^1\text{H NMR}$ (CDCl_3 , 400 MHz, 25 °C): δ 7.85-7.80 (m, 4 H, H7A_{a,b}, H12A_{a,b}), 7.31 (d, 4 H, H6A_{a,b}, H13A_{a,b}, $J = 8.1$ Hz), 5.10 (quin, 1 H, H2G, $J = 5.1$ Hz), 4.34 (dd, 1 H, H3G_a, $J = 11.9$ Hz, 4.5 Hz), 4.24 (dd, 1 H, H3G_b, $J = 12.0$ Hz, 5.8 Hz), 3.73 (t, 2 H, H1G_{a,b}, $J = 5.2$ Hz), 2.74 (t, 2 H, H4A_{a,b}, $J = 7.6$ Hz), 2.69 (t, 2 H, H15A_{a,b}, $J = 7.6$ Hz), 2.40 (t, 2 H, H2A_{a,b}, $J = 7.3$ Hz), 2.32 (t, 2 H, H2S_{a,b}, $J = 7.5$ Hz), 2.06-1.97 (m, 2 H, H3A_{a,b}), 1.69-1.51 (m, 4 H, H16A_{a,b}, H3S_{a,b}), 1.44-1.32 (m, 2 H, H17A_{a,b}), 1.34-1.18 (m, 28 H, H17S_{a,b}, 28xHS_{alk}), 0.94 (t, 3 H, H18A_{a,b,c}, $J = 7.1$ Hz), 0.88 (t, 3 H, H18S_{a,b,c}, $J = 7.1$ Hz).

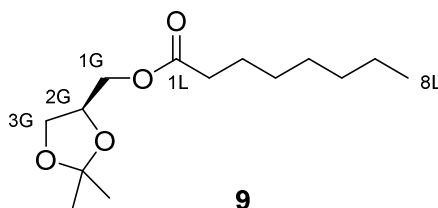
$^{13}\text{C NMR}$ (CDCl_3 , 101 MHz, 25 °C): δ 174.0 (C1S), 173.1 (C1A), 151.5 (C_{azo}), 151.1 (C_{azo}), 146.5 (C_{azo}), 144.4 (C_{azo}), 129.3 (2 C, C_{azo}), 129.2 (2 C, C_{azo}), 123.0 (2 C, C_{azo}), 122.9 (2 C, C_{azo}), 72.4 (C2G), 62.1 (C3G), 61.6 (C1G), 35.7 (C15A), 35.0 (C4A), 34.2 (C2S), 33.6 (C2A), 33.6 (C3S), 29.9-29.7 (m, C_{alk}), 29.6 (C_{alk}), 29.5 (C_{alk}), 29.4 (C_{alk}), 29.3 (C_{alk}), 26.4 (C3A), 25.0 (C16A), 22.9 (C17S), 22.5 (C17A), 14.3 (C18S), 14.1 (C18A).

IR (neat, ATR): $\tilde{\nu} = 3483, 2955, 2917, 2850, 1728, 1711, 1601, 1499, 1472, 1460, 1414, 1379, 1256, 1235, 1214, 1188, 1173, 1138, 1096, 1068, 1052, 1031, 1012, 962, 888, 832, 718, 679$.

HRMS (EI⁺): m/z calcd. for $[\text{C}_{20}\text{H}_{24}\text{N}_2\text{O}_2]^+$: 324.1838, found: 324.1834 ($[\text{M}-\text{e}]^+$).

UV-Vis (25 μM in DMSO): $\lambda_{\text{max}}(\pi-\pi^*) = 340$ nm. $\lambda_{\text{max}}(n-\pi^*) = 442$ nm.

Melting point (°C): 66.5–67.2.

5.4.9.5 – S-2,3-O-Isopropylidene-1-O-octanoyl-*sn*-glycerol (9)

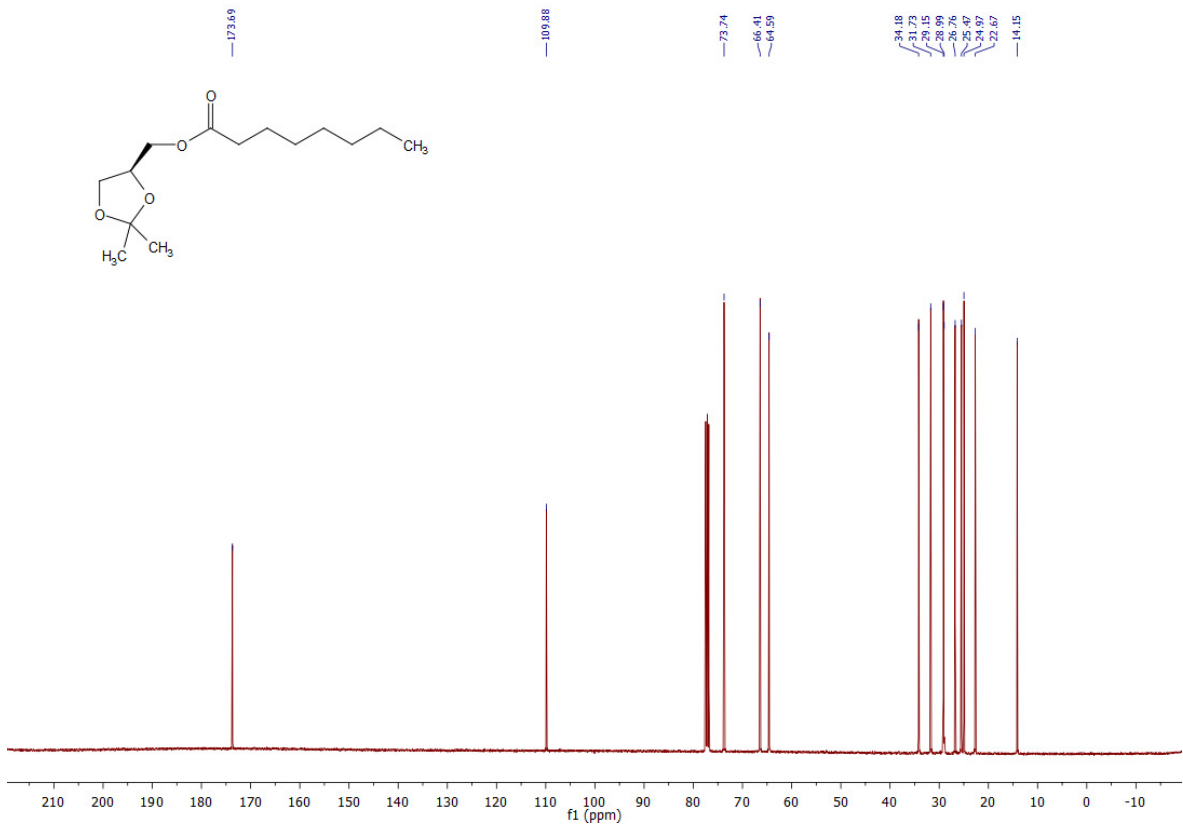
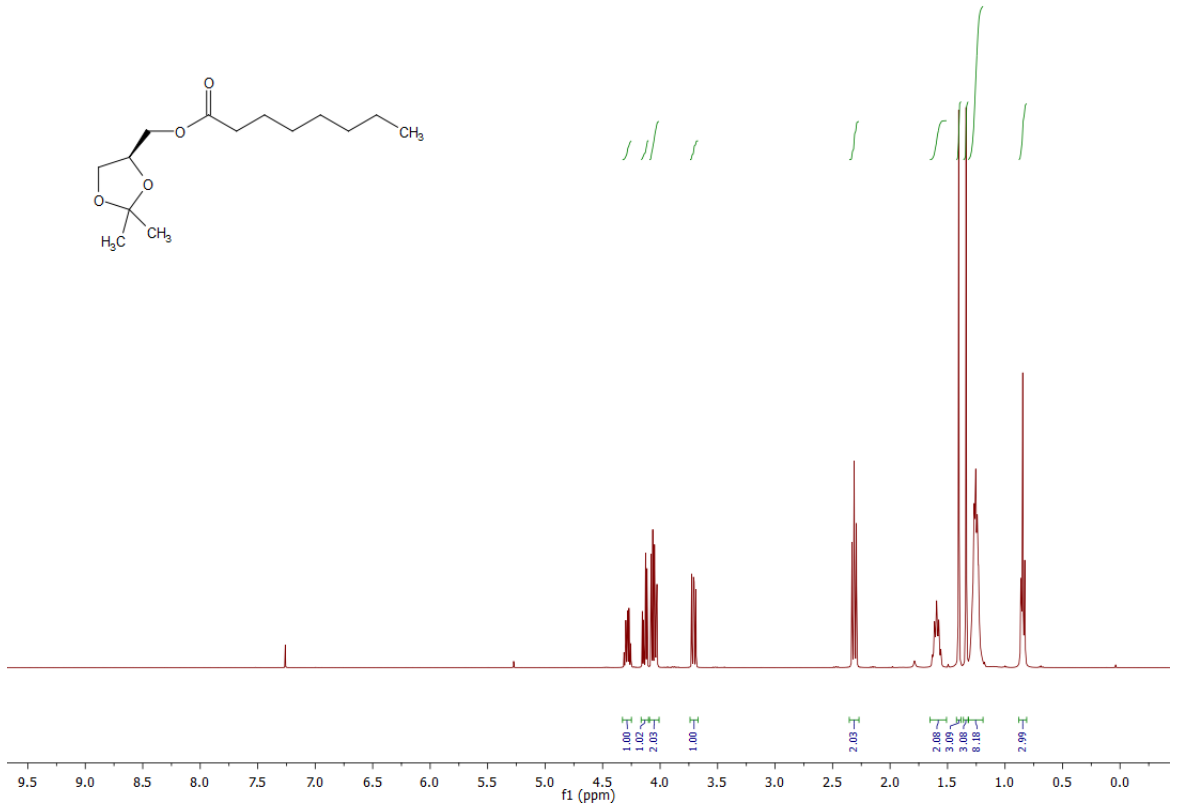
Octanoic acid (490 mg, 3.4 mmol, 1.5 equiv.) was first dissolved in dry CH₂Cl₂ (10 mL) under an argon atmosphere and then NEt₃ (0.310 mL, 2.27 mmol, 1 equiv.) and DMAP (27.7 mg, 0.227 mmol, 0.1 equiv.) were added. The solution was then cooled to 0 °C and then *N,N'*-dicyclohexylcarbodiimide (DCC, 1.171 mg, 5.68 mmol, 2.5 equiv.) was added. This mixture was stirred at 0 °C for 30 min and then the ***R*(-)-2,3-O-isopropylidene-*sn*-glycerol (5)**, 0.280 mL, 2.27 mmol, 1.0 equiv.) was added. The solution was stirred for a further 2 h, and then was diluted with CH₂Cl₂ and washed once with a saturated aqueous NaHCO₃ solution, and twice with H₂O. The organic phase was then dried over Na₂SO₄ and filtered. The filtrate was concentrated under reduced pressure and the resulting oil was purified by flash silica gel chromatography (30 g SiO₂, pre-adsorbed on 1.5 g of SiO₂, 40:1 to 10:1 hexane:EtOAc) to yield **S-2,3-O-isopropylidene-1-O-octanoyl-*sn*-glycerol (9)**, 537 mg, 92%) as a colorless oil.

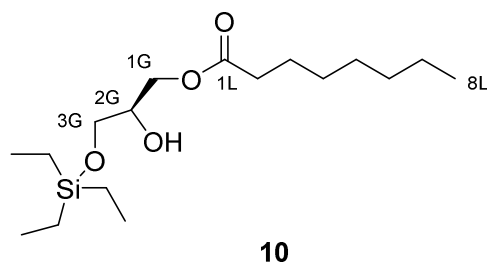
TLC (20:1 hexane:EtOAc): R_f = 0.09.

¹H NMR (CDCl₃, 400 MHz, 25 °C): δ 4.32-4.24 (m, 1 H, H_{2G}), 4.17-4.09 (m, 1 H, HG_{1a}), 4.09-4.00 (m, 2 H, HG_{1b}, HG_{3a}), 3.73-3.68 (m, 1H, H_{3b}) 2.31 (t, 2 H, H_{2L}_{a,b}, J = 7.3 Hz), 1.65–1.54 (m, 2 H, H_{3L}_{a,b}), 1.40-1.33 (s, 6 H, 2xH_{CH3}), 1.31-1.17 (m, 8 H, H_{alk}), 0.84 (t, 3 H, H_{8L}_{a,b,c}, J = 6.7 Hz).

¹³C NMR (CDCl₃, 101 MHz, 25 °C): δ 173.7 (C_{1L}), 109.9 (C_i), 73.7 (C_{Glycerol}), 66.4 (C_{Glycerol}), 66.6 (C_{Glycerol}), 34.2 (C_{2S}), 31.7 (C_{3S}), 29.2 (C_{CH3}), 29.0 (C_{CH3}), 26.8 (C_{alk}), 25.5 (C_{alk}), 25.0 (C_{alk}), 22.7 (C_{alk}), 14.5 (C_{18L}).

HRMS (EI⁺): *m/z* calcd. for [C₁₃H₂₃O₄]⁺: 243.1591, found: 243.1595 ([M-CH₃]⁺).



5.4.9.6 – 1-*O*-Octanoyl-3-*O*-triethylsilyl-*sn*-glycerol (**10**)

S-2,3-*O*-Isopropylidene-1-*O*-octanoyl-*sn*-glycerol (9**, 453.2 mg, 1.75 mmol, 1.0 equiv.)** was first dissolved in dry DCE (6 mL) under an argon atmosphere and then dry DIPEA (1.5 mL, 9.65 mmol, 5.5 equiv.) was added to the solution. The solution was then warmed to 90 °C and TESOTf (1.4 mL, 6.13 mmol, 3.5 equiv.) was added and the reaction stirred for 2 h. The mixture was then diluted with EtOAc (60 mL) and washed with aqueous HCl (0.1 M, 60 mL) and then H₂O (2x60 mL). The organic phase was then dried over Na₂SO₄ and filtered. The filtrate was concentrated under reduced pressure. The resulting oil was dissolved in THF (8 mL) and then aqueous Na₂CO₃ (4 mL, 10% w/w) and I₂ (1.1 g, 4.4 mmol, 2.5 equiv.) were added to the solution. The reaction was stirred for 75 min at room temperature, and was then diluted with EtOAc (70 mL) and washed once with saturated aqueous Na₂S₂O₃ (70 mL) and H₂O (2x70 mL). The organic phase was dried over Na₂SO₄ and filtered. The filtrate was concentrated under reduced pressure and the resulting oil was purified by flash silica gel chromatography (60 g SiO₂, 20:1→15:1→10:1 hexane:EtOAc) to yield **1-*O*-octanoyl-3-*O*-triethylsilyl-*sn*-glycerol (**10**, 211 mg, 36%)** as a colourless oil.

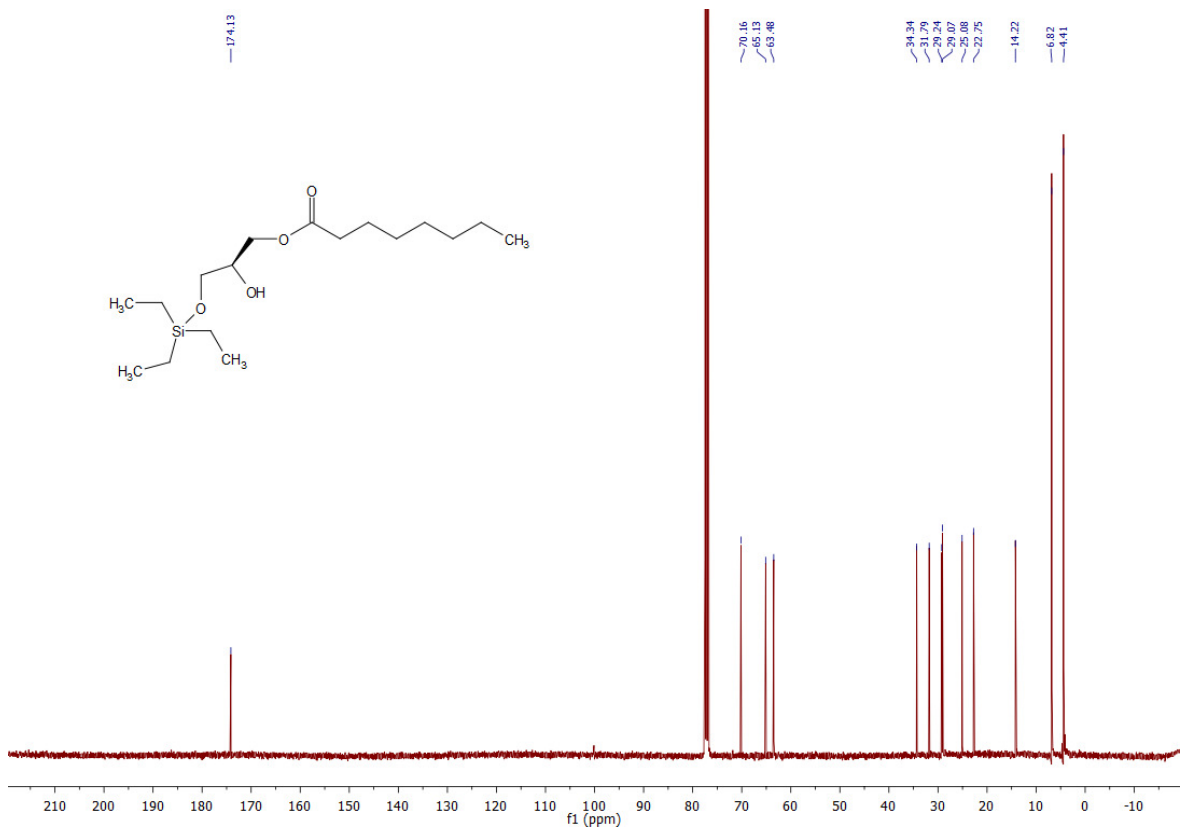
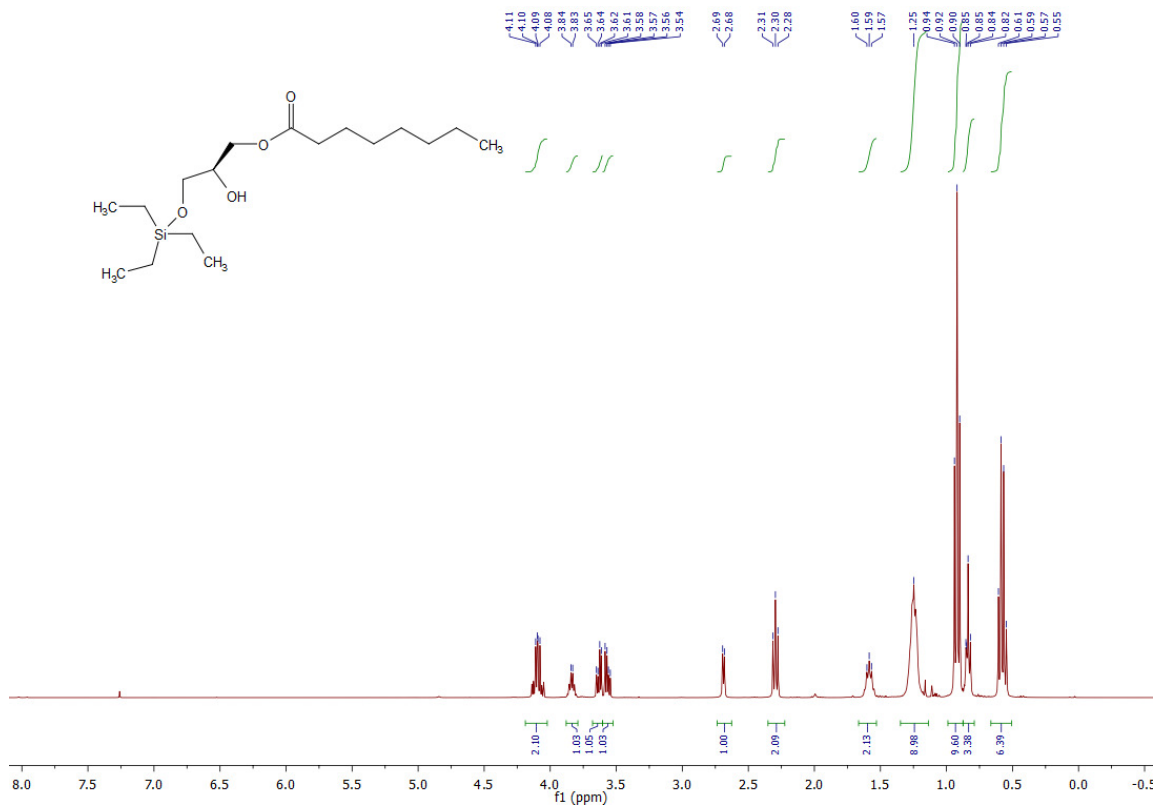
TLC (9:1 hexane:EtOAc): R_f = 0.30.

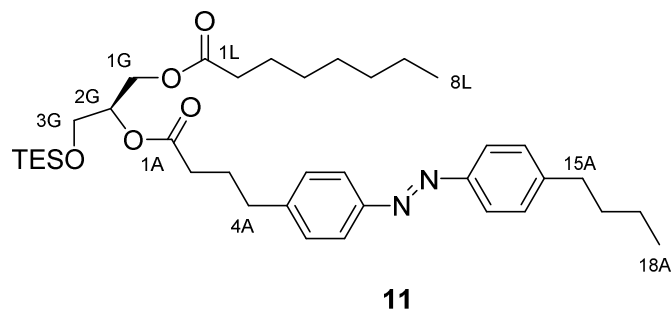
¹H NMR (CDCl₃, 400 MHz, 25 °C): δ 4.19-4.08 (m, 2 H, H1G_{a,b}), 3.98-3.87 (m, 1 H, H2G), 3.63 (dd, 1 H, H3G_a, J₁ = 10.5 Hz, J₂ = 5.3 Hz), 3.56 (dd, 1 H, H3G_b, J₁ = 10.3 Hz, J₂ = 5.4 Hz), 2.69 (d, 1 H, OH, J = 5.4 Hz), 2.34 (t, 2 H, H2_{a,b}, J = 7.5 Hz), 1.67-1.58 (m, 2 H, H3_{a,b}), 1.34-1.20 (m, 8 H, H_{alk}), 0.96 (t, 9 H, 3xCH₃(TES), J = 7.9 Hz), 0.87 (t, 3 H, H8_{a,b,c}, J = 6.9 Hz), 0.61 (q, 6 H, 3xCH₂(TES), J = 7.9 Hz).

¹³C NMR (CDCl₃, 101 MHz, 25 °C): δ 174.1 (C1L), 70.2 (CXG), 65.1, 63.5, 34.3 (C2), 31.8 (C_{alk}), 29.2 (C_{alk}), 29.1 (C_{alk}), 25.1 (C_{alk}), 22.8 (C7L), 14.2 (C8L), 6.8 (3C, 3xCH₃(TES)), 4.4 (3C, 3xCH₂(TES)).

IR (neat, ATR): $\tilde{\nu}$ = 3489, 2955, 2929, 2876, 1740, 1458, 1416, 1380, 1239, 1166, 1100, 1006, 976, 842, 807, 744, 728, 676, 619, 588, 601, 564.

HRMS (ESI⁺): *m/z* calcd. for [C₁₇H₃₇O₄Si]⁺: 333.2461, found: 333.2460 ([M+H]⁺).



5.4.9.7 – 2-O-(4-(4-((4-Butylphenyl)diazenyl)phenyl)butanoyl)-1-O-octanoyl-3-O-triethylsilyl-*sn*-glycerol (11)

FAAzo-4⁵¹ (136.3 mg, 0.42 mmol, 2.0 equiv.) was dissolved in dry CH₂Cl₂ (12 mL) under an argon atmosphere, and then DMAP (5.13 mg, 0.042 mmol, 0.1 equiv.) and EDC (0.11 mL, 0.63 mmol, 3.0 equiv.) were added. The solution was stirred at room temperature for 20 min and then **1-O-octanoyl-3-O-triethylsilyl-*sn*-glycerol (10)**, 68.9 mg, 0.21 mmol, 1.0 equiv.) was added. The solution was stirred overnight at room temperature, diluted with CH₂Cl₂ and then washed three times with H₂O. The organic phase was dried over Na₂SO₄, filtered, and the filtrate was concentrated under reduced pressure. The resulting dark orange oil was purified by flash silica gel chromatography (15 g SiO₂, hexane:EtOAc 20:1→10:1) to yield **2-O-(4-(4-((4-butylphenyl)diazenyl)phenyl)butanoyl)-1-O-octanoyl-3-O-triethylsilyl-*sn*-glycerol (11)**, 77.4 mg, 58%) as an orange oil.

TLC (3:1 hexane:EtOAc): $R_f = 0.48$ (*trans*), 0.30 (*cis*).

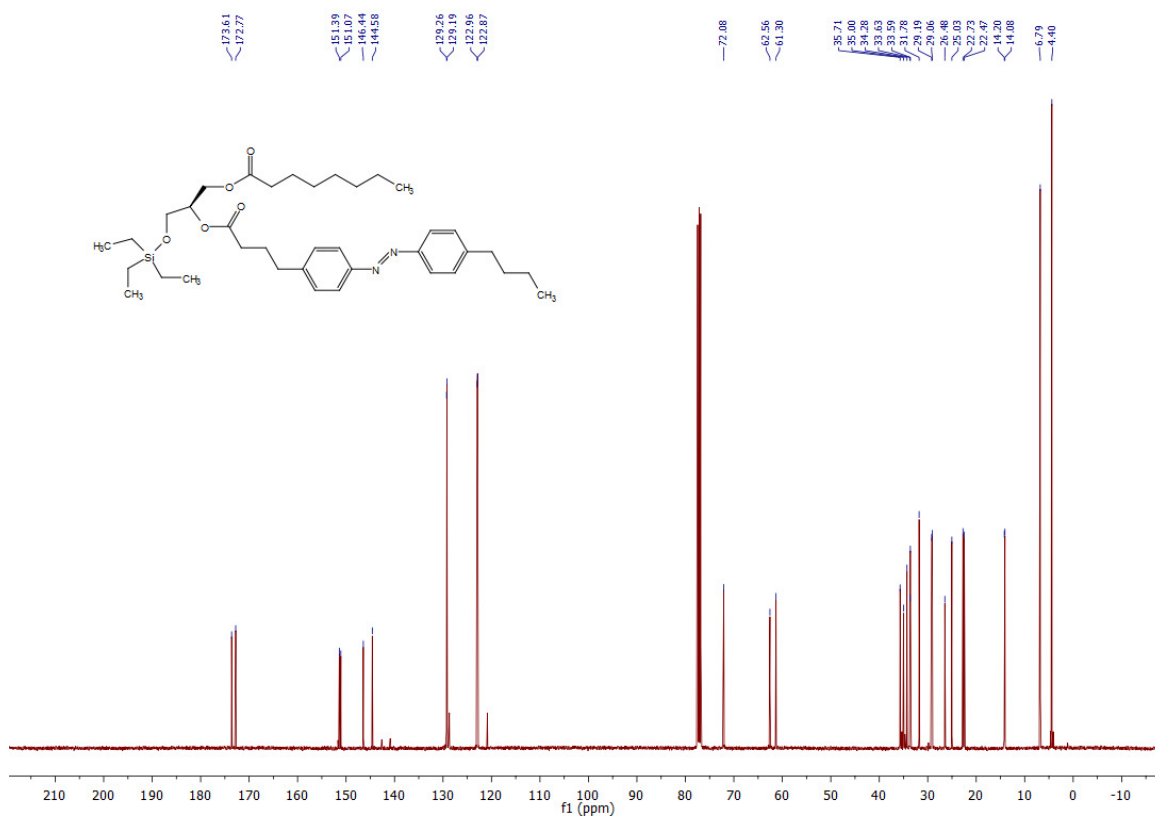
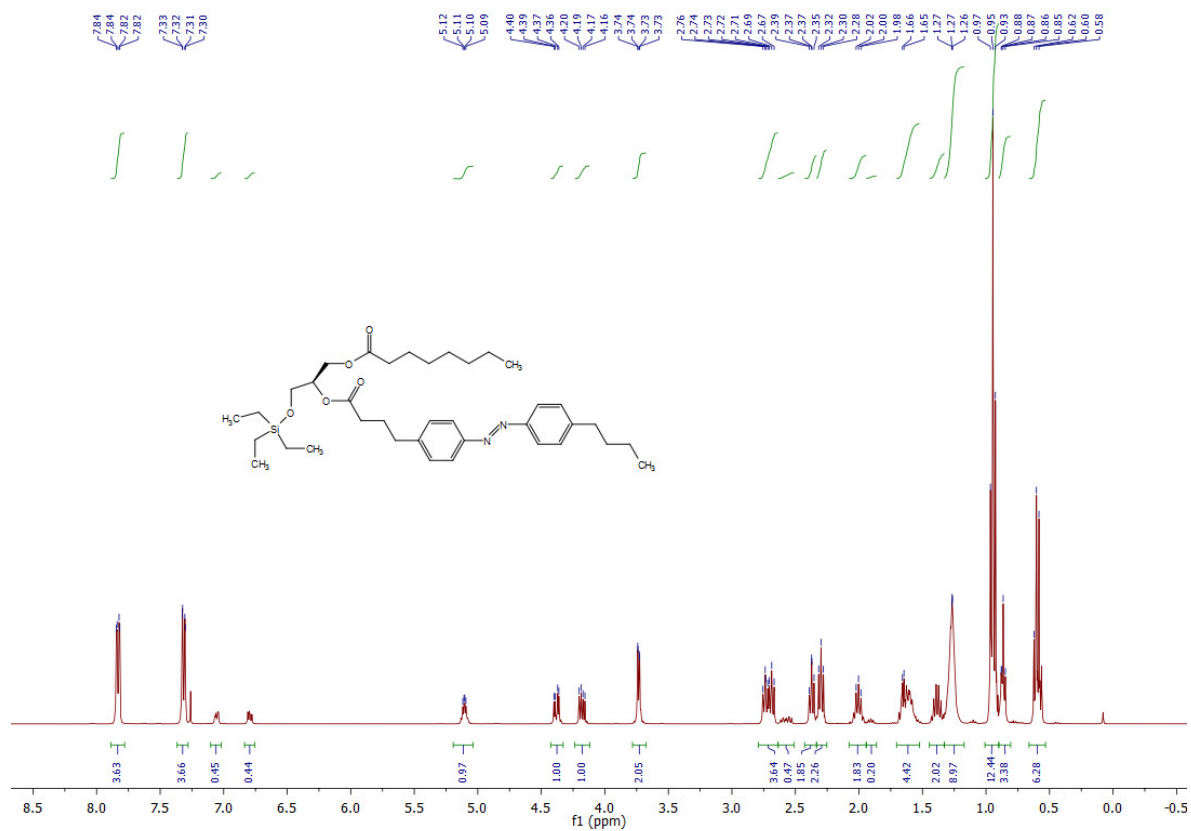
$^1\text{H NMR}$ (CDCl_3 , 400 MHz, 25 °C): δ 7.87-7.79 (m, 4 H, H7A_{a,b}, H12A_{a,b}), 7.31 (d, 4 H, H6A_{a,b}, H13A_{a,b}, $J = 8.7$ Hz), 5.14-5.05 (m, 1 H, H2G), 4.42-4.33 (m, 1H, H1G_a), 4.23-4.13 (m, 1 H, H1G_b), 3.77-3.69 (m, 2 H, H3G_{a,b}), 2.78-2.67 (m, 4 H, H4A_{a,b}, H15A_{a,b}), 2.37 (t, 2 H, H1A_{a,b}, $J = 7.1$ Hz), 2.30 (t, 2 H, H2L_{a,b}, $J = 7.3$ Hz), 2.07-1.95 (m, 2 H, H3A_{a,b}), 1.69-1.52 (m, 4 H, H3L_{a,b}, H16A_{a,b}), 1.44-1.33 (m, 2 H, H17A_{a,b}), 1.33-1.19 (m, 8 H, H_{alk}), 0.99-0.90 (m, 12 H, H18A_{a,b,c}, 3xCH₃(TES)), 0.86 (t, 3 H, H8L_{a,b,c}), 0.59 (q, 6 H, 3xCH₂(TES), $J = 8.0$ Hz).

$^{13}\text{C NMR}$ (CDCl_3 , 101 MHz, 25 °C): δ 173.6 (C1S), 172.8 (C1A), 151.4 (C_{azo}), 151.9 (C_{azo}), 146.4 (C_{azo}), 144.6 (C_{azo}), 129.3 (2 C, C_{azo}), 129.2 (2 C, C_{azo}), 123.0 (2 C, C_{azo}), 122.9 (2 C, C_{azo}), 72.1 (C2G), 62.6 (C3G), 61.3 (C1G), 35.7 (C15A), 35.0 (C4A), 34.3 (C2A), 33.63 (C2A), 33.59 (C3A), 31.8 (C3L), 29.2 (C_{alk}), 29.1 (C_{alk}), 26.5 (C_{alk}), 25.0 (C_{alk}), 22.7 (C_{alk}), 22.5 (C_{alk}), 14.2 (C18L), 14.1 (C18A), 6.8 (3 C, 3xCH₃(TES)), 4.4 (3 C, 3xCH₂(TES)).

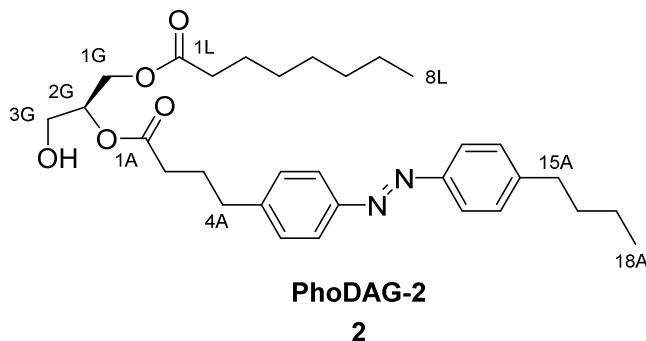
IR (neat, ATR): $\tilde{\nu} = 3028, 2955, 2930, 2874, 2859, 1918, 1739, 1602, 1580, 1498, 1458, 1416, 1378, 1302, 1240, 1226, 1156, 1145, 1104, 1013, 977, 844, 800, 744, 728, 674, 642, 618, 601, 571, 564.$

HRMS (ESI⁺): m/z calcd. for [C₃₇H₅₉N₂O₅Si]⁺: 639.4193, found: 639.4142 ([M+H]⁺).

5 – Photoswitchable diacylglycerols enable optical control of protein kinase C



5.4.9.8 – 2-O-(4-(4-((4-Butylphenyl)diazenyl)phenyl)butanoyl)-1-O-octanoyl-*sn*-glycerol (PhoDAG-2, 2)



2-O-(4-(4-((4-Butylphenyl)diazenyl)phenyl)butanoyl)-1-O-octanoyl-*sn*-glycerol

(PhoDAG-2) was prepared from 2-O-(4-(4-((4-butylphenyl)diazenyl)phenyl)butanoyl)-1-O-octanoyl-3-O-triethylsilyl-*sn*-glycerol (**11**, 28.0 mg, 0.044 mmol, 1.0 equiv.) as described above in the synthesis of 2-O-(4-(4-((4-butylphenyl)diazenyl)phenyl)butanoyl)-1-O-stearoyl-*sn*-glycerol (PhoDAG-1). PhoDAG-2 (13.3 mg, 66%) was isolated as an orange oil. *NOTE: all reactants and reagents were scaled according to molarity.*

TLC (2:1 hexane:EtOAc): R_f : 0.39 (*trans*), 0.28 (*cis*).

$^1\text{H NMR}$ (CDCl_3 , 400 MHz, 25 °C): δ 7.86-7.79 (m, 4 H, H7A_{a,b}, H12A_{a,b}), 7.31 (d, 4 H, H6A_{a,b}, H13A_{a,b}, $J = 8.7$ Hz), 5.15-5.05 (m, 1 H, H2G), 4.37-4.30 (m, 1H, H3G_a), 4.27-4.20 (m, 1 H, H3G_b), 3.76-3.70 (m, 2 H, H1G_{a,b}), 2.74 (t, 2 H, H4A_{a,b}, $J = 7.5$ Hz), 2.69 (t, 2 H, H15A_{a,b}, $J = 7.8$ Hz), 2.40 (t, 2 H, H2A_{a,b}, $J = 7.5$ Hz), 2.36-2.29 (m, 2 H, H2L_{a,b}), 2.07-1.97 (m, 3 H, H3A_{a,b}), 1.70-1.50 (m, 4 H, H16A_{a,b}, HL3_{a,b}), 1.44-1.18 (m, 10 H, H_{alk}), 0.93 (t, 3 H, H18A_{a,b,c}, $J = 7.3$ Hz), 0.90-0.81 (t, 3 H, H8L_{a,b,c}, $J = 7.6$ Hz).

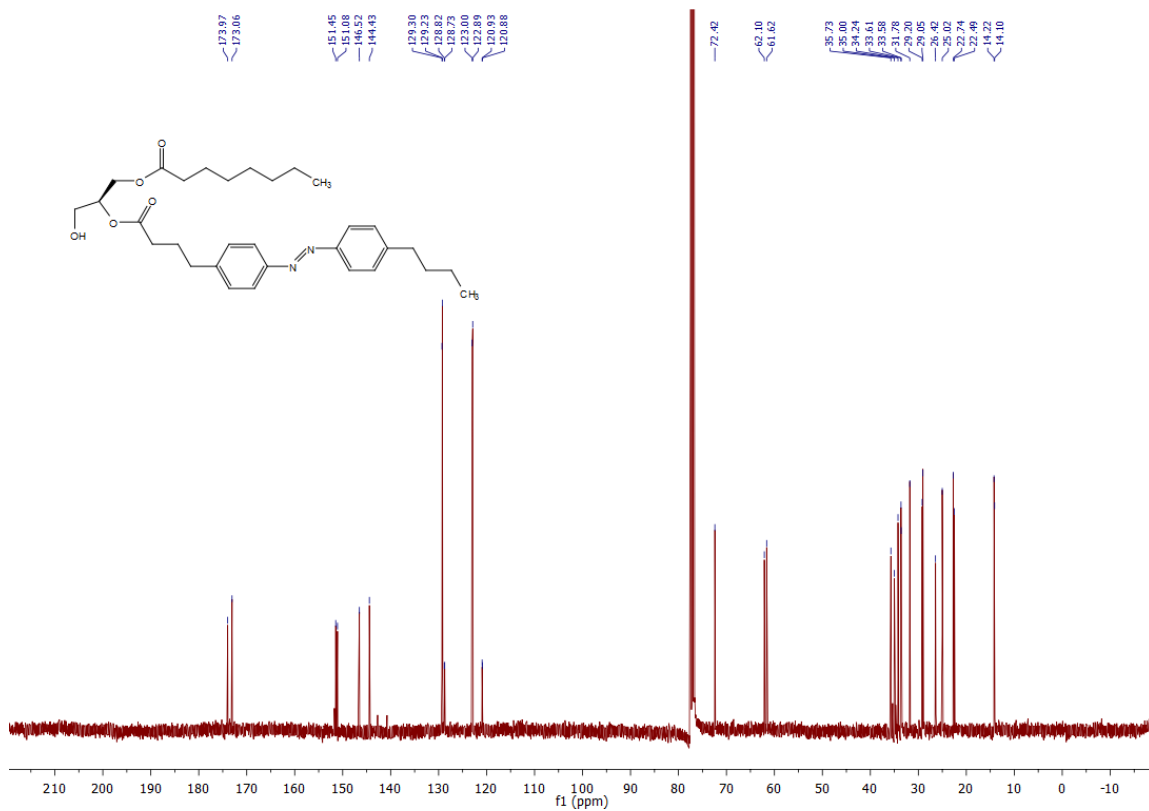
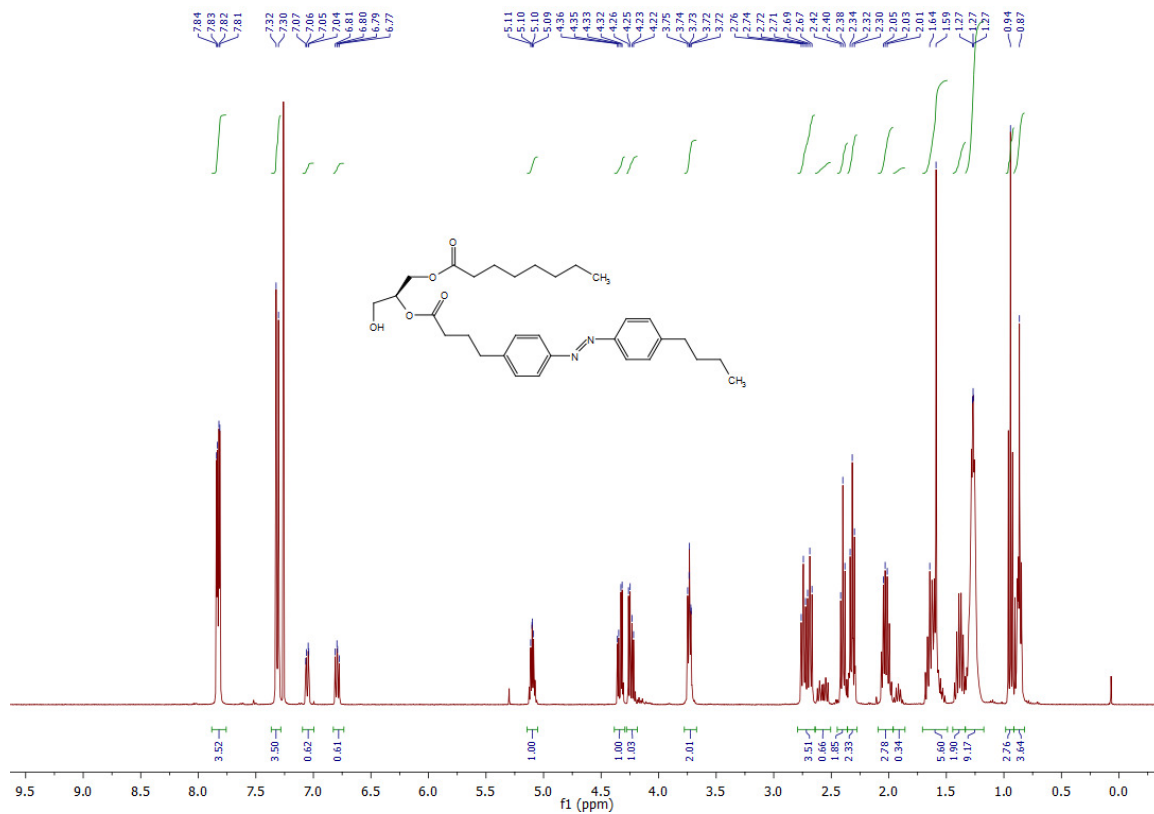
$^{13}\text{C NMR}$ (CDCl_3 , 101 MHz, 25 °C): δ 174.0 (C1L), 173.0 (C1A), 152.8 (C_{azo}), 151.3 (C_{azo}), 146.5 (C_{azo}), 144.4 (C_{azo}), 129.3 (2 C, C_{azo}), 129.2 (2 C, C_{azo}), 123.9 (2 C, C_{azo}), 122.9 (2 C, C_{azo}), 72.4 (C2G), 62.1 (C3G), 61.6 (C1G), 35.7 (C15A), 35.0 (C4A), 34.2 (C2L), 33.61 (C_{alk}), 33.6 (C_{alk}), 31.8 (C_{alk}), 29.2 (C_{alk}), 29.1 (C_{alk}), 26.4 (C3A), 25.0 (C3L), 22.7 (C7L), 22.5 (C17A), 14.2 (C8L), 14.1 (C18A).

IR (neat, ATR): $\tilde{\nu} = 3466, 2956, 2929, 2858, 1739, 1602, 1498, 1458, 1417, 1378, 1225, 1159, 1103, 1051, 1014, 844, 728, 634, 614, 591, 576, 568.$

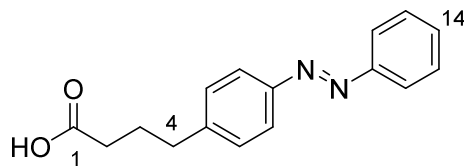
HRMS (EI⁺): m/z calcd. for $[\text{C}_{31}\text{H}_{44}\text{N}_2\text{O}_5]^+$: 524.3250, found: 524.3245 ($[\text{M}-\text{e}]^+$).

UV-Vis (50 μM in DMSO): $\lambda_{\text{max}}(\pi-\pi^*) = 340$ nm. $\lambda_{\text{max}}(n-\pi^*) = 440$ nm.

5 – Photoswitchable diacylglycerols enable optical control of protein kinase C



5.4.9.9 – 4-(Phenyldiazenyl)phenyl butanoic acid (FAAzo-9, 4)



FAAzo-9

4

4-(4-Aminophenyl)butyric acid (200 mg, 1.12 mmol, 1.0 equiv.) was first dissolved in CH_2Cl_2 (20 mL). Nitrosobenzene (143.4 mg, 1.34 mmol, 1.2 equiv.) and AcOH (5 mL) were added, and the solution was then stirred at room temperature overnight. The solvents were then removed under reduced pressure. The resulting crude residue was purified by flash silica gel chromatography (20 g SiO_2 , 99:1 CH_2Cl_2 :AcOH) to yield **4-(phenyldiazenyl)phenyl butanoic acid (FAAzo-9, 4)**, 320.8 mg, quant.) as an orange solid.

TLC (99:1 CH_2Cl_2 :AcOH): $R_f = 0.17$.

$^1\text{H NMR}$ (CDCl_3 , 400 MHz, 25 °C): δ 7.94-7.82 (m, 4 H, H7_{a,b}, H11_{a,b}), 7.55-7.43 (m, 3 H, H13_{a,b}, H14), 7.34 (d, 2 H, H6_{a,b}, $J = 4.0$ Hz), 2.76 (t, 2 H, H4_{a,b}, $J = 7.8$ Hz), 2.42 (t, 2 H, H2_{a,b}, $J = 7.3$ Hz), 2.02 (dd, 2 H, H3_{a,b}, $J = 7.8, 7.3$ Hz).

$^{13}\text{C NMR}$ (CDCl_3 , 101 MHz, 25 °C): δ 178.7 (C1), 152.8 (C11), 151.4 (C8), 144.8 (C5), 131.0 (C14), 129.4-129.2 (4 C, C6_{a,b}, C13_{a,b}), 123.2-122.9 (4 C, C7_{a,b}, C12_{a,b}), 35.0 (C4), 33.2 (C2), 26.2 (C3).

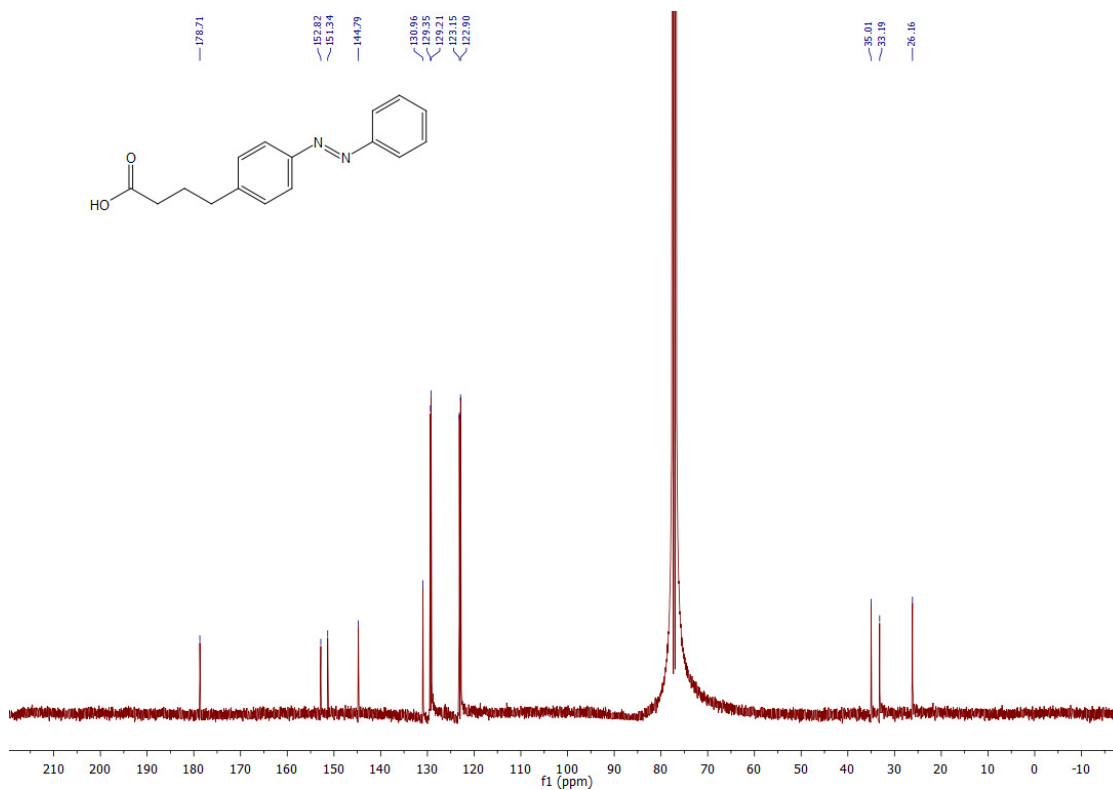
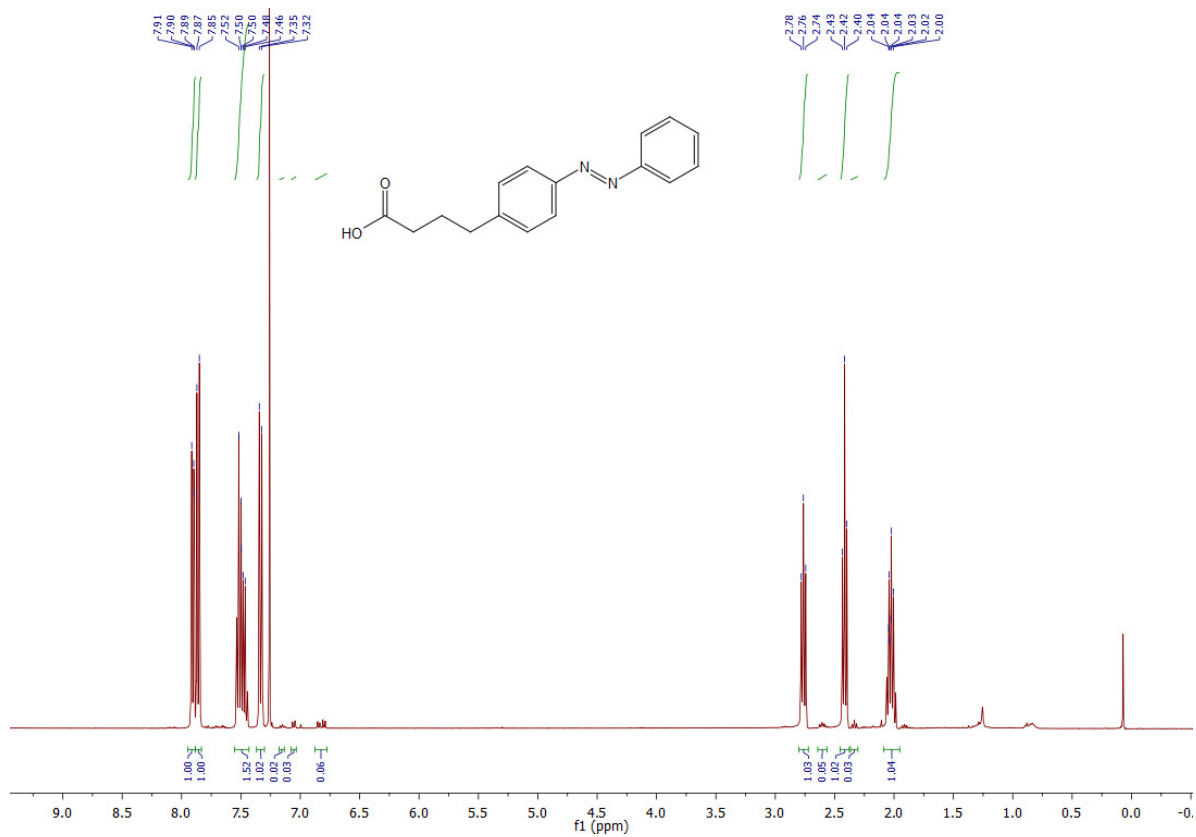
IR (neat, ATR): $\tilde{\nu} = 3041, 2944, 1693, 1601, 1500, 1486, 1462, 1439, 1411, 1339, 1303, 1282, 1252, 1215, 1152, 1106, 1071, 1020, 914, 851, 822, 787, 764, 745, 732, 684, 638, 616, 577, 561$.

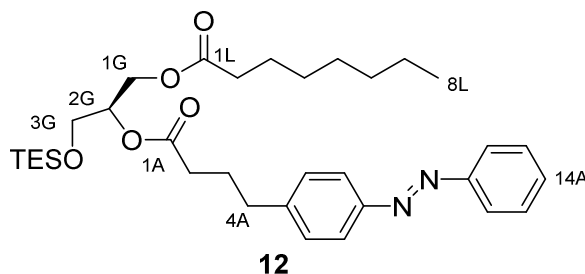
HRMS (EI⁺): m/z calcd. for $[\text{C}_{16}\text{H}_{16}\text{N}_2\text{O}_2]^+$: 268.1212, found: 268.1206 ($[\text{M}-\text{e}]^+$).

UV-Vis (50 μM in DMSO): $\lambda_{\text{max}}(\pi-\pi^*) = 330$ nm. $\lambda_{\text{max}}(n-\pi^*) = 425$ nm.

Melting point (°C): 135.5-137.5.

5 – Photoswitchable diacylglycerols enable optical control of protein kinase C



5.4.9.10 – 2-O-(4-(4-(Phenyldiazenyl)phenyl)butanoyl)-1-O-octanoyl-3-O-triethylsilyl-*sn*-glycerol (12)

4-(Phenyldiazenyl)phenyl butanoic acid (FAAzo-9, 153.4 mg, 0.57 mmol, 2.0 equiv.) was dissolved in dry CH₂Cl₂ (15 mL) under an argon atmosphere. DMAP (3.4 mg, 0.028 mmol, 0.1 equiv.) and EDC (0.15 mL, 0.84 mmol, 3.0 equiv.) were then added to the solution. The mixture was stirred at room temperature for 20 min and then **1-O-octanoyl-3-O-triethylsilyl-*sn*-glycerol (10**, 95.1 mg, 0.28 mmol, 1.0 equiv.) was added. The solution was stirred overnight at room temperature, and was then diluted with CH₂Cl₂ (100 mL) and washed with H₂O (3x50 mL). The organic phase was dried over Na₂SO₄ and then filtered. The filtrate was concentrated under reduced pressure. The residue was purified by flash silica gel chromatography (20 g SiO₂, hexane:EtOAc 20:1→10:1) to yield **2-O-(4-(4-(phenyldiazenyl)phenyl)butanoyl)-1-O-octanoyl-3-O-triethylsilyl-*sn*-glycerol (12**, 100 mg, 61%) as an orange oil.

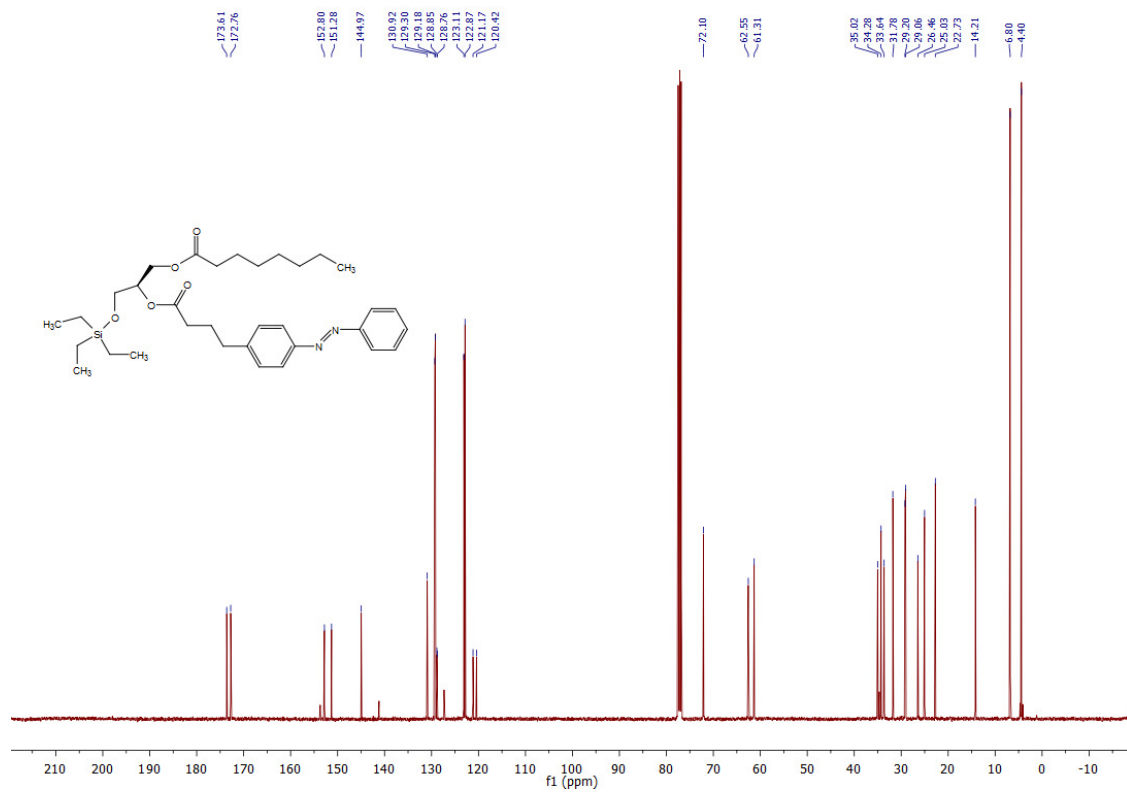
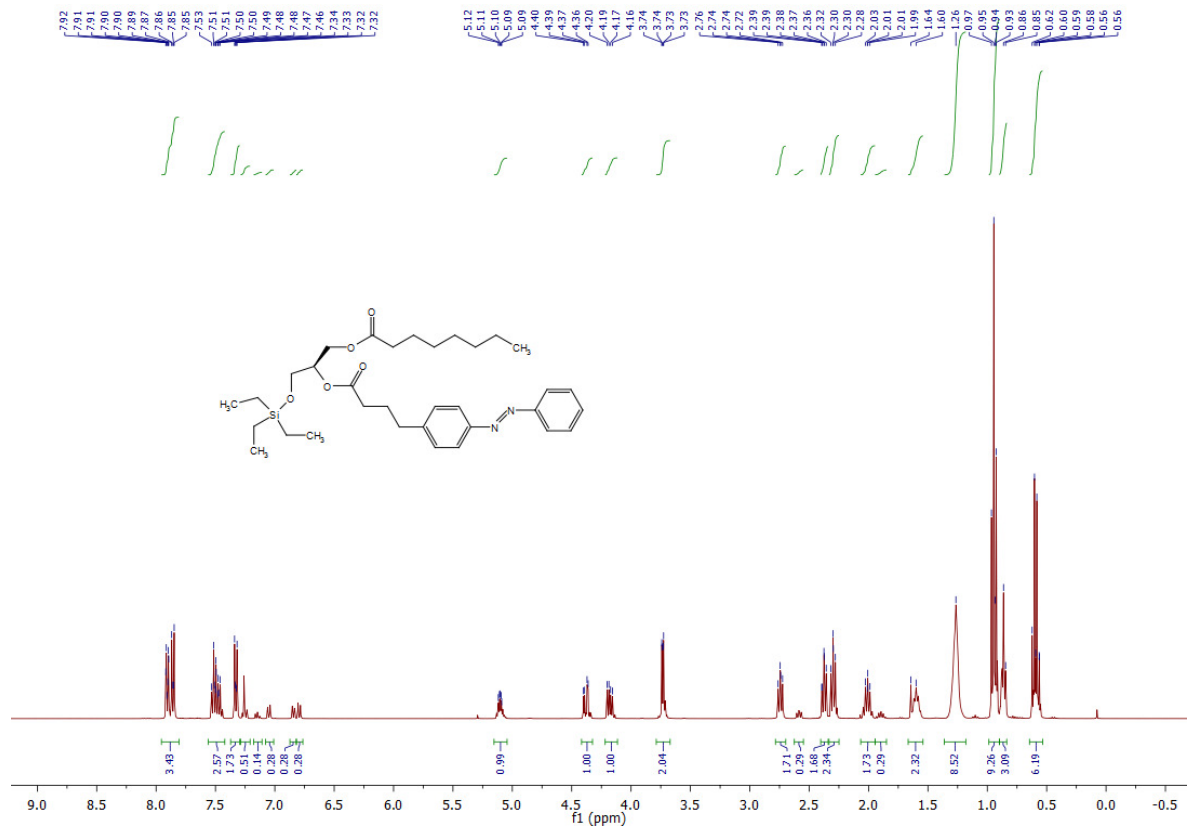
TLC (9:1 hexane:EtOAc): $R_f = 0.43$ (*trans*), 0.25 (*cis*).

$^1\text{H NMR}$ (CDCl_3 , 400 MHz, 25 °C): δ 7.94-7.83 (m, 4 H, H7A_{a,b}, H12A_{a,b}), 7.55-7.43 (m, 3 H, H14A, H13A_{a,b}), 7.33 (d, 2 H, H6A_{a,b}, $J = 8.2$ Hz), 5.15-5.05 (m, 1 H, H2G), 4.41-4.33 (m, 1H, H1G_a), 4.22-4.13 (m, 1 H, H1G_b), 3.78-3.69 (m, 2 H, H3G_{a,b}), 2.74 (t, 2 H, H4A_{a,b}, $J = 7.2$ Hz), 2.38 (t, 2 H, H2A, $J = 7.6$ Hz), 2.30 (t, 2 H, H2L_{a,b}, $J = 7.5$ Hz), 2.08-1.96 (m, 2 H, H3A_{a,b}), 1.64-1.54 (m, 2 H, H3L_{a,b}), 1.34-1.19 (m, 8 H, H_{alk}), 0.94 (t, 9 H, 3xCH₃(TES), $J = 8.3$ Hz), 0.90-0.82 (t, 3 H, H8L_{a,b,c}, $J = 6.9$ Hz), 0.59 (m, 6 H, 3xCH₂(TES), $J = 8.2$ Hz).

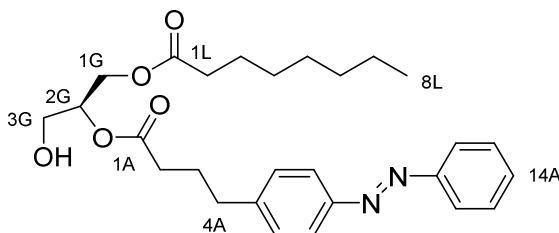
$^{13}\text{C NMR}$ (CDCl_3 , 101 MHz, 25 °C): δ 173.6 (C1L), 172.8 (C1A), 152.8 (C_{azo}), 151.3 (C_{azo}), 145.0 (C_{azo}), 131.0 (C_{azo}), 129.3 (2C, C_{azo}), 129.2 (2 C, C_{azo}), 123.1 (2 C, C_{azo}), 122.9 (2 C, C_{azo}), 72.1 (C2G), 62.6 (C3G), 61.3 (C1G), 35.0 (C4A), 34.3 (C2L), 33.6 (C2A), 31.8 (C_{alk}), 29.2 (C_{alk}), 29.1 (C_{alk}), 26.5 (C_{alk}), 25.0 (C_{alk}), 22.7 (C7L), 14.2 (C8L), 6.8 (3 C, 3xCH₃(TES)), 4.4 (3 C, 3xCH₂(TES)).

IR (neat, ATR): $\tilde{\nu} = 2955, 2930, 2875, 1738, 1603, 1500, 1458, 1415, 1378, 1300, 1240, 1225, 1144, 1103, 1070, 1004, 847, 797, 743, 727, 688, 638, 616, 598, 563$.

HRMS (ESI⁺): m/z calcd. for [C₃₃H₅₁N₂O₅Si]⁺: 583.3567, found: 583.3567 ([M+H]⁺).



5.4.9.11 – 2-O-(4-(4-(Phenyldiazenyl)phenyl)butanoyl)-1-O-octanoyl-*sn*-glycerol (PhoDAG-3, 3)



PhoDAG-3

3

2-O-(4-(4-(Phenyldiazenyl)phenyl)butanoyl)-1-O-octanoyl-*sn*-glycerol (PhoDAG-3) was prepared from **2-O-(4-(4-(phenyldiazenyl)phenyl)butanoyl)-1-O-octanoyl-3-O-triethylsilyl-*sn*-glycerol (12, 22.0 mg, 0.038 mmol, 1 equiv.)** as described above in the synthesis of **2-O-(4-(4-((4-butylphenyl)diazenyl)phenyl)butanoyl)-1-O-stearoyl-*sn*-glycerol (PhoDAG-1)**. **PhoDAG-3 (17.7 mg, quant.)** was isolated as an orange oil. *NOTE: all reactants and reagents were scaled according to molarity.*

TLC (9:1 hexane:EtOAc): $R_f = 0.20$ (*trans*), 0.18 (*cis*).

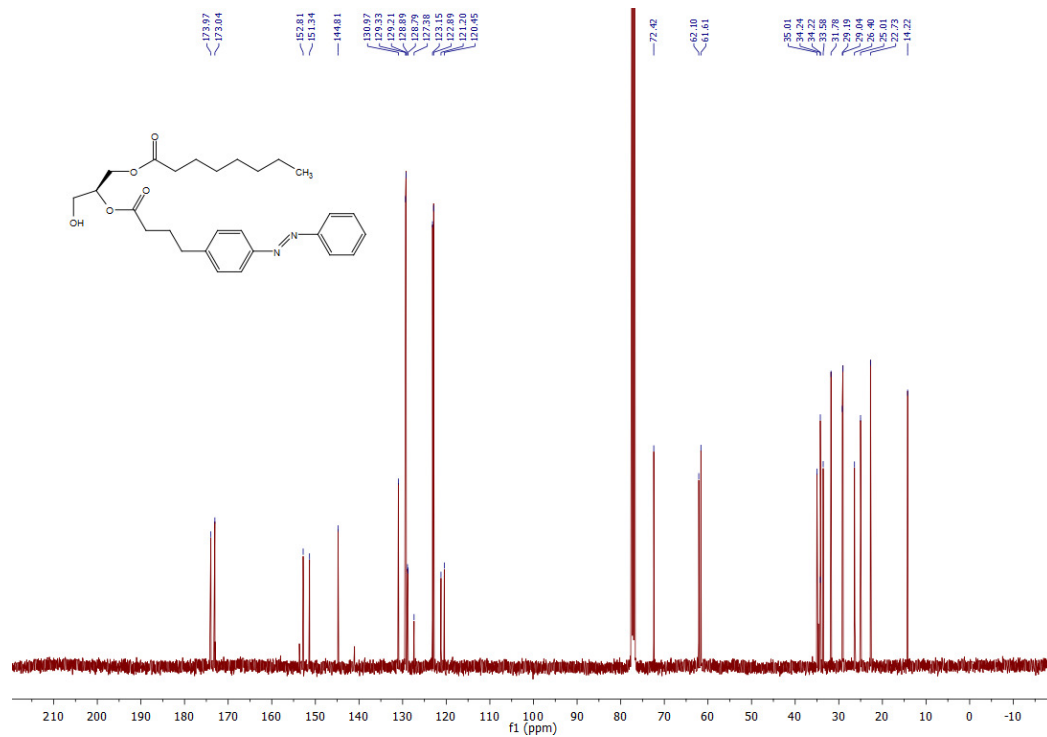
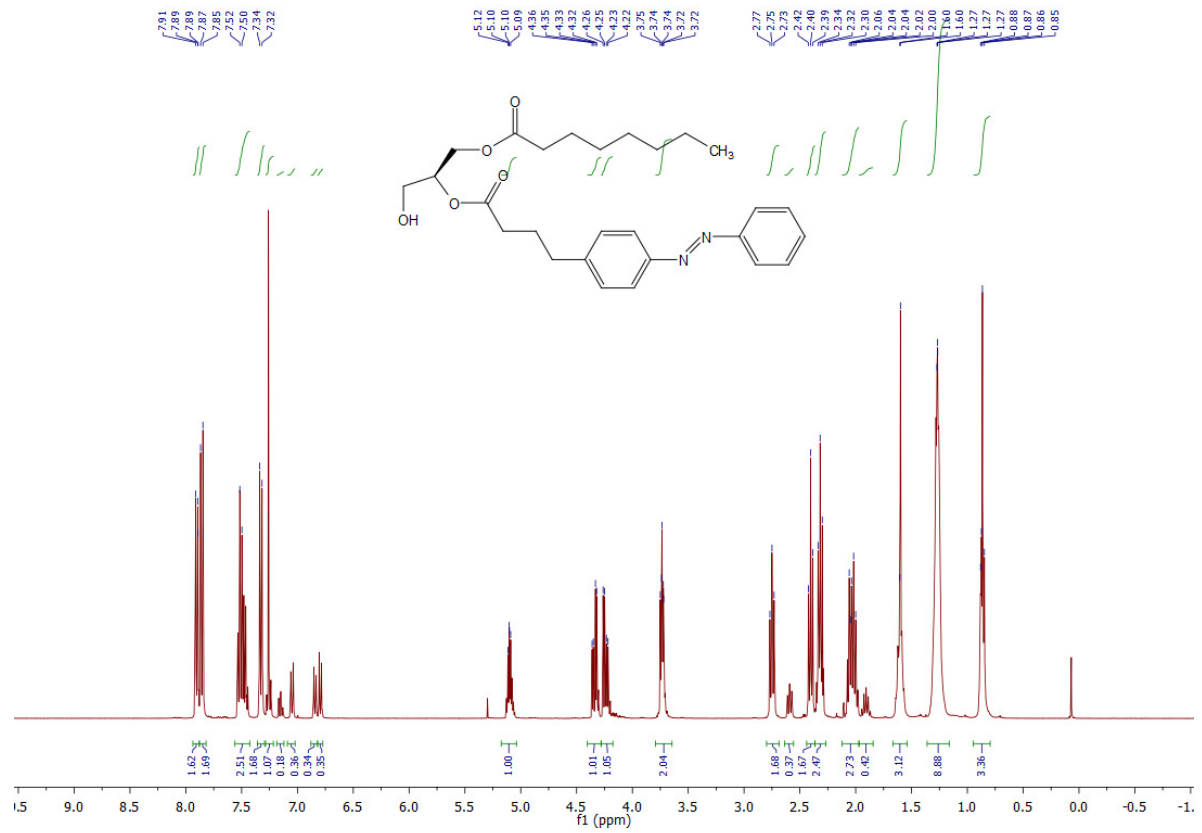
$^1\text{H NMR}$ (CDCl_3 , 400 MHz, 25 °C): δ 7.93–7.83 (m, 4 H, H7A_{a,b}, H11A_{a,b}), 7.55–7.43 (m, 3 H, H14A, H13A_{a,b}), 7.33 (d, 2 H, H6A_{a,b}, $J = 8.3$ Hz), 5.14–5.04 (q, 1 H, H2G, $J = 4.9$ Hz), 4.38–4.29 (m, 1 H, H3G_a), 4.27–4.19 (m, 1 H, H3G_b), 3.78–3.68 (m, 2 H, H1G_{a,b}), 2.75 (t, 2 H, H4A_{a,b}, $J = 7.7$ Hz), 2.40 (t, 2 H, H2A_{a,b}, $J = 7.7$ Hz), 2.32 (t, 2 H, H2L_{a,b}, $J = 7.7$ Hz), 2.07–1.96 (m, 2 H, H3A_{a,b}), 1.65–1.55 (m, 2 H, H3L_{a,b}), 1.34–1.20 (m, 8 H, H_{alk}), 0.90–0.82 (t, 3 H, H8L_{a,b,c}, $J = 7.1$ Hz).

$^{13}\text{C NMR}$ (CDCl_3 , 101 MHz, 25 °C): δ 173.4 (C1L), 173.0 (C1A), 152.8 (C_{azo}), 151.3 (C_{azo}), 144.8 (C_{azo}), 130.9 (C_{azo}), 129.3 (2 C, C_{azo}), 129.2 (2 C, C_{azo}), 123.2 (2 C, C_{azo}), 122.9 (2 C, C_{azo}), 72.4 (C2G), 62.1 (C3G), 61.6 (C1G), 35.0 (C4A), 34.2 (C2L), 33.6 (2 C, C2A, C14A), 31.8 (C6L), 29.2 (C_{alk}), 29.0 (C_{alk}), 26.4 (C_{alk}), 25.0 (C_{alk}), 22.7 (C7A), 14.2 (C8A).

IR (neat, ATR): $\tilde{\nu} = 3466, 2928, 2857, 1739, 1603, 1458, 1416, 1377, 1224, 1157, 1104, 1052, 847, 768, 690, 615, 601, 590, 568, 554$.

HRMS (EI⁺): m/z calcd. for $[\text{C}_{27}\text{H}_{36}\text{N}_2\text{O}_5]^+$: 468.2624, found: 468.2622 ($[\text{M}-\text{e}^-]^+$).

UV-Vis (50 μM in DMSO): $\lambda_{\text{max}}(\pi-\pi^*) = 325$ nm. $\lambda_{\text{max}}(n-\pi^*) = 440$ nm.



6 – Synthesis of photoswitchable glycerophospholipids

6.1 – Introduction

Glycerophospholipids are ubiquitous lipid class which possess a polar headgroup containing a glycerol unit linked to a phosphate at either the *sn*-1 or *sn*-3 positions^{5,161}. Their structures are diverse, as the phosphate can be decorated by a variety of polar units, from the simple choline to more complex units such as serine, *myo*-inositols and sugars. The glycerol hydroxyl groups can also be linked to many different fatty acyl chains, affording a vast number of glycerophospholipids across all types of organisms¹⁶². These amphipathic molecules possess the ability to self-organize into membranes^{1,2}, and are thus found at all levels of organic life. For example, phosphatidylcholines (PCs) have a cylindrical geometry which makes them ideal for forming a planar bilayer. Consequently, they are major components of eukaryotic membranes, and compose >50% of the total phospholipids present¹⁰.

Glycerophospholipids play more than a structural role, as they are ubiquitously involved in cell signaling through several mechanisms¹⁶³. First, they determine the identity and characteristics of the membranes in which transmembrane proteins are folded^{164–167}. Second, they serve as first messengers or allosteric modulators for membrane proteins^{168,169}. Finally, they are also reservoirs of second messengers, as their receptor-mediated hydrolysis by phospholipases releases molecules such as AA, DAG and inositol phosphates^{170,171}. For example, phosphatidylinositol 4,5-bisphosphate (PI(4,5)P₂) is known to directly affect a number of proteins including ion channels, GPCRs, and enzymes^{172–175}. On activation of G_{αq}-coupled GPCRs, PLC cleaves PI(4,5)P₂ into DAG and inositol trisphosphate, which are released into the plasma membrane and cytosol, respectively. The generation of these second messengers leads to the activation of PKC and a rise in [Ca²⁺]_i, triggering a cellular response¹⁷⁶.

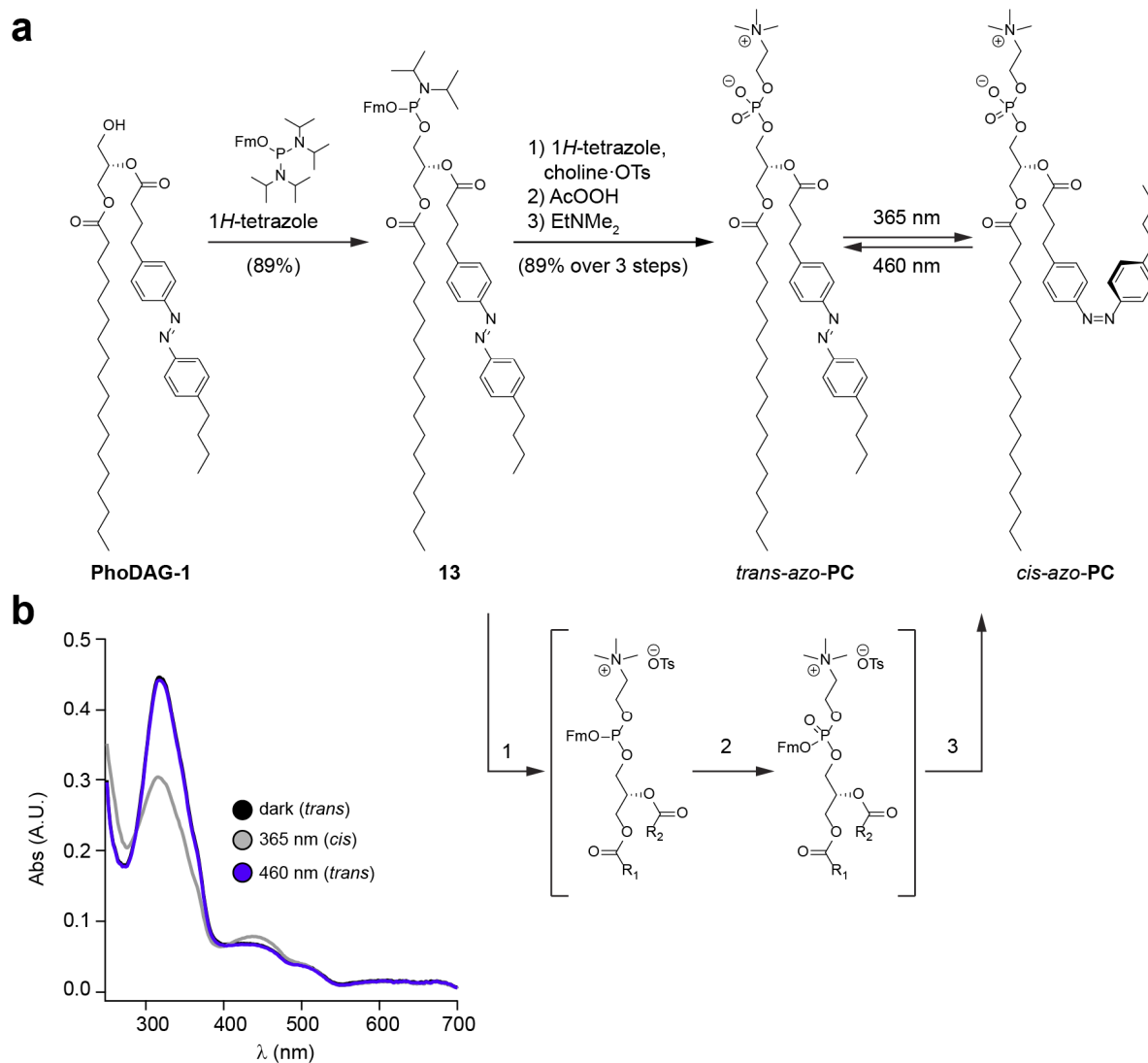
Photochemical tools to probe the biophysical and pharmacological properties of glycerophospholipids remain limited. However, in recent years a few examples have emerged which allow researchers to manipulate glycerophospholipid levels in cells with the spatiotemporal precision of light. Caged lipids²⁴, including caged phosphoinositides^{25,177,178}, phosphatidic acid^{26,179}, phosphatidyl ethanolamine²⁷, and lysophosphatidic acid¹⁸⁰, have shown promise in live-cell experiments. In these examples, caged phosphate groups are employed to block the compounds activity¹⁸¹. On a flash of light, the native lipid is quickly released and a cellular response can be initiated. As uncaging is an irreversible process, this

approach relies on metabolism or transport of the active lipid species to turn the process OFF. Photoswitchable lipids, however, remain a more novel approach. Interestingly, several photoswitchable phosphatidylcholine derivatives were synthesized in the 1980's and their effects in model membrane systems such as monolayers were investigated^{46–48,75}. They were synthesized by the esterification of a *lyso*-phosphatidylcholines with photoswitchable fatty acids. However, the *lyso*-phosphatidylcholine starting materials are quite expensive and no reaction scales, yields or characterization were reported in their synthesis. Since their initial synthesis and evaluation, their application in controlling cell signaling has remained limited. Herein, we describe the syntheses of photoswitchable derivatives of phosphatidylcholine and PI(4,5)P₂. We demonstrate that phosphoramidite chemistry is a high-yielding and efficient approach to rapidly functionalize existing photoswitchable DAGs into more complex glycerophospholipids.

6.2 – Results

6.2.1 – Synthesis and characterization of a photoswitchable phosphatidylcholine

We set our sights first on synthesizing a photoswitchable phosphatidylcholine derivative. For more sophisticated and modern applications, a versatile synthesis must be devised to allow for the preparation of significant amounts of the photoswitchable lipid. We recognized that **PhoDAG-1**⁵² could serve as the backbone for a photoswitchable phosphatidylcholine derivative, now called *azo-PC*. Therefore, an optimized synthetic route was developed which utilized phosphoramidite chemistry to attach the phosphocholine headgroup to **PhoDAG-1** (**Fig. 6.1a**). A 1*H*-tetrazole-mediated coupling of **PhoDAG-1** with *bis*-(9*H*-fluoren-9-ylmethyl)-*N,N*-diisopropylamidophosphite¹⁸¹, a 9-fluorenylmethyl (Fm)-protected phosphoramidite, afforded **13** in high yield. From this phosphoramidite, a sequence of three sequential reactions was optimized to complete the phosphocholine headgroup. A 1*H*-tetrazole-mediated coupling between **13** and choline *p*-toluenesulfonate was immediately followed by oxidation to the phosphate with peracetic acid (AcOOH). A final Fm-deprotection under basic conditions afforded *azo-PC* in an excellent yield of 89% over the three steps. Similar to **PhoDAG-1** and the rest of the FAAzos, *azo-PC* behaved as a regular azobenzene which could be isomerized between its *cis*- and *trans*-states with UV-A and blue light, respectively (**Fig. 6.1b**).



6.2.2 – Design and synthesis of cell-permeable, photoswitchable PI(4,5)P₂

Given our success using phosphoramidite chemistry to modify the polar headgroup of **PhoDAG-1**, we set our sights on the preparation of a photoswitchable derivative of PI(4,5)P₂, which could also be built around the PhoDAG scaffold. However, we recognized that PI(4,5)P₂ is a negatively charged glycerophospholipid, and this could inhibit its ability to reach the inner leaflet of the plasma membrane where it normally exerts its effects. To circumvent this, we designed a “pro-lipid” with esterase-labile protecting groups to mask the charged and polar functional groups of the phosphoinositol headgroup (**Fig. 6.2**). The three free hydroxyl groups would be masked by butanoyl (Bt) protecting groups, while the negatively charged phosphates would be masked by acetoxymethyl (Am)-esters. These protecting groups have been used before to prepare cell-permeant phosphoinositides and phosphates¹⁷⁷. This fully-protected phosphoinositide, *apo-azo-PIP*₂, would therefore be neutral, and more likely to cross the cell membrane. Once inside the cell, intracellular esterases can remove both the butanoyl and Am-ester protecting groups²⁵. The resulting negatively charged photoswitchable *azo-PIP*₂ would remain trapped inside the cell, where it would exert its effects on effector proteins.

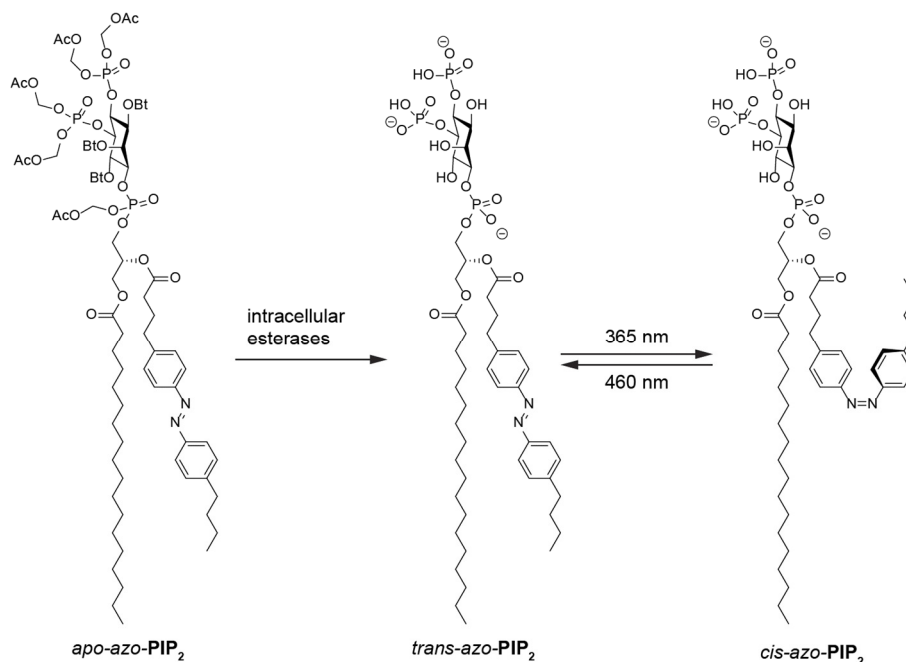


Figure 6.2 | Design of a cell-permeable, photoswitchable PI(4,5)P₂. The chemical structure of *apo-azo-PIP*₂, which is a masked derivative of the photoswitchable phosphoinositide, *azo-PIP*₂. Once inside the cell, the butanoyl and acetoxymethyl ester protecting groups can be cleaved by intracellular esterases, affording the photoswitchable phosphoinositide *azo-PIP*₂, which would remain trapped inside the cell.

We synthesized *apo-azo-PIP*₂ in high yield using phosphoramidite chemistry like that described above for *azo-PC* (Fig. 6.3). A 1*H*-tetrazole-mediated coupling between phosphoramidite **13** and the protected *myo*-inositol **RM-317** (unpublished building block from Prof. Carsten Schultz and Dr. Rainer Müller, EMBL Heidelberg), followed by a sequential oxidation with AcOOH afforded the Fm-protected, phosphoinositide **14** in 78% yield over two steps. Fm-deprotection and acetoxy-methylation using bromomethylacetate then afforded *apo-azo-PIP*₂ in 72% yield. This four-step sequence generated this complex protected glycerophospholipid in very high yield (56% over 4 steps), further demonstrating the versatility of phosphoramidite chemistry in the synthesis of complex glycerophospholipids.

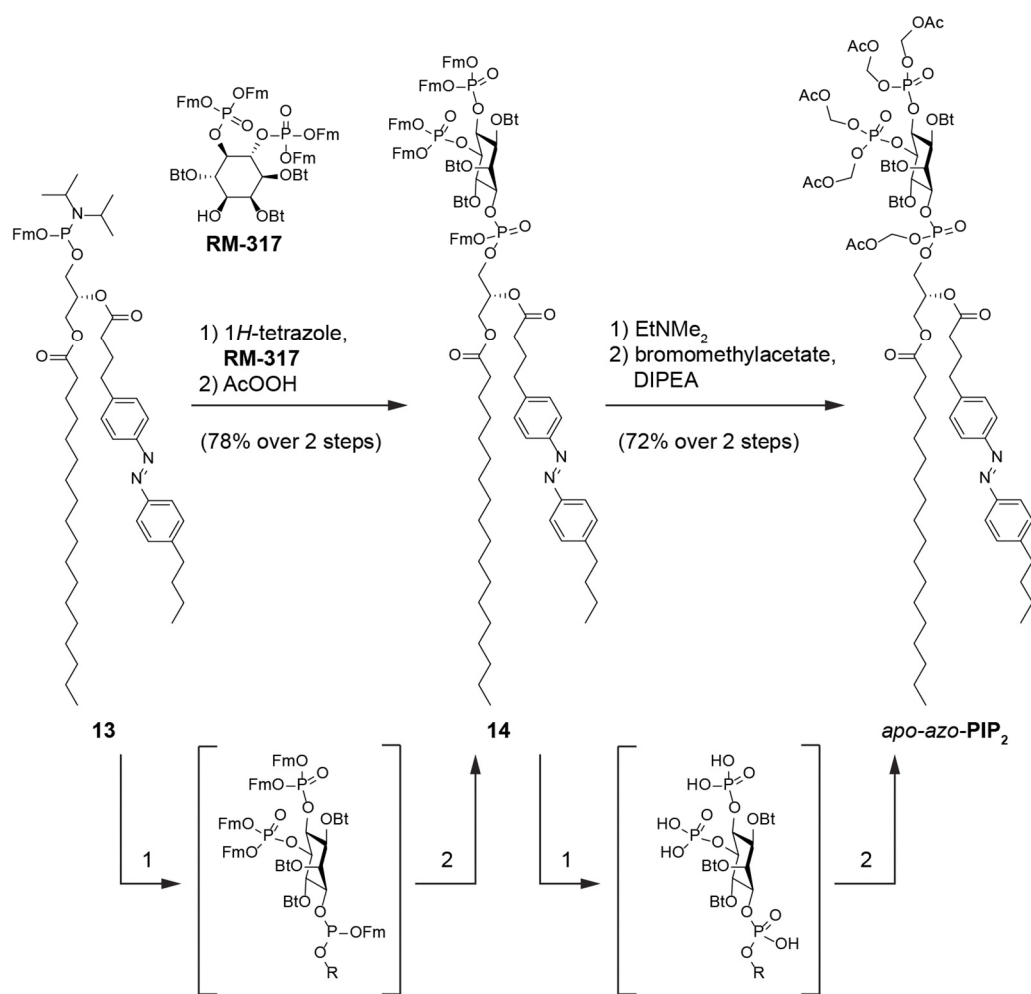


Figure 6.3 | Synthesis of a cell-permeable photoswitchable PI(4,5)P₂. A cell permeable and photoswitchable derivative of PI(4,5)P₂ was synthesized using phosphoramidite chemistry. *apo-azo-PIP*₂ was prepared from phosphoramidite **13** in 56% overall yield over 4 steps.

6.3 – Discussion

In this chapter, we have expanded the scope of photoswitchable lipids into the glycerophospholipid class. We demonstrated that phosphoramidite chemistry is a versatile and high-yielding approach to attach various polar headgroups to pre-existing photoswitchable DAGs. We could install both a simple phosphocholine headgroup and a complex protected phosphoinositide in high yields, and on a comparably large scale. Given the success of this synthetic approach, we envision that phosphoramidite chemistry could also be used to prepare even more photoswitchable glycerophospholipids, for example phosphatidylserine or phosphatidic acid derivatives.

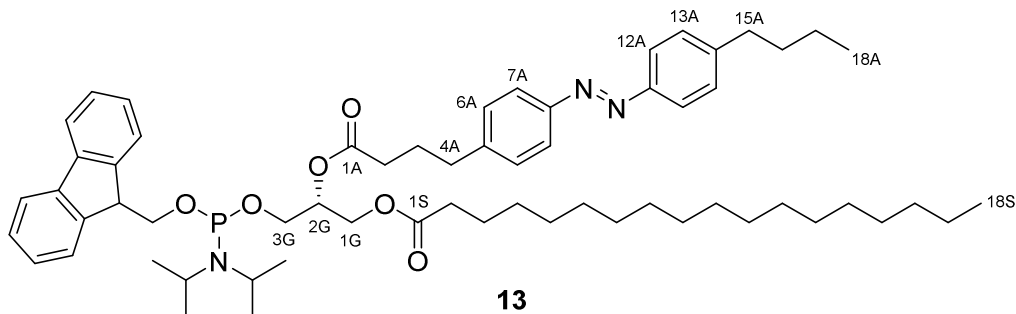
Studies using both compounds are currently underway in our lab and the labs of our collaborators. *azo-PC* is being used in collaborations with Prof. Dr. Thomas Bein (LMU Munich), Prof. Dr. Theobald Lohmüller (LMU Munich), Prof. Dr. Bert Nickel (LMU Munich), Prof. Dr. Joachim Heberle and Prof. Dr. Petra Schwillle (MPI Martinsried). A detailed discussion of this work is not within the scope of this thesis; however, we have demonstrated that *azo-PC* can be incorporated into a variety of artificial membrane systems such as monolayers and vesicles. For example, giant phospholipid vesicles consisting of 100% *azo-PC* can be prepared. Isomerization between the *trans*- and *cis*-forms allows us to control the fluidity of these vesicles and in turn manipulate their shape and structure (unpublished work from the Lohmüller lab). Further investigations utilizing *azo-PC* to control artificial membrane systems are currently ongoing. Similarly, the evaluation of *apo-azo-PIP₂* and its ability to control cell signaling is still underway in collaboration with Prof. Dr. Carsten Schultz (OHSU, EMBL Heidelberg). These efforts remain in the preliminary stage, and will not be discussed further in this thesis. However, given the wide range of physiological processes with which PI(4,5)P₂ is involved¹⁷⁵, there are a large number of potential systems which this tool could be applied to.

In summary, we anticipate that both *azo-PC* and *apo-azo-PIP₂* will be broadly applicable to studying the roles of their parent compounds in membrane biophysics and cell signaling. Similarly, novel glycerophospholipids synthesized using this phosphoramidite chemistry may be useful tools to study the roles of this vast lipid class in cell communication and beyond.

6.4 – Supporting information

6.4.1 – Compound synthesis and characterization

6.4.1.1 – 2-O-(4-(4-((4-Butylphenyl)diazenyl)phenyl)butanoyl)-3-bis-(9H-fluoren-9-ylmethyl)-N,N-diisopropylamidophosphite)-1-O-stearoyl-*sn*-glycerol (13) – (P-diastereomeric mixture)



2-O-(4-(4-((4-Butylphenyl)diazenyl)phenyl)butanoyl)-1-O-stearoyl-*sn*-glycerol

(PhoDAG-1, 1) was prepared as previously described⁵². **PhoDAG-1 (1, 408 mg, 0.614 mmol, 1.0 equiv.)** was suspended in 1*H*-tetrazole solution (1.4 mL, 0.45 M in MeCN, 1.0 equiv.) and the solvent was removed under reduced pressure. The residue was then dissolved in PhMe (5 mL) and the solvent was again removed under reduced pressure. *bis*-(9*H*-fluoren-9-ylmethyl)-*N,N*-diisopropylamidophosphite¹⁸¹ (262 mg, 0.614 mmol, 1.0 equiv.) was dissolved in dry CH₂Cl₂ (5 mL) under argon and then added to the **PhoDAG-1/1*H*-tetrazole** residue under an argon atmosphere at 0 °C. The solution was slowly warmed to room temperature and stirred for 2 h. A solution of NEt₃ in cyclohexane (2% v/v, 5 mL) was then added, and the CH₂Cl₂ was removed under reduced pressure. The solution was directly purified by column chromatography under argon (50 g SiO₂, deactivated first with 10% NEt₃ in cyclohexane, then eluent 1% NEt₃ in cyclohexane) and the product was collected in argon-filled test tubes. The solvent was then removed under reduced pressure to yield a 1:1 *P*-diastereomeric mixture of **2-O-(4-(4-((4-butylphenyl)diazenyl)phenyl)butanoyl)-3-bis-(9*H*-fluoren-9-ylmethyl)-*N,N*-diisopropyl-amidophosphite)-1-O-stearoyl-*sn*-glycerol (13, 542 mg, 89%)** as an orange oil. *Note: the product was always kept under an argon atmosphere and in the presence of NEt₃ to avoid oxidation and decomposition.*

TLC (9:1 cyclohexane:EtOAc): $R_f = 0.90$.

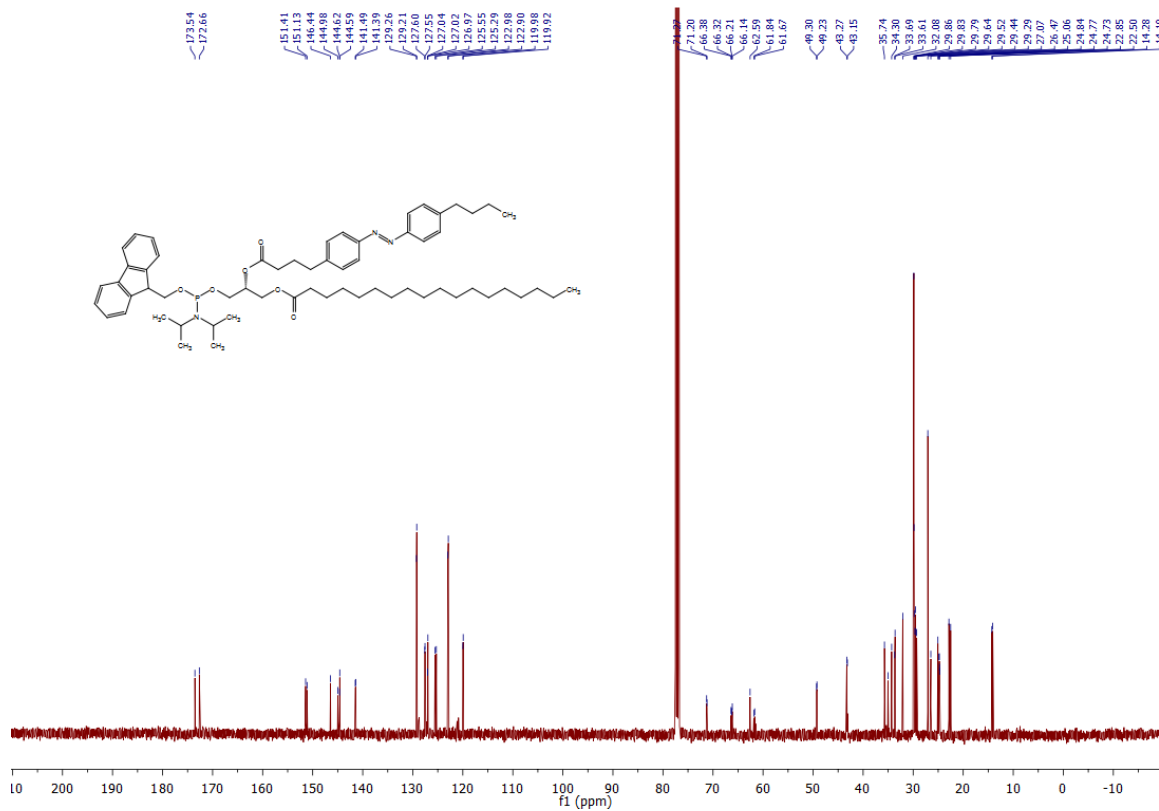
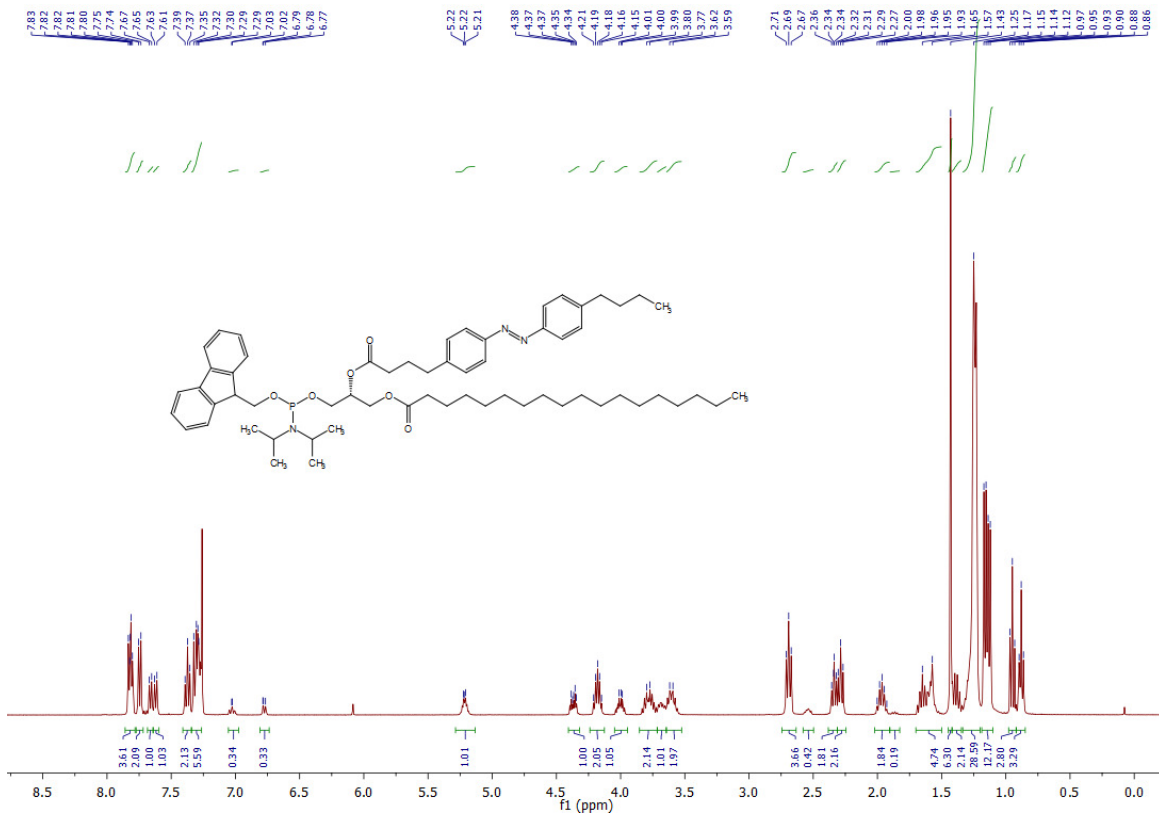
^{31}P NMR (CDCl_3 , 162 MHz, 25 °C): δ 148.2, 148.1.

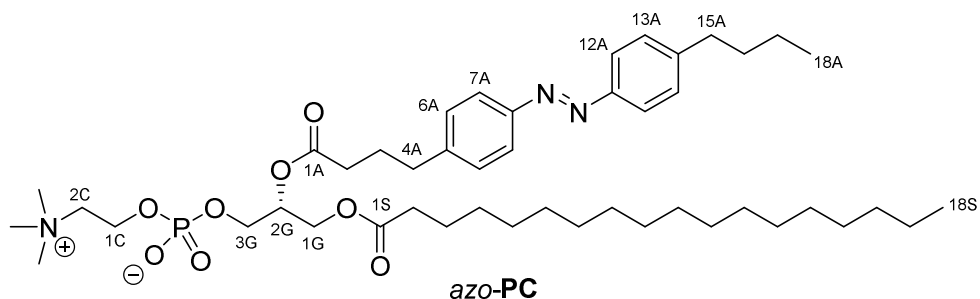
^1H NMR (CDCl_3 , 400 MHz, 25 °C): δ 7.85-7.78 (m, 4 H, H7A_{a,b}, H12A_{a,b}), 7.74 (d, 2 H, 2H_{Fm}, $J = 7.5$ Hz), 7.66 (d, 1 H, H_{Fm}, $J = 7.5$ Hz), 7.62 (d, 1 H, H_{Fm}, $J = 7.5$ Hz), 7.37 (t, 2 H, 2H_{Fm}, $J = 7.3$ Hz), 7.33-7.26 (m, 6 H, H6A_{a,b}, H13A_{a,b}, 2H_{Fm}), 5.25-5.17 (m, 1 H, H2G), 4.40-4.33 (m, 1 H, H_{Fm}), 4.22-4.14 (m, 2 H, H1G_{a,b}), 4.04-3.96 (m, 1 H, H3G_a), 3.84-3.72 (m, 2 H, 2H_{Fm}), 3.72-3.65 (m, 1 H, H3G_b), 3.65-3.53 (m, 2 H, 2H_{CH(iPr)}), 2.69 (t, 4 H, H4A_{a,b}, H15A_{a,b}, $J = 7.8$ Hz), 2.34 (t, 2 H, H2A_{a,b}, $J = 7.2$ Hz), 2.29 (t, 2 H, H2S_{a,b}, $J = 7.6$ Hz), 1.96 (q, 2 H, H3A_{a,b}), 1.70-1.53 (m, 4 H, H16A_{a,b}, H3S_{a,b}), 1.42-1.34 (m, 2 H, H17A_{a,b}), 1.33-1.21 (m, 28 H, H17S_{a,b}, 28xHS_{alk}), 1.18-1.11 (m, 12 H, 12H_{NiPr(CH3)}), 0.95 (t, 3 H, H18A_{a,b,c}, $J = 7.4$ Hz), 0.88 (t, 3 H, H18S_{a,b,c}, $J = 7.1$ Hz).

^{13}C NMR (CDCl_3 , 101 MHz, 25 °C): δ 173.5, 172.7, 151.4, 151.1, 146.4, 145.0, 144.64, 144.62, 141.5, 141.4, 129.3, 129.2, 127.62, 127.58, 127.04, 127.02, 126.97, 125.6, 125.3, 123.0, 122.9, 120.0, 119.9, 71.3, 71.2, 66.4, 66.3, 66.2, 66.1, 62.6, 61.8, 61.7, 49.3, 49.2, 43.3, 43.2, 35.7, 35.0, 34.3, 33.7, 33.6, 32.1, 29.9, 29.84, 29.81, 29.6, 29.5, 29.4, 29.3, 27.1, 26.5, 25.1, 24.84, 24.77, 24.73, 24.66, 22.9, 22.5, 14.3, 14.1.

IR (neat, ATR): $\tilde{\nu} = 2962, 2925, 2855, 1742, 1603, 1498, 1451, 1417, 1396, 1364, 1302, 1200, 1184, 1156, 1102, 1071, 1025, 976, 886, 848, 758, 739$.

HRMS (ESI⁺): m/z calcd. for $[\text{C}_{62}\text{H}_{89}\text{N}_3\text{O}_6\text{P}]^+$: 990.6489, found: 990.6519 ($[\text{M}+\text{H}]^+$).



6.4.1.2 – 2-O-(4-(4-((4-Butylphenyl)diazenyl)phenyl)butanoyl)-3-1-O-stearoyl-*sn*-glycero-3-phosphocholine (azo-PC)

Choline *p*-toluenesulfonate (85 mg, 0.19 mmol, 1.5 equiv.) and a 1*H*-tetrazole solution (1.41 mL, 0.45 M in MeCN, 5.0 equiv.) were combined and the solvent was removed under reduced pressure. The residue was then dissolved in dry CH₂Cl₂ (12 mL) and dry MeCN (12 mL) under an argon atmosphere. **2-O-(4-(4-((4-Butylphenyl)diazenyl)phenyl)butanoyl)-3-bis-(9*H*-fluoren-9-ylmethyl)-*N,N*-diisopropylamidophosphite)-1-O-stearoyl-*sn*-glycerol (**13**, 126 mg, 0.127 mmol, 1.0 equiv.) was dissolved in dry CH₂Cl₂ (12 mL), added to the choline solution and stirred for 30 min at room temperature. After consumption of **13**, the solution was cooled to –10 °C and peracetic acid (AcOOH, 19 μL, 30% in AcOH, 0.25 mmol, 2.0 equiv.) was then added. Stirring was continued and the solution was let warm to room temperature. After 40 min or completion of the reaction as shown by TLC, the solvent was removed under reduced pressure. The residue was then dissolved in MeCN (12 mL), and EtNMe₂ (12 mL) was added. The solution was then stirred for 1 h at room temperature. The solvent was then removed under reduced pressure, and the residue was purified by flash column chromatography (50 g SiO₂, 75:25:4 CHCl₃:MeOH:H₂O) to afford **2-O-(4-(4-((4-butylphenyl)diazenyl)phenyl)butanoyl)-3-1-O-stearoyl-*sn*-glycero-3-phosphocholine (azo-PC**, 94 mg, 89%) as an orange oil.**

TLC (75:25:4 CHCl₃:MeOH:H₂O): R_f = 0.2.

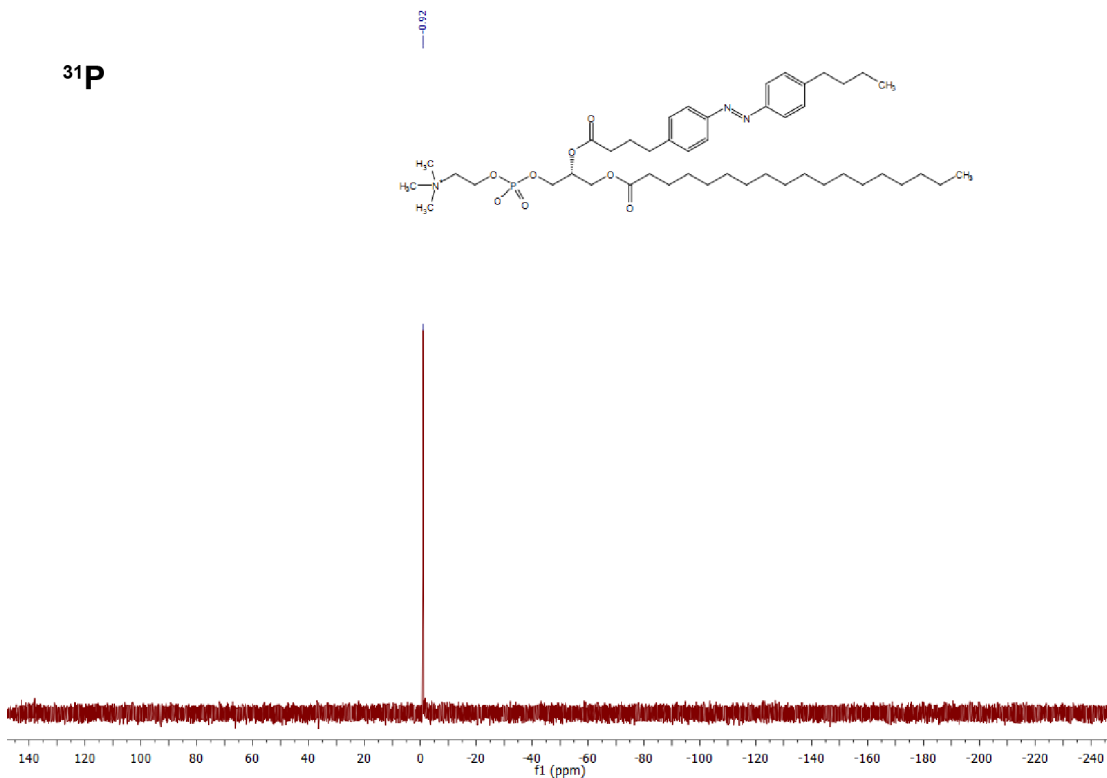
³¹P NMR (CDCl₃, 162 MHz, 25 °C): δ 0.92.

¹H NMR (CDCl₃, 400 MHz, 25 °C): δ 7.88-7.84 (m, 4 H, H7A_{a,b}, H12A_{a,b}), 7.30 (d, 4 H, H6A_{a,b}, H13A_{a,b}, J = 7.9 Hz), 5.27-5.19 (m, 1 H, H2G), 4.39 (dd, 1 H, H3G_a, J = 12.2, 2.9 Hz), 4.30 (br, 2 H, H1C_{a,b}), 4.13 (dd, 1 H, H3G_b, J = 12.1, 7.3 Hz), 3.96 (t, 2 H, H1G_{a,b}, J = 5.9 Hz), 3.78 (br, 2 H, H2C_{a,b}), 3.32 (s, 9 H, 3xCH₃), 2.74-2.63 (m, 4 H, H4A_{a,b}, H15A_{a,b}), 2.36 (t, 2 H, H2A_{a,b}, J = 7.7 Hz), 2.25 (t, 2 H, H2S_{a,b}, J = 7.8 Hz), 2.00-1.91 (m, 2 H, H3A_{a,b}), 1.68-1.58 (m, 2 H, H16A_{a,b}), 1.58-1.49 (m, 2 H, H3S_{a,b}), 1.43-1.32 (m, 2 H, H17A_{a,b}), 1.28-1.18 (m, 28 H, H17S_{a,b}, 26xHS_{alk}), 0.93 (t, 3 H, H18A_{a,b,c}, J = 7.4 Hz), 0.87 (t, 3 H, H18S_{a,b,c}, J = 7.0 Hz).

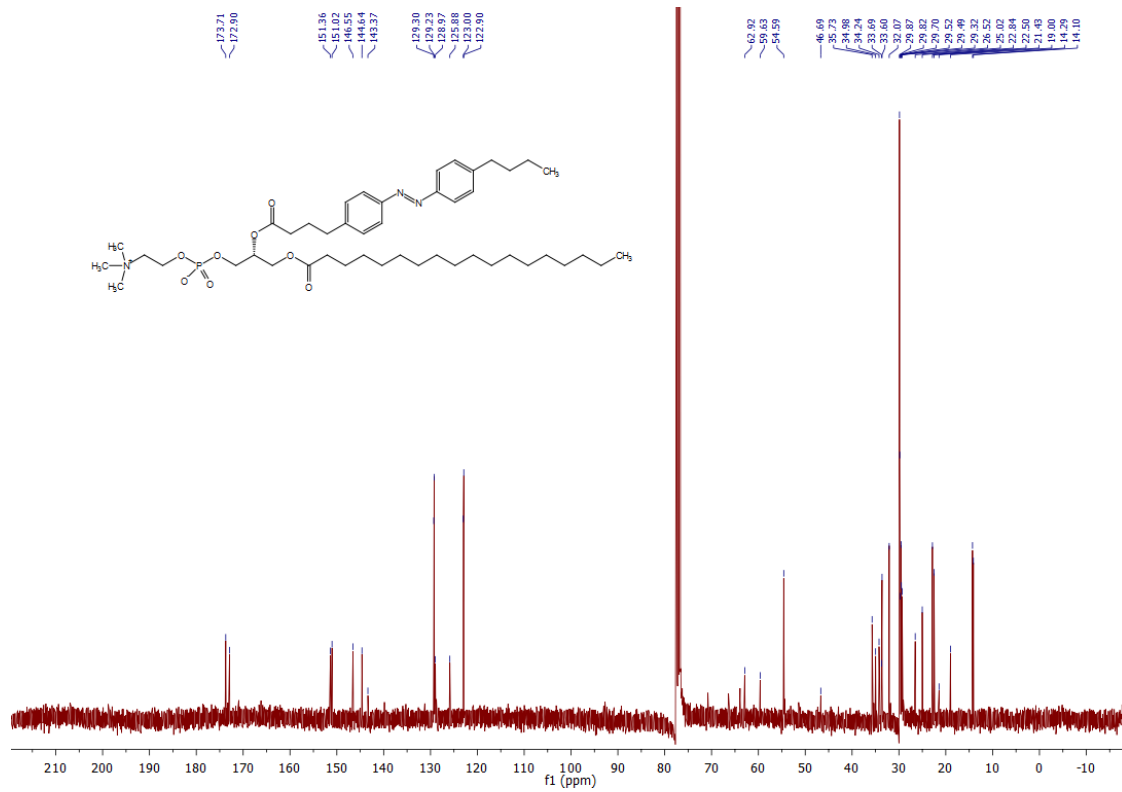
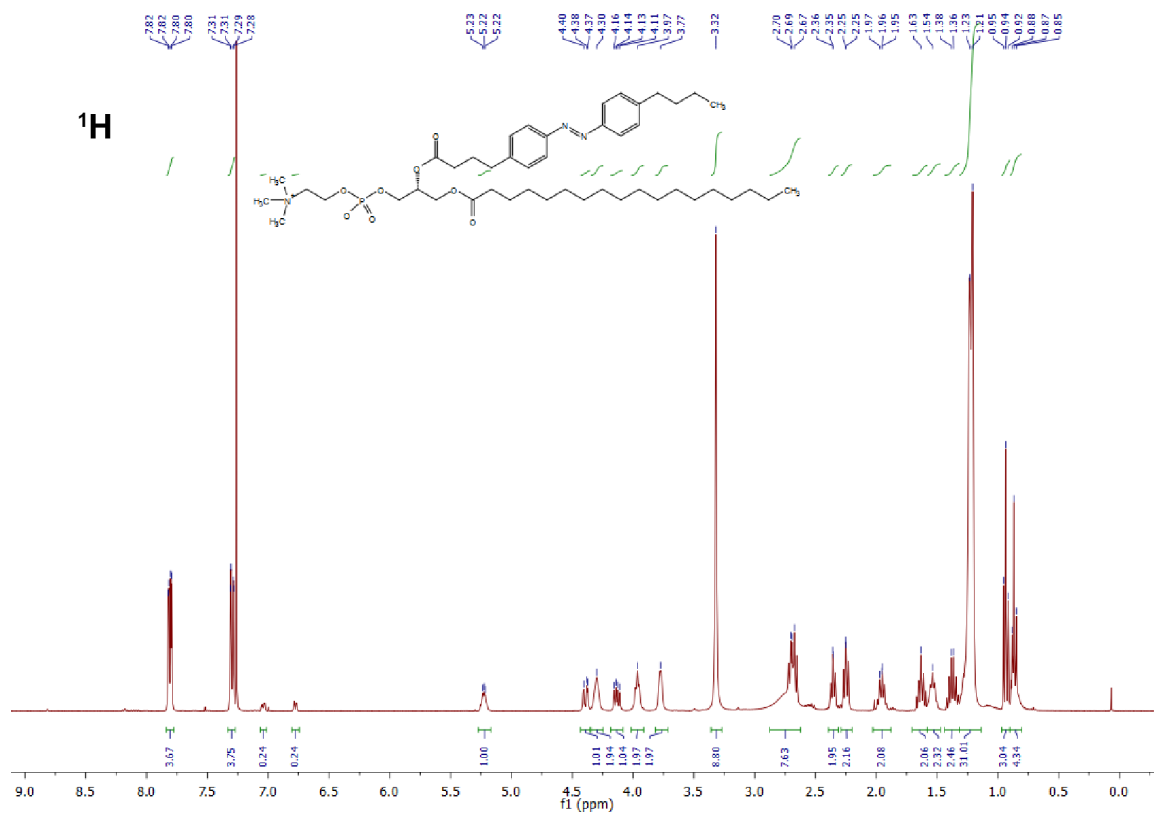
¹³C NMR (CDCl₃, 101 MHz, 25 °C): δ 173.7 (C1S), 172.9 (C1A), 151.4 (C_{azo}), 151.0 (C_{azo}), 146.6 (C_{azo}), 144.6 (C_{azo}), 143.4, 129.3 (2 C, C_{azo}), 129.2 (2 C, C_{azo}), 123.0 (2 C, C_{azo}), 122.9 (2 C, C_{azo}), 70.8, 66.5, 63.9, 62.9, 59.6, 54.6 (3 C, 3xCH₃), 46.7, 35.7, 35.0, 34.2 (C2S), 33.7 (C2A), 33.6, 32.1, 29.9, 29.8, 29.7, 29.5, 29.5, 29.3, 26.5 (C3A), 25.0 (C16A), 22.8, 22.5 (C17A), 21.4, 19.0, 14.3 (C18S), 14.1 (C18A).

IR (neat, ATR): $\tilde{\nu}$ = 2954, 2923, 2853, 1739, 1603, 1462, 1377, 1238, 1180, 1122, 1090, 1066, 1034, 1012, 969, 816, 721, 682.

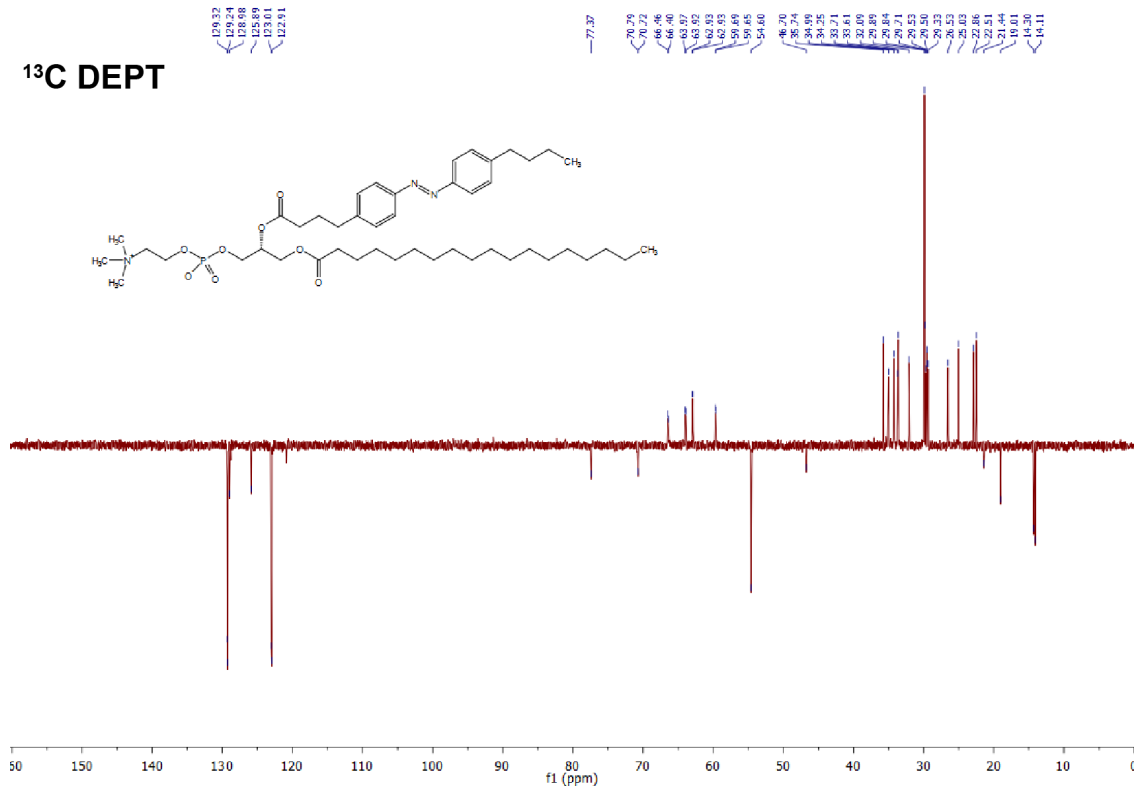
HRMS (ESI⁺): *m/z* calcd. for [C₄₆H₇₇N₃O₈P]⁺: 830.5448, found: 830.5445 ([M+H]⁺).



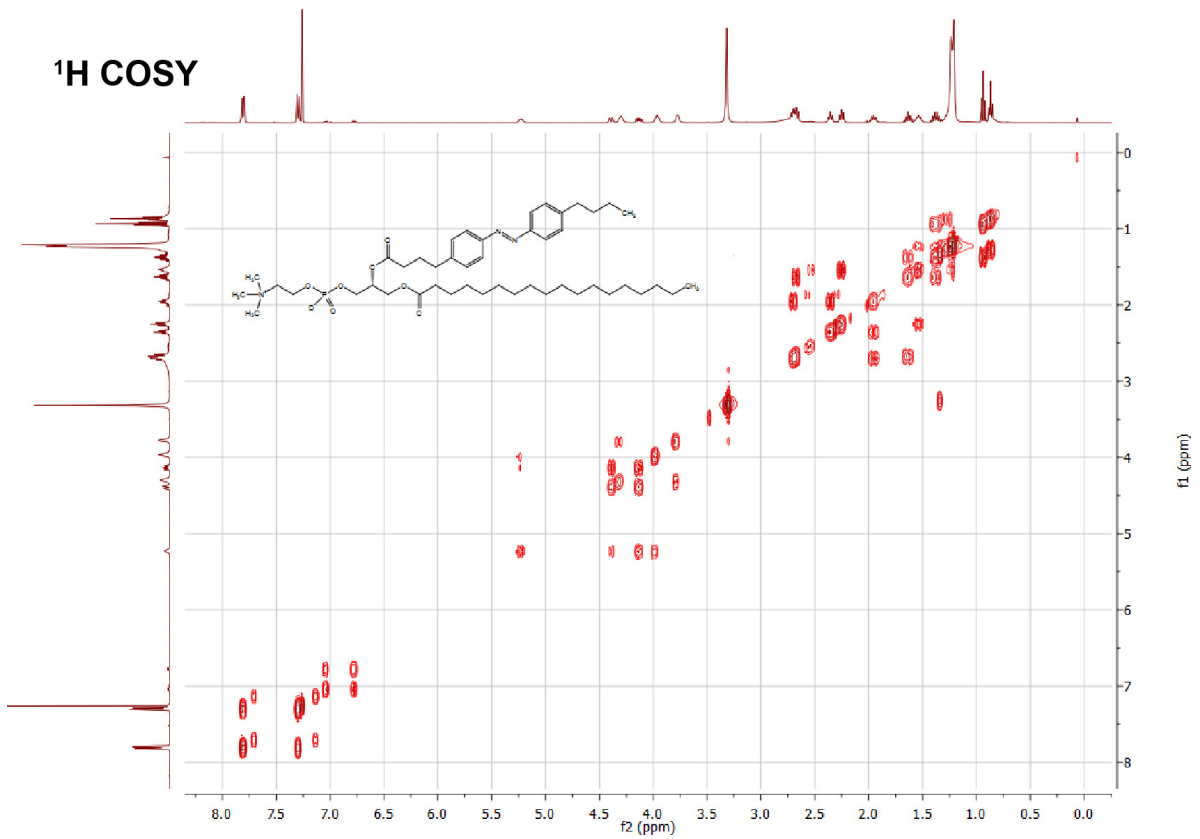
6 – Synthesis of photoswitchable glycerophospholipids

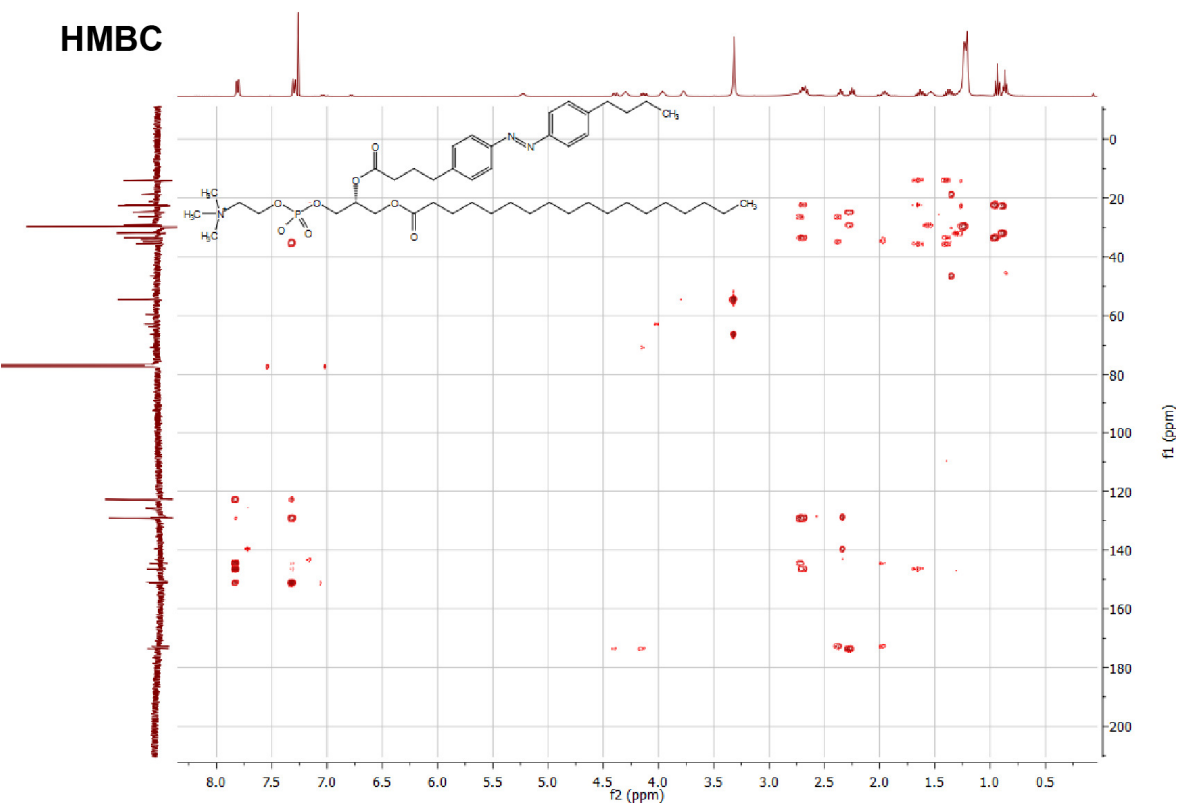
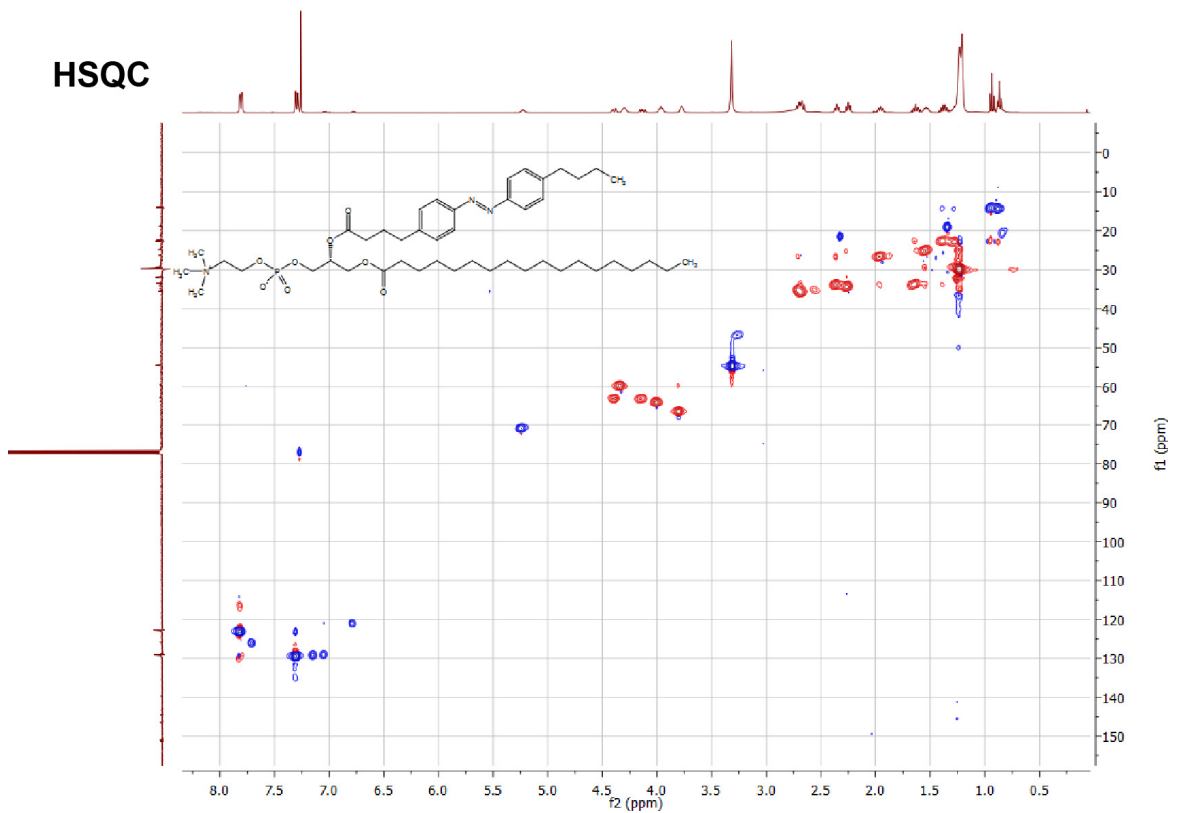


¹³C DEPT

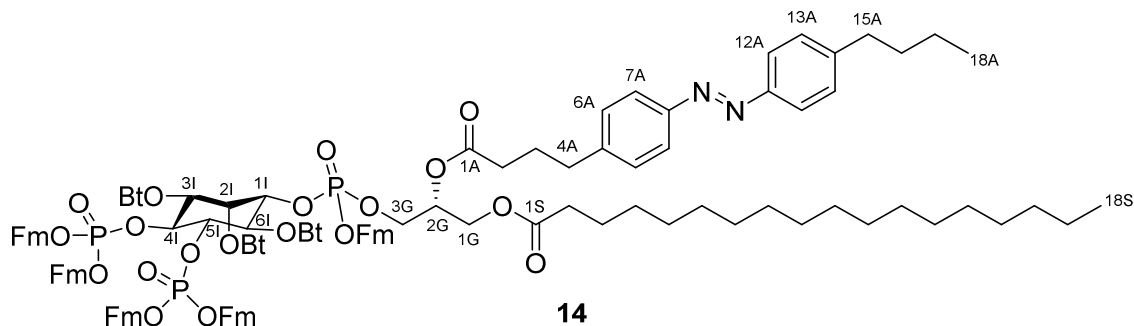


¹H COSY





6.4.1.3 – 2,3,6-*O,O,O*-Tris(butyryl)-4,5-*O,O*-bis(9*H*-fluoren-9-ylmethyl)diphosphoryl-1-*O*-(9*H*-fluoren-9-ylmethyl)-(2'-*O*-(4'-(4'-(4'-butylphenyl)diazenyl)phenyl)butanoyl)-1'-*O*-stearoyl-*sn*-glycero)phosphoryl-*myo*-inositol (14**) - (*P*-diastereomeric mixture)**



RM-317 was obtained from Prof. Dr. Carsten Schultz and Dr. Rainer Müller (OHSU, EMBL Heidelberg). **RM-317** (0.20 g, 0.16 mmol, 1.0 equiv.) was azeotroped twice from MeCN (2 mL). A 1*H*-tetrazole solution (1.7 mL, 0.45 M in MeCN, 0.77 mmol, 4.9 equiv.) was then added, and the solvent was removed under reduced pressure. **2-*O*-(4-(4-(4-Butylphenyl)diazenyl)phenyl)butanoyl)-3-bis-(9*H*-fluoren-9-ylmethyl)-*N,N*-diisopropylamidophosphite)-1-*O*-stearoyl-*sn*-glycerol (**13**, 187 mg, 0.189 mmol, 1.2 equiv.) was dissolved in dry CH₂Cl₂, and this solution was then added to the **RM-317** mixture under an argon atmosphere at room temperature. The solution was then stirred at room temperature for 3 h, diluted with dry CH₂Cl₂ (15 mL) and cooled to –20 °C. AcOOH (42 μL, 30% in AcOH, 0.25 mmol, 1.6 equiv.) was then added and the solution was let warm slowly to room temperature and stirred for 2h. The reaction was monitored by observing consumption of the phosphite by ³¹P NMR. AcOOH (30% in AcOH) was then added at room temperature in aliquots (15 μL) every 30 min until the phosphite was consumed (in this case, 2 further AcOOH aliquots were added). After completion of the oxidation, the solvents were removed under reduced pressure. The residue was purified by flash column chromatography (50 g SiO₂, gradient eluent 5:2 cyclohexane:EtOAc → 2:1 cyclohexane:EtOAc) and then preparative HPLC (C18, gradient 20% EtOAc in MeOH → to 35% EtOAc in MeOH) to afford a 1:1 *P*-diastereomeric mixture of **2,3,6-*O,O,O*-tris(butyryl)-4,5-*O,O*-bis(9*H*-fluoren-9-ylmethyl)diphosphoryl-1-*O*-(9*H*-fluoren-9-ylmethyl)-(2'-*O*-(4'-(4'-(4'-butylphenyl)diazenyl)phenyl)butanoyl)-1'-*O*-stearoyl-*sn*-glycero)phosphoryl-*myo*-inositol (**14**, 268 mg, 78%) as an orange oil.****

TLC (5:2 cyclohexane:EtOAc): R_f = 0.2.

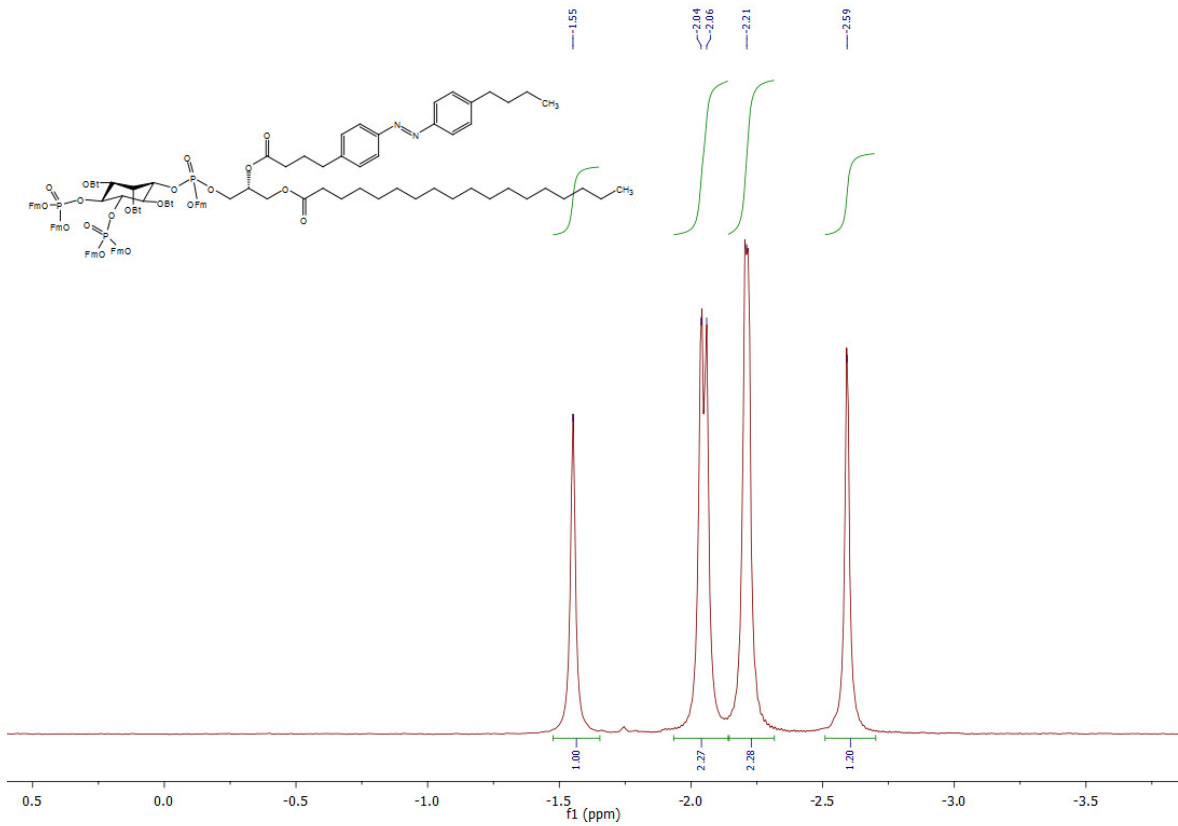
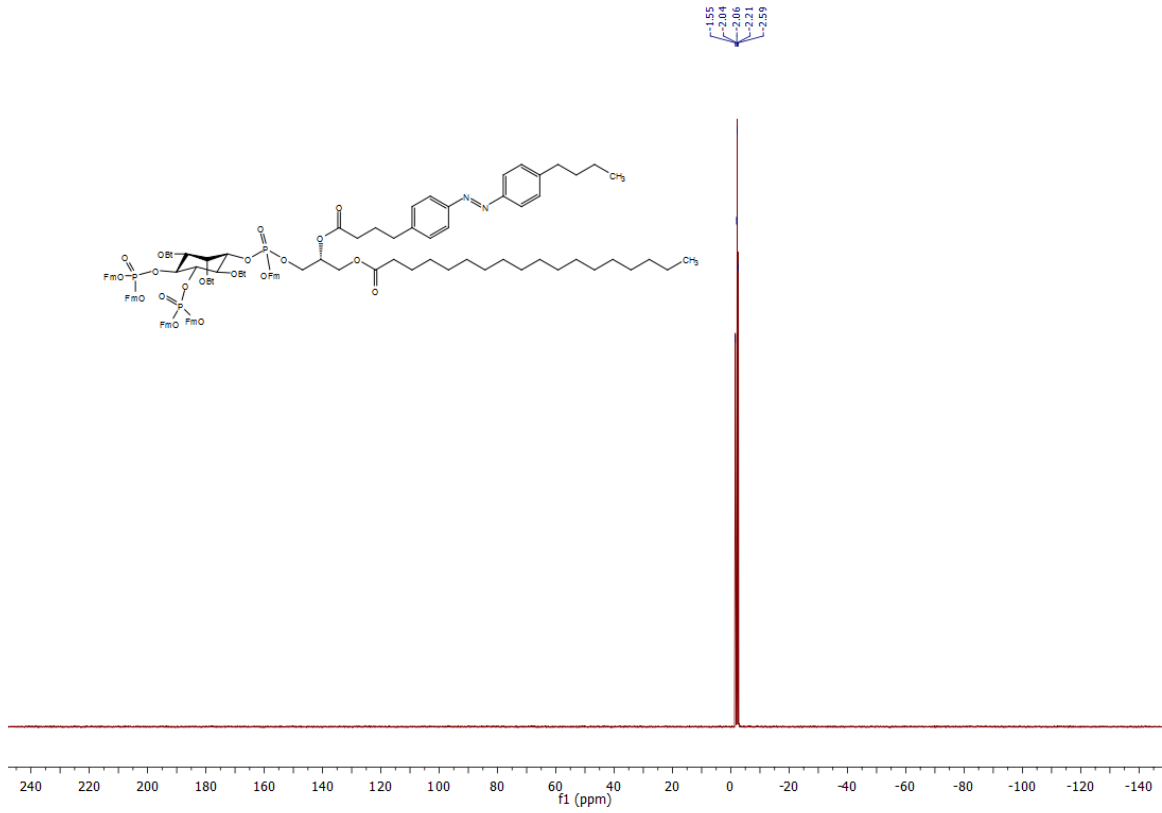
³¹P NMR (CDCl₃, 162 MHz, 25 °C) δ -1.55, -2.04, -2.06, -2.21, -2.59.

¹H NMR (CDCl₃, 400 MHz, 25 °C): δ 7.76-7.70 (m, 6 H), 7.65-7.58 (m, 5 H), 7.58-7.44 (m, 7 H), 7.40 (dd, 2 H, J = 7.5, 3.0 Hz), 7.37-6.98 (m, 26 H), 6.97-6.80 (m, 2 H), 5.57 (t, 1 H, J = 2.8 Hz), 5.42 (t, 1 H, J = 9.9 Hz), 5.19-5.09 (m, 1 H), 5.01-4.93 (m, 1 H), 4.80-4.71 (m, 1 H), 4.48-4.36 (m, 2 H), 4.35-4.24 (m, 4 H), 4.23-4.14 (m, 4 H), 4.11-3.86 (m, 15 H), 2.72-2.46 (m, 4 H), 2.33-2.22 (m, 6 H), 2.17-2.10 (m, 2 H), 2.09-1.79 (m, 4 H), 1.71-1.61 (m, 2 H), 1.60-1.48 (m, 4 H), 1.48-1.33 (m, 4 H), 1.33-1.15 (m, 26 H), 0.95 (t, 3 H, J = 7.4 Hz), 0.92-0.83 (m, 6 H), 0.81-0.73 (m, 6 H).

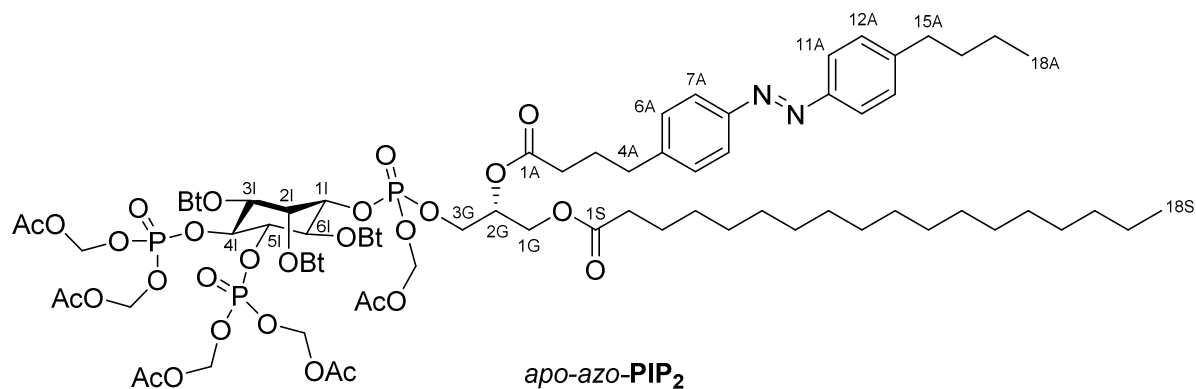
¹³C NMR (CDCl₃, 101 MHz, 25 °C): δ 173.23, 173.20, 172.9, 172.8, 172.4, 172.3, 172.2, 172.1, 151.3, 151.1, 146.4, 144.5, 144.4, 143.3, 143.2, 143.00, 142.95, 142.90, 142.87, 142.72, 142.65, 141.7, 141.60, 141.57, 141.54, 141.50, 141.46, 141.31, 141.29, 141.2, 129.2, 129.1, 128.69, 128.66, 128.3, 128.2, 128.1, 128.02, 127.97, 127.9, 127.8, 127.5, 127.4, 127.3, 127.2, 127.1, 127.0, 125.5, 125.4, 125.3, 125.2, 125.13, 125.05, 124.99, 124.9, 123.0, 122.9, 120.9, 120.8, 120.5, 120.43, 120.35, 120.3, 120.2, 120.09, 120.06, 120.02, 119.98, 119.9, 76.3, 73.1, 72.9, 69.92, 69.86, 69.6, 69.54, 69.47, 68.4, 68.3, 66.1, 65.9, 61.6, 48., 48.0, 47.9, 47.84, 47.76, 35.9, 35.8, 35.70, 35.66, 35.5, 35.3, 35.1, 34.9, 34.6, 34.0, 33.5, 33.4, 33.3, 32.0, 29.80, 29.76, 29.7, 29.6, 29.5, 29.4, 29.2, 26.2, 24.9, 22.8, 22.4, 22.4, 18.6, 18.5, 17.9, 17.7, 17.5, 14.2, 14.04, 14.00, 13.7, 13.62, 13.59, 13.56, 13.5.

IR (neat, ATR): $\tilde{\nu}$ = 3042, 2957, 2925, 2854, 1745, 1603, 1581, 1498, 1478, 1450, 1415, 1379, 1276, 1246, 1154, 1103, 1075, 1012, 989, 942, 908, 868, 841, 784, 756, 738, 727, 668.

HRMS (ESI⁺): *m/z* calcd. for [C₁₂₉H₁₄₇N₂₂O₂]²⁺: 1084.4829, found: 1084.4849 ([M+2H⁺]²⁺).



6.4.1.4 – 2,3,6-O,O,O-Tris-(butyryl)-4,5-O,O-bis(phosphoryl)-1-O-(2'-O-(4'-(4'-(4'-butylphenyl)diazenyl)phenyl)butanoyl)-1'-O-stearoyl-*sn*-glycero)phosphoryl-*myo*-inositol pentakis(acetoxymethyl) ester (*apo*-azo-PIP₂) - (*P*-diastereomeric mixture)



A solution of **2,3,6-O,O,O-tris(butyryl)-4,5-O,O-bis(9*H*-fluoren-9-ylmethyl)diphosphoryl-1-O-(9*H*-fluoren-9-ylmethyl)-(2'-O-(4'-(4'-(4'-butylphenyl)diazenyl)phenyl)butanoyl)-1'-O-stearoyl-*sn*-glycero)phosphoryl-*myo*-inositol (14, 160 mg, 73.8 μ mol, 1.0 equiv.) in CH₂Cl₂ was concentrated from MeCN (2 mL) and dried under vacuum for 30 min. The orange foam was then dissolved in MeCN (3 mL) and EtNMe₂ (3 mL) under an argon atmosphere and stirred for 30 min. The volatiles were then removed under reduced pressure and the resulting orange oil was dissolved in MeCN (2 mL) and again concentrated under reduced pressure. The resulting oil was dissolved in dry MeCN (3 mL) under an argon atmosphere, and to this solution was added sequentially DIPEA (450 μ L, 2.58 mmol, 35 equiv.) and bromomethylacetate (167 μ L, 1.7 mmol, 23.1 equiv.). The solution was stirred for 22 h at room temperature and then PhMe (8 mL) was added and the volatiles were removed under reduced pressure. The resulting orange oil was purified by preparative HPLC (C18, 8:2 MeCN:TBME) to yield **2,3,6-O,O,O-tris-(butyryl)-4,5-O,O-bis(phosphoryl)-1-O-(2'-O-(4'-(4'-(4'-butylphenyl)diazenyl)phenyl)butanoyl)-1'-O-stearoyl-*sn*-glycero)-phosphoryl-*myo*-inositol pentakis(acetoxymethyl) ester (*apo*-azo-PIP₂, 88 mg, 72%) as an orange oil.****

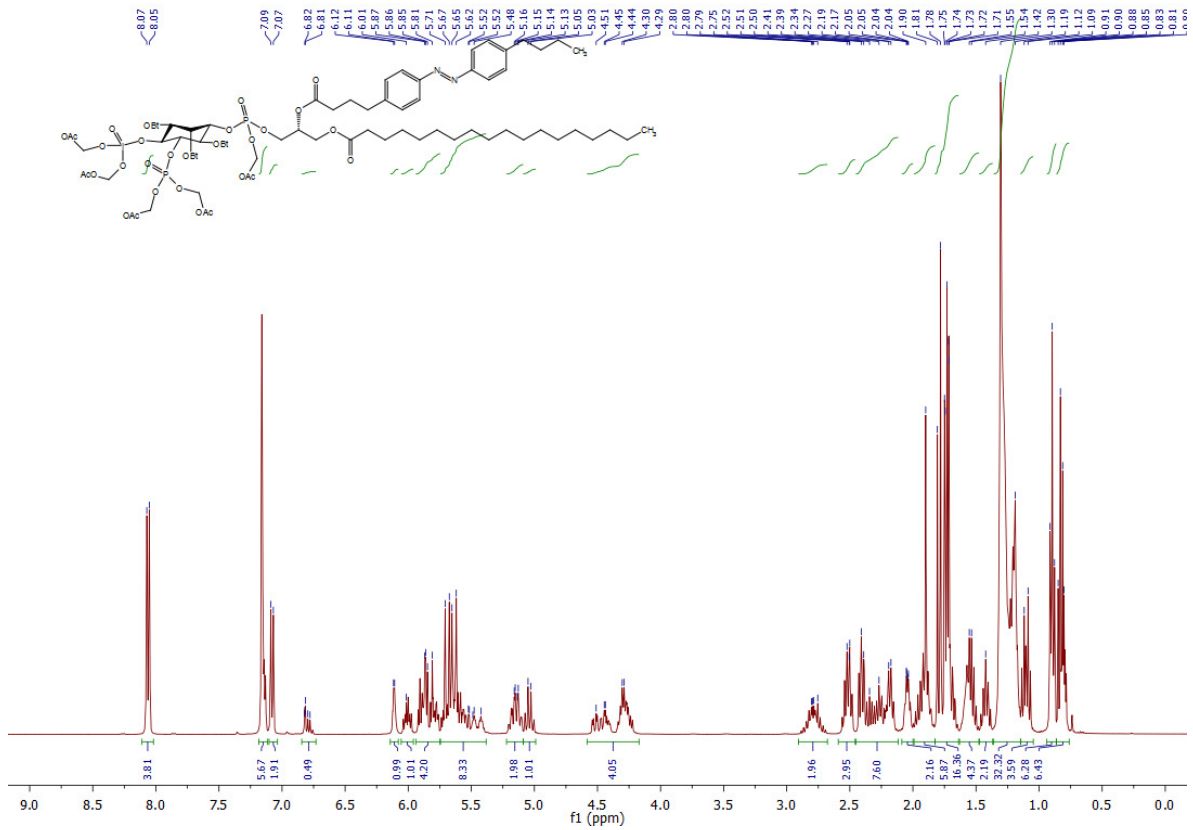
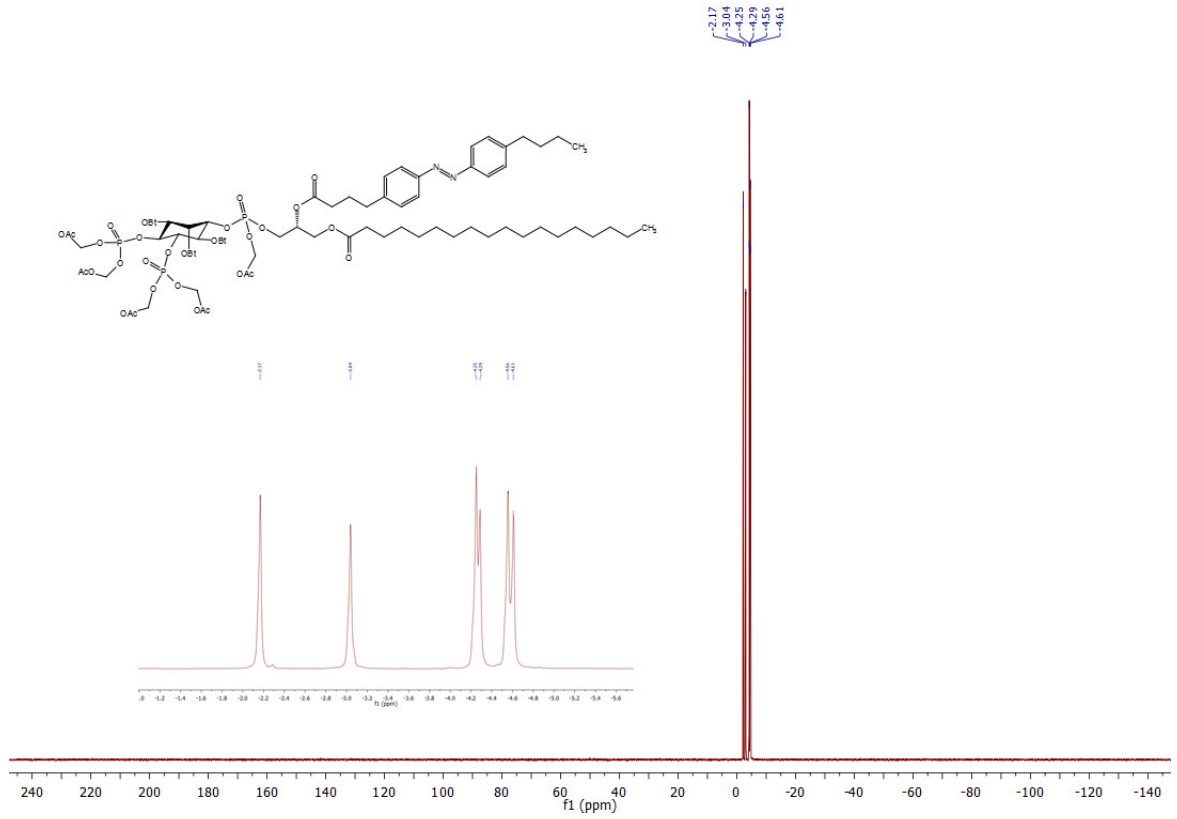
³¹P NMR (C₆D₆, 162 MHz, 25 °C): δ -2.17, -3.04, -4.25, -4.29, -4.56, -4.61.

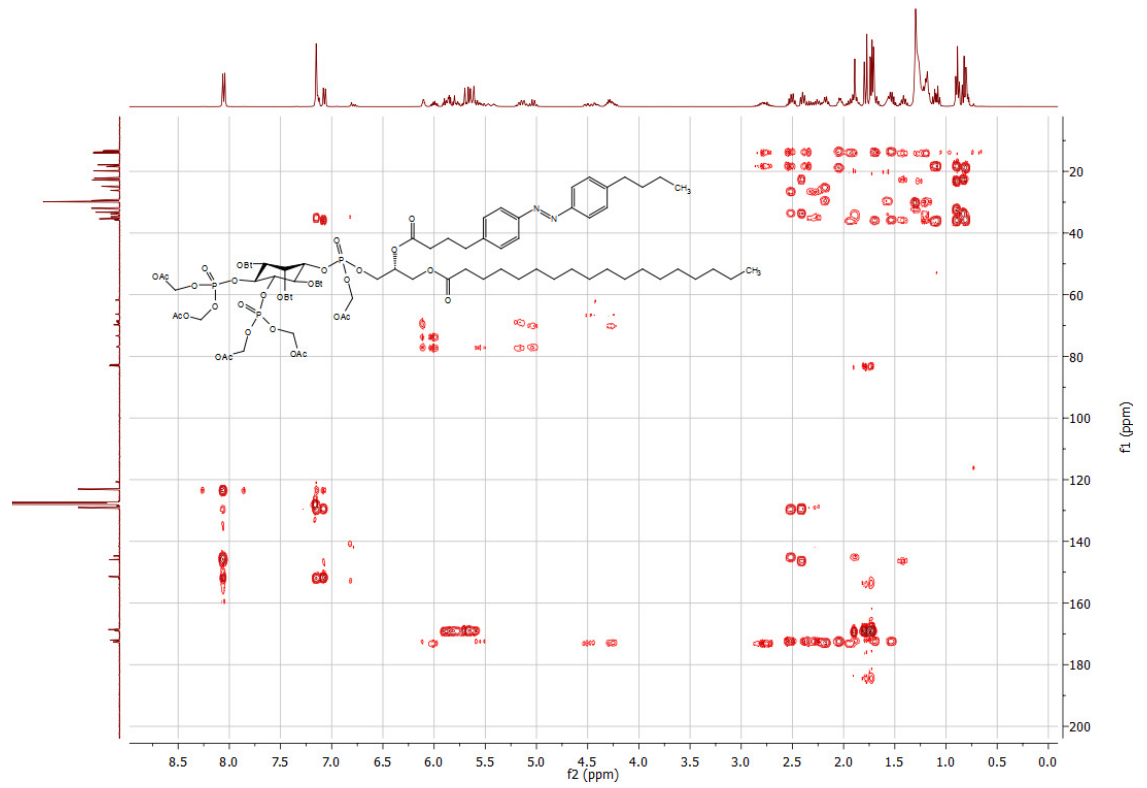
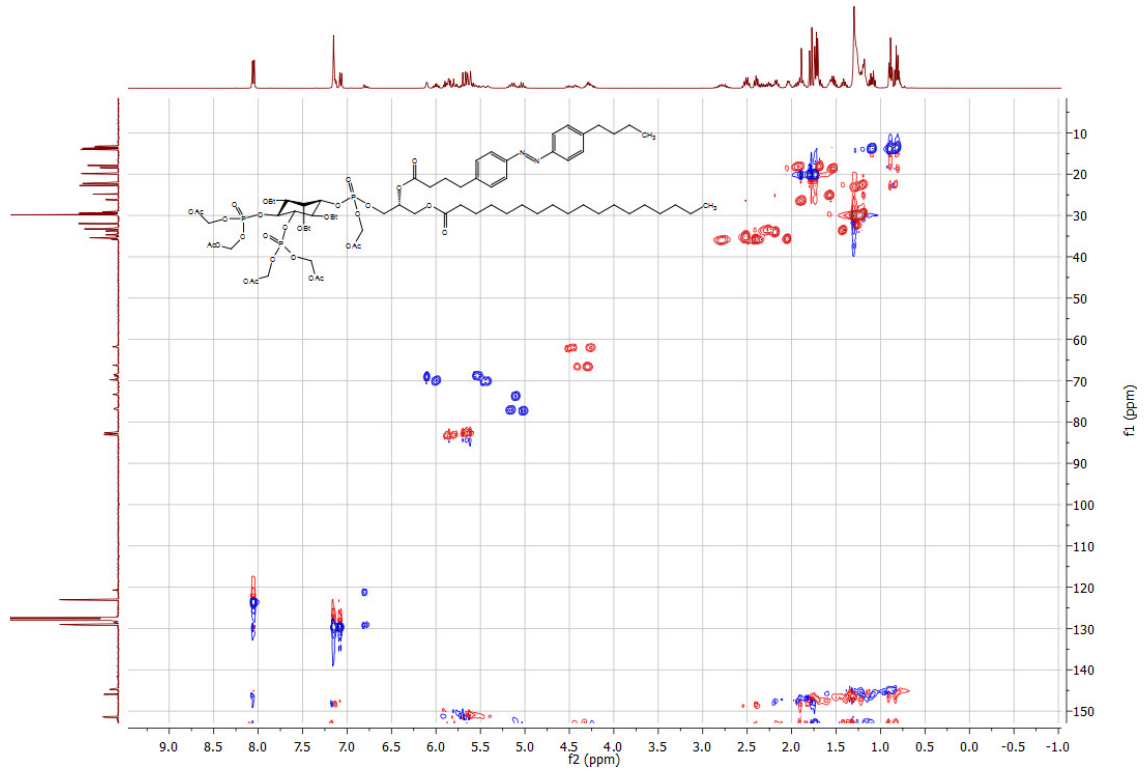
¹H NMR (C₆D₆, 400 MHz, 25 °C): δ 8.06 (d, 4 H, J = 8.1 Hz), 7.17-7.12 (m, 2 H), 7.08 (d, 2 H, J = 8.2 Hz), 6.13-6.09 (m, 1 H), 6.05-5.96 (m, 1 H), 5.93-5.75 (m, 4 H), 5.75-5.39 (m, 8 H), 5.22-5.09 (m, 2 H), 5.08-4.99 (m, 1 H), 4.56-4.19 (m, 4 H), 2.90-2.69 (m, 2 H), 2.57-2.47 (m, 2 H), 2.45-2.12 (m, 8 H), 2.09-2.00 (m, 2 H), 1.99-1.83 (m, 5 H), 1.82-1.63 (m, 16 H), 1.62-1.48 (m, 4 H), 1.47-1.37 (m, 4 H), 1.35-1.15 (m, 28 H), 1.15-1.06 (m, 3 H), 0.90 (t, 6 H, J = 6.8 Hz), 0.86-0.77 (m, 6 H).

¹³C NMR (C₆D₆, 101 MHz, 25 °C): δ 173.2, 173.1, 173.0, 172.9, 172.5, 172.4, 172.42, 172.39, 169.3, 169.2, 169.1, 168.99, 168.97, 168.9, 151.9, 151.7, 146.3, 145.14, 145.10, 129.6, 129.4, 123.5, 123.4, 121.1, 83.6, 83.5, 83.44, 83.39, 83.13, 83.09, 83.05, 83.0, 77.3, 77.1, 73.7, 70.23, 70.16, 70.1, 69.9, 69.2, 69.0, 68.9, 68.8, 66.7, 66.6, 62.2, 62.0, 36.1, 36.0, 35.93, 35.90, 35.78, 35.76, 35.7, 35.07, 35.06, 34.2, 34.1, 33.64, 33.58, 33.5, 32.4, 30.2, 30.2, 30.2, 30.0, 29.9, 29.8, 29.54, 29.52, 26.6, 26.5, 25.2, 23.1, 22.6, 22.5, 20.4, 20.31, 20.29, 20.2, 18.81, 18.76, 18.4, 18.30, 18.28, 14.4, 14.11, 14.08, 14.0, 13.9, 13.8, 13.58, 13.56.

IR (neat, ATR): $\tilde{\nu}$ = 2927, 2856, 1753, 1751, 1602, 1465, 1418, 1371, 1289, 1217, 1156, 1086, 1080, 1008, 970, 870, 827.

HRMS (ESI⁺): *m/z* calcd. for [C₇₄H₁₁₆N₂O₃₂P₃]⁺: 1637.6724, found: 1637.6773 ([M+H]⁺).





7 – Optical control of arachidonate signalling in pancreatic β -cells

7.1 – Introduction

Although minimalistic in structure and most often viewed as subunits of more complex lipids, FAs can have profound effects on cell signaling^{183–186}. Free FAs most often consist of a long, unbranched carbon chain attached to a carboxyl headgroup, which is negatively charged at physiological pH¹³. They are amphiphilic molecules with diverse structures that vary in the chain length and the level of unsaturation. As a unique example, AA is a 20 carbon FA with four non-conjugated *cis* double bonds that affects a variety of transmembrane signaling proteins including GPCRs such as the Free Fatty Acid Receptor 1, also called GPR40¹²². This GPCR responds to long-chain FAs¹⁸⁷, and stimulates a rise in $[Ca^{2+}]_i$ through the activation of PLC via $G_{\alpha q}$ ^{14,188,189}. Various ion channels, including many K^+ channels, are also affected by AA^{183,190,191}, demonstrating its complex pharmacology and vital role within the cell.

Pancreatic β -cells secrete insulin in response to stimulation by glucose (glucose-stimulated insulin secretion, GSIS). When extracellular glucose levels increase, glucose enters β -cells through glucose transporters (GLUT2), where it is metabolized to ATP. The rising cytosolic ATP/ADP ratio leads to the closure of ATP-sensitive K^+ channels (K_{ATP}) in the plasma membrane, resulting in membrane depolarization (**Fig. 7.1**). This induces opening of Ca_v , and increases the $[Ca^{2+}]_i$ concentration, triggering exocytosis of insulin secretory granules. Subsequent activation of K_v and Ca^{2+} -sensitive voltage-dependent K^+ channels leads to repolarization of the membrane, resulting in reduced Ca^{2+} -entry through Ca_v channels, and termination of insulin secretion. Usually, glucose stimulation in β -cells does not induce a single cycle of membrane depolarization-repolarization, but membrane potential oscillations that drive corresponding oscillations in $[Ca^{2+}]_i$ levels. The amplitude and the frequency of these oscillations are dependent on the interplay between K^+ and Ca^{2+} channel activity, and strongly correlate with the amount of insulin secreted^{132,135}. Under physiological conditions, GSIS is determined not only by glucose metabolism (triggering pathway) but is also complemented by the action of messengers which activate GPCRs which further potentiate insulin secretion (amplifying pathway)¹⁹². For example, GPR40 activation is known to intensify GSIS and modulate blood glucose levels^{187,193}. Given its specific localization in insulin-secreting cells, synthetic orthosteric and allosteric GPR40 agonists such as Gw-9508^{194,195} and TAK-875^{196,197} have received significant attention as potential treatments for Type 2 Diabetes Mellitus (T2DM)^{198,199}. T2DM has a complex aetiology, but can be

summarized as a failure of pancreatic β -cells to properly compensate when faced with insulin resistance²⁰⁰. A phase III clinical trial for TAK-875 was recently terminated due to off-target effects and toxicity concerns²⁰¹. Notably, the effects of GPR40 activation on insulin secretion remain elusive due to conflicting results in different experimental settings^{195,202}. As such, tools which could enable precise control over GPR40 signaling may be useful to understand its effect on β -cell function, and could even lead to the development of novel therapeutics²⁰³.

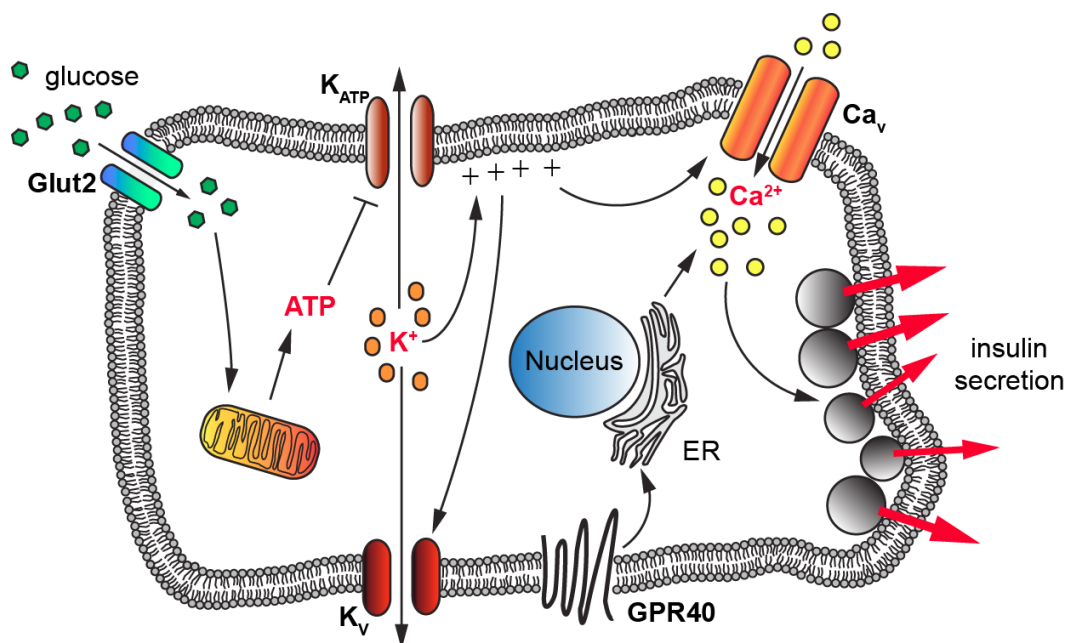


Figure 7.1 | Glucose-stimulated insulin secretion from pancreatic β -cells. Upon uptake into the pancreatic β -cell, glucose is metabolized into ATP. The rising ATP/ADP ratio inhibits K_{ATP} which causes membrane depolarization and the opening of Ca_v . The resulting increased $[Ca^{2+}]_i$ triggers the fusion of secretory granules and the release of insulin. K_v channels work to repolarize the cell, generating oscillations in $[Ca^{2+}]_i$. GPR40 stimulation also leads to increased $[Ca^{2+}]_i$, further potentiating GSIS.

Previous studies in our labs have focused on the development of photoswitchable anti-diabetics such as sulfonylureas and incretins, and have already placed pancreatic β -cell function under the precise spatiotemporal control of light^{204–208}. Complementary to this approach, we showed that a set of photoswitchable FAs, called FAAzOs, can be used as modular building blocks for incorporation into photoswitchable lipids such as DAG^{51–53}, which also affect β -cell $[Ca^{2+}]_i$ activity and insulin secretion. These results suggested that the FAAzOs can mimic highly unsaturated FAs like AA when conjugated to other polar headgroups. However, the pharmacology of the FAAzOs alone remains largely unexplored. Given the sensitivity of GPR40 to unsaturated FAs, we hypothesized that the FAAzOs themselves could

enable optical control of this GPCR. As β -cell activity is known to be regulated by GPR40 and several AA-sensitive K^+ channels, we envisioned they could serve as the perfect model system to evaluate the activity of the FAAzos. Herein, we describe our approach towards to the optical control of FA signaling in the β -cell. We demonstrate that the FAAzos can mimic AA at several different protein targets, enabling photopharmacological control of β -cell function via a new mechanism.

7.2 – Results

7.2.1 – Design and synthesis of photoswitchable arachidonate mimics

Although GPR40 is known to be activated by long-chain FAs such as arachidonic and linoleic acid¹⁴, various aromat-containing carboxylic acids such as Gw-9508 are known to produce a similar effect¹⁸⁵ (**Fig. 7.2a**). Therefore, we reasoned that a photoswitchable FA such as **FAAzo-4** could act as GPR40 agonists as well (**Fig. 7.2b**). We also recognized that the benzyl-aniline moiety of Gw-9508 could be easily substituted by a diazene, and would afford a photoswitchable ligand with little disturbance to the overall size and structure of the drug. Therefore, we synthesized the “azolog” of Gw-9508³⁵, **FAAzo-10**, using the Mills reaction in two steps and 45% overall yield (**Fig. 7.2c**). Like **FAAzo-4**, **FAAzo-10** behaved as a regular azobenzene and could be isomerized between its thermally stable *trans*-form to the *cis*-form with UV-A light (**Fig. 7.2d**). The process could be reversed on irradiation with blue light, and photoswitching could be repeated over many cycles.

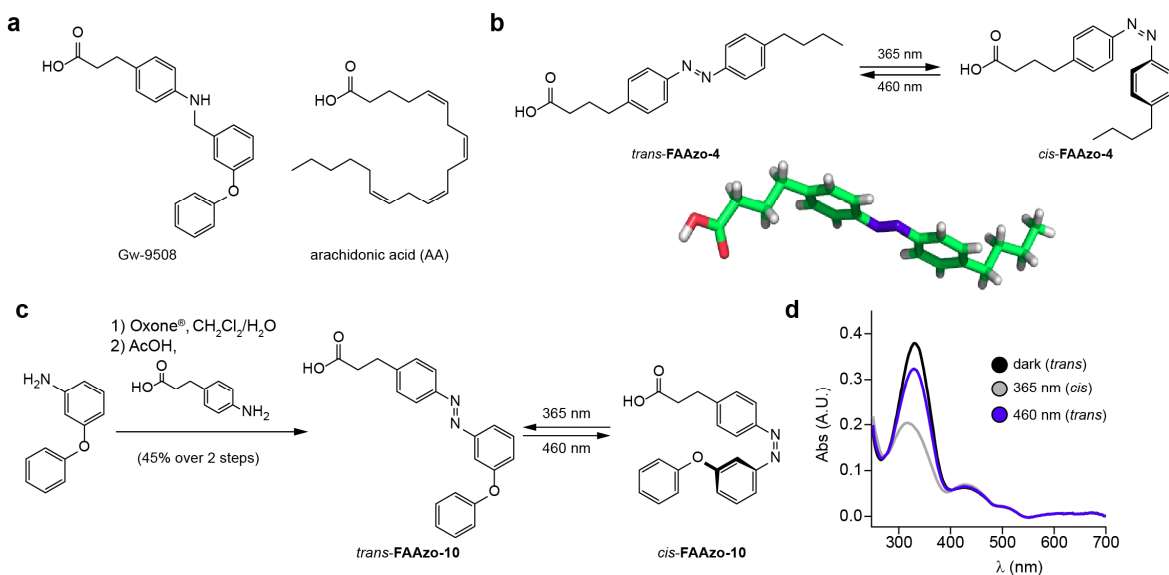


Figure 7.2 | Design and synthesis of photoswitchable GPR40 agonists. (a) The chemical structures of Gw-9508 and AA. (b) Chemical formula and crystal structure of the photoswitchable fatty acid **FAAzo-4**. (c) Chemical synthesis of **FAAzo-10**, the azolog of Gw-9508. (d) The UV-Vis spectra of **FAAzo-10** in its dark-adapted (black), UV-adapted (gray) and blue-adapted (blue) states (20 μ M in PBS).

7.2.2 – Photolipids enable optical control of GPR40 in HeLa cells

Using the genetically encoded fluorescent $[Ca^{2+}]_i$ reporter R-GECO¹²³, we first characterized the effects on GPR40 in HeLa cells with confocal fluorescence microscopy. When transfected with GPR40, a portion of cells displayed spontaneous $[Ca^{2+}]_i$ oscillations without the addition of any external stimuli (**Fig. 7.3a**). Gw-9508 induced a GPR40-dependent increase in the rate and intensity of $[Ca^{2+}]_i$ oscillations that was not affected by UV-irradiation (**Fig. 7.3b**, **Fig. 7.4a**). In cells without GPR40, no response was observed (**Fig. 7.4b,c**). Complementary to this result, we discovered that both **FAAzo-4** (**Fig. 7.3c**, **Fig. 7.4d**) and **FAAzo-10** (**Fig. 7.3d,e**) enabled optical control of $[Ca^{2+}]_i$ levels in HeLa cells expressing GPR40. In both cases, the *trans*-form stimulated an increase in $[Ca^{2+}]_i$. On isomerization to *cis* with $\lambda = 375$ nm irradiation, a sharp decrease in the $[Ca^{2+}]_i$ level was observed. For both compounds, after termination of the irradiation the effect was reversed and an increase in $[Ca^{2+}]_i$ levels was observed. **FAAzo-10** was more potent and active at a much lower concentration when compared to **FAAzo-4** (**Fig. 7.4e**). In control cells lacking GPR40, spontaneous $[Ca^{2+}]_i$ oscillations were not observed, and neither **FAAzo-10** nor **FAAzo-4** affected $[Ca^{2+}]_i$ levels (**Fig. 7.4f-h**). In all cells, histamine (HIS, 10 μ M) was used as a positive control and triggered a large increase in $[Ca^{2+}]_i$ levels on application, independent of GPR40 expression (**Fig. 7.4**). To investigate the downstream effects of GPR40 activation, we expressed the fluorescent DAG reporter C1-GFP, which translocates to the plasma membrane in response to increased DAG-levels following PLC activation¹²⁰. *trans*-**FAAzo-10** triggered C1-GFP translocation towards the plasma membrane, which could be reversed following isomerization to *cis*-**FAAzo-10** (**Figure 7.3f**). This effect could be repeated over many cycles, demonstrating that oscillations in GPR40 and its downstream effectors could be controlled with light.

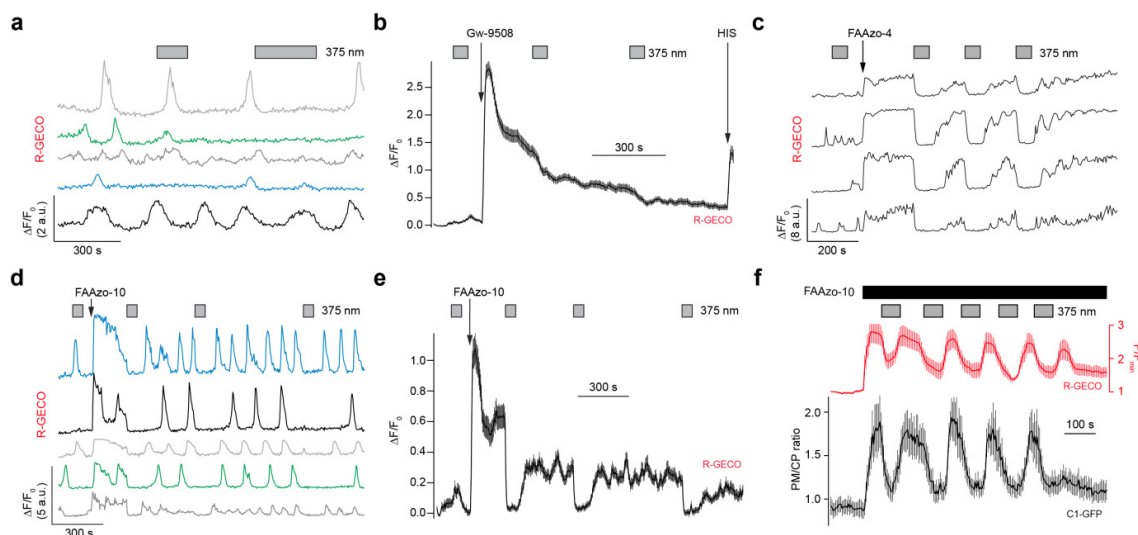


Figure 7.3 | Optical control of GPR40 in HeLa cells. In HeLa cells expressing GPR40, C1-GFP and the $[Ca^{2+}]_i$ reporter R-GECO: **(a)** Spontaneous oscillations of $[Ca^{2+}]_i$ levels were observed without the addition of any compound. **(b)** Gw-9508 (200 nM) caused an increase in $[Ca^{2+}]_i$ levels that was not affected by $\lambda = 375$ nm irradiation. HIS (10 mM) application caused an increase in $[Ca^{2+}]_i$ ($n = 179$ cells from two experiments). **(c)** *trans*-FAAzo-4 (25 μ M) increased $[Ca^{2+}]_i$ levels, and isomerization to *cis*-FAAzo-4 reversed this effect. **(d,e)** FAAzo-10 (200 nM) also behaved as a photoswitchable GPR40 agonist that was more potent in the *trans*-form. Displayed as **(d)** individual $[Ca^{2+}]_i$ traces from representative cells and **(e)** the average $[Ca^{2+}]_i$ level for many cells ($n = 157$ cells from two experiments). **(f)** The fluorescent DAG sensor C1-GFP translocated to the plasma membrane alongside the increase in $[Ca^{2+}]_i$ when stimulated by *trans*-FAAzo-10 (20 μ M, $n = 10$ cells from one representative experiment). Translocation (black) is displayed as the plasma membrane to cytoplasm (PM/CP) C1-GFP fluorescence intensity ratio. Error bars were calculated as \pm s.e.m.

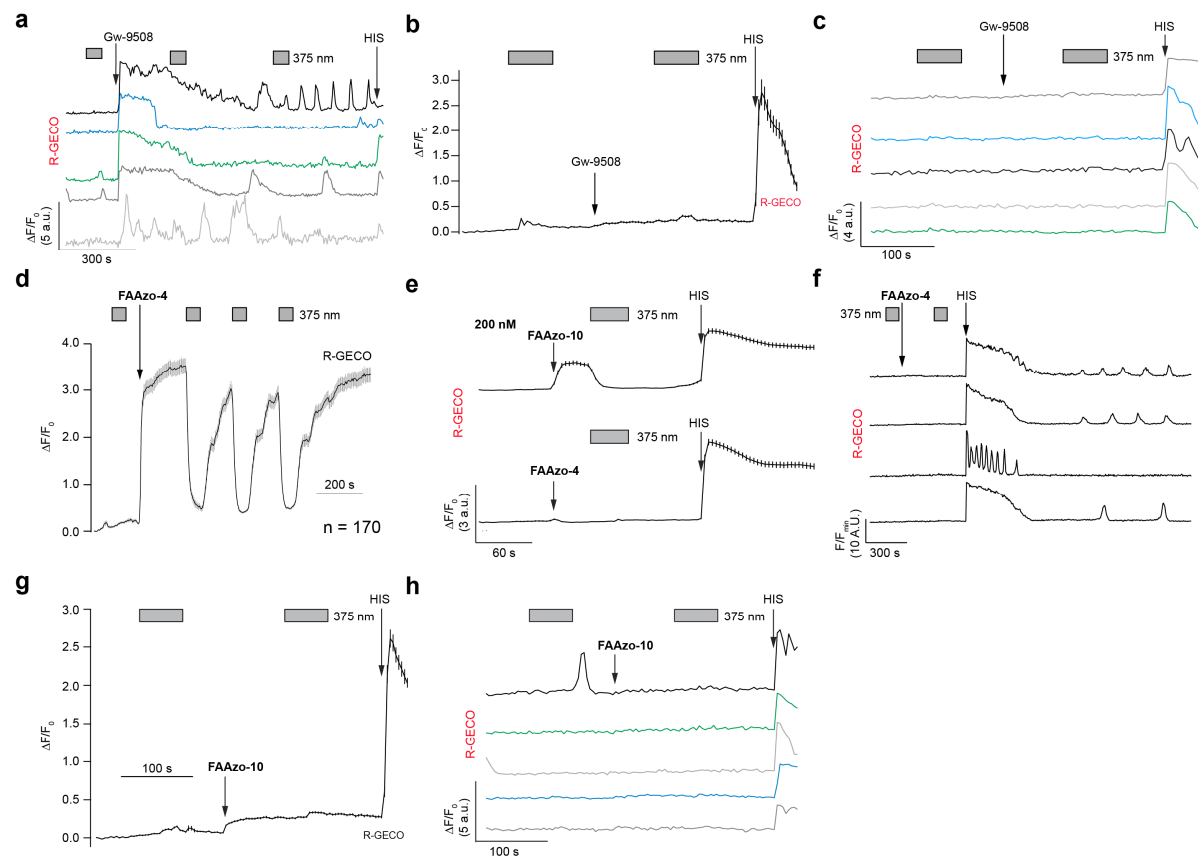


Figure 7.4 | Optical control of GPR40 in HeLa cells. $[Ca^{2+}]_i$ in HeLa cells was monitored using R-GECO. (a) When co-transfected with GPR40, application of Gw-9508 (200 nM) caused an increase in the $[Ca^{2+}]_i$ and oscillation frequency. This was not affected by $\lambda = 375$ nm irradiation. (b,c) Without GPR40, Gw-9508 (up to 20 μ M) did not affect $[Ca^{2+}]_i$ levels. Displayed as (b) an average of many cells ($n = 65$ cells from one experiment) and (c) individual traces from representative cells. HIS (10 mM) was used as a positive control and caused an increase in $[Ca^{2+}]_i$. (d) When co-transfected with GPR40, *trans*-FAAzo-4 (25 μ M) triggered an increase in $[Ca^{2+}]_i$, while isomerization to *cis*-FAAzo-4 reversed this effect ($n = 170$ cells from two experiments). (e) At 200 nM, FAAzo-10 ($n = 153$ cells from two experiments) was active on GPR40 while FAAzo-4 ($n = 211$ cells from two experiments) was not. (f-h) In cells lacking GPR40, neither (f) FAAzo-4 (25 μ M) nor (g,h) FAAzo-10 (200 nM) significantly affected $[Ca^{2+}]_i$ levels. Displayed as (f,h) representative traces from individual cells and (g) the average $[Ca^{2+}]_i$ level from many cells ($n = 159$ cells from two experiments). HIS (10 μ M) was used as a positive control to induce $[Ca^{2+}]_i$. Error bars were calculated as \pm s.e.m.

7.2.3 – Optical control of K⁺ channel activity in β -cells

We used whole-cell electrophysiology in dissociated mouse β -cells to examine the effect of our photoswitchable ligands on K_v channel conductance, a major determinant of the [Ca²⁺]_i oscillation frequency. Like AA, which is known to inactivate K_v^{15,52,136} channels in β -cells, *trans*-**FAAzo-10** reduced channel conductance in the IV-curve in the dark or under blue light (**Fig. 7.5a**). On isomerization to *cis*-**FAAzo-10**, K_v channel activity was restored to a comparable level as the vehicle controls (**Fig. 7.5b**). Application of Gw-9508 reduced channel conductance to a comparable level (**Fig. 7.5b**). Advantageously, **FAAzo-10** could be switched ON and OFF over several cycles, effectively replicating washin and washout of Gw-9508, using only a light stimulus (**Fig. 7.5c**). Voltage ramps were then acquired under varying irradiation wavelengths between $\lambda = 350$ -450 nm. This action spectrum demonstrated that K_v activity could be precisely tuned by changing the irradiation wavelength (**Fig. 7.5d,e**). **FAAzo-4** (50 μ M) behaved in a similar fashion, and reversibly inactivated K_v more strongly in the *trans*-configuration (**Fig. 7.6**).

Gw-9508 was previously shown to potentiate K_{ATP} channels in mouse β -cells¹⁹⁴. Similarly, AA is known to affect K_{ATP} channels in other cell types, however contradicting activities have been observed under different experimental conditions²⁰⁹. We first measured the whole-cell K_{ATP} current from mouse β -cells without extracellular glucose. IV-curves were measured between -110 to -50 mV to exclude any effect of the K_v channels. After dialysis of the cytoplasm with intracellular buffer, the K_{ATP} current increased to a steady state (**Fig. 7.7a,b**). In line with previous reports, Gw-9508 increased the K_{ATP} conductance further, and AA acted in a similar fashion (**Fig. 7.7a,b**). Interestingly, *trans*-**FAAzo-10** behaved differently, and reduced the K_{ATP} conductance, while isomerization to *cis*- reversed the effect entirely (**Fig. 7.7a,c**). Like the effects observed on the K_v channels, **FAAzo-10** activity at K_{ATP} could be fine-tuned by altering the irradiation wavelength (**Fig. 7.7d**). Under blue irradiation the K_{ATP} current was reduced, while the blockade was reversed under UV-A irradiation. UV-A or blue irradiation alone did not affect the K_{ATP} current (**Fig. 7.7e**).

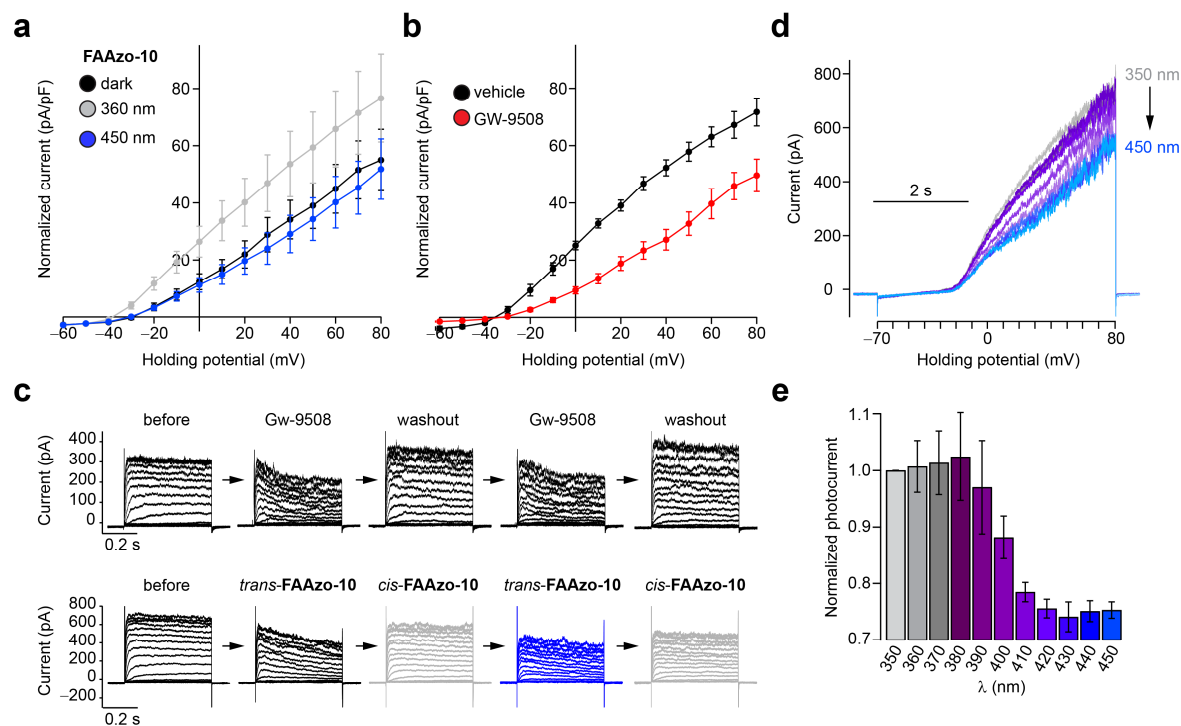


Figure 7.5 | Optical control of β -cell K_v channel activity with FAAzo-10. The whole-cell K_v channel current in dissociated wt mouse β -cells was measured using electrophysiology. **(a)** An IV-plot revealed that in the dark and under blue light, *trans*-FAAzo-10 (20 μ M) reduced the whole-cell K_v current ($n = 7$ cells from 3 animals). Isomerization to *cis*-FAAzo-10 with UV-A light reversed this effect comparable to **(b)** the vehicle control ($n = 6$ cells from 3 animals). Gw-9508 (50 μ M) reduced the K_v conductance to a similar degree ($n = 8$ cells from 2 animals). **(c)** FAAzo-10 could be activated and inactivated over several cycles with irradiation, producing a similar effect to Gw-9508 washin and washout. Shown are IV-steps from -70 to $+80$ mV from representative cells. **(d,e)** An action spectrum between $\lambda = 350$ -450 nm showed that K_v activity could be fine-tuned by changing the irradiation wavelength. Shown are **(d)** sequential voltage ramps (-70 to $+80$ mV) from a representative cell and **(e)** the normalized (to $I_{350\text{nm}}$) current under each λ ($n = 3$ cells from 2 animals). Error bars were calculated as \pm s.e.m.

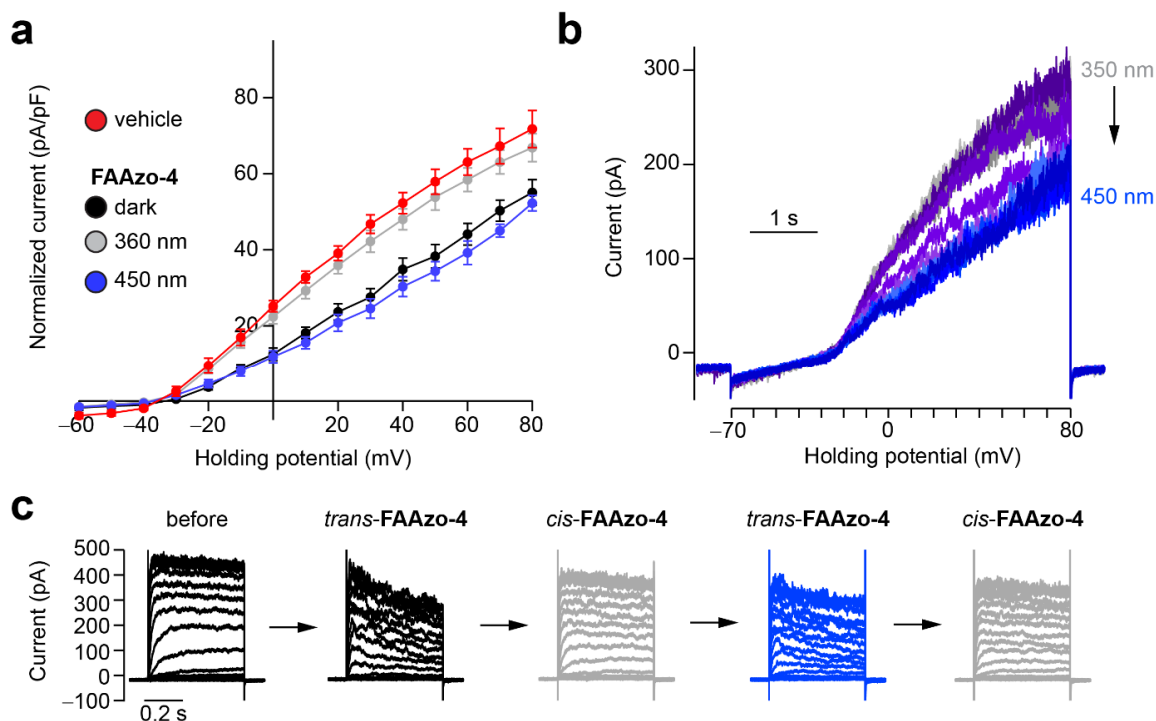


Figure 7.6 | Optical control of β -cell voltage activated K^+ channel activity with FAAzo-4.

The whole-cell K_v channel current in dissociated wt mouse β -cells was measured using electrophysiology. (a) An IV-plot revealed that in the dark (black) under blue (blue) irradiation, *trans*-FAAzo-4 (50 μ M) reduced the whole-cell K_v current ($n = 6$ cells from 2 animals). Isomerization to *cis*-FAAzo-4 with UV-A light (gray) reversed this effect comparable to the vehicle control (red) ($n = 6$ cells from 3 animals). (b) An action spectrum between $\lambda = 350$ -450 nm demonstrates that K_v activity could be fine-tuned with the irradiation wavelength. Shown are sequential voltage ramps (-70 to $+80$ mV) from a representative cell. (c) Isomerization of FAAzo-4 between its *trans*- and *cis*- forms could reversibly inactivate and activate K_v channels over several cycles. Shown are overlaid sequential IV-steps from -70 to $+80$ mV from a representative cell. Error bars were calculated as \pm s.e.m.

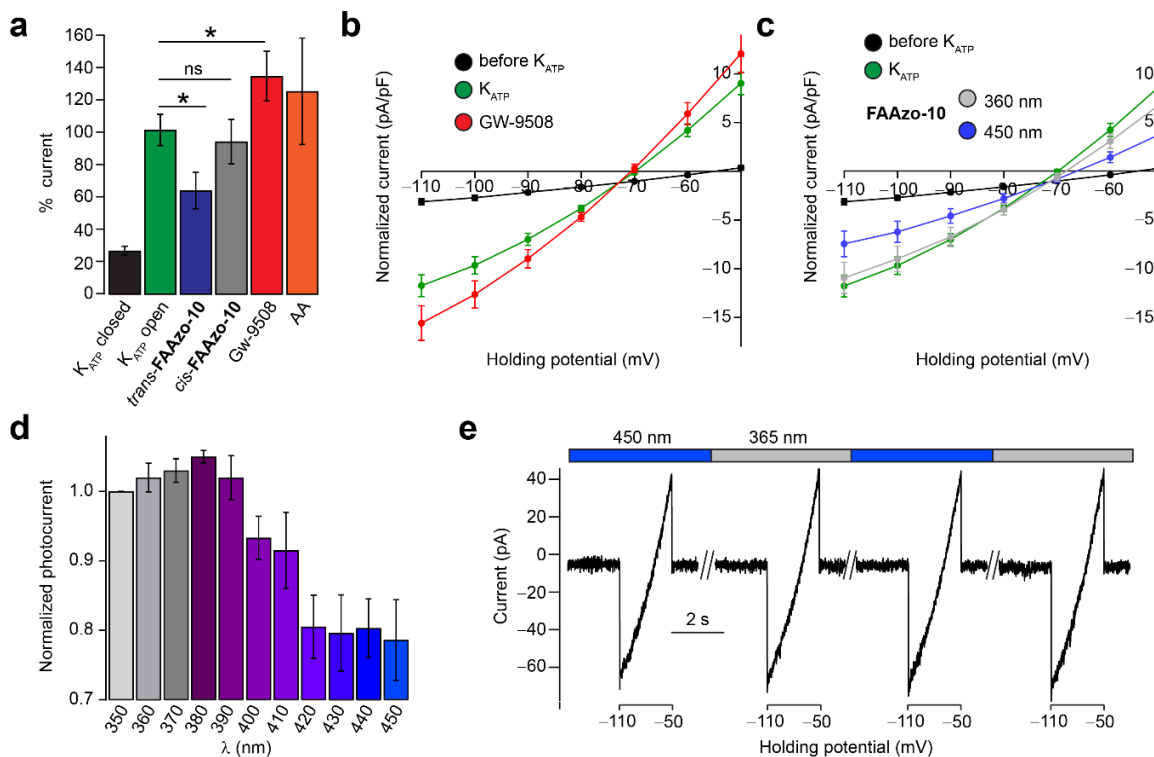


Figure 7.7 | Optical control of β -cell K_{ATP} channels. The whole-cell K_{ATP} current from dissociated mouse β -cells was measured between -110 to -50 mV. (**a-c**) After dialysis of the cytoplasm with the pipette solution, the K_{ATP} current developed to a steady state (black = before, $n = 21$ cells; green = after, $n = 20$ cells; both from 2 animals). Application of Gw-9508 ($20 \mu\text{M}$, red, $n = 9$ cells from 2 animals) and AA ($20 \mu\text{M}$, orange, $n = 4$ cells from 1 animal) increased K_{ATP} conductance. In contrast, the application of *trans*-FAAzo-10 ($20 \mu\text{M}$, blue) decreased the K_{ATP} current, while isomerization to *cis*-FAAzo-10 (gray) reversed this effect ($n = 7$ cells from 2 animals). Data is displayed as (**a**) the % K_{ATP} current (at -110 mV) for multiple cells, normalized to the K_{ATP} open (green) state and (**b,c**) the full IV relationship between -110 to -50 mV. (**d**) In the presence of FAAzo-10, an action spectrum between $\lambda = 350$ - 450 nm revealed that K_{ATP} was inhibited the most under blue irradiation. Irradiation with UV-A light prevented FAAzo-10 from blocking the K_{ATP} current. Displayed as the normalized photocurrent for multiple cells ($n = 3$ cells from one animal, normalized to $I_{350\text{nm}(-110 \text{ mV})}$). (**e**) UV-A and blue irradiation alone did not affect the K_{ATP} current, displayed as sequential voltage ramps under alternating UV-A and blue light from a representative cell. ns = $P > 0.05$, $*P < 0.05$. Error bars were calculated as \pm s.e.m.

7.2.4 – Optical control of $[Ca^{2+}]_i$ oscillations in pancreatic islets

Finally, we evaluated our photoswitchable ligands for their effects on intact pancreatic islets. We used the small-molecule $[Ca^{2+}]_i$ indicator Fluo-8 to monitor $[Ca^{2+}]_i$ oscillations stimulated by a high glucose concentration (11 mM). Similar to the application of Gw-9508 (**Fig. 7.8a,b**) or AA (**Fig. 7.8c**), application of *trans*-**FAAzo-10** caused a marked increase in the $[Ca^{2+}]_i$ oscillation frequency (**Fig. 7.8d**). In line with our previous results, isomerization to *cis*-**FAAzo-10** with $\lambda = 365$ nm irradiation reversed this effect entirely (**Fig. 7.8e**). Lower concentrations of **FAAzo-10** did not affect oscillation frequency in either configuration (**Fig. 7.8f**). **FAAzo-4** behaved in an analogous manner, and reversibly stimulated $[Ca^{2+}]_i$ oscillations in the *trans*- configuration (**Fig. 7.8g,h**). To exclude imaging artefacts, in particular fluorescence quenching, the cells were treated with a methyl ester FAAzo-derivative, **FAAzo-5(OMe)**, which possesses an azobenzene photoswitch with similar spectral characteristics to both **FAAzo-10** and **FAAzo-4**⁵¹. **FAAzo-5(OMe)** did not affect the $[Ca^{2+}]_i$ oscillations in either configuration (data not shown), as methyl esterification of the acid group abolished compound activity. As was previously demonstrated⁵², UV-irradiation alone did not affect oscillatory behavior. We then compared the effects of **FAAzo-10** and Gw-9508 on insulin secretion. At 3 mM glucose, Gw-9508 stimulated an increase in insulin secretion (**Fig. 7.8i**). However, application of **FAAzo-10** in either the *trans*- or *cis*- forms did not affect secretion levels. Further experiments at different glucose concentrations are required to verify this effect, however these results suggest that insulin secretion is not only determined by the $[Ca^{2+}]_i$ oscillation frequency, or that other targets may in fact be affected by the FAAzos as well.

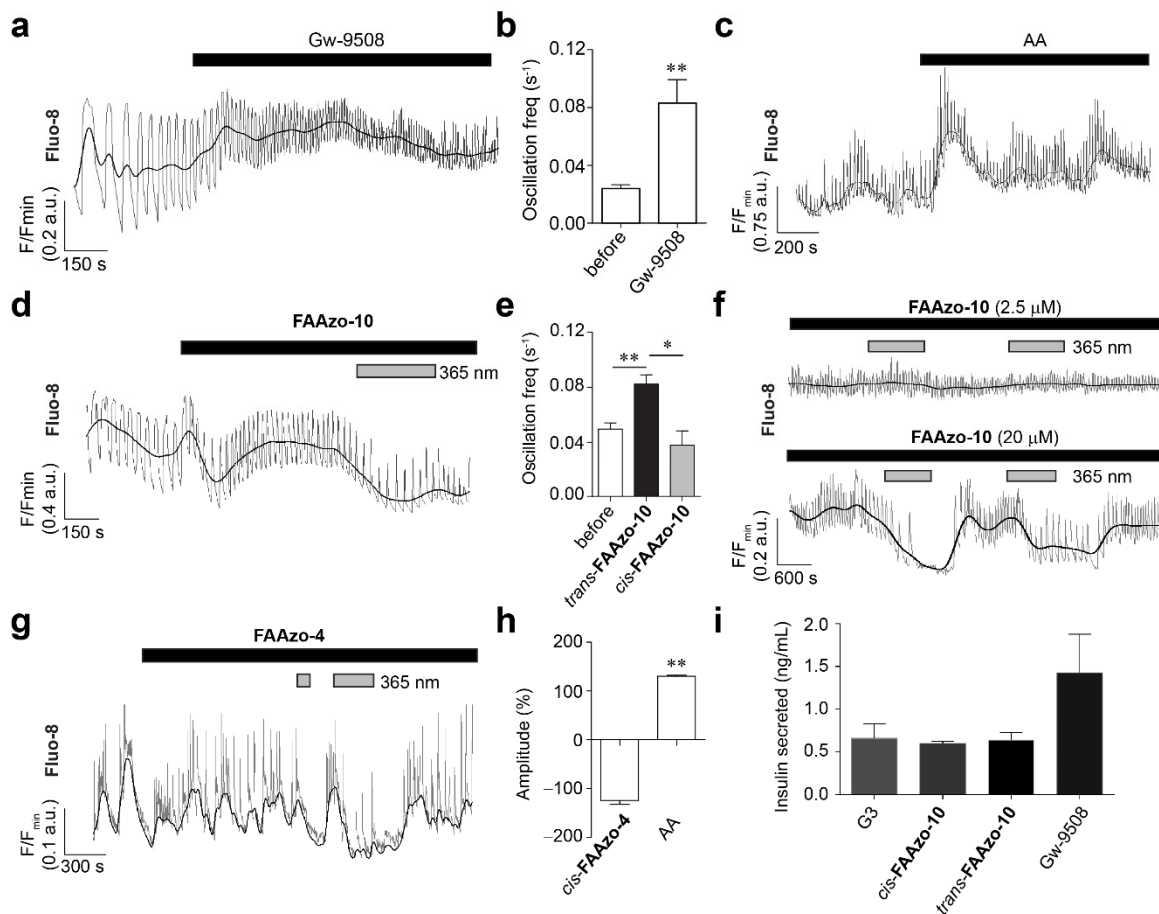


Figure 7.8 | FAAzo-10 enables optical control of $[Ca^{2+}]_i$ oscillations in pancreatic islets. $[Ca^{2+}]_i$ oscillations were stimulated by a high glucose concentration (11 mM) and monitored in intact mouse islets using the fluorescent $[Ca^{2+}]_i$ indicator Fluo-8. (a,b) The application of Gw-9508 (50 μ M) caused an increase in the $[Ca^{2+}]_i$ oscillation frequency. Displayed as (a) a representative trace from a single islet and (b) the oscillation frequency averaged over multiple islets ($n = 6$ islets). (c) Similarly, AA (50 μ M) caused an increase in $[Ca^{2+}]_i$. (d,e) The application of *trans*-FAAzo-10 also caused a marked increase in the oscillation frequency. Isomerization to *cis*-FAAzo-10 with $\lambda = 365$ nm irradiation reversed this effect. Results are displayed as (d) a representative trace from a single islet and (e) the average oscillation frequency from multiple islets ($n = 5$ islets). (f) FAAzo-10 enabled optical control of β -cell $[Ca^{2+}]_i$ oscillations at 20 μ M, but not at 2.5 μ M ($n = 4$ -5 islets). (g,h) Application of *trans*-FAAzo-4 also increased $[Ca^{2+}]_i$ oscillations, while isomerization to *cis*-FAAzo-4 reversed this effect. Displayed as (g) a representative trace from a single islet and (h) the oscillation frequency averaged over multiple islets in the presence of *cis*-FAAzo-4 (50 μ M, $n = 8$ islets) and AA (50 μ M, $n = 6$ islets). (i) At low glucose levels (3 mM), Gw-9508 stimulated insulin secretion, but FAAzo-10 did not ($n = 3$). * $P < 0.05$ and ** $P < 0.01$, Student's t-test or repeated measures ANOVA. Error bars were calculated as \pm s.e.m.

7.3 – Discussion

In summary, this work demonstrates the utility of the FAAzos for manipulating lipid signaling in cells. Both **FAAzo-4** and **FAAzo-10** can mimic AA signaling in a time-controlled manner. Although previous studies involving the FAAzos conjugated to different polar headgroups have all afforded *cis*-active compounds^{51,52}, we found the opposite in this case. Both mimicked the activities of their parent compounds, AA and Gw-9508, with the greatest efficacy in *trans*-form. As such, they behave as a dark-active AA that can be quickly switched OFF and ON again with UV-A and blue irradiation, respectively.

Like AA, these photoswitchable molecules exhibit complex polypharmacology at different targets. They affect GPR40, K_{ATP} and K_v channels, all of which are known to regulate $[Ca^{2+}]_i$ oscillations and GSIS in pancreatic β -cells. Accordingly, we could stimulate glucose-stimulated $[Ca^{2+}]_i$ oscillations in mouse islets on application of either compound in the *trans*-form, while isomerization to *cis*- reduced the effect. However, these results did not translate to the optical control of insulin secretion, which was unaffected by **FAAzo-10** in either the *trans* or *cis*-configurations. A potential explanation is the activation of parallel, non-light-responsive targets, whose activation may counteract any increase in secretion stimulated by the *trans*-ligand at GPR40 or K_v , or K_{ATP} . Nevertheless, we showed that GPR40 agonists like Gw-9508 behave similarly to AA when applied to β -cells, and that their combined effects on GPR40, K_v , and K_{ATP} regulate the intensity and frequency of the $[Ca^{2+}]_i$ oscillations. This complex polypharmacology could also contribute to the varied effects observed using GPR40 agonists in primary vs. model cell lines, as channel expression likely varies between the different cell-types, as was previously alluded to using the PhoDAGs⁵². Moreover, FAs have been shown to alter insulin secretion *via* non-ionic pathways (*e.g.* by acting directly upon the exocytotic machinery through DAG generation) and this could have differential contributions depending on the exact cell-system employed.

Drugs targeting GPR40 for the treatment of T2DM previously received great attention due to the specific localization of the receptor to pancreatic β -cells. Unfortunately, these drugs failed due to adverse side-effects associated with treatment, including liver toxicity. This work demonstrates that GPR40 agonists can have off-target effects on β -cell K^+ channels, and this could be limiting for drug development targeting GPR40. As such, novel molecules must be synthesized to achieve greater specificity towards GPR40 and limit off-target effects. This effort would not only lead to the development of more efficacious photoswitchable ligands, but could even lead to the development of novel therapeutics for T2DM.

7.4 – Supporting information

7.4.1 – Cell culture

HeLa Kyoto cells were grown in 1.0 g/L D-glucose DMEM (GIBCO, cat # 31885-023) supplied with 10% FBS (GIBCO, cat # 10270-106) and 0.1 mg/mL antibiotic Primocin (Invitrogen, cat #ant-pm-1). HeLa cells were first seeded in an 8-well Lab-Tek™ chambered coverslip (ThermoScientific #155411) 24-48 h before transfection at 37 °C and 5% CO₂. Transfection was carried out with FugeneHD (Promega, cat # E2311) in DMEM free of FBS and antibiotics according to the manufacturer's instructions. First, the media was aspirated and the wells were charged with DMEM media (200 μ L per well). A transfection solution containing DMEM (20 μ L per well), cDNA (300 ng total DNA per well) and FugeneHD (1.5 μ L per well) was then added to each well of the 8-well Lab-Tek™. The cells were incubated at 37 °C and 5% CO₂ for 20-24 h before the microscopy experiments were performed.

7.4.2 – Culture of primary mouse pancreatic islets

***Note: Culture of mouse pancreatic islets was performed by Dr. David Hodson and Nick Fine (IMSR Birmingham), and the experimental details are included here for clarity.*

Islets were isolated from C57BL6 and CD1 mice using collagenase digestion, as previously detailed¹⁵⁴. Briefly, following euthanasia by cervical dislocation, the bile duct was injected with a collagenase solution (1 mg/mL) before digestion at 37 °C for 10 min and separation of islets using a Histopaque gradient (1.083 and 1.077 g/mL). Islets were cultured for 24-72 h in RPMI medium supplemented with 10% FCS, 100 U/mL penicillin and 100 μ g/mL streptomycin. All animal work was regulated by the Home Office according to the Animals Act 1986 (Scientific Procedures) of the United Kingdom, as well as EU Directive 2010/63/EU.

7.4.3 – List of utilized cDNA constructs

Name	Characterization
R-GECO ¹²³	red intensimetric $[Ca^{2+}]_i$ sensor
<i>h</i> GPR40 (FFAR1)*	human free fatty acid receptor 1
C1-GFP ¹²⁰	green fluorescent DAG-sensing translocation probe

*This cDNA clone was obtained from the cDNA Resource Center (www.cdna.org).

7.4.4 – Laser scanning confocal microscopy

Imaging of HeLa cells was performed on an Olympus Fluoroview 1200 with a 20x objective, or a 63x oil objective. C1-GFP excitation was performed with $\lambda = 488$ nm laser at low laser power (<3%) and emission was collected at $\lambda = 500$ -550 nm. R-GECO excitation was performed with a $\lambda = 559$ nm laser at low laser power (<3%) and emission was collected at $\lambda = 570$ -670 nm. Compound activation was triggered using the quench function in the Olympus software. Photoactivation was carried out with a $\lambda = 375$ nm laser at 100% intensity. The cells were incubated in imaging buffer (250 μ L, containing in mM: 115 NaCl, 1.2 CaCl₂, 1.2 MgCl₂, 1.2 K₂HPO₄, 20 HEPES, 20 D-glucose) at 37 °C and 5% CO₂ for at least 10 min. Compounds were first solubilized in DMSO at a concentration of 10 mM. This stock was then diluted into imaging buffer (50 μ L) and then added directly to the well containing the cells and imaging buffer.

Imaging of primary rodent pancreatic β -cells was performed on a Zeiss Axiovert M200 coupled to a Yokogawa CSU10 spinning disk head and 10x and 20x objectives. Fluo-8 excitation was performed using a solid-state $\lambda = 491$ nm laser, and emission was collected using a highly sensitive back-illuminated EM-CCD (Hamamatsu C9100-13) at $\lambda = 500$ -550 nm. Photoactivation was carried out using an X-Cite 120 epifluorescence source and a $\lambda = 350 \pm 20$ nm band-pass filter. Islets were imaged in a HEPES-bicarbonate buffer containing (in mM): 120 NaCl, 4.8 KCl, 24 NaHCO₃, 0.5 Na₂HPO₄, 5 HEPES, 2.5 CaCl₂, 1.2 MgCl₂ and 11 D-glucose. Images were processed with Fiji software (<http://fiji.sc/Fiji>) and the resulting data was analyzed in Microsoft Excel, MATLAB and R. The data were then plotted with Igor Pro, Origin and R. ****Note:** $[Ca^{2+}]_i$ imaging of mouse pancreatic islets was performed by Dr. David Hodson and Nick Fine (IMSR Birmingham), and the experimental details are included here for clarity.

7.4.5 – Whole-cell electrophysiology in dissociated mouse β -cells

Two days after culture, primary mouse islets were dissociated into single β -cells using trypsin digestion for 5 min at 37 °C and allowed to attach to poly-L-lysine-coated and acid-etched coverslips overnight in RPMI medium supplemented with 10% FCS, 100 U/mL penicillin and 100 μ g/mL streptomycin at 37 °C and 5% CO₂. Whole cell patch clamp experiments were performed the next day using a standard electrophysiology setup equipped with a HEKA Patch Clamp EPC10 USB amplifier and PatchMaster software (HEKA Elektronik). Micropipettes were generated from “Science Products GB200-F-8P with filament” pipettes using a Narishige PC-10 vertical puller. The patch pipette resistance varied between 4-8 M Ω .

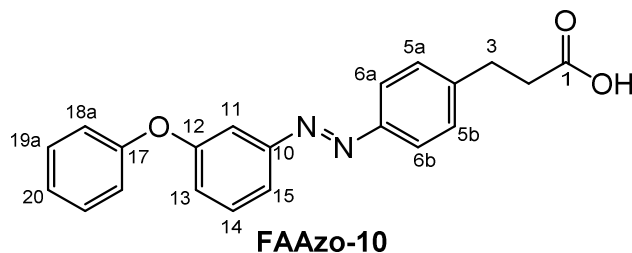
For recording of the K_v current, the bath solution contained (in mM): 119 NaCl, 2 CaCl₂, 4.7 KCl, 10 HEPES, 1.2 MgSO₄, 1.2 KH₂PO₄, 14.4 D-glucose (adjusted to pH 7.3 with NaOH). The intracellular solution contained (in mM): 140 KCl, 1 MgCl₂, 10 EGTA, 10 HEPES, 5 MgATP (adjusted to pH 7.25 with KOH). In voltage clamp mode, voltage steps (500 ms) were applied to the cells from the baseline at –70 mV to +80 mV in 10 mV intervals. The resulting current was averaged between the 400-470 ms range of each voltage step and plotted as a function of the holding potential

For measurement of the K_{ATP} current, the bath solution contained (in mM): 116 NaCl, 3 KCl, 4 CaCl₂, 3 MgCl₂, 25 HEPES (adjusted to pH 7.4 with NaOH). The intracellular solution contained (in mM): 130 K-gluconate, 10 KCl, 10 NaCl, 3 MgCl₂, 4 EGTA, 10 HEPES, 0.3 MgATP (adjusted to pH 7.2 with KOH). In voltage clamp mode, voltage steps (500 ms) were applied to the cells from the baseline at –110 mV to –50 mV in 10 mV intervals. The resulting current was averaged between the 100-450 ms range of the voltage step and plotted as a function of the holding potential.

All cells had a leak current below 15 pA on break-in at –70 mV. And recordings were corrected for the liquid junction potential. The data was analyzed in Igor Pro using the Patcher’s Power Tools (MPI Göttingen) plugin. Current values were extrapolated and processed in Igor Pro and the Microsoft Excel, and the results were again plotted in Igor Pro.

7.4.6 – Compound synthesis and characterization

7.4.6.1 – 3-(4-((3-Phenoxyphenyl)diazenyl)phenyl)propanoic acid (FAAzo-10)



3-phenoxyaniline (112 mg, 0.600 mmol, 2.0 equiv.) was dissolved in CH_2Cl_2 (25 mL), and then an aqueous solution (25 mL) of Oxone[®] (372 mg, 1.20 mmol, 4.0 equiv.) was added. The biphasic mixture was stirred rapidly overnight. The phases were then separated and the organic phase was washed with H_2O (2x30 mL), dried over anhydrous Na_2SO_4 and filtered. The filtrate was concentrated under reduced pressure and the residue was purified by flash silica gel chromatography (10 g SiO_2 , CH_2Cl_2). The fractions containing the green 1-nitroso-3-phenoxybenzene were pooled and 3-(4-aminophenyl)propionic acid (50 mg, 0.30 mmol, 1.0 equiv.) was added alongside AcOH (20 mL). The solution was again stirred overnight at room temperature. The solvents were removed under reduced pressure and the crude residue was purified by flash silica gel chromatography (10 g SiO_2 , 7:3 hexane:EtOAc with 1% AcOH) to yield **3-(4-((3-phenoxyphenyl)diazenyl)phenyl)propanoic acid (FAAzo-10)**, 46.7 mg, 45%) as an orange solid.

TLC (70:30:1 hexane:EtOAc:AcOH): R_f = 0.5 (*trans*), 0.36 (*cis*).

¹H NMR (CDCl₃, 400 MHz, 25 °C): δ 11.33 (bs, 1 H, H_{COOH}), 7.85 (d, 2 H, $\text{H}_{6\text{a,b}}$, J = 8.0 Hz), 7.68 (d, 1 H, H_{15} , J = 7.8 Hz), 7.56 (s, 1 H, H_{11}), 7.48 (t, 1 H, H_{14} , J = 8.0 Hz), 7.41-7.33 (m, 4 H, $\text{H}_{5\text{a,b}}$, $\text{H}_{19\text{a,b}}$), 7.18-7.14 (m, 2 H, H_{13} , H_{20}), 7.10 (d, 2 H, $\text{H}_{18\text{a,b}}$, J = 8.0 Hz), 3.04 (t, 2 H, $\text{H}_{3\text{a,b}}$, J = 7.8 Hz), 2.74 (t, 2 H, $\text{H}_{2\text{a,b}}$, J = 7.6 Hz).

¹³C NMR (CDCl₃, 101 MHz, 25 °C): δ 179.1 (C_1), 158.2 (C_{Azo}), 156.9 (C_{Azo}), 154.2 (C_{Azo}), 151.3 (C_{Azo}), 143.8 (C_4), 130.2 (C_{14}), 130.0 (2 C, $\text{C}_{19\text{a,b}}$), 129.2 (2 C, $\text{C}_{5\text{a,b}}$), 123.8 (C_{20}), 123.3 (2 C, $\text{C}_{6\text{a,b}}$), 121.2 (C_{13}), 119.3 (2 C, $\text{C}_{18\text{a,b}}$), 118.6 (C_{15}), 112.1 (C_{11}), 35.4 (C_2), 30.5 (C_3).

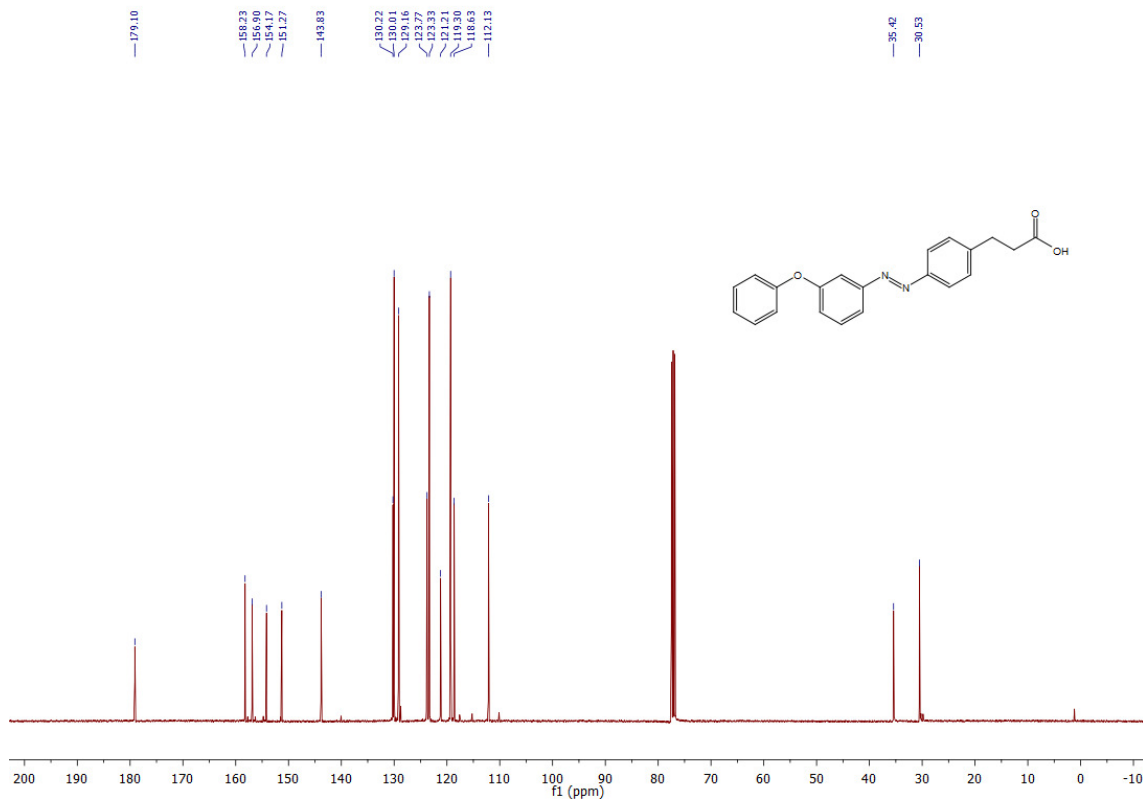
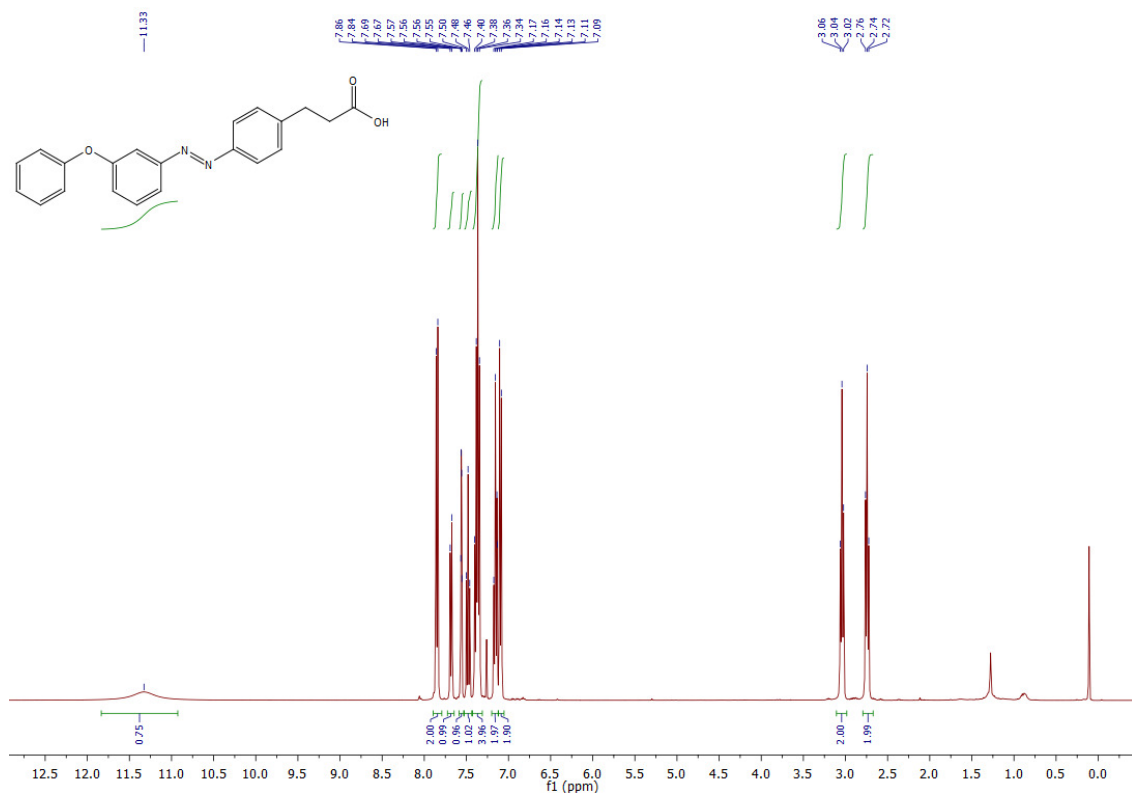
IR (neat, ATR): $\tilde{\nu}$ (cm^{-1}) = 3038, 2924, 2623, 1694, 1602, 1586, 1488, 1437, 1417, 1314, 1277, 1253, 1215, 1166, 1150, 1104, 1072, 1022, 963, 943, 916, 899, 865, 838, 792, 779, 749, 680.

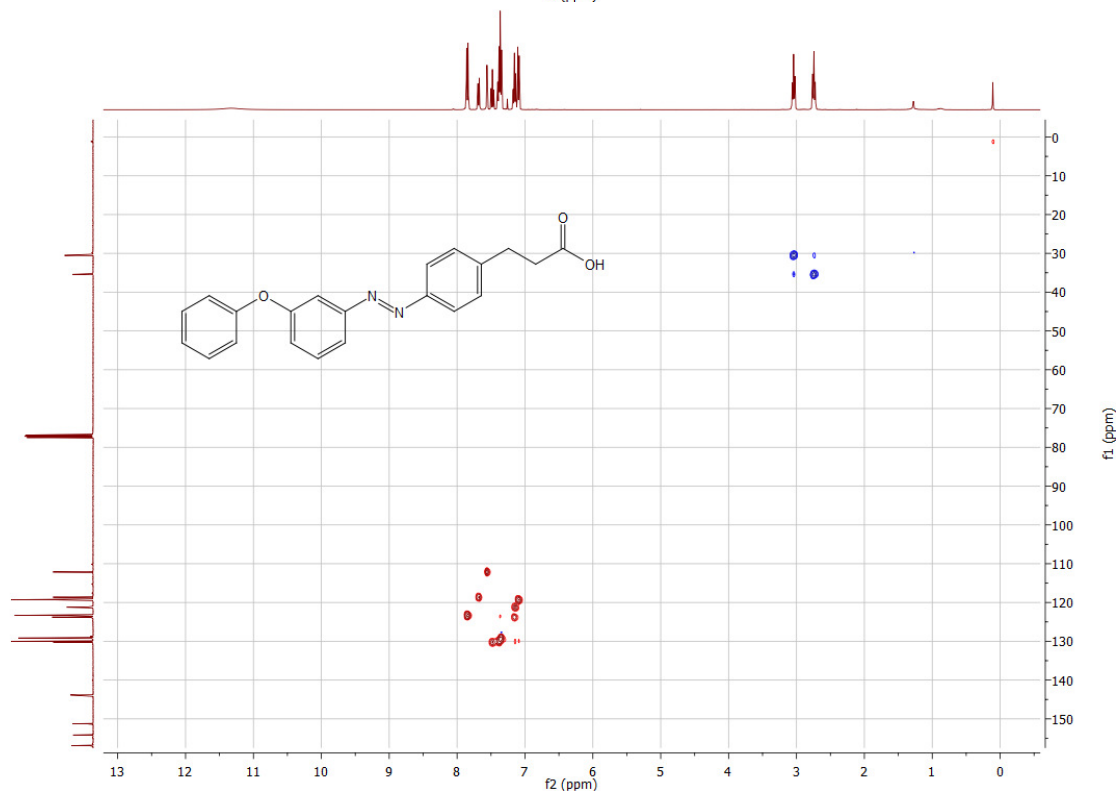
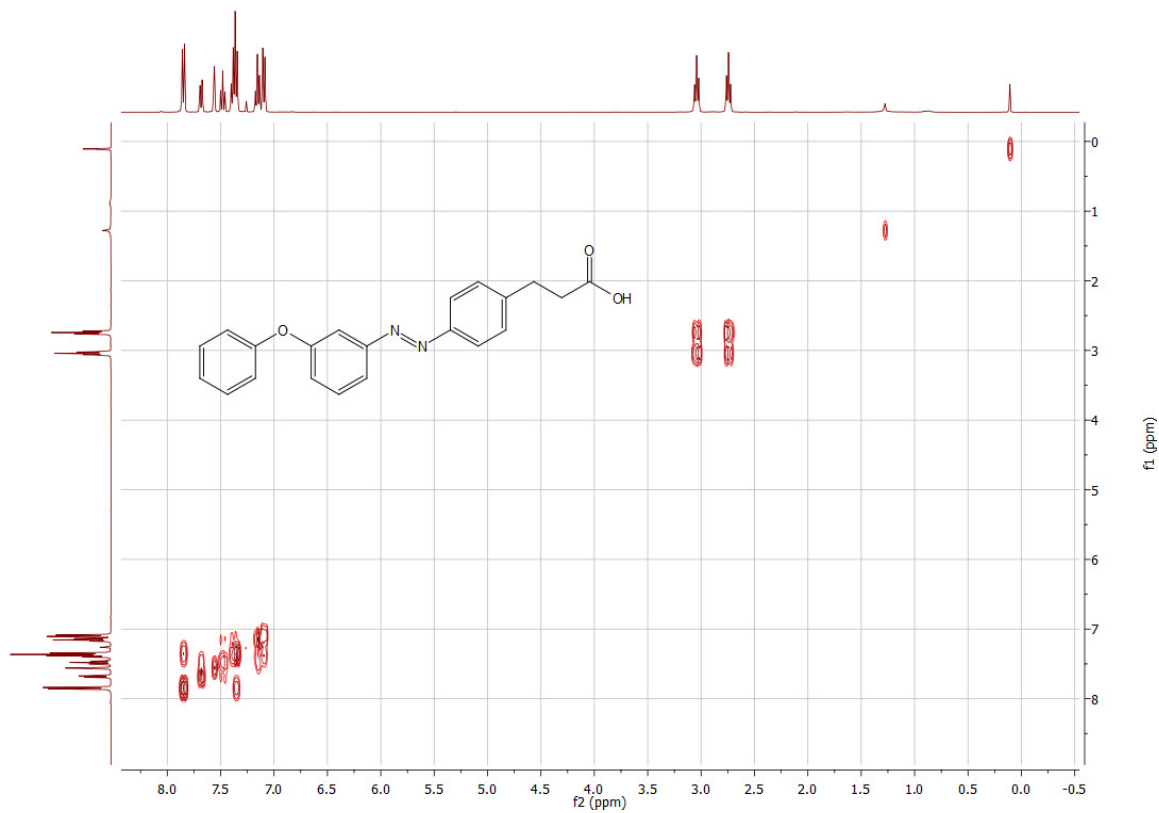
HRMS (ESI⁺): m/z calcd. for $[\text{C}_{21}\text{H}_{19}\text{N}_2\text{O}_3]^+$: 347.1396, found: 347.1390 ($[\text{M}+\text{H}]^+$).

UV-Vis (50 μM in DMSO): $\lambda_{\text{max}}(\pi-\pi^*)$ = 330 nm. $\lambda_{\text{max}}(n-\pi^*)$ = 430 nm.

Melting point (°C): 129.8-132.0.

7 – Optical control of arachidonate signalling in pancreatic β -cells





7.4.7 – Crystallographic data

7.4.7.1 – 4-(((4-Butylphenyl)diazenyl)phenyl)butanoic acid (FAAzo-4)

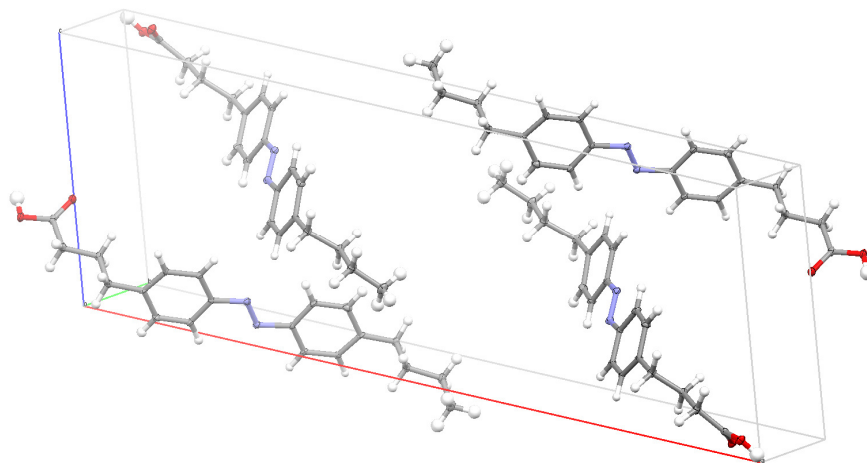


Figure 7.10 | FAAzo-4 unit cell. Displacement ellipsoids are drawn at the 30% probability level.

Net formula = $C_{20}H_{24}N_2O_2$

M_w = 324.41 g/mol

Monoclinic, $P2_1/c$

Diffractometer: Bruker D8Venture

a (Å) = 33.5257(16)

b (Å) = 4.6215(2)

c (Å) = 11.3999(6)

α (°) = 90

β (°) = 99.154(2)

γ (°) = 90

V (Å³) = 1743.79(15)

Z = 4

D_x (g cm⁻³) = 1.236

μ (mm⁻¹) = 0.080

T (K) = 100

Crystal size (mm) = 0.100 × 0.100 × 0.030

Absorption correction: multi-scan

Transmission factor range = 0.8615-0.9585

Reflections measured = 16414

R_{int} = 0.0319

Mean $\sigma(I)$ (I) = 0.0304

θ range = 3.077-26.45

Observed reflections = 2643

x, y (weighting scheme) = 0.0435, 0.4645

Hydrogen refinement: mixed

Reflections in refinement = 3570

Parameters = 279

Restraints = 0

$R(F_{obs})$ = 0.0380

$R_w(F^2)$ = 0.0989

S = 1.018

Shift/error_{max} = 0.001

Max electron density (e Å⁻³) = 0.187

Min electron density (e Å⁻³) = -0.153

8 – Optical control of lipid rafts with photoswitchable ceramides

This work has been published in the *Journal of the American Chemical Society* (2016)⁵³.

8.1 – Introduction

The plasma membrane is not simply a two-dimensional fluid mosaic, but can be laterally organized through the assembly of dynamic lipid domains, the so-called lipid rafts²¹⁰. These segregated domains are thought to permit the two-dimensional organization of membrane components, including both signaling molecules and proteins, leading to the modulation of signaling processes within the plane of the membrane^{12,211–213}. Lipid rafts are structurally and dynamically distinct from the bulk of the lipid bilayer²¹³. They are enriched in specific lipid species such as cholesterol (Chol) and sphingolipids^{214,215}. Moreover, their physical state is more similar to a liquid-ordered (L_o) phase, in contrast to the rest of the plasma membrane, which is assumed to be mainly in the liquid-disordered (L_d) phase. While the most abundant sphingolipid in the plasma membrane is sphingomyelin (SM), in recent years the neutral sphingolipid ceramide (Cer) has received great attention for its effects on membrane structure^{216–221}. This ubiquitous sphingolipid is often considered a second messenger, and is best known for its role in triggering apoptosis, cell-proliferation and cell-cycle arrest^{217,222}. Defects in Cer metabolism are involved in various disease states²²³. In most healthy cells, Cer concentrations are quite low and tightly regulated. However, its generation via the hydrolysis of SM by sphingomyelinase is stimulated by a variety of cell stress signals or other external factors. This can lead to an overall Cer concentration of 10-20% within the membrane, which has a significant effect on the membrane structure^{217,224}. Although structurally similar to DAG, ceramides possess an elevated melting temperature and are known to rigidify lipid membranes^{225,226}. Recent studies in model membrane systems have shown that Cer can trigger the formation of ordered gel-like platforms, and this process is known to be dependent on the length and saturation of its *N*-acyl chain^{227–229}.

Currently, chemical tools used to manipulate lipid membranes have failed to address the features of lipid raft and sphingolipid dynamics. For this, a tighter control of individual membrane components must be achieved than with what is currently available²³⁰. Over the past decades, the emergence of photochemical tools has allowed researchers to translate a light stimulus into a cellular response, with the high degree of spatiotemporal precision

associated with light³⁴. Caged lipids²⁴, whose activities are masked with a photo-*labile* protecting group, have already proven themselves useful to study lipid signaling at the cellular level^{231,232}. In terms of *in vitro* applications, caged ceramides have been shown to modulate lipid domain structure in phase-separated bilayers²⁸; yet the effects observed were quite slow and naturally irreversible, as uncaging is a one-shot process.

An alternative approach utilizes photoswitchable small molecules, such as azobenzene derivatives, to translate optical stimuli into a reversible cellular response. This technique has placed a variety of cellular machinery, including ion channels, GPCR's and enzymes, under the control of light³⁵. The behavior of photoswitchable azobenzene-modified lipids has been evaluated in model membrane systems before, most notably to explore membrane permeability and surface pressure⁴⁵⁻⁴⁷. Photoswitchable amphiphiles have also been used to enable reversible control the lipid domain structure in giant unilamellar vesicles^{49,50}. However, in those studies the photoswitch was incorporated into the polar headgroup of the amphiphile, while the membrane-embedded portion remained unaffected by light.

Recently, we developed a series of photoswitchable fatty acids, the FAAzos, which contain an azobenzene photoswitch along the length of the aliphatic chain⁵¹. The FAAzos can be used as modular building blocks for the construction of more complex photoswitchable lipids, now coined photolipids⁵². Here, we report the incorporation of the FAAzos into the Cer scaffold, which has allowed us to produce, for the first time, a set of intrinsically photoswitchable ceramides, ACes. This approach enables dynamic control over the curvature of the *N*-acyl chain, while still retaining the integrity of the Cer headgroup. Here, we investigate the biophysical properties of this novel class of photolipids within lipid raft-mimicking membrane models using atomic force (AFM) and fluorescence microscopy. In summary, the ACes allow us to restructure, in a reversible manner, ordered lipid domains on isomerization with light.

8.2 – Results

8.2.1 – Synthesis of photoswitchable ceramides

We designed and synthesized three photoswitchable ceramides, ACes (**Fig. 8.1a,b**), which are composed of a sphingosine backbone *N*-acylated with one of the FAAzos. **ACe-1-3** differ in the position of the azobenzene photoswitch from the near to the distal end of the chain, with the diazene unit representing the $\Delta 9$, $\Delta 6$ and $\Delta 12$ positions, respectively. **ACe-1** was prepared in one step by amide coupling between **FAAzo-4**^{47,51} and D-*erythro*-sphingosine in 70% yield (**Fig. 8.1c**). To investigate the photoswitching behavior in a lipid environment, we incorporated **ACe-1** into small unilamellar vesicles (SUVs) (**Fig. 8.1d**). In the dark at room temperature, **ACe-1** existed primarily in the thermally stable *trans*-configuration. Irradiation with UV-A light ($\lambda = 350\text{-}380$ nm) triggered isomerization to the *cis*-configuration (**Fig. 8.1e**). On termination of the irradiation, **ACe-1** relaxed spontaneously back to the *trans*-form with a τ -value of 39 h, and this effect could be reversed by irradiation with blue light. Photoswitching could be repeated over many cycles without fatigue (**Fig. 8.1f**). The average size of the SUVs was 66 ± 2 nm, and was not affected by UV-A or blue irradiation, suggesting that the SUVs were stable on photoswitching. **ACe-2** and **ACe-3** were prepared in an analogous fashion by coupling with **FAAzo-1** and **FAAzo-7**, respectively, and possessed similar spectral characteristics when compared to **ACe-1** (**Fig. 8.2**). As such, the ACes can be described as a classical azobenzenes, whose physical orientation can be reversibly modulated by irradiation with UV-A/blue light.

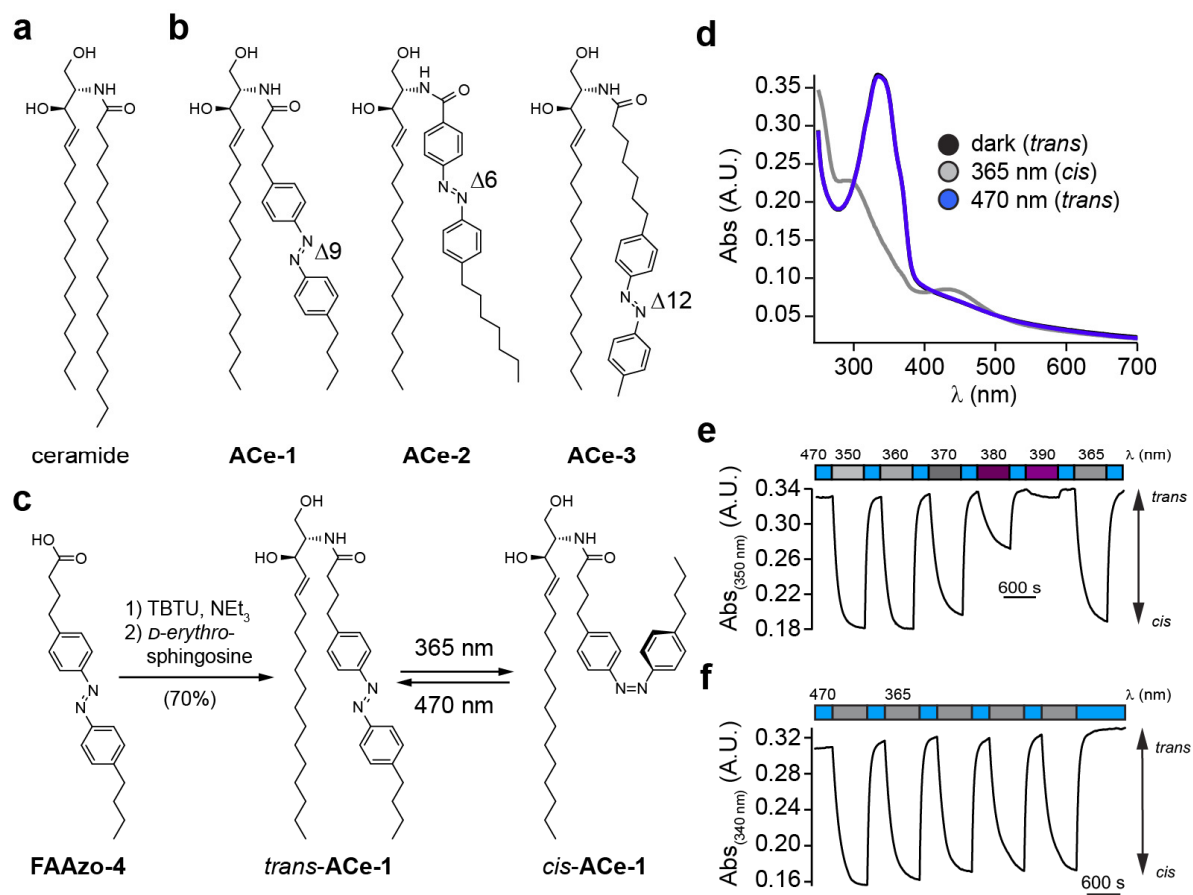


Figure 8.1 | Design and synthesis of photoswitchable ceramides. (a) The chemical structure of C18-ceramide (C18-Cer). (b) The chemical structures of photoswitchable ceramides, **ACE-1-3**. (c) D-erythro-sphingosine was converted to the photoswitchable Cer, **ACE-1**, by peptide coupling with **FAAzo-4**. **ACE-1** isomerized between its *cis*- and *trans*-configurations on UV-A ($\lambda = 365 \text{ nm}$) and blue ($\lambda = 470 \text{ nm}$) irradiation, respectively. (d-f) SUVs containing **ACE-1** (150 μM lipid mixture composed of DOPC:Chol:SM:**ACE-1** 10:6.7:7:3 mol ratio). were analyzed using UV-Vis. (d) The spectra of dark- (black), UV- (gray) and blue-adapted (blue) **ACE-1**. The black trace is superimposed under the blue line. (e) **ACE-1** could be isomerized to its *cis*-configuration with UV-A light ($\lambda = 350\text{-}380 \text{ nm}$). (f) This effect could be reversed with blue light ($\lambda = 470 \text{ nm}$), and could be repeated over many cycles without fatigue.

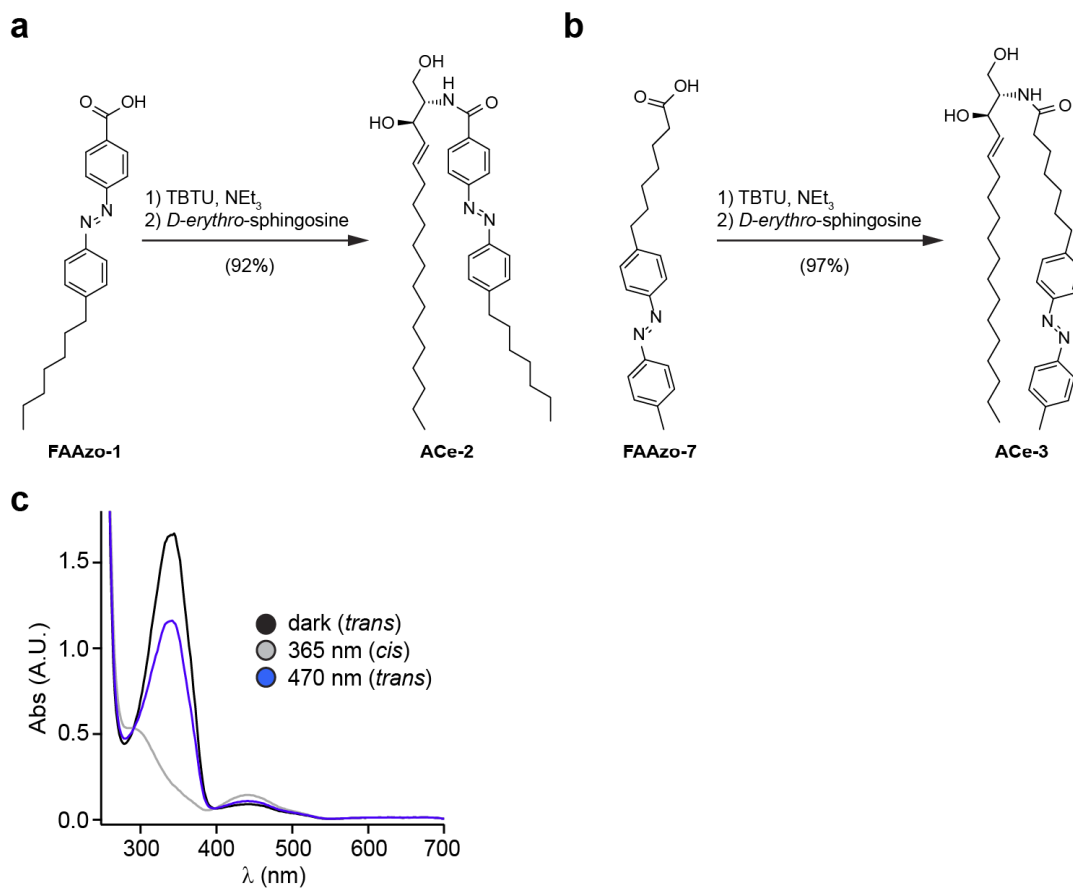


Figure 8.2 | Synthesis of photoswitchable ceramides. The chemical syntheses of photoswitchable ceramides (a) **ACe-2** and (b) **ACe-3**. Both compounds were prepared in high yield via an amide coupling between *D-erythro*-sphingosine and the photoswitchable FAs **FAAzo-1** and **FAAzo-7**, respectively. (c) The UV-Vis spectra of dark- (black), UV- (gray) and blue-adapted (blue) **ACe-1** (50 μ M in DMSO). **ACe-2** and **ACe-3** possessed nearly identical spectral characteristics to **ACe-1** in organic solution.

8.2.2 – Confocal fluorescence microscopy of supported lipid bilayers

In our previous studies, the effect of different ceramides in L_d - L_o phase separated supported lipid bilayers (SLBs) composed of 1,2-dioleoyl-*sn*-glycero-3-phosphocholine (DOPC), Chol, and C18-SM was investigated^{233,234}. Despite the influence of the solid support^{235,236}, SLBs provide us with a practical advantage to study both the spatial and topographical properties of such membranes. Using a similar approach, we prepared lipid mixtures containing molar ratios of 10:6.7:X:Y DOPC:Chol:SM:ACe (with 0.1 mol% ATTO655-DOPE for fluorescence detection), and varied the SM:ACe (X:Y) molar ratio between 9:1, 7:3, 5:5, 2.5:7.5 and 0:10 for all 3 ACes. After deposition of these lipid mixtures on a flat mica surface²³⁷, we analyzed the resulting SLBs using confocal fluorescence microscopy. We discovered that all three ACes formed ordered domains in the 9:1 and 7:3 SM:ACe ratios at room temperature, observed as a decrease in fluorescence intensity in regions of the SLB (**Fig. 8.3a**). However, at the 5:5 ratio, a difference was observed between the three compounds. The **ACe-1** SLB again formed large ordered domains, whereas **ACe-2** prevented the formation of distinguishable domains, and **ACe-3** formed a bilayer with many small domains of a different structure than the **ACe-1** SLB. For SM:ACe ratios of 2.5:7.5 and 0:10, where minimal or no SM is present, a homogeneous L_d phase was observed for all samples, in accordance with previous studies²³⁸.

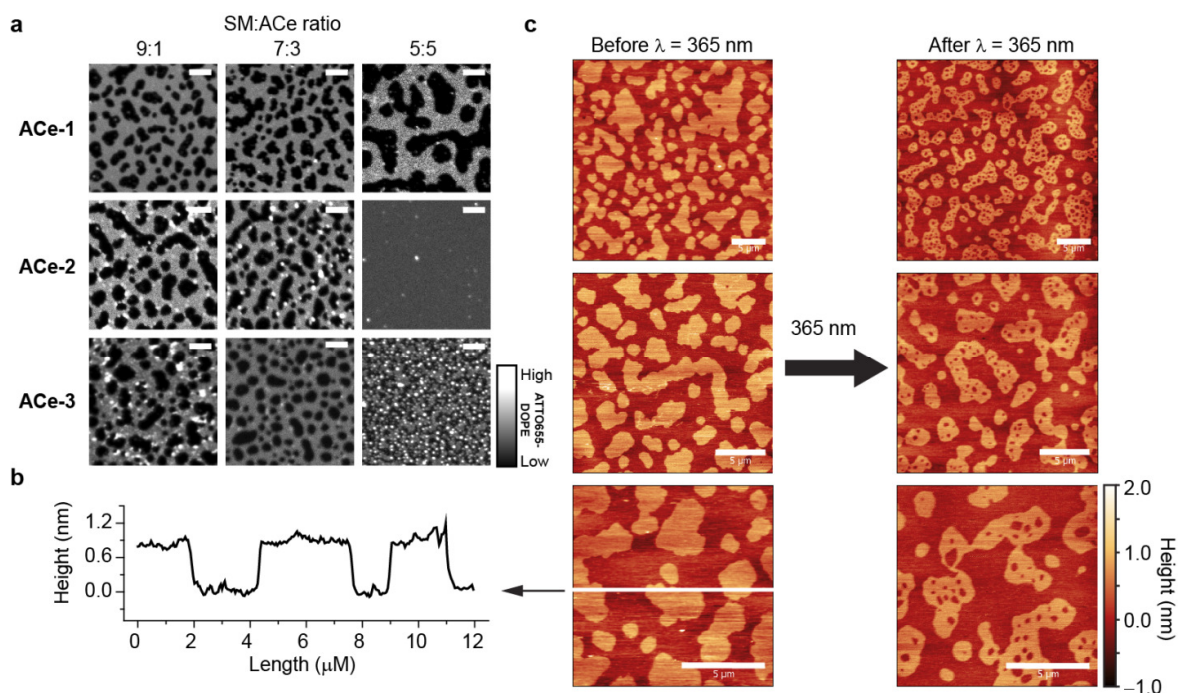


Figure 8.3 | Optical control of ordered lipid domains in supported lipid bilayers (SLBs). (a) Confocal fluorescence images of SLBs containing a quaternary mix of DOPC:Chol:SM:ACe (10:6.7:X:Y mol ratio with 0.1 mol% ATTO655-DOPE). SLBs with SM:ACe X:Y ratios of 9:1, 7:3 and 5:5 are presented for all three ACes. (b) Using AFM, we showed that the ordered (L_o) domains were approximately 0.7-1.1 nm higher than the disordered (L_d) phase in the 7:3 SM:ACe-1 mixture. (c) Representative AFM images of the 7:3 SM:ACe-1 mixture showed that isomerization to *cis*-ACe-1 with $\lambda = 365$ nm irradiation triggered the formation of L_d lakes within the L_o domains. Scale bars = 5 μ m.

8.2.3 – Isomerization to *cis*-ACe-1 triggers a fluidification of ordered domains

Correlated fluorescence and AFM images in contact mode at room temperature of the 7:3 SM:ACe-1 mixture confirmed that we had indeed produced a two phase mixture containing a liquid ordered (L_o) domain, which rested approximately 0.7-1.1 nm above the liquid disordered (L_d) phase (**Fig. 8.3b**). Similarly, the 9:1 and 5:5 SM:ACe-1 mixtures possessed identical height profiles. By measuring the depth of holes found within the SLB, we determined a total SLB thickness of 6-7 nm. On irradiation with UV-A light ($\lambda = 365$ nm, 10 s), a fluidification of the L_o domains was observed and small L_d domains (from here-on called “lakes”, for the sake of clarity) appeared inside the L_o domains (**Fig. 8.3c**). The size of the lakes formed within the L_o domains was proportional to the amount of ACe-1 present in the lipid mixture (**Fig. 8.4**). In the 9:1 SM:ACe-1 mixture, only small fluid domains were observed 1 min after UV-A irradiation. After 5 min they had entirely disappeared, presumably via lateral diffusion of lipids into the nearby L_d phase. In contrast, many fluid lakes were formed in the 7:3 and 5:5 SM:ACe-1 mixtures on UV-A irradiation, and after 5 min most of them had fused to even larger, stable L_d lakes within the L_o domains. In control experiments using C18-Cer, we observed sphingolipid-rich L_o domains that appeared approximately 0.7-1.1 nm above the DOPC-rich liquid disordered (L_d) phase (**Fig. 8.5a**); and Cer enriched gel-like platforms²³⁴ that were 0.4-1.0 nm higher than the L_o phase (**Fig. 8.5b**). As expected, the control SLBs containing C18-Cer were not sensitive to UV-A irradiation (**Fig. 8.5c**). Interestingly, in the case of ACe-1 we were never able to observe the presence of a higher s_o phase; indicating that the formation of such rigid domains may be hindered by the bulkiness of the azobenzene moiety. Using instead a ternary DOPC:SM:ACe-1 mixture (10:7:3 mol ratio) lacking Chol, we could demonstrate that ACe-1 allows the formation of s_o gel-domains (**Fig. 8.6**), similar to what was reported for C16-Cer²³⁹. Analogous to our results in the quaternary mixture, on irradiation with UV-A light, a shrinkage of the s_o domains was observed, as well as small stationary holes within those rigid platforms.

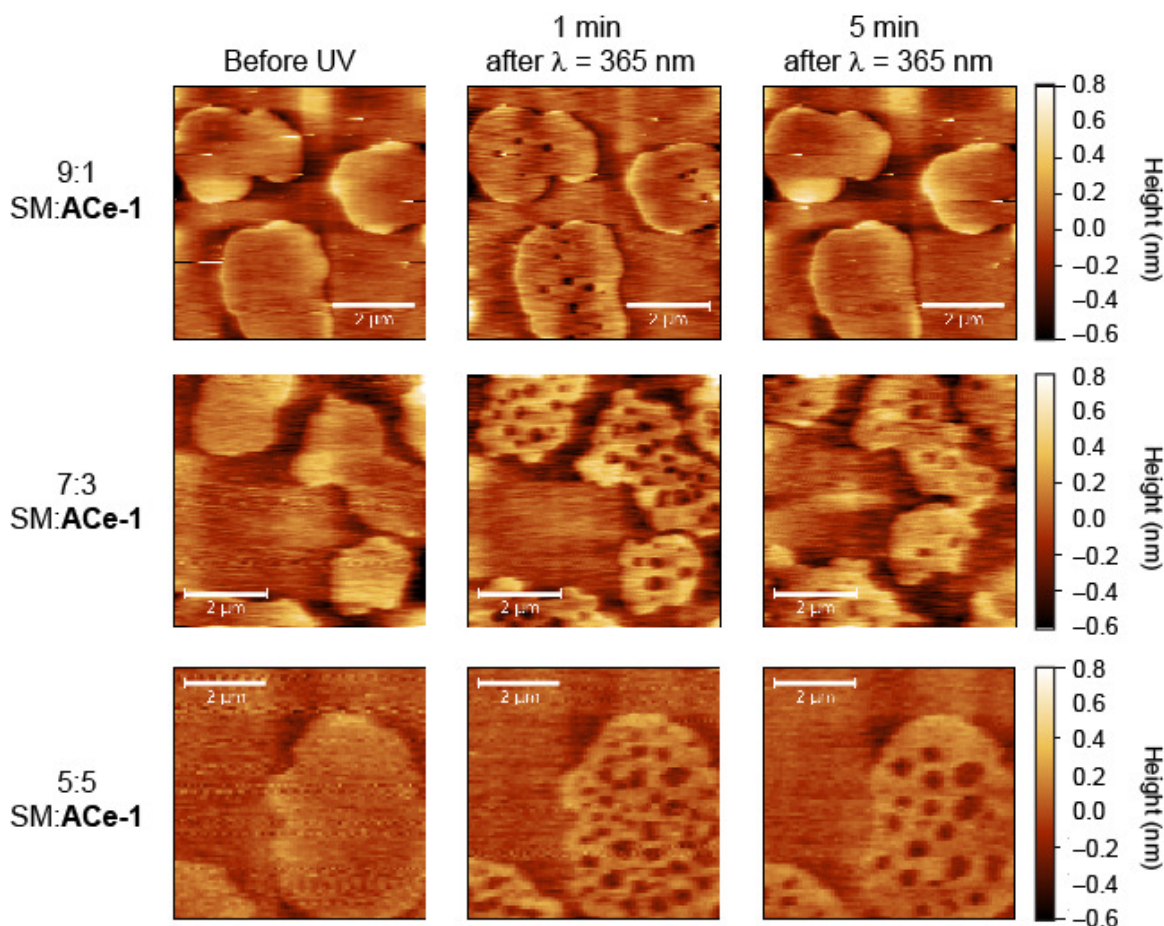


Figure 8.4 | ACe-1 induces a concentration-dependent fluidification within the ordered L_o domains on isomerization to *cis*. SLBs consisting of DOPC:Chol:SM:ACe-1 (10:6.7:X:Y mol ratio) were analyzed using contact mode atomic force microscopy (AFM). The SM:ACe-1 X:Y ratio was varied between 9:1, 7:3 and 5:5. Immediately after irradiation with UV-A light ($\lambda = 365$ nm), small L_d lakes were observed within the L_o domains. In the 7:3 and 5:5 SM:ACe-1 mixtures, those lakes fused together into larger L_d domains and persisted more than 5 min after irradiation. In the 9:1 SM:ACe-1 mixture, the L_d lakes had disappeared 5 min after irradiation. Scale bars = 2 μ m.

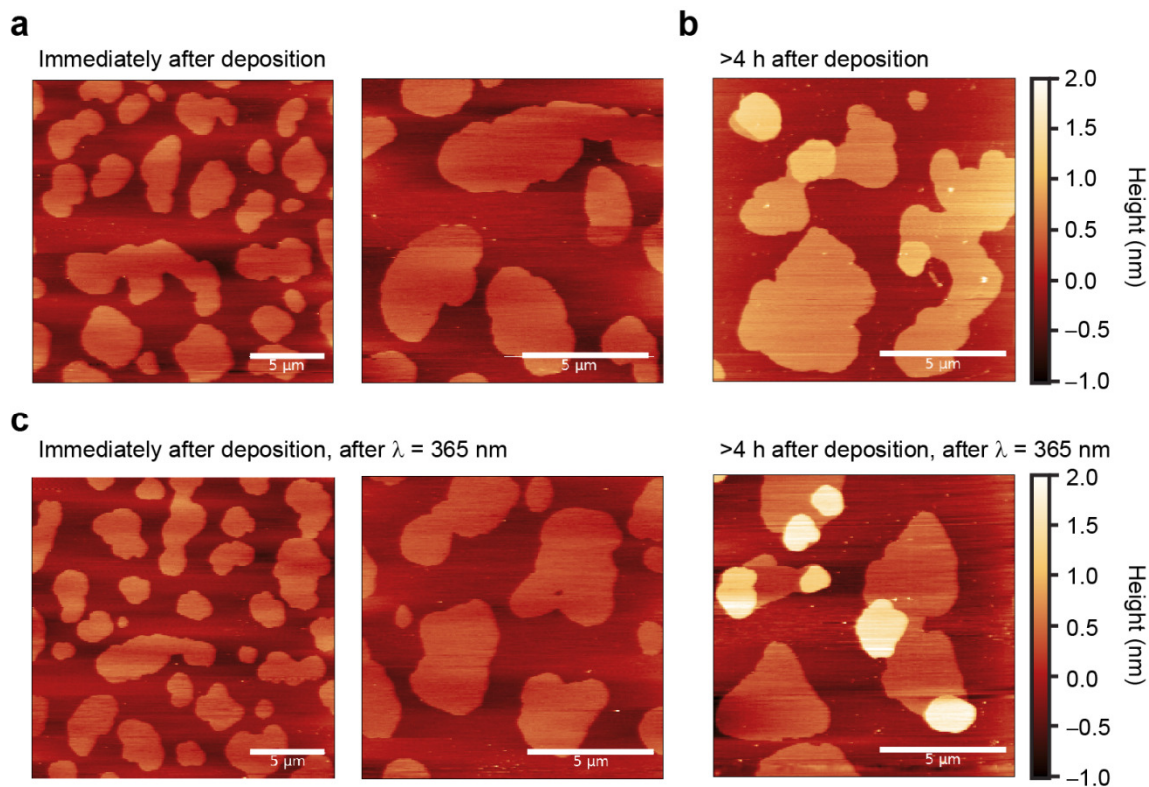


Figure 8.5 | UV-A irradiation does not affect SLBs containing C18-Cer. SLBs consisting of a of DOPC:Chol:SM:C18-Cer (10:6.7:7:3 mol ratio) were analyzed by contact mode AFM, displayed is a representative SLB. **(a)** Immediately after deposition, a two-domain L_d-L_o phase-separated SLB was observed. **(b)** More than 4 h after deposition, a higher Cer-rich gel phase (s_o) appeared inside the L_o domains. **(c)** Irradiation with UV-A light (λ = 365 nm, 10 s) did not affect the structure of the SLB before or after the formation of the s_o phase. Scale bars = 5 μm.

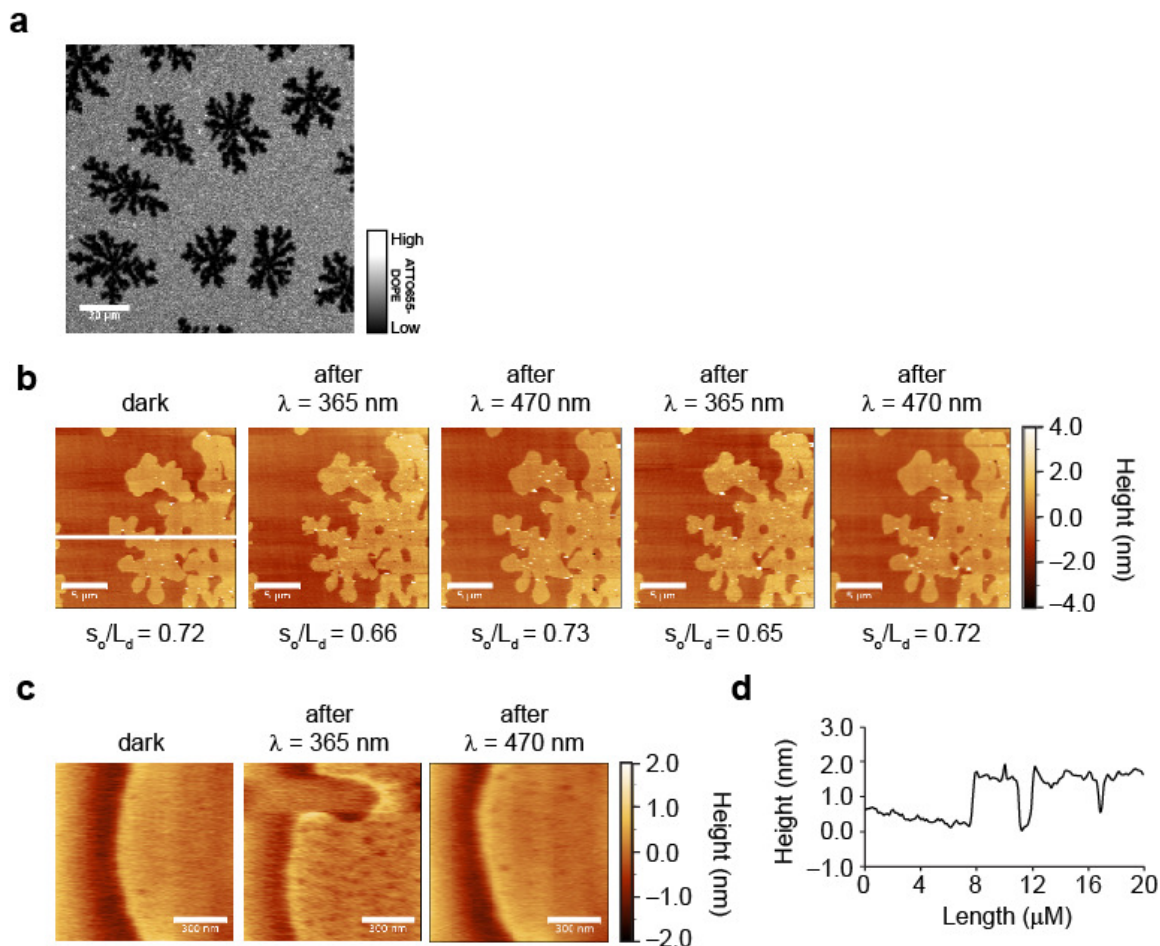


Figure 8.6 | ACe-1 controls domain structure in a ternary lipid mixture. (a) Fluorescence microscopy revealed the presence of gel-like domains in a ternary lipid mixture containing 10:7:3 DOPC:SM:ACe-1 (with 0.1 mol% ATTO655-DOPE) in the presence of *trans*-ACe-1. (b,c) Using AFM, we observed a fluidification of the s_0 domains on $\lambda = 365$ nm irradiation, as they shrunk slightly in size. Small holes were also observed within the domain on isomerization to *cis*. This effect could be reversed with $\lambda = 470$ nm irradiation. (d) The s_0 domains rested approximately 1.5-2.0 nm higher than the L_d domain, displayed as a profile sampled across the white line in b. Scale bars: a = 20 μm , b = 5 μm , c = 300 nm.

8.2.4 – Dynamic control of raft fluidification and rigidification

We next utilized high-speed AFM in intermittent-contact mode (AC mode), which allowed us to acquire images of SLBs (quaternary mixtures) at much higher frame rates to facilitate the observation of domain dynamics on photo-isomerization. In the 5:5 SM:**ACe-1** lipid mixture, we were again able to observe the formation of L_d lakes within the L_o phase on isomerization of **ACe-1** from *trans* to *cis* (**Fig. 8.7a** left). Immediately after irradiation, the newly formed domains were very small and mobile. They laterally diffused towards the L_d phase, or fused together into larger lakes in an effort to reduce surface tension. After equilibration in *cis*, isomerization back to *trans-ACe-1* with blue light ($\lambda = 470$ nm) revealed the immediate formation of small L_o rafts within the fluid L_d phase (**Fig. 8.7a** right, **Fig. 8.7b**). The islands were quite small and rested approximately 1.0-1.5 nm higher than the L_d phase (**Fig. 8.7c**). This height difference is in close agreement with the value obtained for the bilayers under low-speed AFM in contact mode. The small ordered domains quickly disappeared within the first 30 s after blue irradiation, likely due to lipid diffusion into nearby pre-existing L_o domains. By analyzing the fraction of L_d phase compared to L_o phase (L_d/L_o ratio), we showed that the fraction of L_d increased on UV-A irradiation, while the fraction of L_o increased to similar levels as in the dark-adapted state on blue irradiation (**Fig. 8.7a**). This effect could be repeated over several cycles (**Fig. 8.7d**), and demonstrates a change in the phase distribution of **ACe-1** within the SLB on isomerization. This effect could also be observed under fluorescence microscopy, confirming that the fluidification was not an artefact caused by the AFM tip (**Fig. 8.7e**, **Fig. 8.8**). In this case, the dark L_o domains became smaller, brighter and less defined on isomerization to *cis-ACe-1*. On isomerization back to *trans-ACe-1*, the domain structure was slowly restored as the dye diffused out of the ordered domains. For the 7:3 SM:**ACe-1** mixture, the formation of L_o islands within the fluid L_d matrix was also observed on isomerization back to *trans-ACe-1*, however this effect was less prominent when compared to the 5:5 mixture (**Fig. 8.9**).

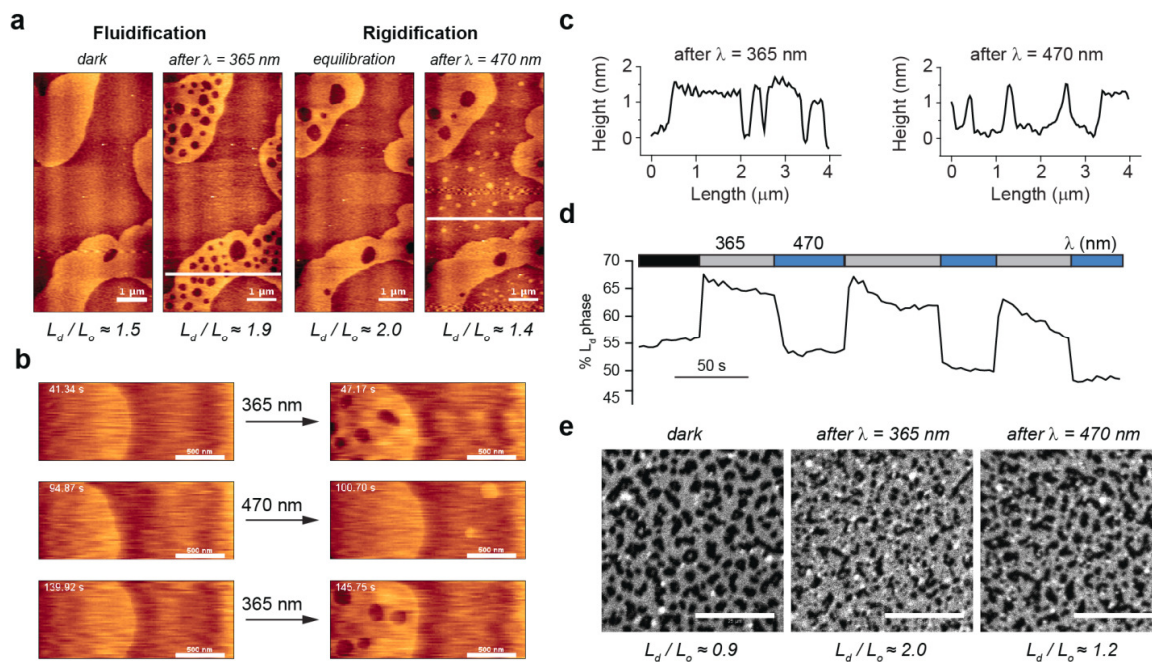


Figure 8.7 | ACe-1 permits reversible remodeling of lipid domains. SLBs containing a DOPC:Chol:SM:ACe-1 (10:6.7:5:5 mol ratio) lipid mixture were prepared and analyzed using high-speed AFM (AC mode). **(a,b)** On isomerization to *cis*-ACe-1, a fluidification inside the L_o domains was observed as fluid L_d lakes formed within them. On isomerization back to *trans*-ACe-1 with $\lambda = 470$ nm blue light, rigidification was observed within the L_d phase as small L_o islands appeared. **(c)** Representative height profiles of the membrane (regions marked with white lines in **a**) after irradiation with $\lambda = 365$ nm and $\lambda = 470$ nm light. **(d)** Fluidification and rigidification could be repeated over multiple cycles, observed as an increase and decrease in the L_d phase. **(e)** Using fluorescence confocal microscopy, we could also observe reversible alterations in the SLB domain structure on UV-A/blue irradiation, with an increased L_d/L_o ratio in the *cis*-form. Scale bars: a,e = 1 μm , b = 500 nm.

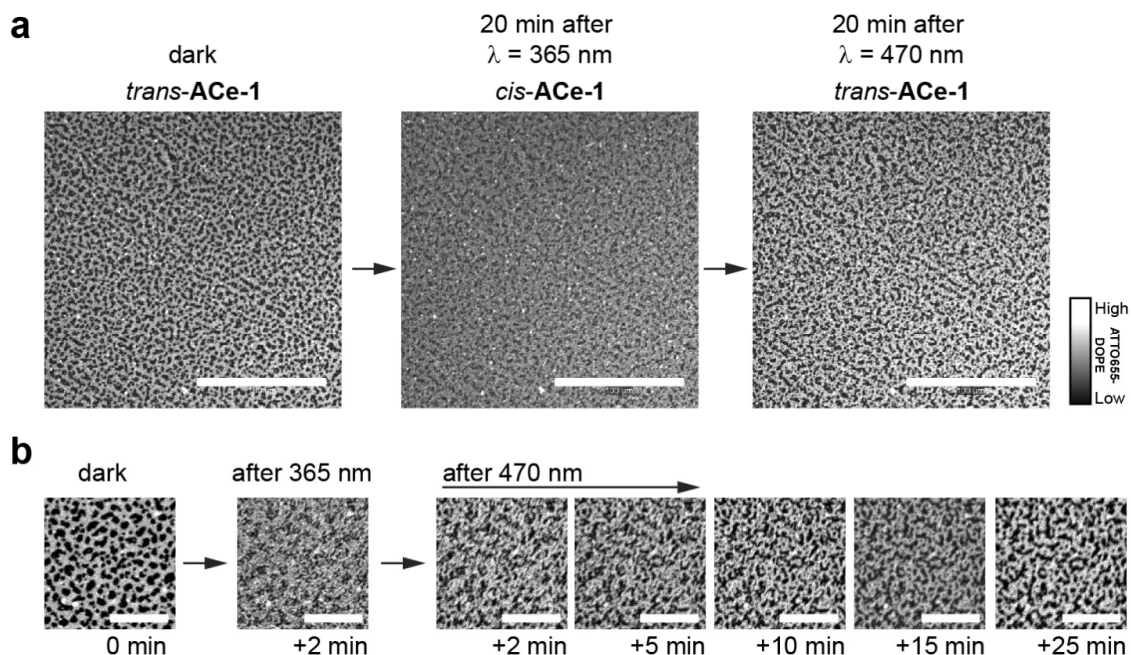


Figure 8.8 | ACe-1 enables optical control of SLB structure. Confocal fluorescence microscopy of an SLB composed of a DOPC:Chol:SM:**ACe-1** (10:6.7:5:5 mol ratio with 0.1% ATTO655-DOPE) revealed L_o domains (dark) within a fluid L_d phase (bright). **(a,b)** On isomerization to *cis-ACe-1* with $\lambda = 365$ nm irradiation (15 s) the dark L_o domains shrank and became less defined. On isomerization back to *trans ACe-1* with $\lambda = 470$ nm irradiation (15 s), the dark L_o domains slowly took shape as the dye diffused back into the fluid domains. Scale bars: a = 100 μm , b = 25 μm .

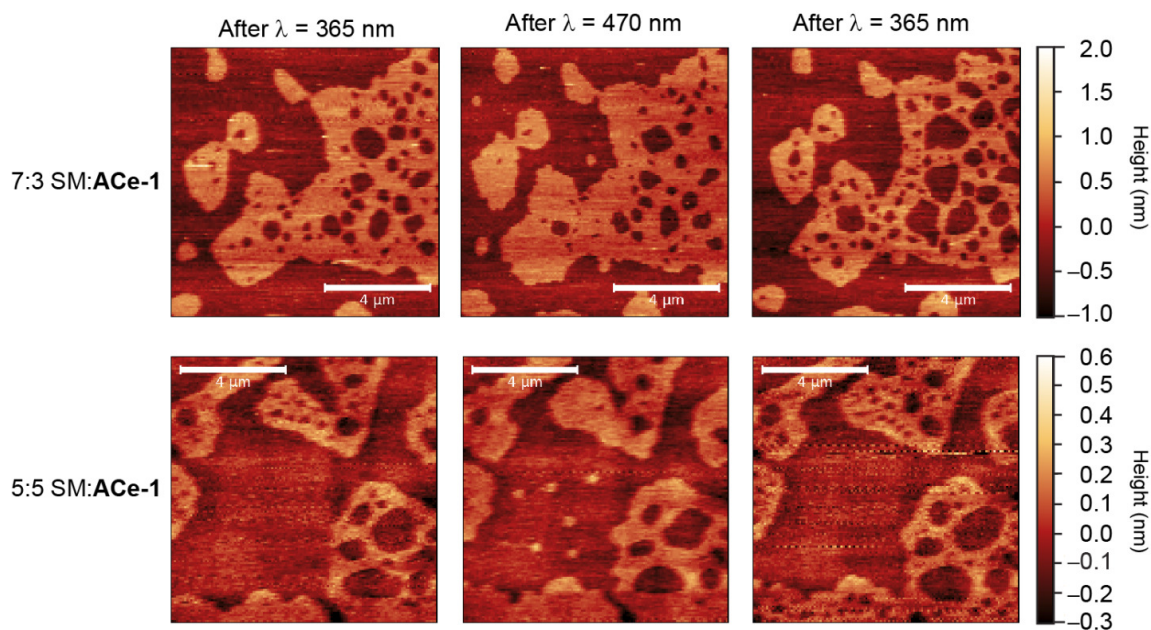


Figure 8.9 | Ordered domains are formed on isomerization from *cis*- to *trans*-ACe-1. SLBs consisting of DOPC:Chol:SM:ACe-1 (10:6.7:X:Y mol ratio) were analyzed using contact mode AFM. On isomerization to *cis*, L_d lakes formed within the L_o domains of the SLB. On blue irradiation and isomerization back to *trans*-ACe-1, L_o islands were immediately observed within the L_d phase. This effect could be repeated over multiple cycles. In the 5:5 SM:ACe-1 mixture, both holes and islands were more pronounced when compared to the 7:3 SM:ACe-1 SLB. Scale bars = 4 μm .

8.2.5 – ACe-2 and ACe-3 affect domain structure on isomerization

Next, we used high-speed AFM to examine different SLB mixtures containing **ACe-2** and **ACe-3** to probe the structure activity relationship between the position of the *N*-acyl azobenzene moiety and the lipid domain structure. In the 7:3 SM:**ACe-2** mixture, only very small and transient L_d lakes were formed inside the L_o domains on isomerization to *cis*-**ACe-2**, while the L_o domains themselves shrunk slightly in size (**Fig. 8.10a**). Irradiation with blue light reversed this effect, as shown by the L_d/L_o ratio. In comparison, photoswitching of **ACe-3** had a greater effect on the SLB structure. In the 7:3 SM:**ACe-3** mixture, large L_d lakes were observed inside the L_o domains on isomerization to *cis*-**ACe-3**, affording a large increase in the L_d/L_o ratio (**Fig. 8.10b**). On isomerization back to *trans* with blue light, L_o islands could be observed within the L_d phase, and the ordered domains again grew to their original size.

In the 5:5 SM:ACe mixtures, a stark difference was observed between **ACe-2** and **ACe-3**. In agreement with our fluorescence microscopy data, the **ACe-2** mixture formed only a flat fluid phase without domains that was not affected by UV-A irradiation (**Fig. 8.11**). In the case of **ACe-3**, however, an inversion of the phases was observed. The SLB consisted primarily of a L_o phase, with smaller embedded L_d domains (**Fig. 8.10c**). Similar to the other lipid mixtures here described, the L_o phase rested 1.0-1.5 nm higher than the L_d domains (**Fig. 8.10d**). On isomerization to *cis*-**ACe-3**, the L_d domains grew dramatically as the fraction of L_o decreased (**Fig. 8.10c,e**). Isomerization back to *trans*-**ACe-3** with blue light reversed this effect, and this behavior could be repeated over multiple cycles. These results suggest that **ACe-3** associates itself much more strongly within the L_o domains when compared to **ACe-2**, and consequently a larger difference in raft structure is induced on photoisomerization. It is likely that the location of the azobenzene unit within **ACe-2**, due to its proximity to the headgroup, interferes with the hydrogen bonding between the Cer headgroup and SM. This decreases its presence within the L_o domains, and thus inhibits its efficacy in modulating the architecture of the SLB. In this case, **ACe-2** behaves more like a short-chain Cer derivative²³⁴, affecting the miscibility and translational order of the L_o domains^{217,240}. In contrast, the azobenzene moiety of **ACe-3** is quite far from the headgroup, which permits its incorporation into the L_o lipid rafts in the *trans*-configuration, and thus **ACe-3** behaves more like a long-chain Cer²³⁴. However, photo-isomerization to *cis*-**ACe-3**, mimics a bend in the *N*-acyl chain, and disrupts its interactions within the rigid domains. Consequently, this effect triggers ACe redistribution into the L_d phase.

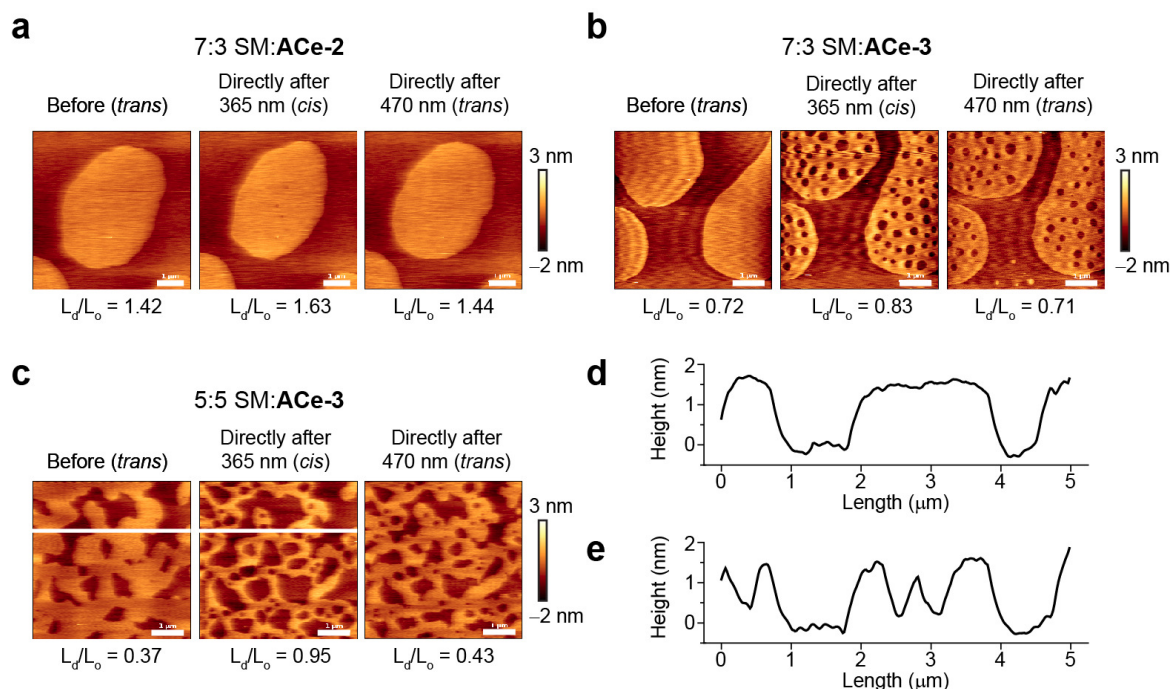


Figure 8.10 | ACe-2 and ACe-3 enable optical control of ordered lipid domains. SLBs containing DOPC:Chol:SM:ACe lipid mixtures (10:6.7:X:Y mol ratio) were analyzed by high-speed AFM (AC mode). **(a)** In the 7:3 SM:ACe-2 mixture, the size of the L_o domains shrunk on isomerization to *cis*-ACe-2. Very few L_d lakes were observed within the L_o domains. On isomerization back to *trans*-ACe-2, the L_o domains grew to their original size. **(b)** In the 7:3 SM:ACe-3 mixture, isomerization had a greater effect on the raft structure, as large L_d lakes and L_o islands were observed on UV-A and blue irradiation, respectively. **(c)** For the 5:5 SM:ACe-3 mixture, an inversion of the L_d - L_o phases was observed. As before, UV-A irradiation significantly increased the amount of the L_d phase, while blue irradiation reversed this effect. **(d,e)** Representative height profiles of the same membrane region (marked with white line) **(d)** before and **(e)** after irradiation with $\lambda = 365$ nm light. After shining UV-A light, L_d lakes resting approximately 1.0-1.5 nm below the L_o phase can be observed. Scale bars = 1 μm .

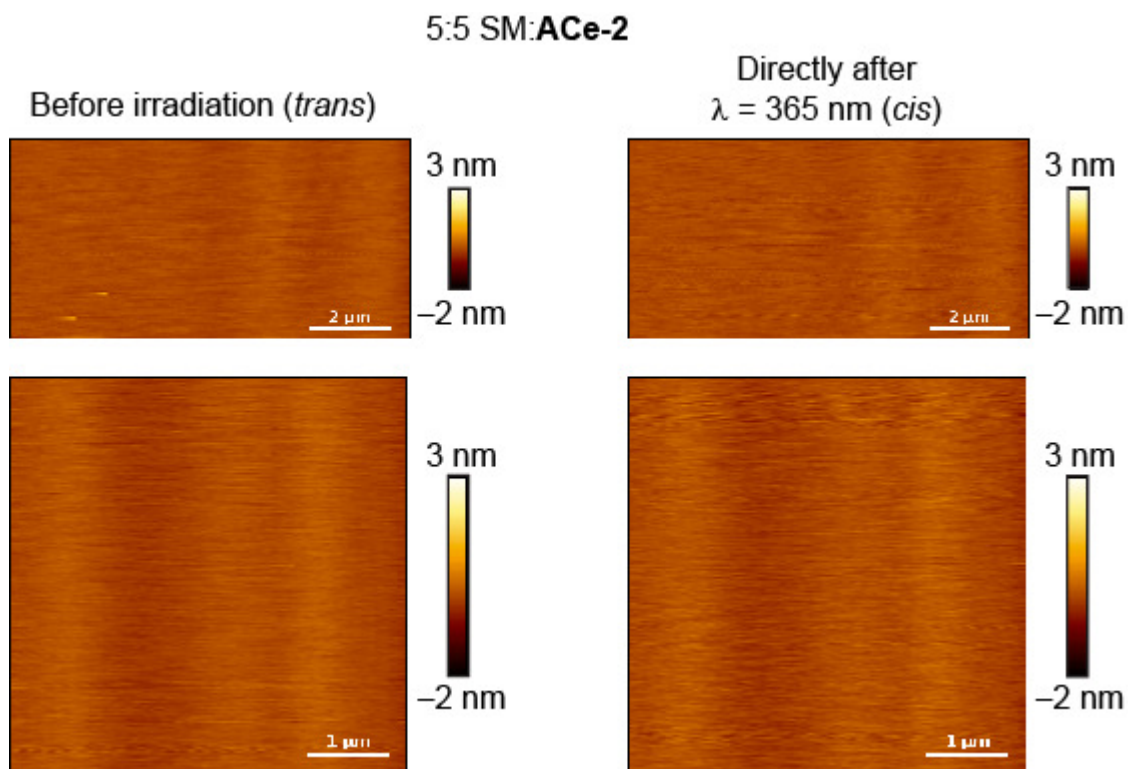


Figure 8.11 | Lipid bilayers containing a 5:5 SM:ACe-2 ratio do not form ordered domains. DOPC:Chol:SM:ACe-2 (10:6.7:5:5 mol ratio) lipid mixtures were analyzed by high-speed AFM and representative AFM images are displayed. Only a single fluid phase was observed, and the SLB was not affected by $\lambda = 365 \text{ nm}$ irradiation. Scale bars = $2 \mu\text{m}$ (top) or $1 \mu\text{m}$ (bottom).

8.3 – Discussion

In conclusion, we demonstrated that ACes in their *trans*-configuration can function similar to Cer in raft-mimicking SLBs. Insertion of the hydrophobic azobenzene into the Cer *N*-acyl chain does not inhibit its interaction with L_o domains. Isomerization from the *trans*- to *cis*-configuration induces a conformational change in the fatty acid structure from a less bent (similar to saturated C18:0), to more bent acyl chain (similar to unsaturated C18:1), respectively; allowing us to locally and effectively control the degree of lipid saturation within the bilayer. This result is in accordance with previous studies utilizing the FAAzos⁵¹, where we demonstrated that they can mimic long and saturated fatty acids in their *trans*-form, whereas they resemble more highly bent fatty acids like arachidonic acid in their *cis*-form. Similar to a previous report investigating the behavior of the unsaturated C18:1-Cer²⁴¹, the bent *cis*-ACes are presumably less soluble within the rigid L_o domains, and therefore prefer to be localized within the fluid phase.

The dynamic manipulation of membrane structure through fluctuations in Cer concentration is thought to be crucial for many biological processes²²⁴, potentially through the lateral segregation of lipids within the plane of the membrane. *In vitro*, we were able to observe the dynamic formation of small transient ordered domains, alongside the growth of existing ones, on isomerization of the ACes from *cis* to *trans*. As such, the ACes may provide biophysical insights on the requirements necessary to form rigid domains in the membrane on the generation of Cer. Effectively, the ACes permit cycling between ceramides with different biophysical characteristics, enabling dynamic and reversible control over the domain structure within model membranes. This characteristic is not shared with other photochemical tools like caged lipids. We hypothesize that the ACes may become useful to study the role of Cer production in the initiation of apoptosis or other signaling cascades. Furthermore, this work demonstrates the utility of the FAAzos as modular building blocks that can be used to construct more elaborate photoswitchable sphingolipids. As such, these tools will enable dynamic control over cell membranes, alongside the proteins with which they interact.

8.4 – Supporting information

8.4.1 – Supported lipid bilayer formation

N-Stearoyl-*D*-erythro-sphingosine (C18-Cer), *N*-stearoyl-*D*-erythro-sphingosylphosphorylcholine (C18-SM, or simply SM), 1,2-dioleoyl-*sn*-glycero-3-phosphocholine (DOPC) and cholesterol (Chol) were purchased from Avanti Polar Lipids (Alabaster, AL, USA). Supported lipid bilayers (SLBs) were prepared by deposition and fusion of small unilamellar vesicles (SUVs) as described elsewhere²³⁷. SUVs composed of DOPC:Chol:SM:C18-Cer and DOPC:Chol:SM:ACe, containing additional 0.1 mol% ATTO655-DOPE (ATTO Technology GmbH, Siegen, Germany), were obtained through bath sonication of multilamellar vesicles. SUV suspensions (1 mM total lipid concentration diluted in a 10 mM HEPES, 150 mM NaCl, pH 7.4 buffer) were deposited in the presence of 2 mM CaCl₂ on freshly-cleaved mica previously glued to glass coverslips. The samples were incubated for 30 min at 65 °C, rinsed with buffer and were then allowed to cool slowly to room temperature for at least 1 h.

SUV size (z-average) was measured at a total 66.7 μM lipid concentration via dynamic light scattering, utilizing a Malvern Zetasizer Nano ZSP (Malvern, Worcestershire, UK) with Hellma SUPRASIL precision quartz cuvettes (10 mm light path).

8.4.2 – Combined atomic force and confocal microscopy

Combined atomic force and confocal microscopy was performed on a JPK Instruments Nanowizard III BioAFM and Nanowizard Ultra (Berlin, Germany) mounted on a Zeiss LSM510 Meta laser scanning confocal microscope (Jena, Germany). Contact-mode AFM imaging was performed with the Nanowizard III head, using uncoated silicon cantilevers CSC38 from MikroMasch (Tallinn, Estonia) with typical spring constants of 0.01-0.2 N/m. The scan rate was typically set between 2-10 Hz. High-speed AFM in AC mode was done with the Nanowizard Ultra head, utilizing USC-F0.3-k0.3 ultra-short cantilevers from Nanoworld (Neuchâtel, Switzerland) with typical stiffness of 0.3 N/m. The cantilever oscillation was tuned to a frequency of 100-150 kHz and the amplitude kept below 10 nm. Scan rate was set to 25-150 Hz. For both modes, images were acquired with a typical 256×256-pixel resolution. All measurements were performed at room temperature. The force applied on the sample was minimized by continuously adjusting the set point and gain during imaging. Height, error, deflection and phase-shift signals were recorded and images were line-fitted as required. Data

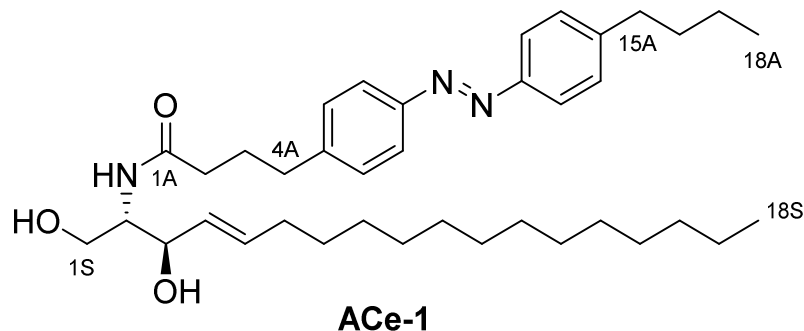
was analyzed using JPK data processing software Version 5.1.4 (JPK Instruments) and Gwyddion Version 2.30 (Czech Metrology Institute).

For the confocal measurements, a $\lambda = 633$ nm He-Ne laser (to excite the 0.1 mol% ATTO655-DOPE added to the lipid mixtures) and a 40 \times NA 1.2 UV-VIS-IR C Apochromat water-immersion objective were used. All measurements were performed at room temperature. Images were typically acquired with a 512 \times 512-pixel resolution at a scan rate of 3.2 μ s per pixel and using a 1 Airy pinhole. Images were further processed with Fiji software (<http://fiji.sc/Fiji>) and the resulting data was analyzed in Microsoft Excel. The data was then plotted using Igor Pro.

8.4.3 – Compound switching on supported lipid bilayers

Compound switching for combined atomic force and confocal microscopy was achieved using a CoolLED pE-2 LED light source (Andover, United Kingdom) for illumination at $\lambda = 365, 425$ and 470 nm. The lightsource was operated at a maximum of 80% power. The light beam was guided by a fiber-optic cable directly through the objective of the microscope via a collimator at the backport side of the microscope.

8.4.4 – Compound synthesis and characterization

8.4.4.1 – *N*-(4-(((4-butylphenyl)diazenyl)phenyl)butanamide)-(2*S*,3*R*)-2-aminoctadec-4-ene-1,3-diol (**ACe-1**)

A solution of **4-(((4-butylphenyl)diazenyl)phenyl)butanoic acid (FAAzo-4)**, 20 mg, 62 μmol , 1.0 equiv.) and *O*-(benzotriazol-1-yl)-*N,N,N',N'*-tetramethyluronium tetrafluoroborate (TBTU), 20 mg, 62 μmol , 1.0 equiv.) in EtOAc (3.0 mL) was treated with NEt_3 (25 mg, 4.0 equiv.) under an argon atmosphere at room temperature. After 1 h, *D*-erythro-sphingosine (24 mg, 0.078 mmol, 1.25 equiv.) was added and stirring was continued at room temperature for 4 h. The solution was then diluted with EtOAc (30 mL) and washed with aqueous NaHCO_3 (2x20 mL) and brine (2x20 mL, 50% saturated) solutions. The phases were separated and the organic solvents were removed under reduced pressure. The residue was then purified by flash silica gel chromatography (3.0 g SiO_2 , 3:1 EtOAc:hexane) to yield ***N*-(4-(((4-butylphenyl)diazenyl)-phenyl)butanamide)-(2*S*,3*R*)-2-aminoctadec-4-ene-1,3-diol (ACe-1)**, 26 mg, 70% as an orange oil.

TLC (EtOAc:hexane, 4:1): $R_f = 0.39$.

$^1\text{H NMR}$ (CDCl_3 , 400 MHz, 25 °C): δ 7.81 (d, 4 H, H7A_{a,b}, H12A_{a,b}, $J = 8.1$ Hz), 7.33-7.28 (m, 4 H, H6A_{a,b}, H13A_{a,b}), 6.33 (d, 1 H, NH, $J = 7.4$ Hz), 5.80-5.71 (m, 1 H, H5S), 5.50 (dd, 1 H, H4S, $J = 15.4, 6.3$ Hz), 4.29-4.25 (m, 1 H, H3S), 3.95-3.86 (m, 2 H, H2S, H1S_a), 3.67 (dd, 1 H, H1S_b, $J = 10.9, 3.1$ Hz), 3.12 (s_{brd}, 2 H, 2xOH), 2.76-2.50 (m, 4 H, H4A_{a,b}, H15A_{a,b}), 2.29-2.17 (m, 2 H, H2A_{a,b}), 2.07-1.96 (m, 4 H, H6S_{a,b}, H3A_{a,b}), 1.69-1.50 (m, 2 H, H16A_{a,b}), 1.44-1.66 (m, 24 H, H_{alk}), 0.94 (t, 3 H, H18A_{a,b,c}, $J = 7.4$ Hz), 0.90-0.85 (m, 3 H, H18S_{a,b,c}).

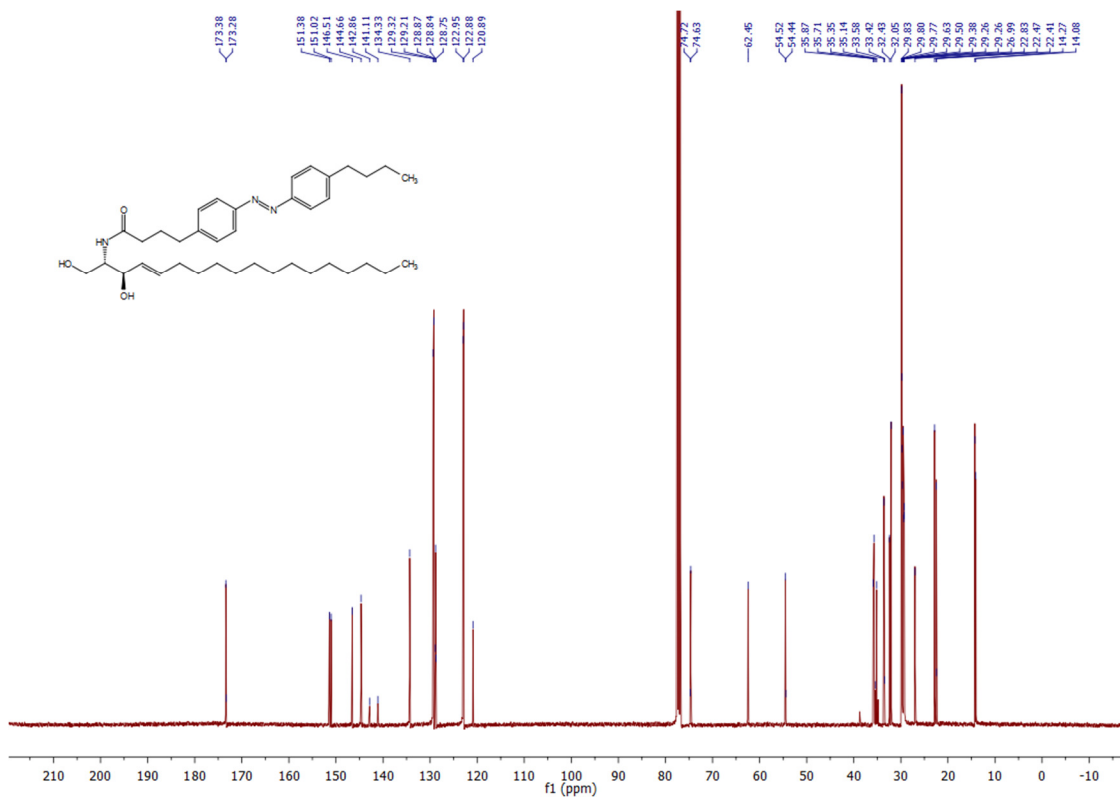
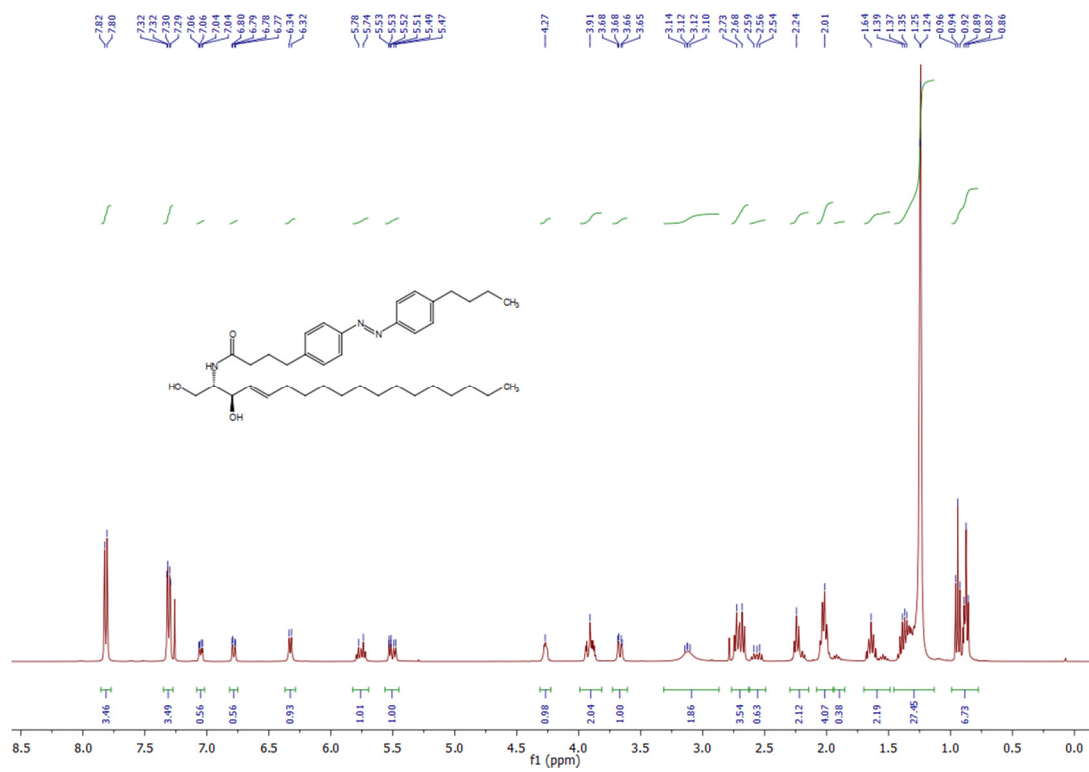
$^{13}\text{C NMR}$ (CDCl_3 , 101 MHz, 25 °C): δ 173.4 (C1A), 151.4 (C_{azo}), 151.0 (C_{azo}), 146.5 (C_{azo}), 144.6 (C_{azo}), 134.3 (C5S), 129.3 (2 C, C_{azo}), 129.2 (2 C, C_{azo}), 128.8 (C4S), 123.0 (2 C, C_{azo}), 122.9 (2 C, C_{azo}), 74.6 (C3S), 62.5 (C1S), 54.5 (C2S), 35.9 (C2A), 35.7 (C_{alk}), 35.1 (C_{alk}), 33.6 (C16A), 32.4 (C6S), 32.1 (C_{alk}), 29.83 (2C, C_{alk}), 29.80 (C_{alk}), 29.77 (C_{alk}), 29.6 (C_{alk}), 29.5 (C_{alk}), 29.4 (C_{alk}), 29.3 (C_{alk}), 27.0 (C_{alk}), 22.8 (C_{alk}), 22.5 (C_{alk}), 14.3 (C18A), 14.1 (C18S).

IR (neat, ATR): $\tilde{\nu} = 3291, 2954, 2918, 2849, 1640, 1602, 1548, 1497, 1466, 1454, 1435, 1417, 1377, 1284, 1224, 1199, 1155, 1107, 1070, 1036, 1013, 982, 959, 914, 850, 839, 721$.

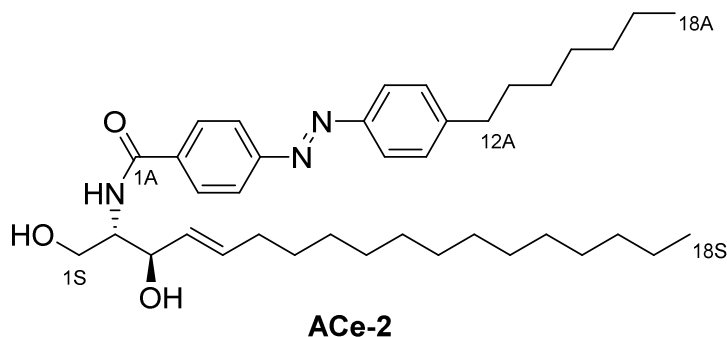
HRMS (EI): m/z calcd. for $[\text{C}_{28}\text{H}_{33}\text{N}_3\text{O}_3]$: 605.4556, found: 605.4563 ($[\text{M}-\text{e}]^+$).

UV-Vis (50 μM in DMSO): $\lambda_{\text{max}}(\pi-\pi^*) = 340$ nm. $\lambda_{\text{max}}(\text{n}-\pi^*) = 435$ nm.

8 – Optical control of lipid rafts with photoswitchable ceramides



8.4.4.2 – *N*-(4-((4-Heptylphenyl)diazenyl)benzamide)-(2*S*,3*R*)-2-aminoctadec-4-ene-1,3-diol (ACe-2)



N-(4-((4-Heptylphenyl)diazenyl)benzamide)-(2*S*,3*R*)-2-aminoctadec-4-ene-1,3-diol (**ACe-2**) was prepared from **4-((4-heptylphenyl)diazenyl)benzoic acid (FAAzo-1, 25 mg, 0.078 mmol, 1 equiv.)** as described above in the synthesis of ***N*-(4-((4-butylphenyl)diazenyl)phenyl)butanamide)-(2*S*,3*R*)-2-aminoctadec-4-ene-1,3-diol (ACe-1)**. **ACe-2** (43 mg, 92%) was isolated as an orange oil. *NOTE: all reactants and reagents were scaled according to molarity.*

TLC (EtOAc:hexane 9:1): $R_f = 0.31$.

¹H NMR (THF, 400 MHz, 25 °C): δ 8.01 (d, 2 H, H_{azo} , $J = 8.3$ Hz), 7.91 (d, 2 H, H_{azo} , $J = 8.2$ Hz), 7.86 (d, 2 H, H_{azo} , $J = 8.1$ Hz), 7.49 (d, 1 H, NH, $J = 8.2$ Hz), 7.36 (d, 2 H, H_{azo} , $J = 8.1$ Hz), 5.77-5.67 (m, 1 H, H_{5S}), 5.59 (dd, 1 H, H_{4S} , $J = 15.6, 6.3$ Hz), 4.39 (d, 1 H, $\text{OH}_{(3)}$, $J = 5.0$ Hz), 4.26 (q, 1 H, H_{3S} , $J = 5.5$ Hz), 4.08-4.00 (m, 1 H, H_{2S}), 3.97 (t, 1 H, $\text{OH}_{(1)}$, $J = 5.5$ Hz), 3.91-3.84 (m, 1 H, H_{1S_a}), 3.75-3.68 (m, 1 H, H_{1S_b}), 2.70 (t, 2 H, H_{12A} , $J = 7.9$ Hz), 2.06-1.96 (m, 2 H, $H_{6S_{a,b}}$), 1.72-1.63 (m, 2 H, $H_{13A_{a,b}}$), 1.40-1.20 (m, 30 H_{alk}), 0.94-0.82 (m, 6 H, $H_{18A_{a,b,c}}$, $H_{18S_{a,b,c}}$).

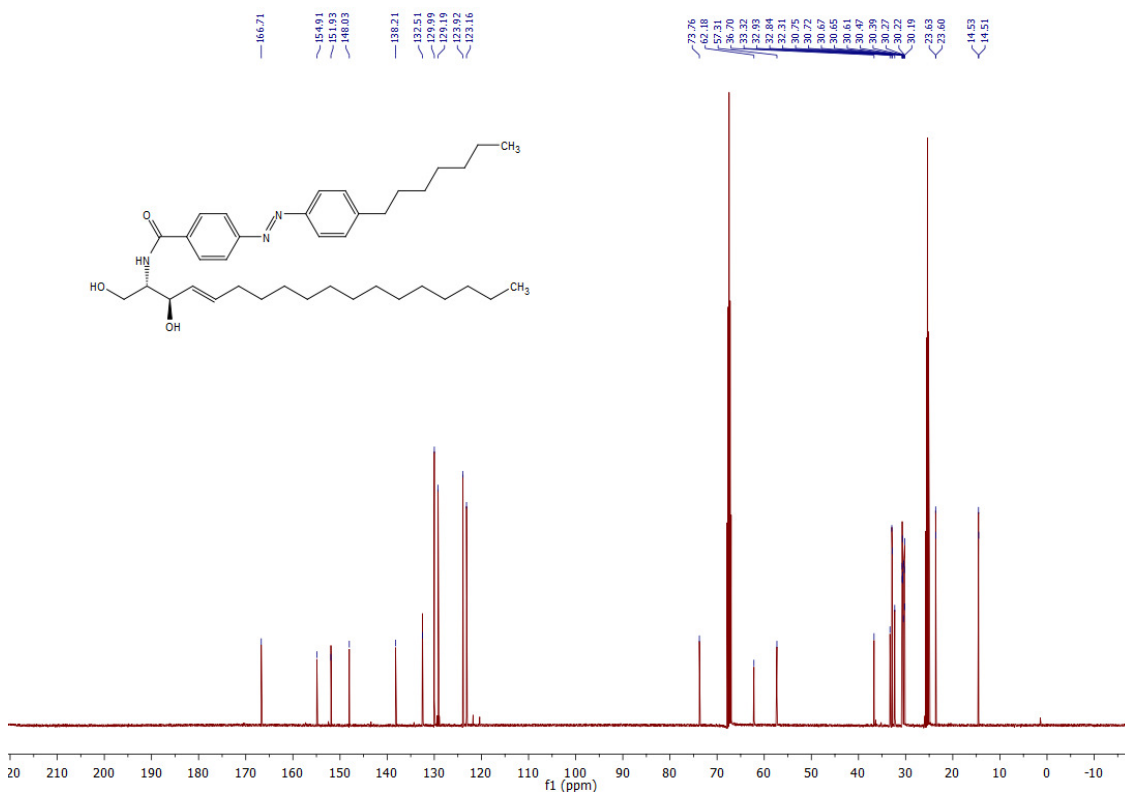
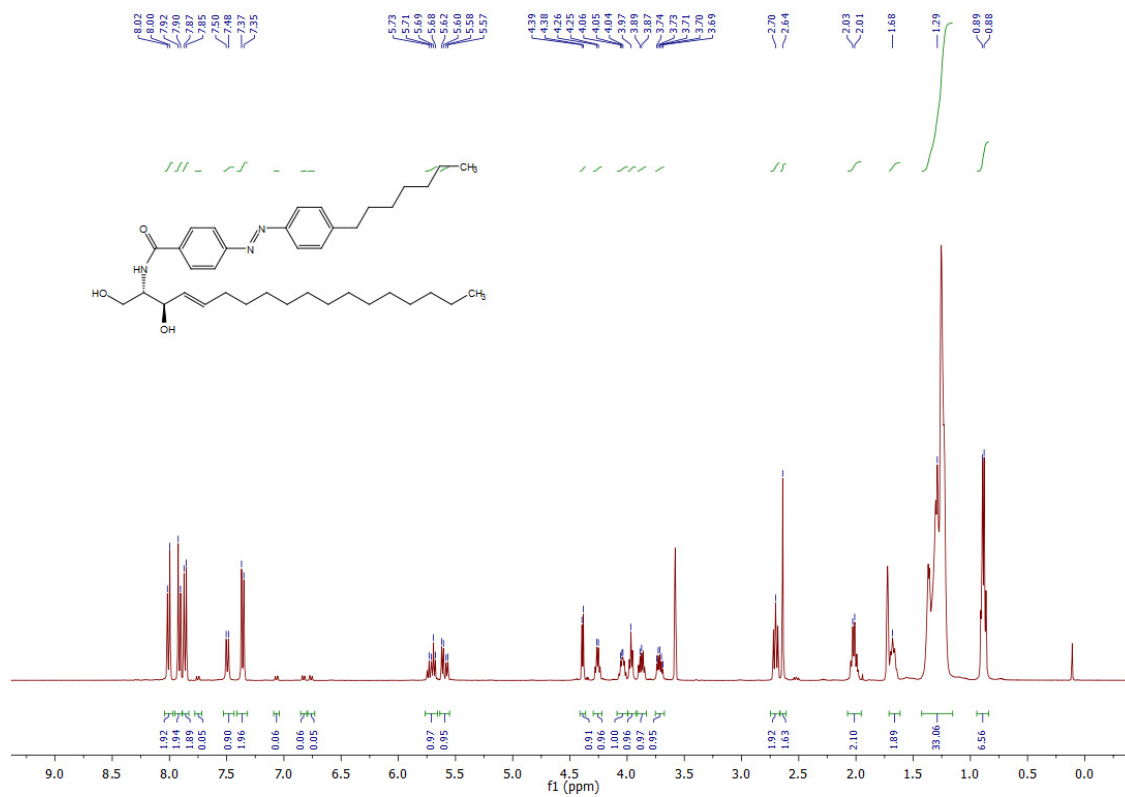
¹³C NMR (CDCl₃, 101 MHz, 25 °C): δ 166.7 (C_{1A}), 154.9 (C_{azo}), 151.9 (C_{azo}), 148.0 (C_{azo}), 138.2 (C_{azo}), 132.5 (2 C, C_{4S} , C_{5S}), 130.0 (2 C, C_{azo}), 129.2 (2 C, C_{azo}), 123.9 (2 C, C_{azo}), 123.2 (2 C, C_{azo}), 73.8 (C_{3S}), 62.2 (C_{1S}), 57.3 (C_{2S}), 36.7 (C_{12A}), 33.3 (C_{6S}), 32.9 (C_{alk}), 32.8 (C_{alk}), 32.3 (C_{13A}), 30.8 (C_{alk}), 30.72 (C_{alk}), 30.67 (C_{alk}), 30.65 (C_{alk}), 30.61 (C_{alk}), 30.5 (C_{alk}), 30.4 (C_{alk}), 30.3 (C_{alk}), 30.22 (C_{alk}), 30.19 (C_{alk}), 23.63 (C_{alk}), 23.60 (C_{alk}), 14.53 (C_{18}), 14.51 (C_{18}).

IR (neat, ATR): $\tilde{\nu} = 3677, 3634, 3301, 2955, 2850, 1634, 1604, 1575, 1539, 1493, 1466, 1414, 1341, 1300, 1259, 1222, 1154, 1101, 1047, 1012, 965, 858, 821, 770, 721$.

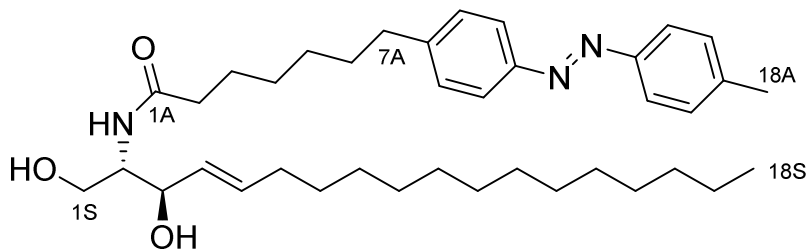
HRMS (EI⁺): m/z calcd. for $[C_{38}H_{60}N_3O_3]^+$: 606.4635, found: 606.4636 ($[M-e]^+$).

UV-Vis (50 μ M in DMSO): $\lambda_{\text{max}}(\pi-\pi^*) = 340$ nm. $\lambda_{\text{max}}(n-\pi^*) = 435$ nm.

8 – Optical control of lipid rafts with photoswitchable ceramides



8.4.4.3 – *N*-(7-(4-(*p*-Tolyldiazenyl)phenyl)heptanamide)-(2*S*,3*R*)-2-aminoctadec-4-ene-1,3-diol (ACe-3)



ACe-3

N-(7-(4-(*p*-Tolyldiazenyl)phenyl)heptanamide)-(2*S*,3*R*)-2-aminoctadec-4-ene-1,3-diol (ACe-3) was prepared from 7-(4-(*p*-tolyldiazenyl)phenyl)heptanoic acid (FAAzo-7, 9.0 mg, 0.028 mmol, 1.0 equiv.) as described above in the synthesis of *N*-(4-(((4-butylphenyl)diazenyl)phenyl)butanamide)-(2*S*,3*R*)-2-aminoctadec-4-ene-1,3-diol (ACe-1). ACe-3 (16.5 mg, 97%) was isolated as an orange solid. *NOTE: all reactants and reagents were scaled according to molarity.*

TLC (9:1 EtOAc:hexane): $R_f = 0.41$.

$^1\text{H NMR}$ (CDCl_3 , 400 MHz, 25 °C): δ 7.84–7.78 (m, 4 H, H10_{a,b}, H15A_{a,b}), 7.33–7.28 (m, 4 H, H9A_{a,b}, H16A_{a,b}), 6.25 (d, 1 H, NH, $J = 7.4$ Hz), 5.82–5.71 (m, 1 H, H5S), 5.52 (dd, 1 H, H4S, $J = 15.5, 6.3$ Hz), 4.33–4.27 (m, 1 H, H3S), 3.98–3.86 (m, 2 H, H2S, H1S_a), 3.68 (dd, 1 H, H15A, $J = 11.2, 3.2$ Hz), 2.79 (s_(br), 2 H, 2xOH), 2.67 (t, 2 H, H7A_{a,b}, $J = 7.5$ Hz), 2.43 (s, 3 H, H18A_{a,b,c}), 2.22 (t, 2 H, H2A_{a,b}, $J = 7.6$ Hz), 2.08–2.00 (m, 2 H, H6S_{a,b}), 1.71–1.59 (m, 4 H, H6A_{a,b}, H3A_{a,b}), 1.43–1.18 (m, 26 H, H_{alk}), 0.87 (t, 3 H, H18S_{a,b,c}, $J = 7.2$ Hz).

$^{13}\text{C NMR}$ (CDCl_3 , 100 MHz, 25 °C): δ 173.9 (C_{azo}), 151.1 (C_{azo}), 151.0 (C_{azo}), 146.1 (C_{azo}), 141.4 (C_{azo}), 143.4 (C_{azo}), 134.4 (C5S), 129.9 (2C, C_{azo}), 129.2 (2C, C_{azo}), 128.9 (C4S), 122.9 (4C, C_{azo}), 74.9 (C3S), 62.6 (C1S), 54.5 (C2S), 36.8 (C2A), 35.9 (C7A), 32.4 (C6S), 32.1 (C_{alk}), 31.2 (C_{alk}), 29.85 (C_{alk}), 29.84 (C_{alk}), 29.82 (C_{alk}), 29.81 (C_{alk}), 29.77 (C_{alk}), 29.64 (C_{alk}), 29.51 (C_{alk}), 29.37 (C_{alk}), 29.25 (C_{alk}), 29.19 (C_{alk}), 29.01 (C_{alk}), 25.7 (C_{alk}), 22.9 (C_{alk}), 21.7 (C18A), 14.2 (C18S).

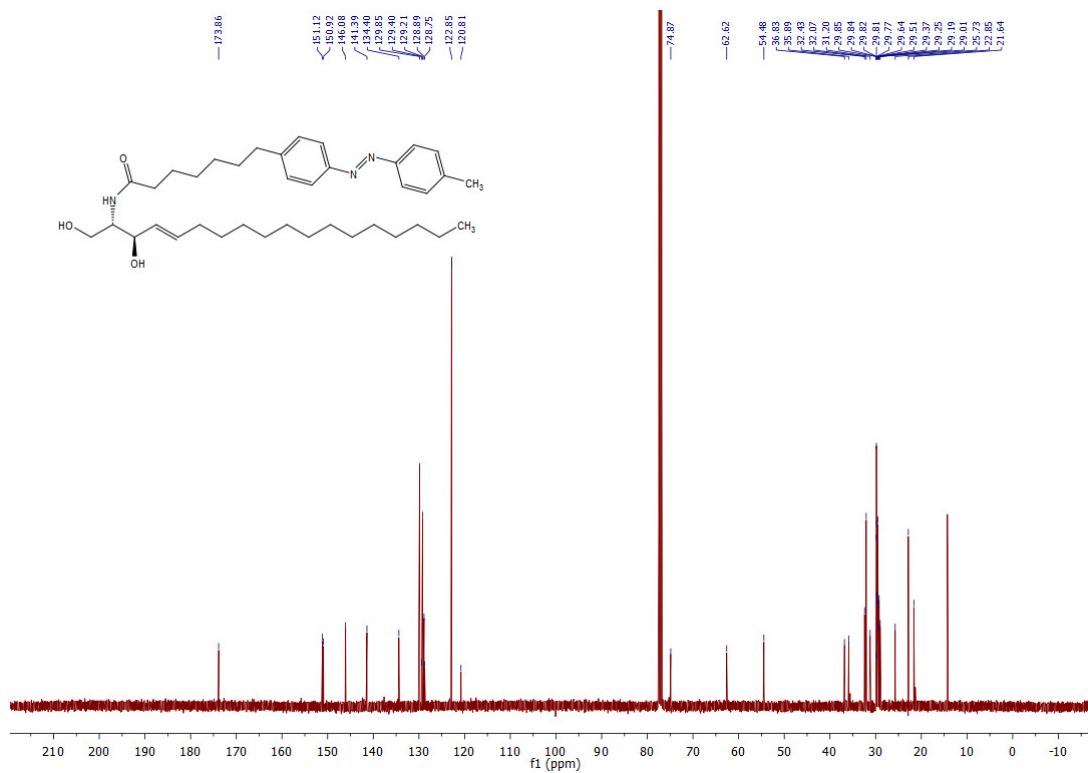
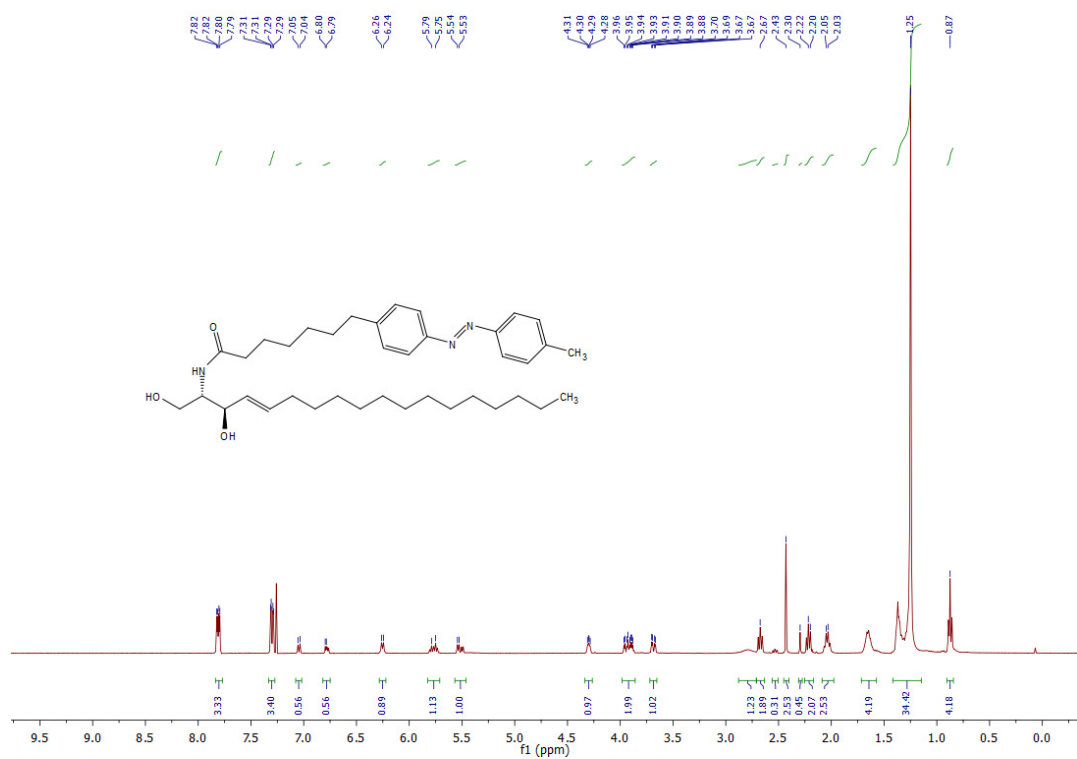
IR (neat, ATR): $\tilde{\nu} = 3564, 3294, 2919, 2850, 1634, 1603, 1539, 1466, 1359, 1155, 1104, 1012, 963, 855, 721$.

HRMS (ESI⁺): m/z calcd. for [C₃₈H₅₉N₃O₃]⁺: 605.4635, found: 606.4635 ([M+H]⁺).

UV-Vis (50 μM in DMSO): $\lambda_{\text{max}}(\pi-\pi^*) = 340$ nm. $\lambda_{\text{max}}(n-\pi^*) = 435$ nm.

Melting point (°C): 103–105.

8 – Optical control of lipid rafts with photoswitchable ceramides



9 – Appendix

9.1 – Abbreviations

1,2-DOG – 1,2-dioctanoyl- <i>sn</i> -glycerol	DCC – <i>N,N'</i> -dicyclohexylcarbodiimide
5-HT – serotonin	DCE – 1,2-dichloroethane
AA – arachidonic acid	DIPEA – <i>N,N</i> -diisopropylethylamine
AC – intermittent contact (AFM mode)	DNA – deoxyribonucleic acid
ACe – <i>azo</i> -ceramide	DOPC – 1,2-dioleoyl- <i>sn</i> -glycero-3-phosphocholine
AcOOH – peracetic acid	DOPE – 1,2-dioleoyl- <i>sn</i> -glycero-3-phosphoethanolamine
AFM – atomic force microscopy	DMAP – 4-dimethylaminopyridine
Am – acetoxymethyl (protecting group)	DMEM – Dulbecco's modified eagle medium
AP – action potential	DMSO – dimethyl sulfoxide
ATP – adenosine 5'-triphosphate	DRG – dorsal root ganglion
ATR – attenuated total reflectance	EDC – 1-ethyl-3-(3-dimethylaminopropyl)carbodiimide
a.u. – arbitrary units	EGTA – ethylene glycol-bis(β -aminoethyl ether)- <i>N,N,N',N'</i> -tetraacetic acid
AzCA – <i>azo</i> -capsaicin	EI – electron ionization
BK – bradykinin	EPSC – excitatory postsynaptic current
Bn – benzyl	ESI – electrospray ionization
BSA – bovine serum albumin	FA – fatty acid
Bt – butyryl (protecting group)	FAAzo – photoswitchable fatty acid
[Ca ²⁺] _i – intracellular Ca ²⁺ concentration	FBS – fetal bovine serum
CAP – capsaicin	FCS – fetal calf serum
Ca _v – L-type voltage-activated Ca ²⁺ channel	Fm – 9-fluorenylmethyl (protecting group)
C-Cl – chelerythrine chloride	FRET – Förster resonance energy transfer
cDNA – complementary deoxyribonucleic acid	GFP – green fluorescent protein
Cer – ceramide	GPCR – G protein-coupled receptor
cg – caged	GSIS – glucose-stimulated insulin secretion
Chol – cholesterol	
CKAR – C kinase activity reporter	
CM-H – C-fiber nociceptor	
CPZ – capsazepine	
DAG – diacylglycerol	

HEPES – 4-(2-hydroxyethyl)-1-piperazineethanesulfonic acid	PMA – phorbol 12-myristate 13-acetate
HIS – histamine	PKC – protein kinase C
Hi-K ⁺ – high potassium	PM/CP – plasma membrane to cytoplasm (translocation quantification ratio)
HRMS – high-resolution mass spectrometry	PTL – photoswitched tethered ligand
HTRF – homogeneous time-resolved fluorescence	RFP – red fluorescent protein
IR – infrared (spectroscopy)	RPMI – Roswell Park Memorial Institute (medium)
<i>i</i> Pr – isopropyl	SAG – 1-O-stearoyl-2-O-arachidonoyl- <i>sn</i> -glycerol
K _{ATP} – ATP-sensitive K ⁺ channel	sEPSC – spontaneous miniature postsynaptic current
K _v – delayed rectifier voltage-gated K ⁺ channel	SLB – supported lipid bilayer
L _d – liquid disordered (domain)	SM – sphingomyelin
L _o – liquid ordered (domain)	s _o – gel-like (domain)
MeCN – acetonitrile	SUV – small unilamellar vesicle
NGM – nematode growth medium	TBME – <i>tert</i> -butyl methyl ether
NMR – nuclear magnetic resonance (spectroscopy)	TBTU – O-(benzotriazol-1-yl)- <i>N,N,N',N'</i> -tetramethyluronium tetrafluoroborate
ns – not significant	TES – triethylsilyl (protecting group)
osc – oscillation	TESOTf – triethylsilyl trifluoromethanesulfonate
PBS – phosphate-buffered saline	THF – tetrahydrofuran
PC – phosphatidylcholine	TLC – thin layer chromatography
PCL – photochromic ligand	TRP – transient receptor potential
PhMe – toluene	UV-Vis – ultraviolet-visible (spectroscopy)
PhoDAG – photoswitchable diacylglycerol	wt – wild type
PI(4,5)P ₂ – phosphatidylinositol 4,5-bisphosphate	
PLC – phospholipase C	

9.2 – General synthetic methods and spectroscopic characterization

All reagents and solvents were purchased from commercial sources (Sigma-Aldrich, TCI Europe N.V., Strem Chemicals, etc.) and were used without further purification unless otherwise noted. Tetrahydrofuran (THF) was distilled under a N₂ atmosphere from Na/benzophenone prior to use. Triethylamine (NEt₃), was distilled under a N₂ atmosphere from CaH₂ prior to use. Further dry solvents such as ethyl acetate (EtOAc), benzene (PhH), dichloromethane (CH₂Cl₂), toluene (PhMe), ethanol (EtOH) and methanol (MeOH) were purchased from Acros Organics as "extra dry" reagents and used as received. Solvents were degassed by sparging the freshly distilled solvent with argon gas in a Schlenk flask under ultra-sonication using a Bandelin Sonorex RK510H ultra-sonic bath for 20 min prior to use. Reactions were monitored by TLC on pre-coated, Merck Silica gel 60 F₂₅₄ glass-backed plates and the chromatograms were first visualized by UV irradiation at $\lambda = 254$ nm, followed by staining with aqueous ninhydrin, anisaldehyde or ceric ammonium molybdate solution (CAM), and finally gentle heating with a heat gun. Flash silica gel chromatography was performed using silica gel (SiO₂, particle size 40-63 μ m) purchased from Merck.

UV-Vis spectra were recorded using a Varian Cary 50 Bio UV-Visible Spectrophotometer with Helma SUPRASIL precision cuvettes (10 mm light path). Switching was achieved using a Polychrome V (Till Photonics) monochromator (intensity vs. wavelength screen, **Fig. 9.1**). The illumination was controlled using PolyCon3.1 software and the light was guided through a fiber-optic cable with the tip pointed directly into the top of the sample cuvette.

All NMR spectra were measured on a BRUKER Avance III HD 400 (equipped with a CryoProbe™). Multiplicities in the following experimental procedures are abbreviated as follows: s = singlet, d = doublet, t = triplet, q = quartet, quint = quintet, sext = sextet, hept = heptet, br = broad, m = multiplet. ¹H chemical shifts are expressed in parts per million (ppm, δ scale) and are referenced to the residual protium in the NMR solvent (CDCl₃: $\delta = 7.26$, D₆-DMSO: $\delta = 2.50$, THF-d₈: $\delta = 3.58$, C₆D₆: $\delta = 7.16$). ¹³C chemical shifts are also expressed in ppm (δ scale) and are referenced to the carbon resonance of the NMR solvent (CDCl₃: $\delta = 77.16$, D₆-DMSO: $\delta = 39.52$, THF-d₈: $\delta = 67.21$, C₆D₆: $\delta = 128.06$). NOTE: Due to the *trans/cis* isomerisation of some compounds containing an azobenzene functionality, more signals are observed in the ¹H and ¹³C spectra than would be expected for the pure *trans*-isomer. Only signals for the major *trans*-isomer are reported, however the identities of the remaining peaks were verified by 2D-COSY, HSQC and HMBC experiments.

Infrared (IR) spectra were recorded as neat materials on a PERKIN ELMER Spectrum BX-59343 instrument. For detection, a SMITHS DETECTION DuraSam-pIR II Diamond ATR sensor was used. The measured wave numbers are reported in cm^{-1} .

Low- and high-resolution electron ionization (EI) mass spectra were obtained on a MAT CH7A mass spectrometer. Low- and high-resolution electrospray ionization (ESI) mass spectra were obtained on a Varian MAT 711 MS instrument operating in either positive or negative ionization modes.

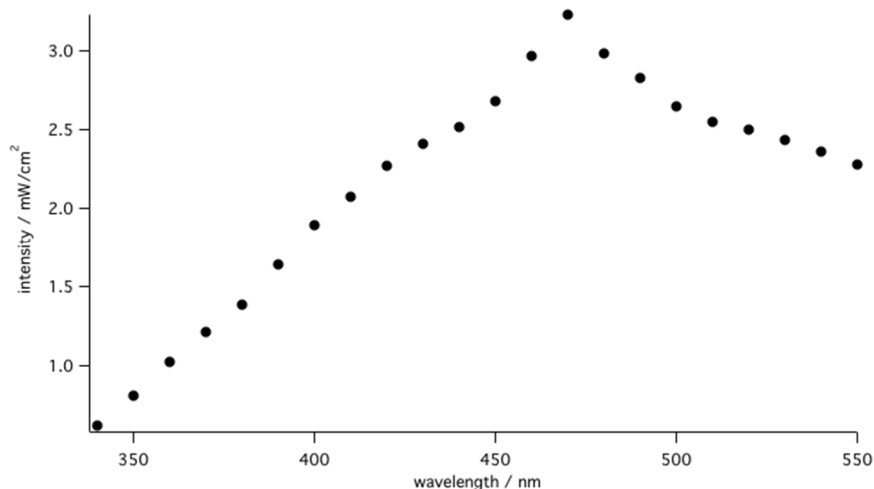


Figure 9.1 | Wavelength vs. intensity screen of the Till Photonics Polychrome V.

9.3 – Data reporting and error analysis

For imaging experiments, “n” is the number of measurements made (individual cells). The number of independent experiments included in each panel is also described in the figure caption. For electrophysiological experiments, “n” represents the number of cells, each of which constitute an independent experiment. For insulin secretion experiments, “n” represents the number of independent experiments performed. For experiments in *C. elegans*, “n” represents the number of animals used, the number of independent experiments is also described in the figure caption. For all figure panels, results are plotted as mean \pm s.e.m., using “n” as the number of samples. Where appropriate, the Mann-Whitney test was used to determine statistical significance.

9.4 – References

1. Tanford, C. *The Hydrophobic Effect: Formation of Micelles and Biological Membranes*. (Wiley, New York, 1980).
2. Kauzmann, W. Some Factors in the Interpretation of Protein Denaturation. *Adv. Protein Chem.* **14**, 1–63 (1959).
3. Singer, S. J. & Nicolson, G. L. The Fluid Mosaic Model of the Structure of Cell Membranes. *Science* **175**, 720–731 (1972).
4. Shevchenko, A. & Simons, K. Lipidomics: coming to grips with lipid diversity. *Nat. Rev.* **11**, 593–598 (2010).
5. Fahy, E. *et al.* A comprehensive classification system for lipids. *J. Lipid Res.* **46**, 839–861 (2005).
6. Dennis, E. A. Lipidomics joins the omics evolution. *Proc. Natl. Acad. Sci.* **106**, 2089–2090 (2009).
7. Yetukuri, L., Ekroos, K., Vidal-puig, A. & Ores, M. Informatics and computational strategies for the study of lipids. *Mol. Biosyst.* **4**, 121–127 (2008).
8. Sud, M. *et al.* LMSD : LIPID MAPS structure database. *Nucleic Acids Res.* **35**, 527–532 (2007).
9. Meer, G. Van. Cellular lipidomics. *EMBO J.* **24**, 3159–3165 (2005).
10. Meer, G. Van, Voelker, D. R. & Feigenson, G. W. Membrane lipids : where they are and how they behave. *Nat. Rev. Mol. Cell Biol.* **9**, 112–124 (2008).
11. Hannun, Y. A. & Obeid, L. M. Principles of bioactive lipid signalling : lessons from sphingolipids. *Nat. Rev. Mol. Cell Biol.* **9**, 139–150 (2008).
12. Simons, K. & Toomre, D. Lipid rafts and signal transduction. *Nat. Rev. Mol. Cell Biol.* **1**, 31–39 (2000).

13. *IUPAC Gold Book - Fatty Acids*. *IUPAC Gold Book* (Blackwell Scientific Publications, 1997). doi:10.1351/goldbook.
14. Briscoe, C. P. *et al.* The Orphan G Protein-coupled Receptor GPR40 Is Activated by Medium and Long Chain Fatty Acids. *J. Biol. Chem.* **278**, 11303–11311 (2003).
15. Jacobson, D. A. *et al.* Kv2.1 Ablation Alters Glucose-Induced Islet Electrical Activity, Enhancing Insulin Secretion. *Cell Metab.* **6**, 229–235 (2007).
16. Wenk, M. R. The emerging field of lipidomics. *Nat. Rev. Drug Discov.* **4**, 594–610 (2005).
17. Gautier, A. *et al.* How to control proteins with light in living systems. *Nat. Chem. Biol.* **10**, 533–41 (2014).
18. Shcherbakova, D. M., Shemetov, A. A., Kaberniuk, A. A. & Verkhusha, V. V. Natural Photoreceptors as a Source of Fluorescent Proteins, Biosensors, and Optogenetic Tools. *Annu. Rev. Biochem.* **84**, 519–550 (2015).
19. Toettcher, J. E., Voigt, C., Weiner, O. D. & Lim, W. The promise of optogenetics in cell biology: interrogating molecular circuits in space and time. *Nat. Methods* **8**, 35–38 (2012).
20. Boyden, E. S., Zhang, F., Bamberg, E., Nagel, G. & Deisseroth, K. Millisecond-timescale, genetically targeted optical control of neural activity. *Nat. Neurosci.* **8**, 1263–1268 (2005).
21. Bernstein, J. G. & Boyden, E. S. Optogenetic tools for analyzing the neural circuits of behavior. *Trends Cogn. Sci.* **15**, 592–600 (2011).
22. Montgomery, K. L., Iyer, S. M., Christensen, A. J., Deisseroth, K. & Delp, S. L. Beyond the brain : Optogenetic control in the spinal cord and peripheral nervous system. *Sci. Transl. Med.* **8**, 1–12 (2016).
23. Nerbonne, J. M. Caged compounds: tools for illuminating neuronal responses and connections. *Curr. Opin. Neurobiol.* **6**, 379–386 (1996).
24. Höglinger, D., Nadler, A. & Schultz, C. Caged lipids as tools for investigating cellular signaling. *Biochim. Biophys. Acta - Mol. Cell Biol. Lipids* **1841**, 1085–1096 (2014).

-
25. Subramanian, D. *et al.* Activation of membrane-permeant caged PtdIns(3)P induces endosomal fusion in cells. *Nat. Chem. Biol.* **6**, 324–326 (2010).
 26. Goedhart, J. & Gadella, T. W. J. Photolysis of Caged Phosphatidic Acid Induces Flagellar Excision in Chlamydomonas. *Biochemistry* **43**, 4263–4271 (2004).
 27. Zhang, Z. & Smith, B. D. Synthesis and Characterization of NVOC-DOPE , a Caged Photoactivatable Derivative of Dioleoylphosphatidylethanolamine. *Bioconjug. Chem.* **10**, 1150–1152 (1999).
 28. Ramirez, D. M. C., Pitre, S. P., Kim, Y. A., Bittman, R. & Johnston, L. J. Photouncaging of ceramides promotes reorganization of liquid-ordered domains in supported lipid bilayers. *Langmuir* **29**, 3380–3387 (2013).
 29. Qiao, L., Kozikowski, A. P., Olivera, A. & Spiegel, S. Synthesis and evaluation of a photolyzable derivative of sphingosine 1-phosphate - caged spp. *Bioorg. Med. Chem. Lett.* **8**, 711–714 (1998).
 30. Tuchinsky, A. & Zehavi, U. Chemoenzymic synthesis of potentially caged glycosphingolipids (GSLs): potentially caged lyso-GM3 and its analogue. *Chem. Phys. Lipids* **92**, 91–97 (1998).
 31. Zehavi, U. Synthesis of potentially caged sphingolipids, possible precursors of cellular modulators and second messengers. *Chem. Phys. Lipids* **90**, 55–61 (1997).
 32. Pelliccioli, A. P. & Wirz, J. Photoremovable protecting groups: reaction mechanisms and applications. *Photochem. Photobiol. Sci.*, **1**, 441–458 (2002).
 33. Fehrentz, T., Schönberger, M. & Trauner, D. Optochemical genetics. *Angew. Chemie - Int. Ed.* **50**, 12156–12182 (2011).
 34. Velema, W. A., Szymanski, W. & Feringa, B. L. Photopharmacology: Beyond proof of principle. *J. Am. Chem. Soc.* **136**, 2178–2191 (2014).
 35. Broichhagen, J., Frank, J. A. & Trauner, D. A Roadmap to Success in Photopharmacology. *Acc. Chem. Res.* **48**, 1947–1960 (2015).

36. Hansen, M. J., Lerch, M. M., Szymanski, W. & Feringa, B. L. Direct and Versatile Synthesis of Red-Shifted Azobenzenes. *Angew. Chem. Int. Ed. Engl.* **128**, 13712–13716 (2016).
37. Konrad, D. B., Frank, J. A. & Trauner, D. Synthesis of Redshifted Azobenzene Photoswitches by Late-Stage Functionalization. *Chem. a Eur. J.* **22**, 4364–4368 (2016).
38. Sadvski, O., Beharry, A. A., Zhang, F. & Woolley, G. A. Spectral Tuning of Azobenzene Photoswitches for Biological Applications. *Angew. Chemie - Int. Ed.* **48**, 1484–1486 (2009).
39. Samanta, S. *et al.* Photoswitching Azo compounds in vivo with red light. *J. Am. Chem. Soc.* **135**, 9777–9784 (2013).
40. Banghart, M., Borges, K., Isacoff, E., Trauner, D. & Kramer, R. H. Light-activated ion channels for remote control of neuronal firing. *Nat. Neurosci.* **7**, 1381–1386 (2004).
41. Broichhagen, J. & Trauner, D. The in vivo chemistry of photoswitched tethered ligands. *Curr. Opin. Chem. Biol.* **21**, 121–127 (2014).
42. Broichhagen, J. *et al.* Orthogonal Optical Control of a G Protein-Coupled Receptor with a SNAP-Tethered Photochromic Ligand. *ACS Cent. Sci.* **1**, 383–393 (2015).
43. Mouro, A. *et al.* Rapid optical control of nociception with an ion-channel photoswitch. *Nat. Methods* **9**, 396–402 (2012).
44. Lerch, M. M., Hansen, M. J., Dam, G. M. Van, Szymanski, W. & Feringa, B. L. Emerging Targets in Photopharmacology. *Angew. Chemie - Int. Ed.* **55**, 10978–10999 (2016).
45. Fujiwara, H. & Yonezawa, Y. Photoelectric response of a black lipid membrane containing an amphiphilic azobenzene derivative. *Nature* **351**, 724–726 (1991).
46. Song, X., Perlstein, J. & Whitten, D. G. Supramolecular aggregates of azobenzene phospholipids and related compounds in bilayer assemblies and other microheterogeneous media: Structure, properties, and photoreactivity. *J. Am. Chem. Soc.* **119**, 9144–9159 (1997).

47. Sandhu, S. S., Yianni, Y. P., Morgan, C. G., Taylor, D. M. & Zaba, B. The formation and Langmuir-Blodgett deposition of monolayers of novel photochromic azobenzene-containing phospholipid molecules. *BBA - Biomembr.* **860**, 253–262 (1986).
48. Eggers, K., Fyles, T. M. & Montoya-Pelaez, P. J. Synthesis and characterization of photoswitchable lipids containing hemithioindigo chromophores. *J. Org. Chem.* **66**, 2966–2977 (2001).
49. Yasuhara, K., Sasaki, Y. & Kikuchi, J. I. A photo-responsive cholesterol capable of inducing a morphological transformation of the liquid-ordered microdomain in lipid bilayers. *Colloid Polym. Sci.* **286**, 1675–1680 (2008).
50. Hamada, T., Sugimoto, R., Nagasaki, T. & Takagi, M. Photochemical control of membrane raft organization. *Soft Matter* **7**, 220–224 (2011).
51. Frank, J. A. *et al.* Photoswitchable fatty acids enable optical control of TRPV1. *Nat. Commun.* **6**, 7118 (2015).
52. Frank, J. A. *et al.* Photoswitchable diacylglycerols enable optical control of protein kinase C. *Nat. Chem. Biol.* **12**, 755–762 (2016).
53. Frank, J. A., Franquelim, H. G., Schwille, P. & Trauner, D. Optical Control of Lipid Rafts with Photoswitchable Ceramides. *J. Am. Chem. Soc.* **138**, 12891–12896 (2016).
54. Wang, X. Lipid signaling. *Curr. Opin. Plant Biol.* **7**, 329–336 (2004).
55. Szallasi, A., Cortright, D. N., Blum, C. A. & Eid, S. R. The vanilloid receptor TRPV1: 10 years from channel cloning to antagonist proof-of-concept. *Nat. Rev. Drug Discov.* **6**, 357–372 (2007).
56. Chuang, H. H. *et al.* Bradykinin and nerve growth factor release the capsaicin receptor from PtdIns(4,5)P₂-mediated inhibition. *Nature* **411**, 957–962 (2001).
57. Clapham, D. E. TRP channels as cellular sensors. *Nature* **426**, 517–524 (2003).
58. Venkatachalam, K. & Montell, C. TRP channels. *Annu. Rev. Biochem.* **76**, 387–417 (2007).

59. Gavva, N. R. Body-temperature maintenance as the predominant function of the vanilloid receptor TRPV1. *Trends Pharmacol. Sci.* **29**, 550–557 (2008).
60. Tominaga, M. *et al.* The cloned capsaicin receptor integrates multiple pain-producing stimuli. *Neuron* **21**, 531–543 (1998).
61. Holzer, P. Local effector functions of capsaicin-sensitive sensory nerve endings: involvement of tachykinins, calcitonin gene-related peptide and other neuropeptides. *Neuroscience* **24**, 739–768 (1988).
62. Caterina, M. J. *et al.* The capsaicin receptor: a heat-activated ion channel in the pain pathway. *Nature* **389**, 816–24 (1997).
63. Jordt, S. E., Tominaga, M. & Julius, D. Acid potentiation of the capsaicin receptor determined by a key extracellular site. *Proc. Natl. Acad. Sci. U. S. A.* **97**, 8134–8139 (2000).
64. Cuypers, E., Yanagihara, A., Karlsson, E. & Tytgat, J. Jellyfish and other cnidarian envenomations cause pain by affecting TRPV1 channels. *FEBS Lett.* **580**, 5728–5732 (2006).
65. Siemens, J. *et al.* Spider toxins activate the capsaicin receptor to produce inflammatory pain. *Nature* **444**, 208–212 (2006).
66. Ross, R. Anandamide and vanilloid TRPV1 receptors. *Br. J. Pharmacol.* **140**, 790–801 (2003).
67. Huang, S. M. *et al.* An endogenous capsaicin-like substance with high potency at recombinant and native vanilloid VR1 receptors. *Proc. Natl. Acad. Sci. U. S. A.* **99**, 8400–8405 (2002).
68. Brand, L. *et al.* NE-19550: a novel, orally active anti-inflammatory analgesic. *Drugs Exp. Clin. Res.* **13**, 259–265 (1987).
69. Melck, D. *et al.* Unsaturated long-chain N-acyl-vanillyl-amides (N-AVAMs): vanilloid receptor ligands that inhibit anandamide-facilitated transport and bind to CB1 cannabinoid receptors. *Biochem. Biophys. Res. Commun.* **262**, 275–284 (1999).

-
70. Davis, J. B. *et al.* Vanilloid receptor-1 is essential for inflammatory thermal hyperalgesia. *Nature* **405**, 183–187 (2000).
 71. Hu, W. P., Guan, B. C., Ru, L. Q., Chen, J. G. & Li, Z. W. Potentiation of 5-HT₃ receptor function by the activation of coexistent 5-HT₂ receptors in trigeminal ganglion neurons of rats. *Neuropharmacology* **47**, 833–40 (2004).
 72. Hanack, C. *et al.* GABA Blocks Pathological but Not Acute TRPV1 Pain Signals. *Cell* **160**, 759–770 (2015).
 73. Mourot, A., Tochitsky, I. & Kramer, R. H. Light at the end of the channel: optical manipulation of intrinsic neuronal excitability with chemical photoswitches. *Front. Mol. Neurosci.* **6**, 5 (2013).
 74. Stein, M., Breit, A., Fehrentz, T., Gudermann, T. & Trauner, D. Optical control of TRPV1 channels. *Angew. Chemie - Int. Ed.* **52**, 9845–9848 (2013).
 75. Morgan, C. G., Thomas, E. W., Yianni, Y. P. & Sandhu, S. S. Incorporation of a novel photochromic phospholipid molecule into vesicles of dipalmitoylphosphatidylcholine. *Biochim. Biophys. Acta - Biomembr.* **820**, 107–114 (1985).
 76. Cao, E., Liao, M., Cheng, Y. & Julius, D. TRPV1 structures in distinct conformations reveal activation mechanisms. *Nature* **504**, 113–118 (2013).
 77. Hellwig, N., Albrecht, N., Harteneck, C., Schultz, G. & Schaefer, M. Homo- and heteromeric assembly of TRPV channel subunits. *J. Cell Sci.* **118**, 917–928 (2005).
 78. Bevan, S. *et al.* Capsazepine: a competitive antagonist of the sensory neurone excitant capsaicin. *Br. J. Pharmacol.* **107**, 544–552 (1992).
 79. Walpole, C. S. *et al.* The discovery of capsazepine, the first competitive antagonist of the sensory neuron excitants capsaicin and resiniferatoxin. *J. Med. Chem.* **37**, 1942–1954 (1994).
 80. Cavanaugh, D. J., Chesler, A. T., Bráz, J. M., Shah, N. M. & Basbaum, A. I. Restriction of TRPV1 to the peptidergic subset of primary afferent neurons follows its developmental downregulation in nonpeptidergic neurons. *J. Neurosci.* **31**, 10119–10127 (2011).

81. Bölcseki, K. *et al.* Investigation of the role of TRPV1 receptors in acute and chronic nociceptive processes using gene-deficient mice. *Pain* **117**, 368–376 (2005).
82. Huang, J., Zhang, X. & McNaughton, P. Inflammatory pain: the cellular basis of heat hyperalgesia. *Curr. Neuropharmacol.* **4**, 197–206 (2006).
83. Sugiuar, T., Bielefeldt, K. & Gebhart, G. F. TRPV1 function in mouse colon sensory neurons is enhanced by metabotropic 5-hydroxytryptamine receptor activation. *J. Neurosci.* **24**, 9521–9530 (2004).
84. Moriyama, T. *et al.* Sensitization of TRPV1 by EP1 and IP reveals peripheral nociceptive mechanism of prostaglandins. *Mol. Pain* **1**, 3 (2005).
85. Ohta, T. *et al.* Potentiation of transient receptor potential V1 functions by the activation of metabotropic 5-HT receptors in rat primary sensory neurons. *J. Physiol.* **576**, 809–822 (2006).
86. Zariwala, H. A. *et al.* A Cre-Dependent GCaMP3 Reporter Mouse for Neuronal Imaging *In Vivo*. *J. Neurosci.* **32**, 3131–3141 (2012).
87. Cavanaugh, D. J. *et al.* Trpv1 reporter mice reveal highly restricted brain distribution and functional expression in arteriolar smooth muscle cells. *J. Neurosci.* **31**, 5067–5077 (2011).
88. Yeh, J. Z. Sodium inactivation mechanism modulates QX-314 block of sodium channels in squid axons. *Biophys. J.* **24**, 569–574 (1978).
89. Binshtok, A. M., Bean, B. P. & Woolf, C. J. Inhibition of nociceptors by TRPV1-mediated entry of impermeant sodium channel blockers. *Nature* **449**, 607–610 (2007).
90. Dong, M., Babalhavaeji, A., Samanta, S., Beharry, A. A. & Woolley, G. A. Red-Shifting Azobenzene Photoswitches for *in Vivo* Use. *Acc. Chem. Res.* **48**, 2662–2670 (2015).
91. Rullo, A. *et al.* Long wavelength optical control of glutamate receptor ion channels using a tetra-*ortho*-substituted azobenzene derivative. *Chem. Commun.* **50**, 14613–14615 (2014).

-
92. Iida, T. *et al.* TRPV1 activation and induction of nociceptive response by a non-pungent capsaicin-like compound, capsiate. *Neuropharmacology* **44**, 958–967 (2003).
 93. Wang, Y. *et al.* Kinetics of Penetration Influence the Apparent Potency of Vanilloids on TRPV1. **69**, 1166–1173 (2006).
 94. Ursu, D., Knopp, K., Beattie, R. E., Liu, B. & Sher, E. Pungency of TRPV1 agonists is directly correlated with kinetics of receptor activation and lipophilicity. *Eur. J. Pharmacol.* **641**, 114–122 (2010).
 95. Liu, L., Lo, Y., Chen, I. & Simon, S. The responses of rat trigeminal ganglion neurons to capsaicin and two nonpungent vanilloid receptor agonists, olvanil and glyceryl nonamide. *J. Neurosci.* **17**, 4101–4111 (1997).
 96. Chou, M. Z., Mtui, T., Gao, Y. D., Kohler, M. & Middleton, R. E. Resiniferatoxin Binds to the Capsaicin Receptor (TRPV1) near the Extracellular Side of the S4 Transmembrane Domain. *Biochemistry* **43**, 2501–2511 (2004).
 97. Jung, J. *et al.* Capsaicin binds to the intracellular domain of the capsaicin-activated ion channel. *J. Neurosci.* **19**, 529–538 (1999).
 98. Vyklický, L., Lyfenko, A., Kuffler, D. P. & Vlachová, V. Vanilloid receptor TRPV1 is not activated by vanilloids applied intracellularly. *Neuroreport* **14**, 1061–1065 (2003).
 99. Zemelman, B. V., Nesnas, N., Lee, G. A. & Miesenbo, G. Photochemical gating of heterologous ion channels: Remote control over genetically designated populations of neurons. *Proc. Natl. Acad. Sci. U. S. A.* **100**, 1352–1357 (2003).
 100. Voets, T. *et al.* The principle of temperature-dependent gating in cold- and heat-sensitive TRP channels. *Nature* **430**, 748–754 (2004).
 101. Moshourab, R. A., Wetzel, C., Martinez-Salgado, C. & Lewin, G. R. Stomatin-domain protein interactions with acid-sensing ion channels modulate nociceptor mechanosensitivity. *J. Physiol.* **591**, 5555–5574 (2013).
 102. García-Domínguez, P. *et al.* A DNA methyltransferase modulator inspired by peyssonenyne natural product structures. *ChemMedChem* **7**, 2101–2112 (2012).

103. Sugimoto, K. *et al.* Protecting-group-free total synthesis of (-)-rhazinilam and (-)-rhazinicine using a gold-catalyzed cascade cyclization. *Angew. Chem. Int. Ed. Engl.* **52**, 7168–7171 (2013).
104. Papahatjis, D. P., Nahmias, V. R., Nikas, S. P., Schimpfen, M. & Makriyannis, A. Design and synthesis of (13S)-methyl-substituted arachidonic acid analogues: templates for novel endocannabinoids. *Chemistry* **16**, 4091–4099 (2010).
105. Reyes, S., Huigens, R. W., Su, Z., Simon, M. L. & Melander, C. Synthesis and biological activity of 2-aminoimidazole triazoles accessed by Suzuki-Miyaura cross-coupling. *Org. Biomol. Chem.* **9**, 3041–3049 (2011).
106. Almena, M. & Mérida, I. Shaping up the membrane: diacylglycerol coordinates spatial orientation of signaling. *Trends Biochem. Sci.* **36**, 593–603 (2011).
107. Brose, N. & Rosenmund, C. Move over protein kinase C, you've got company: alternative cellular effectors of diacylglycerol and phorbol esters. *J. Cell Sci.* **115**, 4399–4411 (2002).
108. Newton, A. C. Protein Kinase C : Structure , Function , and Regulation. *J. Biol. Chem.* **270**, 28495–28498 (1995).
109. Pessin, M. S. & Raben, D. M. Molecular species analysis of 1,2-diglycerides stimulated by alpha-thrombin in cultured fibroblasts. *J. Biol. Chem.* **264**, 8729–8738 (1989).
110. Marignani, P. A., Epand, R. M. & Sebaldt, R. J. Acyl Chain Dependence of Diacylglycerol Activation of Protein Kinase C Activity in Vitro. *Biochem. Biophys. Res. Commun.* **473**, 469–473 (1996).
111. Hofmann, T. *et al.* Direct activation of human TRPC6 and TRPC3 channels by diacylglycerol. *Nature* **397**, 259–263 (1999).
112. Das, J. & Rahman, G. M. C1 Domains : Structure and Ligand-Binding Properties. *Chem. Rev.* **114**, 12108–12131 (2014).
113. Coussens, L. *et al.* Multiple, distinct forms of bovine and human protein kinase C suggest diversity in cellular signaling pathways. *Science* **233**, 859–866 (1986).

-
114. Rhee, J. S. *et al.* β phorbol ester- and diacylglycerol-induced augmentation of transmitter release is mediated by Munc13s and not by PKCs. *Cell* **108**, 121–133 (2002).
115. Wender, P. *et al.* Modeling of the bryostatins to the phorbol ester pharmacophore on protein kinase C. *Proc. Natl. Acad. Sci. U. S. A.* **85**, 7197–7201 (1988).
116. Nadler, A. *et al.* The fatty acid composition of diacylglycerols determines local signaling patterns. *Angew. Chem. Int. Ed. Engl.* **52**, 6330–6334 (2013).
117. Putyrski, M. & Schultz, C. Protein translocation as a tool: The current rapamycin story. *FEBS Lett.* **586**, 2097–2105 (2012).
118. Feng, S. *et al.* A rapidly reversible chemical dimerizer system to study lipid signaling in living cells. *Angew. Chemie - Int. Ed.* **53**, 6720–6723 (2014).
119. Davis, R. J., Ganongq, B. R., Bell, R. M. & Czech, M. P. 1,2-Dioctanoylglycerol. *J. Biol. Chem.* **260**, 1562–1566 (1985).
120. Oancea, E., Teruel, M. N., Quest, A. F. G. & Meyer, T. Green fluorescent protein (GFP)-tagged cysteine-rich domains from protein kinase C as fluorescent indicators for diacylglycerol signaling in living cells. *J. Cell Biol.* **140**, 485–498 (1998).
121. Wuttke, A., Idevall-Hagren, O. & Tengholm, A. P2Y1 receptor-dependent diacylglycerol signaling microdomains in beta cells promote insulin secretion. *FASEB J.* **27**, 1610–1620 (2013).
122. Nadler, A. *et al.* Exclusive photorelease of signalling lipids at the plasma membrane. *Nat. Commun.* **6**, 10056 (2015).
123. Zhao, Y. *et al.* An Expanded Palette of Genetically Encoded Ca^{2+} Indicators. *Science* **557**, 1888–1891 (2011).
124. Plenge-Tellechea, F. & Soler, F. On the inhibition mechanism of sarcoplasmic or endoplasmic reticulum Ca^{2+} -ATPases by cyclopiazonic acid. *J. Biol. Chem.* **272**, 2794–2800 (1997).

125. Corbalán-García, S. & Gómez-Fernández, J. C. Protein kinase C regulatory domains: The art of decoding many different signals in membranes. *Biochim. Biophys. Acta - Mol. Cell Biol. Lipids* **1761**, 633–654 (2006).
126. Kikkawa, U., Matsuzaki, H. & Yamamoto, T. Protein kinase C delta (PKC delta): activation mechanisms and functions. *J. Biochem.* **132**, 831–839 (2002).
127. Reither, G., Schaefer, M. & Lipp, P. PKCalpha: A versatile key for decoding the cellular calcium toolkit. *J. Cell Biol.* **174**, 521–533 (2006).
128. Violin, J. D. & Newton, A. C. Pathway illuminated: visualizing protein kinase C signaling. *IUBMB Life* **55**, 653–660 (2003).
129. Violin, J. D., Zhang, J., Tsien, R. Y. & Newton, A. C. A genetically encoded fluorescent reporter reveals oscillatory phosphorylation by protein kinase C. *J. Cell Biol.* **161**, 899–909 (2003).
130. Toullec, D. *et al.* The Bisindolemaleimide GF 109203X is a Potent and Selective Inhibitor of Protein Kinase C. *J. Biol. Chem.* **266**, 15771–15781 (1991).
131. Herbert, J. M., Augereau, J. M., Gleye, J. & Maffrand, J. P. Chelerythrine is a potent and specific inhibitor of protein kinase C. *Biochem. Biophys. Res. Commun.* **172**, 993–999 (1990).
132. Bergsten, P., Grapengiesser, E., Gylfe, E., Tengholm, A. & Hellman, B. Synchronous oscillations of cytoplasmic Ca²⁺ and insulin release in glucose-stimulated pancreatic islets. *J. Biol. Chem.* **269**, 8749–8753 (1994).
133. Yang, C. & Kazanietz, M. G. Divergence and complexities in DAG signaling: Looking beyond PKC. *Trends Pharmacol. Sci.* **24**, 602–608 (2003).
134. Kurohane Kaneko, Y. *et al.* Depression of Type I Diacylglycerol Kinases in Pancreatic β-Cells From Male Mice Results in Impaired Insulin Secretion. *Endocrinology* **154**, 4089–4098 (2013).
135. Ashcroft, F. M. *et al.* Stimulus-secretion coupling in pancreatic beta cells. *J Cell Biochem* **55S**, 54–65 (1994).

-
136. Jacobson, D. A., Weber, C. R., Bao, S., Turk, J. & Philipson, L. H. Modulation of the Pancreatic Islet beta Cell delayed Rectifier Potassium Channel $K_v2.1$ by the Polyunsaturated Fatty arachidonate. *J. Biol. Chem.* **282**, 7442–7449 (2007).
137. Rutter, G. A. & Hodson, D. J. Beta cell connectivity in pancreatic islets: A type 2 diabetes target? *Cell. Mol. Life Sci.* **72**, 453–467 (2015).
138. Lou, X., Korogod, N., Brose, N. & Schneggenburger, R. Phorbol esters modulate spontaneous and Ca^{2+} -evoked transmitter release via acting on both Munc13 and protein kinase C. *J. Neurosci.* **28**, 8257–8267 (2008).
139. Brose, N., Betz, A. & Wegmeyer, H. Divergent and convergent signaling by the diacylglycerol second messenger pathway in mammals. *Curr. Opin. Neurobiol.* **14**, 328–340 (2004).
140. Basu, J., Betz, A., Brose, N. & Rosenmund, C. Munc13-1 C1 domain activation lowers the energy barrier for synaptic vesicle fusion. *J. Neurosci.* **27**, 1200–1210 (2007).
141. Wierda, K. D. B., Toonen, R. F. G., de Wit, H., Brussaard, A. B. & Verhage, M. Interdependence of PKC-Dependent and PKC-Independent Pathways for Presynaptic Plasticity. *Neuron* **54**, 275–290 (2007).
142. Betz, A. *et al.* Munc13-1 is a presynaptic phorbol ester receptor that enhances neurotransmitter release. *Neuron* **21**, 123–136 (1998).
143. Brose, N., Hofmann, K., Hata, Y. & Sudhof, T. C. Mammalian homologues of *Caenorhabditis elegans* unc-13 gene define novel family of C2-domain proteins. *J. Biol. Chem.* **270**, 25273–25280 (1995).
144. Varoqueaux, F. *et al.* Total arrest of spontaneous and evoked synaptic transmission but normal synaptogenesis in the absence of Munc13-mediated vesicle priming. *Proc. Natl. Acad. Sci.* **99**, 9037–9042 (2002).
145. Bargmann, C. I. & Kaplan, J. M. Signal transduction in the *Caenorhabditis elegans* nervous system. *Annu. Rev. Neurosci.* **21**, 279–308 (1998).
146. Rand, J. B. Acetylcholine. *WormBook*, ed *The C. elegans Research Community* (2007). doi:10.1895/wormbook.1.131.1.

147. Mahoney, T. R., Luo, S. & Nonet, M. L. Analysis of synaptic transmission in *Caenorhabditis elegans* using an aldicarb-sensitivity assay. *Nat. Protoc.* **1**, 1772–1777 (2006).
148. Fleming, J. T. *et al.* *Caenorhabditis elegans* levamisole resistance genes *lev-1*, *unc-29*, and *unc-38* encode functional nicotinic acetylcholine receptor subunits. *J. Neurosci.* **17**, 5843–5857 (1997).
149. Lewis, J. A., Wu, C.-H., Berg, H. & Levine, J. H. The genetics of levamisole resistance in the nematode *Caenorhabditis elegans*. *Genetics* **95**, 905–928 (1980).
150. Fliegl, H., Koehn, A., Haettig, C. & Ahlrichs, R. Ab Initio Calculation of the Vibrational and Electronic Spectra of trans- and cis-Azobenzene. *J. Am. Chem. Soc.* **125**, 9821–9827 (2003).
151. Nolan, C. J., Madiraju, M. S. R., Delghingaro-Augusto, V., Peyot, M.-L. & Prentki, M. Fatty Acid Signaling in the beta-Cell and Insulin Secretion. *Diabetes* **55**, S16–S23 (2006).
152. Hui, X., Reither, G., Kaestner, L. & Lipp, P. Targeted Activation of Conventional and Novel Protein Kinases C through Differential Translocation Patterns. *Mol Cell Biol* **34**, 2370–2381 (2014).
153. Ishihara, H. *et al.* Pancreatic beta cell line MIN6 exhibits characteristics of glucose metabolism and glucose-stimulated insulin secretion similar to those of normal islets. *Diabetologia* **36**, 1139–1145 (1993).
154. Ravier, Magalie, A. & Rutter, Guy, A. in *Mouse Cell Culture* **633**, 171–184 (2010).
155. Ravier, M. A. & Rutter, G. A. Glucose or Insulin, but not Zinc Ions, Inhibit Glucagon Secretion From Mouse Pancreatic alpha-cells. *Diabetes* **54**, 1789–1797 (2005).
156. Dadi, P. K. *et al.* Inhibition of Pancreatic beta-Cell Ca²⁺/Calmodulin-dependent Protein Kinase II Reduces Glucose-stimulated Calcium Influx and Insulin Secretion, Impairing Glucose Tolerance. *J. Biol. Chem.* **289**, 12435–12445 (2014).
157. Bungalossi, A. *et al.* Analysis of neurotransmitter release mechanisms by photolysis of caged Ca²⁺ in an autaptic neuron culture system. *Nat. Protoc.* **7**, 1351–1365 (2012).

-
158. Brenner, S. The genetics of *Caenorhabditis elegans*. *Genetics* **77**, 71–94 (1974).
159. Gaffney, P. R. J. & Reese, C. B. Preparation of 2-O-Arachidonoyl-1-O-stearoyl-*sn*-glycerol and Other Di-O-Acyl Glycerol Derivatives. *Tetrahedron* **38**, 2539–2542 (1997).
160. Chen, C.-Y., Han, W.-B., Chen, H.-J., Wu, Y. & Gao, P. Optically Active Monoacylglycerols: Synthesis and Assessment of Purity. *European J. Org. Chem.* **2013**, 4311–4318 (2013).
161. Working, E. B. The structure of the phospholipids. *Chem. Rev.* **29**, 245–256 (1941).
162. Hishikawa, D., Hashidate, T., Shimizu, T. & Shindou, H. Diversity and function of membrane glycerophospholipids generated by the remodeling pathway in mammalian cells. *J. Lipid Res.* **55**, 799–808 (2014).
163. White, S. H., Ladokhin, A. S., Jayasinghe, S. & Hristova, K. How Membranes Shape Protein Structure. *J. Biol. Chem.* **276**, 32395–32399 (2001).
164. Bogdanov, M., Dowhan, W. & Vitrac, H. Lipids and Topological Rules Governing Membrane Protein Assembly. *Biochem. Biophys. Acta* **1843**, 1475–1488 (2014).
165. Paolo, G. Di & Camilli, P. D. Phosphoinositides in cell regulation and membrane dynamics. *Nat. Rev.* **443**, 651–657 (2006).
166. Hammond, G. R. V *et al.* PI4P and PI(4,5)P₂ are Essential but Independent Lipid Determinants of Membrane Identity. *Science*. **337**, 727–730 (2012).
167. Lemmon, M. A. Membrane recognition by phospholipid-binding domains. *Nat. Rev. Mol. Cell Biol.* **9**, 99–111 (2008).
168. Ufret-Vincenty, C., Klein, R. M., Hua, L., Angueyra, J. & Gordon, S. E. Localization of the PIP₂ sensor of TRPV1 ion channels. *J. Biol. Chem.* **286**, 9688–9698 (2011).
169. Soom, M. *et al.* Multiple PIP₂ binding sites in Kir2.1 inwardly rectifying potassium channels. *FEBS Lett.* **490**, 49–53 (2001).
170. Extons, H. Signaling Through Phosphatidylcholine Breakdown. *J. Biol. Chem.* **265**, 1–4 (1990).

171. Hokin, L. E. Receptors and phosphoinositide-generated second messengers. *Annu. Rev. Biochem.* **54**, 205–235 (1985).
172. Brauchi, S. *et al.* Dissection of the components for PIP₂ activation and thermosensation in TRP channels. *Proc. Natl. Acad. Sci. U. S. A.* **104**, 10246–10251 (2007).
173. Prescott, E. D. & Julius, D. A Modular PIP₂ Binding Site as a Determinant of Capsaicin Receptor Sensitivity. *Science.* **1284**, 1284–1288 (2014).
174. Jiang, Y.-Q., Sun, Q., Tu, H.-Y. & Wan, Y. Characteristics of HCN channels and their participation in neuropathic pain. *Neurochem. Res.* **33**, 1979–1989 (2008).
175. Czech, M. P. PIP₂ and PIP₃: Complex Roles at the Cell Surface. *Cell* **100**, 603–606 (2000).
176. Nishizuka, Y. Intracellular Signaling by Hydrolysis of Phospholipids and Activation of Protein Kinase C. *Science* **258**, 607–614 (1992).
177. Mentel, M., Laketa, V., Subramanian, D., Gillandt, H. & Schultz, C. Photoactivatable and Cell-Membrane-Permeable Phosphatidylinositol. *Angew. Chemie - Int. Ed.* **50**, 3811–3814 (2011).
178. Monteiro, D. *et al.* Phosphoinositides and phosphatidic acid regulate pollen tube growth and reorientation through modulation of [Ca²⁺] and membrane secretion. *J. Exp. Bot.* **56**, 1665–1674 (2005).
179. Cells, F. *et al.* Release of Gelatinase A (Matrix Metalloproteinase 2) Induced by Photolysis of Caged Phosphatidic Acid in HT1080 Metastatic Fibrosarcoma Cells. *J. Biol. Chem.* **270**, 29656–29659 (1995).
180. Hoevelmann, F. *et al.* Optotaxis: Caged Lysophosphatidic Acid Enables Optical Control of a Chemotactic Gradient. *Cell Chem. Biol.* **23**, 1–6 (2016).
181. Dinkel, C., Wichmann, O. & Schultz, C. Versatile reagents to introduce caged phosphates. *Tetrahedron Lett.* **44**, 1153–1155 (2003).

182. Sandhu, S. S. *et al.* The formation and Langmuir-Blodgett deposition of monolayers of novel photochromic azobenzene-containing phospholipid molecules. *BBA - Biomembr.* **860**, 253–262 (1986).
183. Meves, H. Arachidonic acid and ion channels : an update. *Br. J. Pharmacol.* **155**, 4–16 (2008).
184. Salem, N., Litman, B., Kim, H. & Gawrisch, K. Mechanisms of Action of Docosahexaenoic Acid in the Nervous System. *Lipids* **36**, 945–959 (2001).
185. Milligan, G., Shimpukade, B., Ulven, T. & Hudson, B. D. Complex Pharmacology of Free Fatty Acid Receptors. *Chem. Rev.* online (2016).
186. Boland, L. M. & Drzewiecki, M. M. Polyunsaturated Fatty Acid Modulation of Voltage-Gated Ion Channels. *Cell Biochem. Biophys.* **52**, 59–84 (2008).
187. Itoh, Y., Kawamata, Y. & Harada, M. Free fatty acids regulate insulin secretion from pancreatic beta cells through GPR40. *Nature* **422**, 173–176 (2003).
188. Shapiro, H., Shachar, S., Sekler, I., Hershfinkel, M. & Walker, M. D. Role of GPR40 in fatty acid action on the beta cell line INS-1E. *Biochem. Biophys. Res. Commun.* **335**, 97–104 (2005).
189. Schnell, S., Schaefer, M. & Sch, C. Free fatty acids increase cytosolic free calcium and stimulate insulin secretion from beta-cells through activation of GPR40. *Mol. Cell. Endocrinol.* **263**, 173–180 (2007).
190. Meves, H. Modulation of ion channels by arachidonic acid. *Prog. Neurobiol.* **43**, 175–186 (1994).
191. Hamilton, K. L., Syme, C. A. & Devor, D. C. Molecular Localization of the Inhibitory Arachidonic Acid Binding Site to the Pore of hIK1. *J. Biol. Chem.* **278**, 16690–16697 (2003).
192. Rorsman, P. & Braun, M. Regulation of Insulin Secretion in Human Pancreatic Islets. *Annu. Rev. Physiol.* **75**, 155–179 (2012).
193. Stein, D. T. *et al.* Essentiality of Circulating Fatty Acids for Glucose-stimulated Insulin Secretion in the Fasted Rat. *J. Clin. Invest.* **97**, 2728–2735 (1996).

194. Zhao, Y. *et al.* GW9508 inhibits insulin secretion by activating ATP-sensitive potassium channels in rat pancreatic b-cells. *J. Mol. Endocrinol.* **51**, 69–77 (2013).
195. Briscoe, C. P. *et al.* Pharmacological regulation of insulin secretion in MIN6 cells through the fatty acid receptor GPR40: identification of agonist and antagonist small molecules. *Br. J. Pharmacol.* **148**, 619–628 (2006).
196. Yabuki, C. *et al.* A Novel Antidiabetic Drug , Fasiglifam/TAK-875, Acts as an Allosteric Modulator of FFAR1. *PLoS One* **8**, 2–11 (2013).
197. Negoro, N. *et al.* Discovery of TAK-875: A Potent, Selective, and Orally Bioavailable GPR40 Agonist. *ACS Med. Chem. Lett.* **1**, 290–294 (2010).
198. Feng, X. *et al.* GPR40: A therapeutic target for mediating insulin secretion (Review). *Int. J. Mol. Med.* **30**, 1261–1266 (2012).
199. Hara, T., Hirasawa, A., Ichimura, A., Kimura, I. & Tsujimoto, G. Free Fatty Acid Receptors FFAR1 and GPR120 as Novel Therapeutic Targets for Metabolic Disorders. *J. Pharm. Sci.* **100**, 3594–3601 (2011).
200. Rutter, G. A. Nutrient–secretion coupling in the pancreatic islet beta-cell: recent advances. *Mol. Aspects Med.* **22**, 247–284 (2001).
201. Kaku, K., Enya, K., Nakaya, R., Ohira, T. & Matsuno, R. Efficacy and safety of fasiglifam (TAK-975), a G-protein-coupled receptor 40 agonist, in Japanese patients with type 2 diabetes inadequately controlled by diet and exercise: a randomized, double-blind, placebo-controlled, phase III trial. *Diabetes, Obes. Metab.* **7**, 675–681 (2015).
202. Ou, H. *et al.* Multiple mechanisms of GW-9508 , a selective G protein-coupled receptor 40 agonist, in the regulation of glucose homeostasis and insulin sensitivity. *Am J Physiol Endocrinol Metab* **67**, 668–676 (2013).
203. Rendell, M. The Role of Sulphonylureas in the Management of Type 2 Diabetes Mellitus. *Drugs* **64**, 1339–1358 (2004).
204. Broichhagen, J. *et al.* A red-shifted photochromic sulfonylurea for the remote control of pancreatic beta cell function. *Chem. Commun.* **51**, 6018–6021 (2015).

-
205. Broichhagen, J. *et al.* Optical control of insulin release using a photoswitchable sulfonylurea. *Nat. Commun.* **5**, 6116 (2014).
206. Johnston, N. R. *et al.* Beta Cell Hubs Dictate Pancreatic Islet Responses to Glucose. *Cell Metab.* **24**, 389–401 (2016).
207. Broichhagen, J. *et al.* Allosteric Optical Control of a Class B G-Protein-Coupled Receptor. *Angew. Chemie - Int. Ed.* **55**, 5865–5868 (2016).
208. Broichhagen, J. *et al.* Optical Control of Insulin Secretion Using an Incretin Switch. *Angew. Chemie - Int. Ed.* **54**, 15565–15569 (2015).
209. Xu, X. & Lee, K. A. I. S. Dual effects of arachidonic acid on ATP-sensitive K⁺ current of coronary smooth muscle cells. *Am. J. Physiol.* **270**, H1957–H1962 (1996).
210. Simons, K. & Ikonen, E. Functional rafts in cell membranes. *Nature* **387**, 569–572 (1997).
211. Rimmerman, N. *et al.* Compartmentalization of endocannabinoids into lipid rafts in a microglial cell line devoid of caveolin-1. *Br. J. Pharmacol.* **165**, 2436–2449 (2012).
212. Simons, K. & van Meer, G. Lipid sorting in epithelial cells. *Biochemistry* **27**, 6197–6202 (1988).
213. Brown, D. A. & London, E. Functions of lipid rafts in biological membranes. *Annu. Rev. Cell Dev. Biol.* **14**, 111–136 (1998).
214. Eggeling, C. *et al.* Direct observation of the nanoscale dynamics of membrane lipids in a living cell. *Nature* **457**, 1159–1162 (2009).
215. Brown, D. A. & London, E. Structure and function of sphingolipid- and cholesterol-rich membrane rafts. *J. Biol. Chem.* **275**, 17221–17224 (2000).
216. van Blitterswijk, W. J., van der Luit, A. H., Veldman, R. J., Verheij, M. & Borst, J. Ceramide: second messenger or modulator of membrane structure and dynamics? *Biochem. J.* **369**, 199–211 (2003).
217. Castro, B. M., Prieto, M. & Silva, L. C. Ceramide: A simple sphingolipid with unique biophysical properties. *Prog. Lipid Res.* **54**, 53–67 (2014).

218. Goni, F. M. & Alonso, A. Biophysics of sphingolipids I. Membrane properties of sphingosine, ceramides and other simple sphingolipids. *Biochim. Biophys. Acta* **1758**, 1902–1921 (2006).
219. Cremesti, A. E., Goni, F. M. & Kolesnick, R. Role of sphingomyelinase and ceramide in modulating rafts: Do biophysical properties determine biologic outcome? *FEBS Lett.* **531**, 47–53 (2002).
220. Zou, S. & Johnston, L. J. Ceramide-enriched microdomains in planar membranes. *Curr. Opin. Colloid Interface Sci.* **15**, 489–498 (2010).
221. Johnston, I. & Johnston, L. J. Ceramide promotes restructuring of model raft membranes. *Langmuir* **22**, 11284–11289 (2006).
222. Obeid, L., Linardic, C., Karolak, L. & Hannun, Y. Programmed cell death induced by ceramide. *Science* **259**, 1769–1771 (1993).
223. Schmuth, M. *et al.* Permeability barrier disorder in Niemann-Pick disease: Sphingomyelin-ceramide processing required for normal barrier homeostasis. *J. Invest. Dermatol.* **115**, 459–466 (2000).
224. Levade, T. & Jaffrézou, J.-P. Signalling sphingomyelinases: which, where, how and why? *Biochim. Biophys. Acta - Mol. Cell Biol. Lipids* **1438**, 1–17 (1999).
225. Holopainen, J. M., Lehtonen, J. Y. A. & Kinnunen, P. K. J. Lipid microdomains in dimyristoylphosphatidylcholine - Ceramide liposomes. *Chem. Phys. Lipids* **88**, 1–13 (1997).
226. Holopainen, J. M., Subramanian, M. & Kinnunen, P. K. J. Sphingomyelinase induces lipid microdomain formation in a fluid phosphatidylcholine/sphingomyelin membrane. *Biochemistry* **37**, 17562–17570 (1998).
227. Pinto, S. N., Silva, L. C., Futerman, A. H. & Prieto, M. Effect of ceramide structure on membrane biophysical properties: The role of acyl chain length and unsaturation. *Biochim. Biophys. Acta - Biomembr.* **1808**, 2753–2760 (2011).
228. Trajkovic, K. *et al.* Ceramide triggers budding of exosome vesicles into multivesicular endosomes. *Science* **319**, 1244–1247 (2008).

-
229. Megha, Sawatzki, P., Kolter, T., Bittman, R. & London, E. Effect of ceramide *N*-acyl chain and polar headgroup structure on the properties of ordered lipid domains (lipid rafts). *Biochim. Biophys. Acta - Biomembr.* **1768**, 2205–2212 (2007).
230. Edidin, M. The state of lipid rafts: from model membranes to cells. *Annu. Rev. Biophys. Biomol. Struct.* **32**, 257–283 (2003).
231. Shigenaga, A. *et al.* Design and synthesis of caged ceramide: UV-responsive ceramide releasing system based on UV-induced amide bond cleavage followed by *O-N* acyl transfer. *Tetrahedron* **67**, 3984–3990 (2011).
232. Kim, Y. A., Ramirez, D. M. C., Costain, W. J., Johnston, L. J. & Bittman, R. A new tool to assess ceramide bioactivity: 6-bromo-7-hydroxycoumarinyl-caged ceramide. *Chem. Commun.* **47**, 9236–9238 (2011).
233. Chiantia, S. *et al.* Role of ceramide in membrane protein organization investigated by combined AFM and FCS. *Biochim. Biophys. Acta - Biomembr.* **1778**, 1356–1364 (2008).
234. Chiantia, S., Kahya, N. & Schwille, P. Raft domain reorganization driven by short- and long-chain ceramide: A combined AFM and FCS study. *Langmuir* **23**, 7659–7665 (2007).
235. Giocondi, M. *et al.* Surface topography of membrane domains. *Biochem. Biophys. Acta* **1798**, 703–718 (2010).
236. Alessandrini, A. & Facci, P. Phase transitions in supported lipid bilayers studied by AFM. *Soft Matter* **10**, 7145–7164 (2014).
237. Chiantia, S., Kahya, N., Ries, J. & Schwille, P. Effects of ceramide on liquid-ordered domains investigated by simultaneous AFM and FCS. *Biophys. J.* **90**, 4500–4508 (2006).
238. Castro, B. M., Silva, L. C., Fedorov, A., de Almeida, R. F. M. & Prieto, M. Cholesterol-rich fluid membranes solubilize ceramide domains: Implications for the structure and dynamics of mammalian intracellular and plasma membranes. *J. Biol. Chem.* **284**, 22978–22987 (2009).

239. Castro, B. M., de Almeida, R. F. M., Silva, L. C., Fedorov, A. & Prieto, M. Formation of ceramide/sphingomyelin gel domains in the presence of an unsaturated phospholipid: a quantitative multiprobe approach. *Biophys. J.* **93**, 1639–1650 (2007).
240. Goñi, F. M. & Alonso, A. Effects of ceramide and other simple sphingolipids on membrane lateral structure. *Biochem. Biophys. Acta* **1788**, 169–177 (2009).
241. Pinto, S. N., Silva, L. C., de Almeida, R. F. M. & Prieto, M. Membrane domain formation, interdigitation, and morphological alterations induced by the very long chain asymmetric C24:1 ceramide. *Biophys. J.* **95**, 2867–2879 (2008).